rijksuniversiteit
groningen

Advanced Receivers for Submillimeter and Far Infrared Astronomy

Proefschrift

ter verkrijging van het doctoraat in de
Wiskunde en Natuurwetenschappen
aan de Rijksuniversiteit Groningen
op gezag van de
Rector Magnificus, dr. F. Zwarts,
in het openbaar te verdedigen op
maandag 22 december 2008
om 16:15 uur

door

Jacob Willem Kooi

geboren op 12 juli 1960
te Geldrop

Promotores:	Prof. dr. W. Wild Prof. dr. ir. T.M. Klapwijk
Beoordelingscommissie:	Prof. dr. R. F. Peletier Prof. dr. M. W. M. de Graauw Prof. dr. V. Belitsky

ISBN 978-90-367-3653-4

To my wife Helen

and my two sons

David and Andreas

Cover Front: *Caltech Submillimeter Observatory on top of Mauna Kea, Hawaii. Photograph was taken by the author during full moon on October 12, 2006, at 3 o'clock in the morning. Exposure time was 61s, f/5.6, and ISO 200 sensitivity. Projected in the foreground is a high altitude balloon heading for the stratosphere to carry out atmospheric and astrophysical observations.*

– Back: *The Herschel space observatory pointed at star forming regions in M33 (the pinwheel galaxy) in the constellation Triangulum. The distance from our "own" galaxy, the Milky Way, to M33 is approximately 3 million lights years. To avoid attenuation from water in the Earth atmosphere, follow up astrophysical observations may eventually be carried out by aircraft such as Sofia, at low precipitable water vapor sites in Antarctica, the Atacama desert in Chile (not shown), Mauna Kea in Hawaii, and by future space missions.*

Printed by: PrintPartners Ipskamp B.V., Enschede, The Netherlands.

Contents

Chapter 1

Introduction

1.1 Submillimeter and far-infrared astronomy

Modern astronomy started when Galileo Galilei in 1610 pointed a small telescope towards the heavens. It nearly cost him his life and changed the world. Since then we have become aware that most of the light in the universe resides in the infrared and submillimeter region of the electromagnetic spectrum (1 μm – 1 mm). One of the reasons for this is that at large, the universe is a cold and forbidding place. Its low temperature causes the prevalent dust and molecular gas in galaxies, including our own Milky Way, to exhibit an emission peak in the far-infrared and submillimeter wavelength regimes.

The other reason has to do with the expansion of the universe. In the late 1920s Edwin Hubble (California Institute of Technology) made the important cosmological discovery that spectral lines of galaxies are shifted toward the longer wavelength end (red part) of the electro-magnetic spectrum in an amount proportional to their distances. The explanation of this apparent redshift lies with the Doppler effect, which suggests that galaxies move away from each other with velocities proportional to their distance. This has since become known as the "The Hubble law" and implies that the universe is expanding on the whole. Then in 1965 another great cosmological discovery was made by Arno Penzias and Robert Wilson (Nobel Prize 1978), at Bell labs at the time. They discovered that there is a universal microwave radiation, with a spectrum that corresponds to a ~ 3 K blackbody. This has since been confirmed in exquisite detail by COBE [1], NASA's cosmic background explorer mission, designed to measure the diffuse infrared and microwave radiation of the early universe. It was found that the cosmic microwave background (CMB) spectrum is that of a nearly perfect blackbody with a temperature of 2.725 ± 0.002 K (PI: John Mather, Nobel Prize 2006). The success of COBE has been followed up by the Wilkinson Microwave Anisotropy Probe (WMAP) [2], another NASA explorer mission, and soon also with the launch of the European Space Agency (ESA) satellite Planck [3]. Planck has more than fifty times the angular resolution of COBE, and at least ten times the sensitivity. It will, like WMAP, observe the anisotropies of the cosmic microwave background and

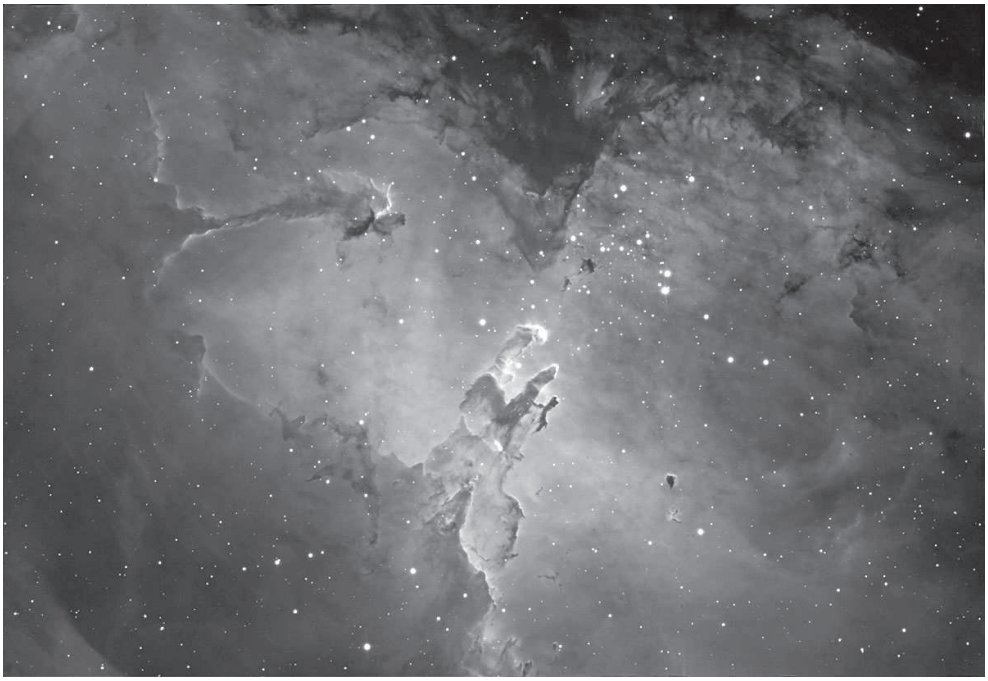

Figure 1.1: Optical image of M16, a young star cluster, surrounded by natal clouds of cosmic dust and glowing gas indicative of HII regions. The region is known as the Eagle Nebula. The dense, dusty columns rising near the center are light-years in length but are gravitationally contracting to form stars. Energetic radiation from the cluster stars erodes material near the tips, eventually exposing the embedded new stars. M16 and the Eagle Nebula lie approximately 7,000 light-years from Earth. Photo: Johannes Schedler (Panther Observatory).

help answer fundamental questions such as: Will the universe continue its expansion forever, what is the nature of the so-called "dark matter" that appears to count for more than 90 % of the total amount of matter in the universe, and furthermore what is "dark energy" in relation to the accelerated expansion of the universe at the earliest epoch of time?

And so we find the submillimeter and far-infrared an interesting wavelength regime (100 μm to 1 mm), one where continuum and line radiation from relatively cool diffuse material, such as interstellar and circumstellar dust and gas, is most abundant (Fig. 1.1). Black bodies with temperatures between 5- and 50 K peak here, and gasses with temperatures between 10 and $\sim$ 200 K emit their brightest molecular and atomic emission lines.

Broadband thermal radiation from dust grains is the most common continuum emission process in this wavelength range. It is also here that luminosities of a wide variety of astronomical sources obscured by interstellar or circumstellar material may be derived. This is because ultraviolet, visible, and near-infrared photons from stars are absorbed by the dust grains in the interstellar medium and re-emitted as a modified graybody spectrum in the far-infrared. And due to a very high optical extinction,

only a small amount of dust suffices to absorb the short-wavelength UV radiation. In this way galaxies, or even quasars, emit a significant fraction of their radiation in the far-infrared. The spectral energy density (SED) of the dust emission in the submillimeter and far-infrared thus provides quantitative information of the temperature distribution of dust particles, their composition, size and spatial distribution. And because submillimeter measurements are little effected by dust extinction, studies of the physical condition and energy balances of nuclear regions in dust enshrouded galaxies are greatly facilitated. As a final note, the submillimeter continuum optical depth provides a direct measure of large dust concentrations, such as are present in protostars, circumstellar disks, or in the large amounts of interstellar gas in galactic nuclei.

Knowledge of the submillimeter and far-infrared spectrum is therefore essential in our understanding of the many complex physical and chemical processes that take place in astrophysical objects. For example, the cooling of giant molecular clouds (GMCs) in star forming regions. It is in these cold and dense molecular clouds where young stars are born.

A striking aspect of submillimeter astronomy is that dust emission, molecular lines, and for example the atomic fine-structure line of C^+, which dominates the gas cooling, are all red shifted to the submillimeter band for distant galaxies. At a redshift of 2–4, galaxy formation in the early universe was most active. Thanks to the expanding universe therefore, lines and dust are seen to shift into the submillimeter band and will be detectable on the ground by large telescopes such as the CSO [4], APEX [5], and in the near future ALMA [6]. Even today Spitzer is surveying large areas of the sky for these early universe objects. Spectroscopic follow-up will be required to determine the physics of galaxy evolution.

It is thus seen that the submillimeter and far-infrared wavelength regimes are critical for astronomy. They contain spectral and spatial information on the early stages of star formation in giant molecular gas clouds, both in our own and external (distant) galaxies, and the cosmic background.

1.1.1 Interstellar medium

The interstellar medium (ISM) is a complex environment that harbors giant molecular clouds out of which stars – and planetary systems – form. Since the creation of the universe the neutral HI dominated medium is enriched by newly synthesized elements from dying stars that have run their course. This complex interplay between stars and the ISM drives the evolution and thus the observational characteristics of our local galaxy (Milky Way) and external galaxies all the way back to the earliest protogalaxies (Fig. 1.2).

Schematically the ISM can be represented by Fig. 1.3 (Walker *et al.*, 2007). The HII region is a heavily ionized and physically hot ($\sim$ 10,000 K) region in close proximity to young stellar objects (YSO). Profuse amounts of high energy far UV photons dominate these regions ionizing everything in their path. This includes atomic nitrogen, that with an ionization potential of 14.52 eV can only exist in the UV dominated HII regions in ionized N^+ form. Also present in the HII region is C^+ with an ionization potential of 11.26 eV.

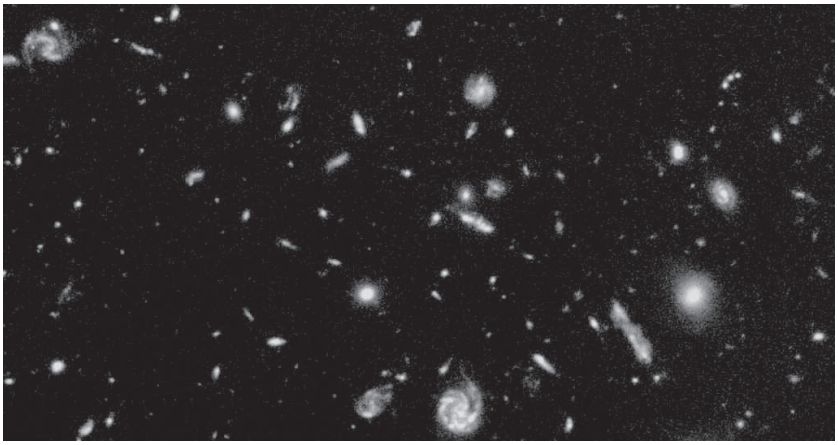

Figure 1.2: Optical image of the Hubble deep field. Shown is a bewildering assortment of galaxies, some of which are close to the beginning of the universe $\sim 13.73 \pm 0.12$ billion years ago. Dying stars in each of these galaxies enrich the local interstellar medium, thereby effecting the evolutionary cycle of galaxy formation including that of our own Milky Way. Photo credit: R. Williams (STScI).

The boundary region between the cooler molecular clouds and HII region is known as the photodissociated region (PDR). Here the overall UV photon energy still dominates the heat budget (6 eV $< h\nu <$ 13.6 eV) and modifies the chemical balance of the molecular cloud. Many of the molecular species (such as CO) are photodissociated and C^+ and C^0 become highly abundant at the expense of CO in this case. As depicted in Fig. 1.3, the interstellar medium has a variety of phases, from very diffuse regions of low hydrogen column density, to dense diffuse warm clouds, as well as photodissociated regions. Large scale shocks produced by supernovae or stars injecting

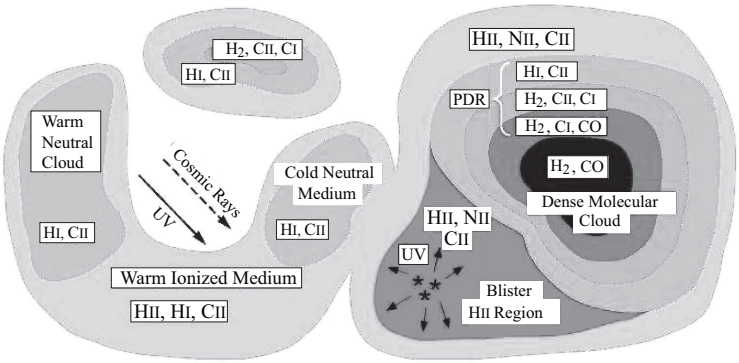

Figure 1.3: Schematic representation of the interstellar medium. The various regions with molecular and atomic content are indicated. The dense molecular cloud cools by means of the emission of photons with energies that correspond to the rotational line transitions of the molecules (C. K. Walker *et al.*, 2007).

matter (outflows) are not uncommon.

Again referring to Fig. 1.3, the neutral HI gas in the interstellar medium is driven via a thermal balance into two phases; the diffuse warm neutral medium (WNM) of $\sim$ 8000 K, and the diffuse cold neutral medium (CNM) at $\sim$ 70 K. Turbulence and shocks will naturally complicate the thermal equilibrium between the two regions. C^+ and neutral atomic hydrogen (HI can be observed with the forbidden hyperfine 21 cm, 1.42040575 GHz, transition) are both present in this neutral medium. In the presence of UV radiation, from say a nearby star, warm diffuse neutral clouds can be destroyed. The resulting ionized region contains in this case hydrogen, carbon and nitrogen ions. Thus we find that ionized carbon is high distributed among the different ISM regions, with N^+ isolated to the more heavily (warm) ionized regions. From this model we find that N^+ emission provides a measure of the ionizing radiation from young massive stars in the ISM. N^+ also has the advantage that it is unaffected by dust extinction. As such ionized nitrogen appears to be a good probe to identify star forming regions. The ratio of C^+/N^+ measures the rate of cloud destruction/formation.

Because molecular hydrogen (H_2) does not have accessible emission line spectra in the submillimeter and far-infrared (the nearest transition lines are in the UV) tracer elements such as C^0, CO, and C^+ are commonly used to study molecular clouds. Atomic carbon (C^0) can be found in all types of neutral clouds, from diffuse (Jenkins & Shaya 1979 [7]) to dense molecular gas (Phillips & Huggins 1981 [8]). C^+ has been seen extensively by COBE throughout the Milky Way and makes a significant contribution to the gas cooling, being so widely distributed (Bennett *et al.* 1994 [9]). Atomic carbon is also found to be a good tracer of molecular gas in molecular clouds. For example, their appears to be a linear correlation between the strength of the C^0 $^3P_1 \rightarrow {}^3P_0$ line at 492 GHz and the $^{13}CO_{J=2\rightarrow1}$ line at 220 GHz (Keene *et al.* 1997 [10]). Higher J CO transitions such as $^{12}CO_{J=7\rightarrow6}$ (807 GHz) trace the warm energetic gas component, whereas higher transitions of HCN and HCO^+ trace the density of the gas that is being warmed by star-formation in clouds and PDRs. Strong mid- and high J rotational line emission is also a signature of shocked gas in the molecular outflows of newly formed stars.

Although emission lines of C^0 and CO arise in principle from different physical regions in an ISM cloud, in actual observations of galactic clouds it is found that CI and CO emissions, on average, seem to come from the same physical region (Phillips *et al.* 2002). This appears to be due to the clumpy or fractal nature of the clouds which allows UV radiation to irradiate regions even deep into the cloud. For external galaxies where individual clouds are unresolved, the different carbon species, including C^+, will be observationally coexistent. In these way line ratios may be compared. It is essential therefore to have a good understanding of nearby galaxies in order to provide templates for more distant unresolved objects.

Aside from ionized carbon, water is also a very important molecule in interstellar chemistry (Tielens 2005) [11]. It can be a dominant reservoir of elemental oxygen in the gas phase, and because of its many levels, water is also an important coolant that can dominate the heat balance of a gas. To study and understand the role of water in the ISM, the high resolution Heterodyne Instrument (HIFI) [12] on Herschel [13], will have as its primary objective (it cannot be done from the ground) the study of a

wide range of H_2O transitions. A second, nearly equally important objective of HIFI, is to study the role of C^+ as the main cooling line in the interstellar medium.

Ionized carbon has a ground-state $^2P_{3/2} \rightarrow {}^2P_{1/2}$ CII atomic fine-structure transition at 158 μm (1.901 THz). The CI atomic carbon (C^0) fine-structure transition falls at 370 μm ($^3P_2 \rightarrow {}^3P_1 = 809$ GHz) and 609 μm ($^3P_1 \rightarrow {}^3P_0 = 492$ GHz). N^+ has two NII ground-state atomic fine-structure transition lines: $^3P_1 \rightarrow {}^3P_0$ at 205.178 μm (1.470 THz) and $^3P_2 \rightarrow {}^3P_1$ at 121.898 μm (2.459 THz). Each of these lines is very narrow (low pressure, low velocity) and high resolution spectroscopic observations are needed to spectrally resolve them. Much of this thesis is devoted to developing the technology that enables these observations.

1.1.2 Star formation

So far we have discussed the various phases of the interstellar medium, but have not yet touched in detail upon the subject of star formation. Stars are found to form in the dense and dusty molecular clouds of the interstellar medium (Figs. 1.1, 1.3). One of the physical properties of the ISM is in the way gas cooling processes allow clouds to collapse to form stars. In particular, cooling happens through line emission from rotationally excited H_2O, diatomic hydride molecules (H_2S, CH, HCl, CH+, NH, ...) and, as we have seen, CI and CII.

1.1.2.1 Molecular clouds

The atomic and isotopic abundances of the ISM provide information on the degree of star-formation activity a given area has suffered. A critical factor in the star-formation process is the cooling mechanism, since a cloud cannot collapse all the way to form a star unless it can purge itself of the heat from its compression under gravity. Such cooling is provided by a variety of molecular transitions in the submillimeter band, but mostly by CO, H_2O, light hydride molecular species, CI, and CII. The densities of interest in star formation, where molecules dominate, span the range from 10^2 cm^{-3} to $> 10^{12}$ cm^{-3}. Shocked regions from supernovae or outflows from young stellar objects (YSO) are likely to experience violent temperature and density increases, possible causing star formation.

The primary manifestation of star formation in the ISM is through molecular outflow. Many deeply embedded sources were first detected this way, and are known as young stellar objects (YSOs). They are surrounded by small 100 AU disk like regions. Complex line profiles may therefore be expected in shocked regions, showing evidence of turbulence, high velocity winds, and pressure broadening in the observed emission lines. To understand the complex interactions in the different regions of the ISM, to overcome spectral blending, line confusion, and to resolve velocities of the various clouds along the line of site, high resolution heterodyne spectroscopy is therefore required.

Since the temperatures in the cold dense molecular gas ranges from approximately 10 K in the cooler regions to 100 – 200 K in the hotter regions (Phillips & Keene 1992 [14]), the corresponding emission has a frequency range ($h\nu \sim k_B T$) of 0.2 – 4 THz. This is also the same range many molecular species have their rotation and

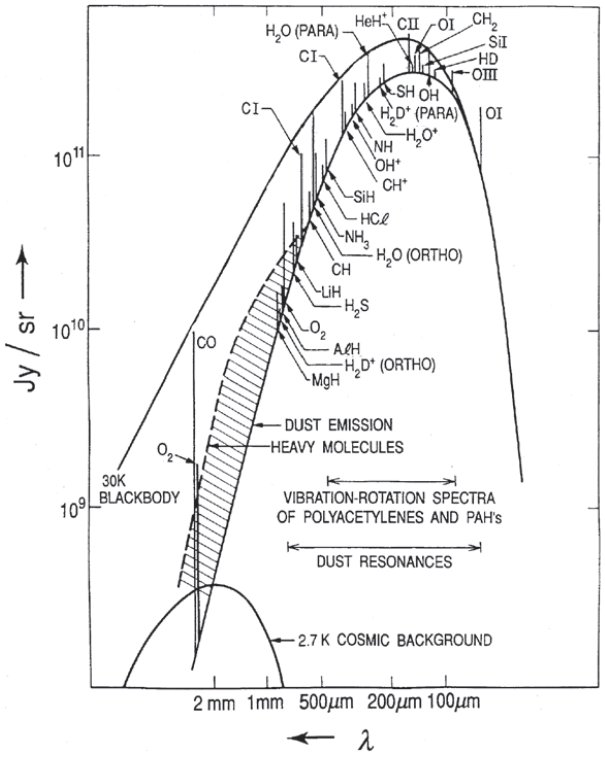

Figure 1.4: Schematic presentation of a 30 K interstellar molecular cloud. The spectrum includes dust continuum, molecular rotation- and atomic fine-structure line emissions (Phillips *et al.* [14]). The suite of lines forms an excellent tool to probe the molecular and ionized gas conditions after young stars disrupt their environment of birth.

atomic fine-structure transitions. In Fig. 1.4 we show a representation of a cloud with 30 K dust and gas temperatures. A blackbody curve bounds the emission with a Wien peak near the 1.9 THz ionized carbon transition. The dust in the cloud is optically thick and has a continuum emission on the blackbody curve. In the millimeter band (shaded areas) heavy molecules with carbon chemistry prevail. In the submillimeter band light molecules with low angular momentum and high rotation speeds dominate. In general the higher-J energy levels probe physically conditions of higher temperature, e.g. $^{12}CO_{J=7\rightarrow6}$ (807 GHz) vs. $^{12}CO_{J=2\rightarrow1}$ (230 GHz). CI and CO are observable in both warm (T>70 K) and cold (T< 20 K) neutral medium clouds, but CII is only observable in warm clouds, and therefore is not a good tracer in a cold cloud.

The many rotational molecular, atomic, and ionic fine-structure lines thus form an excellent probe of the physical and chemical conditions in the molecular cloud, of high velocity stellar winds, protostellar and planet forming regions, galactic nuclei, and galaxy evolution. Analysis of the obtained data provides information on the pressure, elemental and isotopic abundances, molecular inventory of photodissociated

regions, and a general understanding of the interstellar medium.

1.1.2.2 Spectral line surveys

As can be seen from Fig. 1.5, a line survey of the Orion (OMC-1) molecular cloud shows a forest of lines incredibly rich in chemical detail. Among the heavy molecules

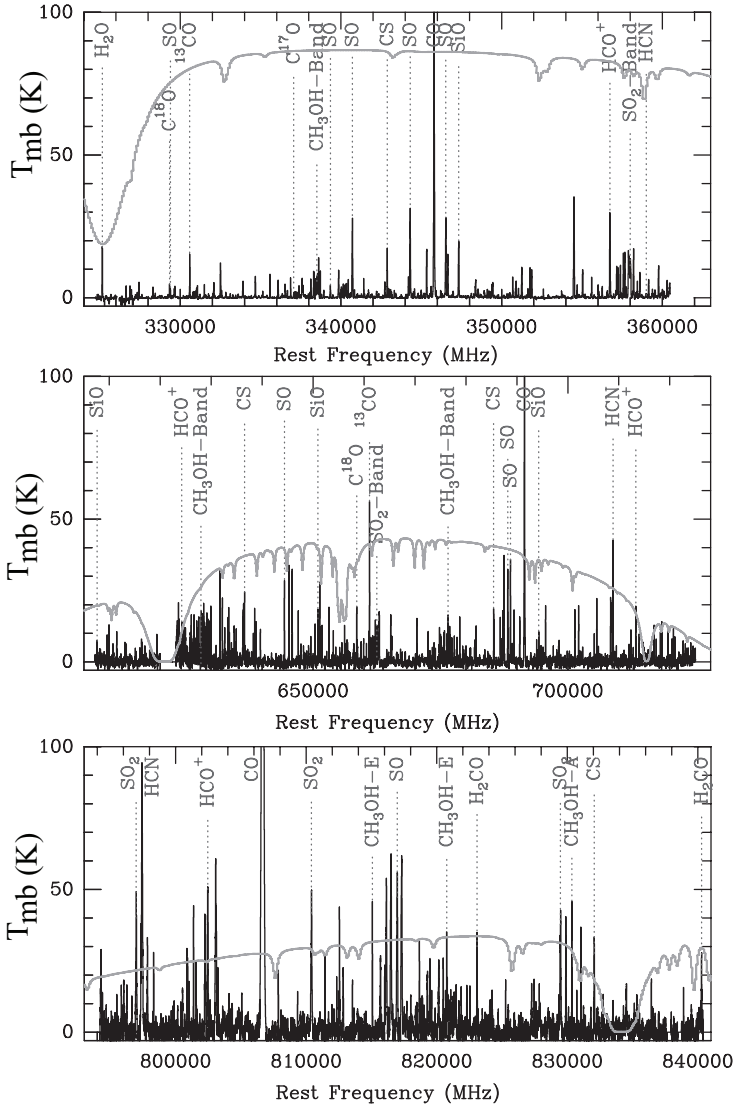

Figure 1.5: *Top*) The Caltech Submillimeter Observatory (CSO) 325 – 360 GHz survey by Schilke *et al.* (1997); *Middle*) CSO 600 – 720 GHz survey by Schilke *et al.* (2001); *Bottom*) CSO 794 – 840 GHz line survey by Mehringer *et al.* (2001). Spectra from E. van Dishoeck [15].

are also some simple light molecules. Surveys such as those shown in Fig. 1.5 thus provide an unbiased view of the molecular inventory of a wide range of objects. Moreover, the large number of lines of individual molecules presented in these spectra allow for a detailed study of the physical conditions in the emitting gas. For example, a spectral survey can tell us when lines are saturated. The line ratios can also provide important information on the temperature and local density, whereas the molecular abundance provides a measure of the evolutionary state of the object. In addition, the cooling rate of the gas can be estimated (CO, CI, H_2O). Surveys also address major questions in star-formation such as: How does the chemical composition depend on the mass and luminosity of an object (Dishoeck 2000 [15]). Measuring the molecular inventory in UV radiation fields, PDR shock regions, and molecular clouds will also aid our understanding of how stars and galaxies form, and why we are here.

The whole question of the gas phase chemistry of molecular clouds thus dependents on a good understanding of the physical conditions, which may be revealed by detailed studies of atomic species. Ground based survey data has provided a complex, yet comprehensive picture of the physical and chemical evolution of star-forming regions. Heterodyne spectroscopy is particular useful in this regard because it has the spectral resolution necessary to resolve the kinematic components of the gas clouds.

1.1.3 Galaxies

Studies of the ISM in our own galaxy, and observations made with large aperture telescopes toward nearby galaxies, can be used as templates for more distant galaxies at z=0.5–3 when galaxy formation was in full swing. The different phases of the ISM are discernable with large aperture telescopes for nearby galaxies in "our" local group, such as M31 (the Andromeda galaxy), M83 (spinwheel galaxy in Hydra), the LMC, SMC and others. Herschel [16] (by virtue of no atmosphere and high spatial resolution, $11.2''$ beam at the 1.901 GHz CII transition) will be especially well suited to study important carbon and water cooling lines. Thanks to the high spectral resolution provided by heterodyne receivers, deconvolution of the observed line profiles can be applied to disentangle the different sources of emission. This technique provides discrimination between the narrow, cold phase lines and the broader (more turbulent) lines from warm ionized gas.

For a long time, detection of extragalactic molecules was restricted to a few molecular species. Even though $\sim$ 30 molecules have been discovered outside the Milky Way, no extragalactic molecular line surveys have been completed. Such line surveys can however provide a detailed (and necessary) comparison of the chemical composition, isotopic abundances, and excitation conditions between extragalactic and galactic sources (Güsten *et al.* [17]). Key extragalactic questions to be addressed may be summarized as: Understanding of the evolution of galaxies, the nature of the interstellar medium, and the process controlling the formation of stars in galaxies.

Being able to study a galaxy with a few beams across will provide a more global aspect of the interstellar medium. Namely, the different antenna beams trace different phases of the ISM (diffuse and molecular clouds, the warm PDRs), and characterize therefore the global properties of the ISM in galaxies. Submillimeter spectroscopy of nearby galaxies is likely to reveal regions of star formation or shock wave activity,

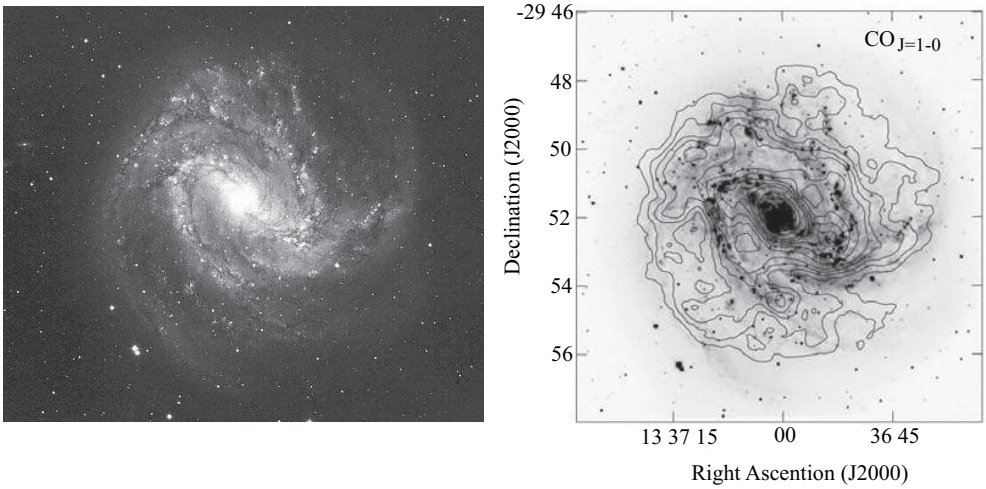

Figure 1.6: *Left*) M83, the spinwheel galaxy in Hydra (AAT). Distance $\sim$ 15 million light years (4.6 Mpc) *Right*) $CO_{J=1\rightarrow 0}$ (115 GHz), Crosthwaite *et al.* (2002), Tmb=55 K. From R. Güsten (2003) [17].

which should provide correlations among the various atomic and molecular species. The correlations obtained in this way tell us about the overall chemistry, and help test physical models for the interstellar medium.

With the Heterodyne Instrument (HIFI) [12] on board Herschel [16], observations of a large number of molecular and atomic transitions detectable in starburst- and the nuclei of nearby galaxies will for the first time enable a detailed analysis of the physical properties, and to some extent the structure of the star forming interstellar medium in these galaxies. In particular, the brightness of C^+ cooling lines will serve as an indicator of high mass star forming rate.

A major challenge for future observations of distant galaxies will be to observe strong emission lines such as CII and the so far unmentioned presence of atomic oxygen (OI), as they redshift into the submillimeter atmospheric windows. Atomic oxygen is also expected to be present in molecular clouds, since the ionization potential is quite high (13.62 eV). OI has two atomic fine-structure transitions in the far-infrared. They are: $^3P_0 \rightarrow {}^3P_1$ at 147 μm (2.060 THz), and $^3P_1 \rightarrow {}^3P_2$ at 63 μm (4.745 THz). To detect these lines at high-redshift, large telescopes and excellent SIS receivers, such as the continuous comparison or correlation receiver of Chap. 8, shall be required. It may in fact be the only method available to learn in detail about the chemical and dynamic processes which take place in high red-shifted galaxies.

1.1.4 Solar system

1.1.4.1 Planets

The discussion should not end without a brief mention of solar system atmospheric chemistry, or planetary aeronomy, since this is also within the capability of heterodyne

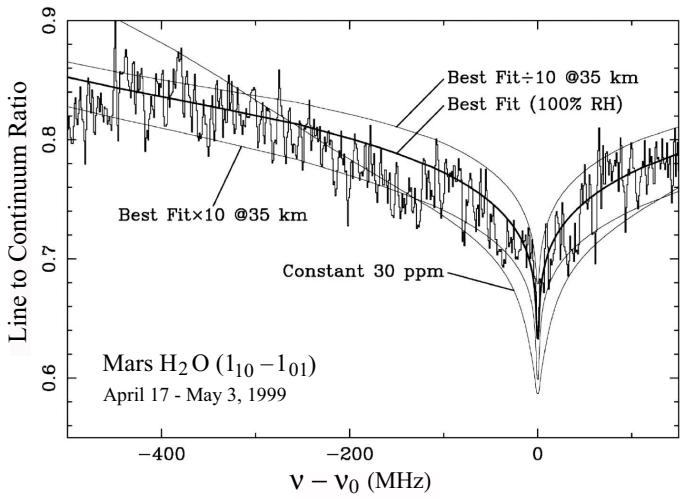

Figure 1.7: Detection of the ground level $1_{10} - 1_{01}$ water line at 556.936 GHz on Mars, as observed by SWAS [18]. Compared are various water distributions (From Gurwell *et al.* 2000 [19].)

receivers. Because of telluric H_2O and O_2 lines, ground based observations of solar system bodies are only possible in the submillimeter atmospheric windows. In the case of airborne platforms such as SOFIA [20] or high altitude ballooning, observations of planetary H_2O remains impossible. Thus observations from space have a distinct advantage over ground based observations, albeit at a much larger expense.

Regardless of these issues, remote sensing in the millimeter and submillimeter is an important tool for studying the chemical composition of atmospheres [21]. Molecular lines are often narrow, though strong H_2O lines can be as wide as 2 GHz, thanks to pressure broadening. Heterodyne spectroscopy provides the capability of measuring individual line shapes, and is therefore especially well suited for vertical profiling of atmospheres. An added advantage of the submillimeter regime is that it is relatively immune to dust extinction, as would be the case with infrared observations.

SWAS [18] and ISO [22] have in fact both detected water in planetary systems. ISO has detected H_2O in the four giant planets, and on Saturn's moon Titan. CO and CO_2 have also been detected by ISO in Jupiter, Saturn, and Neptune, but interestingly not on Uranus. SWAS with its high resolution Schottky based heterodyne receiver (Sec. 3.1) has observed the ground state H_2O $1_{10} - 1_{01}$ line at 556.936 GHz in Jupiter and Saturn. H_2O and CO are thought to be deposited in the upper atmospheres by comets, such as the well observed 1994 Schoemaker-Levy Jupiter impact. In the Martian atmosphere some of the identified molecular species, aside from of course CO_2 are: CO, H_2O, O_2, O_3, and H_2, the latter species observed with FUSE, the far-infrared spectroscopic explorer from NASA [23].

For the high resolution heterodyne instrument on the *Herschel* space observatory [12, 13] the primary science goals are to obtain a detailed characterization of H_2O in the Martian atmosphere. This means measuring a variety of backbone water

transitions, HDO, and isotopic ratios of $H_2^{18}O$ and $H_2^{17}O$. The latter two will establish the important hydrogen/deuterium (H/D) ratio with high precision. Chemically speaking, preferential escape of hydrogen relative to deuterium causes an enrichment of the atmospheric abundance of the latter over geological time. Measurement of atmospheric HDO and H_2O provides an estimate of this enrichment process, and may be compared to the 4.5 billion year atmospheric evolution of for instance the Earth ($H/D \sim 1000$), Venus ($H/D \sim 100$), and comets (next Section). Also anticipated with the Herschel space observatory are searches in the Martian atmosphere for OH, HO_2, H_2O_2. These species are however subject to seasonal variations.

The study of planetary atmospheres provides therefore important clues for understanding the origin, evolution, and formation processes of terrestrial and giant planets. It is clear from everyday experiences on Earth that planetary atmospheres undergo continuous processing through their lifetimes, for example: Volcanism on Io. Both transport (diffusion, convection, escape and winds) and physicochemical effects (photochemistry, electrochemistry, thermochemistry) act to change the state of planetary atmospheres. A high resolving power ($R > 10^6$, Chap. 2) enables the retrieval of the vertical distribution of the observed molecule, the thermal profile, and wind velocity [21]

Submillimeter Fourier-transform spectroscopy ($R \sim 10^4$) such as demonstrated from the CSO by Weinstein and Serabyn (1994) [24], the LWS Fabry-Perot instrument on ISO [25], and the Imaging Fourier Transform Spectrometer instrument (SPIRE) [26] on Herschel are also very important in the study of planetary atmospheres. These instruments provide a lower resolving power than heterodyne instruments, but are able to measure over a far greater instantaneous signal (RF) bandwidth. This is good for lines that are too broad to be detected with a high resolution heterodyne instrument such as troposphere absorption lines.

In the Earth atmosphere ozone (O_3) is a very important trace molecule [27] as it protects the environment from harmful UV-B radiation (for example, the phytoplankton population of Antarctica which affected the entire food chain – from krill to penguins and seals). It is well known that O_3 is a powerful oxidizing agent and that it is readily converted to O_2 via a photosynthesis reaction of UV light, Cl, CLO, NO and NO_2. The highly oxidative OH hydroxyl is the catalyst in this process, and has been found to play a central role in the stratospheric (10 – 50 km) ozone production process [28]. It is however, due to its low abundance (highly reactive, short life time), difficult to observe [29]. In the near future, it may now be possible to observe OH directly via the 1.835 THz, 2.510 THz, and/or 3.545 THz molecular emission line with an HEB heterodyne mixer (Sec. 4.3). For example, with balloon-borne observation from the Terahertz Limb Sounder (TELIS) [30]. As a final word, O_3 also plays an important role in the stratospheric heating/cooling balance. Depletion of ozone in the stratosphere is likely to affect the radiative heat balance in the entire atmosphere, with unforeseen consequences. Some other molecules (green house gasses) that affect the heat balance of the atmosphere, aside from CO_2, are methane (CH_4), and nitrous oxide (N_2O). Both have emission lines in the submillimeter, and are in detectable with the laid out heterodyne techniques of this thesis.

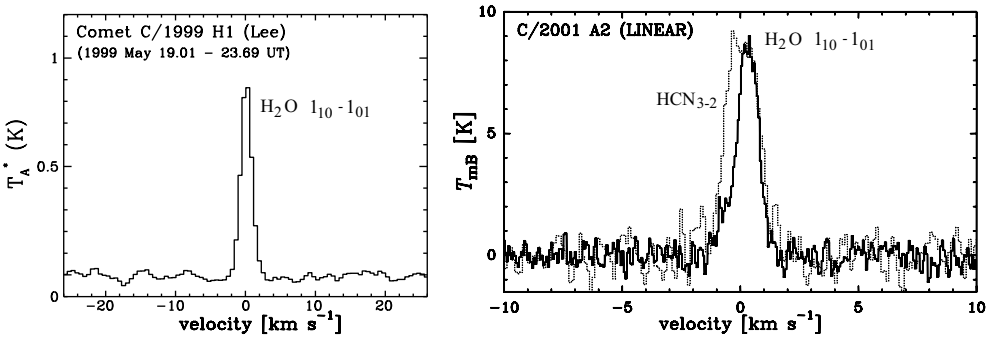

Figure 1.8: *Left*) Detection of the ground level $H_20\ 1_{10} - 1_{01}$ water line at 557 GHz, as observed by SWAS [18] in C/1999 H1 (Lee). (From Neufeld *et al.* 2000 [31]). *Right*) The $H_20\ 1_{10} - 1_{01}$ ground-state water line observed by Odin [32] in comet C/2001 A2 (LINEAR). Overlaid is HCN as observed at the CSO (scale expanded by 10x, dotted line). (From Lecacheux *et al.* 2003. [33]).

1.1.4.2 Comets

Having retained and preserved pristine material from the solar nebula at the moment of their accretion, comets contain unique clues to the history and evolution of the solar system. The study of comets follows the natural progression from interstellar matter to solar system bodies and their formations [34].

Water is the primary constituent of cometary ice, and evaporation drives the dynamics of cometary outgassing at small (< 4) heliocentric distances. Active comets release both gas (mainly water) and dust, with water playing an important role in the thermal balance of a cometary atmosphere as a cooling agent via the emission of its rotational lines. Recent detections of the $H_2O\ 1_{10} - 1_{01}$ ground state rotational transition line at 556.936 GHz by SWAS in Comet C/1999 [31], and in Comet C/2001 by Odin [33] (Fig. 1.8) have shown the possibility of cometary outgassing observations. The spectra of water in comets yields information on the amount of water evaporated from the nucleus, the kinetics of the cometary atmosphere, coma expansion, and provides reference levels for minor volatile abundances. Due to the low escape velocity of cometary gasses, a < 1 kms^{-1} frequency resolution will be required to resolve cometary emission lines. Thus high resolution heterodyne spectroscopy ($R \geq 10^7$, see also Sec. 2.1) will provide the only means available for these kind of observations. As an interesting side note, the vastly improved sensitivity and frequency range of HIFI [12] over the uncooled Schottky mixers (Sec. 3.1) flown onboard SWAS [18], Odin [32], and the microwave radiometer instrument (MIRO) onboard the ROSETTA [35] probe to comet 67P/Churyumov-Gerasimenko (2014), will allow for the study of a number of rotational H_2O transition lines at a variety of comets. Other cometary lines that should be observable with HIFI are: HDO, NH_3, H_2S, OH, CH_2, NH, H_3^+, and OH^+.

Since the cometary gas is cold (10–100 K), the rotational transitions at the lowest energy states are most intense. Thus it is important to look primarily for the fundamental ground state rotational water transition line as was so successfully done with SWAS and Odin.

The deuterium abundance is a key parameter for studying the origin and early evolution of the solar system (previous Section). Simultaneous observations of H_2O and HDO determine the H/D ratio in cometary water. For example, in comet Hyakutake and Hale-Bopp a ratio of ~ 3300 was obtained. This is useful for refinement of theoretical models describing the early solar nebula dynamics. These comets were long period, coming from the Oort cloud (believed to be approximately 1 light-year from the Sun). Measurements of the H/D ratio of comets from the "nearby" Kuiper belt (a bit beyond Neptune at ~ 55 AU) will again help constrain solar nebula models.

Needless to say, due to telluric water vapor, most of these observations can only be done from space.

1.2 Coherent (heterodyne) detection

Atomic and molecular line astrophysics is demanding enhanced capabilities in terms of frequency coverage, spectral resolution, bandwidth, sensitivity, stability (quality of the data products), frequency agility, and ease of use. To help fulfill these demanding requirements, this thesis investigates advanced heterodyne receiver techniques in the submillimeter and terahertz frequency regimes.

1.2.1 Challenges

Coherent detection, the research topic of this thesis, facilitates high resolution spectroscopy by down converting the phase and amplitude of the incoming signal to a much lower intermediate frequency. Hence the terminology "coherent detection". To accomplish this task, a local oscillator signal is required. One of the difficulties of far-infrared heterodyne spectroscopy has been the limited availability of local oscillator (LO) signal power. Recent advances in (waveguide based) local oscillator multiplier technology [36, 37, 38] have opened the field of molecular spectroscopy to ~ 2 THz. Above this frequency Quantum Cascade Lasers (QCL) [39] have in recent years shown much promise. In fact, the QCL can be expected to play a significant role as local oscillator at frequencies where conventional waveguide techniques cease to be practical [40].

Another difficulty has been the lack of sensitive heterodyne mixers at terahertz frequencies. Schottky diode mixers have been available for quite some time, but suffer from a large (mW) LO power requirement. Niobium based Superconductor-Insulator-Superconductor (SIS) mixers, well established in the submillimeter, do not operate in the terahertz due to an energy gap limitation of the superconducting material, and non-negligible parasitic junction capacitance of the tunnel barrier (Chaps. 4 & 5). The introduction of the superconducting NbN-film Hot-Electron Bolometer (HEB) mixer [41] has shown much promise as a moderately sensitive, low LO-power demanding, terahertz mixer.

HEB mixers are thermal devices that operate near the superconducting transition temperature (T_c). By design the hot electron bolometer is planar with very little parasitic device capacitance. As such HEB mixers have no known upper frequency limit, and have demonstrated sensitivities in the terahertz regime that approach six

times the quantum noise limit [42]. This is well beyond the capability of conventional SIS mixers.

Despite some of the for-mentioned advantages of HEB mixers, they do suffer from a number of issues, none the least of which is a limitation in IF bandwidth. The limited IF bandwidth is in large part due to the thermal time constant(s) of the excited (hot) electrons, phonons, and the surrounding bath temperature. In practice the IF gain bandwidth of NbN HEB mixers lies in the range 2.5 – 5 GHz. Though adequate at submillimeter frequencies (200 – 1000 GHz), at terahertz frequencies a 2 – 3 GHz IF bandwidth constrains the obtainable velocity coverage (Doppler shift). This limits observations to galactic sources and some nearby galaxies. A second disadvantage of a small IF bandwidth is the efficiency at which molecular line surveys may be carried out. One of the big challenges in radio astronomy instrumentation is therefore to extend the IF bandwidth of HEB mixers.

Yet another difficulty is the limited sensitivity of HEB mixers. This is due to a relatively low conversion efficiency (-6 to -10 dB) and a high level of thermal noise at the mixer output. A SIS mixer, on the other hand, can have near unity down conversion efficiency [43], and a mixer output noise very close to the quantum noise limit. As a long term goal several groups are trying to extend SIS technology into the terahertz regime with the use of high bandgap materials (Chap. 5).

In case of extended line sources, such as molecular clouds, an improvement in observing efficiency is obtained by combining multiple pixels into a heterodyne array receiver (Chap. 9). This is not unlike multi-pixel charge coupled devices (CCDs) in the optical and near infrared and direct detection bolometer cameras in the submillimeter. In fact, HEB mixers, unlike SIS mixers which have to have a magnetic field applied to suppress Josephson currents, are well suited for array applications.

For point source observations, raw sensitivity with coherent (heterodyne) detection can be attained by utilizing both polarizations, with the use of a continuous comparison or correlation receiver, and for ground based observations the use of a sideband separating mixer [44, 45]. The above mentioned configuration requires two mixing elements. Still further improvement in sensitivity may be gained with the use of balanced configurations. For example, a dual polarization balanced sideband mixer. These receivers configurations are discussed in some detail in Chaps. 3 & 8. Extending this technology to terahertz wavelength will form a significant challenge in the decade(s) to come.

Amplitude instability of the local oscillator (LO) poses a problem to SIS and HEB mixers alike. However, as noted in Chaps. 10, the problem increases in severity with operating frequency. Minute fluctuations in the LO signal, as a consequence of rapid modulation of the LO-mixer standing wave cavity and/or changes in the output power of local oscillator result in a loss of integration efficiency, platforming in the backend spectrometer, and baseline distortion due to imperfect "signal-reference" subtraction. Balanced receivers with inherent common mode amplitude rejection properties (Chap. 8), form an attractive solution to this problem. Moreover, since balanced receivers have built in robustness to excess amplitude modulated (AM) noise from synthesizer driven local oscillator sources, they also facilitate automated (frequency agile) line surveys (Chap. 2).

Instrument stability is also of utmost importance in the case of high-redshift extragalactic observations, where the observed signals are deeply embedded in the noise. Proper system stability ensures efficient integration of the noise with the highest possible fidelity. Since essentially all HEB observations in the terahertz will be done from high elevations, or space (due to telluric H_2O line absorption) it is questionable whether sideband separation in the terahertz frequency range is the correct approach. The challenge that faces HEB receiver development in the terahertz is therefore to construct (balanced) arrays with adequate IF bandwidth. It is the expectation that the theory and techniques outlines in this thesis contribute to this development.

1.2.2 Why high resolution spectroscopy

By virtue of the coherent receiver down-conversion process to an intermediate frequency, it is possible to achieve very high spectroscopic resolution ($R=\nu/\Delta\nu \geq 10^6$), thereby facilitating fine-structure atomic and molecular spectroscopy in the submillimeter and far-infrared. As we have seen, this field encompasses a wide variety of important research topics ranging from protostellar disks and molecular outflows, to galaxy formation.

As was alluded to in the introduction, the detection of dust, or continuum radiation in the submillimeter and terahertz provides a powerful method of studying stars deeply embedded inside dense molecular clouds. It also facilitates the measurement of dust concentrations around protostars, as well as the study of galaxy formation. It is for this reason that a variety highly successful (SCUBA-2, SHARC-2) [46, 47] low resolution direct detection (bolometer) cameras either have been, or are currently in the process of being developed.

To examine the spectral energy density (SED) of objects higher spectral resolution is however needed. For example, the use of an incoherent Fourier transform spectrometer or grating spectrometer provides resolving powers of up to 10,000 (Sec. 2.1). ISO-LWS, the low resolution Fabry-Perot spectrometer ($R \sim 200$) on board ESA's Infrared Space Observatory (ISO) [22] has very successfully obtained spectral information on a wide range of galactic and extragalactic objects. ISO was operational between November 1995 and May 1998. PACS and SPIRE, both low to medium resolution photometer cameras on board the, soon to be launched, Herschel space observatory [16] are expected to study the far-infrared wavelength regime for the first time.

Scientifically speaking, it is currently understood that observations of continuum emission from dust provide insight into the structure of molecular clouds, star forming regions, photodissociated regions (PDRs), and galactic formation (Motte 1998 [48], Dishoeck 2000 [15]), while the spectral energy distribution (SED) provides an indication of the evolutionary state of the objects (Lada 1999) [49]. To study however the physics and chemistry of the gas, only high resolution molecular line observations suffice. For example, the ratios of lines originating at different energy levels of the same molecule provide a convenient way of measuring the temperature structure, local density, and abundance. The ability to disentangle the many gas components responding to these various astrochemical processes requires the high spectral resolution provided by a heterodyne instrument. Given that the research objective of this

thesis is "advanced heterodyne receivers technology", we have ignored in our discussion topics related to the continuum detection of dust, Sunyaev-Zel'dovich effect, and the cosmic background radiation. These are better treated elsewhere in literature.

1.3 Contribution to the field of far-infrared astronomical instrumentation

A global overview of the contributions to the field of far-infrared astronomy is provided in Table 1.1. The following two subsections discuss the thesis outline and impact on astronomy.

Table 1.1: Contributions of this thesis

Chapter	Contribution
4	SIS and HEB mixer fundamentals & technology development.
5	NbTiN film, AlN tunnel barrier, 850 GHz twin-slot mixer.
6	IF bandwidth and mixer gain of NbN HEB mixers
7	High current density (waveguide) AlN-barrier SIS receiver.
8	Balanced, Correlation, and Sideband separating receivers.
9	SIS and HEB mixers on SOI substrates for array applications.
10	HEB stability and the influence of optical standing waves.

1.3.1 Thesis outline

This thesis begins with a brief introduction to the field of submillimeter and terahertz astronomy. From there it proceeds to outline the submillimeter detection and operational requirements in Chap. 2. This is an important Chapter as boundary conditions are defined for the astronomical instrumentation we concern ourselves with.

Once the operational requirements are established a variety of receiver configurations are introduced in Chap. 3. In particular we touch upon the concepts and implementations of the double sideband (DSB) single-ended receiver, the balanced receiver, the correlation receiver, and the sideband separating receiver.

At its core, frequency down-conversion or heterodyning is accomplished with an highly non-linear mixing element. In the submillimeter, below 1000 GHz, SIS tunnel junctions are now commonly employed thanks to their superior conversion gain and sensitivity. In the terahertz regime, at frequencies beyond 1000 GHz, hot-electron bolometer mixers are at the present time the element of choice. The mixing process in both mixers is fundamentally very different. In Chap. 4 we address the physics of each device, and look in detail into a number of device related peculiarities. With the theory covered, the focus shifts in subsequent Chapters to a variety of realized receiver

designs in the laboratory and on the telescope. We address in Chap. 5 an all NbTiN film quasi-optical mixer that operates in the 800 – 920 GHz atmospheric window. As a result of our work, low loss and high energy gap NbTiN superconducting films have been demonstrated, and since then been incorporated in HIFI mixers bands 3, 4, and 5 [50, 51]. Also in Chap. 5 we explore for the first time the use of an AlN tunnel barrier. The results were so impressive that this technology is currently being baselined at institutions like JPL, TU Delft, the University of Virginia, and the University of Köln.

In Chap. 6, our research leads the way to addressing such important issues as the IF bandwidth and mixer gain of (NbN) hot electron bolometers. Then in Chap. 7 a recently installed (at the Caltech Submillimeter Observatory (CSO)) double sideband high-current density AlN-barrier SIS Technology development receiver (Trex) is introduced. Trex was constructed to prove many of the underlying technologies required in advanced receiver designs (Chap. 8). At the present time Trex serves as a facility heterodyne instrument for high spectral resolution wide bandwidth observations, and extended observations with the SMA [52].

In the first part of Chap. 8 we look in detail at the theory, characteristics, and implementation of balanced receivers, designed to cover the important 180 – 720 GHz atmospheric window(s). The second part of Chap. 8 discusses a correlation, or continuous comparison, receiver to operate between 280 – 420 GHz (covers two atmospheric windows with one SIS mixer). Finally, the last Section of Chap. 8 concerns itself with a 600 – 720 GHz (Alma band 9) sideband separating receiver. Theory, implementation, and measurement results are presented. This is the first time a sideband separating receiver has been implemented at such a high frequency. In our treatment, instantaneous signal and IF bandwidth, sensitivity, and sideband ratio are important considerations.

An important, so far un-discussed, receiver concept is the heterodyne focal plane array. Future astronomical developments will increasingly demand the mapping speed enhancement afforded by multi-pixel focal plane arrays. This thesis will devote Chap. 9 towards integrated arrays receivers with actual realized devices and measurement results.

In all of the above outlined receiver designs, instrument stability is of primary importance. It affects the observed baseline quality and integration efficiency. Indeed, there are many ways in which the stability of the receiver may be compromised. The theory and actual measurement results will be presented (Chap. 10).

1.3.2 Impact on astronomy

In the last decade, the field of submillimeter and terahertz astronomy has seen a rapid development. The reasons are many, but several relevant to this thesis stand out: High speed computer technology combined with sophisticated (commercial) electromagnetic simulation software has enabled mixer and local oscillator designs to be much better understood and optimized. A significant amount of money, and thereby expertise, has been injected into the field by large programs such as HIFI [13, 12] and ALMA [6]. In addition there has been a revolution in the automation industry which has enabled commercially viable micro-milling machines. This has allowed waveguide

Table 1.2: Some of the instruments and observatories that have benefited from this work.

Instrument	**Contribution**	**Chapter**
HIFI	Mixer bands 1,3,4,6,7, Systems stability.	4,5,6,8,10
HEAT	HEB mixer, System stability, IF bandwidth.	4,6,10
TELIS	IF bandwidth integrated receivers.	8
STO	HEB mixer, System stability, IF bandwidth.	4,6,10
SuperCam	SIS on SOI, Multi pixel development.	9
ALMA	Band 10: AlN/NbTiN films, Band 5,9: 2SB design.	5,8
Casimir	AlN barrier/NbTiN ground plane.	5
CSO	SIS mixer development, Stability, IF bandwidth.	4,5,7,8,A–C
APEX	Waveguide transition, System stability.	7,A

techniques to be extended to nearly 2 THz [36, 37]. And finally, receiver backend technology has seen a tremendous advancement, to the point where it is now possible to process IF bandwidths of multi-pixel focal plane arrays. Much of the research in this thesis has benefited from the above mentioned revolution.

Many of the ideas and concepts developed in this thesis are either already implemented, or are in the process of being implemented in submillimeter and terahertz instrumentation and telescopes around the world. And, with the high resolution Heterodyne Instrument (HIFI) on ESA's Herschel satellite [16], soon also in space. Table 1.2 serves as a summary.

Examples of instruments and projects that have utilized various aspects of the presented research are, aside from HIFI [12]; the High Elevation Antarctic Telescope (HEAT) [53], the TErahertz and submillimeter LImb Sounder (TELIS) [30], the Stratospheric Terahertz Observatory (STO), SuperCam [54], Atacama Large Millimeter Array (ALMA) [6], Casimir [55], and the Caltech Submillimeter Observatory on top of Mauna-Kea, Hawaii [4].

HEB mixer development for HIFI mixer bands 6 & 7 has encouraged fundamental research into the physics of (NbN) hot electron bolometers at several laboratories, and in particular by Prof. Teun Klapwijk's group at the Kavli Institute of Nanoscience, Delft University of Technology [56, 57, 58, 59]. The research into HEB devices is driven by the urgent need to improve the sensitivity, IF bandwidth and system stability of hot electron bolometers mixers. Much progress has been made in recent years, with issues such as IF bandwidth and mixer gain addressed in Chap. 6 and system stability in Chap. 10.

For HEAT, the hot electron bolometer mixers are anticipated to be fabricated at the TU Delft (NbN films from Gol'tsman group, Moscow State Pedagogical University, Russia [60]). In this case, implications from Chaps. 6 & 10 are directly applicable. Similarly, HEB instrumentation on STO will also benefit directly from the presented research.

IF bandwidth has also been an issue with the integrated flux-flow (SIS) mixers on Telis [30]. Here integrated techniques developed in Chaps. 7 & 8 have been applied

very successfully [61]. In case of the SuperCam [54], the 64 pixel heterodyne array camera from the University of Arizona (Prof. Walker's group), silicon-on-insulator (SOI) technology is employed to produce very thin (3 μm) silicon substrates with gold beam leads. These are needed to move away from conventional single pixel quartz substrates to large format arrays, and to facilitate scalability to terahertz frequencies (Chap. 9).

ALMA mixer band 10 [6] and the Casimir instrument on SOFIA [20] use the NbTiN films and SIS AlN barrier technology of Chap. 5, as developed for HIFI mixer bands 4 & 5 [50, 51]. Furthermore, the ALMA band 5 (163 – 211 GHz) sideband separating mixer work at GARD (Group for Advanced Receiver Development at Chalmers TU, Sweden) [62] employs the quadrature hybrid outlined in Chap 8, and the ALMA band 9 (602 – 720 GHz) sideband separating mixer [63] the research and development of Chaps. 7 & 8.

It should also be observed that instrument stability is a common thread throughout this thesis (Appendix A). It is fair to say that all the above mentioned instruments have benefited from this work. And last but not least, to assist the science at the Caltech submillimeter Observatory, much effort has gone into the development of wide RF and IF bandwidth balanced– and correlation receivers, as outlined in Chap. 8.

Bibliography

[1] [Online]. Available: http://lambda.gsfc.nasa.gov/product/cobe/

[2] [Online]. Available: http://map.gsfc.nasa.gov/

[3] [Online]. Available: http://www.rssd.esa.int/Planck/

[4] [Online]. Available: http://www.submm.caltech.edu/cso/ [Online]. Available: http://www.submm.caltech.edu/cso/receivers/

[5] [Online]. Available: http://www.apex-telescope.org/

[6] [Online]. Available: http://www.alma.info/

[7] Jenkins E.B., & Shaya E.J., *ApJ.*, 231, 55, (1979).

[8] T. G. Phillips and P. J. Huggins, "Abundance of atomic carbon (CI) in dense interstellar clouds," *Astrophys. J.*, vol. 251, pp. 533-540, (1981).

[9] Bennett C.L., Fixsen D.J. *et al.*, "Morphology of the interstellar cooling lines detected by COBE", *ApJ.*, 434, 587, (1994).

[10] Keene, J., Lis, D.C., Phillips, T.G., & Schilke, P., *in Molecules in Astrophysics*: Probes and Processes, ed. E. van Dishoeck (Dordrecht: Kluwer), p. 129, (1997)

[11] A. G. G. M. Tielens, "The Physics and Chemistry of the Interstellar Medium", *Cambridge Univ. Press*, ISBN-10 0-521-82634-9.

[12] Th. de Graauw, N. Whyborn, E. Caux, T. G. Phillips, J. Stutzki, X. Tielens, R. Güsten, F. P. Helmich, W. Luinge, J. Pearson, P. Roelfsema, R. Schieder, K. Wildeman, and K. Wavelbakker, "The Herschel-Heterodyne Instrument for the Far-Infrared (HIFI)", [Online]. Available: herschel.esac.esa.int/Publ/2006/SPIE2006_HIFI_paper.pdf

[13] Th. de Graauw and F. P. Helmich, *Airborne Telescope Systems, in Proc. of the Symposium* "The Promise of the Herschel Space Observatory", edited by G. L. Pilbratt, J. Cernicharo, A. M. Heras, T. Prusti, and R. Harris, (ESA, Toledo, Spain, 2000), "Herschel-HIFI: The heterodyne instrument for the far-infrared", pp. 45., 195-202 (2000). [Online]. Available: www.astro.phys.ethz.ch/herschel/HerschelHifi.pdf

[14] T. G. Phillips and J. Keene, "Submillimeter Astronomy", *Proc. of the IEEE*, Vol. 80, No. 11, Nov. (1992).

[15] E. F. van Dishoeck, "Molecular Line Surveys of Star-Forming Regions with Herschel (First)", *Proc. of 'The promise of FIRST' Symp.*, Toledo, Spain, ESA SP-460, 12-15 Dec., (2000).

[16] [Online]. Available: http://sci.esa.int/

[17] R. Güsten & S. Philipp, "HIFI Core Program: Galaxies and Galactic Nuclei", *SRON*, (2003).

[18] [Online]. Available: http://sunland.gsfc.nasa.gov/smex/swas/

[19] M. A. Gurwell and E. A. Bergin *et. al*, "Submillimeter Wave Astronomy Satellite Observations of the Martian Atmosphere: Temperature and Vertical Distribution of Water Vapor", *ApJ.*, 539, L143, (2000).

[20] [Online]. Available: http://www.sofia.usra.edu/

[21] Th. Encrenaz, B. Bézard, J. Crovisier, A. Coustenis, E. Lellouch, S. Gulkis and S. K. Atreya, "Detectability of molecular species in planetary and satellite atmospheres from their rotational transitions," *Planet. Space Sci.*, Vol. 43. No. 12, pp. 1485-1516, (1995).

[22] [Online]. Available: http://www.sci.esa.int/iso/

[23] V. A. Krasnopolsky and P. D. Feldman, "Detection of Molecular Hydrogen in the Atmosphere of Mars", *Science*, Vol. 294, Nov. (2001).

[24] E. W. Weinstein, and E. Serabyn, "Detection of the 267 GHz J=1-0 rotational transition of PH3 in Saturn with a new Fourier transform spectrometer", *Icarus* 109, pp. 367-381, (1994).

[25] B. M. Swinyard and M. J. Burgdorf *et al.*, "In-orbit performance of the ISO Long Wavelength Spectrometer", *Proc. SPIE*, Vol. 3354, p. 888-899, Infrared Astronomical Instrumentation, Albert M. Fowler; Ed., Aug. (1998).

[26] [Online]. Available: http://www.spire.rl.ac.uk/

[27] P. O. Wennberg, and T. F. Hanisco *et al.*, "Hydrogen Radicals, Nitrogen Radicals, and the Production of O_3 in the Upper Troposphere", *Rev. Sci. Instrum.*, Vol. 279, No. 49 (1998).

[28] S. Miller, M. Birk, F. Schreier, and D. Hausamann, "Airborne far-infrared heterodyne remote sensing of stratospheric OH: a feasability study", *Int. J. Infrared Millim. Waves*, 13, pp. 1241, (1992).

[29] P. O. Wennberg, and R. C. Cohen *et al.*, "An aircraft-borne, laser-induced fluorescence instrument for the *in situ* detection of hydroxyl and hydroperoxyl radicals", *Rev. Sci. Instrum.*, 65, pp. 1858, (1994).

[30] R. W. M. Hoogeveen, P. A. Yagoubov, Q. Kleipool, V. P. Koshelets, S.V. Shitov, B. Ellison, and M. Birk, *in Conf. Digest of the 2004 Joint 29th Int. Conf. on Infrared and Millimeter Waves and 12th Int. Conf. on Terahertz Electronics*, edited by M. Thumm and W. Wiesbeck, (University of Karlsruhe, Karlsruhe, Germany, pp. 581. (2004).

[31] D. A. Neufeld, J. R. Stauffer, E. A. Bergin *et al.*, "SWAS observations of water vapor toward comet C/1999 H1 (Lee). *Astrophys. J.*, 539, L151-L154, (2000).

[32] [Online]. Available: http://www.ssc.se/?id=7180/

[33] A. Lecacheux, N. Biver, J. Crovisier *et al.*, "Observations of water in comets with Odin, *Astron. Astrophys* 402, L55-L58, (2003).

[34] W. M. Irvine, F. P. Schloerb, J. Crovisier, B. Fegley, and M. J. Mumma, "Comets: a link between interstellar and nebular chemistry", in *Protostars and Planets IV*, V. Mannings, A. Boss and S. Russell (Edts), Univ. of Az. Press, Tuscon, Az. 1159-1200, (2000).

[35] [Online]. Available: http://www.esa.int/esaMI/Rosetta/

[36] G. Chattopadhyay, E. Schlecht, J. Ward, J. Gill, H. Javadi, F. Maiwald, and I. Mehdi, "An All Solid-State Broadband Frequency Multiplier Chain at 1500 GHz", *IEEE Transactions on Microwave Theory and Techniques*, Vol. 52, 5, 1538 (2004).

[37] I. Mehdi, E. Schlecht, G. Chattopadhyay, and P. H. Siegel, "THz local oscillator sources: performance and capabilities", *in Proc. of SPIE*, Vol. 4855, edited by T. G. Phillips and J. Zmuidzinas, (SPIE, Waikoloa, USA, 2002), pp. 435.

[38] A. Maestrini, J. S. Ward, H. Javadi, C. Tripon-Canseliet, J. Gill, G. Chattopadhyay, E. Schlecht, and I. Mehdi, "Local Oscilator Chain for 1.55 to 1.75 THz with 100-μW peak power", *IEEE Microwave and Wireless Components Letter*, Vol. 15, 12, pp. 871-873, Dec. (2005).

[39] R. Köhler, A. Tredicucci, F. Beltram, H. E. Beere, E. H. Linfield, A. G. Davies, D. A. Ritchie, R. C. Iotti, and F. Rossi, "Terahertz semiconductor-heterostructure laser", *Nature*, 417, 156 (2002).

[40] J. R. Gao, J. N. Hovenier, Z. Q Yang, J. J. A. Baselmans, A. Baryshev, M. Hajenius, T. M. Klapwijk, A. J. L Adam, T. O. Klaassen, B. S. Williams, S. Kumar, Q. Hu, and J. L. Reno, "A terahertz heterodyne receiver based on a quantum cascade laser and a superconducting bolometer, *Applied Physics Letters*, Vol. 86, 244104 (2005).

[41] Yu. P. Gousev, G. N. Gol'tsman, A. D. Semenov, E. M. Gershenzon, R. S. Nebosis, M. A. Heusinger, and K. F. Renk, "Broadband ultra fast superconducting NbN detector for electromagnetic radiation", *J. Appl. Phys.*, Vol. 75, pp. 3695 (1994).

[42] P. Khosropanah, J. R. Gao, W. M. Laauwen, M. Hajenius, and T. M. Klapwijk, "Low noise NbN hot electron bolometer mixer at 4.3 THz", *Appl. Phys. Lett.*, Vol. 91, 22, 221111, (2007).

[43] J.R. Tucker and M.J. Feldman, "Quantum Detection at Millimeter Wavelengths", *Rev. Mod. Phys.*, Vol. 57, pp. 1055-1113, Oct., (1985).

[44] S. -K. Pan, A. R. Kerr, M. W. Pospiezalski, E. F. Lauria, W. K. Crady, N. Horner, Jr., S. Srikanth, E. Bryerton, K. Saini, S. M. X. Claude, C. C. Chin, P. Dindo, G. Rodrigues, D. Derdall, J. Z. Zhang, and A. W. Lichtenberger, "A Fixed-Tuned SIS Mixer with Ultra-Wide-Band IF and Quantum-Limited Sensitivity for ALMA Band 3 (84-116 GHz) Receivers", *Proc. 15th Int. Symposium on Space Terahertz Technology*, Northampton, MA, Apr., 2004, pp. 62-69.

[45] D. Maier, A. Barbier, B. Lazareff, and K. F. Schuster, "The Alma Band 7 Mixer", *Proc. 16th Int. Symposium on Space Terahertz Technology*, Chalmers, Göteborg, Sweden, May, 2005, S08-02.

[46] M. D. Audley, W. S. Holland, T. Hodson *et al.*, "An update on th eSCUBA-2 project", *In Millimeter and Submillimeter Detectors for Astronomy II. Proc. of the SPIE*, Vol. 5498, J.Zmuidzinas, W.S.Holland, and S.Withington, Eds., pp.6377, Oct. (2004).

[47] [Online]. Available: http://www.submm.caltech.edu/ sharc/

[48] Motte, F., André, P., Neri, R. 1998, *A & A* 336, 150, (1998)

[49] Lada, C. J., *in The Origin of Stars and Planetary Systems*, eds. C. J. Lada and N. D. Kylafis (Dordrecht: Kluwer), p. 142 (1999)

[50] B. D. Jackson, G. de Lange, T. Zijlstra, M. Kroug, J. W. Kooi, J. A. Stern, and T. M. Klapwijk, "Low-Noise 0.8-0.96 and 0.96-1.12 THz Superconductor-Insulator-Superconductor Mixers for the Herschel Space Observatory", *IEEE Trans. Microwave Theory and Techniques*, Vol. 54, No. 2, pp. 547-558, Feb., (2006).

[51] A. Karpov, D. Miller, F. Rice, J. A. Stern, B. Bumble, H. G. LeDuc, J. Zmuidzinas, "Low Noise SIS Mixer for Far Infrared Radio Astronomy", in *Proc. of SPIE*, Volume 5498, Ground-based Telescopes, edited by J.Zmuidzinas, W. S. Holland, and S. Withington, (SPIE, Glasgow, UK, 2004) pp. 616-621.

[52] [Online]. Available: http://sma-www.harvard.edu/

[53] C. K. Walker, C. A. Kulesa, D. R. Golish, A. S. Hedden, K. Jacobs, J. Stutzki, J. R. Gao, J. W. Kooi, D. Glaister, W. Gully, I. Mehdi, M. R. Swain, and P. Siegel, "Forecast for HEAT on Dome A, Antarctica: the High Elevation Antarctic Terahertz Telescope", *in Proc. of SPIE*, Vol. 5498, Ground-based Telescopes, edited by J. Zmuidzinas, W. S. Holland, and S. Withington, (SPIE, Glasgow, UK, 2004), pp. 470.

[54] C. Groppi, C. Walker, C. Kulesa, P. Puetz, D. Golish, P. Gensheimer, A., S. Bussmann, S. Weinreb, T. Kuiper, J. Kooi, G. Jones, J. Bardin, H. Mani, A. Lichtenberger and G. Narayanan, SuperCam, a 64-pixel heterodyne imaging array for the 870 micron atmospheric window. *astro-ph*/0606061 (June 2006).

[55] [Online]. Available: http://www.submm.caltech.edu/sofia/

[56] M. Hajenius, "Terahertz heterodyne mixing with a hot electron bolometer and a quantum cascade laser", Ph. D. thesis, Delft University of Technology, the Netherlands, (2006).

[57] T. M. Klapwijk, R. Barends, J. R. Gao, M. Hajenius, and J. J. A. Baselmans, "Improved superconducting hot-electron bolometer devices for the THz range", *in Proc. of SPIE*, Vol. 5498: Millimeter and Submillimeter Detectors for Astronomy II, edited by J. Zmuidzinas, W. S. Holland, and S. Withington, (Glasgow, Scotland, pp. 129, UK (2004).

[58] R. Barends, "Analyzing superconducting THz Detectors: non-equilibrium double barrier junctions and hot electron bolometer mixers", M.Sc. thesis, TU Delft, (2004).

[59] M. Hajenius, J. J. A. Baselmans, A. Baryshev, J. R. Gao, T. M. Klapwijk, J. W. Kooi, W. Jellema, and Z. Q. Yang, "Full characterization and analysis of a THz heterodyne receiver based on a NbN hot electron bolometer", *J. Appl. Phys.*, Vol. 100, 074507 (2006).

[60] E. M. Gershenzon, G. N. Gol'tsman, I. G. Gogidze, A. I. Eliantev, B. S. Karasik, and A. D. Semenov, "Millimeter and submillimeter range mixer based on electron heating of superconducting films in the resistive state", *Sov. Phys. Superconductivity*, Vol. 3, 1582 (1990).

[61] V. P. Koshelets, A. B. Ermakov, L. V. Filippenko, A. V. Khudchenko, O. S. Kiselev, A. S. Sobolev, M. Yu. Torgashin, P. A. Yagoubov, R. W. M. Hoogeveen, and W. Wild, "Superconducting Integrated Submillimeter Receiver for TELIS", *IEEE Trans. Appl. Superconductivity*, Vol. 17, No. 2, pp. 336-342, Feb., (2007).

[62] [Online]. Available: http://gard04.rss.chalmers.se/

[63] F. P. Mena, J. W. Kooi, A. M. Baryshev, C. F. J. Lodewijk, R. Hesper, G. Gerlofsma, T. M. Klapwijk, and W. Wild, "A Sideband-separating Heterodyne Receiver for the 600−720 GHz Band", *Submitted to IEEE Trans. Microwave Theory and Techniques*, August (2008).

Chapter 2

Submillimeter detection and instrumental requirements

2.1 Introduction/Overview

The submillimeter wavelength band (λ = 100 μm to 1 mm) is a transition region between infrared and millimeter waves. It is a region in which radiometric techniques common to the longer wavelength regime are combined with optical techniques. In this thesis we primarily concern ourselves with advanced heterodyne receiver technology in the submillimeter and far-infrared portion of the electromagnetic spectrum.

At frequencies below 100 GHz coherent (heterodyne) detection is extensively used in for example; mobile phones, satellite communications, and radar applications. The advantage of coherent detection is that by utilizing an intermediate frequency (IF), a nearly arbitrary high spectroscopic resolution (defined as $R = \nu/\Delta\nu$) can be obtained. This is especially useful in the study of atomic and molecular line transitions (Chap. 1). For example, resolution requirements of $R \geq 10^6$ – 10^7 are not uncommon. The actual achievable resolution will depend on the backend (correlator) and phase jitter in the local oscillator. At a rest frequency of 1 THz, a resolving power of $R = 10^6$ – 10^7 corresponds to a spectral resolution bandwidth of 100 KHz – 1 MHz. When expressed in velocity terms (a more practical unit of measure for the astronomer) this equates to $v = c/R = 0.03$ – 0.3 kms^{-1}.

Despite the nearly infinitely high resolution advantage of coherent detection, there are some important drawbacks. Because both amplitude and phase are detected there is an intrinsic lower limit ($h\nu/k_B$), known as the quantum noise limit, on the achievable sensitivity. Here h is Planck's constant, 6.626×10^{-34} J·s, and k_B Boltzmann's constant 1.381×10^{-23} J/K. In practice, depended on the frequency of operation, heterodyne receivers have sensitivities that range from 3 to 10 times the quantum noise temperature. They are also only sensitive to a single radiation mode, and to optimize coupling efficiency from the device to the telescope one polarization (Chaps. 5 – 9) is typically employed. Another very important issue with coherent detectors is the fractionally small detection (IF) bandwidth. Modern heterodyne superconducting-

insulator-superconducting (SIS) receivers (Chaps. 7 & 8) are constructed with a 4 – 8 GHz instantaneous IF bandwidth. However, due to instabilities in the LO pump signal, standing waves in the LO-mixer path, and intrinsic mixer instability not all of this IF bandwidth is available for continuum or spectral energy density (SED) flux detection. The situation is even worse for hot electron bolometer (HEB) mixers, which at best have an instantaneous IF gain bandwidth of 2 – 3 GHz, of which due to excessive $1/f$ noise only $\lesssim$ 500 MHz is available for flux detection. If we take 500 MHz as the upper limit for the total power spectral bandwidth of an HEB mixer, then at 1.9 THz (the important C^+ cooling line) we find that this corresponds to a frequency resolution limit of $R^{min} \sim 4000$, or a maximum velocity coverage of $c/R = 75$ kms^{-1}. As we shall see, this is barely enough for continuum observations toward the galactic center.

Thus we find that coherent detection, though excellent for high resolution spectroscopic astrophysics [1, 2, 3, 4], has limited value in the study of broadband emission from cold interstellar dust, unresolved ultraluminous infrared galaxies, and the cosmic background radiation. This is especially true in the context of low background space observations where the limited sensitivity and instability of coherent detectors is prohibitive in the detection of broadband emission. To address continuum or dust observations incoherent detectors are better suited. In the submillimeter and far-infrared wavelength regime bolometers (heat sensitivity detectors) have been found most sensitive. Though not the subject of this thesis we will outline in Sec. 2.2 the basics of this very important class of incoherent detectors.

Bolometers are insensitive to phase and as such do not have a quantum limit. They are however limited by photon statistics as discussed in Sec 2.2.3. And because the bolometer resolution is set by optical filters (for ground based observations optical filters are ordinarily designed to follow the atmospheric windows), the achievable frequency resolution is very low ($R \sim 10$). To understand why this is advantageous in the study of continuum emission (absorption), one only has to consider that background limited direct detection is best achieved with the instrumental bandwidth matched to the expected resolution of the astronomical source (no excess noise).

From the above discussion, it is evident that there is a large gap between the lowest possible resolving power of coherent ($R \gtrsim 4000$) and incoherent ($R \lesssim 10$) detectors. This gap is filled by a class of medium resolution direct detection instruments that place a Fourier Transform Spectrometer (FTS) in the optical path of a small bolometer array. Good examples of this are SPIFY ($R = 500$ – 10,000) [5], and SPIRE [6], a 3-band Imaging Fourier Transform Spectrometer on the Herschel space observatory [7]. SPIRE has a maximum resolution of $R = 1000$.

The spectral resolution of such instruments can be made variable by adjusting the travel length L of the FTS ($\Delta\nu \approx c/4L$). This technique facilitates, in principle, observations of the galactic center ($c/R = 60$ kms^{-1} with $R = 5000$), nearby galaxies with velocities of 100 – 200 kms^{-1} ($R = 1500$ – 3000), and distant galaxies with $c/R \geq 500$ kms^{-1} ($R \leq 500$). However, by using a FTS a penalty in observation speed is paid by having to sample the source as a function of path length. Thus high resolution scans will take a considerable amount of time. To avoid this time penalty, a grating spectrometer with multiple detector elements may be used. This

technique considerably speeds up the detection process, however at a cost of a fixed frequency resolution. Nikola and Bradford *et al.* have successfully used this method with ZEUS [8], and Z-spec [9]. ZEUS is an echelle grating imaging spectrometer, designed for the JCMT [10], with a resolving power $R \sim 1000$. It operates in the 350 μm and 450 μm atmospheric windows. Z-spec complements ZEUS as it operates in the 190 – 310 GHz atmospheric window. It has a resolution of $R \sim 275$ and is operational at the Caltech Submillimeter Observatory (CSO) [11]. Both instruments are used to search for high redshift CO emission (z = v/c) from ultra luminous galaxies with velocities in excess of 1500 kms^{-1}. In the same category, PACS [12] is also a grating spectrometer with $R^{max} = 4000$. It is to be flown on Herschel space observatory.

As a final note, a new class of direct detectors has recently been introduced by Day and Zmuidzinas *et al.* [13]. These detectors are based on a change in the kinetic inductance component of the surface impedance when a superconducting thin-film material absorbs an optical photon. KIDs as they are known, have the advantage that inherent frequency multiplexing of the output channels greatly facilitates large format camera arrays. In principle this technique circumvents the complicated SQUID multiplexing of superconducting transition edge (TES) arrays [14]. The resolving power of kinetic inductance detectors is determined by an antenna or optical bandpass filter response. As such, KIDs are very low spectral resolution devices.

From the above discussion, it is clear that the optimal detector approach is very much dependent on the scientific goals of the experiment, e.g. spectral resolution, bandwidth, throughput, sensitivity, and instrument stability. With so many approaches to choose from, the instrument designer must carefully consider the scientific goals of the experiment [15].

2.2 Incoherent (direct) detection

As alluded to in the previous Section, heterodyne detection suffers from limited bandwidth and quantum noise. Though suitable for high resolution spectroscopy, the direct or incoherent detection mechanism allows for background limited observations over large bandwidth and low spectral resolution. This facilitates the study of broadband continuum emission from a large variety of galactic and extragalactic sources.

The reason that coherent detectors are subject to a quantum noise limit is that the preservation of signal phase results in an uncertainty in the photon occupation number. When expressed as a temperature, the radiation field that produces an equivalent noise equals $h\nu/2k_B$. It is in the submillimeter wavelength regime that the quantum noise limit becomes comparable, or even exceeds the fundamental photon fluctuation noise (Sec. 2.2.3). A submillimeter direct detector, especially under low background conditions, is therefore always more sensitive than a coherent detector.

In the radio, or longer wavelength regime, the thermal energy (KT) dominates the photon energy ($h\nu$), e.g. $KT \gg h\nu$. In the submillimeter both quantities play an important role. For direct detectors at wavelength long wards of 200 μm the photon energy is however too low to use traditional infrared photoconductive detectors. At these frequencies bolometric detectors have proven very successful, with background

limited performance demonstrated in both single pixel and large format arrays [14].

2.2.1 Bolometers

Bolometers are thermal detectors that are used to sense broadband continuum radiation. These devices respond to the square of the signal input, in contrast to coherent detectors which respond to the product of the local oscillator and signal input (Sec. 2.3). Bolometers can however also be used under suitable conditions as heterodyne mixers. In Chap. 4 we discuss the fundamentals of "hot electron bolometers" (HEBs), and in Chap. 6 the IF bandwidth and mixer conversion gain.

Fig. 2.1 shows the model of a classic bolometer. An incoming photon raises the temperature in the absorber with heat capacity C. In this case the absorbing film is weakly coupled via conductance G to a thermal bath T_0. In its most fundamental form the energy balance of the absorber can be described by

$$C\frac{\partial(T_b - T_0)}{\partial t} + G\Delta T = P_s \ . \tag{2.1}$$

$\Delta T = (T_b - T_0)$ and P_s is the incoming power flow (photons). In steady state $\partial\Delta T/\partial t$=0 and ΔT=P$_s$/G. Solving Eq. 2.1 for T_b yields

$$T_b = T_0 + \frac{P_s}{G}e^{-t/\tau} \ , \tag{2.2}$$

with τ=C/G the thermal time constant of the system. Sensitivity is maximized by reducing G. However, in doing so τ increases. This is generally undesirable. Thus to keep τ small (or constant), the heat capacity of the absorber also needs to be reduced. This is typically achieved by utilizing smaller area devices. And since the resistance of the absorbing film depends on the temperature (T$_b$), a simple current source may be employed to sense the incoming radiation. In practice the situation

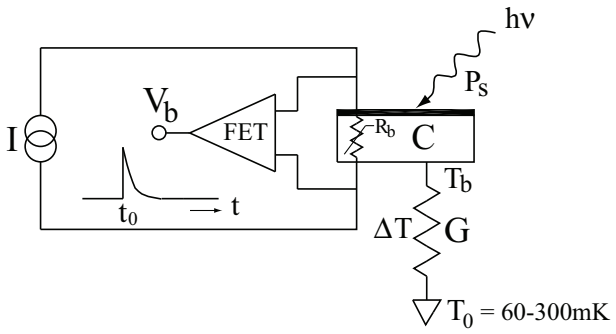

Figure 2.1: Fundamental model of a bolometer. Sensitivity is optimized by reducing the thermal conductance G, thereby increasing ΔT. In doing so the thermal response time τ increases, unless the thermal capacitance C of the absorber is decreased. This is usually accomplished by reducing the area of the bolometer. The bolometer resistance is chosen to be a strong function of temperature at the operating condition.

is a bit more complicated as the bias is ordinarily modulated to stay away from $1/f$ noise in the detector and FET low noise amplifier (Fig. 2.1). It is generally desirable therefore to have the bolometer respond with maximum ΔT, and short thermal time constant τ. This allows for synchronous detection, the rapid differencing of source and background signals (chopping), away from the $1/f$ knee in the power spectrum of the device and atmospheric fluctuation noise. Aside from these issues it is also very important to operate the bolometer as close as possible to the theoretical (photon fluctuation dominated) background, while keeping the bolometer power saturation (linearity) in concurrence with its application.

The signal to noise ratio (SNR) of a direct detector system may be defined as

$$SNR = \frac{P_s}{NEP}\sqrt{2T_{int}}\ , \tag{2.3}$$

where T_{int} is the effective integration time, and the NEP the "Noise Equivalent Power". The factor 2 takes into account a multimode sensitive detector element[1]. Since the NEP of a direct detection system is defined as the rms signal which produces a SNR = 1, we find in the Rayleigh-Jeans limit with $P_s = 2k_B T_s \Delta\nu$ (factor 2 for both polarizations) that the

$$NEP = 2k_B T_s \Delta\nu \sqrt{2T_{int}}\ \ (W/\sqrt{Hz})\ . \tag{2.4}$$

Note that the NEP decreases linearly with decreasing bandwidth ($\Delta\nu$). Thus by increasing the resolving power of the instrument ($\Delta\nu = \nu/R$, Sec. 2.1), for instance by using a FTS or echelle grating, a lower detector NEP will be required to stay background limited.

The responsivity of a bolometer is defined as the change in voltage drop per Watt of absorbed power

$$S_v = \frac{V}{P_s} = I\frac{\partial R}{\partial T}\frac{T}{P}\ \ (V/W)\ . \tag{2.5}$$

S_v can be linked to an NEP via V_n/S_v, where V_n equals the (measured) noise voltage.

Often however it is more convenient to measure the electrical responsivity of a bolometer (S_e) via the so called isothermal technique [16]. In this case the quantum efficiency of the bolometer is not included, e.g. $S_v = \eta_q S_e$. Note that for a high quality bolometer $\eta_q \sim 0.5$. In many cases it is found that the NEP of bolometers scales with the square root of the area. This is certainly the case with the photon fluctuation noise of Sec. 2.2.3. If τ is held constant, then $G \propto A$ and $S \propto A^{-1}$ so that the specific detectivity $D^*=\sqrt{A}/\mathrm{NEP}$ is approximately constant, and thus a useful figure of merit [16].

Aside from fundamental photon fluctuation noise, there are many additional sources of excess noise that contribute to the overall NEP of a bolometer. Examples are the thermal fluctuation noise of the absorbing element (Johnson noise), phonon noise and $1/f$ noise. Of these three Johnson noise is the most dominating. Since these noise sources may be assumed uncorrelated, we can add the mean square fluctuations to estimate the sensitivity of the bolometer, e.g.

[1] In the printed version the factor 2 was erroneously attributed to a 50 % chopping efficiency.

$$NEP^2 = NEP_{ph}^2 + NEP_e^2 \ , \tag{2.6}$$

where

$$NEP_e^2 \approx 4k_B T_b G \ . \tag{2.7}$$

In an ideal detector with background limited performance (BLIP) the first term of Eq. 2.6 dominates. This is the subject of Sec. 2.2.4, however as a frame of reference neutron-transmutation-doped (NTD) germanium thermisters at 300 mK have achieved NEPs of $\sim 1 \times 10^{-16} W/\sqrt{Hz}$ and τ=11 ms [17]. At 100 mK bath temperature the NTD Germanium response improves to $2 \times 10^{-17} W/\sqrt{Hz}$ with a τ=30 ms [18]. Richards *et al.* has reported a NEP as low as $7 \times 10^{-18} W/\sqrt{Hz}$ with a τ=6 ms [16]. And finally, the spider web bolometers developed for SPIRE [6] on Herschel [7] have a rated NEP of $\sim 2 \times 10^{-18} W/\sqrt{Hz}$. The latter value is well below the thermal background provided by the space observatory. For high background ground observations a noise equivalent power on the order of a few times $10^{-15} W/\sqrt{Hz}$, or better, suffices for low resolving powers since atmospheric transmission and emissivity from the sky dominate the noise budget (Sec. 2.2.4).

2.2.2 TES

Classical bolometers as the one described above work very well. However, in the push towards large format cameras (> 300 pixels) there is an issue with the maximum number of signal wires that may be routed in/out of the cryostat. To circumvent this problem, superconducting transition edge sensors (TES) integrated with SQUID multiplexing readout arrays are being investigated. For example, SCUBA-2 is a 10,000 pixel submillimeter camera [14] based on TES technology. The superconducting multiplexing readout is necessary to manage the large number of signal wires coming from the 300 mK work surface.

The TES uses the superconducting film transition where the resistance is an extremely steep function of temperature. Actual sensors are open structure, and do not use a feedhorn or antenna to couple in the radiation. Thus they are sensitive to a field of view (FOV) of $\sim \ \pi$ steradian. To define the beam with a top-hat like telescope illumination, Liot cold stops at various places in the optical chain are being used.

2.2.3 Photon fluctuation noise

As alluded to in the previous Section, fundamental noise in bolometers is limited by fluctuations in the photon arrival rate. This statistical fluctuation with time has to do with the quantum nature of photons, and is known as the background limit. For a single mode, the photon occupation number is given by the Bose-Einstein formula

$$n_0 = \frac{1}{e^{h\nu/k_B T} - 1} \ , \tag{2.8}$$

where T is the effective blackbody radiation temperature. The uncertainty in optical power has been discussed by a great number of people [19, 20, 21] and can for a single mode be expressed as

$$\sigma_{ph}^2 = \frac{(h\nu)^2 \Delta\nu}{\eta_q^2 T_{int}} [\eta_q n_0 (1 + \eta_q n_0)] \ . \tag{2.9}$$

This expression is identical to Lammarre *et al.* [19] with P, the degree of polarization, equal to zero and $A\Omega/\lambda^2 = 1$ (single mode diffraction limited beam). In the radio regime with $k_B T \gg h\nu$ ($n_0 \gg 1$), Eq. 2.9 reduces to the Dicke Radiometer equation (Eq. 3.1). In the optical regime where Poisson statistics dominate, we have $h\nu \gg k_B T$ ($n_0 \ll 1$) and Eq. 2.9 reduces to [20]

$$\sigma_{ph}^2 = \frac{(h\nu)^2 n_0 \Delta\nu}{\eta_q T_{int}} \tag{2.10}$$

In the submillimeter and terahertz, we operate in a regime where $n_0 \sim 1$, and both terms in Eq. 2.9 need to be considered.

To estimate the photon background limit we need to convert σ_{ph} to a noise equivalent power. This can be done by considering how observations are made. To circumvent system instabilities (Appendix A) synchronous detection, e.g. chopping between source and background via a nutating mirror, is usually applied. This reduces the observing efficiency by a factor of two in time. And because the signal for astronomical observations is deeply embedded in the noise, subtraction of the two essentially white noise signals (Gaussian distribution) increases the noise by $\sqrt{2}$. The SNR is thus given by

$$SNR = \frac{P_s}{\sqrt{2}\sqrt{2}\sigma_{ph}} \ . \tag{2.11}$$

Via Eq. 2.3 we obtain the photon noise dominated NEP ($\mathrm{W}/\sqrt{Hz}$), defined in 1 s integration time, as

$$NEP_{ph} = 2\sqrt{2}\sigma_{ph} \ . \tag{2.12}$$

Note that this quantity is referred to the input of the detector.

2.2.4 Emissivity, optical efficiency, and sky noise

Use of a telescope for observations will give additional sources of photon noise, of which the dominant ones are thermal noise due to a finite telescope temperature, and Ohmic loss in the optics chain. There is also the issue of optical coupling efficiency, and for ground based observations the non-negligible thermal noise of a partially transparent sky (Sec. 2.4). To include these effects, we incorporate in Eq. 2.9 the emissivity ε of an equivalent blackbody with radiation temperature T, and transmittance τ. It is important to quantize these numbers if background limited performance (detector noise < photon noise) observations are to be achieved. We thus obtain the generalized variance of the photon noise as

$$\sigma_{ph}^2 = \frac{(h\nu)^2}{\eta_q T_{int}} N_m \Delta\nu (\varepsilon\tau n_0)(1 + \varepsilon\tau n_0 \eta_q) \ . \tag{2.13}$$

N_m are the number of modes (2 for both polarizations). For a perfect blackbody the emissivity equals the absorbtivity or (1-Γ^2), where Γ^2 is the optical voltage reflection coefficient. For metallic mirrors the emissivity can be approximated as ε_m=$0.1\lambda_{\mu m}^{-0.5}$ [19]. Rewriting Eq. 2.13 in terms of the resolving power R and NEP_{ph} yields

$$NEP_{ph}^2 = \frac{8(h\nu)^2}{\eta_q R} N_m \nu(\varepsilon\tau n_0)(1+\varepsilon\tau n_0\eta_q) \quad (W^2/Hz). \tag{2.14}$$

Thus the higher the resolving power the lower the photon noise, and the more sensitive the detector has to be. Note that the NEP_{ph} is referred to the detector input. To refer it to the telescope input, or the top of the atmosphere as the case may be, one has to divide by the instrument optical efficiency (η_{opt}), telescope spillover efficiency (η_s), and atmospheric transmission (η_{atm}).

So far we have ignored the astronomical background. In low background observations (space) galactic and Zodiacal foreground emission can not be ignored. From Lamarre *et al.* [19] we estimate a $\mathrm{NEP}_{ph,space}$ of $2.25\times10^{-18}/\sqrt{R}$ in the 0.3 – 3 THz frequency range. The $\mathrm{NEP}_{ph,space}$ may be added in a statistical manner since the noise is uncorrelated from the other noise sources.

For terrestrial observations the atmospheric transmission, η_{atm}=$e^{-\tau_{atm}}$, is incorporated in the general emissivity via

$$\varepsilon = \varepsilon'_m + (1-\varepsilon'_m)[(1-\eta_s) + \eta_s(1-\eta_{atm})] \ . \tag{2.15}$$

In Eq. 2.15 ε'_m is the overall emissivity of the telescope mirrors, and η_s the telescope spillover, or forward efficiency ($\sim$ 0.9). Defined in this way, (1-η_s) is that part of the beam which terminates somewhere in the (warm) telescope. The sky temperature, for use in the mode occupation number n_0, can be estimated from T_{sky}=$0.95\mathrm{T}_{amb}$. In case of a space telescope T equals the equivalent telescope temperature.

2.2.5 Background limited detection

The next three examples demonstrate the effect that emissive telescope structures and the atmosphere have on the photon background limit. This limit is a useful figure of merit as it sets a sensitivity requirement on the described incoherent detectors.

2.2.5.1 Example 1: A 80 K space telescope

SPIRE [6], the imaging Fourier transform spectrometer instrument on Herschel [7], has a resolving power of $R \sim 1000$. Assuming a telescope emissivity of ε=0.04, telescope temperature of 80 K, 50 % detector quantum efficiency, 50 % instrumental optical efficiency (η_{opt}), frequency of operation 850 GHz (350 μm), sensitivity to both polarizations, and a 90 % spillover efficiency, we find that $n_0 = 0.601$, and that to be background limited the SPIRE detector NEP has to be less than 1.4×10^{-17} W/$\sqrt{Hz}$. In fact the SPIRE detector NEP $\sim 2\times10^{-18}$, which ensures that the instrument is indeed limited by the photon background.

To estimate the NEP referred to the output of the telescope we have

$$NEP_{ph}^{tel} = \sqrt{\left(\frac{NEP_{ph}}{\eta_q \eta_{opt} \eta_s \eta_{atm}}\right)^2 + NEP_{ph,space}^2}\ , \tag{2.16}$$

or $6.4{\times}10^{-17}$ W/$\sqrt{Hz}$ ($\eta_{atm} = 1$).

Note that $n_0 = 0.6$ indicates that we are indeed midway between the optical and radio regimes. In this case, some of the photons are bunched and both terms of Eq. 2.14 need to be used to properly describe the photon statistics.

2.2.5.2 Example 2: A 4 K (cooled) space telescope

Now lets us assume the same specifications as above, but with the telescope cooled to 4 K. In this case the background limit is $1.1{\times}10^{-19}$ W/$\sqrt{Hz}$, a significantly more difficult requirement. $\mathrm{NEP}_{ph}^{tel} = 5.1{\times}10^{-19}$ W/$\sqrt{Hz}$.

2.2.5.3 Example 3: A warm ground based telescope

As a third example let's assume a direct detector with similar specifications as in the example 1, but now located at Chajnantor, Chile. The instrument is again operational in the 350 μm atmospheric window under 0.5 mm (25 percentile) precipitable water vapor condition with an ambient temperature of 273 K and airmass $A = 1.0$. η_s is again 90 %, however the telescope emissivity has increased to 0.1 (larger telescope, higher surface rms and more blockage). From Fig. 2.8 we have an atmospheric transmission of 50 %. ε is therefore 0.64, and n_0=0.861. To achieve BLIP conditions, the bolometer NEP should be $\leq 5.2{\times}10^{-17}$ W/$\sqrt{Hz}$. This is readily achieved with today's technology. Thus to gain more sensitivity one is left with increasing the telescope aperture for point source observations (diffraction limited beam size = 1.22 D/λ) and/or increasing the number of pixels. The NEP referred to the top of the atmosphere (Eq. 2.15) is $4.6{\times}10^{-16}$ W/$\sqrt{Hz}$. Excess voltage noise has been ignored in the discussion, thus the above given NEP is somewhat optimistic. This result is for a resolving power of 1000. For $R = 10$, the NEP referred to the top of the atmosphere becomes $4.6{\times}10^{-15}$ W/$\sqrt{Hz}$.

Some final notes: Johnson (electronics) noise is minimized by lowering the bath temperature T_b (Eq. 2.7). Low background bolometers are therefore operated below 100 mK. For ground based bolometers this requirement may be relaxed to 300 mK as shown by the required NEPs in this example.

Lamarre *et al.* (1995) [19] showed that for a wavelength < 400 μm the telescope temperature is the dominating factor in meeting the background limited BLIP condition. For $\lambda > 400$ μm both emissivity and temperature are important and thus low emissive telescope/mirror designs must be utilized.

2.3 Coherent (heterodyne) detection

In this section we present a variety of coherent detection concepts. These form the basis for the heterodyne detection techniques discussed in this thesis.

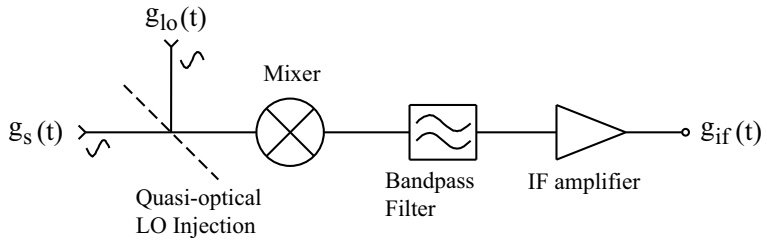

Figure 2.2: Fundamental layout of a heterodyne double sideband (DSB) receiver. The local oscillator signal $g_{lo}(t)$ and input signal $g_s(t)$ are combined and coupled to a non-linear device, "the mixer". In the mixer the two signals are than multiplied, with the difference product (intermediate frequency) filtered and amplified.

A heterodyne receiver down-converts the RF signal to a lower intermediate frequency (IF) without loss of phase. This stands in contrast to the incoherent detection described in the previous Section. The purpose of down-converting the signal to a lower frequency is that commercial low noise electronics can than be used in the signal post detection process.

A characteristic of heterodyne detection is the preservation of signal phase. This feature of the heterodyne down-conversion process is well suited for arraying multiple antennas. This technique is known as interferometry (Chap. 3) and effectively synthesizes a larger telescope area, thereby enhancing the instrument sensitivity. Good examples are ALMA [1], the SMA [4], IRAM [3], and OVRO/CARMA [2]. The IF output signal is usually processed by a high resolution backend spectrometer or correlator. In the case of a single dish antenna an acousto-optical spectrometer (AOS) [22, 23] or fast Fourier transform spectrometer (FFTS) [24] is typically employed. Interferometers (Chap. 3) have their IF outputs signals cross-correlated by either a commercial [25] or custom build digital correlator. The preservation of phase in a heterodyne system is also the foundation of modern day communication systems. Examples include phase modulation in mobile phones, radio communication, and satellite telemetry.

To understand the mechanism of heterodyne detection we depict in Fig. 2.2 the layout of a fundamental double sideband (DSB) heterodyne receiver. The block diagram is very similar to the schematic layout of the single-ended receiver in Fig. 3.2. Refering to Fig. 2.2, the input signal $g_s(t)$ is multiplied by a local oscillator signal $g_{lo}(t)$ as:

$$\begin{aligned} g_s(t) \times g_{lo}(t) &= V_s cos(\omega_s t + \varphi_s) V_{lo} cos(\omega_{lo} t + \varphi_{lo}) \\ &= \frac{V_s V_{lo}}{2} \big[cos[(\omega_s + \omega_{lo}) + (\varphi_s + \varphi_{lo})] + cos[(\omega_s - \omega_{lo}) - (\varphi_s + \varphi_{lo})] \big]. \end{aligned} \tag{2.17}$$

For an ideal mixer with unity mixer gain and $V_s = V_{lo} = 1$, the mixer IF output, after passing through an appropriate bandpass filter, thus becomes

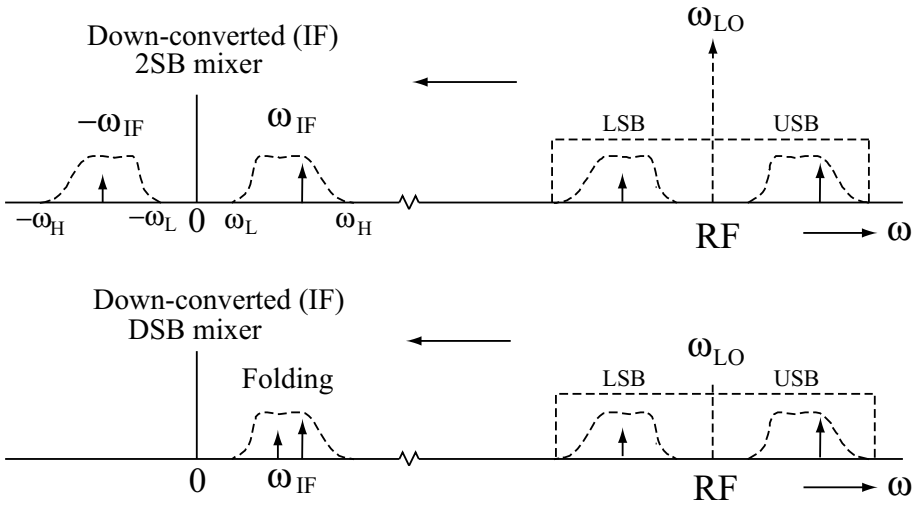

Figure 2.3: Schematic representation of heterodyne detection. The signal of interest is combined with a strong local oscillator signal and down-converted to an intermediate frequency ν_{IF}. *Top*) 2SB mixer. At the mixer IF output a mathematically negative frequency will be positive, with a 180° phase shift. *Bottom*) DSB mixer. See text for details.

$$g_{if}(t) = cos(\mid \omega_s - \omega_{lo} \mid t \mp \varphi_{if}) \ . \tag{2.18}$$

φ_{if} is the down converted phase, $(\varphi_s + \varphi_{lo})$. The sign of φ_{if} depends on whether the IF frequency is mathematically positive or negative. From the above expression it is clear that phase jitter, or frequency modulation noise (FM) on the local oscillator signal will place a limit on the maximum achievable frequency resolution of the down-converted IF signal. In telecommunication systems stringent requirements on the phase stability of local oscillators is therefore a common requirement. From Eq. 2.18 it is evident that if the signal frequency is greater than the LO frequency ($\omega_s > \omega_{lo}$), that the corresponding intermediate frequency is positive. Such a signal is said to be in the upper sideband (USB). If however the signal frequency is less than the LO frequency ($\omega_s < \omega_{lo}$) the intermediate frequency is mathematically negative, and the signal will reside in the lower sideband (LSB). This process is graphically shown in the top panel of Fig. 2.3. Of course negative IF frequencies do not exist (time only moves forward), and the down-converted lower sideband will be present as a positive frequency in the 2SB receiver IF output, albeit with a 180 phase shift. For a double-sideband receiver, the upper and lower sidebands fold in the IF. This is undesirable for many applications, and significant efforts have been expanded to design mixers that separate the upper and lower sidebands at the IF output. In Chap. 3 we take a close look at these mixers configurations, and in Chap. 8 we present the design, fabrication, and measurement of a 600 – 720 GHz [26] sideband separating receiver.

In practice the signal, or astronomical line, will be present in either the upper or lower sideband. The sideband the received signal resides in is often referred to as

the "signal" sideband, with the opposite sideband than being the "image" sideband. These nomenclatures will be used quite extensively in the remaining chapters of the thesis. It should also be noted that an astronomical line placed in the upper sideband will move in a negative frequency direction with increasing LO frequency, whereas an astronomical line in the lower sideband will move in a positive frequency direction with increasing LO frequency. In other words, a change in LO frequency results in either a positive or negative translation, depending which sideband the astronomical line resides in. This feature is extensively used to verify which sideband the received signal resides in. Fig. 2.3 demonstrates this principle.

As a final note, the down-conversion process may also be understood in Fourier space by the principle of frequency shifting [27]. In this case, let $g_s(t)$ again be the RF signal, than

$$\begin{aligned} \mathcal{F}\big[g_s(t)e^{i\omega_s t}\big] &= \int_{-\infty}^{\infty} g_s(t)e^{i\omega_s t}e^{-i\omega t}dt \\ &= \int_{-\infty}^{\infty} g_s(t)e^{-i(\omega-\omega_s)t}dt \\ &= G(\omega-\omega_s)\ . \end{aligned} \tag{2.19}$$

If now $g_{lo}(t) = cos(\omega_{lo}+\varphi_{lo})$ we obtain, using Eulers identity, the spectrum in phasor notation as

$$\mathcal{F}\big[g_s(t)cos(\omega_{lo}+\varphi_{lo})\big] = \frac{1}{2}\Big[G(\omega_s+\omega_{lo})e^{-i\varphi_{if}} + G(\omega_s-\omega_{lo})e^{i\varphi_{if}}\Big] \tag{2.20}$$

Again, by means of an appropriate bandpass filter the difference frequency (IF) can be selected. It is however important to note that there are many occasions where up-conversion, filtering, and down-conversion is more appropriate if interference of harmonic content (intermodulation) is to be avoided. A more detailed description is beyond the scope of this thesis as in the submillimeter and terahertz harmonic content, thanks to device parasitics, can usually be ignored.

2.3.1 Sensitivity of a heterodyne receiver

An important characteristic of heterodyne receivers is the added noise, and efficiency of the down-conversion process. A practical mixer (or amplifier) adds noise in the form of thermal, quantum, flicker ($1/f$), and/or shot noise. In addition, a mixer has conversion efficiency, commonly known as mixer gain. This process is somewhat similar to amplifiers, with the exception that amplifiers have by definition a gain greater than unity, whereas mixers typically exhibit a conversion gain less than unity and have an output frequency that is by definition different from the input frequency. (In Chap. 4 we discuss SIS mixers which due to their quantum nature can in principle have a mixer conversion gain). It is often convenient to consider a mixer, or amplifier, as being lossless with an equivalent noise source at the input. In Fig. 2.4 we demonstrate this mechanism. Mathematically we can describe this situation as

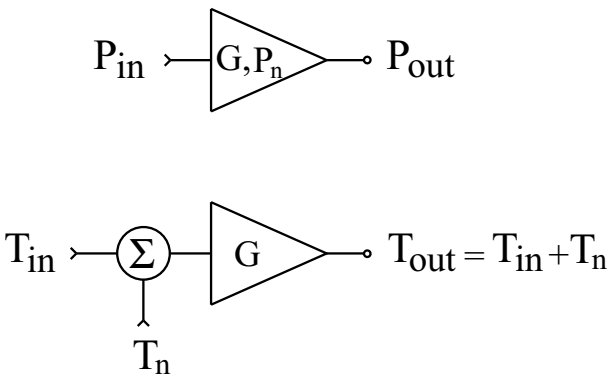

Figure 2.4: *Top*) Definition of equivalent noise power referred to the input of a mixer or amplifier. *Bottom*) Circuit description of an amplifier with noise temperature T_n.

$$P_{out} = G(P_{in} + P_n) \ . \tag{2.21}$$

G is the gain, P_{in} the noise presented to the input, and P_n the equivalent noise temperature of the device. And because radio-astronomy and microwave instrumentation operates in the Rayleigh-Jeans limit of the Planck blackbody power spectrum (a 77 K blackbody has a peak radiation at 3.9 μm, or 76 THz) noise powers are typically expressed in terms of equivalent temperature via P = k_BT. We can therefore re-write Eq. 2.21 as

$$T_{out} = G(T_{in} + T_n) \ , \tag{2.22}$$

and thus the noise refered to the input of the mixer becomes

$$T_n = \frac{T_{out}}{G} - T_{in} \ . \tag{2.23}$$

In electrical engineering applications, it is common practice to express the noise temperature of a device as a noise figure (F) via

$$F_{db} = 10log_{10}(1 + T_n/T_0) \ . \tag{2.24}$$

T_0 is referenced to room temperature, 290 K by definition.
For an ideal instrument with no added noise ($T_n = 0$) and unit conversion gain we have the situation that $T_{in} = T_{out}$. In practice having a heterodyne receiver with a zero Kelvin noise temperature is physically impossible by virtue of the Heisenberg uncertainty principle. This can be understood from the phase coherent down-conversion process where uncertainty in the photon occupation number results in at least half a quantum of noise (hν/2k) being present at the input of the receiver. Whether this half a quantum of noise is attributed to the blackbody input load (the mixer is noiseless in this case), or to the mixer itself is a matter of convention. In actual superconducting heterodyne receivers the sensitivity ranges from a few to 10 times the quantum noise

limit. The Planck formulation of a true blackbody assigns the half a quantum of noise to the mixer. The Callen & Welton definition [28, 29] assigns it to the input load. For reference we give here both definitions. In a unit bandwidth

$$P_{Planck}(T,\nu) = \frac{h\nu}{e^{h\nu/k_BT}-1} = n_0 h\nu, \tag{2.25}$$

and

$$P_{CW}(T,\nu) = \frac{h\nu}{e^{h\nu/k_BT}-1} + \frac{h\nu}{2} = (n_0+\frac{1}{2})h\nu \ . \tag{2.26}$$

In the Rayleigh-Jeans limit ($h\nu \ll k_BT$) $\mathrm{P}_{CW} \sim \mathrm{P}_{RJ}$, and P_{Planck} is always half a photon below P_{CW}.

If we now cascade m devices, each with a noise temperature and gain referred to the input, it is easy to show that the equivalent noise temperature of the cascaded chain will be given by

$$T_{eq} = T_1 + \frac{T_2}{G_1} + \frac{T_3}{G_1G_2} + \cdots + \frac{T_n}{G_1G_2\cdots G_{n-1}} \tag{2.27}$$

This formulism of the equivalent noise temperature of a cascaded chain is useful in determining the overall noise temperature of a receiving system (Eq. 7.6).

To quantify the equivalent noise of a receiver or amplifier the "Y-factor" method is usually employed. Here a blackbody radiator with known (calibration) temperature is connected to the device under test (DUT). Under the assumption that the output of the receiver or amplifier responds linearly to a change in input noise temperature (Eq. 2.22), the equivalent noise temperature is then readily obtained via

$$T_{eq} = \frac{T_{hot} - YT_{cold}}{Y-1} \ . \tag{2.28}$$

Y is the ratio of the corresponding output powers (P_{hot}/P_{cold}). It is common to use the Callen & Welton definition for the equivalent noise temperatures of the blackbody input load. If there is (optical) loss between the blackbody radiator and the device under test, then this may be taken into account via the procedure outlined in Sec. 5.1.2. In receiving systems T_{eq} is usually referred to as T_{rec}^{DSB} with noise being contributed by both sidebands. For an ideal SSB receiver, $\mathrm{T}_{rec}^{SSB} = 2\mathrm{T}_{rec}^{DSB}$. A procedure to derive the DSB receiver noise temperature of a SIS receiver using the Tucker theory (Chap. 4) is provided in Sec. 4.1.7.3.

2.3.2 Conversion of NEP to system noise temperature

It is sometimes convenient to express the NEP ($\mathrm{W}/\sqrt{Hz}$) in temperature units (K). This also facilitates comparison between coherent and incoherent systems. Caution is warranted however when comparing direct detection systems with heterodyne receivers as the former is primarily designed to measure broadband continuum and the latter vibration and rotational atomic and molecular fine line transitions. Nevertheless, for medium resolution direct detection systems such as PACS, SPIRE, Z-Spec, and ZEUS it can be useful.

The noise equivalent flux density, referred to the top of the atmosphere is given by

$$NEFD = \frac{NEP_{ph}}{A_e \Delta\nu} \quad (Jy/\sqrt{Hz}). \tag{2.29}$$

A_e is the effective antenna aperture ($\eta_A A_{tel}$), $\Delta\nu$ the resolution bandwidth (ν/R), and η_A the telescope aperture efficiency. 1 Jy is the unit of flux density, defined as 10^{-26} $\mathrm{Wm^{-2}Hz^{-1}}$. The flux density sensitivity in units of $\mathrm{Wm^{-2}Hz^{-1}}$ of a direct detector is

$$S_v^{dd}(rms) = \frac{NEFD}{\sqrt{n 2 T_{int}}} \ , \tag{2.30}$$

where n is the number of samples taken in case of a FTS direct detector. The factor of two accounts for the on - off source chopping efficiency (50 %).

For a double sideband heterodyne receiver noise temperature T_{rec}^{DSB} the single sideband (SSB) system temperature referred to the top of the atmosphere is given by Eq. 2.41. The antenna temperature, inclusive of a factor 2 due to chopping efficiency (Sec. 2.3.5) can be obtained from the Dicke or radiometer equation (Eq. 3.1)

$$T_A^* = \frac{2 T_{sys}^{SSB}}{\sqrt{\Delta\nu T_{int}}} \quad (K) \ , \tag{2.31}$$

with T_A^* related to the flux density via [30]

$$S_v^{het}(rms) = \frac{2 k_B T_A^*}{A_e \eta_{mb}} \ . \tag{2.32}$$

Note that for a single mode (Gaussian) telescope illumination $A_e\Omega/\lambda^2 = 1$. Equating S_v^{dd} to S_v^{het} and solving for T_{sys}^{SSB} yields

$$T_{sys}^{SSB} = \frac{\eta_{mb} NEP}{4\sqrt{2n} k_B \sqrt{\Delta\nu}} \ . \tag{2.33}$$

For example, the photon background limited direct detector in example 3 (Sec. 2.2.5.3) has, with $n = 1$, and $\eta_{mb} = 0.7$, an equivalent $T_{sys}^{SSB} = 142$ K. This can be compared to the record NbTiN twin-slot DSB receiver of Chap. 5 ($T_{rec}^{DSB} = 205$ K) via Eq. 2.41, by using the same atmospheric and telescope conditions. In this case $T_{sys}^{SSB} = 1580$ K. In other words, we see that the direct detector of example 3 is eleven times more sensitive. Caution is warranted however since we have taken $n = 1$, and have ignored electronic noise in the detector. On a point source, the sensitivity of a FTS based direct detector will decrease by $\sqrt{n}$. This explains the popularity of multi-pixel grating spectrometers such as ZEUS, Z-spec, and PACS [8, 9, 12].

As a final note, the flux density to temperature conversion of a given telescope may be obtained by dividing S_v^{het}/T_A^*. In units of Jy/K this gives

$$\frac{S_v^{het}}{T_A^*} = \frac{2.76 \times 10^3 Jy}{\eta_A A_{tel} \eta_{mb}} \ . \tag{2.34}$$

For the CSO, with a telescope diameter of 10.4 m, a low frequency main beam efficiency of 70 %, and an aperture efficiency of $\sim$ 90 %, $S_v^{het}/T_A^* = 51$ Jy/K. Thus a 150 μK line equates to 7.6 mJy of flux.

2.3.3 IF Bandwidth

Another important mixer parameter is the IF bandwidth. It has direct bearing on the time efficiency of spectral line surveys as demonstrated in Fig. 2.5. It follows that an increased IF bandwidth allows for the simultaneous observation of several (or many) molecular lines. A large IF bandwidth is also important in the measurement of broad emission lines from external galaxies.

Not until quite recent (1995), the IF bandwidth of heterodyne SIS receivers was limited by the availability of low noise amplifiers to approximately 500 MHz. This put a significant constraint on the maximum observable linewidth ($\sim$ 400 kms^{-1} at 345 GHz), and even less at higher frequencies. It meant that only molecular line transitions of galactic sources and some nearby galaxies could be observed. Though considered small these days, it was enormous in comparison to the IF bandwidth afforded by the thermal relaxation time of the InSb hot electron bolometer [31]. These offered IF bandwidth of just a few MHz, and to build up a spectrum the LO had to be scanned!

Today's technology has changed all that. IF bandwidth of 4 GHz, and higher are possible thanks to advances in SIS junction and low noise InP MMIC technology

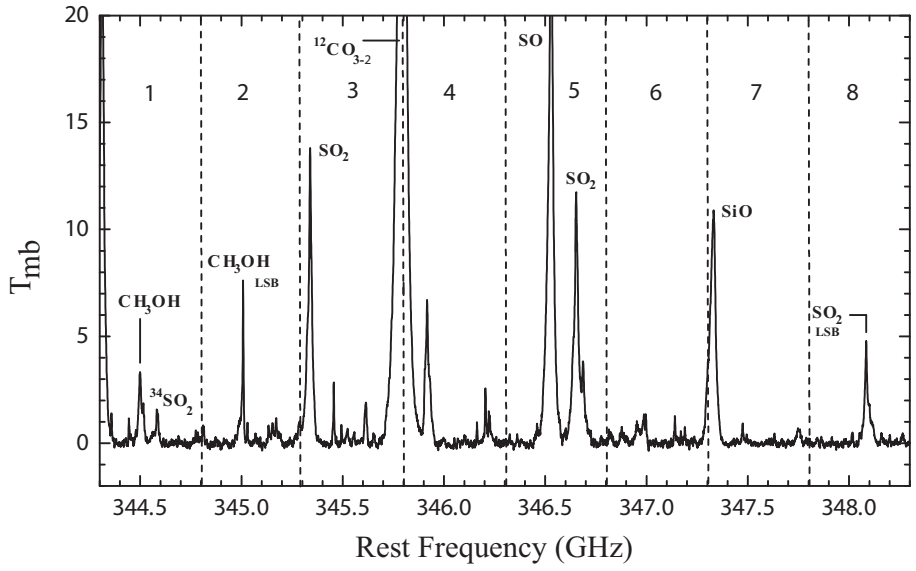

Figure 2.5: Spectrum towards Orion-KL taken from the Caltech submillimeter Observatory. Today's technology provides 4 GHz, or even 8 GHz, of instantaneous IF bandwidth. This has not always been this way. Early on, surveys [35, 36] used IF bandwidth as small as 500 MHz as demonstrated by the dashed lines.

(Chaps. 7 & 8). To demonstrate the significance we show an Orion-KL spectrum obtained with Trex, the technology development receiver described in Chap. 7 [32]. What used to take 8 observations (or 4 with 1 GHz IF bandwidth [33, 34]) now takes just one.

Significant, IF bandwidths of 4 or even 8 GHz allow for observations of distant galaxies with ~ 3000 kms^{-1} linewidth. With the increased IF bandwidth, instrument stability as discussed in Sec. 2.3.5, Chap. 7, and Appendix A becomes of utmost importance.

As a final note, HEB mixers operating in the terahertz regime have a limited IF bandwidth due to the thermal time constants of the electron-phonon interaction time and phonon escape time (Chap. 6). The IF gain bandwidth of NbN based hot electron bolometers is limited to approximately 3 – 5 GHz. In practice essentially all HEB mixers operate at IF frequencies below 4.8 GHz with practical IF passbands of 1 – 2.4 GHz [37, 38]. This puts a similar velocity coverage constraint on the HEB mixers as the SIS mixers experience in the early days. For example, a $\Delta\nu = 1$ GHz at 1.900 THz (C^+) gives maximum velocity resolution of 160 kms^{-1}, just barely enough for observations toward the galactic center. For the HIFI instrument, with an IF bandwidth of 2.4 GHz, a maximum velocity coverage of 380 kms^{-1} at 1.900 THz is possible.

2.3.4 RF Bandwidth

The first submillimeter heterodyne SIS receivers had RF instantaneous bandwidths of just a few GHz [39]. Integrated SIS junction RF matching networks (Sec. 4.1.8) coupled to wide bandwidth (fixed tuned) waveguide probes, and antenna coupled quasi-optical mixers (Chap. 5) changed all that. Today with the advent of high current density AlN barrier junctions and modern electromagnetic simulations tools such as HFSS [40], Sonnet [41], and Supermix [42] instantaneous RF bandwidth of 140 GHz or more are possible (Chap. 7).

HEB mixers, having very little parasitic capacitance, are sensitive to a large range of photon energies. They can be coupled to with either waveguide or open structure antennas (Sec. 4.3). The very large instantaneous RF bandwidth of these devices is liable to result in direct detection (see Sec. 4.3.2), due to a change in heat loading by the different calibration loads. Heat loading on the HEB mixer can however be minimized by either reducing the RF bandwidth (via optical or electrical means) or by reducing the brightness temperature of the calibration loads.

2.3.5 Instrument stability and baseline quality

Throughout the thesis instrument stability is discussed as an important system parameter in establishing time efficient observations. Considering the generally large expense, demand on telescope time, and desired quality of the data products, system stability has become an important design parameter for modern heterodyne instrumentation. In the bottom panel of Fig. 2.6 we depict two simulated spectra from actual HIFI [38] data, as obtained in HEB mixer band 7 during instrument level tests (ILT).

The spectra are shown for four different velocity binning resolutions; native (0.086 kms^{-1}), 1 kms^{-1}, 2 kms^{-1}, and 5 kms^{-1}. To convert the velocity resolution to spectral resolution we use the Doppler relationship $v = c/R$ where $R = \nu/\Delta\nu$. In the example of Fig. 2.6, the LO frequency equals 1.8980 THz (C^+). The corresponding spectral resolution $\Delta\nu$ may thus be obtained as: native 0.5462 MHz [22], 6.33 MHz, 12.67 MHz, and 31.67 MHz. In the top panel of Fig. 2.6 we depict the total power and spectroscopic Allan variance for the total (full) and individual spectrometer subbands. Details on the Allan variance method can be found in Appendix A.

For standard position switch observations the source is observed for a time t_{on}, after which an off-source (t_{off}) reference measurement is taken. The duration of the reference measurement is ordinarily $\sqrt{t_{on}}$. To remove the sky, telescope and instrumental baselines the "on" source signal is subtracted from the "off" source

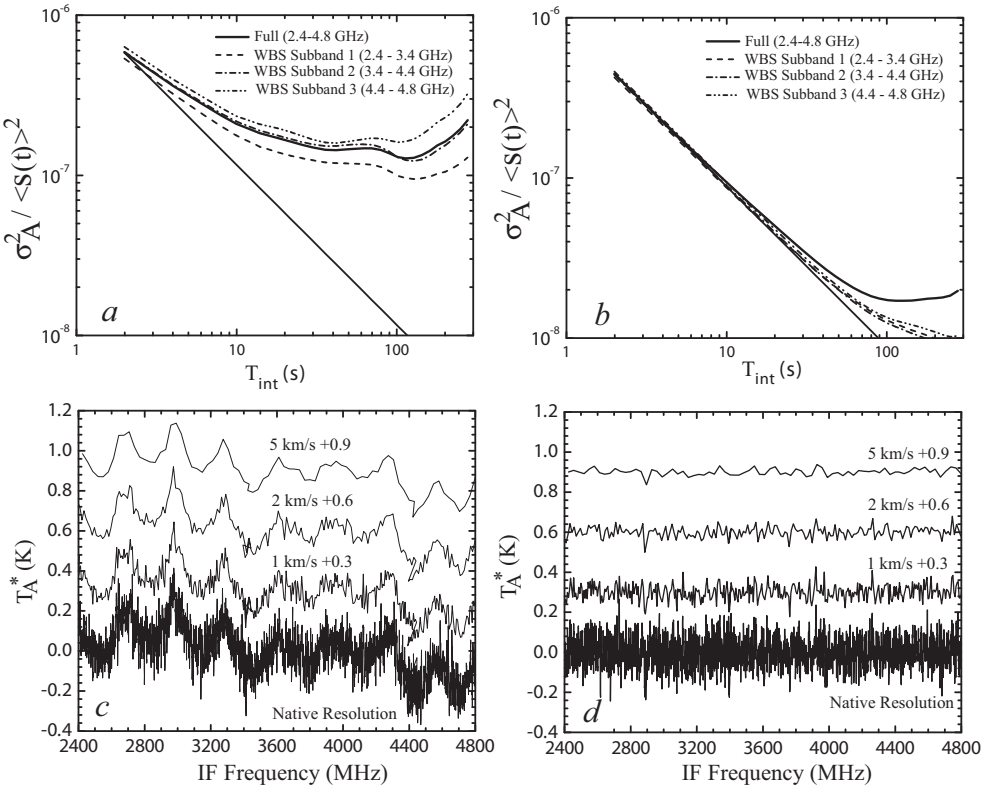

Figure 2.6: *a*) Total power stability of HIFI HEB mixer band 7 at 1.8970 THz. The Allan time, in a fluctuation noise bandwidth of ~ 1.8 MHz, is ≤ 8 s. *b*) Spectroscopic stability (text) with a measured stability time of ~ 80 s. *c*) Synthesized position switched spectrum. Total "on-source" integration time in one 600 s cycle is ~ 464 s, clearly much too long given the stability of the instrument. Severe baseline distortion is the result. *d*) Synthesized double beam switched (DBS) spectrum for different velocity resolutions. Each phase of the chop cycle is 4 s, well below the stability time of the instrument. For a native resolution the theoretical and synthesized 1σ rms noise levels are virtually identical (64 mK vs. 68 mK). Total "on-source" integration time is 2829 s.

signal as part of the calibration routine (Sec. 2.3.6).

For a "stable" receiver (instrument) position switching is the most efficient method of observing, since a relatively large percentage of the time is spent integrating on the source. Unfortunately for HEB based heterodyne receivers, "stable" appears to be a bit of an oxymoron, as evidenced by the total power Allan variance stability measurement of Fig. 2.6a. Typical total power Allan variance times, defined by a $\geq \sqrt{2}$ deviation from the ideal radiometer response, are commonly less than 8 s. The spectroscopic stability is obtained by subtraction of the common mode (Appendix A, Chap. 10), and may be as large as $\sim$ 80 s in a 1.8 MHz noise fluctuation bandwidth ($\Delta\nu$) as evidenced from Fig. 2.6. The data presented here was obtained from measurements on the HIFI instrument [38] during instrument level tests at SRON, the Netherlands. Note that a balanced HEB configuration, by virtue of the in Chap. 8 discussed amplitude noise cancellation properties, is liable to have a significantly enhanced ($\sim$ 10 dB) immunity to environmental and synthesizer induced local oscillator instability (Chap. 10). Recent results by Pantaleev *et al.* appear to bear this out [43].

In panel *c* of Fig. 2.6 we show a synthesized position switched spectrum with an "on-source, slew time, off-source, and again slew time" cycle of 600 s. Total on-source integration time of the entire data set is 2789 s. For the Herschel space observatory the roundtrip slew time is assumed 80 s. In position switch mode, each 600 s cycle thus spends $\sim$ 464 s integrating on the source with the remainder in slew time (80 s) and off-source integration ($\sim$ 56 s). Clearly the "on-off" switching time is way beyond the spectroscopic stability time of the system. This is obvious from the extremely poor baseline quality of Fig. 2.6c.

A far better, though less efficient approach, is to symmetrically beam switch at a rate less than the spectroscopic Allan stability time of the system, by means of nutating mirror. In Fig. 2.6d we show the result of a double-beam switch (DBS) 0.25 Hz "off-on-on-off" chopping pattern. Again each cycle is 600 s and includes one position switch cycle as described above. Including the telescope chopping efficiency and position switch overhead, the total integration time is 2829 s. To estimate T_A^*, and compare it to the 1σ noise obtained from the SSB spectrum of Fig. 2.6d we have included in Eq. 2.31 the chopping efficiency (factor 2 in time), and a factor $\sqrt{2}$ due to the subtraction of two statistically uncorrelated noise levels.

$\Delta\nu$ is the noise fluctuation bandwidth of the spectrometer (1.8 MHz) which is larger than the spectrometer native resolution of 0.5462 MHz. Given a measured DSB HEB receiver noise temperature (in the lower region of the IF band) of $\sim$ 1600 K and assuming equal sideband ratios, we calculate a theoretical 1σ rms noise level of 64 mK. This compares favorably with the, from the spectrum of Fig. 2.6d, obtained 1σ rms noise level of 68 mK (native resolution). Thus we find that symmetric beam switching on time scales less then the spectroscopic Allan time provides proper baseline quality with rms noise levels in agreement with theory. The penalty of differential beam switch measurements over (ideal) position switch measurements is a factor 2 increase in the rms noise level. The overwhelming benefit is of course the quality of the obtained baseline (spectra). The popular use of DBS techniques (analogous to synchronous detection) comes therefore as no surprise.

2.3.6 Calibration

Proper calibration of heterodyne radio-astronomical data is of utmost importance for correct scientific interpretation. To this extent a distinction can be made between space based observations (the HIFI instrument on the Herschel space observatory [44]) and ground based observations [45]. The latter is primarily concerned with the calibration of the Earth atmospheric emission and absorption properties. Due to the short nature of the atmospheric fluctuations ($1/f$ power spectrum), ground based intensity calibrations are naturally exposed to significant errors. This situation allows for some important generalizations and simplifications of the calibration routine. For space based missions the lack of atmosphere puts a more stringent requirement on the amplitude calibration of the instrument. Significant efforts have been expanded by a variety of authors to tackle this problem [44, 45]. For the purpose of this thesis we provide an overview of the problem.

In general, intensity calibration of the astronomical source can be achieved with either a one- or two load chopper wheel. In the first scenario the brightness temperature of an off-source measurement (this includes the atmosphere in case of ground based observations) and a single load with known emissivity is used to derive the proper antenna temperature of the observed astronomical source. In the second scenario the radiation temperatures of both loads are used. The two chopper wheel approach provides a more robust solution since the actual atmospheric temperature, in case of the one load measurement, is difficult to estimate accurately.

One of the difficulties in absolute amplitude calibration are instrumental fluctuations over longer time scales. For SIS receivers this is generally not a problem. The ALMA specification is 10^{-4} in 1 s, which for a properly designed system (no ground loops, minimal thermal fluctuations, optical standing waves...) is not too difficult to achieve. Hot electron bolometer (HEB) mixers on the other hand are intrinsically very sensitive to external influences (Sec. 4.3) and, as may be seen from Fig. 2.6, a total power stability of a few seconds in a 1.8 MHz noise fluctuation bandwidth is unfortunately not unrealistic. In this case the normalized rms noise, $\sigma/\langle s(t)\rangle = 1/\sqrt{\Delta\nu T_{int}}$, is $\sim 5{\times}10^{-4}$. For a 1 GHz total power bandwidth this quantity may be degraded by approximately the square of the bandwidth, e.g. $1.2{\times}10^{-2}$ or about 1 % in 1 s. This is approximately a factor 100 less stable than the ALMA specification. In practice short time scale differential "on-off" source measurements such as the symmetric double beam switching of Fig. 2.6d are needed with HEB based receiver systems.

2.3.6.1 Two-load calibration

For the load calibration procedure to work, the radiation temperature (J_{load}), and coupling efficiency of both sidebands to the calibration load (η_{load}) have to be known. The radiation temperature of a load with physical temperature T may be computed from the Planck formula as

$$J_b = B_\nu(T) = \frac{2h\nu^3}{c^2}\left[e^{h\nu/k_BT} - 1\right]^{-1} . \tag{2.35}$$

Generally speaking, the observed signal will only be in one of the sidebands. Under this condition the equation for T_A^* observed at an airmass A becomes

$$T_A^* = \frac{(V_{source} - V_{sky})}{G_s K \eta_s e^{-A\tau_{atm}}} \ . \tag{2.36}$$

V_{source} is the observed signal, V_{sky} the off-source position, and G_s the fractional signal sideband gain ($G_s + G_i = 1$). For modern large instantaneous RF bandwidth receivers (Sec. 2.3.4) the sideband ratio (G_s/G_i) may, to an error of ≈ 5 %, be approximated as unity. K is a calibration factor. It links the backend spectrometer IF output to the antenna temperature. Following [45], the calibration factor K in case of a two-load chopper wheel can be derived as

$$K = \frac{V_{load1} - V_{load2}}{\eta_{load1}[G_s J^s_{load1} + G_i J^i_{load1}] - \eta_{load2}[G_s J^s_{load2} + G_i J^i_{load2}]} \ , \tag{2.37}$$

with

$$T_A^*(2load) = \frac{(V_{source} - V_{sky})}{(V_{load1} - V_{load2})} \left(\frac{\eta_{load1}[J^s_{load1} + RJ^i_{load1}] - \eta_{load2}[J^s_{load2} + RJ^i_{load2}]}{\eta_s e^{-A\tau_{atm}}} \right). \tag{2.38}$$

In the above equation, η_{load1} and η_{load2} are the respective coupling efficiencies to the load. The superscripts s and i stand for the signal and image sideband. It is apparent from Eq. 2.38 that the atmospheric transmission in zenith, η_{atm}, has to

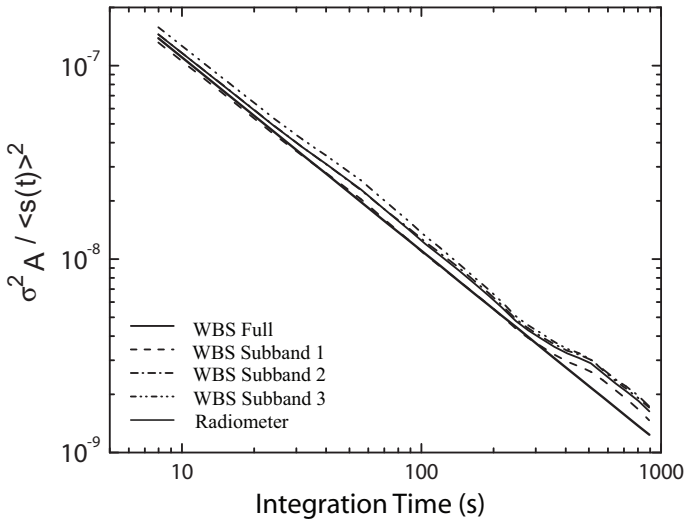

Figure 2.7: Differential stability measured on the HIFI internal loads (physical temperatures of 4 K and 80 K). The result is for the same mixer (B7b, 1.890 THz) as in Fig. 2.6. The results show that the internal load calibration loop is stable to at least 900 s. Thus load intensity and standing wave calibrations with the HIFI HEB mixers may occur on a time scale of at least 15 minutes.

be known accurately. Mangum *et al.* [45] found that for a two-load calibration, an atmospheric opacity accuracy of 1 % corresponds to an ~ 2 % error in the calibration budget. Referring back to Sec. 2.4, this is actually a difficult feat in the upper submillimeter and terahertz frequency bands [46]. For observations from space, the lack of a dominating atmosphere allows a two load calibration to correct for optical standing waves in the obtained spectra (Ossenkopf *et al.* [44]).

To characterize the two-load calibration stability of HIFI [38], differential internal hot (80 K) and cold (4 K) load measurements for all mixer bands, at a variety of LO frequencies have been obtained. In Fig. 2.7 we show the differential internal load stability of HEB mixer band 7 at an LO frequency of 1.890 THz. The result gives a sense for the secondary loop calibration timing. 15 minutes between load calibration appears to be a reasonable value.

2.3.6.2 One-load calibration

The one-load antenna temperature can be derived from Eq. 2.38 by substitution of $V_{load} \rightarrow V_{load1}$, $V_{sky} \rightarrow V_{load2}$, $T_{load} \rightarrow T_{load1}$, and $T_{sky} \rightarrow T_{load2}$. Defining the atmospheric transmission t_{atm} as $e^{-A\tau_{atm}}$ with T_{sky} from Eq. 2.42 and $G_s/G_i = 1$, yields

$$\begin{aligned} T_A^*(1load) &= \frac{V_{source} - V_{Sky}}{\eta_s t_{atm}(V_{load} - V_{sky})}\Big[(J^s_{load} - \eta_s J^s_{sky} - (1-\eta_s)J^s_{spill}) \\ &+ (J^i_{load} - \eta_s J^i_{sky} - (1-\eta_s)J^i_{spill})\Big] \ . \end{aligned} \tag{2.39}$$

Because only one load is used, the sky emission (J_{sky}) must be determined. This is often difficult as the exact brightness temperature of the sky is not known with great precision. We further assume in Eq. 2.39 an equal sideband ratio (true DSB receiver) with 100 % coupling efficiency to the (oversized) warm blackbody calibration load, and ignore the cosmic background radiation temperature (2.725 K). If we further make the simplifying assumption that T_{spill}, T_{sky} and T_{load} have more or less the same physical temperature ($\pm$ 5 % error), and that $\tau^s_{atm} \sim \tau^i_{atm}$ then Eq. 2.39 simplifies to

$$T_A^*(1load') = 2\frac{(V_{source} - V_{sky})}{(V_{load} - V_{sky})} \ . \tag{2.40}$$

Eq. 2.40 is independent of the atmospheric opacity. Of course this solution is a first order approximation and is liable to lead to significant calibration errors, especially above 200 GHz (Fig. 2.8).

From the discussion it is clear that both systematic errors (sideband ratio, load calibration parameters...) and statistical errors (atmospheric opacity, temperature of the atmosphere, integration times on the astronomical source, the loads and the off-source calibration) will be present in the calibration error budget. Calibration uncertainties below ~ 5 %, especially in the upper submillimeter and terahertz frequency bands, will therefore be very difficult to achieve in practice, even with the two-load calibration system. Of all the possible sources of error, atmospheric opacity in the line of site of the observation is the most significant cause of error for ground

based observations. For space based observations the dominant cause of error will likely be the sideband ratio uncertainty.

2.4 Atmospheric transmission

The Earth atmosphere has a large influence on submillimeter and far-infrared observations. For example, due to pressure broadened rotational lines such as H_2O, O_2 (the main culprits) and some minor constituents, observations above $\sim$ 230 GHz suffer from significant atmospheric absorption.

In order to illustrate the atmospheric influence and instrumental system degradation we model the atmosphere above three astronomically interesting sites: Mauna Kea (HI), Chajnantor (Chile), and Sofia. Our calculations use the radiative transfer model "ATM" of Pardo *et al.* [47] which, aside from the above mentioned molecules, also includes the dry air continuum. What is not included in the model are ground (or surface) layer temperature and humidity changes. These typically occur during the daytime by solar heating of the soil. Since most low opacity observations are presumably taken at night, we are allowed to ignore ground effects.

As input to the model we provide the precipitable water vapor (pwv) column height, atmospheric pressure, and temperature. The radiative transfer model output provides the atmospheric opacity, or optical depth, in nepers (τ_{atm}) for a number of molecules. The sum of these can be linked to the atmospheric transmission in zenith via $\eta_{atm} = e^{-\tau_{atm}}$. We shown in Figs. 2.8 & 2.9 the atmospheric transmission in zenith as a function of precipitable water vapor for three high elevation sites. In general the single sideband system noise temperature, assuming unity sideband ratio, referred to the top of the atmosphere is obtained from

$$T_{sys}^{SSB} = 2 * \frac{[T_{rec}^{DSB} + T_{atm}(1 - \eta_s e^{-A \cdot \tau_{atm}})]}{\eta_s e^{-A \cdot \tau_{atm}}}. \tag{2.41}$$

The sky brightness temperature is thus seen to be

$$T_{sky} = T_{atm}(1 - \eta_s e^{-A\tau_{atm}}) \ , \tag{2.42}$$

with the source brightness, as seen from the Earth

$$T_b = T_s \eta_s e^{-A\tau_{atm}} + T_{atm}(1 - \eta_s e^{-A\tau_{atm}}) \ . \tag{2.43}$$

In Eq. 2.43, T_s is the source brightness temperature referred to the top of the atmosphere, and A the airmass (see also Sec. 8.4.3) as measured from zenith. From the above it is evident that both η_{atm} and T_{sys}^{SSB} are a strong function of the precipitable water vapor column directly above the site. Thus knowing the exact column height at the time of the observation is very important since it effects the calibration accuracy of the obtained astronomical data. Though being the subject of the next Sec. 2.3.6, it is important to note that in the submillimeter wavelength regime the sky is usually assumed isothermal and uniform throughout. This allows the atmospheric opacity to be derived from sky dip measurements or by scaling 225 GHz radiometer tipping data [48]. In the higher submillimeter and terahertz frequency regimes (Fig. 2.9)

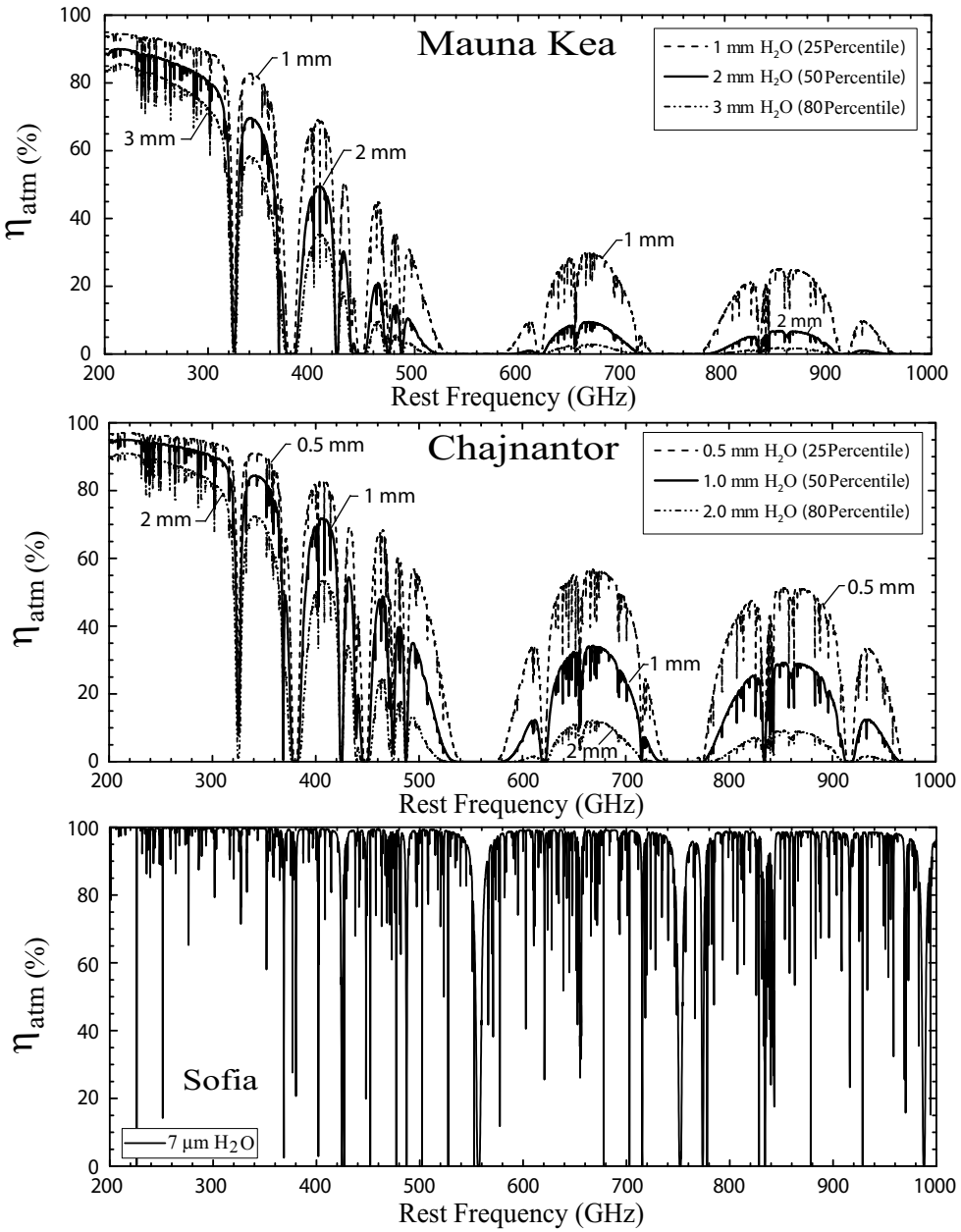

Figure 2.8: *Top*) Submillimeter (200 – 1000 GHz) atmospheric transmission on Mauna Kea (HI) for 25, 50, & 80 observing percentiles. Elevation is 4.2 km, ground temperature 268.15 K, and atmospheric pressure 623 mbar. *Middle*) Atmospheric transmission on Chajnantor(Chile) for 25, 50, & 80 percentiles. Elevation is 5 km, ground temperature is 270 K, and the atmospheric pressure 560 mbar. *Bottom*) Submillimeter atmospheric transmission on the Stratospheric Observatory for Infrared Astronomy (SOFIA) at an altitude of 13.1 km and 7μm of precipitable water vapor. The atmospheric transmission calculations are based on a model (ATM) by J. Pardo *et al.* [47].

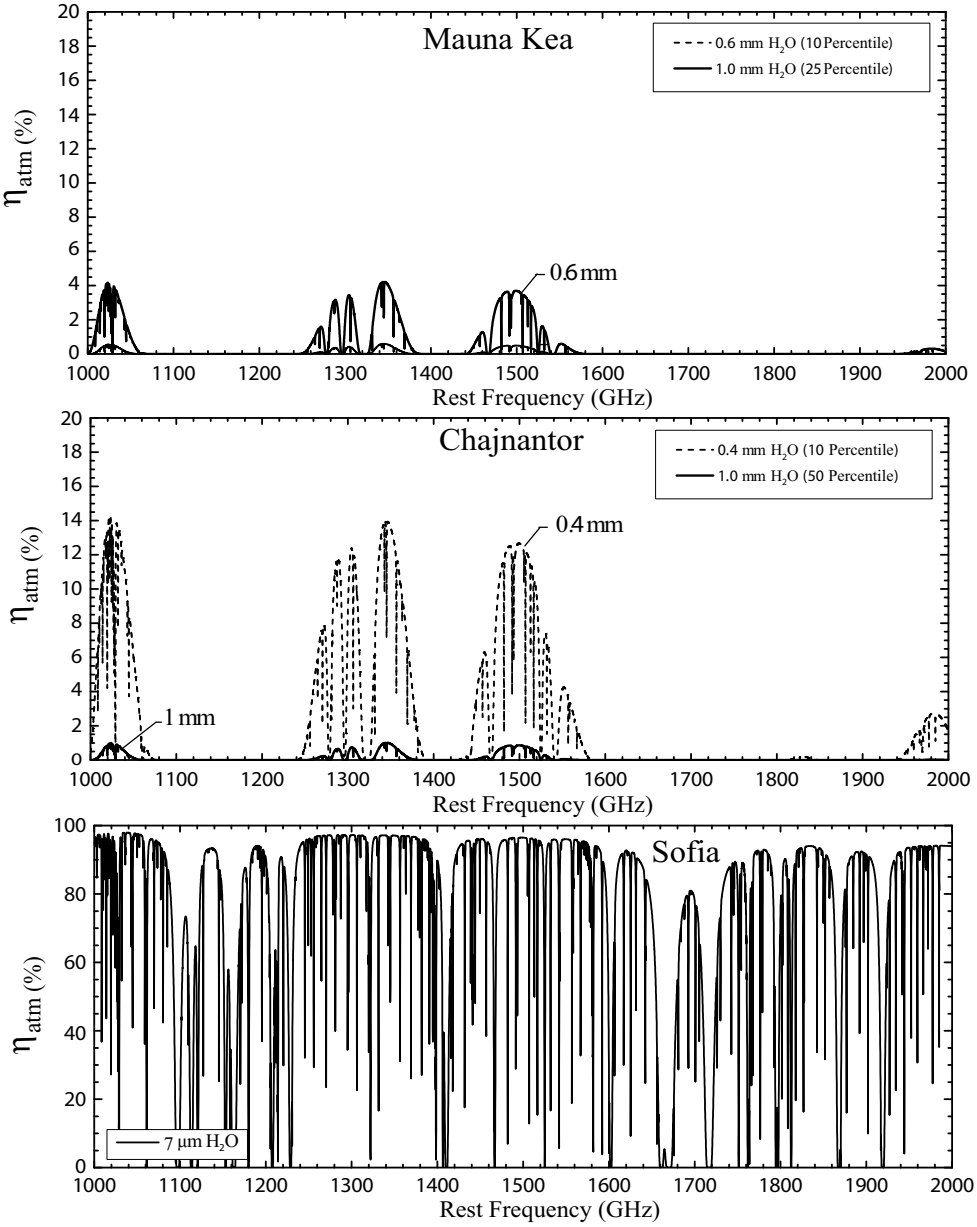

Figure 2.9: *Top*) Terahertz (1 – 2 THz) atmospheric transmission on Mauna Kea (HI) for 10 & 25 observing percentiles. Clearly, the atmosphere prohibits observations in this frequency range. *Middle*) Terahertz atmospheric transmission on Chajnantor(Chile) for 10 & 50 percentiles. The 10 % is averaged over the entire year with the southern hemisphere winters being considerably better (15 %) than the summer time (7 %) [48, 49]. *Bottom*) The terahertz atmosphere from SOFIA for a 7μm column of precipitable water vapor. Above the moist troposphere the atmosphere is essentially dry, and it is in this regime that observations from SOFIA will be most competitive. The atmospheric transmission calculations are based on a model (ATM) by J. Pardo *et al.* [47].

the notion of a stable isobaric atmosphere is not correct. Here real time "FTS" measurements fit to an atmospheric model have proven very successful in obtaining the actual opacity at the frequency of the observation [46]. Of course for space based observations with $\eta_{atm} = 100$ % this discussion does not apply.

2.5 Summary

In this Chapter we took a look at a variety of important submillimeter detection and instrumental requirements. From the discussion it is clear that the design and implementation of far-infrared instrumentation demands a careful case-by-case scientific motivation and outlook. Thus it is the scientific case that motivates a particular instrument design, and not vice versa.

Bibliography

[1] [Online]. Available: http://www.alma.info/

[2] [Online]. Available: http://www.ovro.caltech.edu/mm/

[3] [Online]. Available: http://iram.fr/

[4] [Online]. Available: http://sma-www.harvard.edu/

[5] C.M. Bradford, G.J. Stacey, M.R. Swain, T. Nikola, A.D. Bolatto, J.M. Jackson, M.L. Savage, J.A. Davidson, and P.A.R. Ade, "SPIFI: the First Direct - Detection Imaging Spectrometer for Submillimeter Wavelengths," *Applied Optics*, Vol. 41, No. 13, pp. 2561-2574, May, (2002).

[6] [Online]. Available: http://www.spire.rl.ac.uk/

[7] [Online]. Available: Herschel; http://sci.esa.int/

[8] T. Nikola, S. Hailey-Dunsheath, G. J. Stacey, D. J. Benford, S. H. Moseley, and J. G. Staguhn, "ZEUS: A Submillimeter Grating Spectrometer for Exploring Distant Galaxies", *in Proc. of SPIE*, Vol. 4855, edited by T. G. Phillips and J. Zmuidzinas, (SPIE, Waikoloa, USA, 2002), pp. 88.

[9] C. M Bradford, P. Ade, J. Aguirre, J. J. Bock, M. Dragovan, L. Duband, L. Earle, J. Glenn, H. Matsuhara, B. J. Naylor, H. Nguyen, M. Yun, J. Zmuidzinas, "Z-Spec: a broadband millimeter-wave grating spectrometer: design, construction, and first cryogenic measurements," *in Proc. of SPIE*, Vol. 5498, Ground-based Telescopes, edited by J. Zmuidzinas, W. S. Holland, and S. Withington, (SPIE, Glasgow, UK, 2004), pp. 257.

[10] [Online]. Available: http://www.jach.hawaii.edu/JCMT/

[11] [Online]. Available: http://www.submm.caltech.edu/cso/
[Online]. Available: http://www.submm.caltech.edu/cso/receivers/

[12] [Online]. Available: http://pacs.mpe.mpg.de/

[13] P. K. Day, H. G. LeDuc, B. A. Mazin, A. Vayonakis, and J. Zmuidzinas, "A broadband superconducting detector suitable for use in large arrays", *Nature*, 425, 817-821, Oct. (2003).

[14] M. D. Audley, W. S. Holland, T. Hodson ,M. MacIntosh, I. Robson, K. D. Irwin, G. Hilton, W. D. Duncan, C. Reintsema, A. J. Walton, W. Parkes, P. A. R. Ade, I. Walker, M. Fich, J. Kycia, M. Halpern, D. A. Naylor, G. Mitchell, and P. Bastien, "An update on th eSCUBA-2 project", *In Millimeter and Submillimeter Detectors for Astronomy II. Proc. of the SPIE*, Vol. 5498, J.Zmuidzinas, W.S.Holland, and S.Withington, Eds., pp.63-77, Oct. (2004).

[15] P. L Richards and L. T. Greenberg *IR ad MM waves*, Vol. 6, Appendix I, (Academic, NY 1982).

[16] P. L Richards, "Bolometers for Infrared and Millimeter Waves," *J. Appl. Phys.*, Vol. 76, pp. 1-24, (1994).

[17] D. C. Alsop, C. Inman, A. E. Lange, and T. Wilbanks, "Design and Construction of High Sensitivity Infrared Bolometers for Operation at 300 mK," *Appl. Opt.*, Vol. 31, pp. 6610-6615, (1992).

[18] S. T, Tanaka, A. Clapp, M. Devlin, M. Fisher, C. Hagmann, A. E. Lange, and P. L. Richards, "A 100 mK Bolometric Receiver for Low Background Astronomy", *SPIE Proc., Infrared Detectors and Instrumentation*, 1946, pp. 110, (1993).

[19] J. -M Lamarre, F. -X. Dèsert, and T. Kirchner, "Background limited Infrared and Submillimeter Instruments", *Space Sience Reviews*, Vol. 74, pp. 27-36, (1995).

[20] J. X. Zmuidzinas "Thermal noise and correlations in photon detection", *Applied Optics*, Vol. 42, No. 25, pp. 4989-5008, Sep. (2003).

[21] D. J. Benford, T. R. Hunter, and T. G. Phillips, "Noise equivalent power of background limited thermal detectors at submillimeter wavelength", *Int. J. Infrared and MM. waves*, Vol. 19, pp 931-938, (1998).

[22] R.Schieder, O. Siebertz, F. Schloeder, C. Gal, J. Stutzki, P. Hartogh, V. Natale, "Wide-Band Spectrometer for HIFI-FIRS", *Proc. of "UV, Optical, and IR Space Telescopes and Instruments*", J. B. Breckinridge, P. Jakobsen Eds., SPIE 4013, 313-324, Jul., (2000).

[23] J. Horn, O. Siebertz, F. Schmilling, C. Kunz, R. Schieder, G. Winnewisser, "A 4 x 1 GHz Array Acousto-Optical Spectrometer", *Experimental Astronomy*, Vol. 9, Issue 1, pp. 17-38, Jan., (1999).

[24] B. Klein, S. D. Philipp, I. Krmer, C. Kasemann, R. Gsten and K. M. Menten, "The APEX digital Fast Fourier Transform Spectrometer", *A&A*, pp 454, L29-L32, (2006).

[25] Omnisys Instruments AB, Gruvg. 8 , SE-421 30 Västra Frölunda, Sweden newblock[Online]. Available: http://www.omnisys.se/

[26] F. P. Mena, J. W. Kooi, A. M. Baryshev, C. F. J. Lodewijk, R. Hesper, G. Gerlofsma, T. M. Klapwijk, and W. Wild, "A Sideband-separating Heterodyne Receiver for the 600-720 GHz Band", Submitted to the *IEEE Trans. Microwave Theory and Techniques* in August (2008).

[27] B. P. Lathi, "Modern Digital and Analog Communications Systems" *2nd edition*, ISBN 0-03-027933-X (1989).

[28] H. B. Callen and T. A. Welton, "Irreversibility and generalized Noise", *Phys. Rev.*, Vol. 83, no. 1, pp. 34-40, Jul., (1951).

[29] A. R. Kerr, "Suggestions for Revised Definitions of Noise Quantities, including Quantum effects", *IEEE Trans. Microwave Theory and Techniques*, Vol. 47, No. 3, pp. 325-329, Mar., (1999).

[30] J.D. Kraus, "Radio Astronomy", *2nd Edition*, pp. 7–8.

[31] T. G. Phillips and K. B. Jefferts, "A low temperature bolometer heterodyne receiver for millimeter wave astronomy", *Rev. Sci. Instrum.*, Vol. 44, pp. 1009, (1973).

[32] J. W. Kooi, A. Kovács, M. C. Sumner, G. Chattopadhyay, R. Ceria, D. Miller, B. Bumble, R. LeDuc, J. A. Stern, and T. G. Phillips, "A 275-425 GHz Tunerless Waveguide Receiver Based on AlN SIS Technology", *IEEE Trans. Microwave Theory and Techniques*, Vol. 55, No. 10, pp. 2086-2096, Oct. (2007).

[33] S. Padin and G. Ortiz, "A cooled 1-2 GHz balanced HEMT Amplifier", *IEEE transactions on Microwave Theory and Techniques*, Vol. 39, No. 7, pp. 1239-1243, Jul., (1991).

[34] [Online]. Available: http://www.submm.caltech.edu/cso/receivers/lna.html/

[35] E. C. Sutton, G. A. Blake, C. R. Masson, and T. G. Phillips, "Molecular Line Survey of Orion A from 215 to 247 GHz," *Ap. J. (Suppl.)*, Vol. 58, 341-378, (1985).

[36] "The Contribution of Molecular Line Emission to Broadband Flux Measurements at Millimeter and Submillimeter Wavelengths", Todd Groesbeck, Ph.D. Thesis (Physics, Prof. Tom Phillips, Primary Advisor), California Institute of Technology (1995).

[37] S. Cherednichenko, V. Drakinskiy, T. Berg, P. Khosropanah, and E. Kollberg, "Hot-electron bolometer terahertz mixers for the Herschel Space Observatory", *Rev. Sci. Instruments*, Vol. 79, 034501, (2008).

[38] Th. de Graauw, N. Whyborn, E. Caux, T. G. Phillips, J. Stutzki, X. Tielens, R. Güsten, F. P. Helmich, W. Luinge, J. Pearson, P. Roelfsema, R. Schieder, K. Wildeman, and K. Wavelbakker, "The Herschel-Heterodyne Instrument for the Far-Infrared (HIFI)", [Online]. Available: herschel.esac.esa.int/Publ/2006/SPIE2006_HIFI_paper.pdf

[39] J. W. Kooi, M. Chan, T. G. Phillips, B. Bumble, and H. G. Leduc, "A Low Noise 230 GHz Heterodyne Receiver Employing a 0.25 μm^2 Nb/AlO_x/Nb Tunnel Junction", *IEEE Trans. Microwaves Theory and Techniques*, Vol. 40, No. 5, pp. 812-815, May, (1992).

[40] Ansoft Corporation Four Station Square, Suite 200, Pittsburgh, PA 15219-1119, USA

[41] Sonnet Software, Liverpool, NY, 2005. [Online]. Available: http://www.sonnetusa.com/

[42] J. Ward, F. Rice and J. Zmuidzinas, "Supermix: a flexible software library for high-frequency circuit simulation, including SIS mixers and superconducting components", *Tenth International Symposium on Space Terahertz Technology*, University of Virginia, Charlottesville, VA, Mar. (1999).

[43] D. Meledin, A. Pavolotsky, V. Desmaris, I. Lapkin, C. Risacher, V. Perez, D. Henke, O. Nystrom, E. Sundin, D. Dochev, M. Pantaleev, M. Fredrixon, M. Strandberg, B. Voronov, G. Goltsman, and V. Belitsky, "A 1.3 THz Balanced Waveguide HEB Mixer for the APEX Telescope," accepted for publication in *IEEE Microwave Theory and Technique*, (2008).

[44] V. Ossenkopf, "The intensity calibration of HIFI", *NRAO*, Charlotteville, VA, ALMA Memo 442, Jan., (2003).

[45] J. Mangum, "Load Calibration at Millimeter and Submillimeter Wavelength", *NRAO*, Charlotteville, VA, ALMA Memo 434, Oct., 2002.

[46] S. Paine and R. Blundell, "The Terahertz Atmosphere", in *Proc. 15th Int. Symposium on Space Terahertz Technology*, Northampton, MA, pp. 418-425, Apr., (2004).

[47] J. R. Pardo, J. Cernicharo, and E. Serabyn, "Atmospheric Transmission at Microwaves (ATM): An Improved Model for mm/submm applications", *IEEE Trans. on Antennas and Propagation*, vol. 49, no. 12, pp. 1683-1694, Dec., 2001.

[48] S. Matsushita, H. Matsuo, J. R. Pardo, and S. J. E. Radford, "FTS Measurements of Submillimeter-Wave Atmospheric Opacity at. Pampa la Bola II : Supra-Terahertz Windows and Model Fitting", *PASJ: Publ. Astron. Soc. Japan*, Vol. 51, pp. 603-610 (1999).

[49] S. J. E. Radford, & the ALMA site characterization team, "Conditions for observing with the ALMA at Chajnantor", *at ALMA Science Workshop (NRAO)*, (2004).

Chapter 3

Heterodyne receiver concepts

3.1 Mixing elements

In this Section we give a brief overview of the three most important (non-linear) mixing elements in the submillimeter and terahertz frequency range.

3.1.1 Schottky-diodes

Schottky diodes are fabricated with a metal-semiconductor junction rather than the conventional p-n junction of two semi-conductors. These devices are named after the German physicist Walter H. Schottky, who in 1938 explained the rectifying behavior of the metal-semiconductor contact. In general, Schottky-barrier diodes are majority-carrier devices that do not suffer from the charge-storage effects that limit semiconductor p-n junctions. In the terahertz regime essentially all Schottky diodes are fabricated with GaAs, thanks to the high electron mobility of this semiconductor material. At the metal to (lightly doped) semiconductor interface a voltage dependent potential barrier is created. The result is a strongly non-linear current voltage characteristic that facilitates the mixing (multiplication) process. GaAs is, due to its high mobility and high breakdown voltage the material of choice at microwave frequencies and above. In principle the metal-semiconductor barrier can be created by many metals, however for whisker contacted point-contact devices hard materials such as tungsten or platinum are traditionally employed. Aside from the quality of the I/V curve (sharpness, leakage..) parasitic reactance plays an important role in the RF performance of the device. This is especially true at submillimeter and terahertz frequencies. Not until the late eighties did planar beamlead technology mature enough [1, 2] to make planar Schottky devices viable at frequencies above $\sim$ 200 GHz. This feat is especially impressive considering the potential for parasitic capacitance in a high dielectric material such as GaAs ($C_p = \varepsilon_0 \varepsilon_r A/d$, and ε_r=13.8). ε_0 is the permittivity of free space (8.854×10^{-12} F/m), A the effective area, and d the dielectric thickness.

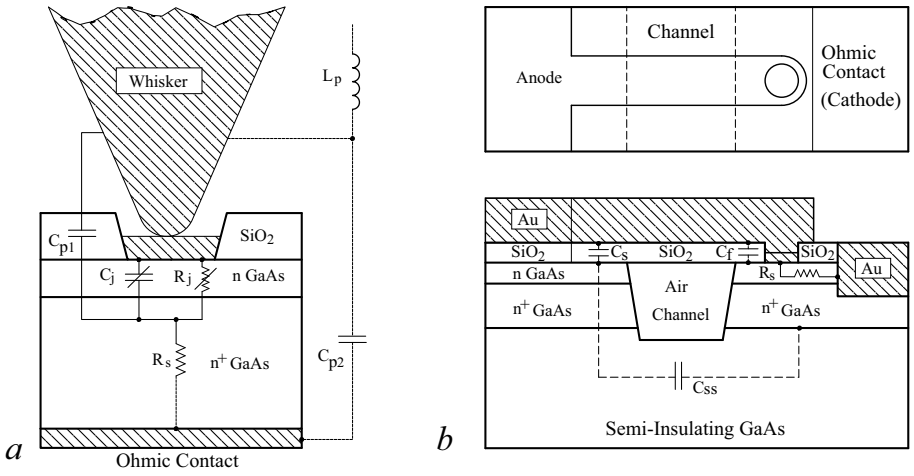

Figure 3.1: *a*) Traditional whisker contacted Schottky diode. *b*) Planar Schottky diode version. To minimize parasitic capacitance the GaAs substrate between the contact pad and anode is etched away, forming an air-channel. The upper frequency is set by the parasitic capacitances C_f, C_s, C_{ss}, the contact resistance R_s, and zero bias junction capacitance C_0. Source: Bishop *et al.* [1, 2].

There are in principle a variety of ways to establish a metal-semiconductor contact. The more traditional whisker contacted Schottky diode, with associated electrical model, is shown in Fig. 3.1a. The cutoff frequency of the diode is set by the series resistance (R_s) and zero bias junction capacitance of the diode. For this reason, a lightly doped epitaxial layer, is grown on top of low resistivity bulk GaAs. To further minimize series resistance, the Ohmic contact resistance of the chip must be of very high quality. The whisker serves as an antenna and couples the incoming radiation from the waveguide [3] or cornercube [4] to the diode.

In Fig. 3.1b we show the planar (modern) version of a Schottky diode. To maximize the frequency response the parasitic capacitance C_f and C_{ss} (in series with C_s) needs to be minimized. This is accomplished by etching a channel directly underneath the anode contact finger. It minimizes not only stray capacitance to the GaAs n-doped substrate but also the pad-pad coupling. R_s, the series resistance of the epilayer, is minimized by positioning the cathode contact pad as close as physically possible to the Schottky barrier interface. For terahertz diodes, typical values of R_s and C_0, the zero bias capacitance in parallel with C_s + C_{ss}, are on the order of 10 Ohm and 2 fF.

From an RF perspective, the advantages of Schottky diode mixers is that they work well into the terahertz, are homogeneous, robust, and do not require cryogenic cooling. They can thus be utilized where cryogenic cooling is not possible or practical. On the flip side, the required LO pump power is quite high, typically a few milliwatt [5, 6]. However if a 10 % reduction in sensitivity can be tolerated than the LO pump level may be reduced by as much as 60 % [7]. Schottky diode mixers have, compared to cryogenic cooled SIS and HEB mixers, a relatively low sensitivity. At 585 GHz, the best reported T_{rec}^{DSB} of Schottky receivers is 1150 K at room temperature, and

880 K cooled [8]. This corresponds to $\sim 32\ h\nu/k_B$, where $h\nu/k_B$ equals the quantum noise limit. For comparison, SIS receivers in this frequency range exhibit typically a sensitivity of $3 - 5\ h\nu/k_B$ (Chap. 7). The receiver noise temperature of Schottky receivers increases with frequency, and reaches $\sim$ 8000 K at 2.5 THz [6] and 70.000 K at 4.75 THz [4], though the latter result may be due to a RF coupling rather than a device issue. In contrast to the relatively low sensitivity, the IF bandwidth of Schottky-diodes has essentially no upper frequency limit [9].

3.1.2 SIS tunnel junctions

Superconductor-insulator-superconductor (SIS) tunnel junctions are quantum mechanical devices whose operation is based on the principle of photon-assisted tunneling [10]. These devices are discussed extensively in this thesis, and we refer to Chaps. 4, 5, 7, 8 & 9 for further detail. Operation of SIS junctions is limited by the energy gap of the superconductor, which for niobium is $\sim$ 1400 GHz.

3.1.3 Hot electron bolometer mixers

Hot electron bolometers rely on a bolometric effect and use the power-law as the mixing principle. "Bolometer" literally means "heat detector", *e.g.* $v(t)^2/R \propto \mathrm{T(t)}$ with $v(t) = v_s \cos(\omega_s t) + v_{LO} \cos(\omega_{LO} t)$. The principle of operation is outlined in Sec. 4.3, with the IF bandwidth, electrothermal feedback, and mixer conversion gain discussed in Chap. 6. Hot electron bolometers do not have an upper frequency limit, unlike SIS junctions, and are currently the element of choice for sensitive high resolution terahertz spectroscopy.

3.2 The single-ended Receiver

In its most basic form, the single-ended double sideband (DSB) mixer was introduced in Chap. 2. For this type of mixer the upper and lower sidebands "fold" in the down-conversion process and are present at the intermediate frequency (IF) output (Sec. 2.3). The invention of the "super-heterodyne" receiver as shown in Fig. 3.2 is credited to E. Armstrong [11] (1920). This technique allows amplification and filtering of the detected signal at an intermediate frequency (IF) where electronic circuits work

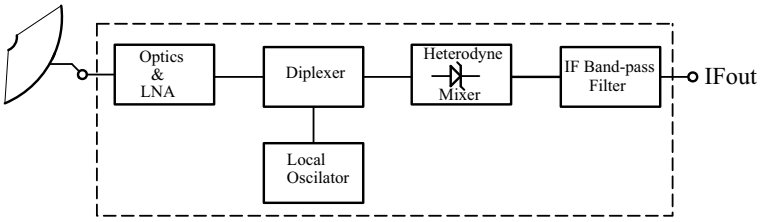

Figure 3.2: Single-ended "super-heterodyne" receiver layout. At frequencies above $\sim$ 100 GHz low noise amplifiers are presently unavailable, and sensitive diode detectors (Sec. 3.1) must be employed.

well. In contrast to the superheterodyne receiver, early radio pioneers like Marconi employed direct down-conversion to baseband techniques without IF conversion. The classical example of this is the AM crystal radio. In practice, due to poor frequency selectivity and front-end filtering, this technique results in a poor signal-to-noise ratio (SNR) at the detector output. These problems were often exacerbated by the inadequate front-end and mixer components at the time. As an interesting side note, modern AM and FM integrated circuits avoid the standard 10.7 MHz and 455 KHz IF frequencies and process the information at a frequency closer to baseband where integrated circuit (op-amps) work well. This avoids the use of large inductors and capacitors needed at the forth mentioned IF frequencies.

The elegance of the single-ended mixer is its simplicity. It is no accident that during WW II, microwave diode mixers experienced, as part of the radar technology development effort, a tremendous boost in frequency range, sensitivity, and reliability. From this early beginning, it has proven very difficult to extend heterodyne principles to submillimeter and terahertz frequencies. It was not until the mid-seventies that technology allowed the first (InSb) hot electron bolometer and SIS mixers [12, 13, 14, 15]. These mixers were single-ended (1 diode) DSB. Even today the majority of submillimeter and terahertz receivers are constructed this way.

Simplicity comes however with some undesirable properties. The mixer has, for example, poor RF/LO isolation and no immunity to intermodulation products or amplitude fluctuations of the local oscillator source. For some applications an additional disadvantage is that both the signal and image sidebands are present at the IF output.

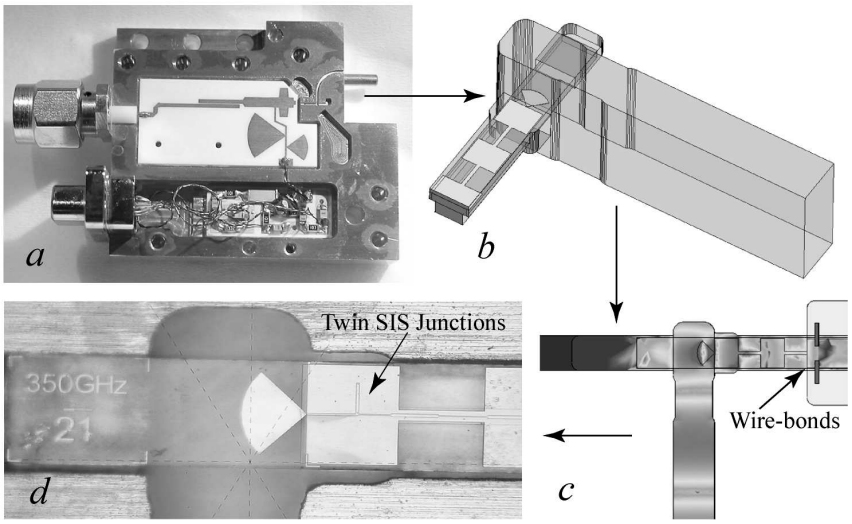

Figure 3.3: A single-ended DSB SIS waveguide mixer operational in the 275 – 425 GHz atmospheric window. a) The basic mixer block. b) Detailed view of the waveguide antenna structure, c) Electromagnetic field distribution, and d) Quartz substrate with radial probe antenna and two AlN tunnel barrier SIS junctions. These also serve as the capacitive element of the RF matching network (Sec. 7.2). Design: J. W. Kooi, Chaps. 7 & 8.

It is not until recent [16, 17, 18] that material and device technology has allowed superior, but also more complex designs to be extended into the submillimeter and terahertz regime [19]. In Chap. 7 of this thesis we describe a recently constructed "Technology demonstration receiver" (Trex). This instrument demonstrates a variety of new techniques that pave the way for the more complex receiver implementations of Chap. 8. The large format array receivers discussed in Chap. 9 are for simplicity's sake of the double sideband type described in Fig. 3.2.

3.3 The switched-load (Dicke) receiver

In their realization essentially all heterodyne mixers suffer from total power gain instability. There are a variety of reasons, most of which are related to the high gain ($\sim$ 80 dB) in the receiving system. Some physical phenomena that effect gain stability are: Sensitivity to temperature fluctuations, bias noise, microphonic pickup, and modulation of standing waves between the LO source and mixer unit (see Chap. 10 for details). To circumvent gain instabilities, with associated loss in sensitivity and baseline distortion, the mixer input may be continuously switched between the antenna and a (cold) load. This switched input scheme, known as Dicke switching, was first introduced by Dicke in 1946 [20].

Without switching, or differential measurements as it is commonly known today, gain instability (Sec. 2.3.5) will limit the baseline quality, calibration accuracy, and integrated rms noise (sensitivity). Schematically the switched receiver is shown in Fig. 3.4.

To demonstrate the effect of gain instability, we show in Fig. 2.6 the total power and spectroscopic stability of HIFI HEB mixer band 7 [21] with associated spectra. The response is typical of many measurements derived during the instrument level test campaign (ILT) [22]. Chap. 10 is in its entirety is devoted to the required switch rate of hot electron bolometer receivers and the effect of standing waves in the optics path. Because of the short stability time (the noise is uncorrelated), we find for HEB receivers differential measurements such as load-chop or double-beam-switch a necessity. This severely limits the position switch time (slew the entire telescope off source for calibration), thereby having a significant impact on the overall observation

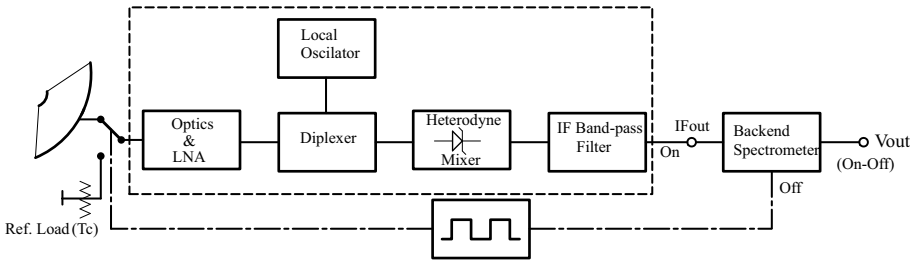

Figure 3.4: Dicke or switched receiver layout [20]. Synchronously switching the receiver input to a reference load on a short time scale ($\sim$ 1 s) subtracts common mode gain fluctuations and drift at the backend spectrometer output. This technique leaves in principle a clean baseline (Fig. 2.6).

strategy.

For all its advantages, the Dicke receiver has the disadvantage of spending half the time looking into a calibration load, rather than on the sky. In addition, due to the "on - off" subtraction of essentially white noise (signal is deeply embedded in the noise) with a Gaussian noise like distribution, the Dicke receiver also exhibits an increased noise level of $\sqrt{2}$. Thus for a differential or switching receiver the sensitivity degrades by a factor of two when compared to an ideal non-switching receiver, e.g.

$$T_A = \frac{2 \cdot T_{sys}^{SSB}}{\sqrt{\eta_c \Delta\nu T_{int}}} \ . \tag{3.1}$$

Here η_c is the chopping efficiency, ~ 90 %, T_{int} the on-source integration time, T_A the rms antenna noise temperature, and $\Delta\nu$ the noise fluctuation bandwidth of the measurement. The factor 2 is a significant loss in sensitivity and corresponds to a factor 4 in integration time over an ideal instrument. To circumvent this problem an interferometer or correlation receiver (Secs. 3.4 & 3.6) may be employed.

3.4 The interferometer receiver

An interferometer utilizes at least two antennas, both pointed at the same source. After correcting for the difference in phase between input signals, a function of antenna separation, the IF signals are cross-correlated at the IF backend processor. As such an interferometer receiver observes the source with 100 % time efficiency. A two element interferometer thus has a sensitivity improvement over the switched (Dicke) receiver of $2\sqrt{2}$, assuming the same system temperature and antenna characteristics. In Fig. 3.5 we show a block diagram of the two element interferometer receiver.

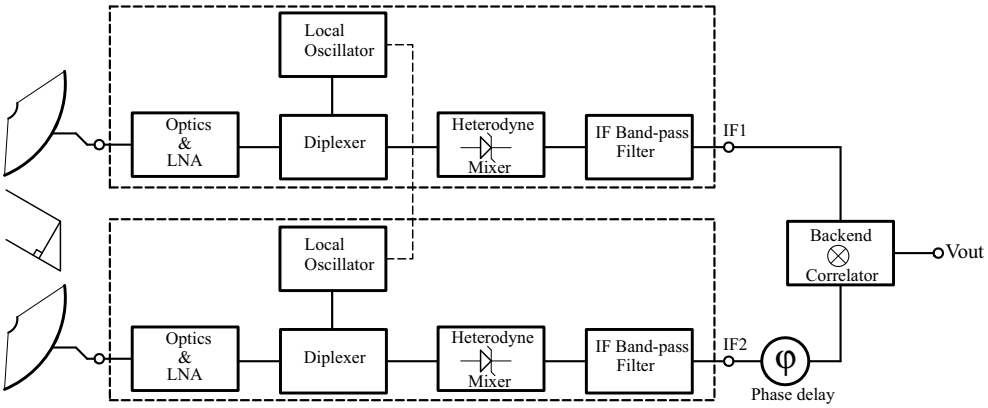

Figure 3.5: Interferometer receiver layout. In this case at least two antennae are pointed at the same source. The local oscillator signal is injected in phase. After correcting for a phase delay due to the baseline offset, the IF signals are cross correlated leaving only the detected signal and residual white noise.

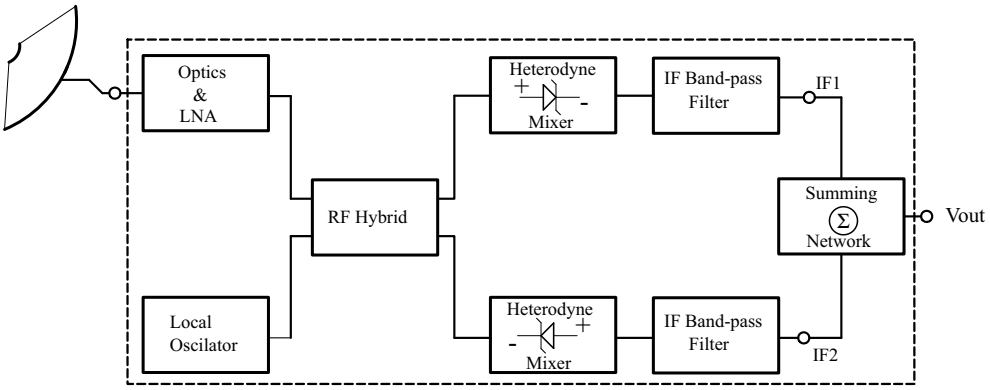

Figure 3.6: Balanced input receiver layout. The RF input hybrid can either be 90° or 180°. In general a 180° input hybrid offers a higher degree of intermodulation noise cancellation and RF/LO port isolation than a 90° input hybrid. When utilizing symmetry in the (SIS) diodes I/V curves, the IF signals may be summed thereby rejecting common mode LO amplitude noise.

3.5 The balanced receiver

A balanced receiver may be constructed with a 90° or 180° input hybrid, and a summing node at the IF output. In general though, a 180° balanced mixer has superior intermodulation and LO/RF port isolation properties than a 90° balanced mixer. At submillimeter or terahertz frequencies, parasitic device capacitance negates the intermodulation problem. However, poor LO/RF port isolation in the 90° balanced mixer remains a problem. It causes LO signal that reflects off the active device to appear at the RF port, hence causing a local oscillator induced optical standing waves in the telescope structure. Such as standing wave is liable to create gain instability at the output of the receiver. Despite this disadvantage, constructed in waveguide the quadrature hybrid is two-dimensional (planar), as opposed to a 180° "magic Tee", and thus much more readily implemented. In Sec. 8.2 we treat the theory and implementation of balanced receivers, and in particular look at the design and implementation of quadrature hybrid balanced receivers in the range 180 – 720 GHz. Fig. 3.6 shows the general layout of a balanced receiver.

3.6 The correlation receiver

In a single dish telescope, a factor two in observing time ($\sqrt{2}$ in sensitivity) may be gained by having one beam continuously on-source with a second beam continuously off-source. Fig. 3.7 shows the block diagram of such a scheme with either a 90° or 180° RF input hybrid. This receiver configuration has the advantage that correlated signals are rejected. Thus by design, gain fluctuations, atmospheric turbulence, and LO standing waves common to both channels are cancelled.

In principle therefore the correlation receiver offers continuous differencing and exquisite baseline quality without platforming and baseline distortion that plague

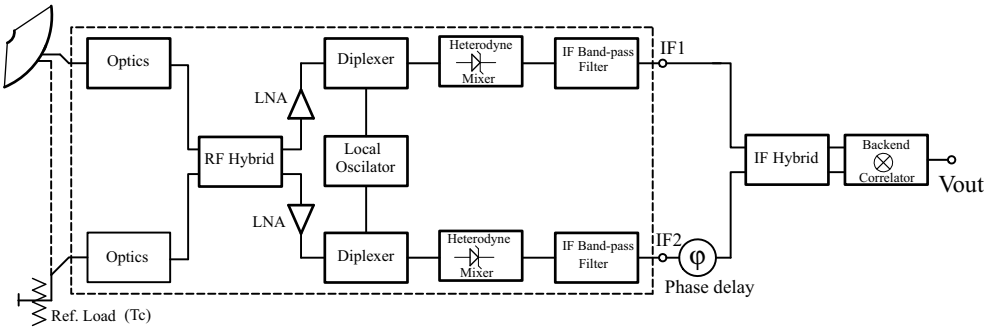

Figure 3.7: Block diagram of a dual-input continuous comparison (correlation) receiver. For symmetry and noise cancellation, the local oscillator signal is injected in phase. The reference beam may be terminated on a radiometric equivalent cold load or on an offset position on the sky. Common mode signals present in both the signal and reference beam are subtracted at the correlated IF output.

more standard receiver configurations. It does however require a reference beam. For the correlation receiver to work optimally, the reference beam has to be 100 % off-source, which is best achieved with point like sources. Note that the reference beam may be terminated on a variable internal cold load, preset to the same temperature as the observed sky brightness. However in this case LO standing waves and atmospheric scintillations are uncommon to both channels, and therefore not subtracted. The correlation receiver is thus found ideally suited for (high redshift extragalactic) point-like observations with spectral lines that are deeply embedded in the noise. In Sec. 8.4, the theory and implementation of a 280 – 420 GHz correlation receiver is treated in detail.

3.7 The sideband separating receiver

The so far described mixers are all double sideband in nature. To separate the signal and image sidebands it is possible to use at the RF input port of the mixer a high-Q filter to suppress one of the sidebands. This technique is narrow band as the RF filter is generally fixed tuned. A more broadband approach is to use a 90° hybrid in both the RF and IF. This shifts the phase of the signal and image sidebands by 180° allowing them to be separated in the IF. Though less common, it is also possible to use a 180° hybrid on the RF input. Fig. 3.8 shows the layout of a sideband separating (2SB) receiver. The theory and implementation of a 600 – 720 GHz 2SB receiver is treated in detail in Sec. 8.5.

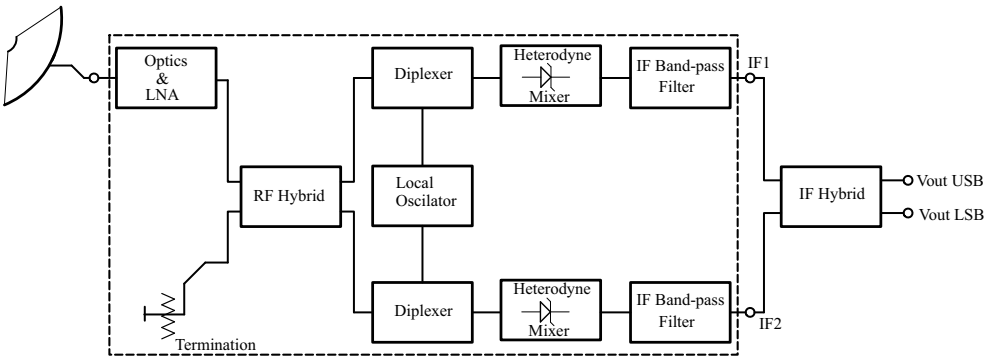

Figure 3.8: Sideband separating receiver layout. The quadrature hybrid at the RF input and IF output functions to shift one of the sidebands 180° with respect to the other. This allows the sidebands to be separated in the IF.

3.8 Summary

We have looked at a variety of mixer and receiver configurations. At frequencies below 100 GHz, advances in microwave monolithic circuit integration (MMIC) design has allowed mixers to be implemented as double or even triple balanced, as well as sideband separating. At submillimeter frequencies and above, due to material limitations (mobility), difficulties in lithography and funding, the vast majority of mixers has until very recent been single-ended (DSB). Thanks however to recent advances in microfabrication, we see today the emergence of more complex mixer designs in the submillimeter and even terahertz frequency regimes. The more advanced receivers are expected to benefit astronomical data quality and speed of operation. We have devoted Chap. 8, and to some extent Chap. 9 to this topic.

Bibliography

[1] W.L. Bishop, K. McKinney, R.J. Mattauch, T.W. Crowe and G. Green, "A Novel Whiskerless Schottky Diode for Millimeter and Submillimeter Wave Applications," *Proceedings of the 1987 IEEE MTT-S International Symposium*, Las Vegas, Nev., 607-610, June (1987).

[2] W.L. Bishop, E.R. Meiberg, R.J. Mattauch and T.W. Crowe, "A Micron Thickness, Planar Schottky Diode Chip for Terahertz Applications with Theoretical Minimum Parasitic Capacitance," The *1990 IEEE MTT-S International Microwave Symposium*, Dallas, TX, pp. 1305-1308, May (1990).

[3] A. R. Kerr, "Low-noise room-temperature and cryogenic mixers for 80-120 GHz", *IEEE Trans. Microwave Theory Tech.*, Vol. 23, No. 10, pp. 781-787, Oct., (1975).

[4] A. L. Betz and R. T. Borejko, "A practical Schottky mixer for 5 THz", in *Proc. 7th Int. Symp. on Space Terahertz Technology*, edited by R. M. Weikle, G. M. Rebeiz, T. W. Crowe, (University of Virginia, Charlottesville, USA), pp. 503 (1996).

[5] B. N. Ellison, B. J. Maddison, C. M. Mann, D. N. Matheson, M. L. Oldfield, S. Marazita, T. W. Crowe, P. Maaskant, and W. M. Kelly, in *Proc. of the 7th Int. Symp. on Space Terahertz Technology*, edited by R.M. Weikle, G.M. Rebeiz, T.W. Crowe, (University of Virginia, Charlottesville, USA), "First results for a 2.5 THz Schottky diode waveguide mixer", pp. 494., (1996).

[6] M. C. Gaidis, H. M. Pickett, C. D. Smith, R. P. Smith, S. C. Martin, and P. H. Siegel, "A 2.5 THz receiver front-end for spaceborne applications", *IEEE Trans. Microwave Theory Technol.*, Vol. 48, pp. 733, (2000).

[7] J. L. Hesler, T. W. Crowe, W. L. Bishop, R. M. Weikle, II, R. F. Bardley, and S-K. Pan, "The Development of Planar Schottky Diode Waveguide Mixers at Submillimeter Wavelength", The *1997 IEEE MTT-S International Microwave Symposium*, pp. 953-956, June (1997).

[8] J. L. Hesler, W. R. Hall, T. W. Crowe, R. M. Weikle, B. S. Deaver, "Submm wavelength waveguide mixers using planar Schottky barrier diodes", in *Proc. 7th Int. Symp. on Space Terahertz Technology*, edited by R. M. Weikle, G. M. Rebeiz, T. W. Crowe, (University of Virginia, Charlottesville, USA), pp. 462 (1996).

[9] M. Morgan and S. Weinreb, "A monolithic HEMT diode balanced mixer for 100-140 GHz", in *Proc. of IEEE MTT-S Intl. Microwave Symposium*, edited by B. Sigmon, (IEEE, Phoenix, AZ), pp. 99, (2001).

[10] J. R. Tucker and M. J. Feldman, "Quantum detection at millimeter wavelengths", Rev. Mod. Phys., Vol. 57, 1055, (1985).

[11] E. H. Armstrong, "Methods of receiving high frequency oscillations", *US Patent* 1342885, Jun. 8, (1920).

[12] T.G. Phillips and K.B. Jefferts, "A cryogenic bolometer heterodyne receiver for millimeter wave astronomy", *Review of Sci. Instrumentation*, Vol. 44, 1009, (1973).

[13] T.G. Phillips and K.B. Jefferts, "Millimeter-Wave Receivers and their Applications in Radio Astronomy", *IEEE Trans. Microwave Theory and Techniques*, Vol. 54, No. 2, pp. 1290-1292, Dec., (1974).

[14] P. L. Richards, T. -M. Shen, R. E. Harris, and F. L. Lloyd, "Superconducting-insulator-superconducting quasiparticle junctions as microwave photon detectors", *Appl. Phys. Lett.*, Vol. 36(6), pp. 480-482, Mar., (1980).

[15] G. J. Dolan, R. A. Linke, T. C. L. G. Sollner, D. P. Woody, and T. G. Phillips, "Superconducting Tunnel Junctions as Mixers at 115 GHz", *IEEE Trans. Microwave Theory and Techniques*, Vol. 29, No. 2, pp. 87-91, Feb., (1981).

[16] A. R. Kerr and S. -K. Pan, "Design of Planar Image Separating and Balanced SIS Mixers", *NRAO*, Charlotteville, VA, ALMA Memo 151, March. (1996).

[17] A. R. Kerr and S. -K. Pan, "A single chip Balanced SIS Mixer for 200-300 GHz", *NRAO*, Charlotteville, VA, ALMA Memo 308, May. (2000).

[18] G. Chattopadhyay, D. Miller, H. G. LeDuc, and J. Zmuidzinas, "A 550-GHz Dual Polarized Quasi-Optical SIS Mixer," *Proc. 10^{th} International Symposium of Space Terahertz Technology*, Charlottesville, Virginia, March 16-18, (1999), pp. 130-143.

[19] D. Meledin, A. Pavolotsky, V. Desmaris, I. Lapkin, C. Risacher, V. Perez, D. Henke, O. Nystrom, E. Sundin, D. Dochev, M. Pantaleev, M. Fredrixon, M. Strandberg, B. Voronov, G. Goltsman, and V. Belitsky, "A 1.3 THz Balanced Waveguide HEB Mixer for the APEX Telescope," accepted for publication in *IEEE Microwave Theory and Technique*, (2008).

[20] J.D. Kraus, "Radio Astronomy", *2nd Edition*, Ch. 7, McGraw-Hill, New York, (1966).

[21] Th. de Graauw and F. P. Helmich, Airborne Telescope Systems, in Proc. of the Symposium "The Promise of the Herschel Space Observatory", edited by G. L. Pilbratt, J. Cernicharo, A. M. Heras, T. Prusti, and R. Harris, (ESA, Toledo, Spain, 2000), "Herschel-HIFI: The heterodyne instrument for the far-infrared",

pp. 45.
http://astro.estec.esa.nl/first/Publ/2001/sp460_toledo_hifi.pdf, 195-202 (2000).

[22] J. W. Kooi, V. Ossenkopf, M. Olberg, R. Shipman, and R. Schieder, "Instrument Stability, as measured during the ILT phase", *HIFI internal report*, 30 Nov. (2007).

Chapter 4

Fundamentals of SIS and HEB mixers*

4.1 SIS mixers: Introduction

A Superconductor-Insulator-Superconductor (SIS) junction is a "sandwich" of two superconductors separated by a very thin insulator layer. The quantum mechanical nature of SIS tunnel junctions lies in the way charge carriers with quantized energy levels (Cooper pairs and quasiparticles) tunnel through the barrier. Heterodyne mixers based on Cooper pair tunneling are known as as Josephson mixers, whereas mixers based on quasi (single) particle tunneling are referred to as SIS mixers. It is the latter, and its application to advanced receivers designs, that we concern ourselves with in this thesis.

The quantum generalization of super-Schottky diodes was laid out by Tucker and Millea in 1978 [1], with a follow up paper in 1979 by Tucker [2] on the theory of quantum limited detection in superconducting tunnel junctions. The key features of this theory are the prediction of quantum limited mixer noise and unlike classical mixers, the possibility of RF-IF conversion gain. For this phenomenon to occur the tunnel junction has to exhibit an extremely nonlinear I/V curve. In the case of a SIS junction, this is achieved by the very sharp onset of quasiparticle tunneling beyond a dc threshold voltage equal to the energy gap of the superconductor (Fig. 4.1).

In the first part of this Chapter, we cover some of the fundamental underpinnings needed in the understanding and design of SIS mixers. Some of the discussion is seen to follow the excellent review by Tucker and Feldman in 1985 [3]. The second part of

*The material described in this Chapter has been published in the following papers: J. W. Kooi , M. Chan, B. Bumble, and T. G. Phillips, *Int. J. IR and MM Waves*, Vol. 15, No. 5, May, (1994), J. W. Kooi, F. Rice, G. Chattopadhyay, S. Sundarum, S. Weinreb and T. G Phillips, *Proc. 10^{th} Int. Symp. Space Terahertz Technology*, University of Virginia, Va, Mar., (1999), J. W. Kooi, G. Chattopadhyay, M. Thielman, T. G. Phillips, and R. Schieder, *Int. J. IR and MM Waves*, Vol. 21, No. 5, May, (2000), J. W. Kooi, J. Pety, B. Bumble, C. K. Walker, H. G. LeDuc P. L. Schaffer, and T. G. Phillips, *IEEE Trans. Microwave Theory and Techniques*, Vol. 46, No. 2, pp. 151-161, Feb., (1998).

this Chapter concerns itself with the theory of HEB mixers.

4.1.1 Photon-assisted quasiparticle tunneling

The physical phenomena that provides the basis of SIS mixer theory is photon-assisted tunneling by quasiparticles across a thin, typically 10 – 20 Å, Al_2O_3 or as of late AlN barrier (Chap. 7). This effect was first discovered by Dayem and Martin in 1962 [4], and theoretically explained by Tien and Gordon soon afterwards in 1963 [5]. It is made possible by a significant overlap of the wave functions on either side of the tunnel barrier. And because insulators have typically a ~ 0.5 eV barrier to electrons, tunneling is the only significant source of current at the small bias voltages (< 10 mV) and temperatures (< 5 K) at which niobium junctions operate.

In a superconductor at the lowest-energy quantum state (T=0 K), electrons are bound into Cooper pairs. This occurs in certain metals due to phonon-mediated attraction between two electrons with equal momenta but opposite spin, and at a temperature below which it is energetically favorable for Cooper pairs to "condense" into the ground, or lowest-energy state [6]. In an SIS junction at 0 K, the superconductors on either side of the barrier are thus seen to be in the ground state. From the BCS theory (Bardeen, Cooper, Schriefer (1957)) [7] we understand that each electron in a Cooper pair has a binding energy Δ. The minimum energy for excitation of a Cooper pair above the ground state is therefore 2Δ. This breaking energy is known as the superconducting energy gap and is the energy required to produce two single-particle excitations from a Cooper pair. Following BCS as given in Tinkham [6] the energy of the quasiparticle excitation is

$$E = \sqrt{\varepsilon^2 + \Delta^2} \tag{4.1}$$

where ε is the normal state quasiparticle energy measured relative to the Fermi level. The density of states $N_S(E)$ for quasiparticles in a superconductor then becomes

$$N_S(E) = N_N(\varepsilon)\frac{d\varepsilon}{dE} \ . \tag{4.2}$$

And because we are only interested in energies ε a few meV from the Fermi energy, we are allowed to take $N_N(\varepsilon)=N_N(0)$. Thus $N_N(0)$ represents the density of state in the normal metal above the superconducting transition. Using Eq. 4.1 we find

$$N_S(E) = N_N(0)\frac{E}{\sqrt{E^2-\Delta^2}}, \quad E > \Delta \tag{4.3}$$

and

$$N_S(E) = 0, \quad E < \Delta \ . \tag{4.4}$$

From this discussion it is evident that no quasiparticle states are allowed for $E < \Delta$, e.g. in the *gap*. The divergence in the density of states near the gap is illustrated graphically in the semi-conductor energy level diagram of Fig. 4.1 for two scenarios; without and with photon assisted tunneling. It is interesting to observe that it is the

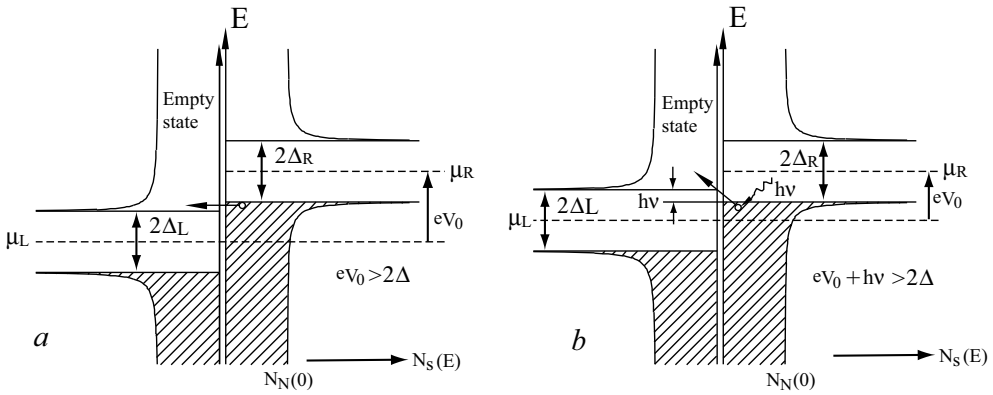

Figure 4.1: Semiconductor picture for a SIS tunnel junction. *Left*) Density of states vs. energy for quasiparticle tunneling at the same energy level. μ_R and μ_L are the electron Fermi levels on both sides of the barrier. Applying a voltage potential V_0 shifts the Fermi level of one side with respect to the other. *Right*) photon assisted tunneling.

divergence in the density of states that is responsible for the very nonlinear SIS I/V curve of Fig. 4.2.

Referring to Fig. 4.1a, the onset of quasiparticle tunneling takes place at a dc voltage $eV_0 = 2\Delta$. At this potential a single electron is able to tunnel through the barrier leaving an un-paired quasiparticle behind. In Fig. 4.1b we depict the process we are most concerned with, photon-assisted tunneling. In this scenario the photon energy + dc bias voltage should be greater than 2Δ ($h\nu + eV_0 > 2\Delta$) for electrons to be able to tunnel through the barrier. Referring again to the energy diagram, the superconducting energy gap voltage may now be defined as

$$V_{gap} = \frac{2\Delta}{e} \ . \tag{4.5}$$

In Fig. 4.2a we show an ideal I/V curve at 0 K. The sharp rise in current at the gap is, as was seen, due to the divergent density of states just above and below the gap. From Tinkham [6] the direct current through the tunnel junction may be calculated as

$$I(V_0) = C \int_{-\infty}^{\infty} \frac{dN_S(E)}{dE} \frac{dN_S(E+eV_0)}{dE} \Big[f(E+eV_0) - f(E) \Big] dE, \tag{4.6}$$

where N_S is given by Eqs. 4.3 & 4.4 and f(E) the Fermi-Dirac distribution

$$f(E) = \frac{1}{e^{E/(k_B T)} + 1} \ . \tag{4.7}$$

In Eq. 4.7, k_B is Boltzmann's constant and T the temperature of the superconducting material.

In practice a SIS junction is not ideal, and certainly not operated at 0 K. For this reason we show in Fig. 4.2b a measured unpumped I/V curve of a high current density

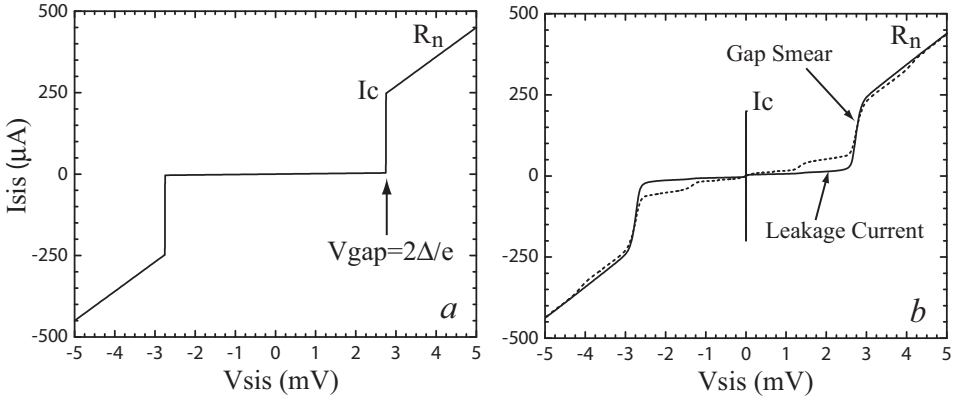

Figure 4.2: *Left*) Ideal high-current density AlN-barrier SIS I/V curve at 0 K (Eq. 4.6). The gap voltage is 2.77 mV, R_n 10.6 Ω, and $I_c \sim 200$ μA. *Right*) The actual measured I/V curve. All parameters are the same, except for a 70 μV gap smear and R_{sg} / R_n ratio (leakage) of 13.7. Superimposed is a photon assisted tunnel current corresponding to 345 GHz submillimeter irradiation. The critical current I_c is given by Eq. 4.9.

AlN-barrier SIS junction. Superimposed on the I/V curve is the critical current (Sec. 4.1.2). The important junction defining parameters are; gap voltage, subgap leakage current, gap smearing, and the critical current. The gap voltage is a function of the superconductor (2Δ). The critical current is a constant determined by the superconducting energy gap and normal state resistance of the junction (Sec. 4.1.2), and the gap smearing and leakage current a quality factor related to the manufacturing process and operating temperature. At 0 K (no thermal excitation of quasiparticles), any residual subgap leakage is the result of single electron and/or Multiple-Andreev Reflections (MAR) through pinholes in the barrier (Sec. 7.2.4). The sharpness of the gap is found to relate to the mixer conversion gain via Z_{01} in Eq. 4.39, itself a function of the dc I/V curve and its Kramers-Kronig transform (Sec. 4.1.4).

Superimposed on the unpumped I/V curve in Fig. 4.2b is a 345 GHz quantized photon assisted tunnel current. This tunnel current is made possible when $V_0 + nh\nu/e \geq V_{gap}$, with n an integer corresponding to the number of photons absorbed by a quasiparticle. The absorption probability (Eq. 4.7) decreases rapidly as the photon number increases. For n=1 the photon step at $V_0 = V_{gap} - h\nu/e$ arises from electrons absorbing a single photon and being able to tunnel across the barrier. The photon step directly above the gap at $V_0 > V_{gap}$ arises from electrons absorbing a photon and making a transition to a higher energy level where the density of states is lower. However, when $V_0 > V_{gap} + h\nu/e$ emission as well as absorption of a photon with energy $h\nu$ is possible. This is evident in the current rise at $V_0 = V_{gap} + h\nu/e$. Thus a SIS junction biased at V_0 will respond to radiation in the frequency range $e(V_{gap} - V_0) < h\nu < e(V_{gap} + V_0)$.

4.1.2 The Josephson effect

In addition to quasiparticle induced tunnel current, a barrier potential between two superconductors (SIS) also supports Cooper pair tunneling. This phenomena was first predicted by Josephson in 1962, and is known as the "dc Josephson effect" [8]. For his prediction Josephson shared in 1973 the Nobel Prize in Physics with Esaki and Giaever, co-discoverers of the tunneling phenomena in solids. The Cooper pair induced tunnel current was found to depend on the phase difference φ of the superconducting wave functions across the barriers

$$I = I_c sin(\varphi) \ . \tag{4.8}$$

I_c is the critical current which, referring to Fig. 4.2b, is the maximum possible zero-voltage current that can be passed. Since at zero-voltage the phase can take any value, the current will vary between -I_c and +I_c.

From microscopic theory it is understood that I_c is a constant that depends on the barrier and junction area according to

$$I_c = \frac{\pi\Delta}{2eR_n} tanh\left(\frac{\Delta}{2k_BT}\right) \ \approx \ \frac{\pi}{4}\frac{V_{gap}}{R_n} \ . \tag{4.9}$$

For bulk niobium, with a 2Δ energy gap voltage of 2.8 mV, the critical current amounts to $\sim$ 1.9 mV/R_n. Rewriting Eq. 4.9 in terms of a of current density yields

$$J_c = \frac{\pi}{4}\frac{V_{gap}}{(R_nA)} \ . \tag{4.10}$$

If a constant voltage is applied across the barrier, we understand from the Josephson relations that the phase difference varies in time according to

$$\frac{d\varphi}{dt} = \frac{2eV_0}{h} \ . \tag{4.11}$$

Integrating Eq. 4.11 with respect to time yields $\varphi = \varphi_0 + 2eV_0t/h$. This implies an oscillating current at a frequency $\nu = 2eV_0/h$. The latter equation is referred to as the "ac-Josephson effect", and corresponds to a frequency of 484 GHz/mV. Though useful for an accurate determination of voltage standards, Cooper pair tunneling is undesirable in SIS junctions.

In a LO pumped mixer Josephson oscillations are excited at discrete voltages S_n, known as Shapiro steps [9]. S_n(mV) $= nh\nu_{lo}/2e = n\nu_{lo}/484$ GHz, where n is an integer. Biasing on a Shapiro step results in large excess noise in the mixer with subsequent unstable receiver behavior. Fortunately magnetic fields may be used to suppress Cooper pair tunneling in a SIS quasiparticle mixer. This is based on the fact that I_c is a function of the magnetic field flux Φ threaded through the barrier region. For rectangular junctions the critical current is modulated in a Fraunhofer like diffraction pattern

$$I_c = I_c(0)\left|\frac{sin(x)}{x}\right| \ , \quad x = \frac{\pi\Phi}{\Phi_0} \ . \tag{4.12}$$

Φ_0 the magnetic flux quantum $h/2e$. To fully suppress the Josephson effect one flux quantum should be threaded through the barrier region. The magnetic field necessary is approximately $B = \Phi_0/t(d+2\lambda)$, where t is the length of the junction size perpendicular to the direction of B-field, d the barrier thickness, and λ the magnetic penetration depth. For a typical 1 μm^2 junction with λ=100 nm and a 1 nm barrier thickness the magnetic field required is $\sim$ 100 Gauss. It may be seen [6] that for circular junctions the modulation of the critical current follows an Airy pattern

$$I_c = 2I_c(0)\left|\frac{J_1(x)}{x}\right| \ , \quad x \sim \frac{\Phi}{\Phi_0} \ , \tag{4.13}$$

where J_1 is the Bessel function of the first kind. We refer to Sec. 4.1.11 for an actual measurement of the critical current suppression in a SIS junction as a function of magnetic field.

4.1.3 Network representation

Tucker [2] and Feldman [3] laid out the quantum theory of heterodyne mixing in SIS mixers. On a very global level, this theory consists of three components: The interaction of the local oscillator signal on the SIS tunnel junction (LO pumped I/V curve), the mixing or down conversion process of RF signals to an intermediate frequency (IF), and the addition of noise in this conversion process.

In the context of the discussion, we introduce a network representation describing the coupling of a current source (LO) to a load (SIS junction). The voltage diagram is shown in the left panel of Fig. 4.3.

For heterodyne mixing the current, or admittance, representation shown in the right panel of Fig. 4.3 is the more useful one. In this case the LO signal is shunted by an internal embedding admittance Y_{emb} in parallel with the complex junction admittance Y_{RF}. The embedding admittance represents the mixer mount, and includes

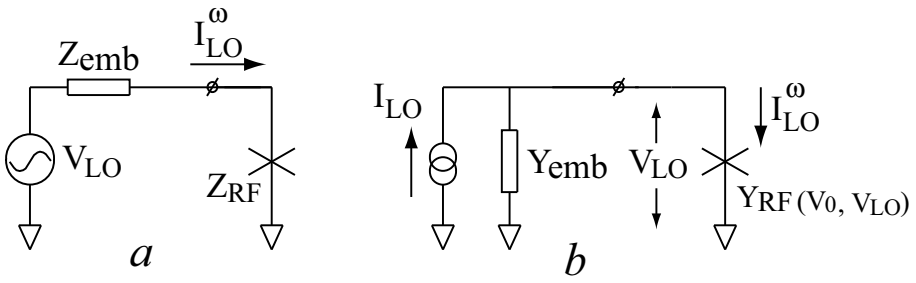

Figure 4.3: *a*) Voltage representation of a LO signal source with internal embedding impedance Z_{emb} driving the complex SIS load Z_{RF}. *b*) Current representation of the same lossless circuit. The admittance network is a more useful model to describe the interaction of the LO current with the embedding and junction admittances. The parasitic junction capacitance is included in the embedding admittance. The currents are a function of dc bias voltage (V_0) and applied LO voltage (V_{LO}).

the SIS junction parasitic capacitance (Table 4.1). As shall be seen, Y_{RF} is a function of bias and LO voltage, and can be obtained from the dissipative and reactive current components through the junction, Eqs. 4.24 & 4.25, once the LO pump level ($\alpha \equiv eV_{LO}/\hbar\omega$) has been established. Y_{emb} on the other hand can be obtained from electro-magnetic (em) simulation analyses [10, 11]. This has not always been the case. Before the advent of em-simulation tools, obtaining an accurate estimation for the embedding admittance was very difficult. Scaled mixer mount models were frequently employed for example.

From network theory we know that the maximum power transfer occurs when $Y_{emb} = Y^*_{RF}$ and thus $G_{emb} = G_{RF}$. This is a resonance condition and much effort is typically expanded to maximize the frequency range (RF bandwidth) over which this condition can be approximated (Sec. 4.1.8). The actual power dissipated in the junction in this scenario is

$$P_{av} = \frac{|I^2_{LO}|}{8G_{emb}} \ . \tag{4.14}$$

4.1.4 Current in an SIS junction

Due to the quantum nature of the quasiparticle tunnel current, nonlinear equations described by a Taylor series or Fourier analysis are no longer possible. To this extent the averaged quantized nonlinear quasiparticle tunnel current, based on the transfer Hamiltonian formulation of tunneling put forward by Cohen *et al.* [12], and work by Ambegaokar and Baratoff [13] to describe Cooper pair tunneling, was formulated by Werthamer [14] in 1966 as

$$\langle I(t)\rangle = Im \int_{-\infty}^{\infty} d\omega' d\omega'' W(\omega') W^*(\omega'') e^{-i(\omega'-\omega'')t} j(V_0 + \hbar\omega'/e) \ . \tag{4.15}$$

V_0 is the SIS bias voltage, and $W(\omega)$ the phase factor. The time dependent voltage across the junction is then obtained from the Fourier transform of $W(\omega)$

$$\int_{-\infty}^{\infty} d\omega' W(\omega') e^{-i\omega' t} = exp\Big[-\frac{ie}{\hbar}\int^t dt'[V(t') - V_0]\Big] \ . \tag{4.16}$$

In Eq. 4.15 $j(V)$ is a complex function, known as the current response function, and is given by

$$j(V) = iI^0_{dc}(V_0) + I_{KK}(V_0) \ . \tag{4.17}$$

For the special case of a time-independent potential $W(\omega) = \delta(\omega)$, the left side of Eq. 4.15 reduces to the dc (no LO irradiation) I/V curve of the tunnel junction,

$$I^0_{dc}(V_0) = Im[j(V_0)] \ . \tag{4.18}$$

Note that Im$[j(V_0)]$ is the dissipative part of the response function and can be measured directly (Fig. 4.4). The real part of the response function Re$[j(V_0)]$ characterizes the reactive portion of the tunnel current, and it can be related to the dissipative part through a Kramers-Kronig transform

$$I_{KK}(V_0) = Re[j(V_0)] = P\int_{-\infty}^{\infty} \frac{dV'}{\pi} \frac{I^0_{dc}(V') - V'/R_n}{V' - V_0} \ . \tag{4.19}$$

I^0_{dc} denotes the (measured) unpumped dc I/V curve, V' the measured I/V curve voltage, R_n the junction normal state resistance, and P an indication that the Cauchy principal value is taken. In practice the I_{KK} is evaluated numerically from the unpumped dc I/V curve. We find therefore that the ac response for quasiparticle tunneling is completely characterized by the measured I/V curve through Eqs. 4.15 – 4.19. The reactance obtained from $I_{KK}(V)$ is non-classical, and is in addition to the ordinary geometric junction capacitance.

To derive the current expressions of a SIS junction under irradiation of a monochromatic local oscillator signal we make the assumption that the large geometric capacitance effectively shunts all harmonics. Strictly speaking this is not necessarily the case for modern SIS junctions at frequencies $\hbar\omega \leq \ eV_{gap}/2$, and likely results in an over estimation of the available mixer gain [3]. Ignoring harmonic effects, the time dependent voltage across the tunnel barrier is of the form

$$V(t) = V_0 + V_{LO}cos(\omega t) \ . \tag{4.20}$$

Solving Eq. 4.15 by means of Eq. 4.16 the local oscillator current in the junction can be found

$$I_{LO}(t) = Im \sum_{n,m=-\infty}^{\infty} J_n(\alpha)J_{n+m}(\alpha)e^{+im\omega t} i(V_0 + n\hbar\omega/e) \ , \tag{4.21}$$

where J_n is the n-th Bessel function of the first kind, and α the LO pumping parameter $eV_{LO}/h\nu$. The average current induced by the local oscillator thus contains components at all harmonic frequencies with amplitudes

$$\begin{aligned} 2a_m &= \sum_{n=-\infty}^{\infty} J_n(\alpha)\big[J_{n+m}(\alpha) + J_{n-m}(\alpha)\big] I^0_{dc}(V_0 + n\hbar\omega/e) \ , \\ 2b_m &= \sum_{n=-\infty}^{\infty} J_n(\alpha)\big[J_{n+m}(\alpha) - J_{n-m}(\alpha)\big] I_{KK}(V_0 + n\hbar\omega/e) \ . \end{aligned} \tag{4.22}$$

However since the harmonics from the LO are, to a first order, shunted by the geometric junction capacitance we are justified to limit the summation of m to +1, 0, -1. The LO pumped dc I/V characteristic is provided by m=0 as

$$I_{dc}(V_0, V_{LO}) = a_0 = \sum_{n=-\infty}^{\infty} J^2_n(\alpha) I^0_{dc}(V_0 + n\hbar\omega/e) \ . \tag{4.23}$$

The dissipative, in phase current I'_{LO} through the junction at the LO frequency ω is given by $2a_1$

$$I'_{LO}(V_0, V_{LO}) = 2a_1 = \sum_{n=-\infty}^{\infty} J_n(\alpha)\big[J_{n-1}(\alpha) + J_{n+1}(\alpha)\big] I^0_{dc}(V_0 + n\hbar\omega/e) \ , \quad (4.24)$$

and the reactive current component through the junction I''_{LO} is obtained from $2b_1$ as

$$I''_{LO}(V_0, V_{LO}) = 2b_1 = \sum_{n=-\infty}^{\infty} J_n(\alpha)\big[J_{n-1}(\alpha) - J_{n+1}(\alpha)\big] I_{KK}(V_0 + n\hbar\omega/e) \ , \quad (4.25)$$

In this way the complex LO induced current through the junction may be defined

$$I^{\omega}_{LO}(V_0, V_{LO}) = I'_{LO} + iI''_{LO} \ . \quad (4.26)$$

When we now refer back to Fig. 4.3b we see that the total LO current for a lossless RF circuit equals $I_{LO}(V_0, V_{LO}) = Y_{emb}V_{LO} + I^{\omega}_{LO}(V_0, V_{LO})$. As we have seen, the embedding environment is determined by the waveguide transition, tuning circuit, and the junction's geometric capacitance. The LO induced SIS current and RF embedding impedance can be calculated in a way described by Skalare [15]. This method is known as the "RF voltage matching method" and matches the RF junction voltage ($V^k_{LO} = \alpha^k\hbar\omega/e$) at each point k of the pumped IV curve (V^k_0). With this set of points (all belonging to the first photon step), the parameters $|I_{LO}|$ and Y_{emb} which minimize the function

$$\sum_k \big||I_{LO}|^2 - |Y_{emb}.V^k_{LO} + I^{\omega}_{LO}(V^k_0, V^k_{LO})|^2\big| \quad (4.27)$$

may be found.

These days modern em-simulation software [10, 11], as well as custom circuit tools such as, for example, Supermix or Pcircuit [16, 17], provide a means of establishing the RF embedding environment of the SIS tunnel junction. It is this method that we employ in the design of the tunerless, large fractional RF bandwidth, SIS mixers in this thesis. As a final note, V_{LO} is strictly speaking a function of V_0, due to the fact that the RF input impedance of the tunnel junction depends on bias voltage. However a constant α is often a fairly good first order assumption as seen in Fig. 4.6b [18].

In Fig. 4.4 we show the nonlinear behavior and quantum response of a high current density AlN-barrier SIS junction. The bias voltage is normalized to V_{gap}, and the impedance to the normal state resistance R_n. Fig. 4.4a depicts the unpumped dc I/V curve and its Kramers-Kronig transform. The single SIS junction current represents half of the measured AlN barrier twin-junction current presented in Chap. 7. This junction is baselined for the balanced- and correlation mixers discussed in Chap. 8. The junction has a quality factor R_{sg}/R_n=14, gap voltage of 2.77 mV, gap smear of $\pm$ 70 μV, and normal state resistance of 10.6 Ω. Fig. 4.4b shows the unpumped I/V curve overlaid with two photon-assisted quasiparticle tunneling steps correspondent to an LO pump level (α) of 0.4 and 0.8. In Fig. 4.4c we show the junction's quantum conductance, which may be derived from I'_{LO}/V_{LO} (Eq. 4.24). The junction's

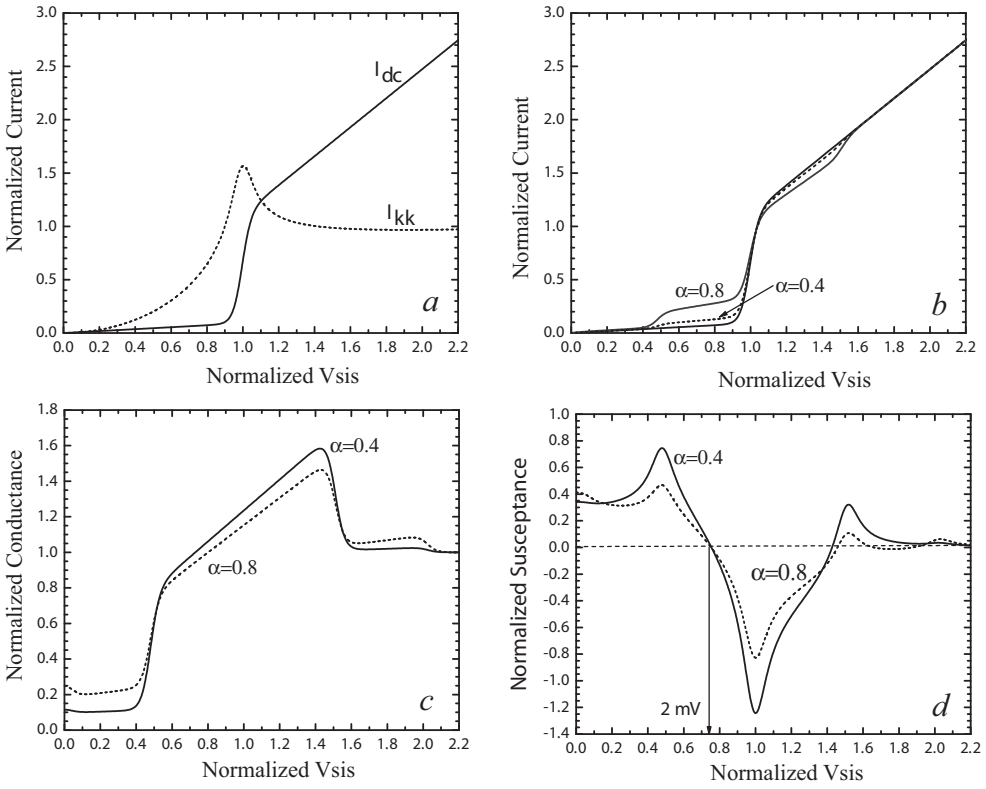

Figure 4.4: *a*) Unpumped dc I/V curve with its Kramers-Kronig transform. In the example we use the high J_c AlN-barrier SIS junction of Chap. 7. The SIS bias voltage is normalized to V_{gap}, the impedance to the normal state resistance R_n, and the current to the top of the gap (198 μA). *b*) Example of photon assisted tunneling with a fixed α of 0.4 and 0.8. The LO frequency is 345 GHz which corresponds to an energy 1/2 V_{gap} (niobium). *c*) Normalized RF conductance (G_{RF}) as a function of bias voltage and LO pump level. *d*) Normalized RF susceptance (B_{RF}) under the same conditions. Optimal mixer conversion gain is typically found with $B_{RF} \sim 0$.

quantum susceptance is shown in Fig. 4.4d and is derived from I''_{LO}/V_{LO} (Eq. 4.25). The RF susceptance changes from capacitive to inductive, and back to capacitive as a function of bias voltage and location of the photon step.

Again referring to Fig. 4.3b, a capacitive RF embedding admittance can, under appropriate conditions, tune out the inductive susceptance of the tunnel junction close to V_{gap}. This causes a strong absorption of the incident LO signal, a slight increase in the LO pump level $\alpha(V_0)$ of the junction, and a positive sloped LO pumped I/V curve. For an inductive embedding susceptance, the opposite occurs. Close to the gap there is a large mismatch, and $\alpha(V_0)$ decreases. The drop in a LO signal on the junction results in a (undesirable) negative sloped LO pumped I/V curve. For further details we refer to G. de Lange Ph.D. dissertation [18].

4.1.5 Small-signal 3-port mixer model

The linear network representation of a heterodyne mixer is shown in Fig. 4.5. With the LO pumping parameter α known (previous Section) the small-signal mixing products can now be determined. Under the simplifying assumption that the large geometric capacitance of the SIS junction shunts all harmonics, the local oscillator frequency ω is seen (Chap. 3) to mix with the IF output frequency ω_0 as

$$\omega_m = m\omega + \omega_0 \ , \quad m = -1, 0, 1 \ . \tag{4.28}$$

In this notation $\omega_{-1} = \omega_I$ represents the image sideband, and $\omega_1 = \omega_S$ the signal sideband. In general each of the sidebands is terminated by an admittance Y_m.

The purpose of the mixer is to convert the incoming signal to an output frequency ω_0 at the IF output port Y_0, itself terminated into the (frequency dependent) complex load admittance Y_L of the IF matching network and low noise amplifier. To take into account the interaction between the ports, the small-signal voltage and current components can be linearly related by an admittance matrix $Y_{mm'}$

$$i_m = \sum_{m'} Y_{mm'} v_{m'} \ . \tag{4.29}$$

The values of the admittance matrix elements $Y_{mm'}$ are determined by the nonlinearity of the dc I/V curve (Eqs. 4.18 & 4.19) and the LO pumping parameter α. Expanding Eq. 4.29 in the individual elements (m = -1, 0, 1) and including the load admittance at the signal (Y_S), IF output (Y_L), and image (Y_I) ports gives

$$\begin{bmatrix} i_1 \\ i_0 \\ i_{-1} \end{bmatrix} = \begin{bmatrix} Y_{11} + Y_S & Y_{10} & Y_{1-1} \\ Y_{01} & Y_{00} + Y_L & Y_{0-1} \\ Y_{-11} & Y_{-10} & Y_{-1-1} + Y_I \end{bmatrix} \begin{bmatrix} v_1 \\ v_0 \\ v_{-1} \end{bmatrix} \ , \tag{4.30}$$

The admittance matrix elements are obtained by expanding the total current through the junction barrier and identifying those terms that are linear in the small-signal

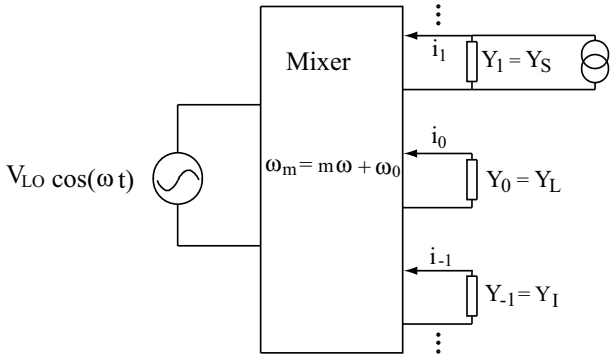

Figure 4.5: Schematic diagram of the heterodyne mixer with LO pump signal ω. In the matrix formalism the signal sideband frequency ω_1=ω_S, the image sideband ω_{-1}=ω_I, and the IF ω_0=ω_{IF}. All ports are terminated with an admittance Y_m.

voltage limit. The result [3] is of the form $Y_{mm'} = G_{mm'} + iB_{mm'}$ with

$$G_{mm'}(V_0, V_{LO}) = \frac{e}{2\hbar\omega_{m'}} \sum_{n,n'=-\infty}^{\infty} J_n(\alpha) J_{n'}(\alpha) \delta_{m-m',n'-n} \times \{[I^0_{dc}(V_0 + n'\hbar\omega/e + \hbar\omega_{m'}/e) - I^0_{dc}(V_0 + n'\hbar\omega/e)] + [I^0_{dc}(V_0 + n\hbar\omega/e) - I^0_{dc}(V_0 + n\hbar\omega/e - \hbar\omega_{m'}/e)]\} , \quad (4.31)$$

and

$$B_{mm'}(V_0, V_{LO}) = \frac{e}{2\hbar\omega_{m'}} \sum_{n,n'=-\infty}^{\infty} J_n(\alpha) J_{n'}(\alpha) \delta_{m-m',n'-n} \times \{[I_{KK}(V_0 + n'\hbar\omega/e + \hbar\omega_{m'}/e) - I_{KK}(V_0 + n'\hbar\omega/e)] - [I_{KK}(V_0 + n\hbar\omega/e) - I_{KK}(V_0 + n\hbar\omega/e - \hbar\omega_{m'}/e)]\} . \quad (4.32)$$

Thus we find that the small-signal admittance matrix elements separate into conductance elements $G_{mm'}$ and reactive elements $B_{mm'}$, which are fully determined by the dc I/V curve, its Kramers-Kronig transform, and LO pump level α.

To calculate the mixer conversion gain we need to know the output power delivered to an arbitrary IF load (Y_L) at the IF output port of the mixer. This includes the parasitic junction and RF matching network capacitance, shunted by the input admittance of the IF matching network and/or first low noise amplifier. This output power may be written in the form $G_L|v_0|^2/2$. To obtain v_0 the admittance matrix has to be inverted into an impedance matrix with elements $Z_{mm'}$

$$v_m = \sum_{m'} Z_{mm'} I'_m . \quad (4.33)$$

Normalizing the resulting $Z_{mm'}$ to Z_{00}, the internal IF output port impedance of the mixer, the output voltage at the IF port may be then obtained

$$v_0 = Z_{00} \sum_m \lambda_{0m} I_m . \quad (4.34)$$

$\lambda_{0m} = Z_{0m}/Z_{00}$ and does not depend on the output load termination $Y_0 = Y_L$.

For a double sideband mixer, the dissipated output power from the signal and image sidebands equals

$$P_{out} = \frac{1}{2} G_L |v_0|^2 = \frac{1}{2} G_L \left[|Z_{01}|^2 |I_S|^2 + |Z_{0-1}|^2 |I_I|^2 \right] . \quad (4.35)$$

$|Z_{01}|, |Z_{0-1}|$ describe the coupling from the signal and image sidebands to the mixer IF output. The available signal power in both sidebands is then given by

$$P_{in} = \frac{|I_S|^2}{8G_S} + \frac{|I_I|^2}{8G_I} , \quad (4.36)$$

and thus the DSB mixer conversion gain (P_{out}/P_{in}) may be derived as

$$G_{mix}^{DSB}(V_0, G_S, G_I, G_L, V_{LO}) = 4G_L\left[G_S|Z_{01}|^2 + G_I|Z_{0-1}|^2\right] . \quad (4.37)$$

In case of an ideal DSB mixer with equal sideband ratio and signal/image termination, $Z_{01} = Z_{0-1}$ and Eq. 4.37 reduces to

$$G_{mix}^{DSB}(V_0, G_S, G_L, V_{LO}) = 2G_L G_S|Z_{01}|^2 . \quad (4.38)$$

For an ideal SSB mixer, the image sideband is terminated into 0 K, and Eq. 4.37 simplifies to

$$G_{mix}^{SSB}(V_0, G_S, G_L, V_{LO}) = L^{-1} = 4G_L G_S|Z_{01}|^2 . \quad (4.39)$$

4.1.6 Noise properties

The noise properties of a mixer can also be described using the multiport network of Fig. 4.5. Fundamentally there are two dominant noise sources in an SIS mixer, noise due to thermally excited quasiparticles and shot noise due to the large local oscillator pump current. Thermal noise from the port terminations may be neglected. Following Tucker and Feldman [3], the noise power coupled into an IF load is

$$P_{noise} = G_L \sum_{m,m'} Z_{0m} Z_{0m'} H_{mm'} . \quad (4.40)$$

$H_{mm'}$ is known as the current noise correlation matrix and describes the generation and mutual correlation between the two dominant noise sources at different frequencies. Tucker [2] derived the correlation matrix and found the mixer noise temperature in the form

$$k_B T_{mix}^{LO} = \frac{1}{4G_S|\lambda_{01}|^2} \sum_{m,m'} \lambda_{0m}\lambda_{0m'}^* H_{mm'} , \quad (4.41)$$

with

$$\begin{aligned} H_{mm'}(V_0, V_{LO}) = \frac{e}{2\hbar\omega_{m'}} \sum_{n,n'=-\infty}^{\infty} & J_n(\alpha) J_{n'}(\alpha) \delta_{m-m',n'-n} \\ & \times \{coth[(eV_0 + n'\hbar\omega + \hbar\omega_{m'})/2k_BT] I_{dc}^0(V_0 + n'\hbar\omega/e + \hbar\omega_{m'}/e) \\ & + coth[(eV_0 + n\hbar\omega - \hbar\omega_{m'})/2k_BT] I_{dc}^0(V_0 + n\hbar\omega/e - \hbar\omega_{m'}/e)\} . \end{aligned} \quad (4.42)$$

Thus the contribution to the total mixer noise (T_{mix}) is due to a combination of shot noise generated from the dc bias (V_0) and shot noise from the LO induced tunnel current. Not included in the Tucker noise analysis are multiple Andreev reflections (MAR) through pinholes in the (non-ideal) barrier [19]. This may be accounted for as described in Sec. 7.2.4. Another noise source not included is quantum noise due to vacuum zero-point fluctuations of the electromagnetic field. This half-a-photon noise,

$\hbar\omega/2k_B$, is due to the Heisenberg uncertainty principle and may either be included as part of the mixer noise, or as part of the mixer input signal [20, 21]. In practice the half-a-photon noise is attributed to the blackbody input load in accordance with Callen & Welton [22] and is in agreement with the Tucker theory [2]. Including the half-a-photon noise as part of the incoming radiation also works out favorably in terms of the mixer and receiver noise temperature. For a SSB mixer the minimum noise temperature, referred to the output of the mixer, is $\hbar\omega/k_B$ with half-a-photon added by the SSB mixer. For a DSB receiver, it can be shown that the minimum noise temperature referred to the input of the mixer is 0 K [2], and that the minimum noise temperature referred to the output of the mixer equals $\hbar\omega/2k_B$ K [20].

4.1.7 SIS Mixer properties

4.1.7.1 RF reflection coefficient

An important property in the design of SIS mixers is the RF input reflection coefficient. For each sideband, this quantity may be calculated once the embedding impedance Y_{emb} and intrinsic input admittance Y_{RF} of the tunnel junction is known. To obtain the junction admittance, the complex large signal LO current through the SIS junction of Eq. 4.26 is divided by $V_{LO}(V_0)$, itself obtained from a fit to the LO pumped I/V curve

$$Y_{RF}(V_0, V_{LO}) = \frac{I^{\omega}_{LO}}{V_{LO}(V_0)} \ . \tag{4.43}$$

As we have seen $V_{LO}(V_0)$ is, strictly speaking, a (small) function of bias voltage for a capacitively tuned SIS junction. However, to a good first order approximation V_{LO} can be assumed constant on the first photon step below the gap. In addition, judging from Eqs. 4.24 & 4.25 the RF junction admittance at the LO, signal, and image sideband of a DSB mixer will be similar. It is also important to note that Y_{RF} is independent of the sideband and IF load termination. When the LO voltage is smaller than the photon step, e.g. $\alpha = eV_{LO}/\hbar\omega < 1$, Y_{RF} can be approximated by

$$\begin{aligned} Y_{RF}(V_0, V_{LO}) = {} & \frac{e}{2\hbar\omega} J_0(\alpha)^2 \left[I^0_{dc}(V_0 + \hbar\omega/e) - I^0_{dc}(V_0 - \hbar\omega/e) \right] \\ & + i \frac{e}{2\hbar\omega} J_0(\alpha)^2 \left[I_{KK}(V_0 + \hbar\omega/e) - 2I_{KK}(V_0) + I_{KK}(V_0 - \hbar\omega/e) \right]. \end{aligned} \tag{4.44}$$

It can be seen that Eq. 4.44 reduces to the classical conductance dI_{dc}/dV_0 with the susceptance term $\rightarrow 0$ when $\hbar\omega/e$ is smaller than the dc nonlinearity of the gap. Assuming that the RF embedding impedance is known [10, 11, 17], the RF reflection coefficient may now be found

$$S11_{RF}(V_0, V_{LO}) = \left| \frac{Y^*_{emb} - Y_{RF}}{Y^*_{emb} + Y_{RF}} \right| . \tag{4.45}$$

To minimize reflections between the mixer and the telescope (the secondary mirror) $S11_{RF}$ should preferably be kept $>$ -6 dB.

4.1.7.2 IF output admittance and conversion gain

In 1981 Shen [23] presented a paper describing the quasiparticle conversion gain in SIS mixers. He formulated the intrinsic mixer output admittance Y_{IF} as

$$Y_{IF}(V_0) = \frac{1}{Z'_{00}} \ , \tag{4.46}$$

where Z' denotes the augmented Z matrix ($Y^{-1}_{mm'}$) with IF load admittance $Y_L = Y_0{=}0$ ($Z_L = \infty$). For a double sideband mixer, with $Y_1 = Y^*_{-1} = Y_S = G_S{+}iB_S$, the output admittance is real due to symmetry in the Y matrix. In this case Y_{IF} can also be obtained by subtracting the load conductance from the total mixer conductance at the IF output frequency:

$$Y_{IF}(V_0) = G_{IF} = Y_{00} = \frac{1}{Z_{00}} - G_L \ . \tag{4.47}$$

From the above expressions, it is evident that Y_{IF} does not depend on the IF load conductance G_L. The quantity G_{IF} can be derived from the subgap slope of the LO pumped I/V curve (Fig. 4.4b). Knowing Y_{IF} and Y_L the IF reflection coefficient may be calculated

$$S11_{IF}(V_0) = \left| \frac{Y^*_L - Y_{IF}}{Y^*_L + Y_{IF}} \right| . \tag{4.48}$$

Following Shen, the mixer conversion gain of Eq. 4.39 can be separated into a coupling factor η_{IF} and intrinsic mixer gain factor L_0^{-1} according to

$$\begin{aligned} G^{SSB}_{mix}(V_0, G_S, G_L, V_{LO}) = L^{-1} &= \eta_{IF} L_0^{-1} \\ &= \left(\frac{4 G_{IF} G_L}{|Y_{IF} + Y_L|^2} \right) \left(\frac{G_S}{G_{IF}} |\lambda_{01}|^2 \right) . \end{aligned} \tag{4.49}$$

From the above analysis, it is clear that a matched condition is obtained at the IF output port of the mixer, when $G_L = |G_{IF}|$ and $B_L = -B_{IF}$. Following this thread, when the mixer output conductance is positive we find that $\eta_{IF} = 1$ and that the SSB mixer gain equals the intrinsic mixer gain, e.g. $L^{-1} = L_0^{-1}$. When however the mixer output conductance is negative $\eta_{IF} = 0$ and infinite mixer gain is possible. Feldman [24] has shown that under the condition of a negative IF match, the reflection coefficient at the signal, image, and every harmonic sideband will tend to infinity. Needless to say, this is a condition to be avoided.

The derived analysis is valid under the condition that the susceptance of the geometric SIS junction capacitance is sufficiently small to be ignored. This is certainly the case for intermediate frequencies around 1 GHz. However when the mixer IF is increased to 8 GHz, or above, the parasitic susceptance can no longer be ignored, and causes the mixer gain to roll off. In Sec. 4.1.10 we present a case study and offer a solution with a more integrated IF circuit approach.

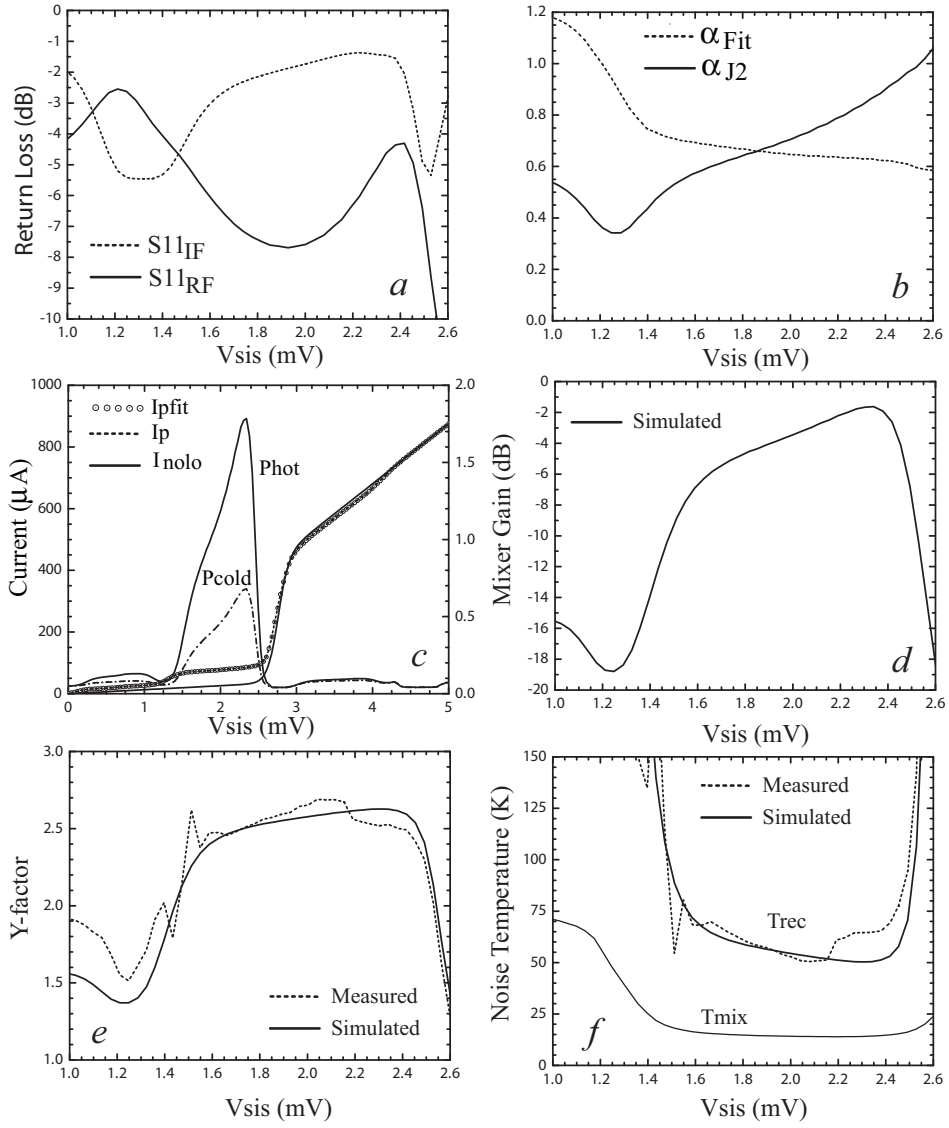

Figure 4.6: *a*) Calculated input and output return loss as a function of SIS bias voltage (345 GHz). The from simulation obtained RF embedding admittance is 160.2+i28.4 mS. The IF load admittance is 28.1+i41.9 mS. *b*) $V_{LO}(V_0)$ obtained from a fit against the measured LO pumped I/V curve. Note that α_{Fit} may be approximated as a constant (0.65). α_{J2} represents the LO pumping on the second junction (text). *c*) Heterodyne response. T^*_{hot}=267.3 K, and T^*_{cold}=73.2 K. In deriving the input noise temperatures (Fig. 5.3) we find a best fit to measurement with a front-end optics loss t_{RF}=0.9156, and physical temperature T_a=24.6 K. *d*) Derived DSB mixer gain. *e*) Simulated and measured Y-factor. *f*) DSB receiver and mixer noise temperature. In the mixer noise we have included 1 $\hbar\omega/k_B$ K of photon noise.

4.1.7.3 Calculated receiver performance

With the embedding admittance, LO pump level, and IF load admittance established, Tucker's three port approximation can then be used to calculate the mixer noise temperature and DSB mixer conversion gain G_{mix}^{DSB}. Once these quantities are obtained, the IF output power P_{IF} may be obtained via

$$P_{IF}^{DSB}(V_0, V_{LO}) = k_B\big[(T_{load}^{*} + T_{mix}) \cdot G_{mix}^{DSB} + T_{IF}\big]BG_{IF} \ . \tag{4.50}$$

T_{load}^{*} represents the effective noise temperature at the input of the mixer and depends on the optical loss in front of the mixer (Sec. 5.1.2). B is the IF bandwidth and T_{IF} the equivalent IF noise temperature referred to the input of the low noise IF amplifier. To experimentally derive the IF noise temperature we use the shot noise from the SIS junction, when biased above the gap, as a calibrated noise source. For details on this procedure, we refer to Chap. 7. Once the hot and cold load IF response is known, the receiver noise temperature may then be calculated via the well known Y-factor method ($Y = P_{hot}^{IF}/P_{cold}^{IF}$), with

$$T_{rec}^{DSB}(V_0, V_{LO}) = \frac{T_{hot} - YT_{cold}}{Y - 1} \ . \tag{4.51}$$

In Fig. 4.6a we depict the calculated input and output return loss of an AlN based SIS mixer design at 345 GHz (Chap. 7). In the calculations we have fit the measured LO pumped I/V curve with the unpumped I/V curve of Fig. 4.4. This provides $\alpha(V_0)$ according to Eq. 4.23, and is indeed reasonably constant on the first photon step below the gap (Fig. 4.6b). Since there are two junctions (Sec. 7.2.2), distanced 54.9 μm via a 10.31 Ω transmission line (63.58° phase at 345 GHz), the LO voltage across the second junction can also be calculated (α_{J2} in Fig. 4.6b). In Fig. 4.6c we depict the simulated heterodyne response, as well as the fitted $\alpha(V_0)$ LO pumped I/V curve. The shape of the hot and cold (heterodyne) response is slightly different than that obtained from measurement (Fig 7.10). This is attributed to the effect of higher order harmonics, which have been ignored in the simplified 3-port Tucker model. Fig. 4.6d shows the calculated DSB mixer gain. Finally, in Figs. 4.6e, f we plot the calculated DSB receiver and mixer noise temperature and Y-factor against measured values at 345 GHz. Despite the simplification of ignoring higher order harmonics, the 3-port Tucker model fits the measured data quite well. To calculate the receiver noise temperature we use the Callen & Welton [22] formulism with half a photon of noise, due to zero-point vacuum fluctuations, included as part of the input blackbody radiation load.

4.1.8 RF matching networks below the energy gap

As is clear from Fig. 4.4d, for bias voltages on the first quasiparticle step, the junction's quantum susceptance (B_{RF}) is approximately zero with the junction susceptance dominated by the parasitic barrier capacitance, C_j. The general expression for the RF conductance of a LO-pumped SIS junction with arbitrary upper and lower sideband response and harmonics is well described by Eq. 4.31.

Under the assumption of being in the low LO power limit where $\alpha \equiv eV_{lo}/\hbar\omega < 1$, having equal sideband response functions, and that the LO harmonics are shorted by the large parasitic junction capacitance, we are allowed to use the approximate, but simplified, solution of Eq. 4.44. Here $G_{RF} = \mathrm{Re}[Y_{RF}]$ and is given by the slope of the line joining points on the pumped IV curve one photon step above and below the dc bias point [25]. R_{RF} (G_{RF}^{-1}) ranges from $R_n/3$ in the lower part of the sub-millimeter band to R_n for frequencies $\geq$ 500 GHz. The admittance of the junction can thus be described as

$$Y_{RF} = (Y_{RF} + i\omega C_j) \tag{4.52}$$

with the value of C_j, the geometric junction capacitance, determined by the thickness and material properties of the barrier (Table 4.1).
The RF conductance varies slowly with frequency and for our design purposes can be assumed constant.

The coupling efficiency between the antenna and junction has the form

$$\eta(\omega) = \frac{4G_{RF}G_p}{\mid Y_{RF} + Y_p \mid^2}. \tag{4.53}$$

Y_p is the waveguide probe admittance which, by design, has an approximately constant admittance locus (Chap. 7). To achieve optimum coupling it is required that Y_p=Y_{RF}^*. The simplest way to achieve this condition is to tune out the junction susceptance with an open or closed transmission line in parallel to the junction (commonly referred to as open or closed ended stub).

The admittance of a transmission line with a characteristic admittance $Y_0 = Z_0^{-1}$ is given by

$$Y_s = Y_0 \frac{Y_l + iY_0 tan(\beta l)}{Y_0 + iY_l tan(\beta l)} \ . \tag{4.54}$$

β is the propagation constant = $2\pi/\lambda$, Y_l the load admittance at the end of the transmission line, and βl the electrical length. For $Y_l = 0$ (open circuit) the input susceptance becomes

Table 4.1: Specific capacitance of selected tunnel barriers as a function of current density (fF/μm^2), as used in the SIS junction designs of this thesis. Estimated error bars are $\lesssim$ 10 %. Source: JPL

Material	**J_c=7 kA/cm^2**	**J_c=10 kA/cm^2**	**J_c=25 kA/cm^2**
AlO_x	60	82	–
AlN †	65	75	90
MgO	100	140	–

† Recent measurement at TU Delft indicate that the specific capacitance of AlN may be as low as 60 fF/μm^2 at J_c=25 kA/cm^2 [26].

$$B_s = iY_0 tan(\beta l) \tag{4.55}$$

The shunt susceptance of the open ended stub cancels the junction susceptance for $Y_0 = \omega C_j$ and $l = 3/8\ \lambda$, giving 100 % coupling efficiency provided that the probe admittance is real and equals the RF conductance of the junction G_{RF}.

Similar results can be obtained with a shorted $1/8\ \lambda$ transmission line or an ideal inductor. The latter requires a series capacitance to allow the junction to be dc biased and as such is difficult to realize at submillimeter wavelengths. For a $1/8\ \lambda$ shorted stub we obtain

$$B_s = -iY_0 cot(\beta l) \tag{4.56}$$

The shorted stub provides a larger frequency range over which a match to the junction can be achieved. This can be observed by comparing the derivatives of Eq. 4.55 and Eq. 4.56.

It can be shown that the open-circuited stub has a theoretical bandwidth of $\approx 0.35\ \kappa^{-1}$ while the short-circuited stub has a bandwidth of $\approx 0.93\ \kappa^{-1}$, where $\kappa \equiv \omega R_{RF} C_j \sim \omega R_n C_j$. From a fabrication point of view both tuning networks suffer from being critically tuned, and in practice it has proven difficult to design a tuning stub that resonates at the design frequency. This is largely due to uncertainties in the manufacturing process and properties of niobium at 4 K.

These problems can to some extent be overcome by the use of a "twin-junction" matching network [27] or "end-loaded" tuning circuit [28, 29]. The "twin-junction" matching network works by putting a short length of transmission line ($\sim 63°$ at 345 GHz for the AlN-barrier designs presented in Chaps. 7 & 8) between two SIS junctions. In this manner the complex impedance of one junction, after transformation by the transmission line, is equal to the complex conjugate of the other.

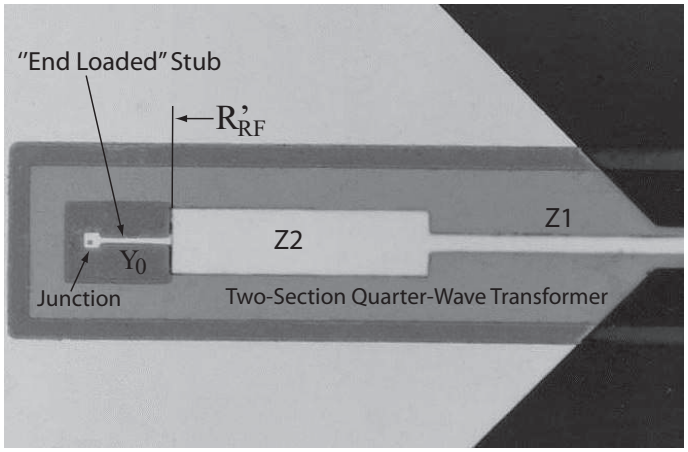

Figure 4.7: Layout of the "end-loaded" stub RF matching network. The junction is located inside a 5 x 5 μm^2 pad. At 345 GHz the width and electrical length of the "end-loaded" stub are 2 μm and 39.8° respectively.

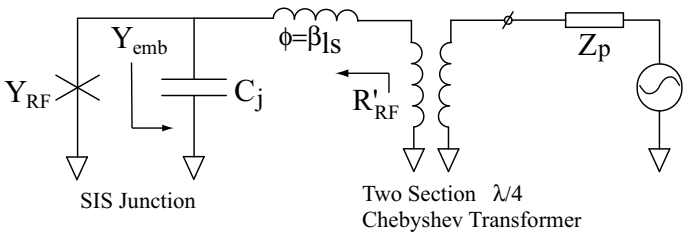

Figure 4.8: Electrical diagram of the RF matching network in Fig. 4.7.

In the remainder of this Section, we concentrate on the "end-loaded" stub RF matching network of Figs. 4.7 & 4.8, where a small section transmission line is placed in series with the junction. This results in the transformation of the complex junction admittance, Y_{RF} to a small but real impedance.

Consider a transmission line with a characteristic admittance $Y_0=\omega C_j$ and a load $Y_l=Y_{RF}$. Using Eq. 4.54 we calculate the electrical length of the "end-loaded" stub (βl_s) for which the imaginary part of Y_s equals zero.

$$tan(\beta l_s) = \frac{Z_0^2}{2}\left(\sqrt{G_{RF}^4 + 4Y_0^4} - G_{RF}^2\right) \ , \tag{4.57}$$

where Z_0 is the characteristic impedance (Y_0^{-1}) of the transmission line. We can simplify Eq. 4.57 for $G_{RF} < Y_0$,

$$tan(\beta l_s) \simeq 1 - \frac{1}{2\kappa^2} \ , \quad \kappa = \omega R_{RF} C_j > 1.2 \ . \tag{4.58}$$

Combining Eq. 4.58 and Eq. 4.54 we now solve for the real part of the transformed junction admittance.

$$G'_{RF} \simeq Y_0\left(\frac{\kappa(2\kappa^2-1)}{2\kappa^4 - 2\kappa^3\sqrt{\kappa^2-1} - 1}\right) \ , \quad l = l_s \ . \tag{4.59}$$

For $\omega R_{RF} C_j \gg 1$ Eq. 4.59 simplifies to

$$R'_{RF} \approx \frac{R_{RF}}{2\kappa^2} \ , \tag{4.60}$$

where R'_{RF} is the transformed resistance of a junction connected to an "end-loaded" stub of electrical length βl_s (Fig. 4.8). Then expressing Eq. 4.59 in terms of the electrical length of the series transmission line we find

$$R'_{RF} \approx R_{RF} cos(2\beta l_s) \ . \tag{4.61}$$

Thus, as the frequency increases we find from Eq. 4.58 that the stub length $l_s \rightarrow \pi/4$, which reduces R'_{RF} to a very small value (Fig. 4.9, Eq. 4.61). This is a serious drawback of the "end-loaded" stub. For frequencies above 500 GHz it gets more and

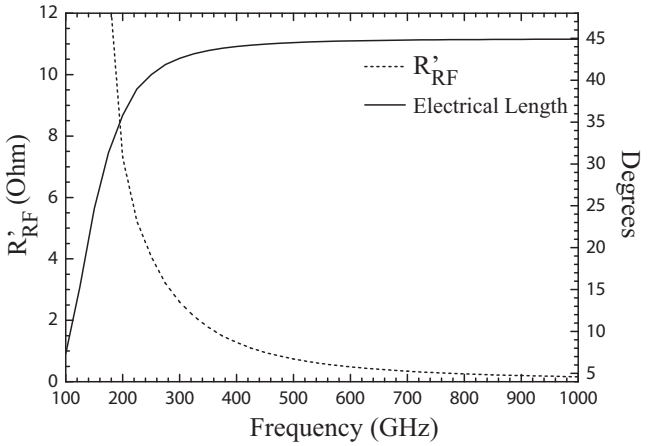

Figure 4.9: The real part of the transformed junction impedance R'_{RF} and electrical length of the "end-loaded" stub (Eq. 4.57), as a function of frequency. The junction's RF conductance is obtained from Tucker's theory. The calculations assume a 0.5 μm^2 junction area, and a 85 fF/μm^2 specific capacitance.

more difficult to transform R'_{RF} to match the probe impedance over a reasonable bandwidth.

To transform R'_{RF} to Z_p^*, we used a two section equal-ripple Chebyshev transformer [30]. Given the Bode-Fano criterion [31, 32], which dictates that ωRC $\leq \pi$ $\ln(\rho_m^{-1})$, this type of transformer provides the maximum bandwidth while allowing a tolerable pass band ripple. If we define ρ_m as the maximum allowed voltage reflection

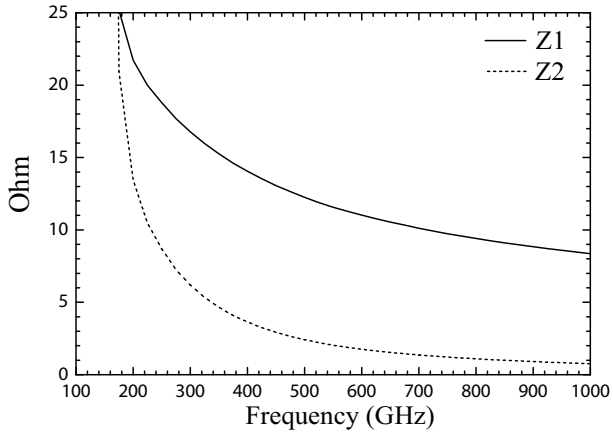

Figure 4.10: Characteristic impedances of an equal-ripple two-section Chebyshev quarter-wave transformer needed to transform R'_{RF} (Fig. 4.9) to a 40 Ω probe impedance. Above 500 GHz, $Z_2 < 2\ \Omega$ which makes implementation difficult.

coefficient of the passband ripple (Fig. 4.11), we can derive the impedances for the two quarter-wave sections that give the widest possible fractional bandwidth

$$Z_1^2 = Z_p\sqrt{R'_{RF}Z_p}\sqrt{\frac{1-\rho_m}{1+\rho_m}} \tag{4.62}$$

$$Z_2^2 = R'^2_{RF}\sqrt{\frac{Z_p}{R'_{RF}}}\sqrt{\frac{1+\rho_m}{1-\rho_m}}\ . \tag{4.63}$$

Z_1 is the high impedance section that connects to the waveguide probe. Z_2 is the low impedance section and attaches to the "end-loaded" stub (Fig. 4.7). Using Eq. 4.60 we can express Z_1 and Z_2 in terms of κ and the RF junction resistance

$$Z_1^2 \approx \frac{Z_p}{\kappa}\sqrt{\frac{R_{RF}Z_p}{2}}\sqrt{\frac{1-\rho_m}{1+\rho_m}}\ , \quad \kappa \gg 1 \tag{4.64}$$

$$Z_2^2 \approx \frac{R_{RF}}{4\kappa^3}\sqrt{2R_{RF}Z_p}\sqrt{\frac{1+\rho_m}{1-\rho_m}}\ , \quad \kappa \gg 1\ . \tag{4.65}$$

Eqs. 4.64 & 4.65 show that $Z_1 \propto \kappa^{-0.5}$ and $Z_2 \propto \kappa^{-1.5}$. For frequencies in the upper half of the submillimeter band Z_2 becomes very small. It is in practice difficult to realize a very low impedance superconducting microstrip transmission line because its aspect ratio, (length/width), becomes rather small. Connecting the high impedance "end-loaded" stub to a low impedance transmission line results in a large discontinuity, which adds an additional parasitic series inductance, thereby increasing the effective electrical length of the "end-loaded" stub, shifting the resonance down in frequency. This is an especially serious effect for frequencies above 500 GHz where the center frequency of the RF matching network is critically dependent on the "end-loaded"

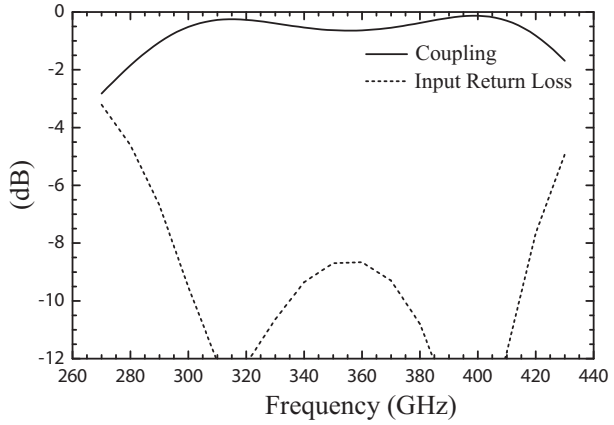

Figure 4.11: Input reflection coefficient and coupling efficiency of an "end-loaded" stub connected to a 50 Ω, 0.49 μm^2, Nb/AlO$_x$/Nb tunnel junction. The designed in-band RF reflection coefficient is -9 dB, which was a trade off between maximum RF bandwidth and optimum impedance match.

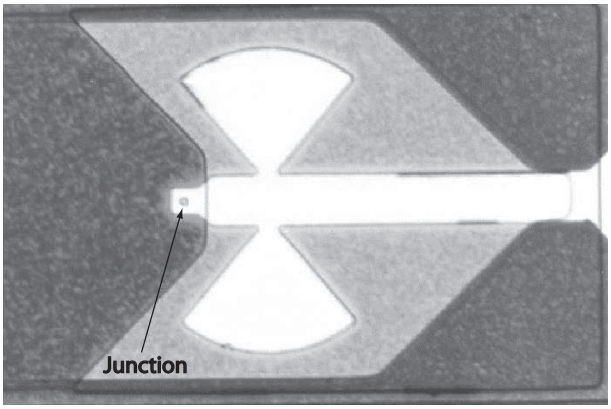

Figure 4.12: 1000× photograph of the junction and "butterfly" matching network. The junction size is 0.75 μm on a side.

stub's electrical length (Fig. 4.9). Fig. 4.10 depicts the calculated impedances of a two section quarter-wave transformer in the submillimeter band for a worst case in-band reflection coefficient, ρ_m, of -9 dB.

To avoid the issue of very small R'_{RF} values above $\sim$ 500 GHz we have introduced a "butterfly" RF matching network which constitutes a hybrid between a "end-loaded" and radial stub matching network. In Fig. 4.12 we show a photograph of the actual device as used in the 600 – 720 GHz receiver at the Caltech Submillimeter Observatory, Mauna Kea, HI [33]. Instead of transforming the junction impedance to a real impedance, we make the transformed impedance slightly inductive, which when presented with a shunt capacitance (parallel radial stubs) transforms the impedance to $\approx$ 3.5 Ω. A single section quarter wave transformer is then used to transform to the desired antenna or probe impedance. The advantages of this kind of matching scheme are several: First, the "end-loaded" stub length can be extended beyond $\pi/4$, which eases the constraints on the photolithography. Secondly, there is no large discontinuity. The latter greatly simplifies RF circuit models [11].

The microstrip transmission line properties are calculated based on expressions by Hammerstad & Jensen [34]. To take into account the finite complex conductivity of the superconductor (Eqs. 4.99 – 4.100), the transmission line properties have been modified following Kautz & Whitaker [35, 36]. For a more detailed discussion we refer to Zmuidzinas and Bin *et al.* [16, 37].

4.1.9 Sensitivity to operating temperature

Radiometer stability can be compromised when the mixer or IF amplifier (LNA) are subjected to temperature fluctuations. A slow change in the physical temperature of the mixer, or amplifier, results in a change in receiver gain. As a consequence, temperature fluctuations manifest themselves as low frequency drift noise at the output of the receiver [38, 39].

Because most, if not all, sensitive receivers require some kind of active cooling

system, it is of interest to quantify the maximum allowed temperature drift given a certain Allan variance system stability time (Appendix A). Lets assume an IF output signal of the form

$$s(t) = s_o(1 + g_t t). \tag{4.66}$$

Here g_t is defined as the normalized drift in system gain, and s_o the nominal total power at t=0. Defining m_t as the slope of the IF output drift with respect to time, it can be seen that $g_t = m_t/s_o$. If we take two contiguous measurements, one on source and one as reference, in a time period 2 T and define

$$z(T) = [s(T) - r(T)]/r(T) \ , \tag{4.67}$$

we obtain the variance of the relative drift

$$\sigma^2_{drift} \ = \ \langle z(T)^2 \rangle - \langle z(T) \rangle^2 \ . \tag{4.68}$$

Since the mean of $z(T) = 0$, Eq. 4.68 simplifies to

$$\sigma^2_{drift} = \langle [(s(T) - r(T))/r(T)]^2 \rangle \ = \ (g_t \cdot T)^2 \ . \tag{4.69}$$

This corresponds to a $\beta = +2$ slope for the drift contribution in an Allan plot (Figs. 7.14 & 10.5). At the same time we have for the radiometric noise (Eq. 10.1, Appendix A)

$$\sigma^2_{rf} = \langle [(s(T) - r(T))/r(T)]^2 \rangle \ = \ \frac{2}{\Delta\nu \cdot T} \ , \tag{4.70}$$

where $\Delta\nu$ is the bandwidth and T is the integration time of the data sample. Using the constant c to represent $1/f$ electronic noise, we obtain the general Allan variance form

$$\sigma^2_A(T) = (g_t \cdot T)^2 + \frac{2}{\Delta\nu \cdot T} + c \ . \tag{4.71}$$

Differentiating with respect to T provides the Allan stability time minima

$$T_A = (g_t^2 \Delta\nu)^{-\frac{1}{3}} \ . \tag{4.72}$$

Eq. 4.72 can now be re-written so that given a desired Allan stability time we obtain an estimate for the maximum allowed rate of change in system gain

$$g_t \ = \ ({T_A}^3 \cdot \Delta\nu)^{-\frac{1}{2}} \ . \tag{4.73}$$

For example, if a radiometer requires a broadband total power continuum detection of 4 GHz and has a required Allan stability time of 1 s, we find a maximum allowed drift in system gain of $1.4 \cdot 10^{-3}$ %/s (5.7 %/hour).

Having calculated the allowed gain drift, we can now get an idea of the maximum temperature fluctuation a niobium based SIS mixer and low noise cryogenic GaAs HEMT amplifier may be subjected to. Re-writing Eq. 4.66 to include a temperature dependence gives

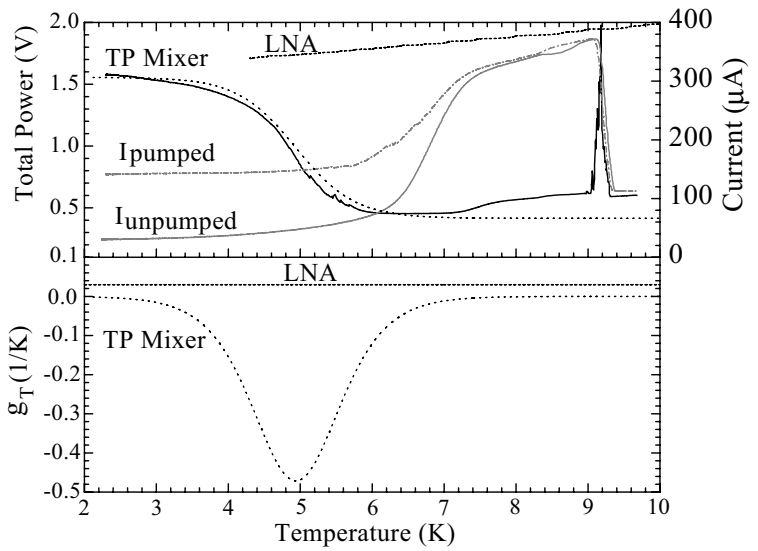

Figure 4.13: SIS mixer and LNA gain sensitivity as a function of temperature. Note the large difference in sensitivity to temperature between the LNA and LO pumped SIS mixer. The pumped and unpumped SIS current has been included for reference. In the experiment the SIS junction was constant voltage biased at 2.2 mV, the peak of the total power response at 4.2 K. The computed normalized slope $g_T = (1/so \cdot dP/dT)$ is shown in the bottom half of the figure and used in Eq. 4.75. Above 9.2 K the niobium film ceases to be a superconductor and the LO pumped junction current drops sharply.

$$s(t) = s_o[1 + g_T(T - T_o)] \ . \tag{4.74}$$

g_T in the above equation is defined as the (to the IF signal output) normalized temperature dependent drift of the system. If we now let m_T be the measured drift slope (dP/dT), a property of the SIS mixer and amplifier, then $g_T = m_T/s_o$.

To obtain m_T for a typical GaAs LNA and LO pumped SIS mixer [40], we performed the following experiments: First, the LNA was gradually heated from 4.2 K to 10 K in a time span of 1 hour (LNA input load at 4.2 K), while continuously recording the IF total power and amplifier physical temperature. In the second experiment we pumped the SIS mixer with LO power and over the course of an hour varied its temperature from 2.16 K to 9.6 K. The temperatures referred to in the text were measured at the outside of the mixer and amplifier block. During the LO pumped mixer experiment the LNA remained unheated at 2.16 K. In Fig. 4.13a we show the measured IF output power as a function of temperature. The normalized temperature dependent drift (g_T) is shown in Fig. 4.13b. It is clear that the SIS mixer has a negative temperature dependence, while the low noise amplifier has a positive and constant temperature dependence.

As the physical temperature of the mixer in Fig. 4.13 is changed from 2.16 K to 6 K we see the mixer output noise drop in an exponential manner. The dotted line in Fig. 4.13a is a best fit Fermi function. As the temperature of the mixer block

is increased from 2.16 K to 6 K only a minimal change in the junction's unpumped current (shot noise) is observed. The change in total power is to a very large extent caused by the temperature dependent conversion gain of the mixer. Above 7.2 K we observe a jump in total power, which is attributed to the by now large leakage current (shot noise) in the junction. At 9.2 K the niobium film ceases to be a superconductor and the LO pumped junction current drops sharply. Note, that the SIS mixer conversion gain sensitivity to temperature peaks around 4.9 K. This is unfortunately close to the 4.2 K bath temperature SIS mixers usually operate at (1 Bar atmospheric pressure). Moving to a high altitude site (600 mBar) improves the mixer conversion gain by $\sim$ 7–8 % [41] and reduces the mixer's sensitivity to temperature fluctuations. Reducing the helium bath temperature to 1.5 K reduces the temperature sensitivity to a minimum. It is interesting to note that the mixers in the HIFI instrument on Herschel [42] operate at a physical temperature of 2.2 K.

Combining Eqs. 4.66 & 4.74 we obtain the maximum allowed temperature change

$$\delta T = t \cdot \frac{g_t}{g_T} \ . \tag{4.75}$$

g_t is derived from Eq. 4.73 with g_T obtained from the bottom panel of Fig. 4.13(b).

In the example of the 4 GHz IF bandwidth total power continuum detection (worst case scenario) we estimate a maximum allowed gain drift of $14 \cdot 10^{-4}$ %/s, given a 1 s Allan time. At 4.2 K this gain drift equates to an allowed temperature drift of 470 μK/s for a GaAs LNA, and 66 μK/s for a LO pumped SIS mixer! In high resolution spectroscopy mode with a channel bandwidth of 100 KHz, a 1 s Allan stability time, and 4.2 km altitude helium bath temperature of 3.6 K, we find a maximum allowed temperature fluctuation of 106 mK/s for the low noise amplifier and 48 mK/s for the SIS mixer (13.8 mK/s at 4.2 K bath temperature).

4.1.10 IF bandwidth

As was seen in Chap. 1, there is a strong interest to increase the IF bandwidth of SIS receivers in order to facilitate extragalactic observations and spectral line survey efficiency. However, increasing the IF bandwidth generally also means increasing the IF operating frequency of the mixer, because it is very difficult to achieve a good IF impedance match to a low noise amplifier (LNA) for more than an octave bandwidth. Complicating the matter is that available cryogenic isolators, positioned between the mixer and low noise amplifier, nearly always have less than one octave of bandwidth. An alternative to increasing the IF bandwidth beyond an octave is to integrate a low noise amplifier directly into the mixer block, thereby minimizing the distance between the junction and LNA [43]. This is the approach taken with SuperCam in Chap. 9.

The IF output impedance Z'_{00} (Eq. 4.46) of a LO pumped SIS junction is typically 8–10 times the normal state resistance [44, 45]. Following the discussion in Sec. 4.1.7.2, the intrinsic mixer IF output admittance Y_{IF} is shunted by the parasitic capacitance of the junction and that of the RF matching network. Table 4.1 provides the specific capacitance for a variety of SIS tunnel barriers at a given current density. The RF matching network required to match the LO pumped SIS junction admittance (Eq. 4.44) to the waveguide embedding impedance (Sec. 4.1.8, Chap. 7) is commonly

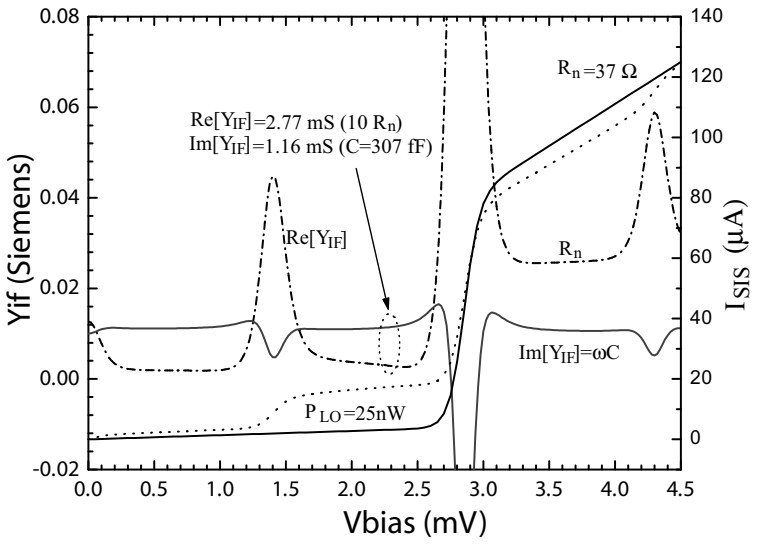

Figure 4.14: IF output admittance of a LO pumped SIS junction at 345 GHz. The combined RF matching network and parasitic junction capacitance is 260 fF. The embedding impedance locus is centered at 40 - i20 Ω, the IF frequency 6 GHz, and the junction R_nA product 18 $\Omega - \mu m^2$. The real part of the IF impedance is close to 10 R_n, while the imaginary part corresponds to a 307 fF capacitance. Of this 47 fF is quantum susceptance. Calculations are derived from Supermix [17].

implemented in microstrip mode, and fabricated with either SiO or SiO_2 as the dielectric between the wire layer and ground-plane. For example, the JPL process uses 450- and 200 nm thick SiO (ε_r=5.6) dielectric layers whereas UVa uses SiO_x with an (ε_r=4.3). The relatively high dielectric constant of SiO_x guarantees that any type of RF matching network implemented in microstrip introduces significant parasitic capacitance, thereby limiting the obtainable IF bandwidth of the mixer [29, 46].

Now consider the ωR_nC product of a SIS junction. For a niobium SIS junction with AlO_x barrier and current density (J_c) of 7–10 kA/cm^2, the ωR_nC product is ~ 1 at 100 GHz. In contrast, an AlN barrier junction with J_c=25 kA/cm^2 has an ωR_nC product of 1 at $\sim$ 180 GHz (Chap. 7).

It can be seen that the combined junction and RF matching network geometric capacitance is nearly the same for all microstrip tuned SIS devices. This is especially so if one considers that the fabrication process for SIS junctions is universal. We are justified therefore to do a case study of the popular and widely used "end-loaded" stub RF matching network, without losing too much generality [28, 47, 48, 49]. As an example we investigate a SIS junction/RF matching network with a combined parasitic capacitance of 260 fF at the IF Port of the mixer. Superconducting mixer calculations using Supermix [17, 50] have been performed in order to better understand the IF output conductance, optimum IF load impedance and IF frequency limitations of the SIS mixer.

In Fig. 4.14 we plot the junction IF output admittance as a function of bias voltage. For reference sake we show the pumped and unpumped IV curves as well.

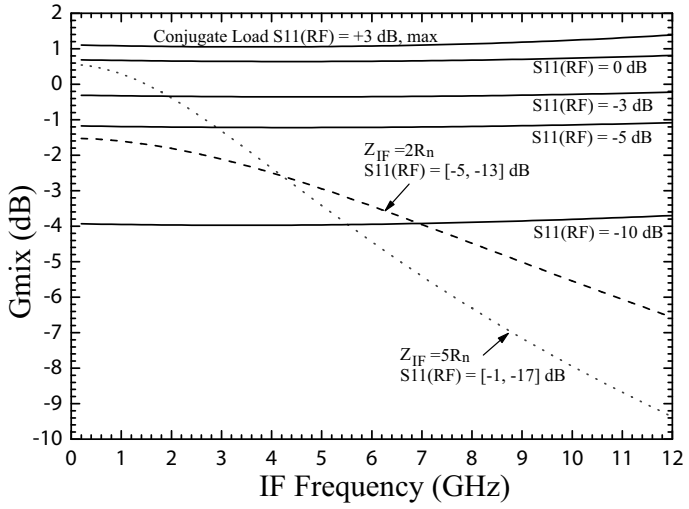

Figure 4.15: Mixer gain and RF reflection, S11(RF), as a function of IF frequency for different IF terminations loads. Presenting a conjugate load results in mixer gain and a large RF reflection (+3 dB). Presenting a real load such as 2 R_n or 5 R_n is adequate at the lower IF frequencies, but results in a large loss in mixer performance at IF frequencies above 8 GHz. The frequency independent mixer gain (horizontal lines) occurs when the IF termination includes a negative shunt capacitance. Unfortunately such a design is physically unrealizable. A good alternative is shown in Fig. 4.16.

The IF frequency is 6 GHz, and 3 harmonics were used in the harmonic balance part of the program. The junction IF output impedance consists of a real part (10 R_n) shunted by a capacitive component of 307 fF. This includes the quantum susceptance, and is a more accurate value than the estimated 260 fF mentioned earlier. To see how the junction's IF admittance varies as a function of IF frequency we ran the mixer simulation from 0.5 to 12 GHz. The result is shown in Fig. 4.15. The IF junction admittance is comprised of a parallel RC network, with $R = 10\ R_n$ and $C = 307$ fF.

Intuitively one may think that it is best to conjugate match the mixer IF output admittance. However, aside from mixer gain, this also provides a +3 dB reflection gain [S11(RF)] at the RF input port of the mixer (Eq. 4.30, top curve Fig. 4.15)! Reflection gain is liable to causes significant standing waves (VSWR) between the mixer and the telescope, with baselines distortions likely at the output of the back-end spectrometer. A more suitable value for S11(RF) is $\geq$ -5 dB, which results in a slightly reduced mixer gain but much more stable instrument (Sec. 7.2.2).

To achieve a broad IF bandwidth, an IF matching network with integrated tuning circuit is needed *before* the IF signal is taken off chip (via an inductive bondwire). A natural design is the Chebyshev impedance transformer, implemented for example in co-planar wave (CPW) with a capacitance integrated on chip. This is the approach we have taken with the high current density AlN barrier SIS junctions design for the Caltech submillimeter Observatory (Chaps. 7 & 8). This concept has also been very successfully applied to the integrated receiver of Koshelets *et al.* [51]).

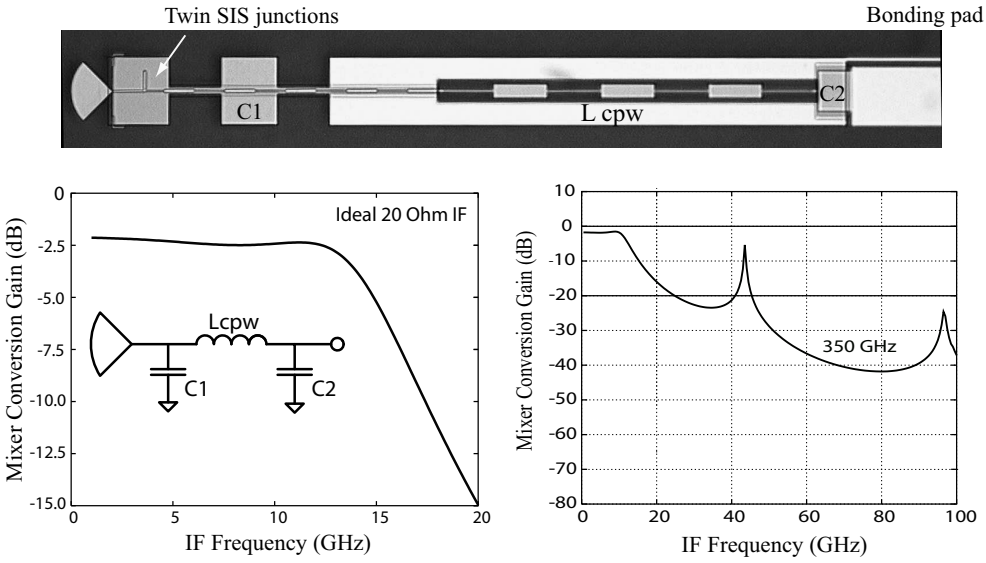

Figure 4.16: IF response of the new high current density AlN-barrier SIS junctions with on-chip IF matching. For a more detailed description refer to Chaps. 7 & 8.

In Fig. 4.16 we show an actual 380 – 520 GHz twin-SIS junction mixer chip with integrated IF. The theoretical IF response is flat to $\sim$ 13 GHz when terminated into a 20 Ohm load. Above 13 GHz the IF frequency response rolls off as a second order pole due to the integrated capacitance. This helps minimize saturation in the SIS junctions [52] (Chap. 7). It should be noted that this circuit is critically

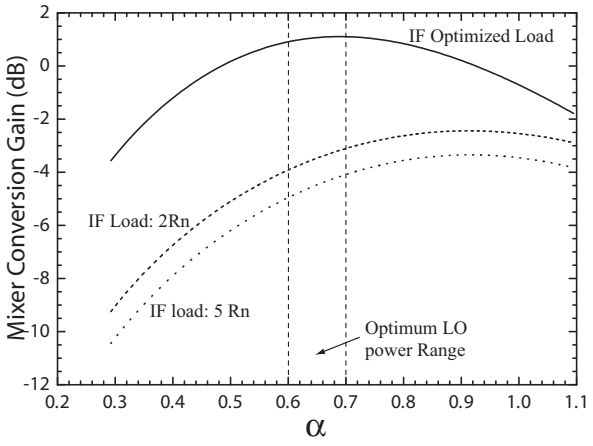

Figure 4.17: Mixer conversion gain as a function of LO power (α) for various IF load terminations. IF frequency is 6 GHz, LO frequency 345 GHz, and the R_nA product 18 Ω-cm^2.

tuned, and that deviations from perfection will cause the IF passband to have a more characteristic "double-tuned" response. And finally, in Fig. 4.17 we present the calculated mixer conversion gain as a function of LO power at the junction. Optimal LO pumping is found with $\alpha \equiv eV_w/\hbar\omega = 0.75$. For an $R_n = 37\ \Omega$ this corresponds to a LO power level at the junction of $\sim$ 30nW. For comparison, the LO power required to optimally pump a high current density AlN barrier junction with $R_nA = 7.6$, and similar device area, $\sim$ 75 nW. The twin SIS junctions of Chap. 7 requires approximately 150 nW.

4.1.11 SIS mixer stability as a function of magnetic field

Now that we have an understanding of the theoretical relationship between magnetic field and the ac Josephson effect (Sec. 4.1.2), and the SIS tunnel junction as a phase coherent photon detector, it becomes constructive to investigate the quasiparticle mixer heterodyne system stability (Sec. 2.3.5 and Appendix A) as a function of magnetic field.

For this measurement we used the recently installed "Technology development receiver" (Trex), at the Caltech submillimeter Observatory (CSO) in Hawaii. The mixer employs a twin AlN barrier high current density SIS junction as described in Chap. 7. By design the SIS junctions are rectangular in shape (0.7 x 1.0 μm on a side), e-beam defined, and oriented 45° to the magnetic field in the plane of the junction (Fig. 7.4). The projected junction geometry thus approximates that of a diamond rather than a rectangle or circle. Judging from the measured shape of the critical current vs. magnetic field in Fig. 4.18 this does indeed appear to be the case [53]. We

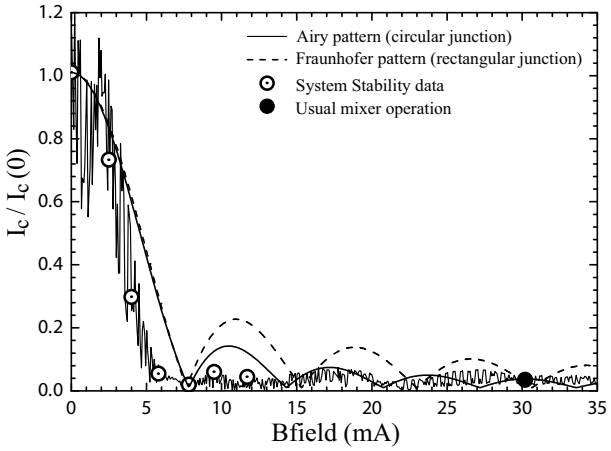

Figure 4.18: Measured critical current (I_c) vs. magnetic field coil current for Trex, the technology development receiver of Chap. 7. Stars indicate at which magnetic field setting the system stability data was taken. The mixer is usually operated around 30 mA to avoid mixer conversion gain (text). However the best total power and spectroscopic stability is obtained at the first Josephson null (7.8 mA), which corresponds to one flux quantum ($h/2e = 2.07 \times 10^{-15}$ Wb) of magnetic field through the barrier.

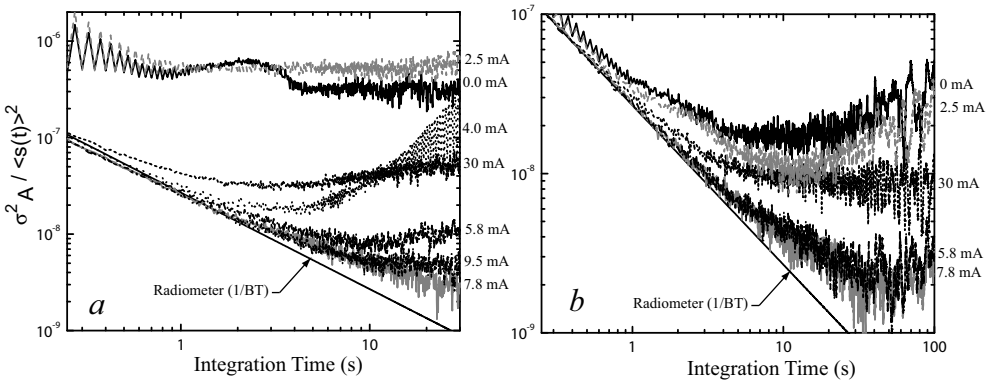

Figure 4.19: System stability as a function of applied magnetic field. *Left*) Total-power Allan variance. For very small magnetic field settings, there is large excess (Josephson oscillations) noise. A clear optimum is visible at the first Josephson null (7.8 mA). Operating the mixer at a 30 mA magnetic field current setting (4^{th} Josephson null) actually degrades the stability performance. *Right*) Spectroscopic Allan variance. We find a factor of two deviation from radiometric noise at $\sim$ 16 s. This is for a magnetic field current setting of 7.8 mA and corresponds to approximately 80 s in a 1.5 MHz noise fluctuation bandwidth. As with the continuum stability results, operation near the 4^{th} Josephson null (30 mA) is non-optimal. A $\pm$ 40 % current deviation from the 1^{st} Josephson null appears acceptable.

find therefore that junction geometry affects the shape, and how broad a minimum in the critical current suppression can be achieved. In Chap. 9 we discuss SIS junctions fabricated by the University of Virginia (Lichtenberger *et al.*) for SuperCam, a 64 pixel heterodyne focal plane array. The tunnel junctions are circular, and the critical current vs. magnetic field suppression is expected to follow an Airy pattern.

In the experiment we limit ourselves to a fixed 345 GHz LO frequency, a bias voltage of 2.25 mV, and local oscillator pump level of 85 μA. These bias settings are optimal for this particular junction design (Sec. 7.3.2). From the above discussion, we understand that the 3^{rd} Shapiro step is at 2.138 mV, 0.11 mV below the chosen bias voltage. In this regard the experiment should be considered as "nominal", and not as a worst case scenario.

The system stability was measured at a variety of carefully chosen magnetic field settings. As seen from Fig. 4.19 the first null corresponds to 7.8 mA. However, as was noted in Chap. 7, appreciably more current is needed (30 mA) to slightly suppress the superconducting energy gap and thereby avoid mixer gain and unwanted interference from ac-Josephson oscillations mixing with the third harmonic of the LO signal (Sec. 7.3.2). The latter can possibly effect the calibration accuracy of the instrument. Slightly complicating the situation is that the parallel twin-SIS junctions form a SQUID, or superconducting quantum interference device. This explains the sawtooth like modulation on top of the measured data, its periodicity set by the self inductance of the twin-junction loop. To derive the continuum and spectroscopic mixer stability (Appendix A) two fixed tuned 35 MHz bandpass filters with center frequency of 5 and 7 GHz were used, similar to the setup in Fig. 10.1. In this way two IF channels are formed in the middle of the 4 – 8 GHz receiver IF passband. This

allows the spectroscopic Allan variance to be established (Sec. 10.2.1). The interest of the experiment is to establish the location, and to which precision the Josephson effect (Cooper pair tunneling through the barrier) needs to be suppressed, as this has significant bearing on automated tuning algorithms and baseline quality/distortion.

Throughout the experiment the receiver beam terminated into a 290 K hot black body. The measured Y-factor was 2.6, which corresponds to a receiver noise temperature of 50 K. As for the LO source, we used a fundamental Gunn oscillator (Carlstrom *et al.*) and a VDI [54] ×4 multiplier. The Gunn was left free running after a substantial warm-up period of $\sim$ 12 hours. Any (slow) drift will only manifest itself in the total power Allan variance at long time scales and is therefore of no concern in this experiment. In the spectroscopic Allan variance the drift component is common to both IF channels, and is removed in the analysis.

Judging from Fig. 4.19 the total power Allan variance exhibits large excess noise (Josephson oscillations) for very small magnetic field settings. A clear optimum is visible at the first Josephson null (7.8 mA, Fig. 4.18). Operating the mixer near the 4^{th} Josephson null (30 mA) actually degrades the stability performance. A factor two deviation in continuum stability from radiometric performance occurs at $\sim$ 8 s. Given the 35 MHz 8-pole filter passband, and assuming a drift slope $\beta = 2$ (Appendix A), this equates to a total power stability of $\sim$ 38 s in a (typical) 1.5 MHz spectrometer noise fluctuation bandwidth. The spectroscopic Allan variance deviates a factor two from radiometric noise at $\sim$ 16 s. This is again at the first Josephson null and corresponds to approximately 80 s in a 1.5 MHz noise bandwidth. Note that the large excess noise at zero magnetic field is to a large extent removed by the zero's order baseline subtraction of the spectroscopic Allan variance calculation. Quite unexpected, 1 s double beam switch (DBS) spectroscopic observations are actually possibly (spectroscopic Allan time $\sim$ 2 s) with no applied magnetic field! Of course the line intensity calibration will be terrible (Sec. 2.3.6). As with the continuum stability results, operation near the 4^{th} Josephson null (30 mA) is non-optimal. In the experiment the two IF channels are 2 GHz apart (5 and 7 GHz), and it may be expected that spectroscopic subtraction improves with closer channel spacing (Josephson noise more correlated).

This information is particular relevant for extragalactic observations, where due to the generally wide emission linewidths and weak line intensities, binning of spectrometer channels to 100 MHz is not uncommon. In this case operation on, or near, the 1^{st} Josephson null is important. For narrow line observations the data suggests that the magnetic field current setting is reasonably relaxed, with $\pm$ 40 % from the optimal setting an acceptable limit. As a final note, the experiment was performed on an IR labs LHe cryostat. System stability performance with closed cycle refrigerators is expected to be somewhat reduced due to microphonic modulation of the LO - mixer standing wave (Chap. 10) [55].

4.2 Electrodynamics and the non-local anomalous limit

4.2.1 Transmission line model

To propagate the RF and LO signals to the described SIS tunnel junction (mixing element), superconducting transmission lines are typically employed. Below the superconducting energy gap (2Δ) superconductors exhibit no loss to direct currents (dc), and very low loss to alternating currents (ac). Above the energy gap the situation changes as RF and LO photons have enough energy to break electron pairs in the superconducting film. This phenomena causes large absorption loss (attenuation) in the superconducting films in front of the mixing element, with significantly degraded mixer sensitivity as a result. In this Section we take a closer look at the anomalous skin effect in superconductors, and the associated complex conductivity and surface impedance (loss) above and below the energy gap. We start our discussion with the general transmission line model as shown in Fig. 4.20.

R represents the resistance due to the finite conductivity of the conductor, and G the shunt conductance due to dielectric loss in the material between conductors. L and C are the transmission line series inductance and shunt capacitance per unit length. From network theory we have what is known as the "telegraph" equations:

$$\frac{dV_s}{dz} = -(R + i\omega L)I_s, \quad \frac{dI_s}{dz} = -(G + i\omega C)V_s \ . \tag{4.76}$$

Combining the above with Maxwell's curl equations for a uniform plane wave yields the frequency dependent complex constant of a lossy medium

$$\gamma = \alpha + i\beta = \sqrt{(R + i\omega L)(G + i\omega C)} \ . \tag{4.77}$$

The propagating electric field in the z-direction thus has the form

$$E_{xs} = E_{x0}e^{-\alpha z} \cdot e^{-i\beta z} \ . \tag{4.78}$$

α is known as the attenuation constant (Nepers/m), and β as the phase constant (Rad/m) with $V(z) = V(0)e^{-\gamma z}$, and $I(z) = I(0)e^{-\gamma z}$. Since the power transmitted is equivalent to $Re[V(z)I(z)^*]$ we find that

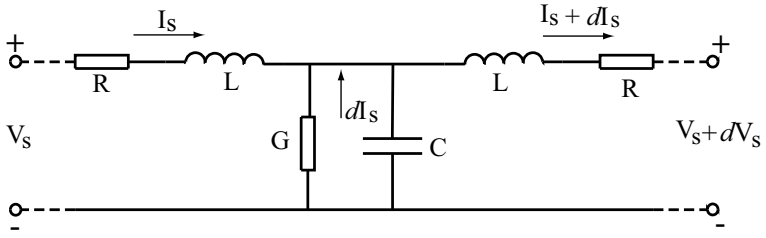

Figure 4.20: Lumped element equivalent circuit of a transmission line.

$$P(z) = P(0)e^{-2\alpha z} \ . \tag{4.79}$$

Thus the power attenuation is 2α. The characteristic impedance of the lossy transmission line can now be defined as

$$Z_0 = \frac{V(z)}{I(z)} = \frac{R + i\omega L}{\gamma} = \sqrt{\frac{R + i\omega L}{G + i\omega C}} \ , \tag{4.80}$$

which for a lossless transmission line reduces to the familiar $Z_0 = \sqrt{L/C}$ expression. In the above expression the phase constant $\beta = 2\pi/\lambda$ and the phase velocity $v = \omega/\beta$. For a lossless transmission line $\alpha = 0$ and $\gamma = i\beta$. It may be readily observed that $v = 1/\sqrt{LC}$. Dispersion on the transmission line occurs when β is a non-linear function of frequency (the phase velocity is different for different frequencies). Related to this discussion is group delay, defined as $v_g = d\omega/d\beta$. For narrow band signals (for example HDTV in the submillimeter wavelength regime) v_g should ideally be zero. Finally, the quality factor of a lossy transmission line equals

$$Q_L = \frac{\omega LC}{RC + GL} = \frac{\beta}{2\alpha} \ . \tag{4.81}$$

If we can ignore the substrate conductance G then we see that Eq. 4.81 reduces to the classical formulism $Q = \omega L/R$. We will use this knowledge in Chap. 5 where we discuss the effect of transmission line loss above the superconducting energy gap.

4.2.2 Plane waves in lossy dielectrics

All dielectric materials have some conductivity G. In the context of our discussion on loss, it is constructive to have a brief overview of dielectric loss. Again from Maxwell's equations the complex propagation constant for a lossy slab of material can be obtained

$$\gamma = i\omega\sqrt{\mu\varepsilon}\sqrt{1 - i\frac{\sigma}{\omega\varepsilon}} \ , \tag{4.82}$$

with the intrinsic complex impedance [56] derived as

$$\eta = \sqrt{\frac{i\omega\mu}{\sigma + i\omega\varepsilon}} \ . \tag{4.83}$$

μ is the permeability of the lossy material ($\mu = \mu_r\mu_0$). For non-magnetic materials $\mu_r = 1$ and μ equals the permeability of free space ($\mu_0 = 4\pi 10^{-7}$ H/m). ε is the permittivity, obtained from the material's dielectric constant (ε_r) times the permittivity of free space ($\varepsilon_0 = 8.85410^{-12}$ F/m). For free space Eq. 4.83 reduces to $\eta = \sqrt{\mu_0/\varepsilon_0} = 377\ \Omega$.

If there is loss in the material ε will be complex ($\varepsilon' - i\varepsilon''$). The real part is the material dielectric constant, whereas the imaginary part accounts for loss due to damping of vibrating dipole moments [57]. For free space, being lossless and real,

$\varepsilon' = \varepsilon_0$. The loss tangent of the material is defined as the ratio of the conduction current to displacement current density and becomes

$$\tan\delta = \frac{\sigma}{\omega\varepsilon} = \frac{\omega\varepsilon'' + \sigma}{\omega\varepsilon'} \ , \tag{4.84}$$

with $\varepsilon = \varepsilon_r\varepsilon_0$ (1 - i $tan\delta$). From general circuit design principles the quality factor (Q) of a tuned, or resonating, circuit is defined as

$$Q = \frac{StoredEnergy}{Loss\ per\ Radian} = \frac{\omega}{\Delta\omega} = \frac{1}{tan\delta} \tag{4.85}$$

Thus a low loss dielectric material exhibits a high Q. This is important not only in the context of Kinetic Inductance Detectors (KID's) [58], but also the RF tuning circuits we concern ourselves with (Sec. 4.1.8). The $\omega R_n C$ (Q) of AlO_x barrier SIS junctions in the submillimeter ranges from 2–8, and even less for AlN barrier SIS devices. This is much lower than the SiO_x dielectric loss ($tan\delta$ at 100 GHz $\approx 10^{-3}$ [59]), and we are justified in ignoring dielectric material loss, e.g. $G \cong 0$ in Fig. 4.20.

4.2.3 Plane waves in good conductors

For a perfect conductor the current density at any point within the conductor is related by

$$\mathbf{J} = \sigma\mathbf{E} \ . \tag{4.86}$$

In case of a good conductor the loss tangent factor $\sigma/\omega\varepsilon \gg 1$ and Eq. 4.82 reduces to

$$\gamma = i\omega\sqrt{\mu\varepsilon}\sqrt{-i\frac{\sigma}{\omega\varepsilon}} = (1+i)\sqrt{\frac{\mu\omega\sigma}{2}} \ . \tag{4.87}$$

The conduction current at any point within the conductor becomes

$$J_x = \sigma E_x e^{-\delta_c z} cos(\omega t - \delta_c z),\ \delta_c = \sqrt{\frac{2}{\mu\omega\sigma}} \ . \tag{4.88}$$

$\delta_c = \sqrt{2/\mu\omega\sigma}$ is known as the classical skin depth, and represents the distance at which the current density decreases by e^{-1}, or 63.2 %. For example, room temperature aluminum has a conductivity of $\sigma_{300K} = 3.82 \cdot 10^7$ S/m, so that at 500 GHz $\delta_c^{300K} =$ 115 nm. At cryogenic temperatures σ_{4K} in thin-films is known to improve by a factor 5–10 so that δ_c^{4K} at 500 GHz $\sim$ 40–55 nm. Given that the electron mean free path l_e of aluminum is $\approx$ 16 nm, we find that $\delta_c \gg l_e$. This condition is known as the "local limit", e.g. the limit where local-electrodynamics such as presented here apply. The power loss (heat) due to the skin depth in a good, but non-perfect, conductor may be obtained from Eq. 4.79.

The intrinsic impedance of the conductor is $\eta = i\omega\mu/\gamma$ and simplifies in a good conductor to

$$\eta(\omega) = (1+i)\sqrt{\frac{\omega\mu}{2\sigma}} = (1+i)\frac{1}{\sigma\delta_c} \ . \tag{4.89}$$

η is known as the complex surface impedance (Z_s) in a bulk metal. The real part of the surface impedance equals $R_s(\omega) = Re(\eta) = \rho/\delta_c$ ($\Omega/\Box$), and can be related to the average dissipated power (conductor loss) and free space impedance via

$$P = \frac{2 \mid E_0 \mid^2 R_s}{\eta_0^2} \ , \quad \eta_0 = \sqrt{\frac{\mu_0}{\varepsilon_0}} = 377\ \Omega \ . \tag{4.90}$$

The surface resistance contributes to the series impedance of the transmission line and the surface reactance to L, as shown in Fig. 4.20. For the microstrip tuning networks we concern ourselves with (Fig. 4.7), the attenuation due to the conductor loss may be approximated by

$$\alpha \cong \frac{R_s}{Z_0 W} \quad (Np/m) \ , \tag{4.91}$$

where Z_0 equals the characteristic impedance, and W the width of the microstrip transmission line [60].

4.2.4 Surface impedance of normal metals

The general (non-bulk) equation for the surface impedance takes the form

$$Z_s(\omega) = R_s + iX_s = \frac{E_x(0,\omega)}{\int_0^d dz J_x(z,\omega)} \ , \tag{4.92}$$

where d is the thickness of the thin-film conductor. As was seen, the real part of the surface impedance contributes to the loss in the (microstrip) transmission line, and the imaginary component to the transmission line inductance. In Eq. 4.92 $E_x(0,\omega)$ is $\parallel$ at the surface, with $J_x(z,\omega)$ the current density into the conductor at a depth z. In the local limit, the electric field penetration depth is long in comparison to the electron mean free path, e.g. $\delta_c \gg l_e$ and the surface impedance for an arbitrary film thickness d may be solved from Maxwell's equations as

$$Z_s(\omega) = \sqrt{\frac{i\omega\mu_0}{\sigma}} coth\Big(d\sqrt{i\omega\mu_0\sigma}\Big) \ . \tag{4.93}$$

At cryogenic temperatures and microwave frequencies (or higher) when the metal mean free path $\geq \delta_c$, a non-local form must be assumed for $\mathbf{J}$ and $\mathbf{E}$. Pippard (1954) [61] proposed a replacement of the vector local current density $\mathbf{J}$ with a volume current density in a region around $\mathbf{r}$, such that [6, 62]

$$\mathbf{J}(\mathbf{r}) = \frac{3\sigma}{4\pi l_e} \int \frac{\mathbf{R}\big[\mathbf{R}\cdot\mathbf{E}(\mathbf{r}+\mathbf{R})\big]e^{-R/l_e}dV'}{R^4} \ . \tag{4.94}$$

dV' is an infinitesimally small volume at location $\mathbf{r}+\mathbf{R}$. In the limit of infinite conductor thickness ($d \to \infty$) Reuter-Sondheimer [63] obtained a simple expression for the surface impedance in the extreme anomalous limit ($l_e \gg \delta_c$)

$$Z_s(\omega) = \frac{1}{3^{1/2}\pi^{1/3}}(1+\sqrt{3}i)\mu_0^{2/3}\omega^{2/3}\left(\frac{l_e}{\sigma}\right)^{1/3} , \tag{4.95}$$

with the anomalous skin penetration depth as

$$\delta_a = \left(\frac{2\sqrt{3}l_e}{\pi}\right)^{\frac{1}{3}} \cdot \delta_c^{2/3} . \tag{4.96}$$

Judging from Eq. 4.95 we see that the surface impedance in the extreme anomalous limit only depends on the material properties l_e, σ which are nearly temperature independent. It is also interesting to observe that in all cases $\delta_a > \delta_c$. For normal metals σ is real if we ignore possible time relaxation effects at very high frequencies.

As an example, for a typical thin-film wire layer (Fig. 4.7) with thickness $d =$ 200 nm, aluminum metal with resistivity $\rho_{4K} = 1/\sigma \sim$ 0.5 $\mu\Omega$-cm, the mean free path is $\sim$ 250 nm [64]. At 500 GHz $\delta_c = 39$ nm, and we find that $l_e > \delta_c$ and $l_e \sim d$. This places Al at 4 K in the anomalous, rather than extreme anomalous limit. A method to calculate Z_s in the anomalous limit is given by Kautz [65] and solved numerically by Bin and Zmuidzinas *et al.* [16]. Bin found good agreement between the normal and anomalous skin depth, with a 40 % underestimation of Z_s when calculated in the extreme anomalous limit. In Fig. 4.22 we plot the complex surface impedance of Al in the local limit (Eq. 4.93), and compare it to that of Nb and NbTIN as calculated from the Mattis-Bardeen theory in the extreme-anomalous or local limit.

4.2.5 Surface impedance of superconductors

From the BCS theory we understand that pair formation between electrons is energetically advantageous. An attractive force between two electrons, with equal but opposite momenta and spin, occurs when the exchange of phonons (quantum of thermal energy) is taken into consideration. At temperatures below T_c two electrons are than bound in what is known as Cooper pairs and condense until an equilibrium is reached. At 0 K all Cooper pairs occupy the same minimum state, known as the BCS ground state where each electron has a binding energy $\Delta(0) = 1.764 k_B T_c$.

The average separation distance between two electrons forming a Cooper pair is called the coherence length ξ_0. The coherence length is the smallest size wave packet superconducting charge carriers can form. From an uncertainty-principle argument, $\xi_0 \simeq \hbar v_F / k_B T_c$, where v_F equals the Fermi velocity. In practice ξ_0 ranges from 0.1 – 1 μm, and is analogous to the mean free electron path length in the non-local electrodynamics of normal metals. Due to the large coherence length, the Cooper pairs are found to be highly overlapping.

A second, so far undiscussed phenomena is the so called "Meissner effect" (1933) [66]; the fact that magnetic flux is completely excluded from the interior of a superconductor. Similar to the exponential decay of an electric field in a normal metal, the magnetic flux density inside a superconductor was proposed by London [67] to decay as $B(z) = B_0 e^{-z/\lambda_L}$. In practice the measured magnetic penetration depth λ is larger than λ_L and can be linked via the Pippard coherence length $\xi^{-1} = \xi_0^{-1} + l_e^{-1}$.

In materials with impurities and alloys $\lambda = \lambda_L(\xi/\xi_0)^{1/2}$, and has a temperature dependence

$$\lambda(T) \approx \frac{\lambda(0)}{\sqrt{1-\left(\frac{T}{T_c}\right)^4}} \ . \tag{4.97}$$

This is the situation we concern ourselves with, and it is known as the "dirty limit" with $l_e \ll \xi$. This condition is similar to that of high T_c superconductors which exhibit very short coherence lengths and operate in the local regime ($\xi \ll \lambda$). It is interesting to note that near T_c all superconductors become local.

Empirically, the resistivity, critical temperature, and magnetic penetration depth obey the BCS relation [68, 69]

$$\lambda = \left[\frac{\rho(\mu\Omega - cm)}{T_c(K)}\right]^{1/2} \times \ 100 \ nm \ . \tag{4.98}$$

As a practical example, thin-film niobium is found to have a normal state resistivity of 5 $\mu\Omega$-cm, $\xi_0 = 37$ nm, $l_e = 11$ nm, and a $T_c = 9.2$ K. The latter values correspond to a magnetic penetration depth $\lambda_{nb}(0) = 75$ nm, and compares well with the measured bulk ($d = \infty$) penetration depth of 85 nm. With $l_e \ll \xi$ niobium is in the "dirty regime". NbTiN films have a measured resistivity [70] in the range 70–100 $\mu\Omega$-cm, depending on the quality of the film deposition, and with a $T_c \sim 15.2$ K exhibit a penetration depth around 200–250 nm. This is very similar to NbN, another "dirty limit" superconductor. For all of these superconductors the surface impedance needs

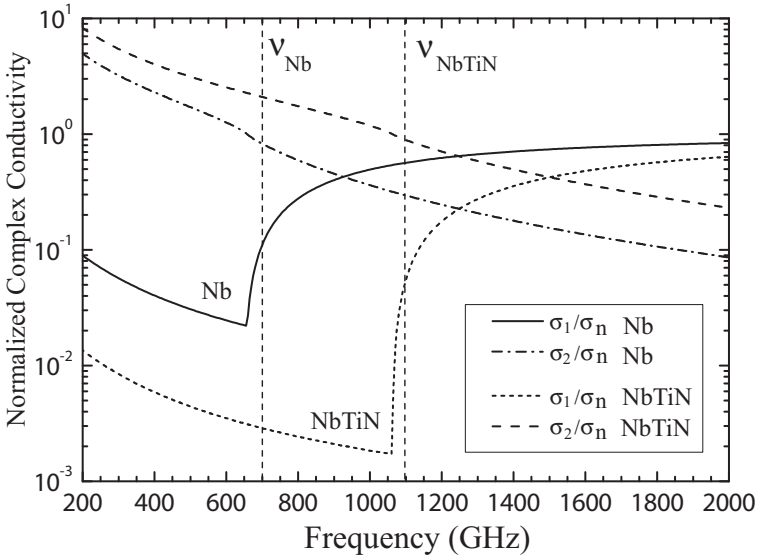

Figure 4.21: Calculated complex conductivity for niobium ($T_c = 9.2$ K, $2\Delta/e = 2.8$ mV) and NbTiN (T_c=15.3 K, $2\Delta/e = 4.4$ mV). For niobium the normal state resistivity $\rho_n = 5$ $\mu\Omega$-cm, and for good quality NbTiN films $\rho_n \sim 80$ $\mu\Omega$-cm.

to be calculated with the skin effect in the anomalous limit, as laid out by Mattis and Bardeen in 1958 [71]. Pöpel [72] carried out the numerical double integration to obtain the surface impedance for thin-films and found that if the thickness is $\geq$ 3 λ, the bulk limit solution is a good approximation of the exact solution. For thin niobium films the "bulk approximation" appears appropriate, however for NbTiN films as discussed in Chap. 5 this is not quite the case.

Nonetheless we can simplify our task by representing the superconductor with a complex conductivity [6, 73] $\sigma_s = \sigma_1 - i\sigma_2$ as obtained from the Mattis-Bardeen theory in the extreme-anomalous limit, where a local approximation can be made, and substitute σ_s in the expression for the surface impedance in the local limit of Eq. 4.93. Once the normal state conductivity σ_n, measured just above T_c, and the energy gap are known, σ_1 and σ_2 can then be obtained from:

$$\frac{\sigma_1}{\sigma_n} = \frac{2}{\hbar\omega}\int_{\Delta}^{\infty} dE[f(E) - f(E+\hbar\omega)]\frac{E^2+\Delta^2+\hbar\omega E}{\sqrt{E^2-\Delta^2}\sqrt{(E+\hbar\omega)^2-\Delta^2}}$$
$$+\frac{1}{\hbar\omega}\int_{\Delta}^{\hbar\omega - Delta} dE[1-2f(\hbar\omega - E)]\frac{\hbar\omega E - E^2 - \Delta^2}{\sqrt{E^2-\Delta^2}\sqrt{(\hbar\omega-E)^2-\Delta^2}}\ , \qquad (4.99)$$

$$\frac{\sigma_2}{\sigma_n} = \frac{1}{\hbar\omega}\int_{\Delta-\hbar\omega,-\Delta}^{\Delta} dE[1-2f(E+\hbar\omega)]\frac{E^2+\Delta^2+\hbar\omega E}{\sqrt{E^2-\Delta^2}\sqrt{(E+\hbar\omega)^2-\Delta^2}}\ . \qquad (4.100)$$

$f(E)$ is the Fermi-Dirac distribution as given in Eq. 4.7. In Fig. 4.21 we show the (calculated) normalized complex conductivity. The first term of Eq. 4.99 describes the scattering of thermally excited normal electrons. The second term describes the creation of photon-excited quasiparticles, and is zero for $\hbar\omega < 2\Delta$. Eq. 4.100 describes the "kinetic" inductance caused by Cooper pairs. The lower limit of the integral becomes $-\Delta$ for $\hbar\omega > 2\Delta$.

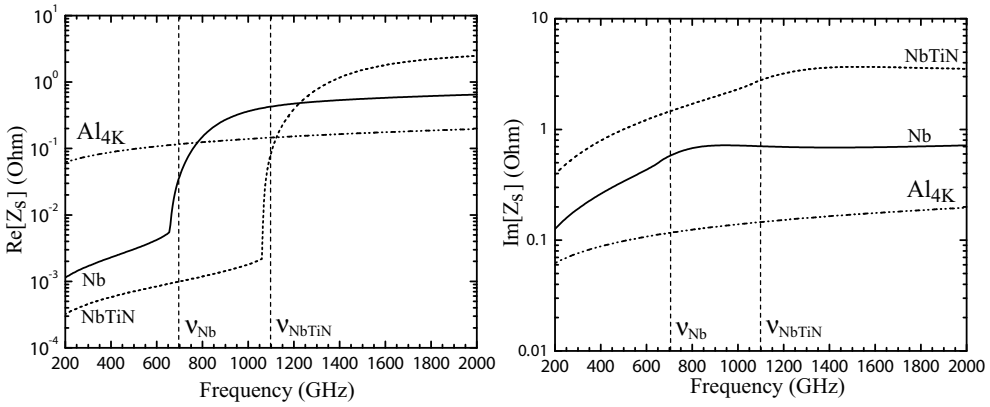

Figure 4.22: Calculated real (*left*) and imaginary part (*right*) of the surface impedance for niobium, NbTiN, and Aluminum at 4 K in the local limit (Eq. 4.93). See text for details.

In Fig. 4.22 we show the real and imaginary components of the complex surface impedance for Nb and NbTiN. Overlaid is the surface impedance of thin-film aluminum (200 nm) calculated in the local limit. Bin *et al.* showed good agreement between the local, or "dirty" limit, calculation and the rigorous non-local Mattis-Bardeen numerical integration for thick films. The approximation of the extreme anomalous limit (Eq. 4.95) showed an under estimation of R_s by as much at 40 %. Above $\sim$ 800 GHz the real part of the Al surface impedance (loss) is less that that of Nb. It should be noted that below the energy gap the surface impedance of a superconductor is purely inductive (Rs $\sim$ 0, Fig. 4.22 left panel) and given by $X_s = \omega\mu_0\lambda$. For Nb this corresponds to a surface inductance $L_s = \mu_0\lambda \sim 0.11$ pH/$\square$, and for NbTiN 0.3 pH/$\square$ [69]. In Chap. 5 we have a closer look at the first all-NbTiN film SIS mixer (Nb junctions), designed to operate in the 800 – 920 GHz atmospheric window. It also served as a demonstration receiver for HIFI [42] mixer bands 3–5 on the Herschel far-IR space observatory. As of this writing the all-NbTiN mixer of Chap. 5 remains the most sensitive heterodyne receiver in this frequency range.

4.3 HEB mixers: Introduction

Hot electron bolometer mixers (HEBs) consist of a strip of thin film superconducting material. As the name implies, HEB mixers work on the principle of the bolometric effect, which utilizes the strongly non-linear temperature dependent resistance of the superconductor as a bases for the heterodyne mixing process (Sec. 2.3). In the terahertz regime, well above the energy gap of the thin-film superconducting material, incident photons are able to break Cooper pairs (Sec. 4.1.1) and a uniform heating across the superconducting bridge may be assumed. To dissipate the incident power and have a reasonable response time, a bolometer needs to be coupled to a thermal reservoir. It is the mechanics of the heat capacity, and thermal conductance that governs the HEB response function.

For the HEB to function as a heterodyne mixer, both LO (V_{LO}) and RF (V_s) signals need to be present. The power dissipated in the bridge with dc resistance R_0 is therefore

$$P_B(t) = \frac{[V_{LO}cos(\omega_{LO}t) + V_s cos(\omega_s t)]^2}{2R_0} \ . \tag{4.101}$$

The resulting IF beat frequency is than $V_{IF}(t) = \frac{1}{2}V_{LO}V_s cos(|\omega_{LO} - \omega_s|)t$. To function as a terahertz heterodyne mixer, the time response of the HEB mixer is required to be on the order of tenth of pico-seconds (IF bandwidth should at least be several GHz and preferably more). This has been the subject of much research, with Chap. 6 devoted to this subject in its entirety.

In Fig. 4.23*a* we show a scanning electron microscope (SEM) close up of the HEB bridge. Typical dimensions are 1 μm by 0.1 μm and up to 4 μm by 0.4 μm. To couple the RF and LO signals to the HEB, quasi-optical antenna structures such as shown in Fig. 4.24 are typically employed [74, 75]. This is opposed to submillimeter receivers which are predominantly waveguide based (Chaps. 7-9). To facilitate low loss coupling of terahertz radiation to the HEB contact pads, the antenna structures are ordinarily

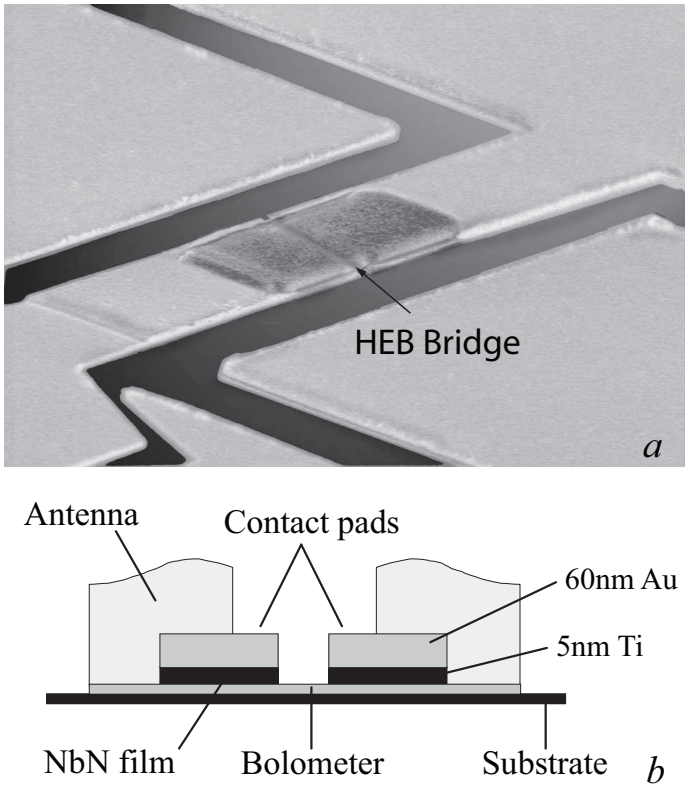

Figure 4.23: *Top* (a) Close up SEM picture of a 1 μm by 0.15 μm hot electron bolometer (HEB). As is evident from the photograph, the NbN bridge is covered with a protective resist mask. *Bottom* (b) Cross-section of the HEB and contact pad. Photograph courtesy TU Delft. See text for details.

made of high quality gold. A cross-section of the contact pads is shown in (Fig. 4.23*b*). The contact pad consists of 60 nm Au with a 5 nm Ti adhesion layer underneath. In the conventional fabrication process of the HEB mixer, the deposition of the contact pads is done without any cleaning of the NbN film. Thus it is to be expected that a contact resistance exists between the NbN film and the contact pad. The presence of such a contact resistance has been reported in literature [76, 77, 78] and explains why the device resistance of HEB mixers is always higher than expected, as based on the bolometer size and NbN sheet resistance. It goes without saying that the performance of the HEB mixer depends strongly on the (thermal) boundary conditions. A contact resistance between the NbN film and the contact forms a barrier for the hot electrons diffusing out of the bolometer. It also changes the effective length of the bolometer, because the contact resistance determines the length over which RF current flows through the NbN film. For a more detailed discussion on this subject we refer to Baselmans & Hajenius *et al.* [79, 80].

In Fig. 4.24b we show the HEB connected to a twin-slow antenna [74, 81]. A very similar device is currently in operation in the HIFI instrument of the Herschel space

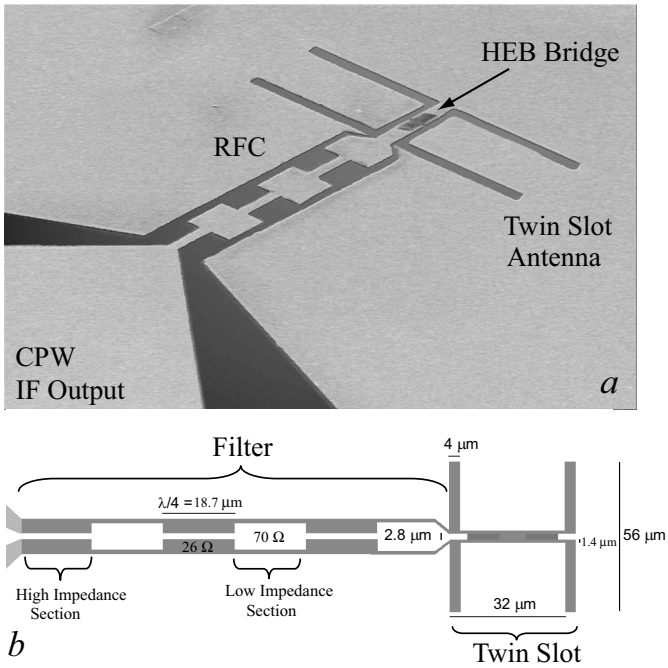

Figure 4.24: *Top* (a) SEM picture of a twin-slot antenna coupled HEB mixer. The IF output is taken via a 4 section high-low impedance CPW implemented RF choke as shown in the bottom panel. Photograph courtesy TU Delft. *Bottom* (b) Layout of the 1.6 THz twin-slot HEB mixer. The HEB bridge is symmetrically centered on the twin-slot antenna.

observatory [42]. The use of a twin-slot open structure antenna over, for example, a very broad bandwidth non-resonant spiral antenna offers the advantage that the "radiated" beam has a fixed polarization and a high level of "Gaussisity" [82]. We refer to Chap. 5 for further details on the twin-slot antenna in the context of SIS mixers.

As was seen earlier, the physical properties of the NbN film are essential to the HEBs operating principle. Well below the critical temperature of the superconductor the electron-phonon coupling is weak, and to a first order the electron gas may be treated as separate from the phonon system. The electron-electron interaction is however strong, and incident radiation will tend to thermalize the electrons before being dissipated to the surrounding phonon bath. As a result the thermally excited "hot" electrons have an equilibrium temperature that is higher than that of the lattice (phonons). Since heated electrons have a small heat capacity c_e, the corresponding thermal response time can be short [83], typically ≤ 3 ps for NbN films [84]. However, cooling of the "hot" electrons is another matter. This involves the transfer of energy to phonons (quantum of thermal energy), which by design either escape predominantly into the substrate (film thickness $d < 6$ nm), as would be the case of "phonon cooled" hot electron bolometers, or diffuse out of the Au contact pads (length of the superconductor strip $<$ electron diffusion length) in the case of "diffusion cooled"

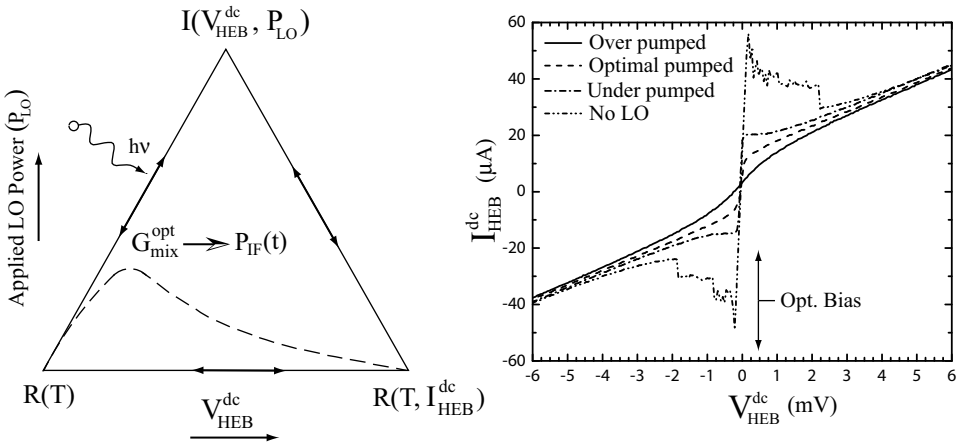

Figure 4.25: *Left*) Graphical representation of the HEBs device physics. DC bias is in the horizontal direction and applied LO bias in the vertical direction. At the lower left corner is $R(T)$, which is the intrinsic device resistance at temperature T. At the lower right is $R(T, I^{dc}_{HEB})$, the resistance as a function of temperature and dc HEB current [85, 86]. At the top we depict $I(V^{dc}_{HEB}, P_{LO})$, which is the current voltage characteristic as a function of bias voltage and local oscillator power. The dashed curve follows the HEB mixer conversion gain. Optimal mixer gain is typically achieved at 0.5 mV bias. The level of LO power (heating) depends on the volume (area) of the bridge. *Right*) Four I/V curves as a function of LO power. Applying a LO signal raises the electron temperature in the center of the bridge to the transition temperature (T_c), as shown in Fig. 4.26.

HEBs. The electron-phonon interaction time is determined by the film thickness as τ_{eph}=500T$^{-1.6}$ ps·K [83, 87].

As an example; for a NbN HEB with a 10 K electron temperature $\tau_{eph} \sim 12$ ps (Table 6.1). The heat transfer rate of phonons in the film to phonons in the substrate is known as the phonon escape time τ_{esc} and may be approximated by $10.5d$ ps/nm [88, 89]. For a typical NbN film thickness of 6 nm, this corresponds to an escape time of approximately 60 ps (Table 6.1). The described time constants can be used in the Perrin-Vanneste linearized two-temperature model [90] of Chap. 6 to estimate the IF bandwidth of the hot electron bolometer. It is found that the shorter the phonon escape time (thinner films), and the higher the electron temperature (T_c), the larger the IF bandwidth becomes [91, 92, 93].

To better appreciate the complex physical interactions that govern the HEB mixer, we depict in the left panel of Fig. 4.25 a diagram with the various processes. The dashed curve in the middle of the triangle indicates the condition for optimal mixer gain. In the right panel of Fig. 4.25 we show four I/V curves under various LO pump conditions. Without application of LO power (heating) there is up to a critical current (I_c), in this case ~ 50 μA, no substantial resistance in the NbN film. As the current approaches the critical current of the superconducting film, free vortices pairs created by the increase in temperatures and current enhanced two-dimensional (2D) phase slip events, or flux flow, give rise to a resistance and thus a voltage drop across the type III superconductor. Understanding this mechanism, Barends *et al.* [94] showed that this consideration leads to a correct description of the dc I(V) curve.

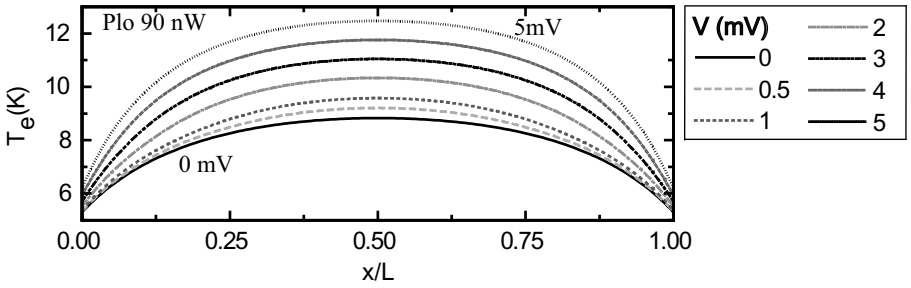

Figure 4.26: Calculated electron temperature profile along the length of the bridge at P_{LO}=90 nW at various dc bias voltages. The metal contacts on both sides of the bridge are assumed to be at a phonon temperature of 4.2 K. The calculation is performed using the heat-balance approach described in Sec. 6.2

With no LO power applied, the so developed resistance is negative and results in bias oscillations. This is evidenced from the unpumped I/V curve in Fig. 4.25. The onset of the vortex creation region is, under idealized conditions known as the Berezinskii-Kosterlitz-Thouless transition and has an electron temperature $T_{KT} < T < T_c$. In Fig. 4.25a we depict the condition of no LO power along the horizontal axis with $R(T) \rightarrow R(T, I^{dc}_{HEB})$.

Since the HEB is contacted on both sides by the antenna (Fig. 4.24), we find that under heating (LO or bias) "hot" electrons in close proximity to the contact pads diffuse out to this equilibrium reservoir. Note that heated electrons can be formed by application of LO power, or by application of a bias voltage. At the extremities of the HEB bridge, near the contact pads, the electron temperature will therefore take on the ambient temperature of the antenna. In the center of the bridge, there will be, due to the poor thermal conductivity of the superconducting film (decoupled electrons/phonons), a localized heating of the electrons. This effect results in a distributed temperature profile in the bridge, as shown in Fig. 4.26, and is governed by coupled differential heat balance Eqs. 6.1 and 6.2. In the center of the bridge the electron temperature rises to just above T_c which causes a breakdown in the coherent superconducting state. It is this mechanism that governs the heterodyne mixing process in hot electron bolometers.

The combined heating effect of LO signal and dc bias voltage brings the device to the optimal operating conditions for mixing (the electron temperature in the center of the bridge is approximately T_c). The application of LO signal and dc bias thus gives rise to a number of interacting and dissipative mechanisms. The result is that under normal operating conditions several processes occur simultaneously, not the least of which is the spatial variation of electron temperature across the bridge. It is therefore virtually impossible to learn about the underlying HEB physics based purely on measurements of the device under full operating conditions. The physical processes shown in Fig. 4.25a, as well as material and geometric properties such as the electron-phonon interaction time τ_{eph}, phonon escape time τ_{esc}, and electron/phonon specific heat capacity ratio c_e/c_{ph} (IF bandwidth, Chap. 6) all play a role in determining the heterodyne response of the hot electron bolometer mixer [95].

4.3.1 Electro-thermal Feedback and IF Standing Waves

As we have seen in Sec. 4.3, hot electron bolometers are thermal devices that operate near the superconducting transition temperature. It should not come as a surprise therefore that voltage reflections at the IF port influence the operation of the bolometer. This principle is known as electro-thermal feedback, or self heating, and is demonstrated in Fig. 4.27. In the past, primarily as a matter of convenience, the IF embedding impedance (Z_L) has usually been treated as a frequency independent resistance (50 Ω). This is however an over-simplification, and one that can have significant implication on the actual mixer operation.

In Chap. 6 we derive an expression for the conversion gain of the HEB mixer based on the standard lumped element model [96, 97]

$$\eta(\omega) = \frac{2\alpha^2 p_{lo}}{\chi^2 \cdot P_{dc}} \left| \frac{R_o Z_L}{(R_o + Z_L)^2} \cdot \frac{C^2}{[\Psi(\omega) + \Gamma_{if}\ C]^2} \right| \ . \tag{4.102}$$

Included in the bolometric responsivity (Eq. 6.15) is the complex embedding impedance Z_L, and reflection coefficient

$$\Gamma_{if} = \frac{R_o - Z_L}{R_o + Z_L} \ . \tag{4.103}$$

p_{lo} in Eq. 4.102 is the LO power at the device, and can be estimated from the isothermal technique [81, 98]. χ describes the ratio of LO power to dc power heating efficiency, C the self heating parameter [98, 99], $\Psi(\omega)$ the time dependent modulation of the electron temperature, and R_o the dc resistance at the operating point of the mixer (Re[Z_o]). The parameter $\Gamma_{IF}C$ represents the electro-thermal feedback and is zero for $Z_L = R_o$.

To demonstrate the electro-thermal feedback, we use as an example the HIFI HEB mixer band 6 & 7 IF design (Kooi *et al.*, 2004 [100]). Shown in Fig. 4.28a is the HEB mixer chip connected via a set of triple wirebonds to an IF circuit board. A 206 mm coaxial cable connects the IF board and bias Tee to a SRON/Kuo-Lian 2.4 – 4.8 GHz InP 2-stage HEMT low noise amplifier (LNA) with 26 dB gain and 5 K noise temperature. Due to lack of space, the scientific requirement of having

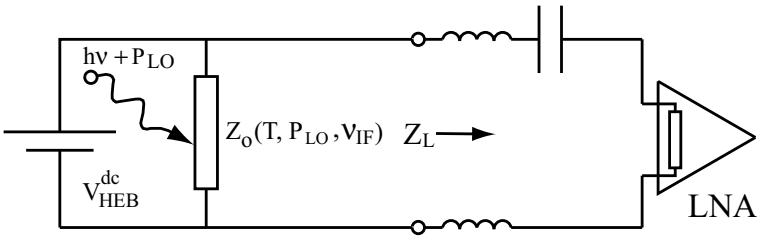

Figure 4.27: The principle of electro-thermal feedback in hot electron Bolometers (HEBsH). Voltage reflections from the IF signal chain induce a current in the bolometer, which results in a temporal redistribution of the localized heating in the bridge. The result is a small shift in the mixer operating point and subsequent modulation of the IF output signal. In an actual mixer, the IF embedding impedance is both complex and a function of frequency.

at least 2.4 GHz of instantaneous IF coverage, and the non-existence of a space-qualified isolator, it was decided not to use an isolator in the IF signal chain. To help minimize standing waves between the HEB mixer and low noise amplifier, extensive electromagnetic field simulations [10] were performed. The 3D model of the HEB mixer chip, CPW-microstrip transition, dc-blocking capacitor, and coaxial transition is shown in Fig. 4.28b.

Based on the lumped element expression of the HEB mixer conversion gain of Eq. 4.102, the effect of IF reflections can now be taken into account. This is shown in Fig. 4.29. It should be noted that the conversion gain model remains linked to a lumped element model, and as such deviations can be expected in extreme conditions. In the left panel of Fig. 4.29 we show $(\Psi(\omega)+\Gamma_{if}C)$. At low IF frequencies $\Psi(\omega) \sim 1$. $\Psi(\omega)^{-1}$ is plotted in Fig. 6.6, and can to a first order be approximated as a single pole roll off, hence the monotonic rise in $(\Psi(\omega)+\Gamma_{if}C)$. IF reflections cause a modulation of the electron temperature $\Psi(\omega)$ via Γ_{IF}. In the right panel of 4.29 we depict $C/(\Psi(\omega)+\Gamma_{if}C)$. It is evident that, by design, in the 2.4 – 4.8 GHz IF passband the

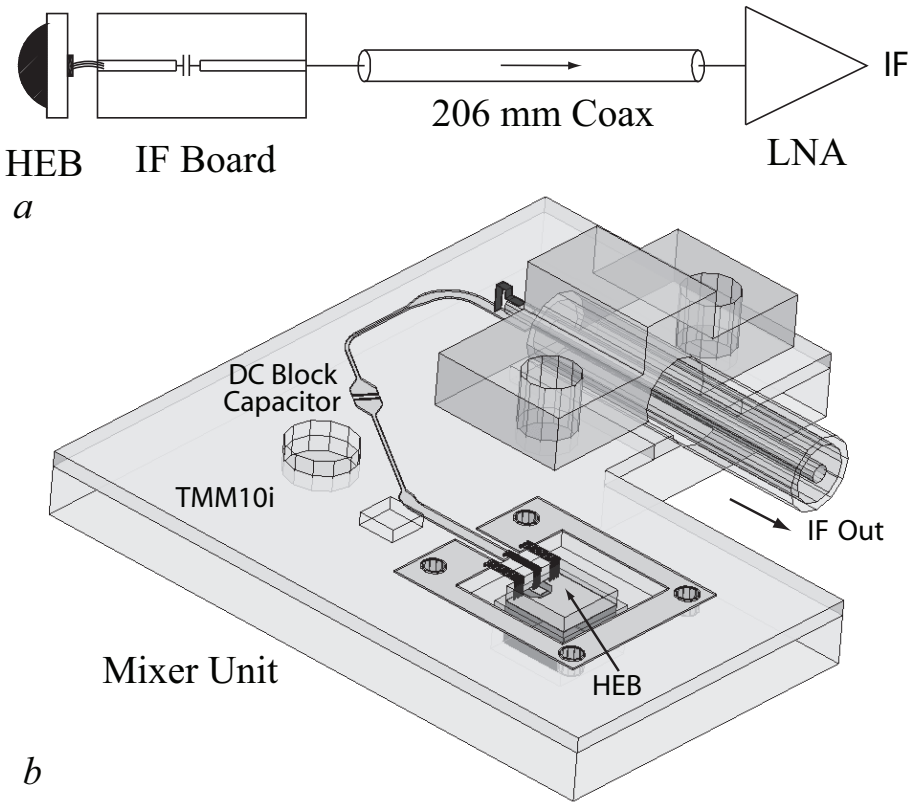

Figure 4.28: *Top*) (a) Layout of the 2.4 – 4.8 GHz HIFI band 6, 7 HEB mixer and IF signal chain. Due to space and availability no isolator is used. *Bottom*) (b) Mixer unit IF board layout. Included are the CPW-microstrip transition, dc blocking capacitor, and 50 Ω coaxial transition.

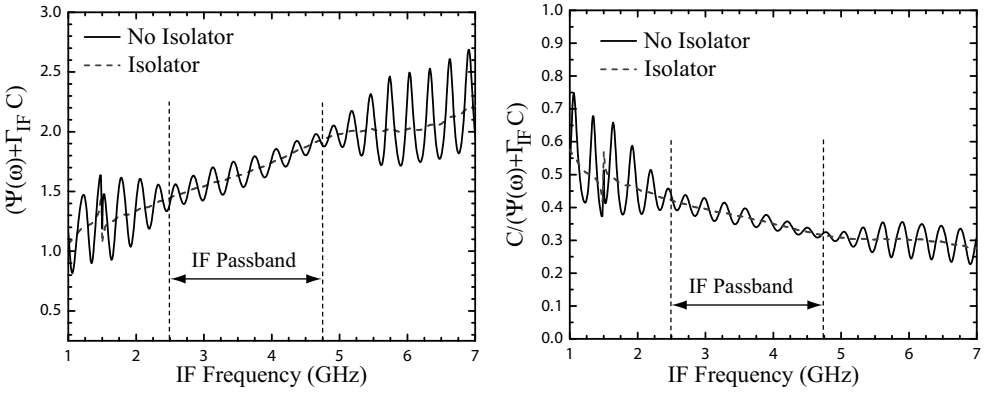

Figure 4.29: *Left*) $(\Psi(\omega) + \Gamma_{if}C)$ as a function of IF frequency. At low IF frequencies $\Psi(\omega) \sim 1$. By design, the IF standing wave modulation has been minimized in the 2.4 – 4.8 GHz IF passband. *Right*) $C/(\Psi(\omega) + \Gamma_{if}C)$ as a function of IF frequency. At low IF frequencies the electro-thermal effect is most pronounced. $\Psi(\omega)$ is the time dependent modulation of the electron temperature.

electro-thermal feedback modulation is minimized. The ripple period is $\sim$ 300 MHz, and corresponds to the physical distance of the 206 mm coax cable plus IF circuit board ($\sim$ 50 mm).

Fig. 4.30 shows the system performance of the HIFI band 6 & 7 HEB mixers. Panel *a* of Fig. 4.30 shows the system IF gain with and without isolator. The discovery of large excess receiver noise (not shown) in "HIFI-like" system measurements (no isolator and 200 mm coax cable) motivated a re-design of the mixer unit IF circuit board (Fig. 4.28b, [100]) and an investigation of the HEB mixer IF output impedance (Chap. 6). The embedding impedance presented at the HEB IF output port is shown in Fig. 4.30b, both with and without an isolator. It should be noted that the original HIFI HEB IF passband was specified to operate between 4 – 8 GHz. As shown in Chap. 6, a 4 – 8 GHz passband for NbN films is an almost impossible technical requirement, and a scientific compromise was found with a 2.4 – 4.8 GHz IF passband. Unfortunately, due to ferro-magnetic material properties, cryogenic isolators in this frequency range are essentially non-existent. The proper solution to this dilemma is to integrate a low noise amplifier (MMIC) into the mixer block, similar to what has been done by Morales *et al.* [101]. Given the constraints of HIFI however, this was not an option, and the redesigned IF circuit board of Fig. 4.28b was implemented instead.

The HEB mixer conversion gain is shown in panel *c* for three situations; with and without isolator, and based purely on the model without IF reflections (no electro-thermal feedback). This plot should be compared to Fig. 6.5 in which we show actually measured data with a much simpler IF board (Fig. 6.2) and wideband MMIC IF amplifier [102]. Finally, the calculated receiver noise temperature is provided in Fig. 4.30d. In the calculation we assume a 80 % optical transmission, 350 K mixer noise temperature, and a 6 K IF (based on measurements) noise temperature. The result is in good agreement with actual HIFI measured receiver system temperatures.

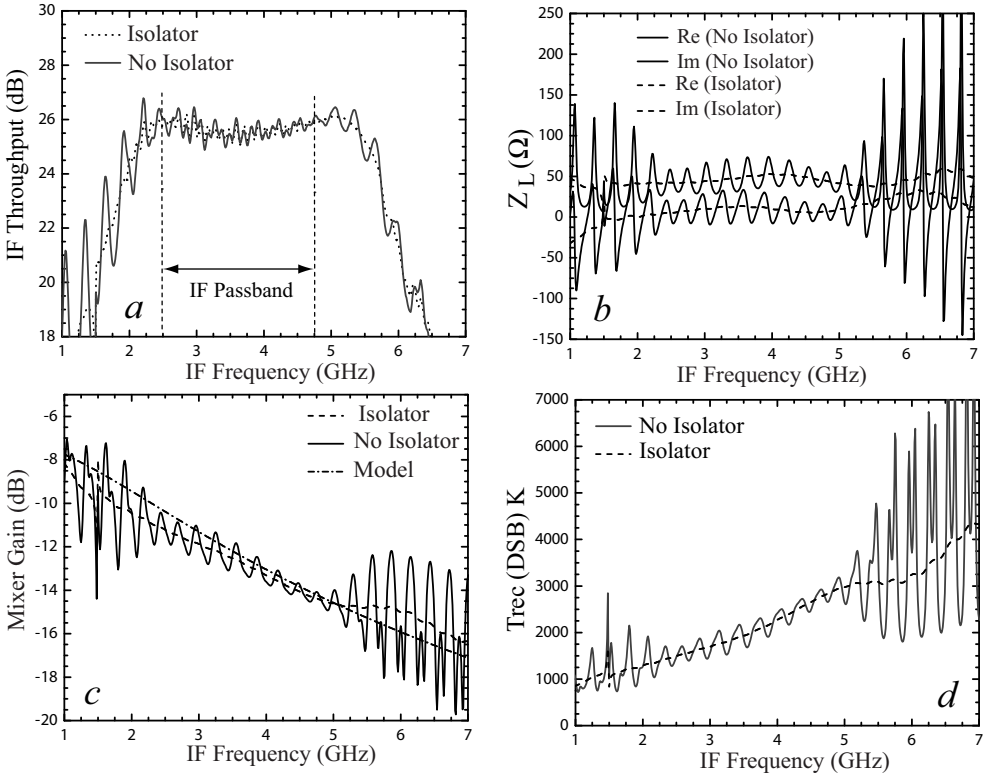

Figure 4.30: *a*) IF passband of the IF circuit board and SRON InP 2-stage low noise amplifier. The passband specification is 2.4 – 4.8 GHz. *b*) Complex embedding impedance Z_L with and without (ideal) isolator *c*) Calculated mixer gain. The model shows the expected roll of in mixer gain without electro-thermal feedback ($R_o = Z_L$). *d*) Calculated receiver noise temperature. Note the slope and standing wave modulation across the IF passband. Before the IF re-design of Fig. 4.28 the large excess noise outside the IF passband, has in fact been observed on occasion in the IF passband.

As a final point of interest we show a measured vs. modeled residual standing wave of HIFI mixer band 6 in Fig. 4.31. The spectrum is obtained by the division of two internal "cold" (4.2 K) load measurements at two different 4 s periods, 1640 s apart in time. HIFI housekeeping telemetry indicates a small change in the HEB mixer current, indicative of a drift in LO signal. This in term results in a slight redistribution of the HEB temperature profile of Fig. 4.26, T_e in Table 6.1, and thus a slight change in the mixer conversion gain. By fitting our model to the measured spectra, and taking the ratio, we obtain a residual very similar to the measurement, providing confidence in the physical model.

4.3.2 Investigation of direct detection

It is often of interest to reduce the LO power requirement of HEB mixers operating in the terahertz frequency regime. A simple way to accomplish this is to downsize the

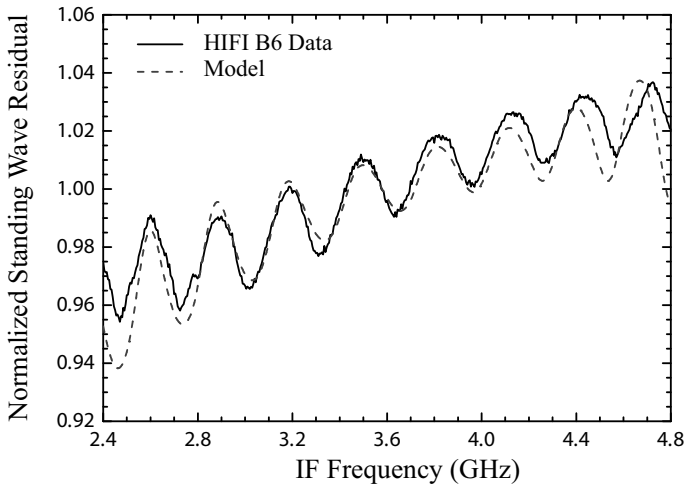

Figure 4.31: Measured vs. fitted residual IF standing wave, $\Delta P/\langle P\rangle$, of HIFI mixer band 6 for two 4 s observations, 1640 s apart on an internal calibration load. The normalized change in HEB current, $\Delta I^{dc}_{HEB}/\langle I^{dc}_{HEB}\rangle$, is 1.62 %. This corresponds to a $\Delta P/\langle P\rangle$ of $\sim$ 2.5 %, so that the IF power to dc current conversion ratio $(\Delta P \cdot \langle I^{dc}_{HEB}\rangle/\Delta I^{dc}_{HEB} \cdot \langle P\rangle)$ equals 1.53. Note the good agreement between model and measurement. For additional details we refer to Sec. 4.3.1.

mixer volume. However, when integrated with the large instantaneous RF bandwidth of quasi-optical antennas, reducing the HEB volume enhances the direct detection response of the mixer. Before continuing the discussion, it should be noted that the HEB mixers under investigation are fabricated on high purity silicon, with 3.5–6 μm thick NbN films from the Moscow Pedagogical State University [103, 104]. The critical temperature of the films is $\sim$ 9.7 K. I_c, the critical current, is approximately 70 μA, and the normal state resistance, as measured just above T_c, $\sim$ 170 Ω. The bridge area is 1 x 0.15 μm, and is very similar to the HEB mixer area used on HIFI (Sec. 4.3.2.1).

Biasing the described small volume HEB mixers at, or near, the optimal operating point causes a small change in mixer bias current when the input signal is switched between a "hot" (290 K) and "cold" (80 K) load. This change in mixer current is due to direct- or continuum detection, and alters the IF output impedance and mixer gain of the HEB mixer in a small but noticeable manner. The direct detection response thus modulates the standing wave between mixer and LNA (Fig. 4.30), which results in a non-perfect subtraction of the hot and cold IF output signals, similar to what is shown in Fig. 4.31 although at a much lower amplitude. Use of an isolator between the HEB and LNA will reduce the direct detection modulation of the IF signal, however changes in the mixer conversion gain remain present.

The direct detection current in an HEB mixer becomes prominent when the RF power from the calibration load, absorbed in the bridge, is non-negligible compared to the absorbed LO– plus dc power, thus upsetting the intricate heat balance in the bridge. In case of the small area hot electron bolometer, the measured [105] LO power requirement at the input of the cryostat was $\sim$ 100 nW. This compares well

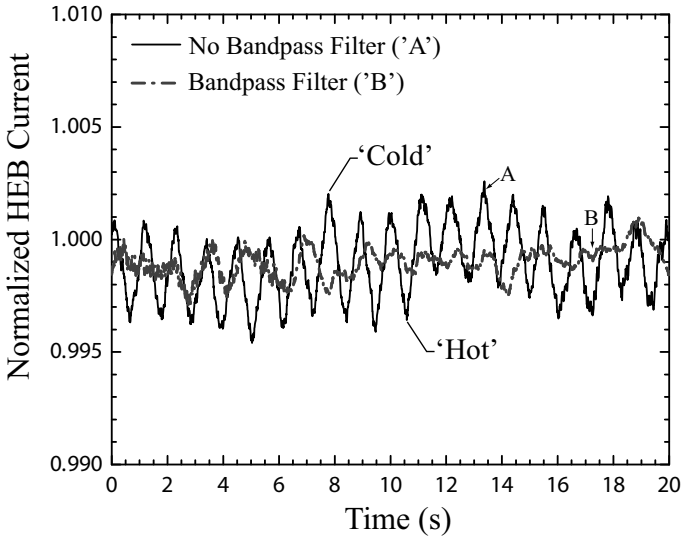

Figure 4.32: The normalized chopped "hot" load (296 K) minus "cold" ($\sim$ 105 K) time response of a small area (1 x 0.15 μm area) HEB mixer. The solid line is without a RF bandpass filter, whereas the dashed curve is the response with a (cooled) 200 GHz bandpass filter. The HEB mixer was biased at 0.5 mV and 10 μA of current (I^{dc}_{HEB}). $\Delta I^{dc}_{HEB}/\langle I^{dc}_{HEB}\rangle = 0.338$ % without the bandpass filter, and 0.130 % with the bandpass filter (factor of 2.5 reduction). The effect on sensitivity is shown in Fig. 4.33.

with the 60 nW LO power requirement obtained from the isothermal technique [95]. The difference between both methods is attributed to a small mismatch between the mixer and local oscillator beam waists [106].

To quantify the direct detection effect we can estimate the effective input power of the loads in the Rayleigh-Jeans limit as

$$P_{RF} = k_B \Delta\nu T_{load} \ . \tag{4.104}$$

T_{load} is the effective "hot" and "cold" load temperature as described in Fig. 5.3, and $\Delta\nu$ the instantaneous bandwidth, estimated to be 900 GHz in case of the twin-slot antenna of Fig. 4.24. In the experiment the "hot" and "cold" loads are external to the cryostat. Provided an optical transmission of $\sim$ 90 %, T_{load} is estimated, using the Callen & Welton formulism [20, 22], as 296 K and 105 K respectively. For the "hot" load this equates to a radiative load of 3.7 nW, while for the "cold" load 1.3 nW of continuum loading is present on the bridge area. It is the difference in power, 2.4 nW, that changes the thermal equilibrium of the hot electron bolometer, and is responsible for the direct detection effect in the HEB mixer. Given an optimum dc bias of 0.5 mV and 8–10 μA of current, approximately 5 nW of dc power loading is present as well. The total (P_{dc} + P_{LO}) dissipation of our small volume device therefore equals $\sim$ 65 nW. Thus we find that switching between the room temperature and liquid nitrogen calibration load changes the power budget in the bolometer bridge by 3.6 %. This is large enough to noticeably alter the bias point of the mixer.

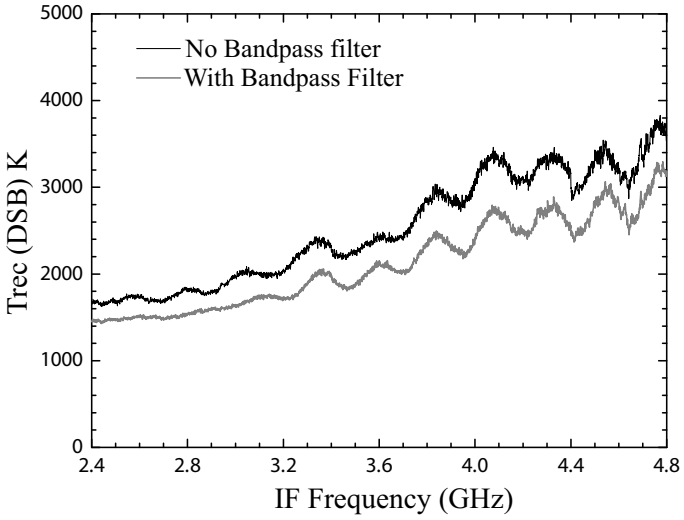

Figure 4.33: Measured receiver noise temperature on HIFI FM HEB mixer B6L, S/N 10 with and without bandpass filter. The application of a bandpass filter reduced the receiver noise temperature, as referred to the input of the mixer, by $\sim$ 17 %. Note also the roll-off in sensitivity across the IF band. This is related to the IF response time of the HEB (Chap. 6). Operating frequency was 1616 GHz.

In Fig. 4.32 we show the normalized direct detection current, defined as $I_{DD}/\langle I^{dc}_{HEB}\rangle$ with $I_{DD} = (I_{hot} - I_{cold})$, with and without a narrow passband RF metal mesh filter [107], as measured on the HIFI HEB mixer B6, S/N 10 flight model. For this device the bridge area was 1 x 0.15 μm. The bandpass filter has a 90 % transmission in a 200 GHz band around 1.6 THz at 4.2 K. Thus the difference in radiated signal power in the presence of the cooled metal mesh bandpass filter is $\sim 1/5^{th}$ of the signal power without the filter, or about 0.8 % of the total 65 nW power budget. The measured reduction in direct detection current in the case of metal mesh filter is $\sim$ 2.5. Though diminished, even with the 200 GHz passband filter a small amount of direct detection remains. It is important to observe that I_{DD} is always negative, in agreement with results reported [108, 109, 110, 111]. This indicates that the difference in RF power between the 105 K and 295 K load changes the bias current of the mixer in the same manner as a decrease in P_{LO}. As a consequence the hot load output power is evaluated at a slightly lower bias current than the cold load output power. And because the mixer output power is a function of bias current, the Y-factor is influenced by a shift in bias current and hence an error is introduced into the calibration procedure [110]. It is interesting to note that the best sensitivity found for small 1.0 μm $\times$ 0.1 μm area devices, once corrected for direct detection, is identical to the best sensitivity (700 K) reported in a spiral-antenna coupled, large area (4.0 μm $\times$ 0.4 μm) HEB mixer at the same frequency [79, 95].

In Fig. 4.33 we show the averaged receiver noise with and without a 1.6 THz bandpass filter. Spectrometer integration time was set to 5 s, a value known the be on the edge of the intrinsic total power stability of HEB mixer's (Fig. 2.6). The

bandpass filter has a cold loss of approximately 10 %. For the "RF bandpass filter measurement" the LO power had to be increased slightly so as to keep the HEB mixer current at the same level for both measurements. With the narrow passband metal mesh RF filter in place the receiver noise temperature decreased $\sim$ 17 %. This is in agreement with the detailed experiment of [110].

4.3.2.1 HIFI

In the actual HIFI instrument, the calibration loads are cryogenic (80 K and 4 K). We can thus expect a factor three reduction in the signal input "hot" load radiation temperature, and because a Martin-Pupplet style diplexer is employed to inject the LO signal another factor of $\sim$ 2 by the reduction in RF passband. The actual HIFI bridge area is 2.0×0.1 μm^2 (length $\times$ width) with a critical current of 200 μA [112]. If approximate linear behavior is assumed, we estimate an HIFI HEB mixer direct detection current of 0.06–0.08 % of the operating current.

To quantify the HEB mixer direct detection in HIFI under calibration conditions (internal "hot" and "cold" load), we have determined the amplitude variation and statistics of the HEB current and IF output power from 35 long duration ($>$ 40 min), 4 s phase differential (chopped) internal load stability measurements [113]. For this we use the HEB current as recorded in the instrument level test (ILT) housekeeping. These data were acquired at $\sim$ 1 Hz. In Fig. 4.34 we show as an example a FFT spectrum of the HEB mixer band 6 current during 0.25 Hz chopped load operation. Timing errors in the housekeeping data likely cause the apparent 50 ms shift in time.

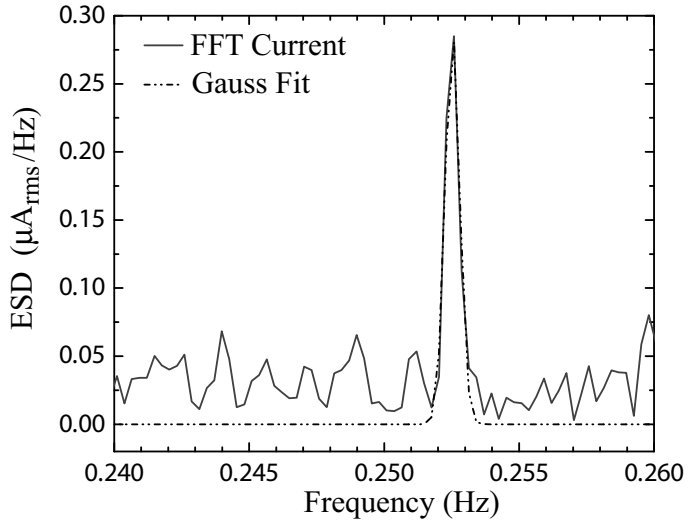

Figure 4.34: Direct detection as measured in B6b of the HIFI instrument at 1673.5 GHz. The direct detection current is obtained from Eq. 4.105. In this particular example, E_{fit}=0.702 μA/Hz, and N=3600. The from the FFT calculated normalized direct detection current equals 0.1 % with $\langle I^{dc}_{HEB} \rangle = 50$ μA. The calibration loads are switched at a rate of 1/4 Hz.

A Hanning window is applied in the Fourier transform to take into account the finite data set. To estimate the direct detection current from the energy spectral density (ESD), we first find the power under the FFT peak by fitting a Gaussian to the spectrum. From this we obtain the detection current I_{DD} via

$$I_{DD} = \frac{E_{fit}}{2\sqrt{2}NF_{han}} \quad (\mu A). \tag{4.105}$$

E_{fit} is the power under the Gaussian, N the number of data samples (3600 in the case of Fig. 4.34), and F_{han} 1.4657. The factor 2 in Eq. 4.105 accounts for the frequency folding in the FFT, and the $\sqrt{2}$ converts the rms to a peak current value. For all 35 data samples, we derive in this manner a normalized direct detection current $I_{DD}/\langle I^{dc}_{HEB}\rangle = 0.103 \pm 0.043$ %. This is slightly higher than the crudely estimated value of 0.06–0.08 %, not a surprise. The change in standing wave amplitude (not shown) due to the direct detection current has a mean value of 0.2 %. This value goes directly into the calibration error budget. The thus obtained direct detection IF power-to-current conversion ratio $(\Delta P \cdot \langle I^{dc}_{HEB}\rangle)$ / $(\Delta I^{dc}_{HEB} \cdot \langle P\rangle)$ for HIFI equals 2.10, slightly higher than the obtained ratio of 1.53 in Fig. 4.31.

4.3.3 Effect on instrument calibration

The astronomical consequences of the direct detection lie in the absolute, or total power, calibration accuracy of the measurement. To properly correct for the direct detection effect the local oscillator power needs to be (slightly) increased when switching from a "hot" to "cold" calibration load. This is needed to ensure that the HEB bias current remains constant. However such a procedure requires a very accurate control of the LO output power, for example via a precise rotation of a polarizing grid in the LO path of the mixer, as in [110]. For the HIFI instrument under discussion such a complication would be prohibitive.

As we have seen, another technique to reduce the direct detection is to minimize the total power difference between the hot and cold load, e.g. reduce the temperature difference between the calibration loads. This is done for HIFI, and results in a 0.2 % direct detection calibration error. Alternatively, the calibration load brightness temperature may be reduced by including in the optics path a narrow RF bandpass metal mesh filter [107] or by utilizing a waveguide, rather than open-structure antenna design.

4.3.4 Parametric stability

As part of the HIFI instrument level test program (ILT), parametric studies of the HEB mixer band 6 & 7 were performed. For the HIFI instrument the LO is subdivided into subbands "a, b". For example, mixer band 6b refers to HEB mixer band 6, LO subband "b". In Fig. 4.35 we show a representative subset of the parametric stability tests at a LO frequency of 1666 GHz (B6b) and 1773.5 GHz (B7a). Two situation were examined: Spectroscopic system stability (Appendix A) as a function of LO pump power (HEB current), and spectroscopic system stability as a function of HEB bias voltage.

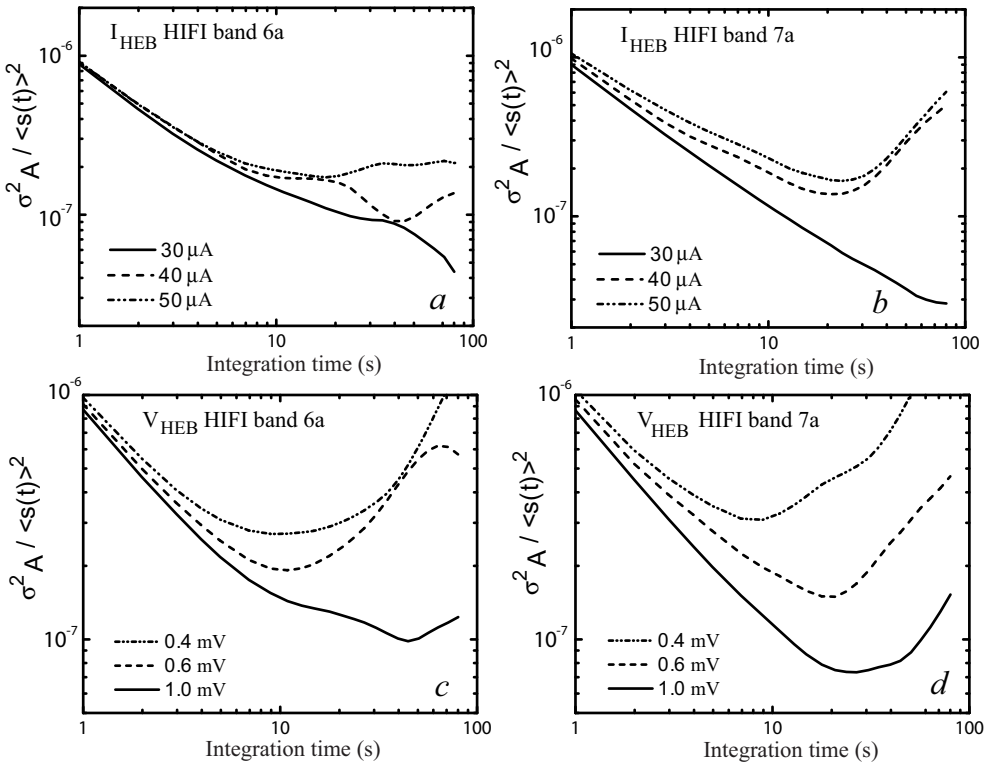

Figure 4.35: *a*) Normalized spectroscopic stability as a function of LO pump level. HEB mixer band 6b. 30 μA is slightly over pumped, 40 μA optimally pumped, and 50 μA slightly under pumped. The LO frequency is 1666 GHz. See also the I/V curves of Fig. 4.25b. *b*) Same as *a*), except for HEB mixer band 7a and at an LO frequency of 1773.5 GHz. *c*) Band 6b normalized spectroscopic stability as a function of HEB mixer bias voltage. Optimal sensitivity is ordinarily achieved around 0.5 mV. *d*) Band 7a normalized spectroscopic stability as a function of HEB mixer bias voltage. At a tradeoff of some sensitivity, a higher bias voltage improves the spectroscopic instrument stability.

In the top panel of Fig. 4.35 (*a, b*) we show the normalized spectroscopic Allan variance as a function of LO power. For both mixer bands 30 μA is slightly over pumped, 40 μA optimally pumped, and 50 μA on the verge of being under pumped. Slightly over pumping the HEB mixer from a stability point of view appears beneficial. This is understood to be the combined effect of a slight decrease in sensitivity and increase in required LO pump level (see also Fig. 4.25b). Higher LO power levels generally cause the W-band power amplifiers in the LO chain to run more saturated, thereby clipping the amplitude modulated (AM) noise on the LO carrier signal [114]. Consistent also is the trend that lower LO power (HEB current) results in a reduced Allan time, around 10 s in our case. This agrees with the picture that AM noise is present on the LO carrier, and that saturation of the LO chain power amplifiers is highly important.

In the bottom panel of Fig. 4.35 (*c, d*) we show the normalized spectroscopic Allan

variance as a function of bias voltage for a nominal LO pump level. Again we have a consistent trend with higher HEB bias voltages providing more stable behavior. At the larger (1 mV) bias voltage this is simply related to the sensitivity of the HEB mixer, e.g. the less sensitive the mixer the less sensitive it will also be to AM local oscillator noise. However between 0.4 and 0.6 mV the sensitivity of the mixer is more or less constant and the instability is likely the result of how close the mixer is biased to the (known) instability region [81]. From this discussion it is evident that slightly over pumping the HEB mixer (20 %), while biasing it above the nominal operating voltage (20 %) enhances the mixer stability, and thereby the integration efficiency and baseline quality.

4.4 Summary

In this Chapter we have taken a close look at the fundamental theory of both SIS and HEB mixers. We have seen that the described mixers operate on a completely different physical mechanism (quasi-particle tunneling vs. bolometric effect). SIS mixers suffer from a large intrinsic capacitance, related to the superconducting-insulator-superconducting geometry of barrier. To compensate (or tune out) this large parasitic capacitance imaginative tuning structures have been devised. The geometry of HEB mixers lacks the parasitic capacitance, making it in principle easy to connect to over a very broad RF bandwidth. However, the lack of geometric capacitance can also result in significant direct detection, which in actual application adversely effects absolute calibration accuracy.

Yet another significant difference between SIS and HEB mixers is that the SIS mixers have an upper frequency limit of 4Δ, or two times the superconducting energy gap. For niobium this equates to $\sim$ 1400 GHz. Hot electron bolometer mixers do not operate on this principle, and in fact are preferably operated above the superconducting energy gap (2Δ) of the material. In this way Cooper pairs are broken and uniform heating may be assumed in the bridge. An additional feature HEB mixers lack is the need to suppress Cooper pair tunneling through a tunnel barrier. This is known as the Josephson effect, and causes large excess noise in the SIS mixer when left unsuppressed (by application of a suitable magnetic field). Despite some of these advantages, HEB mixers generally exhibit considerably higher conversion loss than SIS mixers, which are capable, due to their quantum mechanical nature, of conversion gain. The higher conversion loss of HEB mixers leads to a generally lower mixer and receiver noise temperature. At approximately 1 THz both mixer types become competitive in sensitivity. This is primarily due to the Ohmic loss in the SIS RF matching network.

Because HEB mixers are thermal devices, in contrast to SIS tunnel junctions, the IF response is governed by several time constants: The electron-electron interaction time which is very fast (ps), the electron-phonon interaction time ($\sim$ 12 ps for NbN) and the phonon escape time to the surrounding substrate ($\sim$ 50 ps for thin film NbN). This time dependence causes the HEB mixer IF response to roll off above several GHz. This is an important drawback of HEB mixers, whose function is primarily in the terahertz frequency regime where astronomical lines have significant Doppler

broadening. A significant effort (and success) has been expanded to improve the IF response of HEB mixers (Chap. 6). SIS mixers do not have an IF frequency limitation, and can in principle be operated at IF frequencies of tenth of GHz. As we have seen in this Chapter, the thermal nature of HEB mixers also results in an electrothermal feedback mechanism, with reflected IF currents changing the heat balance in the HEB bridge. This is a process unknown to SIS mixers.

As a final note, SIS receivers generally have markedly better stability performance than HEB mixers. The improved stability of SIS receivers over HEB receivers is most likely related to the susceptibility of either device to fluctuations in local oscillator power, optical standing waves, and electronic noise. It is certainly the case that HEB mixers, being thermal devices that operate primarily in the terahertz regime, face a much more challenging operating environment than SIS mixers. Chap. 10 is devoted to this subject.

Bibliography

[1] J. R. Tucker and M. F. Millea, "Photon detection in nonlinear tunneling devices", *Appl. Phys. Lett.*, Vol. 33, 7, pp. 611-613, (1978).

[2] J. R. Tucker, "Quantum Limited Detection in Tunnel Junction Mixers", *IEEE J. Quantum Electronics*, Vol. 15, pp. 1234, (1979).

[3] J. R. Tucker, and M. J. Feldman, "Quantum Detection at Millimeter Wavelengths", *Rev. Mod. Phys.*, Vol. 57, pp. 1055-1113, Oct., (1985).

[4] A. H. Dayem, and R. J. Martin, *Phys. Rev. Lett.* Vol. 8, pp. 246, (1962).

[5] P. K. Tien and J. P. Gordon, "Multiphoton Process Observed in the Interaction of Microwave fields with the Tunneling between Superconductor Films", *Phys. Rev.* Vol. 129, pp. 647, (1963).

[6] M. Tinkham, "Introduction to Superconductivity", *New York: McGraw-Hill*, (1975).

[7] J. Bardeen, L. N. Cooper, and J. R. Schrieffer, "Theory of Superconductivity", *Phys. Rev*, Vol. 108, pp. 1175 (1957).

[8] B. D. Josephson, "Possible new Effects in Superconductive Tunneling", *Phys. Lett.* Vol. 1, pp. 251, (1962).

[9] S. Shapiro and A. D. Little, "Josephson current in Superconducting Tunneling: The effect of Microwaves and other Observations", *Phys. Rev. Lett.*, Vol. 11, No. 2, pp. 80-82, Jul. (1963).

[10] HFSS, Ansoft Corporation, Pittsburgh, PA, 2005.

[11] SONNET, Sonnet Software, Liverpool, NY, 2005.

[12] M. H. Cohen, L. M. Falicov, and J. C. Phillips, "Superconductive tunneling", *Phys. Rev. Lett.*, Vol. 8, pp. 316-318, (1962).

[13] V. Ambegaokar and A. Baratoff, "Tunneling between Superconductors", *Phys. Rev. Lett.*, Vol. 11, pp. 1364, (1963).

[14] N. R. Werthamer, "Nonlinear Self-Coupling of Josephson Radiation in Superconducting Tunnel Junctions", *Phys. Rev*, Vol. 147, pp. 225 (1996).

[15] A. Skalare, "Determining embedding circuit parameters from dc measurements on quasiparticle mixers", *Int. Jr. IR and MM Waves*, Vol. 10, no. 11, pp. 1339-1353, (1989).

[16] M. Bin, "Low-noise THz Niobium SIS Mixers", Ph.D. Dissertation (1997), California Institute of Technology, Pasadena, Ca 91125.

[17] J. Ward, F. Rice and J. Zmuidzinas, "Supermix: a Flexible Software Library for High-Frequency Circuit Simulation, including SIS Mixers and Superconducting Components", *Proc. 10^{th} Int. Symposium on Space Terahertz Technology*, Charlottesville, VA, Mar., (1999), pp. 269–281.

[18] G. de Lange, "Quantum Limited Heterodyne detection of 400-840 GHz Radiation with Superconducting Nb Tunnel Junctions", Ph.D. Dissertation, University of Groningen, (1994).

[19] P. Dieleman, H. G. Bukkems, T. M. Klapwijk, M. Schicke, and K. H. Gundlach, "Observation of Andreev Reflection Enhanced Shot Noise", *Phys. Rev. Lett.*, Vol. 79, pp. 3486-3489 , Nov., (1997).

[20] A. R. Kerr, M. J. Feldman, S. K. Pan, "Receiver Noise Temperature, the Quantum Noise Limit, and the Role of the Zero-Point Fluctuations", *Electron. Div.*, NRAO, Charlottesville, VA, Internal Rep. 304, Sep., (1996).

[21] A. R. Kerr, "Suggestions for Revised Definitions of Noise Quantities, including Quantum effects", *IEEE Trans. Microwave Theory and Techniques*, Vol. 47, No. 3, pp. 325-329, Mar., (1999).

[22] H. B. Callen and T. A. Welton, "Irreversibility and generalized Noise", *Phys. Rev.*, Vol. 83, no. 1, pp. 34-40, Jul., (1951).

[23] T. M. Shen, "Conversion gain in millimeter wave quasi-particle heterodyne mixers", *IEEE J. Quantum Electronics*, Vol. 17, No. 7, pp. 1151-1165, (1981).

[24] M. J. Feldman, "Some analytical and intuitive results in the quantum-theory of mixing", *J. Appl. Physics*, Vol. 53, No. 1, pp. 584-592, (1982).

[25] E.C. Sutton, "A Superconducting Tunnel Junction Receiver for 230 GHz", *IEEE Trans. Microwave Theory and Techniques*, Vol. MTT-31, No. 7, pp. 589-592, (1983).

[26] C. F. J. Lodewijk, T. Zijlstra, S. Zhu, F. P. Mena, A. M. Baryshev, and T. M. Klapwijk, "Bandwidth limitations of Nb/AlN/Nb SIS mixers around 700 GHz," submitted to *IEEE Trans. Appl. Superconductivity* (2008).

[27] V. Y. Belitsky, M. A. Tarasov, S. A. Kovtonjuk, L. V, Filippenko, and O. V. Kaplunenko, "Low-noise completely quasi-optical SIS receiver for radioastronomy at 115 GHz", *Int. J. IR and MM Waves*, Vol. 13, pp 389-396, (1992).

[28] K. Jacobs, U. Kotthaus, and B. Vowinkel, "Simulated Performance and Model Measurements of an SIS Waveguide Mixer using Integrated Tuning Structures", *Int. J. IR and MM Waves*, Vol 13, No. 1, pp. 15-26, (1992).

[29] T. H. Büettgenbach, H. G. LeDuc, P. D. maker, and T. G. Phillips, "A Fixed Tuned Broadband Matching Structure for Submillimeter SIS Receivers", *IEEE Transactions on Applied Superconductivity*, Vol. 2 (3), pp 165-175, Sep. (1992).

[30] "Foundations for Microwave Engineering", McGraw-Hill Physical and Quantum Electronics Series, (1966).

[31] H. W. Bode, "Network Analysis and Feedback Amplifier Design", *Van Nostrand*, N.Y. (1945).

[32] R. M. Fano, "Theoretical Limitations on the Broad-Band Matching of Arbitrary Impedances", *Journal of the Franklin Institute*, Vol. 249, pp. 57-83, Jan. (1950), and pp. 139-154, Feb. (1950).

[33] J. W. Kooi, M. S. Chan, H. G. Leduc, and T. G. Phillips, "A 665 GHz Waveguide Receiver Using a Tuned 0.5 μm^2 Nb/AlO$_x$/Nb Tunnel Junction", *Proc. 7th Int. Symp. Space Terahertz Technology, Charlottesville*, Va, Mar., (1996).

[34] E. Hammerstad and O. Jensen, "Accurate models for microstrip computer-aided design, *IEEE MTT-S*, Int. Microwave Symp. Dig., pp. 407-409, May. (1980).

[35] R. L. Kautz, "Picosecond pulses on superconducting striplines", *J. Applied Physics*, Vol. 49, pp. 308-314, (1978).

[36] J. F. Whitaker, R. Sobolewski, D. R. Dykaar, T. Y. Hsiang, and G. A. Mourou, "Propagation model for ultrafast signals on superconducting dispersive striplines", *IEEE Trans. Microwave Theory and Techniques*, Vol. MTT-36, No. 2, pp. 277-285, Feb. (1988).

[37] J. Zmuidzinas and H. G. LeDuc, "Quasi-Optical Slot Antenna SIS Mixers", *IEEE Trans. Microwave Theory and Techniques*, Vol. MTT-40, pp. 1797-1804, (1992).

[38] J. W. Kooi, G. Chattopadhyay, M. Thielman, T. G. Phillips, and R. Schieder, "Noise Stability of SIS receivers", *Int J. IR and MM Waves*, Vol. 21 (5) (2000).

[39] A Baryshev, R Hesper, G Gerlofsma, M Kroug, and W Wild, "Influence of Temperature Variations on the Stability of a Submm Wave Receiver", *Proc. 14th Int. Symp. Space Terahertz Technology*, (2003).

[40] G. Chattopadhyay, D. Miller, H. G. LeDuc, and J. Zmuidzinas, "A dual-polarized quasi-optical SIS mixer at 550 GHz", *IEEE Trans. Microwave Theory and Techniques*, Vol. 48, No. 10, pp. 1680-1686, Oct., (2000).

[41] J. W. Kooi, J. Pety, B. Bumble, C. K. Walker, H. G. LeDuc P. L. Schaffer, and T. G. Phillips, "A 850 GHz Waveguide Receiver Employing a Niobium SIS Junction Fabricated on a 1μm Si_3N_4 Membrane", *IEEE Trans. Microwave Theory and Techniques*, Vol. 46, No. 2, pp. 151-161, Feb., (1998).

[42] Th. de Graauw, N. Whyborn, E. Caux, T. G. Phillips, J. Stutzki, X. Tielens, R. Güsten, F. P. Helmich, W. Luinge, J. Pearson, P. Roelfsema, R. Schieder, K. Wildeman, and K. Wavelbakker, "The Herschel-Heterodyne Instrument for the Far-Infrared (HIFI)", [Online]. Available: herschel.esac.esa.int./Publ/2006/SPIE2006_HIFI_paper.pdf

[43] S. Padin, D. P. Woody, J. A. Stern, H. G. LeDuc. R. Blundell, C. -Y. E. Tong, M. W. Pospieszalski "An integrated SIS mixer and HEMT IF amplifier", *IEEE Trans. Microwave Theory and Techniques*, Vol. MTT-44, No. 6, pp. 987-990, Jun., (1996).

[44] A. R. Kerr, S.-K. Pan, and S. Withington, "Embedding Impedance Approximations in the Analysis of SIS Mixers", *IEEE Trans. Microwave Theory and Techniques*, Vol. MTT-41, No. 4, pp. 590-594, Apr., (1992).

[45] Ke and M. J. Feldman, "Optimum Source Conductance for high Frequency Superconducting Quasiparticle Receivers", *IEEE Trans. Microwave Theory and Techniques*, Vol. MTT-41, No. 4, pp.600-604, Apr., (1992).

[46] A. R. Kerr, "Some fundamental and practical limits on broadband matching to capacitive devices and the implications for SIS mixer design", *IEEE Trans. Microwaves Theory and Techniques*, Vol. 43, No. 1, pp. 1-13, Jan., (1995).

[47] J. W. Kooi, M. Chan, B. Bumble, T. G. Phillips, "A low noise 345 GHz waveguide receiver employing a tuned 0.50 μm^2 Nb/AlO_x/Nb tunnel junction", *Int. J. IR and MM Waves*, Vol. 15, No. 5, May., (1994).

[48] J. W. Kooi, M. Chan, B. Bumble, H. G. Leduc, P.L. Schaffer, and T. G. Phillips, "230 and 492 GHz Low-Noise SIS Waveguide Receivers employing tuned Nb/AlO_x/Nb tunnel junctions", *Int. J. IR and MM Waves*, Vol. 16, No. 12, pp. 2049-2068, Dec. (1995).

[49] C. E. Honigh, S. Haas, D. Hottgenroth, K. Jacobs, J. Stutzki, "Low-noise broadband fixed tuned wave-guide mixers at 660 and 800 GHz", *IEEE-Applied Physics*, Vol. 7(2), Part 3, pp. 2582-2586, Jun., (1997).

[50] J. W. Kooi, F. Rice, G. Chattopadhyay, S. Sundarum, S. Weinreb and T. G Phillips, "Regarding the IF Output Conductance of SIS Tunnel Junctions and the Integration with Cryogenic InP MMIC Amplifiers", *Proc. 10^{th} Int. Symp. Space Terahertz Technology*, University of Virginia, Va, Mar., (1999).

[51] V. P. Koshelets, A. B. Ermakov, L. V. Filippenko, A. V. Khudchenko, O. S. Kiselev, A. S. Sobolev, M. Yu. Torgashin, P. A. Yagoubov, R. W. M. Hoogeveen, and W. Wild, "Superconducting Integrated Submillimeter Receiver for TELIS", *IEEE Trans. Appl. Superconductivity*, Vol. 17, No. 2, pp. 336-342, Feb., (2007).

[52] A. R. Kerr "Saturation by Noise and CW Signals in SIS Mixers", *Proc. 13th Int. Symposium on Space Terahertz Technology*, Harvard University, Mar., (2002), pp. 11-22.

[53] A. Karpov, D. Miller, F. Rice, J. A. Stern, B. Bumble, H. G. LeDuc, J. Zmuidzinas, "Low Noise SIS Mixer for Far Infrared Radio Astronomy", in *Proc. of SPIE*, Vol. 5498, Ground-based Telescopes, edited by J.Zmuidzinas, W. S. Holland, and S. Withington, (SPIE, Glasgow, UK, 2004) pp. 616-621.

[54] Virginia Diodes Inc., 321 West Main Street, Charlottesville, VA 22903, USA.

[55] J. W. Kooi, J. J. A. Baselmans, A. Baryshev, R. Schieder, M. Hajenius, J. R. Gao, T. M. Klapwijk, B. Voronov, and G. Gol'tsman, "Stability of Heterodyne Terahertz Receivers", *Journal of Applied Physics*, Vol. 100, 064904, Sep. (2006).

[56] W. H. Hayt, JR., "Engineering Electromagnetics", *McGraw-Hill*, 4th Edition, (1981).

[57] D. M. Pozar, "Microwave Engineering", *John Wiley & Sons*, Inc., 3rd Edition, (2005).

[58] P. K. Day, H. G. LeDuc, B. A. Mazin, A. Vayonakis, and J. Zmuidzinas, "A broadband superconducting detector suitable for use in large arrays", *Nature 425*, 817-821, Oct. (2003).

[59] A. Vayonakis, "Precision measurements of the properties of thin-film superconducting microstrip lines at 100-500 GHz", *Proc. 14th Int. Symp. Space Terahertz Technology*, (2003).

[60] I. J. Bahl and D. K. Trivedi, "A Designer's Guide to Microstrip Line", *Microwaves*, pp. 174-182, May (1977).

[61] A. B. Pippard, "Metallic conduction at high frequencies and low temperatures", *Advances in Electronics and Electron Physics*, Vol. 1, pp. 1-45, L. Marton Ed. NY: Academic Press, (1954).

[62] J. H. Hinken, "Springer-Verlag: Berlin Heidelberg, (1989).

[63] G. E. H. Reuter, and E. H. Sondheimer, "The theory of the anomalous skin effect in metals", *Proc. Roy. Soc.*, (London), vol. A195, pp. 336-364, (1948).

[64] A. F. Mayadas, "Intrinsic Resistivity and Electron Mean Free path in Aluminum films", *J. Appl. Physics*, Vol. 39, No. 9, pp. 4241-4245, Aug. (1968).

[65] R. L. Kautz, "Miniaturization of normal-state and superconducting striplines", *J. Res. Natl. Bureau Std.*, vol. 84, no. 3, pp. 247-259, (1979).

[66] W. Meisner, R. Ochsenfield, "Ein neuer Effekt bei Eintritt der Supraleitung", *Naturwissenschaften* 21, p. 787, (1933).

[67] F. London and H. London, "The Electromagnetic Equations of the Supraconductor", *Proc. Royal Soc. London* (A), p. 71-88, (1935).

[68] A. Cucolo, A. Nigro, and R. Vaglio, "Surface impedance of NbN superconducting thin-films by Josephson measurements", *J. Low Temp. Phys*, Vol. 69, pp. 363-376, (1987).

[69] J. Zmuidzinas, J. Kooi, J. Kawamura, G. Chattopadhyay, B. Bumble, H. G. LeDuc, and J. A. Stern, "Development of SIS mixers for 1 THz *Proc. SPIE*, Vol. 3357, pp. 53-61, (1998).

[70] J. Kawamura, J. Chen, D. Miller, J. W. Kooi, J. Zmuidzinas, B. Bumble, H. G. LeDuc, J. A. and Stern, "Low-noise Submillimeter-wave NbTiN Superconducting Tunnel Junction Mixers", newblock *Applied Physics Letters*, Vol. 75, 4013-4015, (1999).

[71] D. C Mattis and J. Bardeen, "Theory of the Anomalous Skin Effect in Normal and Superconducting Metals", *Phys. Rev.*, Vol. 111, no. 2, pp. 412-417, Jul., (1958).

[72] R. Pöpel, "Surface Impedance and reflectivity of superconductors", *J. Appl. Phys*, Vol. 66, 5950 (1989).

[73] R. E. Glover, *III, Phys. Rev.* Vol. 110, pp.771 (1958).

[74] W. F. M. Ganzevles, L. R. Swart, J. R. Gao, P. A. J. de Korte, and T. M. Klapwijk, "Direct response of microstrip line coupled Nb THz hot-electron bolometer mixers", *Appl. Phys. Lett.*, Vol. 76, pp. 3304 (2000).

[75] P. Focardi, A. Neto, and W. R. McGrath, "Coplanar-waveguide-based terahertz hot-electron-bolometer mixers mproved embedding circuit description", *IEEE Trans. Microwave Theory Technol.*, Vol. 50, 10, pp. 2374-2383, Oct., (2002).

[76] A. D. Semenov, H. -W. Hbers, J. Schubert, G. N. Gol'tsman, A. I. Elantiev, B. M. Voronov, and E. M. Ger-shenzon, "Design and per-formance of the lattice-cooled hot-electron terahertz mixer," *J. Appl. Phys.*, Vol.88, p.6758, (2000).

[77] P. Khosropanah, T. Berg, S. Cherednichenko, H. Merkel, S. Svechnikov, V. Drakinsky, E. Kollberg, and G.Gol'tsman, "Geometry dependence of the performance of NbN heterodyne hot electron bolometer super-conducting mixers," *Proc. EUCAS*, (2003).

[78] S. Miki, Y. Uzawa, A. Kawakami, and Z. Wang, "IF bandwidth and noise temperature measurements of NbN HEB mixers on MgO substrates," *IEEE Trans. Appl. Supercond.*, Vol. 11, no.1, p.175, (2001)

[79] J. J. A. Baselmans, M. Hajenius, J. R. Gao, T. M. Klapwijk, P. A. J. de Korte, B. Voronov, and G. Gol'tsman, "Doubling of sensitivity and bandwidth in phonon cooled hot electron bolometer mixers", *Appl. Phys. Lett.*, 84, pp. 1958, (2004).

[80] M. Hajenius, J. J. A. Baselmans, J. R. Gao, T. M. Klapwijk, P. A. J. deKorte, B.Voronov, and G. Gol'tsman, "Low noise NbN supercon-ducting hot electron bolometer mixers at 1.9 and 2.5 THz," *Supercond. Sci. Technol.*, Vol. 17, pp. S224S228, (2004).

[81] M. Hajenius, J. J. A. Baselmans, A. Baryshev, J. R. Gao, T. M. Klapwijk, J. W. Kooi, W. Jellema, and Z. Q. Yang, "Full characterization and analysis of a THz heterodyne receiver based on a NbN hot electron bolometer", *J. Appl. Phys.*, Vol. 100, 074507 (2006).

[82] D. F. Filipovic, S. S. Gearhart, and G. M. Rebeiz, "Double-Slot Antennas on Extended Hemisherical and Elliptical Silicon Dielectric Lenses", *IEEE Transactions on Microwave Theory and Techniques*, Oct. (1993).

[83] E. M. Gershenzon, G. N. Gol'tsman, I. G. Gogidze, A. I. Eliantev, B. S. Karasik, and A. D. Semenov, "Millimeter and submillimeter range mixer based on electron heating of superconducting films in the resistive state", *Sov. Phys. Superconductivity*, Vol. 3, pp. 1582, (1990).

[84] P. Khosropanah, "NbN and NbTiN hot electron bolometer THz mixers", Ph. D. thesis, Chalmers University of Technology, Sweden, (2003).

[85] T. M. Klapwijk, R. Barends, J. R. Gao, M. Hajenius, and J. J. A. Baselmans, "Improved superconducting hot-electron bolometer devices for the (THz) range", *Proc. of SPIE*, Vol. 5498: Millimeter and Submillimeter Detectors for Astronomy II, edited by J. Zmuidzinas, W. S. Holland, and S. Withington, Glasgow, Scotland, UK (2004), pp. 129.

[86] R. Barends, "Analysing superconducting THz Detectors: non-equilibrium double barrier junctions and hot electron bolometer mixers", M. Sc. thesis, TU Delft, (2004).

[87] Yu. P. Gousev, G. N. Gol'tsman, A. D. Semenov, E. M. Gershenzon, R. S. Nebosis, M. A. Heusinger, and K. F. Renk, "Broadband ultrafast superconducting NbN detector for electromagnetic radiation", *J. Appl. Phys.*, Vol. 75, pp. 3695, (1994)
Note that the paper is supposed to report measured electron-phonon time τ_{e-ph}, but the thermal time constant τ_{th} instead of τ_{e-ph} was mistakenly plotted in Fig. 4 of this paper according to private communication with one of the authors (G. Gol'tsman). Note also that the τ_{e-ph} extrapolated for 10 K from $\tau_{e-ph} \approx 500T^{-1.6} psK^{1.6}$ was measured separately by K. S. Il'in, G. N. Gol'tsman, and B. M. Voronov, in Proc. of the 10^{th} Int. Symp. on Space Terahertz Technol., edited by T. W. Crowe and R. M. Weikle, UVa, Charlottesville, USA, (1999), pp. 390.

[88] S.B. Kaplan, *J. Low Temp. Phys.* Vol. 37, 343, (1979).

[89] A. D. Semenov, R. S. Nebosis, Yu. P. Gousev, M. A. Heusinger, and K. F. Renk, "Analysis of the nonequilibrium photoresponse of superconducting films to pulsed radiation by use of a two-temperature model", *Phys. Rev. B*, Vol. 52, 581 (1995).

[90] N. Perrin and C. Vanneste, "Dynamic behavior of a superconductor under time dependent external excitation", *J. Physique.*, Vol. 48, 1311 (1987).

[91] Y. B. Vachtomin, M. I. Finkel, S. V. Antipov, B. M. Voronov, K. V. Smirnov, N. S. Kaurova, V. N. Drakinski and G. N. Gol'tsman, "Gain bandwidth of phonon cooled HEB mixer made of NbN thin film with MgO buffer layer on Si", *Proc. 13th Int. Symp. on Space Terahertz Technology*, Harvard University, MA, USA, (2002), pp. 259.

[92] R. S. Nebosis, A. D. Semenov, Yu. P. Gousev, and K. F. Renk, "Rigorous analysis of a Superconducting Hot-Electron Bolometer Mixer: Theory and Comparison with Experiment", *Proc. 7th Int. Symp. on Space Terahertz technology*, Charlottesville, VA, (1996), pp. 601-613.

[93] J. W. Kooi, J. J. A. Baselmans, J. R. Gao, T. M. Klapwijk, M. Hajenius, P. Dieleman, A. Baryshev, and G. de Lange, "IF Impedance and Mixer Gain of NbN Hot-Electron Bolometers", *Journal of Applied Physics*, Vol. 101, 044511, Feb. (2007).

[94] R. Barends, M. Hajenius, J.R. Gao, and T.M. Klapwijk, Current-Induced Vortex Unbinding in Bolometer Mixers *Appl. Phys. Lett*, Vol. 87, (2005).

[95] M. Hajenius, "Terahertz heterodyne mixing with a hot electron bolometer and a quantum cascade laser", Ph. D. thesis, TU Delft, The Netherlands, (2007).

[96] B.S. Karasik and I. Elant'ev, "Noise temperature limit of a superconducting hot-electron bolometer mixer", *Appl. Phys. Lett.*, Vol. 68, pp. 853 (1996).

[97] Yu. P. Gousev, G. N. Gol'tsman, A. D. Semenov, E. M. Gershenzon, R. S. Nebosis, M. A. Heusinger, and K. F. Renk, "Broadband ultra fast superconducting NbN detector for electromagnetic radiation", *J. Appl. Phys.*, Vol. 75, pp. 3695 (1994).

[98] H. Ekström, B. Karasik, E. Kollberg, and K. Yngvesson, "Conversion gain and noise of niobium superconducting hot-electron mixers", *IEEE trans Microwave Theory and Techniques*, Vol.43, pp. 938, (1995).

[99] P. J. Burke, R. J. Schoelkopf, and D. E. Prober, "Mixing and Noise in diffusion and phonon cooled superconducting hot-electron bolometers", *J. Appl. Phys.*, Vol. 85, No. 3, Feb. (1999).

[100] In 2004 the IF matching network was re-designed by the author in an effort to eliminate excess noise in HIFI mixers bands 6 & 7. It is now understood that the observed excess noise was caused by standing waves between the mixer and low noise amplifier, modulating the temperature balance in the HEB bridge via an electrothermal feedback mechanism.

[101] F. Rodriguez-Morales, S. Yngvesson, "Integrated THz receivers based on NbN HEB mixers and InP MMIC IF amplifiers", *IEEE MTT-S Int.* Vol. 1, pp. 435-438, 12-17 Jun., (2005).

[102] S. Weinreb, WBA13 MMIC Low Niose Amplfier, private communication.

[103] P. Yagoubov, G. Gol'tsman, B. Voronov, L. Seidman, V. Siomash, S. Cherednichenko, and E. Gershenzon, "The bandwidth of HEB mixers employing ultra thin NbN films on sapphire substate", *Proc. 7th Int. Symposium on Space Terahertz technology*, Charlottesville, VA, (1996), pp. 290-302.

[104] H. Ekström, E. Kollberg, P. Yagoubov, G. Gol'tsman, and E. Gerhenzon, "Gain and noise bandwidth of NbN hot-electron bolometric mixers", *Appl. Phys. Lett.*, Vol. 70 (24), pp. 3296-3298, 16 Jun., (1997).

[105] J. J. A. Baselmans, M. Hajenius, J. R. Gao, A. Baryshev, J. W. Kooi, T. M. Klapwijk, B. Voronov, P. de Korte, and G. Gol'tsman, "NbN Hot Electron Bolometer Mixers: Sensitivity, LO Power, Direct Detection and Stability", *IEEE Trans. Applied Supercon*, Vol. 15, No. 2, pp. 484-489, Jun., (2005).

[106] W. Jellema, "private communication."

[107] QMC Instruments Ltd., Cardiff University, Cardiff, U.K.

[108] Yu. B. Vachtomin, S. V. Antipov, S. N. Maslennikov, K. V. Smirnov, S. L. Polyakov, N. S. Kaurova, E. V. Grishina, B. M. Voronov, and G. N. Gol'tsman, *Proc. 15th Int. Symp. on Space Terahertz technology*, Northampton, MA, (2004).

[109] S. Svechnokov, A. Verevkin, B. Voronov, E. Menschikov, E. Gershenzon, and G. Gol'tsman, *Proc. 10th Int. Symp. on Space Terahertz technology*, UVa, Charlottesville, pp. 44., (1999).

[110] J. J. A. Baselmans, A. Baryshev, S. F. Reker, M. Hajenius, J. R. Gao, T. M. Klapwijk, Yu. Vachtomin, S. Maslennikov, S. Antipov, B. Voronov, and G. Gol'tsman, "Direct detection effect in small volume hot electron bolometer mixers", *Appl. Phys. Lett.* Vol. 86, 163503, (2005).

[111] J. Kawamura, C. -Y. E. Tong, R. Blundell, D. C. Papa, T. R. Hunter, F, Patt, G. Gol'tsman, and E. Gershenzon, *IEEE Trans. on Appl. Supercond.* Vol. 11, pp. 952 (2001).

[112] S. Cherednichenko, V. Drakinskiy, T. Berg, P. Khosropanah, and E. Kollberg, "Hot-electron bolometer terahertz mixers for the Herschel Space Observatory", *Rev. Sci. Instruments*, Vol. 79, 034501, (2008).

[113] R. Higgins, "private communication."

[114] N. Erickson, "AM Noise in Drives for Frequency Multiplied Local Oscilators", *Proc. 15th Int. Symp. on Space Terahertz technology*, Northampton, MA, (2004), pp. 135-142.

Chapter 5

Quasi-optical mixers*

5.1 Introduction

Some of the difficulties that face heterodyne mixers, implemented in conventional waveguide at frequencies that approach (or exceed) a terahertz, are machining of the small dimensions and loss in the waveguide. In this Chapter we have a look at a 800 – 950 GHz quasi-optical mixer that was installed at the Caltech Submillimeter Observatory, Mauna Kea, HI in 2000. As of this writing the instrument is still the most sensitive of its kind in the world. This is related to the use of a high energy gap NbTiN superconducting film, rather than niobium (or metallic) film, as part of the front-end RF matching network. Before proceeding to discuss the all-NbTiN quasi-optical mixer, we shall first have a closer look in Sec. 5.1.2 at the treatment of absorption loss, and will discuss ways around it.

5.1.1 Waveguide Loss

From Sec. 4.2.3 we understand that metallic conductors operate in a local state with $l_c \ll \delta_c$. The (Ohmic) absorption loss of a fundamental TE_{10} mode waveguide can then be related to the skindepth and surface roughness [1, 2] via,

$$\alpha(\nu) = \frac{\lambda_o}{b \cdot \lambda_g}\Big(\frac{\pi \cdot \Psi}{\lambda_o \cdot \eta \cdot \sigma}\Big)^{\frac{1}{2}} \cdot \left[1 + \Big(\frac{\lambda_g}{2a}^2\Big) \cdot \big(1 + 2 \cdot \frac{b}{a}\big)\right] \cdot 8.686 \;\; dB/m. \tag{5.1}$$

λ_o is the wavelength in air, a and b the waveguide dimensions, and ν_c the cutoff frequency of the waveguide TE_{10} mode (c/2a). In addition, c is the speed of light, η the free space impedance (377 Ω), σ the electrical conductivity, and Ψ an efficiency

*The material described in this chapter has been published in the following papers: J. W. Kooi, J. Kawamura, J. Chen, G. Chattopadhyay, J. R. Pardo, J. Zmuidzinas, T. G. Phillips, B. Bumble, J. Stern, and H. G. LeDuc, in *Int. J. IR and MM Waves*, Vol. 21, No. 9, Sep., (2000),
J. Kawamura, J. Chen, D. Miller, J. W. Kooi, J. Zmuidzinas, B. Bumble, H. G. LeDuc, J. A. and Stern, *Applied Physics Letters*, 75, 4013-4015, (1999).

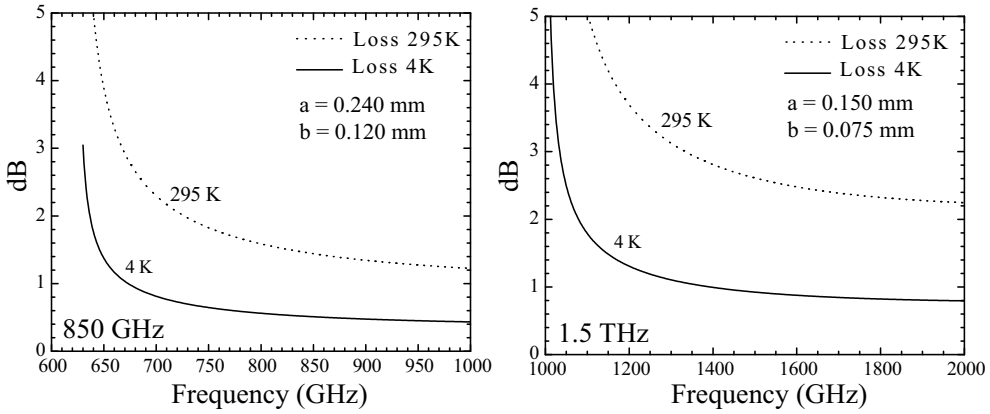

Figure 5.1: Calculated waveguide loss at 295 K and 4 K. *Left*) 850 GHz. *Right*) 1.5 THz. In the calculations, the efficiency factor Ψ, due to surface roughness in the waveguide is constant (1.5). The waveguide physical length is 10 mm.

factor to account for surface roughness and anomalous skin effect upon cooling (1.5). The guide wavelength is obtained from

$$\lambda_g = \frac{\lambda_o}{\sqrt{1-(\nu/\nu_c)^2}}. \tag{5.2}$$

To see the significance we show in Fig. 5.1 the loss of a 10 mm waveguide at 850 GHz and 1.5 THz. The physical temperatures of the waveguide are 290 K and 4 K. A 10 mm waveguide run may be considered the minimum practical distance between an active device and the output port of the mixer block (Fig. 8.7). Ψ is assumed constant (1.5) under the assumption that in the terahertz regime electro-chemical techniques allow etching of smooth walled waveguides [3]. More complex structures will inevitably have higher loss. As a reference, the electrical conductivity for various metals and alloys is compiled in Table 5.1.

To circumvent the problem of machinability and Ohmic loss, a variety of open structure mixers have been introduced [4, 5], with the twin-slot mixer [6, 7] the most popular. To a large extent this is due to the superior optical properties of the double-slot antenna.

To date the vast majority of all heterodyne quasi-optical mixers are implemented as single-ended DSB mixers (Sec. 3.2). A notable exception is the dual polarization twin-slot mixer by Chattopadhyay *et al.* [8]. Like their waveguide counterparts, open structure mixers have issues as well. Most notably beam steering, alignment accuracy between mixer chip and lens, Gaussisity of the beam, astigmatism, variation in beam divergence (waist), and in the case of log periodic antennas [5] a frequency dependent polarization. Due to these issues the quasi-optical mixer finds its use mainly above $\sim$ 800 GHz, where traditional waveguide techniques become either too difficult to machine or too costly. A noted exception is the superconducting integrated receiver [9, 10] which utilizes on chip real estate to combine a twin-slot coupled SIS mixer,

Table 5.1: Electrical conductivity of selected metals and alloys (bulk). The conductivity improvement upon cooling depends on the purity of the metal. Alloys have therefore a very limited improvement. Like alloys, thin-films too have less of a conductivity improvement (RRR = $\sigma_{4K}/\sigma_{300K}$ = 5–10) than bulk metals. The reason for this is that σ_{300K} is highly dependent on the quality of the film deposition.

Material	σ_{295K} $(10^7 \cdot \mathbf{S/m})$	σ_{4K} $(10^7 \cdot \mathbf{S/m})$
Ag	6.21	$\leqslant 10^4$
Au	4.54	$\leqslant 2500$
Al-6063	3.65	$\leqslant 10^4$
Cu	5.88	$\leqslant 10^4$
Ni	1.43	$\leqslant 2500$
Brass	1.39	2.326
Constantan	0.190	0.227
CuNi	0.39	0.43
Monel	0.20	3.3
Stainless Steel	0.10	0.125

flux-flow local oscillator, and IF matching circuitry [11].

5.1.2 Absorption loss above the superconducting energy gap

In Sec. 4.1.1 we saw that photons have enough energy to break Cooper-pairs above the superconducting energy gap ($2\triangle$). This results in a large absorption loss in the thin-film RF matching network in front of the mixer. To minimize the absorption loss (calculated to be 50–65 % per wavelength at 850 GHz for niobium) it is important to keep the RF matching network as simple and short as possible. In Fig. 5.2 we compare the calculated coupling efficiencies of a radial stub and "end-loaded" stub (Fig. 4.7) RF matching network, centered at 850 GHz [12, 13].

Although the "end-loaded" stub matching network is successfully used with SIS devices below the gap frequency, above the gap wiring loss prohibits its use. To include the effect of loss, we introduce an attenuator in front of the mixer with transmission t_{RF} at a physical temperature T_a. This is graphically represented in Fig. 5.3. In this way the lossless Tucker analysis [14] described in Chap. 4 can be applied.

The actual superconducting loss in the thin-film microstrip RF matching network is determined by the surface impedance, which for a superconductor is obtained from measuring the normal state dc conductivity just above the gap, and by solving the Mattis-Bardeen theory in the local limit (Sec. 4.2.5). With the complex conductivity known, the actual superconducting microstrip properties can then be calculated [15, 16, 17].

If R_l is the Ohmic loss in the RF matching network microstrip transmission line, then the shunt conductance in parallel with the RF junction admittance Y_{RF} (Eq. 4.43) is found to have the form

$$G_p = \frac{1}{R_l(1+Q_L^2)} \ . \tag{5.3}$$

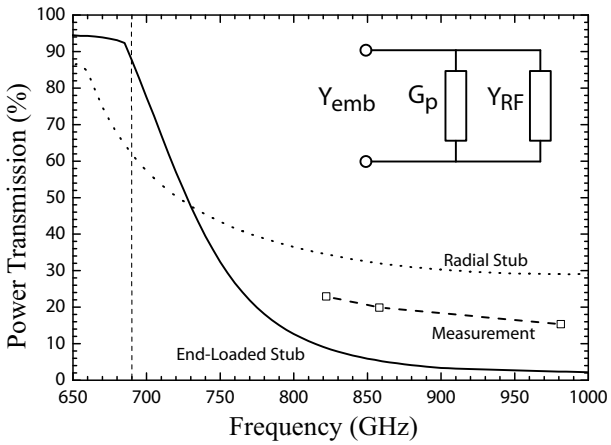

Figure 5.2: Coupling efficiency calculations assuming a conjugate matched "radial" and "end-loaded" stub RF matching network. Overlaid is the calculated efficiency from measured heterodyne data (dashed line) [18]. The loss in the RF choke structure and "Bowtie" antenna are not included in the simulated result. Material is niobium.

G_p represents a loss factor in parallel with Y_{RF} (Fig. 5.2) and Q_L the quality factor of a lossy transmission line, as defined by Eq. 4.81. As seen in Sec. 4.1, and Fig. 4.4d in particular, optimal mixer conversion gain is typically achieved with the junction quantum susceptance $B_{RF} \sim 0$, and the parasitic junction capacitance tuned out by the RF matching network. In this case, $G_{RF} \sim Y_{RF}$. For frequencies above the gap G_{RF} is slightly less than G_n, the junction normal state conductance. Since in our case, $Q_L^2 \gg 1$ Eq. 5.3 simplifies to

$$G_p \simeq \frac{B_{ms}^2}{G_l} \ , \tag{5.4}$$

with B_{ms} the shunt susceptance of the inductive transmission line. Under this condition t_{RF} of Fig. 5.3 may be obtained from

$$t_{RF} = \frac{G_{RF}}{G_{RF} + G_p} \ . \tag{5.5}$$

Several important observations can now be made: Power coupled to the junction is maximized by employing small area devices which decrease the transmission line susceptance B_{ms}. Second, loss in the RF matching network can be reduced

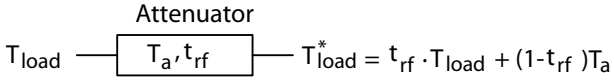

Figure 5.3: RF attenuator port model in front of the mixer. T_a is the physical temperature of the attenuator. The attenuator takes into account the front-end optics loss and absorption loss in the niobium film of the tuning circuit.

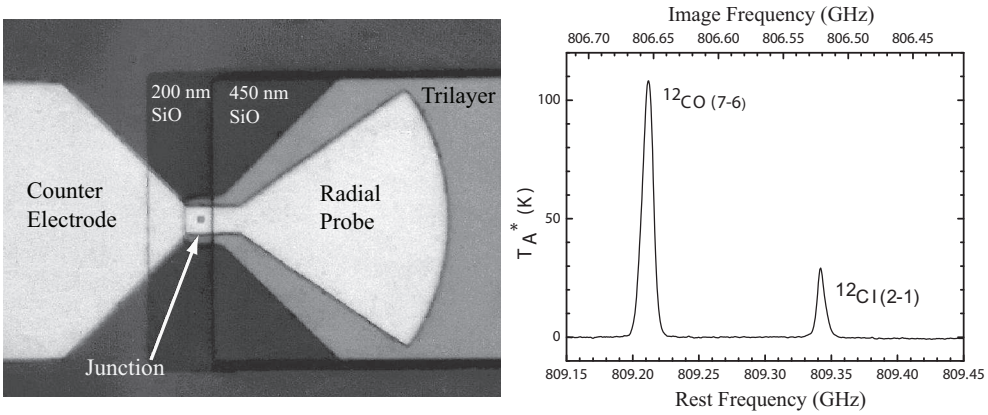

Figure 5.4: *Left*) 1000× photograph of the junction on silicon membrane. The transmission line length is 2.5 μm on 450 nm SiO and terminates in a radial stub with a fan angle of 70 degrees. The junction size in the center of the "Bowtie" antenna is 0.55 μm on a side. *Right*) $^{12}CO_{J=7\rightarrow6}$ (807 GHz) and detected atomic carbon, CI $^3P_2 \rightarrow {}^3P_1$ (809 GHz) in the Orion Bar region, at the Caltech Submillimeter Observatory. System temperature and total integration time were $\sim$ 4400 K and 47 minutes respectively. The main beam efficiency measured on Mars (10″ diameter) was 33 %, with an approximate zenith atmospheric transmissions of 40 %.

by maximizing the SiO insulating layer thickness to transmission line width ratio (R_l minimized). In our case we have opted for an insulator thickness of 450 nm, which is a standard process in the JPL-MDL junction fabrication process. Lastly, by employing high current density devices (Chaps. 7 & 8) we increase G_{RF}, via G_n, and thus increase the fraction of power coupled to the SIS device [19, 20].

In Fig. 5.4 we show a close-up of an all niobium radial probe RF matching network/SIS junction on a 1 μm thick silicon-nitride membrane with an AlO_x barrier [18]. This device formed a first step towards integrated array receivers (Chap. 9). It was installed at the CSO in 1997, and replaced in 2000 with the more sensitive all NbTiN quasi-optical mixer. The details of the all NbTiN quasi-optical mixer are discussed in the remainder of the Chapter. It is interesting to observe that a radial stub matching network has a relative narrow instantaneous bandwidth below the superconducting energy gap while above it the frequency response is broadened by the dispersive loss in the superconducting film.

An alternative to the use of superconducting transmission lines are normal metals such as gold (Au) or Aluminum (Al) [21, 22]. It is however required that any metals employed are compatible with the SIS fabrication process. Even though pure Au and Al conductivity improves by a factor of 5–10 when cooled to 4 K, these metals exhibit high loss when compared to an ideal superconductor, such as niobium. Above 800 GHz however the loss of Au/Al transmission lines becomes less than that of niobium ($\approx$ 40 % loss per wavelength). The same is true for NbTiN at $\nu > 1100$ GHz, as shown in Fig. 5.5, and as obtained from the discussion in Sec. 4.2.4. It is also possible to use high current density (AlN-barrier) tunnel junctions to reduce the loss in normal metal transmission lines. This technique has been successfully applied by

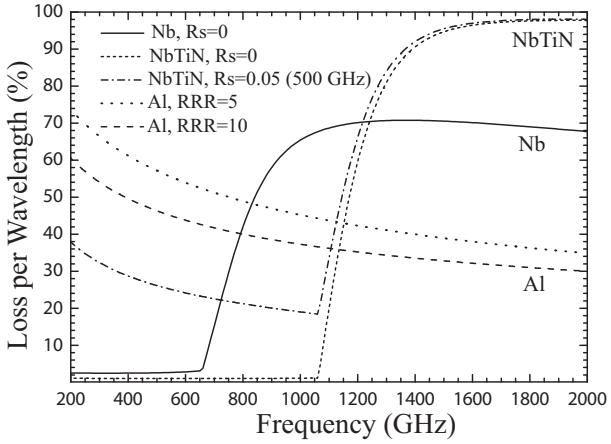

Figure 5.5: RF loss of a 5 μm microstrip transmission line made of three different materials. SiO substrate thickness is 400 nm, dielectric constant 5.6, substrate loss tangent 0.0015, and film thickness 300 nm. Nb has a T_c = 9.2 K, V_{gap}=2.8 mV, and ρ_n=5 $\mu\Omega$-cm. The NbTiN properties are T_c=15.3 K, V_{gap}=4.4 mV, and ρ_n=80 $\mu\Omega$-cm. The room temperature resistivity of the Al film is 2.45 $\mu\Omega$-cm. For details on the surface impedance calculation in the extreme anomalous, or local limit we refer to Sec. 4.2.

Karpov it et al. in the HIFI mixer band 5 design [20].

In the remainder of the Chapter we focus on the use of NbTiN to mitigate film loss above $\sim$ 680 GHz. As of this writing, the mixer remains the most sensitive of its kind in the 800 – 920 GHz frequency range. Fig. 5.5 shows the material loss for a variety of films. It is clear that NbTiN is a very promising material, even in the presence of moderate surface resistance [23].

5.2 Physical implementation of a 850 GHz twin-slot mixer

In Fig. 5.6 we show the layout of the 850 GHz AlN-barrier twin-slot junction. The quasi-optical mixer uses an extended hyper-hemispherical or elliptical lens [24] to couple the incoming radiation to a double-slot antenna. Here we describe a mixer that was installed at the CSO [25] in 2000 to cover the 800 – 920 GHz atmospheric window.

The twin-slot antenna (Zmuidzinas *et al.*) [6, 26] works by generating a voltage that is 180 degrees out of phase due to symmetry (inset Fig. 5.6). This sets up a virtual ground in the center of the tuning structure. The junction capacitance is tuned out by the shunt inductance of the microstrip line connecting the two junctions (D/2). At very high frequencies, the tuning inductor (D/2) becomes very small [27] and any kinetic inductance presented by the SIS junctions becomes proportionally more significant. To circumvent this problem, we introduced in 2000 "long" e-beam (sub-micron) junctions. For the HEB mixers, discussed in Sec. 4.3, tuning out of device

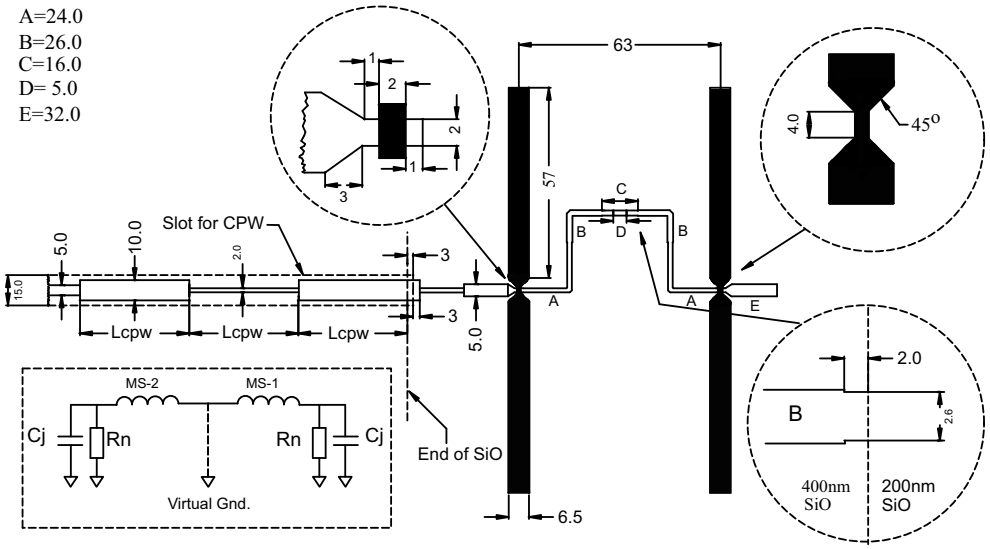

Figure 5.6: Twin-slot antenna with a NbTiN wire layer (top) and ground (bottom) layer. The actual SIS junctions are made of Nb with an AlN tunnel barrier. Device details in table 5.2.

capacitance is not an issue. This is an advantage of HEB mixers over SIS mixers in that these devices have a planar geometry (Fig. 4.23) with very little parasitic capacitance.

In the twin-slot design of Fig. 5.6 the IF output is coplanar-waveguide (CPW), with the slot antennas terminated by a open-ended microstrip line. Both serve to minimize parasitic capacitance, which is important if the IF bandwidth is to be maximized.

5.3 Optics

In 1993 Filipovic *et. al.* published a comprehensive paper [24] on the far-field patterns and Gaussian coupling efficiencies of double-slot antennae placed on hemispherical lenses with different radii (R) and extension length (L). In the original twin-slot mixer [7, 27] the L/R ratio was 0.291, which is the hyper-hemispherical position. This L/R ratio produces a fast $f/2.5$ beam at the e^{-2} power contour. To match the $f/4.2$ optics of the telescope [25] we required a L/R ratio of 0.335. Note that with the twin slot antenna located in an elliptical focus position, a collimated beam is obtained.

The lens diameter was chosen 6.35 mm (0.25 inches) which minimizes the virtual waist distance. It was also the smallest practical size possible, especially when the criticality of the SIS chip alignment to the extended hemispherical lens is considered. The maximum theoretical Gaussian coupling efficiency of $L/R = 0.335$ turns out to be slightly worse (5 %) than with the original $L/R = 0.291$. This tradeoff was considered acceptable in light of the fact that the successful cooled optics scheme of the 850 GHz waveguide mixer (Si_3N_4 membrane with $Nb/AlO_x/Nb$ junction [18], Sec. 9.2) could

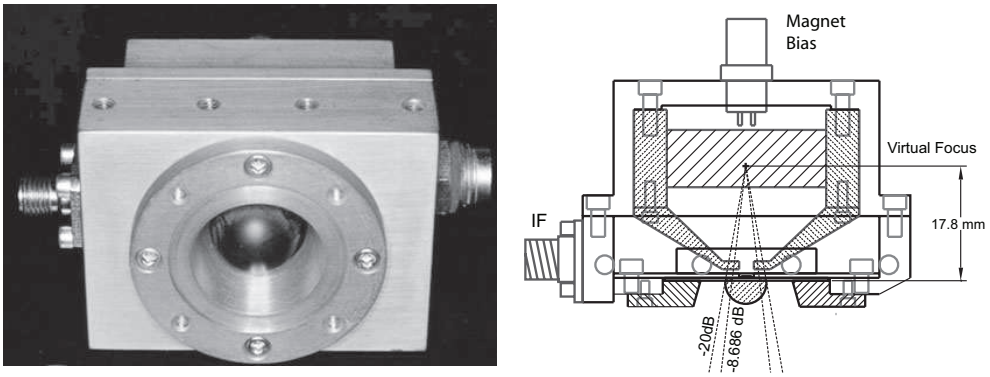

Figure 5.7: Optical configuration of the twin-slot mixer as described by Zmuidzinas *et al.* Modified mixer block with a L/R ratio of 0.335 and 12.7 mm diameter silicon lens. The virtual focus is $\approx$ 17.8 mm behind the planar twin-slot antenna. The lens material is high resisitivity silicon, and has been antireflection coated to minimize loss.

now be re-implemented for the twin-slot NbTiN mixer. Fig. 5.7 shows the mixer block and a graphical representation.

5.4 Nb/AlN/NbTiN SIS junction with NbTiN wire layers

The 800 – 920 GHz frequency band lies entirely above the superconducting energy gap of niobium (690 GHz), a commonly used superconductor for SIS junctions (Chap. 4). To prevent large absorption loss in the ground plane and wire layers, NbTiN

Table 5.2: Device parameters

Parameter	**Range**
R_nA	20 Ω-μm^2
Junction area	0.25 μm x 2.6 μm
Wiring thickness	250 nm
Ground-plane thickness	300 nm
SiO dielectric thickness	400 nm
SiO dielectric constant	5.6
Tanδ SiO	0.0015
NbTiN film properties	ρ_n = 80 $\mu\Omega$-cm
	λ = 230 nm
	T_c = 15.3 K
Nb film properties	ρ_n = 5 $\mu\Omega$-cm
	λ = 80 nm
	T_c = 9.2 K
Specific capacitance AlN_x	85 fF/μm^2

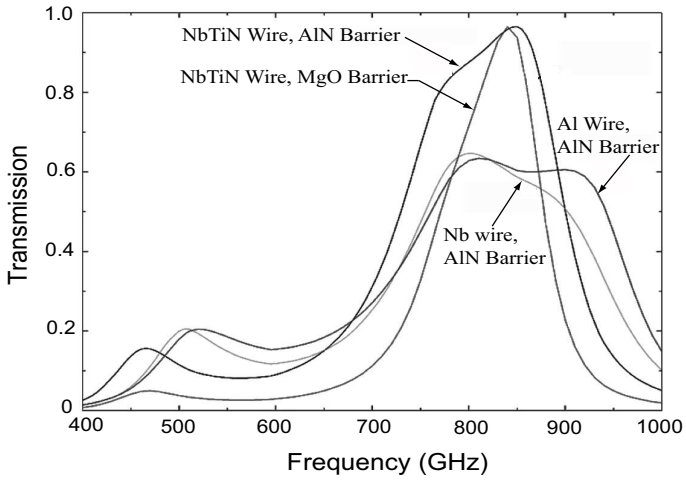

Figure 5.8: Circuit simulations of 4 different style SIS junction, and tuning structure configurations. In all cases the ground plane is NbTiN. Design was optimized for 850 GHz. The simulated bandwidth of the NbTiN/AlN/NbTiN tunnel junction with NbTiN thin-film wire layer & ground plane is $\sim$ 130 GHz, which agrees well with the measured heterodyne response presented in Fig. 5.9. MgO barriers have large specific capacitance (140 fF/μm^2), and thus exhibit narrower bandwidth the AlN barrier SIS junctions. Note that moderate current density (J$_c$=10 kA/cm^2) SIS junctions were employed in the designs of this chapter. The higher current density junctions of Chap. 7 & 8 provide $\sim$ 180 GHz of instantaneous RF bandwidth.

was utilized for the first time. In the described design the actual SIS junctions were fabricated with an AlN tunnel barrier, Nb top electrode, and NbTiN counter electrode. Even today, the performance and material composition of this device remains unique. The reason for this is that it has proven very difficult to grow a high quality (low temperature) epitaxial NbTiN wire (top) layer without degrading the quality of the SIS junction. Similar devices used in HIFI mixer bands 3, 4, and 5 all use an Al wire layer as substitute [19, 28]. The material and device parameters are shown in Table 5.2.

Heterodyne and extensive direct detection measurements with a Fourier Transform Spectrometer (FTS), indicate that NbTiN films have a low surface resisitivity, about 0.1 $\Omega/\square$ at 600 GHz or less. The details of the fabrication process, the FTS measurement results, and actual device parameters are presented in a publication by Kawamura *et al.* [29]. The junctions used for this work have a critical current density of 10 kA/cm^2. The measured leakage current in the junction [30] at 2 mV is 7.4 μA. This corresponds to a R$_{subgap}$ to R$_n$ ratio of 15. Being a hybrid junction, the energy gap was expected to be at 4 mV (Δ_{Nb} + Δ_{NbTiN}), however the actual measured gap voltage is 3.2 mV (2Δ/h $\approx$ 800 GHz). The most plausible explanation is that the NbTiN counter electrode, in the vicinity of the barrier, is of poor quality. In Fig. 5.8 we show circuit simulations of twin-slot mixers with a variety of material compositions.

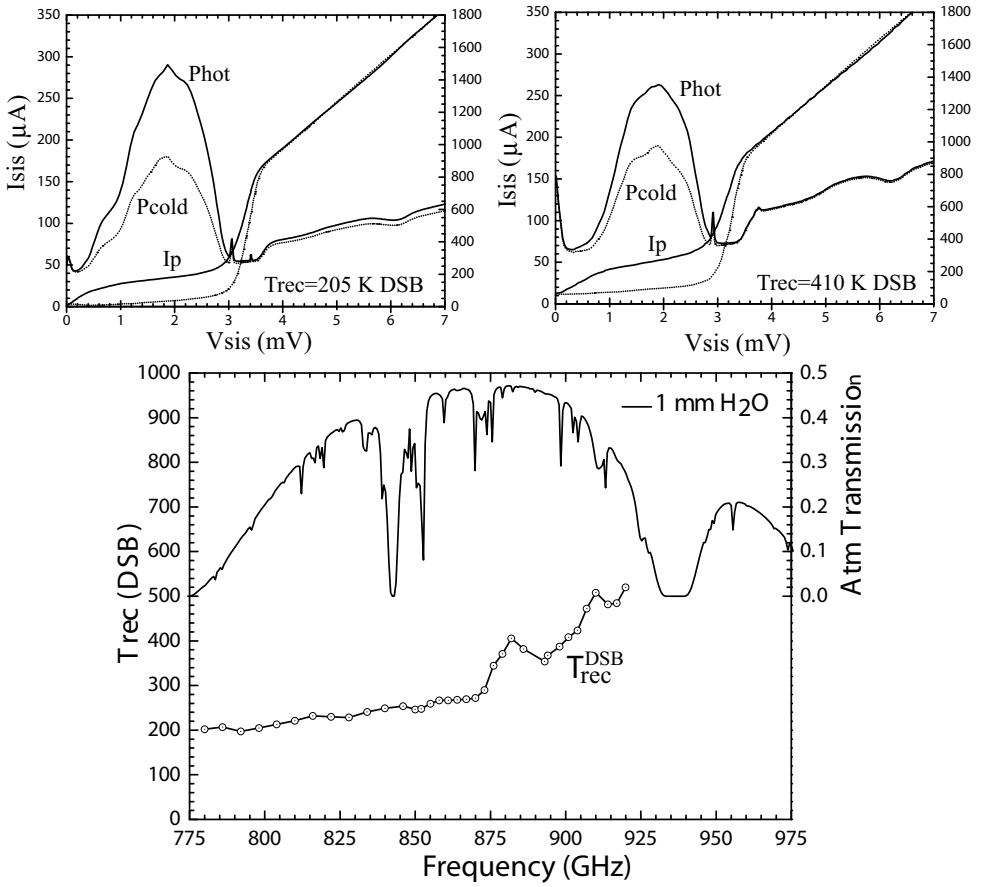

Figure 5.9: Top: 800 GHz and 900 GHz heterodyne response. Bottom: Receiver sensitivity of the all NbTiN twin-slot open structure receiver as measured at the Caltech Submillimeter Observatory (CSO). All results are with a 1 – 2 GHz IF.

5.5 Performance

Fig. 5.9 shows the heterodyne response at 800 GHz and 900 GHz as measured at the Caltech Submillimeter Observatory (CSO). These results are obtained with an all NbTiN wire and ground layer, and twin Nb/AlN/NbTiN SIS junctions. Note how with increasing frequency the width of the photon step decreases. This is indeed expected for frequencies above 2Δ (800 GHz), as the photon step from the negative bias side partially cancels the photon step from the positive bias side (V_{gap} – hν/e = -0.4 mV at 900 GHz). The optimal bias condition across the entire frequency band is 2.10 mV. The LO pump current is $\sim$ $I_c/3$ or 40 μA, I_c being the critical current of the junction.

The improvement over the in 1997 installed all-niobium waveguide receiver [18] is primarily due to the decrease in NbTiN wire layer and ground plane transmission

Table 5.3: Measured and calculated receiver parameters at V_{sis} = 2.10 mV. Results presented are with a 1 – 2 GHz intermediate frequency.

Parameters	**800 GHz Data**	**900 GHz Data**
T_{rec} (K) DSB	205	410
T_{opt} (K)	70	100
T_{IF} (K)	22	41
$t_{RF} \cdot G_{mix}^{DSB}$ (dB)	-7.2	-9.9
T_{mix} (K)	43	55
$h\nu/k$ (K)	38	43
T_{LNA} (K) †	4.2 ± 0.3	4.2 ± 0.3
$\Gamma_{beamsplitter}$ (%)	14	18
Z_p (Ω)	129	80.5
R_n (Ω)	17.8	17.8
Z_{IF} (Ω)	90	90

† Measured

line loss (∼5 dB). Note that the front-end optics and IF configurations are identical between the two systems! In the text all noise temperatures are calculated using the Callen & Welton defined blackbody radiation temperature [31, 32]. The receiver and mixer properties are summarized in Table 5.3. Optics loss is derived from the intersecting line technique, described by Blundell [33], Ke, and Feldman [34] *et al.*

$t_{RF} \cdot G_{mix}^{DSB}$ is the total mixer conversion gain which includes optics loss in front of the mixer. T_{mix} is the mixer noise temperature (referred to the input): (T_{rec} - T_{opt} - T_{IF}) · ($t_{RF} G_{mix}^{DSB}$), and T_{IF} the total IF noise contribution. T_{LNA} is the actual measured noise temperature of the low noise amplifier directly following the mixer. Z_p is the subgap differential resistance obtained from the LO pumped IV curve and is needed to take reflection loss in the shot noise calculations into account. The IF matching network presents a 90 Ω impedance to IF output port of the mixer. As of the writing of this thesis this receiver remains the most sensitive every build in this frequency range.

5.6 Astronomical observations

Among the first observations [35] carried out with the new receiver we performed 10″ resolution maps of two contiguous HDO transitions: $J_{Ka,Kb} = 2_{1,2} \rightarrow 1_{1,1}$ at 848.9619 GHz, and $J_{Ka,Kb} = 1_{1,1} \rightarrow 0_{0,0}$ at 893.6387 GHz towards Orion IRc2. The weather conditions during the observing runs (January and March 2000) were excellent and provided average zenith transmissions above Mauna Kea as high as ∼ 38.5 % (849 GHz) and ∼ 42 % (886 GHz). This resulted in SSB system temperatures at 849 GHz as low as 1700 K at the elevation of the source (70 deg) at the beginning of the observations. Integration time for each point was 3 minutes.

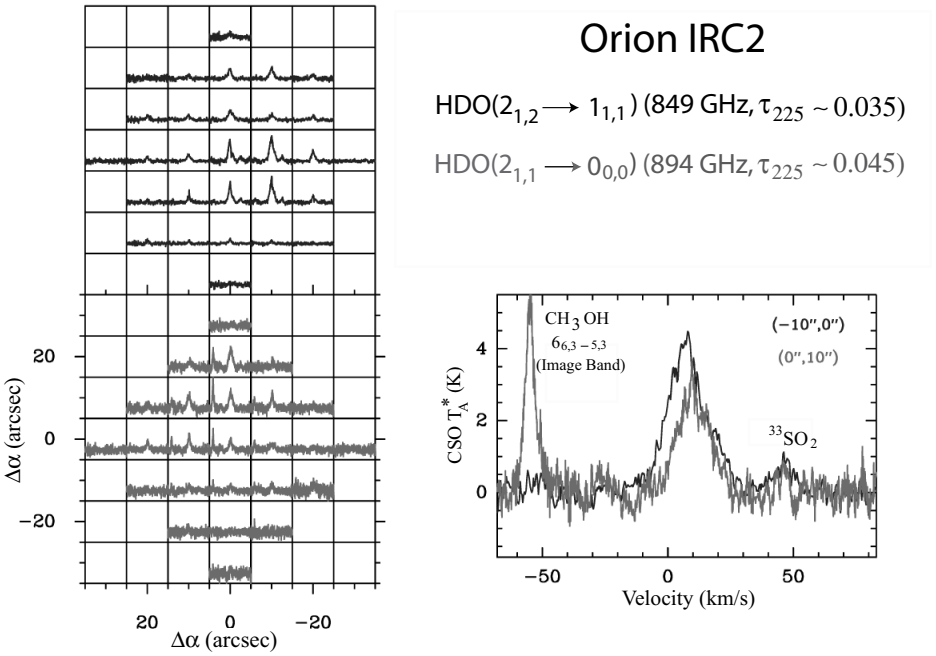

Figure 5.10: First Detection of HDO($2_{1,2} \rightarrow 1_{1,1}$) and HDO($1_{1,1} \rightarrow 0_{0,0}$) in Orion-IRc2.

The observations show a compact source for both HDO lines ($\sim 45''$). The data have been modeled using the same LVG model previously used by Cernicharo [36] *et al.* for their analysis of the emission of H_2O at 183.31 GHz and 325.15 GHz (this last line observed also at the CSO) towards the same source. These two H_2O lines have a maser nature in Orion IRc2, so the newly observed (thermal) HDO lines place better constraints on the density, temperature, and H_2O abundance estimates of the emitting regions.

5.7 Summary

A 850 GHz quasi-optical receiver has been presented. It was installed at the Caltech Submillimeter Observatory [25] in 2000. To circumvent absorption loss in the superconducting film, due to the braking of Cooper pairs, the junction uses NbTiN wiring with an AlN tunnel barrier for the first time. This technological feat provides for a record heterodyne sensitivity in the 350 μm atmospheric window. A method for dealing with the absorption loss in front of the mixer is presented. HIFI mixers bands 3, 4, and 5 have all benefited from the development presented in this Chapter.

Bibliography

[1] A. J. Baden Fuller, Microwaves, 2^{nd} Edition, Pergamon Press, (1979).

[2] G. A. Edis, "Measurements and Simulations of Overmoded Waveguide Components at 70 – 118 GHz, 220 – 330 GHz, and 610 – 720 GHz", *NRAO*, Charlotteville, VA, ALMA Memo 467, May. 29, (2003).

[3] A. Pavolotsky, D. Meledin, C. Risacher, M. Pantaleev, and V. Belitsky, "Micromachining Approach In Fabricating of THz Waveguide Components", *EMN04*, 20-21 Oct., Paris, France, (2004).

[4] M. J. Wengler, D. P. Woody, R. E. Miller, and T. G. Phillips, "A low noise receiver for millimeter and submillimeter wavelength," *Int. J. IR and MM Waves*, Vol. 6, pp. 697-706, Aug., (1985).

[5] T. H. Büttgenbach, R. E. Miller, M. J. Wengler, D. M. Watson, and T. G. Phillips, "A Broad-band Low Noise SIS Receiver for Submillimeter Astronomy", *IEEE Trans. Microwave Theory and Techniques*, Vol. 36, No. 12, pp. 1720-1726, Dec., (1988).

[6] V. Y. Belitsky, M. A. Tarasov, S. A. Kovtonjuk, L. V. Filippenko, and O. V. Kaplunenko, "Low Noise completely quasi-optical SIS receiver for radio astronomy at 115 GHz", Int, *J, IR and MM Waves*, Vol. 13, pp. 389-396, Apr., (1002).

[7] J. Zmuidzinas and H.G LeDuc, "Quasi-optical slot antenna SIS mixers, *IEEE Trans. Microwaves Theory and Techniques*, Vol. 40, No. 9,pp. 1797-1804, Sept. (1992).

[8] G. Chattopadhyay, D. Miller, H. G. LeDuc, and J. Zmuidzinas, "A dual-polarized quasi-optical SIS mixer at 550 GHz," *IEEE Trans. Microwave Theory and Techniques*, Vol. 48, No. 10, pp. 1680-1686, Oct., (2000).

[9] V. P. Koshelets and S. V. Shitov, "Integrated Superconducting Receivers", *Superconductor Science and Technology*, Vol. 13, pp. R53-R69, (2000).

[10] V. P. Koshelets, "Superconducting Integrated Receiver for TELIS", *IEEE Trans. Appl. Supercond.*, Vol. 15, pp. 960-963, (2005).

[11] V. P. Koshelets, A. B. Ermakov, L. V. Filippenko, A. V. Khudchenko, O. S. Kiselev, A. S. Sobolev,
M. Yu. Torgashin, P. A. Yagoubov, R. W. M. Hoogeveen, and W. Wild, "Superconducting Integrated Submillimeter Receiver for TELIS", *IEEE Trans. Appl. Supercond*, Vol. 17, no. 2, pp. 336-342, Jun., (2007).

[12] J. W. Kooi, M. Chan, B. Bumble, T. G. Phillips, "A low noise 345 GHz waveguide receiver employing a tuned 0.50 μm^2 Nb/AlO$_x$/Nb tunnel junction", *Int. J. IR and MM Waves*, Vol. 15, No. 5, May., (1994).

[13] J. W. Kooi, M. Chan, B. Bumble, H. G. Leduc, P. L. Schaffer, and T. G. Phillips, "230 and 492 GHz Low-Noise SIS Waveguide Receivers employing tuned Nb/AlO$_x$/Nb tunnel junctions," *Int. J. IR and MM Waves*, Vol. 16, No. 12, pp. 2049-2068, Dec., (1995).

[14] J. R. Tucker and M. J. Feldman, "Quantum Detection at Millimeter Wavelengths", *Rev. Mod. Phys.*, Vol. 57, pp. 1055-1113, Oct., (1985).

[15] J. F. Whitaker, R. Sobolewski, D. R. Dykaar, T. Y. Hsiang, and G. A. Mourou, "Propagation model for ultrafast signals on superconducting dispersive striplines", *IEEE Trans. Microwave Theory and Techniques*, Vol. MTT-36, No. 2, pp. 277-285, Feb., (1998).

[16] R. L. Kautz, "Picosecond pulses on superconducting striplines", *J. Applied Physics*, Vol. 49, pp. 308-314, (1978).

[17] E. Hammerstad and O. Jensen, "Accurate models for microstrip computer-aided design, *IEEE MTT-S, Int. Microwave Symp. Dig.*, pp. 407-409, May. (1980).

[18] J. W. Kooi, J. Pety, B. Bumble, C. K. Walker, H. G. LeDuc, P. L. Schaffer, and T. G. Phillips, "A 850 GHz Waveguide Receiver Employing a Niobium SIS Junction Fabricated on a 1μm Si$_3$N$_4$ Membrane", *IEEE Trans. Microwave Theory and Techniques*, Vol. 46, No. 2, pp. 151-161, Feb., (1998).

[19] A. Karpov, D. Miller, F. Rice, J. A. Stern, B. Bumble, H. G. LeDuc, and J. Zmuidzinas, "Low Noise SIS Mixer for Far Infrared Radio Astronomy", in *Proc. of SPIE*, Volume 5498, Ground-based Telescopes, edited by J.Zmuidzinas, W. S. Holland, and S. Withington, (SPIE, Glasgow, UK, 2004) pp. 616-621.

[20] A. Karpov, D. Miller, F. Rice, J. A. Stern, B. Bumble, H. G. LeDuc, and J. Zmuidzinas, "Low Noise 1 THz-1.4 THz Mixers using Nb/Al-AlN/NbTiN SIS Junctions", *IEEE Transactions on Applied Supercon.*, Vol. 17 (2), pp. 332-346, Jun. (2007).

[21] M. Bin, M. C. Gaidis, J. Zmuidzinas, T. G. Phillips, and H. G. Leduc, "Quasi-Optical SIS mixers with Normal-Metal Tuning Structures", *IEEE Transactions on Applied Supercon*, Vol. 7 (2), Part 3, pp 3584-3588, Jun. (1997).

[22] P. Dieleman, T.M. Klapwijk, J.R. Gao, and H. van de Stadt, "Analysis of Nb superconductor-insulator-superconductor tunnel junctions with Al striplines for THz radiation detection", *IEEE Trans. Applied Superconductivity*, Vol. 7, pp 2566-2569, (1997).

[23] J. Zmuidzinas, J. Kooi, J. Kawamura, G. Chattopadhyay, B. Bumble, H. G. LeDuc, and J. A. Stern, "Development of SIS Mixers for 1 THz", *SPIE; International Society for Optical Engineering Proceedings*, Kona, Hawaii, (1998).

[24] D. F. Filipovic, S. S. Gearhart, and G. M. Rebeiz, "Double-Slot Antennas on Extended Hemispherical and Elliptical Silicon Dielectric Lenses", *IEEE Transactions on Microwave Theory and Techniques*, Oct., (1993).

[25] T. G. Phillips, "The Caltech Submillimeter Observatory", IEEE 1-4244-0688, Sep., (2007).

[26] J. Zmuidzinas, H. G. Leduc, J. A. Stern, and S. R. Cypher, "Two-junction tuning circuits for submillimeter SIS mixers, "*IEEE Transactions on Microwave Theory and Techniques*, Vol. MTT-42, No. 4, pp 698-706, Apr., (1994).

[27] M. Gaidis, H. G. LeDuc, M. Bin, D. Miller, J. A. Stern and J. Zmuidzinas, " Characterization of low noise quasi-optical SIS mixers for the Submillimeter Band", *IEEE transactions on Microwave Theory and Techniques*, Vol. 44, No. 7, pp. 1130-1139, Jul., (1996).

[28] B. D. Jackson, G. de Lange, T. Zijlstra, M. Kroug, J. W. Kooi, J. A. Stern, and T. M. Klapwijk, *"Low-Noise 0.8-0.96 and 0.96-1.12 THz Superconductor-Insulator-Superconductor Mixers for the Herschel Space Observatory"*, *IEEE Trans. Microwave Theory and Techniques*, Vol. 54, No. 2, pp. 547-558, Feb., (2006).

[29] J. Kawamura, J. Chen, D. Miller, J. Kooi, J. Zmuidzinas, B. Bumble, H. G. LeDuc, and J. A. Stern, "Low-Noise Submillimeter-wave NbTiN superconducting tunnel junction mixers", *Applied Physics Letters*, Vol. 75, Num. 25, Dec., (1999).

[30] P. Dieleman, H. G. Bukkems, T. M. Klapwijk, M. Schicke, and K. H. Gundlach, "Observation of Andreev reflection enhanced shot noise," *Phys. Rev Letters*, Vol. 79, pp. 3486-3489, (1997).

[31] H. B Callen and T. A. Welton, "Irreversibility and generalized noise," *Phys. Rev.*, Vol. 83, no. 1, pp 34-40, Jul., (1951).

[32] A. R. Kerr, M. J. Feldman, and S. K. Pan, "Receiver noise temperature, the quantum noise limit, and the role of zero-point flucuations, "*NRAO*, Charlottesville, VA, Electron. Div., Internal Rep. 304, Sep. (1996).

[33] R. Blundell, R. E. Miller, and K. H. Gundlach, "Understanding noise in SIS receivers," *Int, J. Infrared and Millimeter Waves*, Vol. 13, no. 1, pp 3-26, (1992).

[34] Q. Ke and M. J. Feldman, "A technique for noise measurements of SIS receivers," *IEEE transactions on Microwave Theory and Techniques*, Vol. 42, pp. 752-755, Apr., (1994).

[35] J. R. Pardo, J. Cernicharo, F. Herpin, J. Kawamura, J. W. Kooi, and T. G. Phillips, "Deuterium Enhancement in Water toward Orion IRc2 Deduced from HDO Lines above 800 GHz", *Astrophysical Journal*, Vol. 562, pp. 799-803, Dec., (2001).

[36] J. Cernicharo, J. R. Pardo, E. Gonzalez-Alfonso, E. Serabyn, T. G. Phillips, D. Benford, and D. Mehringer, "Physical conditions in shocked regions of Orion from ground-based observations of H2O", *Astrophysical Journal*, Vol. 520, L131-L134, (1999).

Chapter 6

IF impedance and mixer gain of NbN hot-electron bolometers*

Abstract - The intermediate frequency (IF) characteristics, the frequency dependent IF impedance, and the mixer conversion gain of a small area Hot Electron Bolometer (HEB) have been measured and modeled. The device used is a twin slot antenna coupled NbN HEB mixer with a bridge area of 1 μm x 0.15 μm, and a critical temperature of 8.3 K. In the experiment the local oscillator (LO) frequency was 1.300 THz, and the intermediate frequency (IF) 0.05 – 10 GHz. We find that the measured data can be described in a self consistent manner with a thin film model presented by Nebosis *et al.* [Proceedings of the Seventh International Symposium on Space Terahertz Technology, Charlottesville, VA 1996 (unpublished), pp. 601–613], that is based on the two temperature electron-phonon heat balance equations of Perrin-Vanneste[J. Phys. Vol. 48, 1311 (1987)]. From these results the thermal time constant, governing the gain bandwidth of HEB mixers, is observed to be a function of the electron-phonon scattering time, phonon escape time, and the electron temperature. From the developed theory the maximum predicted gain bandwidth for a NbN HEB is $\sim 5.5 - 6$ GHz. In contrast, the gain bandwidth of the device under discussion was measured to be $\sim$ 2.3 GHz which, consistent with theory, is attributed to a somewhat low critical temperature and non-optimal film thickness (6 nm).

*This Chapter is published as J. W. Kooi, J. J. A. Baselmans, J. R. Gao, T. M. Klapwijk, M. Hajenius, P. Dieleman, A. Baryshev, and G. de Lange, in the *Journal of Applied Physics*, **101**, 044511, Feb. (2007).

6.1 Introduction

Traditionally hot electron bolometer mixers [1], based on InSb, suffer from small (<10 MHz) IF bandwidths, due to a relatively long electron relaxation time. To enhance the science that may be done with these devices, there has in recent years been a strong push to expand the gain and noise bandwidth of hot electron bolometers. Success has been achieved with the use of ultra thin ($\approx 4-6$ nm) NbN superconducting films with very short phonon escape times [2]. The majority of such films have been supplied by the Moscow Pedagogical State University [3] [4]. In previous work, measurement and analysis of the IF impedance and gain bandwidth of large area NbN phonon-cooled hot electron bolometers was performed by Rodrigues-Morales and Yngvesson [5]. The analysis was, however, based on model that uses a single time constant to describe the electron temperature relaxation time [6].

Initially, HEB mixers were analyzed as lumped element transition-edge sensors [7] [8]. The strong temperature dependence of the resistance at the transition to the superconducting state was taken as a sensitive measure of variations in the electron temperature. In practice HEBs are operated at an elevated electron temperature created by dc bias and applied local oscillator (LO) signal. These conditions have led to a reanalysis of the physical conditions during mixing. Initially, mixing was understood to be the result of a heating induced, fully normal (Ohmic) electronic "hot spot" [9], and more recently due to a distributed temperature profile [10] [11] in response to temperature and current induced local resistivity. In general, HEB analyses have focused on taking into account all contributions to the power fed into the electron system, balanced by losses due to diffusion and electron-phonon relaxation. In recent work [12] it became clear that the dc current-voltage characteristics could not be described on the basis of power and electron temperatures alone. It turned out important to include the physical process, that acts as the source of resistance in a superconducting film close to its transition temperature. This resistance is known to appear due to temperature and current enhanced two-dimensional (2D) phase slip events or flux flow. It was shown [12] that this consideration leads to a correct description of the dc I(V) characteristics. It is assumed that the underlying physics is analogous to the Berezinskii-Kosterlitz-Thouless treatment, in which for thin superconducting films above a characteristic temperature $T > T_{KT}$ pairs of free vortices with plus and minus signs and core radii ξ ($\sim$ 4nm for NbN) are created.

In the present manuscript we focus on the dynamic processes that govern the HEB mixer gain, IF impedance, and gain bandwidth. It is assumed that the mixing process at THz frequencies is controlled by the quadratic response to voltage, leading to an intermediate frequency signal in the electron temperature. We will assume that the vortex processes relevant at dc are too slow to follow the responses at THz and IF frequencies. We find that the two temperature electron cooling model introduced by Perrin-Vanneste [13], and expanded upon by Nebosis, Semenov, Gousev, and Renk (NSGR) [14] is very adequate in describing the IF response. The NSGR model includes an electro-thermal feedback mechanism that modulates the mixer's inhomogeneous non-linear mixing region via complex IF voltage reflections. It is this feedback mechanism that is responsible for fluctuations in the receiver noise temperature.

In this paper we present a unique data set and demonstrate that the modified NSGR model provides a self consistent set of parameter values in good agreement with literature and measurement. The obtained parameter values may then be used to explore the maximum achievable bandwidth of NbN based HEBs, and provide guidance toward possible material improvement.

6.2 Theory

At RF frequencies with h$\nu \gg 2\Delta$, power is absorbed uniformly in a bridge with fixed cross-sectional area. Applying a LO signal the electron temperature in the bridge modulates with $[sin(\omega_{LO}t) + sin(\omega_s t)]^2$, resulting in a modulation of the electron temperature at the difference frequency (IF) between ω_{LO} and ω_s. Since the upper frequency limit for non-equilibrium responses of the superconductors is set by the superconducting energy gap we assume that the vortex processes cannot follow the RF signals.

At IF frequencies the free vortex density modulation as a result of current is, when compared to the electron temperature, expected to be a lower order effect. In addition, though Knoedler and Voss have measured phase slip induced shot noise up to 100 KHz [15], the recombination/annihilation rate of free vortices at the intermediate frequencies we concern ourselves with are thought to be too slow to follow the IF. We will therefore assume that at the IF frequencies the temporal response is predominantly connected to the electron temperature (∂R/∂T). This allows the use of the NSGR model, where the non-thermal action of the current (∂R/∂I) has been neglected.

The primary cooling mechanism of quasi-particles in the superconducting film occurs via electron-phonon interaction, while the phonons, raised to a temperature that closely follows the electron temperature, escape into the substrate. Due to the thin (3.5–6 nm) film and strong coupling to the substrate, diffusion via the metal contact pads is assumed negligible in determining the temporal response. For this reason diffusion has been neglected in the NSGR model. Important to our discussion are the strongly temperature dependent heat capacities of the electrons, $c_e(T_e)$, and phonons, $c_{ph}(T_{ph})$. Following the two temperature analysis of Perrin-Vanneste [13], coupled differential equations are used, one for the electron temperature T_e and one of the phonon temperature T_{ph}, to describe the heat balance in the film:

$$c_e \frac{\partial T_e}{\partial t} = P_{dc} + p_{lo} - p_{eph} \ , \tag{6.1}$$

$$c_{ph} \frac{\partial T_{ph}}{\partial t} = p_{eph} - p_{phs} \ . \tag{6.2}$$

The powers are per unit volume, with P_{dc} and p_{lo} due to dc and LO power induced heating. p_{eph} describes the power transfer between the quasi-particles and the phonons, and p_{phs} the transfer between phonons and substrate (with a bath temperature T_0).

$$p_{eph} = A_e({T_e}^n - T_{ph}^n), \quad A_e = \frac{c_e}{n{T_e}^{n-1}\tau_{eph}} \ , \tag{6.3}$$

$$p_{phs} = A_{ph}(T_{ph}^4 - {T_0}^4), \quad A_{ph} = \frac{c_{ph}}{nT_{ph}^3\tau_{esc}} \ . \tag{6.4}$$

For NbN, n $\sim$ 3.6 [16] [17]. Both p_{eph} and p_{phs} are assumed uniform in the bridge apart from their temperature dependence [14] [18]. In reality, the temperature profile across the bridge is a function of position [11] [12], and even though this has not been taken into account in the NSGR model, we are able to achieve good fits between model and measurement. Future models may be improved by taking the distributed temperature profile across the bridge into account.

To obtain a general solution to the heat balance equations, one has to make a certain assumption on how the local resisitivity depends on current and electron temperature. Following Nebosis *et al.*, we obtain

$$Z = \frac{d}{dI}[I \cdot R(I, T_e)] = R(I, T_e) + I\frac{\partial R}{\partial I} + I\frac{\partial R}{\partial T_e}\frac{\partial T_e}{\partial I} \ , \tag{6.5}$$

where term $\frac{\partial R}{\partial I}$ is ignored at IF frequencies. $Z(\omega)$, the frequency dependent HEB output impedance, may be found by assuming that a small perturbation in the current, $dI = \delta I e^{i\omega t}$, causes a change in the electron temperature $dT_e = \delta T_e e^{i(\omega t + \varphi 1)}$, and phonon temperature $dT_{ph} = \delta T_{ph} e^{i(\omega t + \varphi 2)}$. Substituting these partials into the linearized ($T_e \sim T_{ph} \ll 2T_0$) heat balance Eqs. 6.1 & 6.2 and solving it together with Eq. 6.5 gives

$$Z(\omega) = R_o \cdot \frac{\Psi(\omega) + C}{\Psi(\omega) - C} \ . \tag{6.6}$$

Strictly speaking the simplification that $T_e \sim T_{ph}$ holds (Sec. 6.6), however the assumption that $T_{ph} \ll 2T_0$ and that of a uniform temperature distribution in the bridge is not entirely valid as it approximates a lumped element model. It does however provide a convenient closed form solution that fits the measured data. In Eq. 6.6, $\Psi(\omega)$ represents the time dependent modulation of the electron temperature, ω the IF radial frequency, R_o the dc resistance at the operating point of the mixer, and C the self heating parameter [19] [20]. The latter is important as it forces the complex part of the impedance (Eq. 6.6) to be zero at very low and very high IF frequencies. $\Psi(\omega)$ is defined by three time constants, τ_1, τ_2, τ_3:

$$\Psi(\omega) = \frac{(1 + i\omega\tau_1)(1 + i\omega\tau_2)}{(1 + i\omega\tau_3)}. \tag{6.7}$$

The self heating parameter C can be described as

$$C = \frac{I^2}{V}\frac{\partial R}{\partial T_e}\left(\frac{\tau_{eph}}{c_e} + \frac{\tau_{esc}}{c_{ph}}\right) \tag{6.8}$$

with dV/dI the differential resistance at the operating point. In the transfer function $\Psi(\omega)$; τ_1, τ_2, τ_3 may be solved as

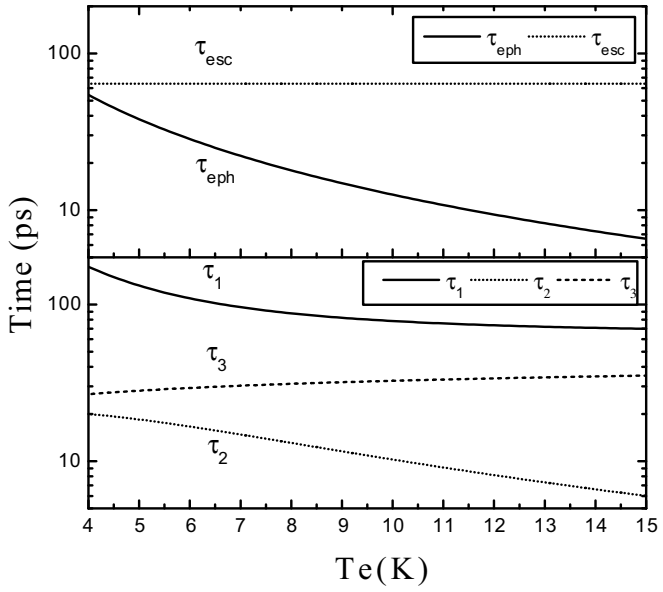

Figure 6.1: Discussed time constants and their electron temperature relationship. The NbN τ_{eph}, τ_{esc}, and the heat capacity ratio c_e/c_{ph} (not shown) are obtained from literature and serve to constrain the impedance and mixer gain models. A 6 nm thick NbN film is estimated from transmission electron microscopy (TEM) measurements, with values for τ_1, τ_2, τ_3 derived from Eqs. 6.9 – 6.11. Actual fit values for τ_{eph}, τ_{esc}, and c_e/c_{ph} for different HEB bias and LO pump conditions are shown in Table 6.1.

$$\tau_1^{-1}, \tau_2^{-1} = \frac{\Omega}{2}\left(1 \mp \sqrt{1 - \frac{4{\tau_{eph}}^{-1}{\tau_{esc}}^{-1}}{\Omega^2}}\right) , \tag{6.9}$$

with

$$\Omega = \left(1 + \frac{c_e}{c_{ph}}\right) \cdot \tau_{eph}^{-1} + \tau_{esc}^{-1} , \tag{6.10}$$

and

$$\tau_3^{-1} = \frac{c_e}{c_{ph}}{\tau_{eph}}^{-1} + {\tau_{esc}}^{-1} . \tag{6.11}$$

In Fig. 6.1 we plot the phonon escape time and electron-phonon scattering time with the corresponding $\Psi(\omega)$ time constants as a function of electron temperature for a 6 nm NbN superconducting film.

To derive an expression for the conversion gain of the mixer, we use standard lumped element formalism to obtain the frequency selective responsivity [8] [21] [22] of a bolometer, but with the single pole time constant replaced by the more general

temperature dependent electron transfer function $\Psi(\omega)$. Included in the responsivity is a complex load impedance Z_L, which connects across the output port of the bolometer, and the HEB output reflection coefficient Γ_{if}. In this manner the self heating electro-thermal feedback, due to (complex) voltage reflections between mixer and IF circuitry, may be taken into the account.

$$S(\omega) = \frac{dV_l}{dP} = \frac{\alpha}{\chi \cdot I} \frac{Z_L}{R_o + Z_L} \frac{C}{(\Psi(\omega) + \Gamma_{if}\ C)}\ , \tag{6.12}$$

with

$$\Gamma_{if} = \frac{R_o - Z_L}{R_o + Z_L}. \tag{6.13}$$

Here α represents the RF coupling factor, and I the signal current through the load (and device). Fundamentally the bolometer responsivity of Eq. 6.12 remains linked to the lumped element model, and a modification is needed to properly account for the different heating efficiencies of LO and dc signal power [10]. This parameter is symbolized by χ, and is an inverse measure of the width of the distributed temperature profile in the bridge. At high bias power $\chi \sim 1$, whereas at low dc bias and incident LO power χ may be as large as 3. Obtained values for χ in the context of the present analysis are found in Table 6.2. In this formalism, the direct detection (bolometric) response of the hot electron bolometer [23] may be accounted for by a change in χ, bias current, and R_o. Regardless of these adjustments, the modified NSGR hot electron bolometer responsivity remains an approximation of the physical dynamics inside the bridge area [12], albeit a good one.

Note that because the IF load impedance connected to the mixer is in general complex, it is important to use the complex responsivity, and not the absolute responsivity, $|S(\omega)|$, to reflect the true nature of the electro-thermal feedback on the conversion gain, $\eta(\omega)$. To find the (complex) conversion gain of the mixer, we use the standard expression

$$\eta(\omega) = \frac{2S(\omega)^2}{Z_L} p_{lo}\ . \tag{6.14}$$

After substitution of Eq. 6.12, and making the assumption that most of the signal current through the device is in fact dc bias current, i.e. $P_{dc}{=}I^2 \cdot R_o$ we find after some algebraic manipulation the magnitude of the conversion gain as

$$\eta(\omega) = \frac{2\alpha^2 p_{lo}}{\chi^2 \cdot P_{dc}} \left| \frac{R_o Z_L}{(R_o + Z_L)^2} \cdot \frac{C^2}{[\Psi(\omega) + \Gamma_{if}\ C]^2} \right|. \tag{6.15}$$

where p_{lo} is the LO power at the device, as estimated from the isothermal technique [24, 25].

6.3 Experiment and calibration

In the described experiment, we use a sub-micron twin-slot NbN HEB mixer chip (M12-F2) with a bridge area of 1 μm x 0.15 μm [2]. Before processing the starting

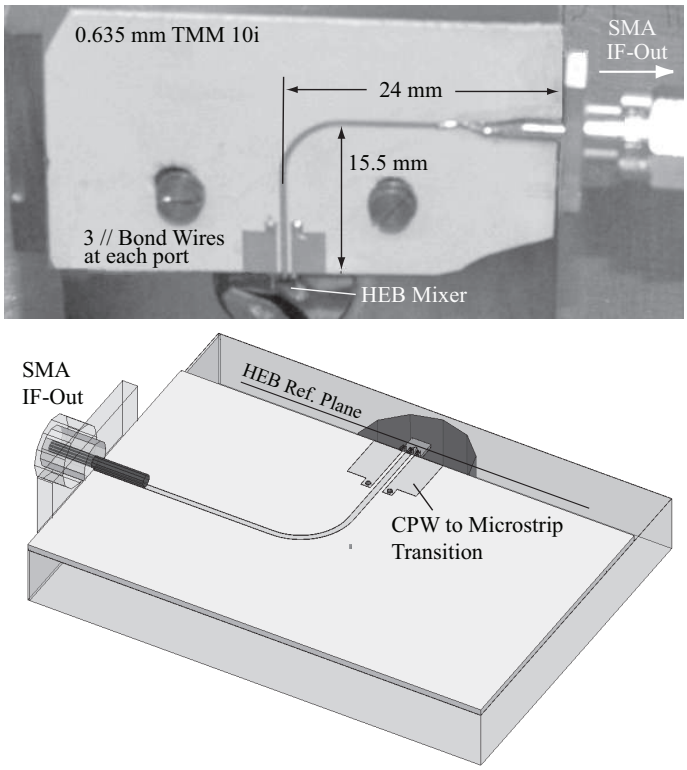

Figure 6.2: *Top*) Photograph of the IF board used in the experiment. The curved transmission line is 50 Ω. *Bottom*) 3D model used to deembed the measurements to the HEB mixer IF output port. For this HFSS [26] was employed, which provided a full 3D electromagnetic computation of the IF circuit board, and associated S-parameters.

film had a T_c of 9.5 K. After fabrication the critical temperature of the sub-micron area HEB lowered to 8.3 K. Details on the device's noise temperature, mixer gain as a function of bias, and R-T curve maybe found in a separate paper by Yang *et al*. [27]. To obtain the 1.3 THz [28] LO pumped HEB IF impedance the following procedure was used: At 4.2 K we measured the complex reflection coefficient of the mixer block IF output with a vector network analyzer (VNA). The output power of the VNA was -65 dBm, low enough not to disturb the HEB I/V curve. To improve the signal to noise, 64 measurements were averaged. Included in the VNA measurement is a bias-tee. As shown in Fig. 6.2 we used HFSS [26], a full three-dimensional (3D) finite element electromagnetic field simulator, to obtain a 2 port S-parameter model of the mixer block IF circuit, including wire bonds, via holes, and air space. Finally, to obtain the actual LO pumped HEB IF impedance, a linear circuit simulator [29] was employed to deembed the IF circuit from the VNA measurement. Further details on the calibration method may be found at [30]. Though not applied here, it is also possible to eliminate the need of a full deembedding of the HEB mixer IF circuitry by using the mixer itself as a calibration source. This can be achieved with the HEB

inside the cryostat. Here we use the HEB in its superconducting state as a short, and the HEB at 20 K as a load with known impedance. Measuring the full S11 reflection coefficient at both states enables a full calibration of the VNA, with the reference plane at the HEB bridge itself. This technique eliminates the need of a 3D electromagnetic simulation, facilitating experimental analysis.

6.4 IF impedance

In Fig. 6.3 we show the bias points at which reflection and mixer gain measurements in the experiment were obtained. The bias points are chosen strategically along three (over, optimal, and under-pumped) LO levels. The measured HEB IF impedance and mixer conversion were fitted against the model using Eqs. 6.6 – 6.11 to determine the IF impedance, and Eq. 6.16 to obtain the mixer gain (Sec. 6.5). It was found essential to use both the measured impedance and calibrated mixer gain data to obtain a self consistent fit for τ_{eph}, τ_{esc}, and the temperature dependent c_e/c_{ph} ratio.

Fig. 6.4 represents a subset of the data presented in Ref. [30]. We find that particularly in the under pumped LO situation, that the HEB IF impedance demonstrates large real and reactive components. It is here that the mean electron temperature is lowest. For all bias conditions [30] in the range 0 – 3 GHz, where the mixer gain is optimal, the real and imaginary components of the IF impedance are most dynamic, and a proper match to 50 Ohm is difficult. The reason for this behavior is that the effect of τ_1 and τ_3 in the time dependent electron temperature, $\Psi(\omega)$, is largest in this frequency range (see also Fig. 6.6). The electrothermal feedback, via voltage reflections of the HEB mixer, is therefore most pronounced in the IF region with optimal mixer gain.

The input parameters for the fit procedure, and resulting values for the fit pa-

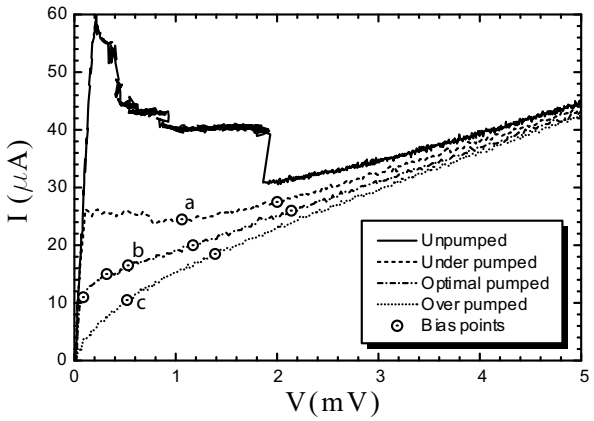

Figure 6.3: Unpumped, under pumped, optimal pumped, and over pumped I/V curves. Circles indicate the bias points where reflection and mixer gain measurements were obtained. a, b, and c refer to the impedances shown in Fig. 6.3.

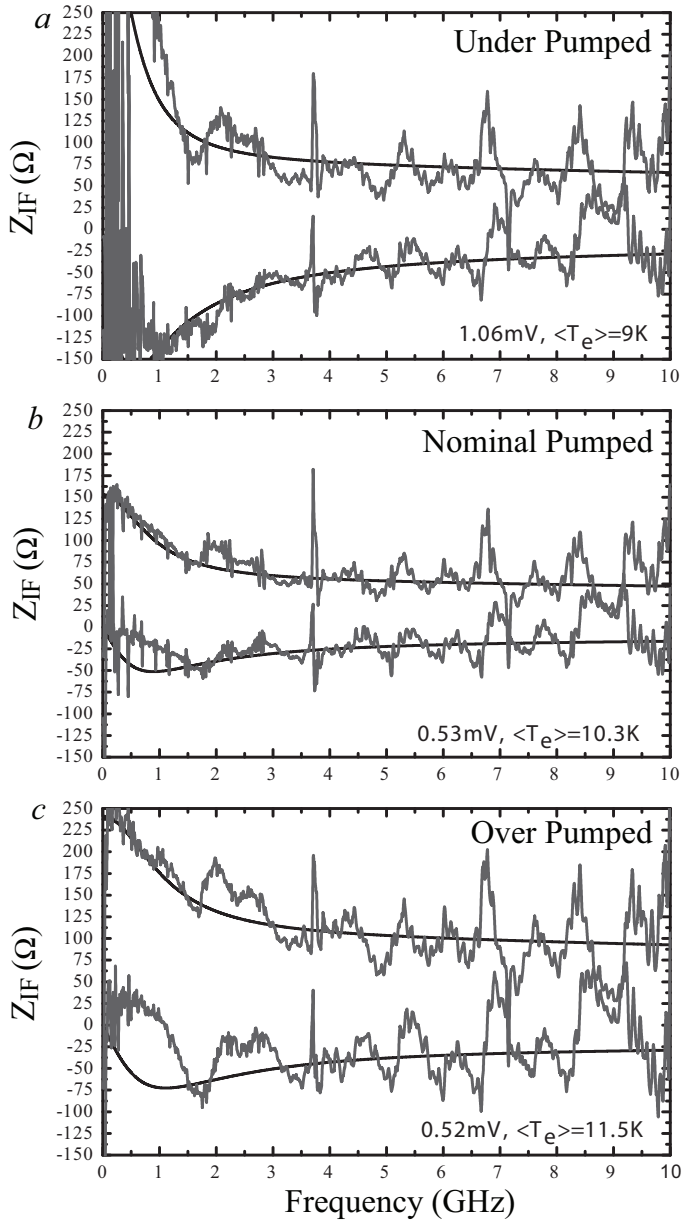

Figure 6.4: Measured and modeled IF impedance for a variety of bias and LO pump power conditions. The mean electron temperature is a fit parameter in the model and is found, consistent with theory, to increase with the LO pump level. Refer to Fig. 6.5 for related mixer gain and Table 6.1 & 6.2 for additional details.

rameters are shown in Table 6.1. They provide interesting statistics on the material

properties of the NbN film, and assumptions of the temperature dependence of τ_{eph}, and c_e/c_{ph} used in literature. For example, the mean escape time for phonons into the substrate is 64 ± 4.9 ps. Using the empirical relationship that $\langle\tau_{esc}\rangle \sim$ 10.5 d (ps/nm) [31] [32], we find a suggestive NbN film thickness of 6.1 ± 0.46 nm. This is supported by a recent study of the film by Transmission Electron Microscopy (TEM), in which the measured thickness is 6 ± 1 nm instead of the intended 3.5 nm thickness [33]. In addition, the temperature relationship of the electron-phonon interaction time, and the ratio of the electron-phonon heat capacities may, to a first order, be verified. Using the empirical relationships that for thin NbN films, $\tau_{eph} \approx 500\ T^{-1.6}$ (ps·K) [22] and $c_e/c_{ph} \approx 18.77\ T^{-2}$ [32], we obtain an estimate for the mean (or effective) electron temperature in the NbN bridge. The last two columns in Table 6.2 show the calculated results. The mean electron temperature, $\langle T_e\rangle = \langle T_e(eph) + T_e(c_e/c_{ph})\rangle$ is reported in Fig. 6.4, and shows a consistent trend with bias and LO pump level [10] [11].

6.5 Mixer conversion gain and the effect of electro-thermal feedback

To properly model the HEB mixer conversion gain, the effect of voltage reflections on the electron temperature and subsequent mixing efficiency ($\partial R/\partial T$) will need to be

Table 6.1: HEB Parameters for different bias conditions. Units of dV/dI, R_o, R_o^* are in Ω, τ_{esc} and τ_{eph} in ps, $T_e(eph)$ and $T_e(c_e/c_{ph})$ in Kelvin. Each row has three data sets $(Z_{re}, Z_{im}, G_{mix})$ which are used to obtain a self consistent set of fit values. The first three columns (dV/dI, R_o, C) are derived from the measured I/V curve. The three primary fit parameters are τ_{esc}, τ_{eph}, c_e/c_{ph}. These determine the electron temperature time dependence. For some bias and LO settings it was found that that the dc resistance at the operating point (R_o) and self heating parameter(C) needed adjustment. The modified values are depicted by R_o^* and C^*. Especially in the more extreme bias states did we find significant changes to R_o and C. This is likely due to the lumped element nature of the NSGR model, which does not completely account for all the dynamics inside the bridge area (Ref. [12]).

Vbias	dV/dI	R_o	C	R_o^*	C^*	τ_{esc}	τ_{eph}	c_e/c_{ph}
0.09mV Opt	42	7.5	0.69	10.0	0.55	45.8	15.8	0.24
0.32mV Opt	110	21.3	0.67	27.5	0.62	65.4	12.7	0.22
0.53mV Opt	167	31.2	0.68	37.0	0.61	72.0	12.3	0.18
1.17mV Opt	168	58.5	0.48	58.5	0.48	65.8	10.3	0.15
2.14mV Opt	169	82.3	0.34	82.3	0.34	58.4	7.3	0.10
20.0mV Opt	150	140	0.034	140	0.033	—	—	—
1.06mV Under	600	42.4	0.87	52.4	0.77	65.2	14.9	0.24
2.00mV Under	230	71.4	0.53	66.0	0.33	68.2	9.1	0.13
0.52mV Over	80	52.0	0.21	70.0	0.55	70.2	10.0	0.15
1.39mV Over	127	77.2	0.24	50.0	0.24	65.4	7.7	0.11

Table 6.2: Mixer Gain Parameters. χ describes the ratio of LO power to dc power heating efficiency. ν_{NSGR} is the modeled -3 dB gain bandwidth (GHz), and ν_{exp} the experimentally obtained -3 dB gain bandwidth. p_{lo} in nW, and the LO frequency 1.3 THz (Ref. [28]). $T_e(eph)$ and $T_e(c_e/c_{ph})$ are mean electron temperatures inferred from fit values of τ_{eph} and c_e/c_{ph} in Table 6.1, and the obtained temperature relationships from literature (Refs. [22], [31], and [32]).

Vbias	χ	ν_{NSGR}	ν_{exp}	p_{lo}	$T_e(eph)$	$T_e(c_e/c_{ph})$
0.09mV Opt	2.632	2.10	1.8	55	8.6	8.9
0.32mV Opt	1.632	1.95	2.0	55	9.9	9.3
0.53mV Opt	1.365	2.20	2.3	55	10.2	10.3
1.17mV Opt	1.118	3.00	3.2	55	11.3	11.4
2.14mV Opt	0.978	3.80	4.0	55	13.9	13.7
20.0mV Opt	—	—	—	—	—	—
1.06mV Under	1.114	2.40	2.4	29	9.0	8.9
2.00mV Under	0.854	3.15	3.4	29	12.2	12.3
0.52mV Over	2.623	2.95	3.0	72	11.5	11.4
1.39mV Over	1.379	3.00	3.3	72	13.5	13.4

taken into account. This is important as voltage reflections at the IF port cause, via a self heating electro-thermal feedback mechanism, fluctuations in the mixer gain.

From experience it is known that there are some discrepancies between measurement and theory with existing HEB mixers models. One of these is due to an over simplification of the IF impedance presented to the hot electron bolometer mixer [4] [5] [8] [10] [14]. In nearly all instances, the IF impedance used in the electro-thermal feedback formulism is assumed real. In actuality the IF impedance presented to the active device is both complex and frequency dependent. Because, as part of the deembedding exercise, an accurate 3D EM model [26] of the IF embedding circuit inclusive of discontinuities and wire bonds was developed, it can now also be used to accurately predict the IF impedance presented to the HEB mixer chip. With this information we can calculate Γ_{if} and $[R_o \cdot Z_L/(R_o + Z_L)^2]$ in Eq. 6.15. A second problem with the traditional (idealized) mixer gain calculations is that it does not include a mechanism to account for parasitic device reactance. These can, for example, be introduced in the HEB mixer stripline circuitry, contact pads, and capacitance across the bridge. It is however also possible that it is related to an incomplete model of the HEB mixer. Since parasitic device reactance is not taken into account in the "idealized" responsivity formulism of Eq. 6.12, it may be advisable to include them. We find experimentally that the addition of a 10 GHz ($\tau = 15.8\ ps$) fixed frequency pole to Eq. 6.15 helps to improve the high frequency accuracy of the modeled conversion gain. At low IF frequencies where the vast majority, if not all, of the HEBs operate the addition of an added pole to $\eta(\omega)$ and $Z(\omega)$ is of little consequence.

A final issue that needs addressing is the need for an efficiency factor. It is known, for example, that the hot electron bolometer mixer conversion gain and LO pumped I/V curves are RF frequency dependent. This is understood to be due to the heating

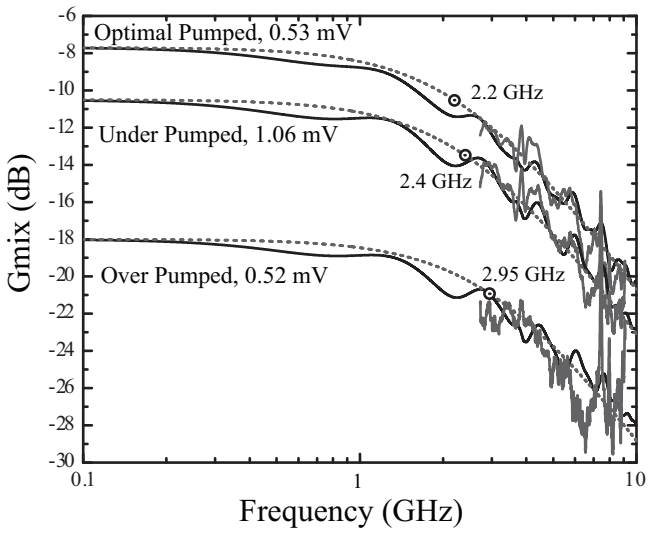

Figure 6.5: Measured and modeled HEB mixer conversion gain as a function of IF frequency for the three bias conditions in Fig. 6.4. The -3 dB gain roll-off shifts to higher frequency with increased LO power. This is understood to be caused by the increased mean electron temperature. The effect of electro-thermal feedback is taken into account by means of the (modeled) complex IF load impedance. Details in Table 6.1 & 6.2.

efficiency of the "hot" electrons, and the distributed temperature profile in the bridge (χ, Sec. 6.2). The HEB mixer gain modified for device parasitics and heating efficiency may thus be rewritten as

$$\eta(\omega) = \frac{2\alpha^2 p_{lo}}{\chi^2\ P_{dc}} \left| \frac{1}{(1+i\omega\tau_p)^2} \frac{R_o\ Z_L}{(R_o+Z_L)^2} \frac{C^2}{[\Psi(\omega)+\Gamma_{if}\ C]^2} \right|, \tag{6.16}$$

where $\tau_p \approx 15.8$ ps. Note that τ_p is device and application dependent. α, the optical coupling factor is estimated to be 0.66 (-1.8 dB). In Fig. 6.5 we show the measured and modeled mixer gain for three different bias and LO pump conditions. Fit parameters for the entire data set are shown in Table 6.1 & 6.2. Based on these results, Eq. 6.16 is seen to accurately describe both the amplitude and frequency dependence of the HEB mixer conversion gain.

Some observations can be made: First, to minimize receiver noise temperature modulation across the IF operating bandwidth, one has to carefully consider ways to minimize the complex part of Z_L at the superconducting bridge such that Γ_{if} is frequency independent. Secondly, setting $Z_L \approx R_o$ such that $\Gamma_{if} \rightarrow 0$ not only minimizes the frequency dependent modulation of $\eta(\omega)$, but also maximizes the mixer gain. To do so in practice, it is desirable to terminate the reflected noise wave by means of a balanced amplifier, or isolator between the mixer unit and the first low noise amplifier. It is also requires a good understanding of the IF circuit (matching network and bias tee) including wire bonds that connect the HEB mixer chip.

To better understand how the time dependent electron transfer function and the

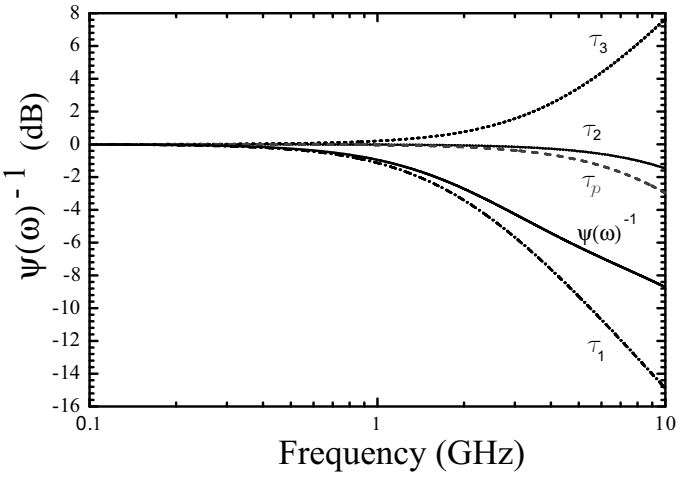

Figure 6.6: $\Psi(\omega)^{-1}$ (dB), the time dependent transfer function of the electron temperature at 0.53mV bias and optimal LO pump level. $\tau_1 = 87.1$ ps, which results in a pole at 1.83 GHz. $\tau_2 = 10.1$ ps with a pole at 15.8 GHz, and $\tau_3 = 35.0$ ps with a zero at 4.55 GHz. Also shown is τ_p which accounts for device parasitics. The poles and zero effectively synthesize a "single" 2.20 GHz pole. To increase the IF bandwidth, the time response of $\Psi(\omega)$ will need to be increased.

parasitic device capacitance determine the HEB gain bandwidth and overall slope, we plot in Fig. 6.6 $\Psi(\omega)^{-1}$, and the transfer functions $(1+i\omega\tau_1)^{-1}$, $(1+i\omega\tau_2)^{-1}$, $(1+i\omega\tau_3)$, and $(1+i\omega\tau_p)^{-1}$ at 0.53mV bias and optimal LO signal level. Here τ_3 (4.55 GHz) is seen to slightly compensate τ_1 (1.83 GHz), whereas τ_2 (15.8 GHz) enhances the effect of τ_1, though to a very small extent. Adding τ_p to take into account residual device parasitics, we effectively synthesize a 2.20 GHz pole in $\eta(\omega)$ as indicated in Eqn. 6.16. This is also depicted by ν_{NSGR} in Table 6.2. As may be seen from Table 6.2, the IF bandwidth is bias and LO power dependent. By biasing the HEB mixer at a higher bias voltage (electron temperature), IF bandwidth and conversion efficiency may to some extent be traded off. This effect is in good agreement with results from literature [4] [6] [34] [35].

6.6 Increasing the IF bandwidth of hot electron bolometers

For many radio-astronomy and atmospheric science applications, the 2 – 3 GHz IF bandwidth reported here would be too small. Since $\Psi(\omega)^{-2} \propto \eta(\omega)$, it is meaningful to study the time dependent electron temperature to gain insight into ways in which the HEB mixer IF bandwidth may be enhanced. A close inspection of Eqs. 6.10 & 6.11, as shown in Fig. 6.7, indicates that a rise in the electron and phonon temperature results in a faster response time, and therefore an improved gain bandwidth. The physical explanation is that with increasing temperature the phonon specific heat (c_{ph}) increases faster than the electron specific heat (c_e). Phonons are thus seen to

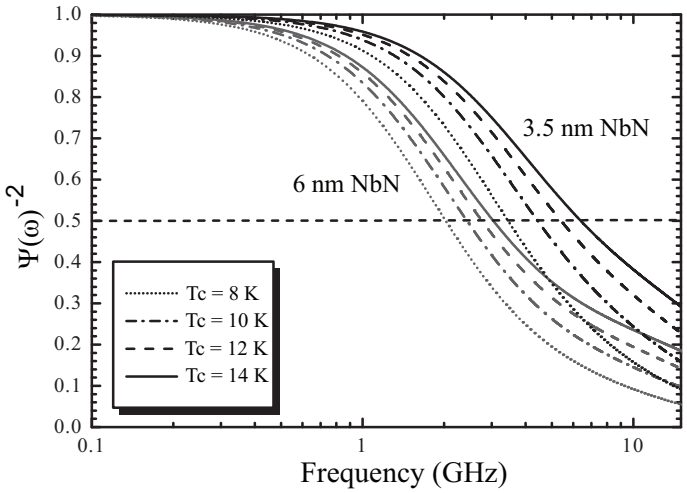

Figure 6.7: $\Psi(\omega)^{-2}$ as a function of IF frequency for a 3.5 nm and 6 nm thickness NbN film of different T_c. $\Psi(\omega)^{-2}$ can be interpreted as the relative conversion gain without the effect of electro-thermal feedback. For an optimized NbN mixer the maximum gain bandwidth is projected to be on the order of 5.5 – 6 GHz.

act as an important intermediate heat bath between the electron gas and substrate. Note that for thinner films this effect is enhanced. Because thin films of NbN can have different critical temperatures depending on deposition conditions and thickness, it is important that both the critical temperature and thickness of the film be optimized. As a colorrary, use of higher T_c materials with strong electron-phonon interaction and a short phonon escape time should also be of benefit. Thus by reducing the film thickness one can increase the IF bandwidth, while for a given thickness an increased T_c will also result in an increased bandwidth (Fig. 6.7).

The temperature dependence in Fig. 6.7 is derived under the assumption that $T_e \sim T_{ph}$. To estimate the difference between T_e and T_{ph} for actual operating conditions, T_e and T_{ph} were calculated, using Eqs. 6.1 & 6.2. Under these conditions T_{ph} is approximately 0.8 T_e, which in view of the small difference, suggests that the Perrin-Vanneste two temperature model is applicable to the hot electron bolometers under discussion. In the case of the homogeneous model, the T_c of the film is thus found to be a measure of the electron temperature. However there is a distributed temperature profile [10]- [12] in HEB mixers, which inevitably leads to deviations from the uniform temperature calculations of Perrin-Vanneste. The temperature in the center of the HEB bridge, depending on for example the interface transparency of the contacts and the operating condition, can in general exceed the critical temperature of the film (Table 6.1). It may therefore be argued that the IF bandwidth follows the T_c dependence as shown in Fig. 6.7, with possibly an enhanced bandwidth as a result of higher electron temperature due to device size, interface contact transparency, high bias, or over-pumped LO. The by the co-authors reported IF bandwidth measurement of 6 GHz [34] was performed on a much larger area device (4 x 0.4 μm),

with clean contacts that are not necessarily the same as the device under discussion. Although not fully understood, the result remains within the theoretical possibly of the presented analysis.

6.7 Conclusion

A deembedding technique is demonstrated to obtain the IF impedance of a small area ($0.15\ \mu\text{m}^2$) phonon cooled HEB under a variety of bias and LO pump level conditions. In the same setup the HEB mixer conversion gain has, at an LO frequency of 1.3 THz, been measured in a 2.5 – 9 GHz IF bandwidth.

To understand the observations, we have successfully modeled the HEB IF impedance and mixer conversion gain based on a two-temperature electron cooling model first introduced by Perrin-Vanneste, and expanded upon by Nebosis *et al*. Good agreement in both amplitude and frequency between model and theory is obtained, and we are able to extract from the NSGR model values for the electron-phonon interaction time τ_{eph}, the phonon escape time τ_{esc}, and the ratio of the electron and phonon specific heat capacity c_e/c_{ph}. Indirectly, using published temperature and thickness relationships for NbN, we are able to infer the effective electron temperature of the bridge as a function of bias, LO pump level, and the thickness of the NbN film (6 nm for the device in this experiment). As the electron temperature of the bridge varies, the electron transfer time changes, influencing the IF impedance and mixer gain bandwidth. Because the phonon and electron heat capacity ratio for NbN is a strong function of temperature, it is found that along with a reduction in film thickness it is also important to maximize the critical temperature of the film. Using NSGR model we are able to infer a maximum achievable IF bandwidth of NbN film HEBs of $\sim 5.5 - 6$ GHz.

Finally, by using the complex IF impedance presented to the HEB chip we are able to demonstrate the effect of electro-thermal feedback on the mixer gain. Flat mixer gain (receiver noise temperature) within IF band may only be achieved if the variance of the complex load impedance presented to the HEB mixing chip is small in comparison to the hot electron bolometer dc resistance at its operating point. Mixer gain is maximized when both the load impedance presented to the HEB device is real, close to the dc resistance of the device, and the power exchange function χ close to unity. Thus, using the modified NSGR model with a knowledge of the IF load impedance presented to the HEB mixer and a measured (LO pumped) I/V curve, expressions for the impedance and mixer gain of thin NbN films may now be derived.

Bibliography

[1] T.G. Phillips and K.B. Jefferts, "A cryogenic bolometer heterodyne receiver for millimeter wave astronomy", "*Review of Sci. Instrumentation*, Vol 44, 1009, (1973).

[2] S. Cherednichenko, P. Yagoubov, K. Il'in, G. Gol'tsman and E. Gershenzon, "Large bandwidth of NbN phonon cooled hot-electron bolometer mixers on sapphire substrates", *Proc. 8^{th} Int. Symp. on Space Terahertz Technology*, Cambridge, MA, (1997), p. 245.

[3] P. Yagoubov, G. Gol'tsman, B. Voronov, L. Seidman, V. Siomash, S. Cherednichenko, and E. Gershenzon, "The bandwidth of HEB mixers employing ultra thin NbN films on sapphire substate", "*Proc. 7^{th} Int. Symposium on Space Terahertz technology*, Charlottesville, VA, (1996), pp. 290-302.

[4] H. Ekström, E. Kollberg, P. Yagoubov, G. Gol'tsman, and E. Gerhenzon, "Gain and noise bandwidth of NbN hot-electron bolometric mixers" *Appl. Phys. Lett.*, Vol. 70 (24), pp. 3296-3298, 16 June (1997).

[5] F. Rodriques-Morales and K.S. Yngvesson, "Impedance and bandwidth characterization of NbN hot electron bolometric mixers", *Proc. 14^{th} Int. Symp. on Space Terahertz Tech.*, UAz, (2003).

[6] B. Karasik and W. McGrath, "Microwave transmission technique for accurate impedance characterization of superconducting bolometer mixers", *Infrared and Millimeter Waves*, Vol. 20, No. 1, (1999).

[7] D. E. Prober, *Appl. Phys. Lett.*, Vol. 62, 2119 (1993).

[8] B.S. Karasik and I. Elant'ev, "Noise temperature limit of a superconducting hot-electron bolometer mixer", *Appl. Phys. Lett.*, Vol. 68, 853 (1996).

[9] D. Wilms Floet, E. Miedema, T. M. Klapwijk, and J. R. Gao, *Appl. Phys. Lett.*, Vol. 74, 433 (1999).

[10] H. F. Merkel, P. Khosropanah, D. W. Floet, P. A. Yagoubov, and E. L. Kollberg, "Conversion gain and fluctuation noise of phonon-cooled hot-electron Bolometers in hot-spot regime", *IEEE Trans. Microwave Theory and Techniques*, Vol. 48, No. 4, 690, April (2000).

[11] T. M. Klapwijk, R. Barends, J. R. Gao, M. Hajenius, and J. J. A. Baselmans, Proc. SPIE 5498, p. 129 (2004).

[12] R. Barends, M. Hajenius, J.R. Gao, and T.M. Klapwijk, Current-Induced Vortex Unbinding in Bolometer Mixers *Appl. Phys. Lett*, Vol. 87, (2005).

[13] N. Perrin and C. Vanneste, "Dynamic behavior of a superconductor under time dependent external excitation", *J. Physique.*, Vol. 48, 1311 (1987).

[14] R. S. Nebosis, A. D. Semenov, Yu. P. Gousev, and K. F. Renk, "Rigorous Analysis of a Superconducting Hot-Electron Bolometer Mixer: Theory and Comparison with Experiment", "*Proc. 7th Int. Symp. on Space Terahertz Tech.*, Charlottesville, VA, (1996), pp. 601-613.

[15] C. M. Knoedler and R. F. Voss, "Voltage noise measurement of the vortex mean free path in superconducting granular tin films", *Physical Review B*, Vol. 26, No. 1, 449-451, July (1982).

[16] E. M. Gershenson, G. N. Gol'tsman, I. G. Gogidze, Yu, P. Gousev, A. I. Elant'ev, B.S. Karasik, and A. D. Semenov, *Sov. Phys. Superconductivity*, Vol. 3, 1582 (1990).

[17] B.S. Karasik and I. Elant'ev, *Proc. 6th Int. Symp. on Space Terahertz Technology*, Caltech, Pasadena, Ca, (1995), p. 229.

[18] E. M. Gershenson, G. N. Gol'tsman, A. I. Elant'ev, B.S. Karasik, and S. E. Potoskuev, *Sov. J. Low Temp.*, Vol. 14, 414 (1988).

[19] H. Ekström, B. Karasik, E. Kollberg, and K. Yngvesson, "Conversion gain and noise of niobium superconducting hot-electron mixers", *IEEE trans Microwave Theory and Techniques*, Vol.43, pp. 938, (1995).

[20] P. J. Burke, R. J. Schoelkopf, and D. E. Prober, "Mixing and Noise in diffusion and phonon cooled superconducting hot-electron bolometers", *J. Appl. Phys.*, Vol 85, No. 3, Feb. (1999).

[21] D. F. Fillipovic, S. S. Gearhart, and G. M. Rebeiz, *IEEE Transactions on Microwave Theory and Techniques*, Vol. 41, pp. 1738, (1993).

[22] Yu. P. Gousev, G. N. Gol'tsman, A. D. Semenov, E. M. Gershenzon, R. S. Nebosis, M. A. Heusinger, and K. F. Renk, "Broadband ultra fast superconducting NbN detector for electromagnetic radiation", *J. Appl. Phys.* Vol. 75, 3695 (1994).

[23] J.J.A. Baselmans, A. Baryshev, S.F. Reker, M. Hajenius, J.R. Gao, T.M. Klapwijk, Yu. Vachtomin, S. Maslennikov, S. Antipov, B. Voronov, and G. Gol'tsman. "Direct detection effect in small volume hot electron bolometer mixers", *Appl. Phys. Lett.*, Vol. 86, 163503 (2005).

[24] M. Hajenius, J. J. A. Baselmans, A. Baryshev, J. R. Gao, T. M. Klapwijk, J. W. Kooi, W. Jellema, and Z. Q. Yang. "Full characterization and analysis of a THz heterodyne receiver based on a NbN hot electron bolometer", *J. Appl. Phys.,* Vol. 100, 074507 (2006).

[25] In ref. [24] it was found that the isothermal technique is an adequate method of estimating the LO power needed to pump a HEB mixer. It was also found that designing an optical coupling scheme that is capable of matching the highly divergent beam from the Silicon lens antenna with more than 50% of efficiency is challenging.

[26] Ansoft Corporation, Pittsburgh, PA 15219, USA.

[27] Z. Q. Yang, M. Hajenius, J. J. A. Baselmans, J. R. Gao, B. Voronov, and G. Gol'tsman, "Reduced noise in NbN hot electron bolometer mixers by annealing", *Supercond. Sci. Technol.*, Vol. 19, L9-L12 Rapid Com, (2006).

[28] Virginia Diodes, Inc., Charlottesville, VA 22902-6172, USA.

[29] Microwave office, Applied Wave Research Inc. El Segundo, CA 90245, USA.

[30] J. W. Kooi, J. J. A. Baselmans, J. R. Gao, T. M. Klapwijk, M. Hajenius, P. Dieleman, A. Baryshev, and G. de Lange, "IF Impedance and Mixer Gain of NbN Hot-Electron Bolometers", *Journal of Applied Physics*, Vol. 101, 044511, Feb. (2007).

[31] S.B. Kaplan, *J. Low Temp. Phys.*, Vol. 37, 343(1979).

[32] A. D. Semenov, R. S. Nebosis, Yu. P. Gousev, M. A. Heusinger, and K. F. Renk, "Analysis of the nonequilibrium photoresponse of superconducting films to pulsed radiation by use of a two-temperature model", *Phys. Rev. B*, Vol. 52, pp. 581 (1995).

[33] J. R. Gao, M. Hajenius, F. D. Tichelaar, B. Voronov, E. Grishina, T. M. Klapwijk, G. Gol'tsman, and C. A. Zorman, "Can NbN films on 3C-SiC/Si change the IF bandwidth of hot electron bolometer mixers?", *Proc. 17^{th} International Symposium on Space Terahertz Technology*, 10-12 May, Paris, France, (2006).

[34] J.J.A. Baselmans, J M.Hajenius, R. Gao, T.M. Klapwijk, P.A.J. de Korte, B. Voronov, G. Gol'tsman, "Doubling of sensitivity and bandwidth in phonon cooled hot electron bolometer mixers" *Appl. Phys. Lett.*, Vol. 84, 1958, (2004).

[35] K. V. Smirnov, Yu. B. Vachtomin, S. V. Antipov, S. N. Masalennikov, N. S. Kaurova, V. N. Drakinsky, B. M. Voronov, G. N. Gol'tsman, "Noise and gain performance of spiral antenna coupled HEB mixers at 0.7 THz and 2.5 THz", *Proc. 14^{th} Int. Symp. on Space Terahertz Technology*, UAz, (2003).

Chapter 7

A 275–425 GHz tunerless waveguide receiver based on AlN SIS technology*

Abstract - We report on a 275 – 425 GHz tunerless waveguide receiver with a 3.5 – 8 GHz intermediate frequency (IF). As mixing element, we employ a high-current-density Nb-AlN-Nb superconducting-insulating-superconducting (SIS) tunnel junction. Thanks to the combined use of AlN-barrier SIS technology and a broad bandwidth waveguide to thin-film microstrip transition, we are able to achieve an unprecedented 43 % instantaneous bandwidth, limited by the receiver's corrugated feedhorn.

The measured double-sideband (DSB) receiver noise temperature, uncorrected for optics loss, ranges from 55 K at 275 GHz, 48 K at 345 GHz, to 72 K at 425 GHz. In this frequency range the mixer has a DSB conversion loss of 2.3 ± 1 dB. The intrinsic mixer noise is found to vary between 17 – 19 K, of which 9 K is attributed to shot noise associated with leakage current below the gap. To improve reliability, the IF circuit and bias injection are entirely planar by design. The instrument was successfully installed at the Caltech Submillimeter Observatory (CSO), Mauna Kea, HI, in October 2006.

*This Chapter is published as J. W. Kooi, A. Kovács, M. C. Sumner, G. Chattopadhyay, R. Ceria, D. Miller, B. Bumble, R. LeDuc, J. A. Stern, and T. G. Phillips, in the *IEEE Trans. Microwave Theory and Techniques*, Vol. 55, No. 10, pp. 2086-2096, Oct. (2007).

7.1 Introduction

All the pre-existing Superconducting-Insulating-Superconducting (SIS) waveguide receivers at the Caltech Submillimeter Observatory (CSO), Mauna Kea, HI, use waveguide tuners to achieve sensitivities a few times the quantum noise limit. Each of these receivers has played a pioneering role in the submillimeter field. However modern astronomy is demanding more capability in terms of sensitivity, bandwidth, stability, frequency agility, and ease of use. To facilitate these requirements, technological advances of the past decade have enabled receiver designers to construct tunerless receivers with expanded IF bandwidths at sensitivities a few times the quantum noise limit. Although different in detail and configuration, advanced receiver designs now feature prominently in, for example, the Heterodyne Instrument for the Far-Infrared (HIFI) on the Herschel satellite [1], ALMA [2], the Plateau de Bure interferometer (IRAM) [3], the Atacama pathfinder experiment (APEX) [4], TELIS [5], and the Harvard-Smithsonian Submillimeter Array (SMA) [6].

To upgrade the heterodyne facility instrumentation at the CSO, four tunerless balanced-input waveguide receivers have been designed to cover the 180 – 720 GHz frequency range [7, 8]. These receivers will allow dual-frequency (two-color) observations in the 230/460 GHz and 345/660 GHz atmospheric windows. The IF bandwidth of the CSO receivers will increase from the current 1 GHz to 4 GHz, though in principle 12 GHz is possible. For spectroscopic studies of distant galaxies, a complementary two-channel 275 – 425 GHz balanced continuous-comparison (correlation) receiver [9] is also under construction. Balanced configurations were chosen for their inherent local oscillator (LO) amplitude noise cancellation properties, facilitating the use of synthesizer-driven LO chains. Unique to the CSO, broad RF bandwidth is favored, allowing the same science to be done with fewer instruments. To maximize the RF bandwidth, we explore the use of high-current-density AlN-barrier SIS technology in combination with a broad bandwidth full-height waveguide to thin-film microstrip transition. Additional advantages of AlN tunnel barriers, in comparison to AlO_x-barriers, are enhanced chemical robustness and a low ωRC product (increased RF bandwidth). Even if optimal RF bandwidth is not a requirement, a low ωRC product provides a more homogeneous frequency response and increased tolerance to errors in device fabrication.

To validate the many technologies used in the design process, we have constructed a technology demonstration receiver ("Trex") to cover the important 275 – 425 GHz atmospheric windows. The design principles laid out in this paper are directly applicable to the entire set of new CSO receivers. The receiver offers a 43 % RF bandwidth, nearly 50 % wider than the ALMA band 7 275 – 373 GHz specification [10], and limited to a large extent by the corrugated feedhorn characteristics.

7.2 Instrument design

7.2.1 Broad bandwidth waveguide–to–microstrip Transition

Traditionally the majority of SIS and HEB waveguide mixers employ planar probes that extend all the way across the waveguide [11]- [15]. An important reason for the popularity of this design is the convenience with which the active device can be biased and the IF signal extracted. Unfortunately, the "double-sided" (balanced) probe exhibits a rather poor RF bandwidth ($\leq$ 15 %), when constructed in full-height waveguide. When the height of the waveguide is reduced by 50 %, the probe's fractional bandwidth improves dramatically to a maximum of about 33 %. These results can be understood in that the popular double-sided probe is essentially a planar variation of the well known Eisenhart and Khan waveguide probe [16]. Borrowing from Withington and Yassin's assessment [17], the real part of the probe's input impedance is influenced in a complex way by the parallel sum of individual non-propagating modal impedances, and as such, is frequency dependent. By lowering the height of the waveguide, the effect of non-propagating modes may be reduced [18]- [21].

An alternative approach is to use an asymmetric probe that does not extend all the way across the waveguide. For this kind of probe, the modal impedances add in series. The real part of the input impedance depends only on the single propagating mode

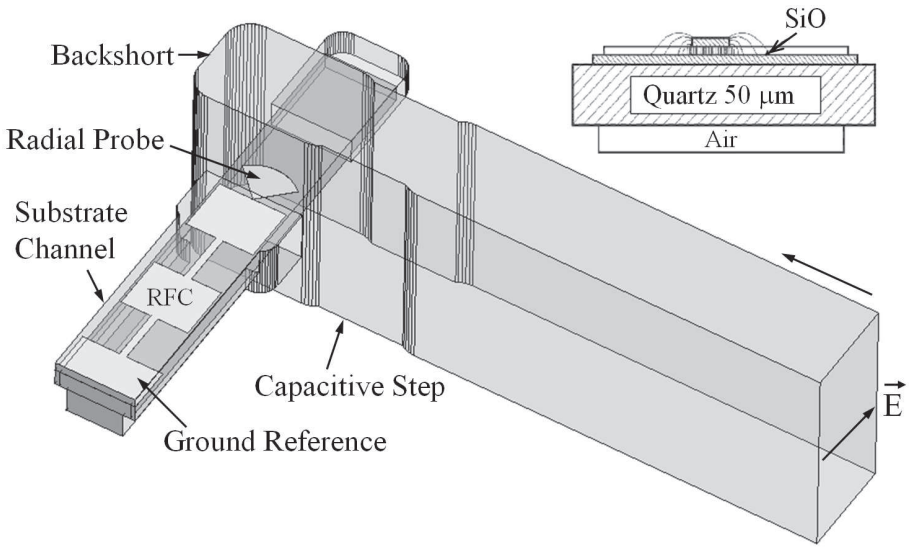

Figure 7.1: Isometric view of the waveguide transition. The 90° radial probe couples very efficiently to the fundamental TE_{10} waveguide mode. It is important to have the probe situated on a suspended dielectric as this maximizes the width of the substrate and makes room for the radial fan. Widening of the substrate channel around the first section of the RF choke serves to reduce the imaginary component of the probe impedance. To help reduce the probe's input return loss and increase the RF bandwidth even further, the addition of a small capacitive waveguide tuning step in front of the radial probe is found useful. Dimensions are provided in Table 7.1.

Table 7.1: Parameters used for the 270 – 430 GHz Design

Substrate material	quartz
Waveguide size (μm)	580 x 270
Probe radius (μm)	112
Substrate width (μm)	200
Substrate thickness (μm)	50
Air height above substrate (μm)	25
Air height below substrate (μm)	50
Backshort-substrate distance (μm)	103
Backshort radius (μm)	70
Probe impedance (Ω)	47 + i3

and is relatively frequency independent. These probes are typically implemented in full-height waveguide, which minimizes conduction loss and reduces the complexity of fabrication. A rectangular version of the "one-sided" probe has been used quite extensively by microwave engineers [22, 23], was introduced to the submillimeter community by Kerr *et al.* [24] in 1990, and is currently part of the baseline design for ALMA band 3 and 6 [25, 26]. The radial probe described here represents an attempt to extend the use of radial modes to the waveguide coupling problem [27]. From a practical point of view, the radial probe can be quite naturally made to feed a thin-film microstrip or co-planar wave (CPW) line that has a small line width and thin insulator [28, 29].

If very broad-band operation is desired, a further improvement in the probe's performance can be achieved by adding a simple capacitive waveguide tuning step in front of the probe (Fig. 7.1). Typically, a 15 % reduction in waveguide height is adequate to tune out most of the probe's residual reactance. The length of the step is on the order of the waveguide height dimension. Because some of the reactance in the probe is tuned out by the step, the distance between the substrate and backshort must be increased by 1.5 – 2.0 % λ_g. This increase in distance represents an added advantage to using a waveguide step, as it reduces machining difficulty. Fig. 7.2 depicts the radial probe input return loss and impedance locus.

To simplify the way the IF signal is extracted, it is possible to go across the waveguide with an inductive quarter-wavelength meandering transmission line [30]-[32]. In this case, care must be taken not to excite modes that result in high-Q resonances in the probe's passband. Through extensive simulations [33], we find that going across the waveguide in this manner reduces symmetrically the transition bandwidth by ~ 7 %, which is likely to be acceptable for many applications. To match the very large instantaneous RF bandwidth afforded by an AlN-barrier twin-junction SIS matching circuit, we have opted in our design for the 100 % asymmetric radial probe.

7.2.2 New set of SIS junctions

Circuit design of the high-current-density niobium SIS junctions (four frequency bands) was done at Caltech with fabrication at JPL.

The new SIS tunnel junctions all share the same 50 μm thick quartz wafer. The design employs twin SIS junctions [34] with AlN-barriers and a current density of 25 kA/cm^2. In our design we have used Supermix [35, 36], a flexible software library for high-frequency harmonic-balanced mixer and superconducting circuit simulation, in combination with extensive 2D and 3D EM-field analysis of the RF and IF embedding circuitry [33], [37]. Based on extensive simulation, the twin-junction RF matching network was found to exhibit a slightly larger RF bandwidth than the more common single-junction RF matching network [38, 39]. The AlN-barrier SIS junction $[R_nC]^{-1}$ product is 164 GHz, similar to the bandwidth afforded by the thin-film waveguide transition, and high enough to avoid the Body-Fano bandwidth limitation. As part of the AlN-barrier characterization process at JPL, the specific junction capacitance is estimated 80 fF/μm^2. To minimize saturation ($\delta V_{sis} \propto [P_{sig}R_n]^{0.5}$), while maintaining reasonably sized junction areas, we decided on a 5.4 Ω twin junction normal state resistance. The calculated bias voltage variation (δV_{sis}) between 0 K and 300 K loads is 80 μV rms, assuming a 160 GHz RF noise bandwidth. From the curvature of the measured total-power response we estimate the saturation ≤ 1 %.

Matching to an intermediate IF impedance of 20 Ω is realized on-chip (Fig. 7.3). The choice of this impedance is dictated by the limited available real estate, and the need to minimize gain compression [40]. To transform the 20 Ω mixer-chip IF output impedance to a 50 Ω load, an external matching network/bias tee is employed

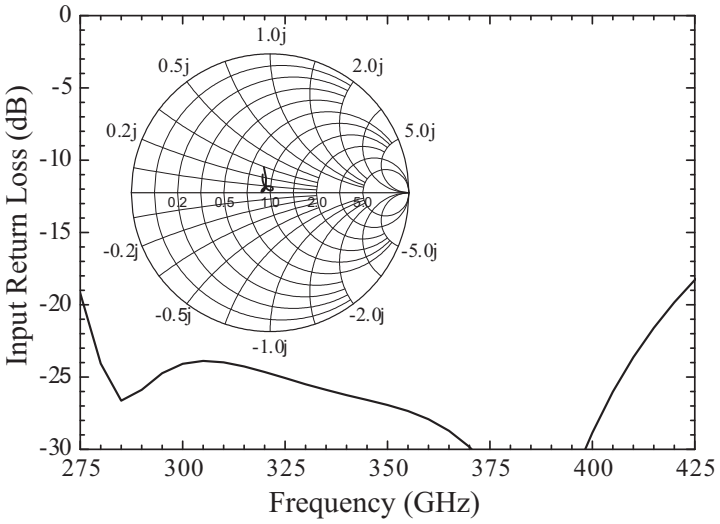

Figure 7.2: Input return loss of the fixed tuned full-height waveguide transition. The fractional bandwidth of the 350 GHz full-height waveguide radial probe is $\approx$ 45 %, 95 % of a standard TE_{10} fundamental waveguide band. The impedance locus of the probe is 47 + i3 Ω.

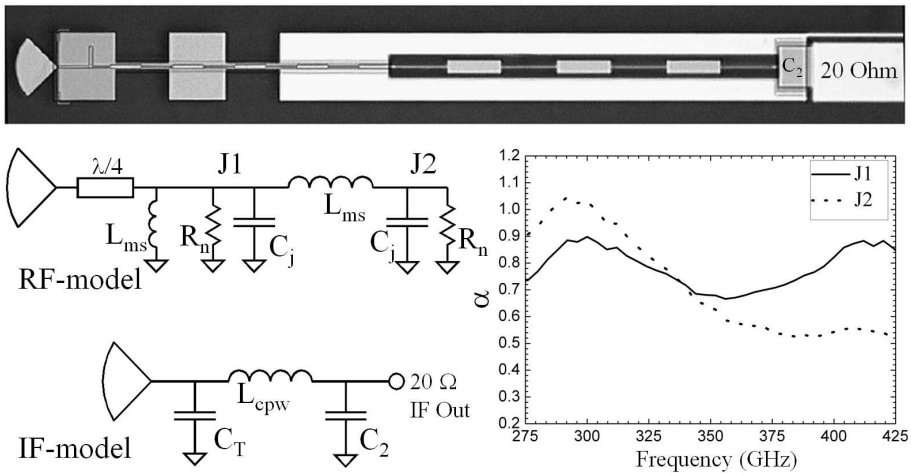

Figure 7.3: 350 GHz junction layout and simulated LO pumping parameter α. The radial probe antenna is visible on the left side. The IF signal is taken out via a microstrip RF choke (on 300 nm SiO, ε_r=5.6) that connects to a high impedance CPW transmission line (inductive) and integrated shunt capacitor (C_2). This L–C mechanism provides a π tuning network with the combined capacitance of the probe, twin-junction RF tuning structure, and microstrip RF matching network (C_T). The passband is optimized to cover 1 – 13 GHz. To minimize gain compression, the integrated shunt capacitor also serves to terminate out-of-band broadband noise. The IF impedance presented to the twin SIS junctions is 14 Ω, $\sim$ 2.7 R_n.

(Sec. 7.2.5). The mixer design has been optimized for minimum noise temperature and optimal conversion gain from 275 – 425 GHz, while simultaneously regulating the RF and IF input return loss to $\geq$ 8 dB. The latter is important as reflections from the RF or IF port can lead to mixer instability (Sec. 7.3.4). In Fig. 7.4, we show a photograph of the mixer chip positioned in the waveguide. Short parallel wire bonds provide the ground contact.

The tunnel junction under discussion is from batch B030926. It has a measured R_nA product of 7.6 $\Omega\mu m^2$, a junction area of 1 x 0.7 μm^2, R_{sg}/R_n ratio of 13.8 at 2.0 mV bias, and a 5.32 Ω normal-state resistance. At the CSO, on top of Mauna Kea, a lower LHe bath temperature (3.67 K) results in a subgap leakage current reduction of 10 % (R_{sg}/R_n = 15). For the two successful batches produced by JPL, the specifications are shown in Table 7.2.

7.2.3 Nb/AlN$_x$-Al/Nb junction fabrication

Devices are fabricated on z-cut crystalline-quartz wafers 250 μm thick, 76 mm in diameter, and polished on both sides. Magnetron sputter deposition and room-temperature nitride growth is done in-situ. For this we use a load-locked ultra-high vacuum system with a typical base pressure of 2 x 10^{-7} Pa. The trilayer is deposited by a lift-off process employing a multi-layer photolithographic technique using PMMA under AZ5214 photoresist. Optical lithography is accomplished by means of a GCA model 6300 i-line (365 nm) wafer stepper / aligner tool. The resulting undercut structure allows for

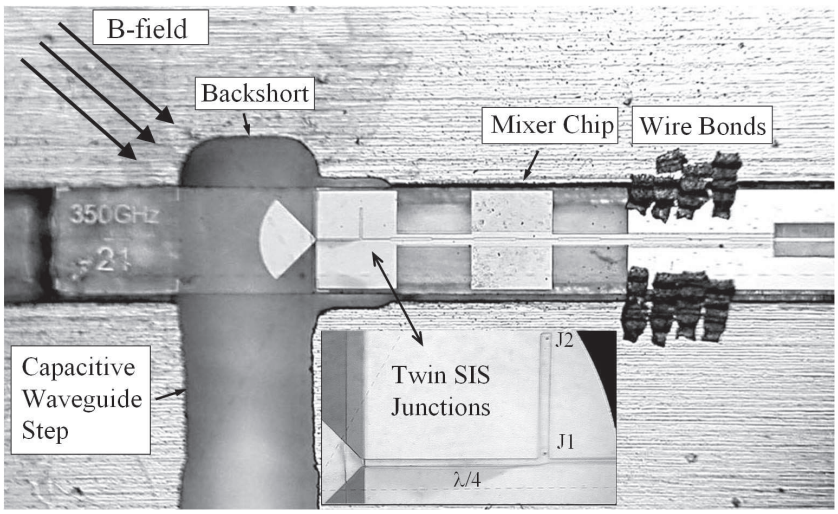

Figure 7.4: The 350 GHz mixer chip mounted in the IF channel with the radial probe extruding into the waveguide. Note the capacitive waveguide step directly in front of the probe. Wirebonds are used to provide the ground reference.

clean lift-off of the sputtered films. This step forms the ground plane structure with layers of 180 nm Nb base, 6 nm Al, AlN_x, and 80 nm Nb counter-electrode. AlN_x barrier formation is done with a pure N_2 low-pressure plasma. The substrate is held at ground potential and an opposing electrode is driven by a 13.5 MHz source to create the N_2 plasma. A rectangular junction mesa, the smallest being 1.0 μm x 0.5 μm in area, is defined by direct-write-electron-beam lithography in a 100 nm thick PMMA stencil. Chromium is deposited through the PMMA stencil and serves as an etch mask over 500 nm of polyamide. Contact regions of the trilayer are then protected by adding a photoresist stencil. The combined chromium + photoresist/polyamide

Table 7.2: Device Parameters

Parameter	**B030925**	**B030926**	**Specification**
R_n (Ω)	11.8	10.9	10.9 ± 15 %
C_s (fF/μm^2)	80	80	± 10 %
Area (μm^2)	0.7	0.7	1 x 0.7 ± 15 %
R_nA ($\Omega\mu$m^2)	8.28	7.63	7.6 ± 15 %
R_{sg}/R_n	9-11	10-12	15
Vgap (mV)	2.55-2.60	2.68-2.75	2.90
Nb Top (nm)	420	420	400 ± 20 %
SiO (nm)	320	320	300 ± 15 %
Nb Bottom (nm)	210	210	200 ± 20 %

structure is etched using an oxygen reactive ion etch (RIE). The polyamide remaining defines an isolation window and junction mesa for subsequent Nb RIE. To achieve Nb etch directionality, we utilize a gas mixture of 62 % CCl_2F_2 + 31 % CF_4 + 7 % O_2.

Electrical isolation of the base electrode from the microstrip wire layer is provided by thermal evaporation of 300 nm of SiO. Samples are rotated at a slight tilt angle during SiO deposition to assure good isolation and self-aligned lift-off with the polyamide. Lift-off is then accomplished by dissolving the polyamide in resist stripper containing NMP.

The waveguide probe and wire layer is formed by a blanket deposition of 400 nm Nb. RIE etching with an OiR620 photoresist stencil defines this pattern. Gold contacts are patterned by lift-off of films done by evaporation. As a final step, the substrates are diced into near cm^2 size chips and diagnostic sites are tested. The thick chips were lapped by Ron Kehl Engineering [41], down to 50 μm thickness, with the individual mixer elements diced out at JPL using a Disco saw and diamond/Ni blade.

7.2.4 Multiple Andreev Reflection (MAR)

It is found, not surprisingly, that high-current-density (J_c) AlN-barrier tunnel junctions exhibit a larger leakage current than commonly used lower-J_c AlO_x tunnel junctions (R_{sg}/R_n ratios of 10–14 vs. 20–35). To investigate the contribution of the higher subgap leakage to the intrinsic mixer noise, we apply a technique described by Dieleman *et al.* [42]. In that analysis, the noise spectral density below the energy gap is modeled by summing the thermalized single-electron tunnel current (I_{tun}) with a charged quantum transport current (I_{mar}) that results from MAR through pinholes in the barrier. We find that

$$S_I(V) = 2eI_{tun} + 2q(V)I_{mar}, \quad q(V) = (1 + 2\Delta/eV), \tag{7.1}$$

with $2\Delta/e = 2.75$ mV for our AlN junctions. Rearranging Eq. 7.1 by defining r=I_{tun}/I with I=(I_{tun}+I_{mar}) gives

$$S_I(V) = 2eI\left[1 + \frac{2\Delta}{eV}(1 - r)\right]. \tag{7.2}$$

The noise contribution of the junction to the IF output is then given by

$$P_{IF} = G_{IF}B\left[\frac{S_I(V)R_d}{4}(1 - \Gamma_{IF}^2)\right], \tag{7.3}$$

where

$$\Gamma_{IF} = \frac{R_d - Z_0}{R_d + Z_0} \tag{7.4}$$

G_{IF} is the IF gain, B the IF bandwidth, R_d the differential resistance obtained from the measured unpumped I/V curve, and Z_0 the IF impedance. To properly account for all the subgap mixer output noise, we need a 10 % MAR current. When compared to an idealized junction with R_{sg}/R_n=30, we conclude that 90 % of the enhanced

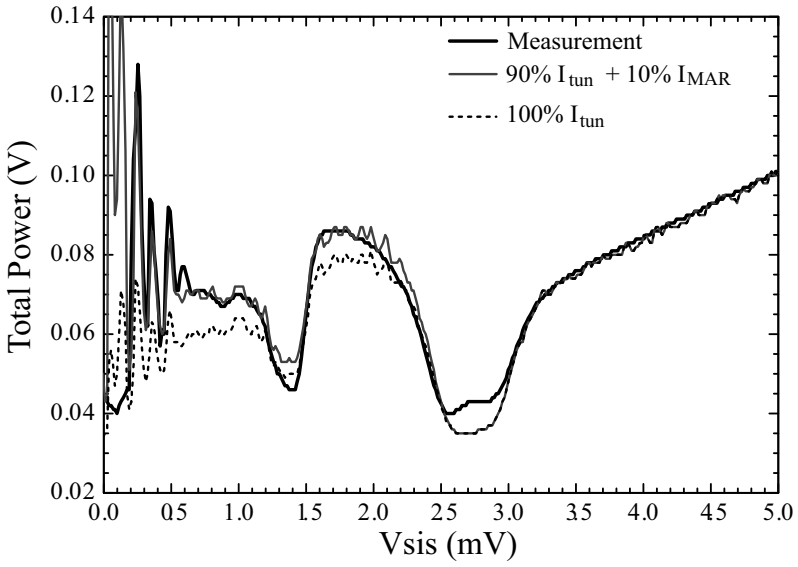

Figure 7.5: Measured mixer output noise compared to single-electron and MAR-enhanced shot noise. A 10 % MAR current (Fig. 7.5) accounts for all of the excess subgap noise, indicative that nearly all of the shot noise is due to single-electron transport in the barrier. The total intrinsic shot + MAR noise in the junction at 2 mV bias is 8.9 K, $\sim$ 45 % of the derived mixer noise (Sec. 7.3.2).

subgap noise is due to single-electron tunneling. From this the net increase in mixer noise is estimated to be 8.9 K.

In Sec. 7.3.2 we calculate the IF noise contribution by biasing the junction above the gap. In this case the current will be entirely due to single-electron tunneling. T_{shot} may then be found in the traditional way:

$$T_{shot} = \frac{eR_dI}{2k_B} coth\left(\frac{eV}{2k_BT}\right). \tag{7.5}$$

7.2.5 Planar 4 – 8 GHz IF matching network, dc-break, bias Tee, and EMI filter

In a practical mixer configuration, the active device is terminated into a desired IF load impedance, the bias lines filtered and injected via a bias tee, and the output dc decoupled. The dc block is usually accomplished with a small surface-mount capacitor contacted in series by either a soldered contact or wire bond. As a consequence, parasitic resonances at the upper end of the IF band are easily excited. Moreover, since the dc-blocking capacitor passes the mixer IF output current, a failure would be catastrophic. Indeed, component failure can occur in may ways, the most obvious perhaps due to mechanical stress from repeated cryogenic thermal cycles. As an alternative we investigate the use of parallel-coupled suspended microstrip lines [43]- [45]. An important advantage of this planar approach is that it offers accurate modeling

with 3D EM field-simulation software [33].

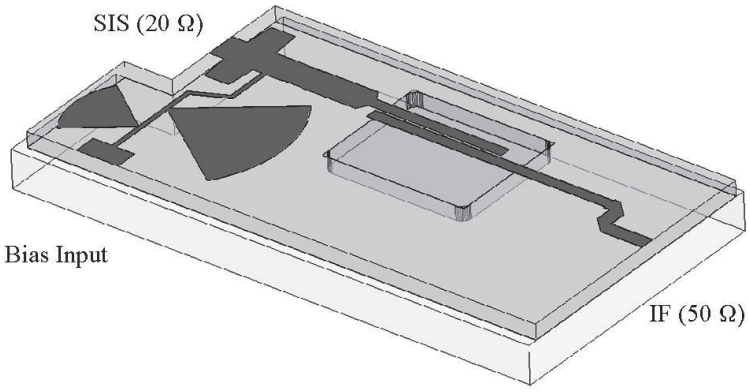

Figure 7.6: IF configuration with a 3 – 9 GHz passband response. The combined IF match, dc-break, bias tee, and EMI filter are planar by design. Design parameters are provided in Table 7.3.

As shown in Fig. 7.6, the suspended coupled microstrip lines act as a compact band-pass filter. For this filter to work, the ground plane directly underneath the filter needs to be removed. The IF board is optically positioned on top of a machined cutout (resonant cavity) by a set of alignment holes. The advantages of this technique are simplicity of design (only one lithography step) and improved reliability. The disadvantage at lower IF frequencies is size, $\lambda_g/4$. To secure the alumina board [46] to the Au plated brass mixer block we use an indium alloy paste [47]. Repeated thermal cycles have proven successful, an indication that the thermal expansion of the dissimilar materials does not pose a significant problem.

Details of the blocking filter are summarized in Table 7.3. The spacing S, and

Table 7.3: Coupling Parameters of Fig. 7.6

Substrate	Alumina
ε_r	9.80
H_{sub} (μm)	635
W (μm)	480
L (mm)	5.72
S (μm)	120
H_{cav} (μm)	585
H_{air} (mm)	2.5
L_c x W_c (mm)	5.08 x 6.1

H_{sub} denotes the substrate height, W the width of the coupled lines, L their length, S the spacing, H_{cav} the cavity depth, H_{air} the air height above the substrate, L_c the cavity length, and W_c the cavity width. Center frequency is 6 GHz.

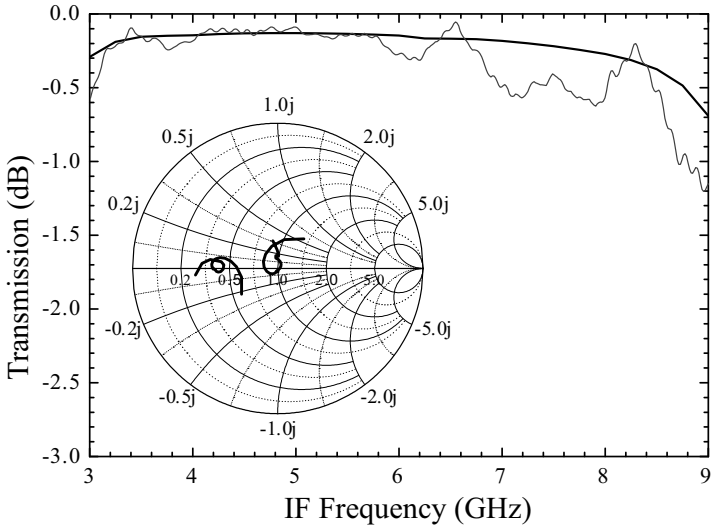

Figure 7.7: Simulated and measured coupling efficiency into a 50 Ω load (see also Fig. 6). Inset: Simulated complex impedance towards the SIS chip (20 Ω) and IF output (50 Ω).

cavity depth H_{cav} set the coupling. Tolerance values should be held to $\pm$ 5 %. Performance curves for IF coupling efficiency and impedance are shown in Fig. 7.7. In principle the twin-junction SIS design offers a 1 – 13 GHz IF passband response. However, due to availability of low noise cryogenic components, we have chosen a design to match the 4 – 8 GHz low noise InP amplifier (LNA) from Chalmers University (Sec. 7.2.6) and the 4 – 8 GHz cryogenic isolator [48].

7.2.6 4 – 8 GHz low noise cryogenic amplifier

In collaboration with Chalmers University in Sweden and NASA's Jet Propulsion Laboratory, we have acquired extremely low noise (2.2 K) 4 – 8 GHz indium phosphide (InP) cryogenic high-electron-mobility transistor (HEMT) amplifiers [49, 50]. The dc power consumption is $\approx$ 10 mW, allowing the amplifier to be mounted on the LHe stage, and the input return loss 18 dB. The amplifier gain is 25 dB (2 stages). To add additional gain at the 4K stage, we use a cryogenic GaAs MMIC from Prof. Weinreb's group at the California Institute of Technology [51] as a second low noise amplifier. This amplifier offers excellent performance, with a gain of 25 dB and a noise temperature of 5 K.

7.2.7 Cooled optics

The receiver noise temperature is critically dependent on optical loss in front of the mixer. This can be understood from

$$T_{rec}^{DSB} = T_{rf} + \frac{T_{mix}}{G_{rf}} + \frac{T_{IF}}{G_{rf} G_{mix}^{DSB}}. \tag{7.6}$$

G_{mix}^{DSB} is the double-sideband mixer gain, G_{rf} the front-end optics transmission coefficient, T_{rf} the optics noise temperature, T_{IF} the IF noise temperature, and T_{mix} the intrinsic mixer noise. We have minimized the optics noise by careful selection of the infrared blocking filters and vacuum window, and by using a cooled off-axis elliptical mirror. Fig. 7.8 depicts some of the receiver hardware mounted on the cryostat LHe stage.

For optimal RF bandwidth and performance, we use a corrugated feedhorn [52] with $\sim$ 43 % fractional bandwidth. The design is based on numerical simulations of a 180 – 280 GHz feedhorn with 64 sections by J. Lamb [53]. Calculated input return loss of the horn is better than 18 dB, the cross-polar component less than -32 dB, and the phase front error 0.1. At 345 GHz the horn has a f/2.42 beam divergence. The optics is designed to provide a 11.8 dB frequency-independent illumination of the telescope's secondary mirror [54]. To check the level of cross-polarization and off-axis aberration of the elliptical mirror (M6) design, a physical optics calculation [55] was done by Jellema and Finn [56]. In our design the second focus of the elliptical mirror is positioned at the 77 K (LN_2) stage of the cryostat. This allows the use of a 32 mm diameter pressure window (7 ω_o). The infrared blocking filters on the 4 K

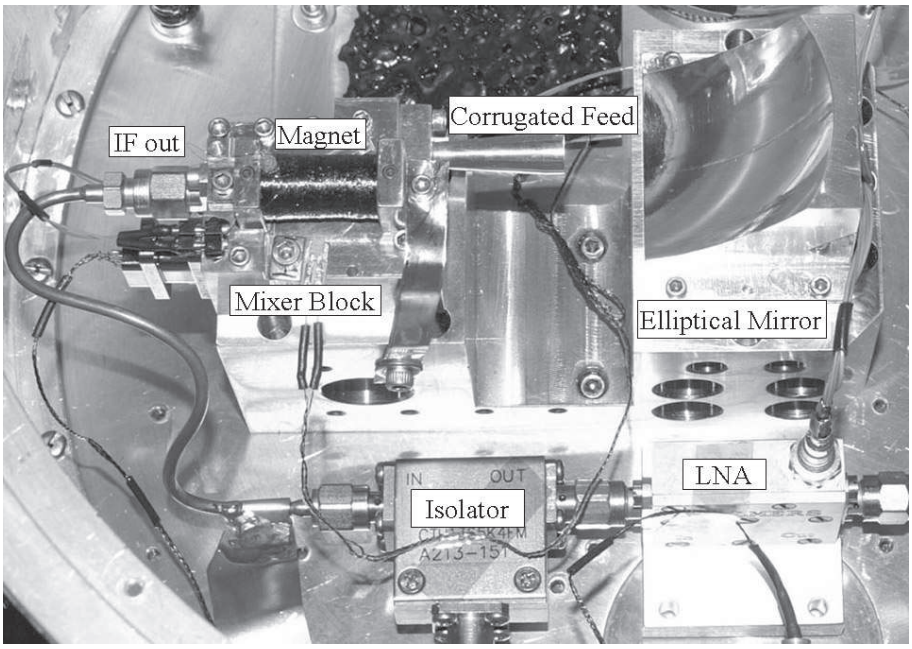

Figure 7.8: The mixer, off-axis elliptical mirror, 4 – 8 GHz isolator, and low noise amplifier are all situated on the LHe stage. The Infrared Labs Dewar is mounted upside-down in the Cassegrain focus of Caltech Submillimeter Observatory (CSO).

and 77 K stages are made of one layer (100 μm) G104 and one layer (200 μm) G108 Zitex (30–60 % porous Teflon [57]), separated by $\sim$ 40 μm vacuum via a precision-cut circular HDPE spacer. This design has a better than 99 % transmission from 280 – 420 GHz, while photon scattering leads to a loss of $\approx$ 98.5 % per sheet in the thermal infrared [58].

The vacuum window is made of 715 μm high-density polyethylene (HDPE) that is antireflection coated with one layer (150 μm) G106 Zitex on one side, and one layer (200 μm) G108 on the other. Calculated transmission is better than 98 % across the 280 – 420 GHz frequency band. As a "glue" to make the porous Teflon stick to the HDPE we used 50 μm thick LDPE [59]. This material has a melting point just below that of HDPE, and under pressure on a hot plate the "sandwich" of Zitex-LDPE-HDPE-LDPE-Zitex fuses together. Fourier transform spectrometer (FTS) transmission measurements confirm the excellent transmission properties of these windows. To inject the local-oscillator signal [60] we use a 25 μm quasi-optical Mylar beamsplitter with a calculated reflection of 4.9 % at 345 GHz (G_{bs} in Table 7.4). Standing waves between the telescope secondary mirror and cryostat are minimized by tilting the vacuum window and IR blocks at 5° angles.

7.3 Receiver performance

7.3.1 Fourier transform spectrometer measurements

To investigate the coupling to the twin SIS junction RF matching network, we have measured the direct-detection response of the mixer with a Fourier transform spectrometer (FTS). The result, overlaid with the derived mixer conversion gain and Supermix simulation, is shown in Fig. 7.9.

A few points are noteworthy. First, the response bandwidth is limited by the corrugated feedhorn ($\sim$43 % fractional bandwidth), more or less 20 GHz symmetrically on either side. Second, the direct-detection response is centered on 350 GHz. This argues for the accuracy of the computer simulations and quality of the device fabrication.

7.3.2 Heterodyne results and discussion

In Fig. 7.10 we show the measured heterodyne response and associated local-oscillator pumped and unpumped I/V curves at 280, 345, and 424 GHz. Optimal mixer bias occurs between 2.1 – 2.2 mV for all frequencies (see also Fig. 7.11). Optimal LO pump current is 80 – 85 μA, which is 55 – 60 μA over the dark current. From this we calculate that $\alpha \equiv eV_{LO}/\hbar\omega = 0.64$ at 345 GHz, corresponding to an available LO power at the two junctions of 160 nW. The magnetic field required to suppress the Josephson current to a first minima (1 flux quantum) results in an unexpectedly good receiver noise temperature at frequencies below 370 GHz. This effect is understood to be due to ac-Josephson oscillations mixing with the third harmonic of the LO signal. By softening the gap with a stronger magnetic field (2^{nd} null), the harmonic conversion efficiency is reduced, alleviating the problem. The generation of significant

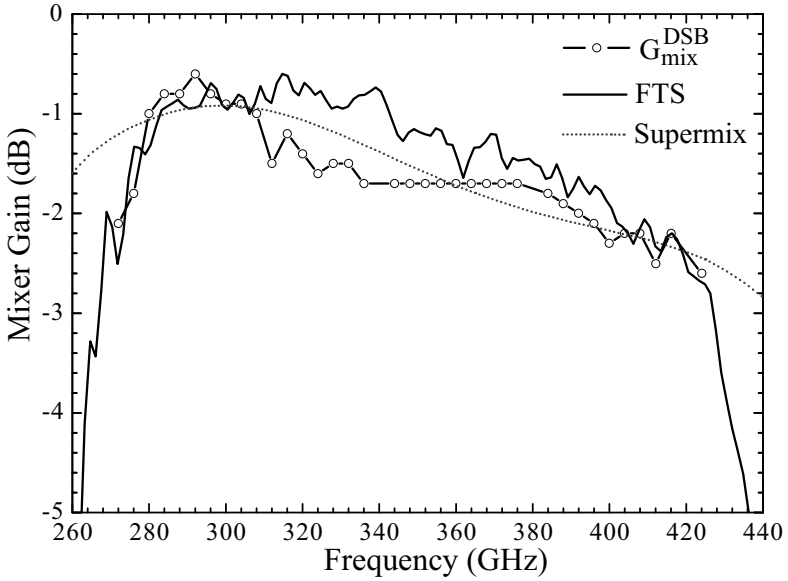

Figure 7.9: FTS measurement superimposed with the mixer conversion gain and "Supermix" simulation (no optics/waveguide). The RF bandwidth is limited, 20 GHz on either side, by the frequency response of the corrugated feedhorn. The waveguide cutoff frequency is 250 GHz.

amounts of harmonic content may be characteristic of high current density AlN-barrier SIS junctions. Operating the mixer at the second Josephson null reduces the mixer conversion gain by $\sim$ 1.5 dB, and has a minimal impact on the receiver noise temperature. The input loads (T_h, T_c) are defined using Callen & Welton formalism [62, 63], where the vacuum zero-point fluctuation noise is included in the blackbody radiation temperature. At the frequencies of interest this approaches the Rayleigh-Jeans limit.

As a general principle the receiver should not be biased for maximum G_{mix}^{DSB}, which occurs when the IF output power is optimized. Rather, the mixer should be biased for optimal sensitivity (Fig. 7.11). This in effect is similar to "noise matching" as opposed to "power matching" of low noise amplifiers.

To characterize the IF noise contribution, Rudner *et al.* [64], and Woody *et al.* [11], proposed to use the unpumped junction above the gap voltage as a calibrated shot noise source (Eq. 7.5). Studies by Dubash *et al.* [65, 66] quantitatively verified that the noise current of an unpumped SIS junction above the gap is in fact the shot noise associated with the direct current. Using this technique the IF noise contribution and mixer conversion gain were computed as explained by Wengler and Woody [67].

To understand the optics loss in front of the mixer, we employ a technique, commonly known as the "intersecting-line technique", described by Blundell *et al.* [61] and Ke and Feldman [68]. We find between 280 – 424 GHz a front-end equivalent noise temperature (T_{rf}) of 19 – 30 K. This includes thermal noise injected via the room-temperature 25 μm Mylar beamsplitter. The uncorrected optical efficiency

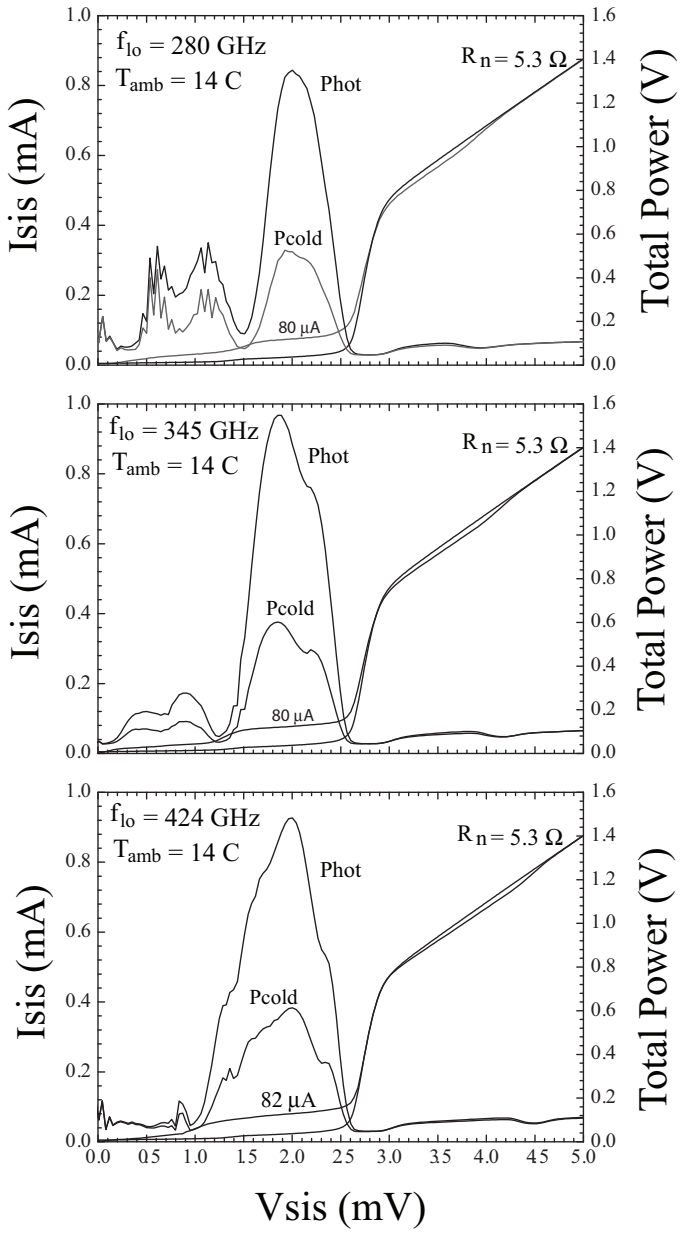

Figure 7.10: Measured heterodyne response at 280, 345, and 424 GHz at the Caltech Submillimeter Observatory (4200 m). Optimal bias ranges from 2.1 – 2.2 mV with an LO pump current of 57 – 60 μA over the leakage current (25 μA). At 345 GHz this corresponds to $\alpha \equiv eV_{LO}/\hbar\omega = 0.64$. The combined twin-junction normal-state resistance (R_n) equals 5.32 Ω and the resistive subgap-to-R_n ratio $\simeq$ 15.

(G_{rf}), referred to 290 K, is found to range from -0.29 dB at 280 GHz to -0.46 dB at 424 GHz. Correcting for the beamsplitter loss (G_{bs}), the optical efficiency of the pressure window, IR blocks, and cooled optics is therefore -0.14 dB ($\sim$ 96.7 %), consistent with the optics design outlined in Sec. 7.2.7. It should be noted that the "intersecting-line technique" is likely to include some small correction factors because the mixer is not perfectly matched and/or operating in true DSB mode [68]. From fits to our data, the magnitude of this factor is found experimentally to be $\hbar\omega/2k$.

The measured receiver noise temperature at 345 GHz is 48 K DSB. From the shot noise calculations we obtain at 345 GHz an overall mixer conversion gain of

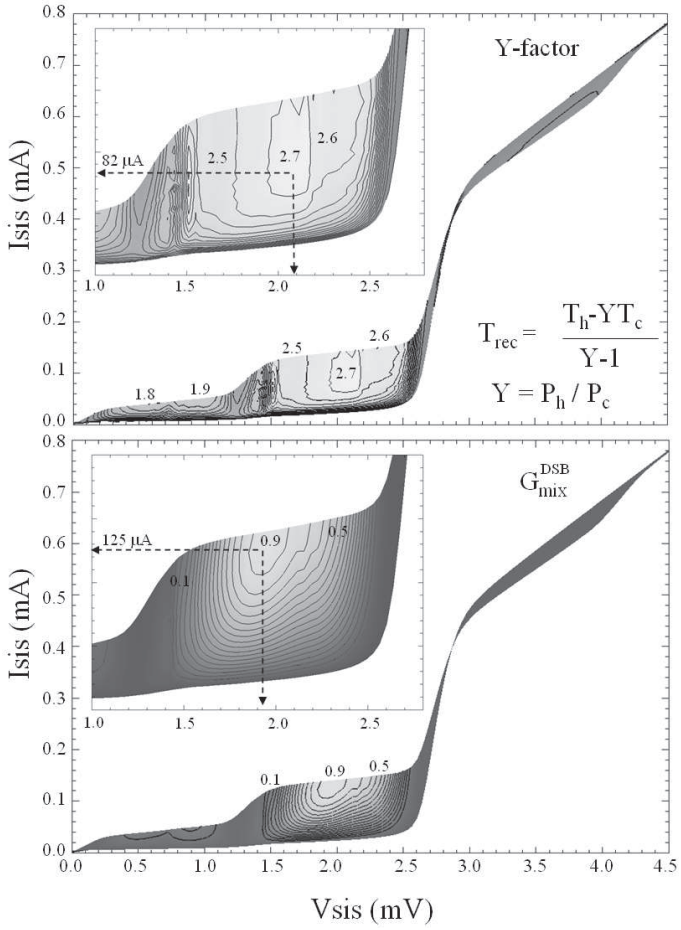

Figure 7.11: *Top*) Y-factor (sensitivity) as a function of mixer bias and local-oscillator pump current. Optimal sensitivity occurs around 2.1 mV and 82 μA. *Bottom*) Conversion gain (linear) vs. mixer bias and LO pump current. Maximum conversion gain (IF power) occurs at 1.9 mV bias and 125 μA of LO pump current. Contour lines are in steps of 0.1, and the LO pump frequency is 345 GHz. Biased at optimal sensitivity, the mixer gain drops from 0.9 to 0.6 (-2.3 dB).

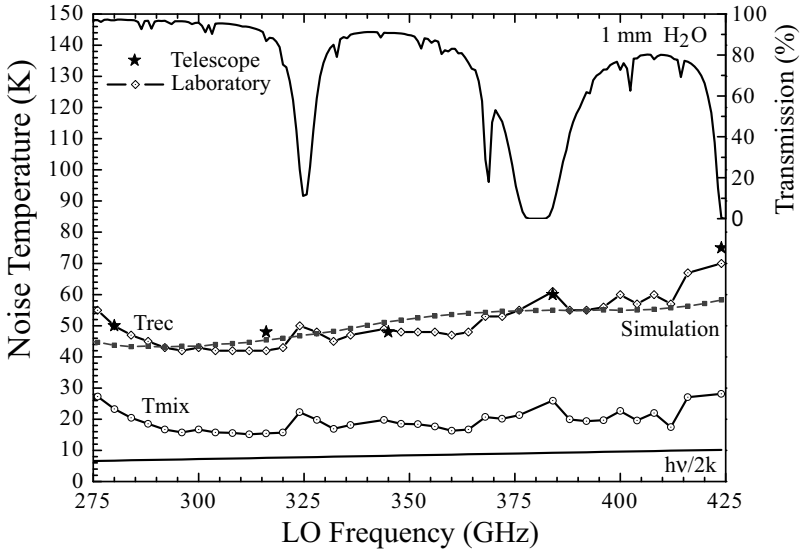

Figure 7.12: Measured receiver and mixer noise temperature in the laboratory and at the telescope. The dotted line represents the simulated result. All noise temperatures are uncorrected for optical loss. The atmospheric window for 1 mm of precipitable water is shown for reference. T_{mix} includes, due to leakage current below the gap, 9 K of MAR-enhanced shot noise. In the calculations the radiometric hot and cold blackbody temperatures are assumed to be in the Rayleigh-Jeans limit.

-2.3 dB, and mixer noise temperature of 19.8 K. Of this ∼9 K is due to leakage current in the AlN tunnel barrier. The obtained IF noise temperature is 3.8 K and the IF noise contribution to the receiver budget 7.0 K. These values are in good

Table 7.4: Measured and calculated receiver parameters. Refer to Eq. 7.6 for details. *T_{mix} includes 9 K of MAR-enhanced shot noise.

Parameters	**280 GHz**	**345 GHz**	**424 GHz**
T_{rec}^{DSB} (K)	50	48	72
T_{rf} (K)	19	21	30
T_{IF} (K)	3.8	3.8	3.8
T_{mix} (K)*	23.3	19.8	28.2
G_{mix}^{DSB} (dB)	-1.6	-2.3	-3.2
G_{rf} (dB)	-0.29	-0.32	-0.46
G_{bs} (dB)	-0.15	-0.22	-0.32
$T_{mix}/(G_{rf})$ (K)	25	21.3	31.3
$T_{IF}/(G_{rf}G_{mix}^{DSB})$ (K)	7.5	7.0	9.0
Measured α	0.66	0.64	0.62

agreement with simulation. A detailed breakdown of the noise budget is provided in Table 7.4. In Fig. 7.12 we show the heterodyne response from 275 – 425 GHz as measured in the laboratory and at the observatory on top of Mauna Kea, Hawaii. For the balanced heterodyne receivers currently under development, the DSB receiver response is expected to improve in sensitivity by 9 – 20 K in the 275 – 424 GHz frequency range due to a reduction in thermal noise and LO amplitude noise.

7.3.3 IF response

The 345 GHz IF response of the mixer is shown in Fig. 7.13. The data was obtained in a 30 MHz resolution bandwidth by scanning a YIG filter [69] from 3.5 – 8 GHz at 15 MHz intervals. At each frequency the hot and cold response was measured using an automated chopper wheel. This technique allows efficient integration of the noise in a time frame less than the Allan variance stability time of the instrument ($\sim$ 9 s in a 30 MHz IF channel bandwidth). Between 7 – 8 GHz we see the noise rise from 50 K to 70 K DSB. Extensive electromagnetic field simulations [33, 37] compared to measured IF output data, point to a problem in the assumed "infinite" CPW ground plane and 1-mm-long IF bond wire. Because the on-chip IF matching circuit is highly tuned, a slight mistuning in one or more of its components results in a double-peaked passband response. Computer simulations show a mixer IF passband peak at 4 GHz,

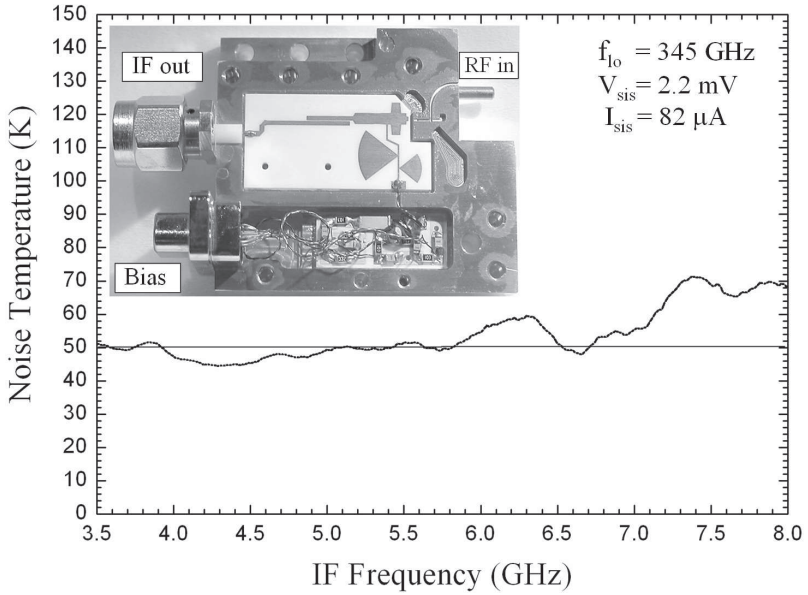

Figure 7.13: Receiver noise temperature across the IF band. The rise at 7 GHz is attributed to a slight mistuning of the junction's double-tuned IF response. Computer simulations suggest that this can be corrected with additional wirebonds to ground at the integrated capacitor, and reduction in the IF contact wirebond length (1 mm at present). The equivalent noise bandwidth of the mixer is $\sim$ 5 GHz.

and a 3 dB dip at 8 GHz. Fortunately this issue is easily solved with the addition of extra ground contacts in the vicinity of the integrated capacitor (Fig. 7.3) and a reduction of the IF bond wire length. Due to this effect the 4 – 8 GHz receiver noise temperature is slightly weighted toward the 3.5 – 6 GHz range (Table 7.4).

7.3.4 Stability

In general, receiver instabilities lead to a loss in integration efficiency and poor baseline quality [70]. Throughout the design process, attention has been given to the multiplicity of factors that degrade the stability of the instrument. These include improved SIS and LNA bias electronics, voltage-divider networks in the SIS mixer and cryogenic low-noise amplifiers, enhanced thermal design of the room-temperature IF amplifiers, careful elimination of all ground loops, and the use of twisted-pair wires in the cryostat to minimize microphonic pickup. The resulting Allan variance stability plot is shown in Fig. 7.14.

It has been found [71, 72] that fluctuations with a $f^{-\alpha}$ power spectrum show up in the Allan variance plot as $T_{int}^{\alpha-1}$, with T_{int} defined as the integration time. If we let $\beta = \alpha - 1$, the shape of the Allan variance is found to follow

$$\sigma_A^2(T_{int}) = aT_{int}^{-1} + b + cT_{int}^{\beta} \ , \tag{7.7}$$

where a, b, c are constants. The first term, with β = -1, represents radiometric (white) noise. In a log-log plot it has a slope of -1 (Fig. 7.14). This type of frequency-independent (uncorrelated) noise integrates down with the square-root of time according to the well-known radiometer equation [73]

$$\sigma = \frac{\langle s(t) \rangle}{\sqrt{\Delta\nu T_{int}}} \ . \tag{7.8}$$

Here s(t) is the measured detector IF output signal in the time domain, and $\Delta\nu$ the equivalent IF noise-fluctuation bandwidth of the system. The last term in Eq. 7.7 represents drift noise. In between these two limits a certain amount of gain-fluctuation or flicker noise with a $1/f$ noise power spectral distribution may exist ($\beta = 0$). The intercept between radiometric and drift noise is the Allan minimum time of the system (T_A). From our measured data we calculate a total-power Allan minimum time of 2.5 s and a noise-fluctuation bandwidth of 4.6 GHz, consistent with the IF passband shown in Fig. 7.13.

If the stability were to be limited by drift noise alone, the Allan variance time would scale with IF bandwidth as

$$T_A' = T_A(\Delta\nu/\Delta\nu')^{\frac{1}{1+\beta}} \ . \tag{7.9}$$

T_A is the measured Allan variance time in a noise-fluctuation bandwidth $\Delta\nu$, and T_a' the expected Allan stability time in bandwidth $\Delta\nu'$. Note that for optimal observing efficiency integrations time should be kept well below the Allan minimum stability time of the system. In our case a 50 % loss in integration efficiency is incurred at T_{int}=1 s ($\Delta\nu$ = 4.6 GHz). Using Eq. 7.9, this corresponds to approximately 100 s in a 2 MHz spectrometer channel noise-bandwidth. These results are measured with

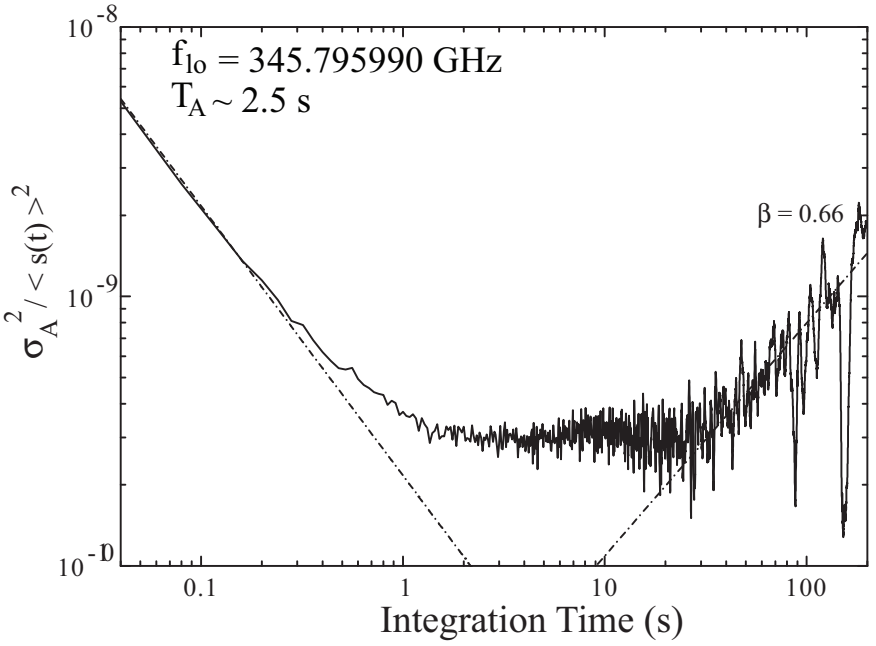

Figure 7.14: Measured total-power (continuum) Allan variance on a room-temperature blackbody as a function of integration time with the instrument mounted on the telescope. From the Allan variance analysis we derive a drift slope of 0.66 and a noise-fluctuation bandwidth ($\Delta\nu$) of 4.6 GHz. At 1 s, a factor of 1.5 is lost in the total-power integration efficiency. For reference, this corresponds to approximately 100 s in a typical 2 MHz spectrometer channel.

the instrument mounted on the telescope and are a factor 6–8 times better than the existing facility heterodyne receivers. For comparison, the ALMA [74] specified goal for total-power gain stability (∂G/G) at 1 s is 10^{-4}. The results presented here equate to a normalized total-power gain stability ($\sigma/\langle s(t)\rangle$) of 1.5 x 10^{-5}.

7.3.5 Observations

In October 2006 we observed the ^{12}CO$_{J=3\rightarrow 2}$ (345.796 GHz) transition in the hot core regions around Orion IRC2 and W3 at the CSO (Fig 7.15). The single-sideband (SSB) system temperature, airmass, and integration times were 1380 K, 1.31, and 8.4 minutes for the Orion observation, and 1430 K, 1.45, and 10.1 minutes for the W3 observation. Consistent with our optics design, fits to beam measurements on the telescope's secondary mirror give a Gaussian illumination with 11.5 dB edge taper. From this and knowledge of the primary surface roughness (20 μm), we estimate a main-beam efficiency of $\sim$ 75 %. The weather conditions were poor during our engineering run with a 225 GHz zenith atmospheric opacity (τ_{225}) $\geq$ 0.205. At 345.796 GHz this translates into an air-mass corrected, on-source opacity (τ) of 0.92 for Orion and 1.02 for W3 [75].

The measured SSB system temperatures (T_{sys}^{SSB}) are consistent with those ob-

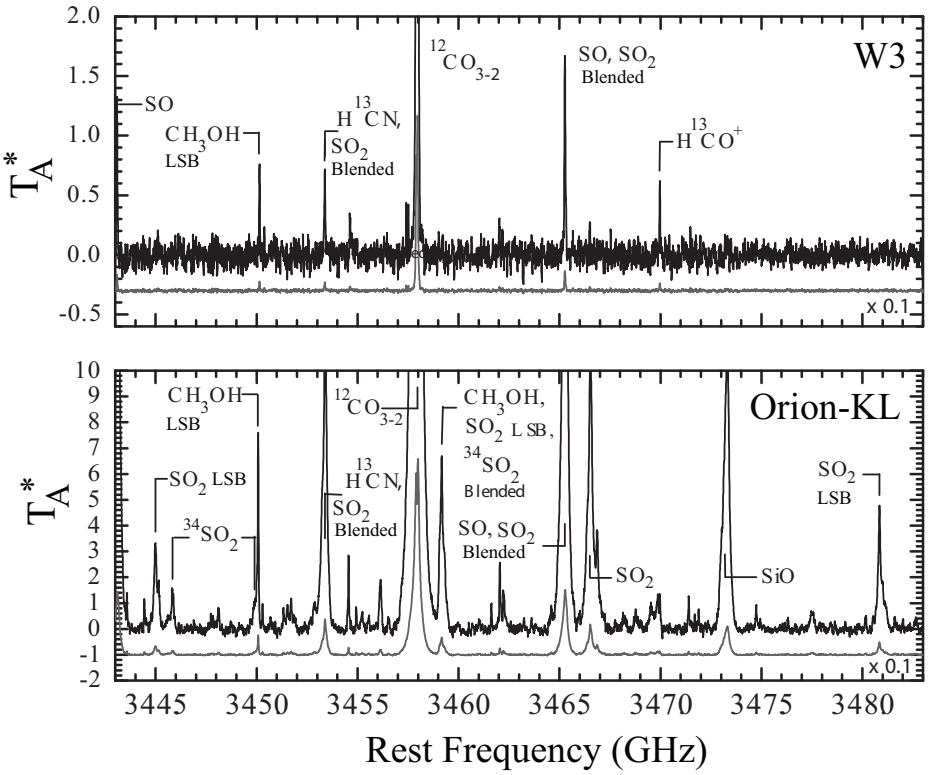

Figure 7.15: Test spectra taken at the Caltech Submillimeter Observatory in October 2006 of the hot core around Orion IRC2 and W3 in $^{12}CO_J = 3 \rightarrow 2$. Due to time constraints and poor weather pointing was non-optimal. Line identifications based on Schilke *et al.* [76] and Helmich *et al.* [77].

tained from theory

$$T_{sys}^{SSB} = 2\Big(\frac{T_{rec}^{DSB} + (1 - \eta_s e^{-\tau})T_{sky}}{\eta_s e^{-\tau}}\Big) \ . \tag{7.10}$$

η_s, the hot spillover efficiency, is 90 % and was obtained from sky-dip measurements in July of 2006. The physical temperature of the sky (T_{sky}) is estimated to be $\sim$ 275 K. Given a 50 K DSB receiver noise temperature (Fig. 7.12) we obtain a theoretical T_{sys}^{SSB} of 1260 K for Orion-KL, and 1450 K for W3. This includes a respective SSB atmospheric noise contribution of 825 K and 970 K. In the event an SSB receiver with 10 dB sideband rejection ratio (ALMA) and T_{rec}^{SSB} = 2 x T_{rec}^{DSB} had been used for the observations the SSB system temperatures are estimated to have been 820 K and 940 K. Though much improved over the single-ended DSB receiver (a factor of 2.4 in integration time), the system temperature would still be limited by the sky.

7.4 Conclusion

We have discussed the design, development, and installation of a 275 – 425 GHz tunerless heterodyne receiver. By combining AlN-barrier high-current-density (25 kA/cm^2) SIS technology with a full-height waveguide to thin-film microstrip transition, we are able to achieve an unprecedented 43 % instantaneous bandwidth, limited primarily by the mixer corrugated feedhorn.

From 275 – 425 GHz we measure a receiver noise temperature of 40 – 72 K DSB. In this frequency range the mixer gain is relatively constant at -2.3 ± 1 dB. The optimal mixer bias is found between 2.1 – 2.2 mV, with an LO pumped SIS current of 55 – 60 μA over the 25 μA leakage current at all frequencies. These parameters allow for easy automation of the instrument.

The high-current-density AlN-barrier devices are found to have a somewhat higher leakage current than is commonly observed in lower-current-density AlO_x tunnel junctions. We find that below the gap, 90 % of the leakage current induced shot noise is via single-electron tunneling, with only 10 % due to multiple Andreev reflections. The total MAR enhanced shot noise is $\sim$ 8.9 K. This accounts for $\sim$ 45 % of the obtained 19.8 K intrinsic mixer noise temperature.

To optimize integration efficiency and baseline quality, a significant effort has been expended to achieve maximum instrument stability. The measured total-power stability on the telescope is $\sim$ 2.5 s in 4.6 GHz, or about 100 s in a 2 MHz noise-fluctuation bandwidth. This is a factor 6 – 8 times better than the existing facility heterodyne instrumentation.

Bibliography

[1] [Online]. Available: http://www.sron.nl/divisions/lea/hifi/

[2] [Online]. Available: http://www.alma.info/

[3] [Online]. Available: http://iram.fr/

[4] [Online]. Available: http://www.apex-telescope.org/

[5] [Online]. Available: http://www.sron.nl/

[6] [Online]. Available: http://sma-www.harvard.edu/

[7] J.W. Kooi, A. Kovács, S. Kaye, J. Dama, J. Zmuidzinas, and T.G. Phillips, "Heterodyne Instrumentation Upgrade at the Caltech Submillimeter Observatory" *Proc. SPIE*, Vol. 4855, pp. 265-278, Feb., (2003).

[8] J. W. Kooi, A. Kovács, B. Bumble, G. Chattopadhyay, and M. L. Edgar, S. Kaye, R. LeDuc, J. Zmuidzinas, and T. G. Phillips "Heterodyne Instrumentation Upgrade at the Caltech Submillimeter Observatory II" *Proc. SPIE*, Vol. 5498, pp 332-348, Jun., (2004).

[9] C. R. Predmore, N. R. Erickson, G. R. Huguenin, and P. Goldsmith, "A Continuous Comparison Radiometer at 97 GHz" *IEEE Microwave Theory and Techniques*, Vol. MTT-33, No. 1, Jan., (1985).

[10] D. Maier, A. Barbier, B. Lazareff, and K. F. Schuster, "The Alma Band 7 Mixer", *Proc. 16th Int. Symposium on Space Terahertz Technology*, Chalmers, Göteborg, Sweden, May, (2005), S08-02.

[11] D. P. Woody, R. E. Miller, and M. J. Wengler, "85-115 GHz Receivers for Radio Astronomy", *IEEE Trans. Microwave Theory Tech.*, Vol. 33, pp. 90-95, February, (1985).

[12] B. N. Ellison and R. E. Miller, "A Low Noise 230 GHz SIS Receiver," *Int. J. IR and MM Waves*, Vol. 8, 609-625, Jun., (1987).

[13] J. W. Kooi, M. Chan, T. G. Phillips, B. Bumble, and H. G. Leduc, "A low Noise 230 GHz Heterodyne Receiver employing 0.25 μm^2 Area Nb/AlO$_x$/Nb Tunnel Junctions," *IEEE Microwaves Theory and Techniques*, Vol. 40, pp. 812-815, May, (1992).

[14] C. K. Walker, J. W. Kooi, M. Chan, H. G. Leduc, P. L. Schaffer, J. E. Carlstrom, and T. G. Phillips, "A Low-noise 492 GHz SIS Waveguide Receiver," *Int. J. IR and MM Waves*, Vol. 13, pp. 785-798, Jun., (1992).

[15] J. H. Kawamura, T. R. Hunter, C.-Y. E. Tong, R. Blundell, Q. Zhang, C. A. Katz, D. C. Papa and T. K. Sridharan, "First Image with the CfA Superconducting HEB Receiver: The Protostellar Outflow from IRAS 20126 + 4104 in CO (J=7-6)," *Pubs. Astronomical Soc. Pacific*, Vol. 111, pp. 1088-1094, Sep., (1999).

[16] R. L. Eisenhart and P. J. Khan, "Theoretical and Experimental Analysis of a Waveguide Mounting Structure", *IEEE Microwave Theory and Techniques*, Vol. MTT-19, pp. 706-717, Aug., (1971).

[17] S. Withington and G. Yassin, "Analytical Expression for the Input Impedance of a Microstrip Probe in Waveguide," *Int. J. IR and MM Waves*, Vol. 17, pp. 1685-1705, Nov., (1996).

[18] C-Y. E. Tong, R. Blundell, and S. Paine, "Design and Characterization of a 250-350-GHz Fixed-Tuned Superconductor-Insulator-Superconductor Receiver", *IEEE Microwave Theory and Techniques*, Vol. MTT-44, pp. 1548-1556, Sep., (1996).

[19] Y. Delorme, M. Salez, B. Lecomte, I. Péron, F. Dauplay, A. Féret, J. Spatazza, J. -M. Krieg, and K. F. Schuster, "Space-Qualified SIS Mixers for Herschel Space Observatory's HIFI Band 1 Instrument", *Proc. 16th Int. Symposium on Space Terahertz Technology*, Chalmers, Göteborg, Sweden, May, (2005), S08-05.

[20] C. F. J. Lodewijk, M. Kroug, and T. M. Klapwijk, "Improved Design for Low Noise Nb SIS Devices for Band 9 of ALMA (600-720 GHz)", *Proc. 16th Int. Symposium on Space Terahertz Technology*, Chalmers, Göteborg, Sweden, May, (2005), S03-05.

[21] B. D. Jackson, G. de Lange, T. Zijlstra, M. Kroug, J. W. Kooi, J. A. Stern, and T. M. Klapwijk, "Low-Noise 0.8-0.96- and 0.96-1.12 THz Superconductor-Insulator-Superconductor Mixers for the Herschel Space Observatory", *IEEE Microwave Theory and Techniques*, Vol. MTT-54, No. 2, pp. 547- 558, Feb., (2006).

[22] Y-C Leong and S. Weinreb, "Full-band Waveguide-to-Microstrip Probe Transitions" *IEEE Microwave Theory and Techniques*, Digest of Papers, Anaheim, CA, 13-19 Jun., (1999).

[23] J. H. C. van Heuven, "A new Integrated Waveguide-Microstrip Transition", *IEEE Microwave Theory and Techniques*, Vol MTT-24, pp. 144-147, Mar., (1976).

[24] A. R. Kerr and S. K Pan, "Some recent Developments in the Design of SIS Mixers,", *Int. J. IR and MM Waves*, Vol. 11, no. 10, pp. 1169-1187, Nov., (1990).

[25] A. R. Kerr, "Elements for E-plane Split-Block Waveguide Circuits", NRAO, Charlottesville, VA, [Online]. Available: http://www.alma.nrao.edu/memos/html-memos/alma381/memo381.pdf

[26] S. -K. Pan, A. R. Kerr, M. W. Pospiezalski, E. F. Lauria, W. K. Crady, N. Horner, Jr., S. Srikanth, E. Bryerton, K. Saini, S. M. X. Claude, C. C. Chin, P. Dindo, G. Rodrigues, D. Derdall, J. Z. Zhang, and A. W. Lichtenberger, "A Fixed-Tuned SIS Mixer with Ultra-Wide-Band IF and Quantum-Limited Sensitivity for ALMA Band 3 (84-116 GHz) Receivers", *Proc. 15th Int. Symposium on Space Terahertz Technology*, Northampton, MA, Apr., (2004), pp. 62-69.

[27] S. Withington, G. Yassin, J. Leech, and K. G. Isaak, "An Accurate Expression for the Input Impedance of One-Sided Microstrip Probes in Waveguide", *Proc. 10th Int. Symposium on Space Terahertz Technology*, Charlottesville, Va, Mar., (1999), pp. 508-518.

[28] J.W. Kooi, G. Chattopadhyay, S. Withington, F. Rice, J. Zmuidzinas, C.K. Walker, and G. Yassin, "A Full-Height Waveguide to Thin-Film Microstrip Transition with Exceptional RF Bandwidth and Coupling Efficiency", *Int J. IR and MM Waves*, Vol. 24, No. 3, pp. 261 - 284, Sept., (2003).

[29] A. Navarrini, B. Lazareff, D. Billon-Pierron, and I. Peron, "Design and characterization of 225-370 GHz DSB and 250-360 GHz SSB full height waveguide SIS mixers", *Proc. 13th Int. Symposium on Space Terahertz Technology*, Harvard University, Mar., (2002), pp. 33-40.

[30] C. Risacher, V. Vassilev, A. Pavolotsky and V. Belitsky, "Waveguide-to-Microstrip Transition with Integrated Bias-T", *IEEE Microwave and Wireless Components Letters"*, Vol. 13, No. 7, pp. 262 - 264, Jul., (2003).

[31] C. Risacher, V. Belitsky, V. Vassilev, I. Lapkin, and A. Pavolotsky, "A 275-370 GHz SIS Receiver with Novel Probe Structure", *Int. Journal Infrared and Millimeter Waves*, Vol. 26, No. 6, pp. 867 - 880, May, (2005).

[32] F. P. Mena, J. W. Kooi, A. M. Baryshev, C. F. J. Lodewijk, R. Hesper, G. Gerlofsma, T. M. Klapwijk, and W. Wild. "A Sideband-separating Heterodyne Receiver for the 600−720 GHz Band", Submitted to the *IEEE Trans. Microwave Theory and Techniques* in August (2008).

[33] HFSS, Ansoft Corporation, Pittsburgh, PA, (2005).

[34] V. Y. Belitsky, M. A. Tarasov, S. A. Kovtonjuk, L. V, Filippenko, and O. V. Kaplunenko, "Low-noise completely quasi-optical SIS receiver for radioastronomy at 115 GHz," *Int. J. IR and MM Waves*, Vol. 13, pp 389-396, (1992).

[35] J. Ward, F. Rice and J. Zmuidzinas, "Supermix: a Flexible Software Library for High-Frequency Circuit Simulation, including SIS Mixers and Superconducting Components", *Proc. 10th Int. Symposium on Space Terahertz Technology*, Charlottesville, VA, Mar., (1999), pp. 269–281.

[36] F. Rice, M. Sumner, J. Zmuidzinas, R. Hu, H. LeDuc, A. Harris, and D. Miller, "SIS mixer Design for a Broadband Millimeter Spectrometer Suitable for Rapid Line Surveys and Redshift Determinations", *in Proc. SPIE*, Kona, HI, (2002), Vol. 4855, pp. 301-311.

[37] SONNET, Sonnet Software, Liverpool, NY, 2005.

[38] J. W. Kooi, M. Chan, B. Bumble, H. G. LeDuc, P. L. Schaffer, and T. G. Phillips, "180425 GHz low noise SIS waveguide receivers employing tuned Nb/AIOx/Nb tunnel junctions", *Int. Journal Infrared Millim. Waves*, Vol. 15, no. 5, pp. 783-805, May, (2004).

[39] D. Maier, S. Devoluy, M. Schicke, and K. F. Schuster, "230 GHz SSB SIS Mixer for Band 3 of the new Generation Receivers for the Plateau de Bure Interferometer", newblock *Proc. 16th Int. Symposium on Space Terahertz Technology*, Chalmers, Göteborg, Sweden, May, (2005), S03-02.

[40] A. R. Kerr, "Saturation by Noise and CW Signals in SIS Mixers", *Proc. 13th Int. Symposium on Space Terahertz Technology*, Harvard University, Mar., (2002), pp. 11-22.

[41] R. Kehl Engineering, 384 Umbarger Rd., Units B & C, San Jose, Ca 95111.

[42] P. Dieleman, H. G. Bukkems, T. M. Klapwijk, M. Schicke, and K. H. Gundlach, "Observation of Andreev Reflection Enhanced Shot Noise", *PhysRevLett*, Vol. 79, pp. 3486-3489 , Nov., (1997).

[43] W. Menzel, L. Zhu, K. Wu, and F. Bögelsack, On the design of novel compact broadband planar filters, *IEEE Trans. Mircowave Theory Tech.*, Vol. 51, no. 2, pp. 364-370, Feb. (2003).

[44] G. de Lange, SRON, NL, Private Communication, (2003).

[45] H. Golstein, SRON, NL, Private Communication, (2003).

[46] American Technical Ceramics, One Norden Lane, Huntington Station, NY 11746, USA.

[47] Indium Corporation of America, Indalloy paste, #290, www.indium.com

[48] Pamtech, 4053 CalleTesoro, Camarillo, Ca 93012, USA.

[49] N. Wadefalk, A. Mellberg, I. Angelov, M. Barsky, S. Bui, E. Choumas, R. Grundbacher, E. Kollberg, R. Lai, N. Rorsman, P. Starski, J. Stenarson, D. Streit, and H. Zirath, "Cryogenic, Wide-band, Ultra-low-noise IF Amplifiers operating at Ultra-Low DC-Power," *IEEE Trans. Microwave Theory and Techniques*, Vol. 51, No. 6, pp. 1705-1711, Jun., (2003).

[50] N. Wadefalk, Caltech, Private Communication, (2005).

[51] N. Wadefalk and S. Weinreb, "Very Low-Noise Amplifiers for very Large Arrays," *IEEE MTT-S Int. Microwave Symp.* Dig., Long Beach, CA, Jun., 2005.

[52] Custom Microwave Inc., 940 Boston Avenue Longmont, CO 80501, USA.

[53] J. Lamb, Caltech, Private Communication, (2003).

[54] P. F. Goldsmith, *QuasiOptical Systems*, Piscataway, NJ: IEEE Press, 1998.

[55] TICRA Engineering, ticra@ticra.com

[56] W. Jellema, and T. Finn, SRON, NL. Private Communication, (2005).

[57] Saint-Gobain Performance Plasics Inc., 150 Dey Rd., Wayne, NJ 07470, USA.

[58] D. J. benford, M. C. Gaidis, and J. W. Kooi, Transmission Properties of ZITEX in the Infrared to Submillimeter *Proc. 10^{th} Int. Symposium on Space Terahertz Technology*, 402, Mar., (1999), pp. 402-411.

[59] Carlisle Plastics Company, Inc., 320 South Ohio Avenue, New Carlisle, OH 45344, USA.

[60] Virginia Diodes Inc., 321 West Main Street, Charlottesville, VA 22903, USA.

[61] R.Blundell, R. E. Miller, and K. H. Gundlach, "Understanding Noise in SIS Receivers," *Int. J. IR and MM Waves*, Vol. 13, No. 1, pp. 3-26, Jan., (1992).

[62] H. B. Callen and T. A. Welton, "Irreversibility and generalized Noise," *Phys. Rev.,* Vol. 83, no. 1, pp. 34-40, Jul., (1951).

[63] A. R. Kerr, M. J. Feldman, and S. K. Pan, "Receiver Noise Temperature, the Quantum Noise Limit, and the Role of the Zero-Point Fluctuations," *Electron. Div., NRAO, Charlottesville*, VA, Internal Rep. 304, Sep., (1996).

[64] S. Rudner, M. J. Feldman, E. Kollberg, and T. Claeson, "Superconducting-Insulator-Superconducting Mixing with Arrays at Millimeter-Wave Frequencies", *J. Applied Physics*, Vol. 52, pp. 6366-6371, (1981).

[65] N. B. Dubash, G. Pance, and M. J. Wengler, "Photon Noise in the SIS detector", *IEEE Trans. Microwave Theory Tech.*, Vol. 42, no. 4, pp. 716-725, Apr. (1994).

[66] N. B. Dubash, M. J. Wengler, and J. Zmuidzinas, "Shot Noise and Photon-Induced Correlations in 500 GHz SIS Detectors", *IEEE Trans. Applied Superconductivity*, Vol. 5, no. 2, pp. 3308-3311, Jun., (1995).

[67] M. J. Wengler, and D. P. Woody, "Quantum Noise in Heterodyne Detection", *IEEE J. Quantum Electronics*, Vol. QE-23, no.5, pp. 613-622, May, (1987).

[68] Q. Ke and M.J. Feldman, "A Technique for Noise Measurements of SIS Receivers", *IEEE Trans. Microwave Theory Tech.*, Vol. 42, No. 4, pp. 752-755, Apr., (1994).

[69] "Micro Lambda Wireless, Inc. 46515 Landing Pkwy., Fremont, CA 94538-6421.

[70] J. W. Kooi, G. Chattopadhyay, M. Thielman, T.G. Phillips, and R. Schieder, "Noise Stability of SIS Receivers," *Int J. IR and MM Waves*, Vol. 21, No. 5, pp. 689-716, May, (2000).

[71] R. Schieder and C. Kramer, "Optimization of Heterodyne Observations using Allan Variance Measurements", *Astron. Astrophys*, Vol. 373, pp. 746-756, Jul., (2001).

[72] V. Ossenkopf, "The stability of spectroscopic instruments: A unified Allan variance computation scheme", *A & A*, Vol. 479, 915-926 (2008).

[73] J. D. Kraus, *Radio Astronomy*, New York: McGraw-Hill, 1966, Ch. 3 and 7.

[74] M. A. Holdaway, "Effects of Atmospheric Emission Fluctuations and Gain Fluctuations on Continuum Total Power Observations with ALMA", *NRAO*, Charlotteville, VA, ALMA Memo 490, Mar. 30, (2004).

[75] J. R. Pardo, J. Cernicharo, and E. Serabyn, "Atmospheric Transmission at Microwaves (ATM): An Improved Model for mm/submm applications", *IEEE Trans. on Antennas and Propagation*, Vol. 49, no. 12, pp. 1683-1694, Dec., (2001).

[76] P. Schilke, T. D. Groesbeck, G. A. Blake, and T. G. Phillips, "A line Survey of Orion KL from 325 to 360 GHz", *Astrophys. J.*, Ser. 108, pp. 301-337, Jan., (1997), suppl.

[77] F.P. Helmich, and E. F. van Dishoeck, "Physical and chemical variations within the W3 star-forming region, II. The 345 GHz spectral line survey, *Astrophys. J.*, Ser. 124, pp. 205-253, Aug., (1997), suppl.

Chapter 8

Advanced receiver implementations*

8.1 Introduction

In this Chapter we look at three advanced submillimeter and far-infrared coherent detection schemes; the balanced-, correlation-, and sideband separating receiver. Depending on the application, each receiver configuration offers certain advantages. These, along with the theory and implementation are discussed at some length in this Chapter.

A balanced receiver arrangement provides a high level of amplitude noise immunity and utilizes all of the available LO power. These features facilitate automation, for example, by means of a synthesized local oscillator source. A noted disadvantage of balanced mixers is that the sidebands at the mixer IF output remain convolved (DSB). For the Caltech Submillimeter Observatory (CSO) [1, 2], balanced mixers were judged most promising, being able to facilitate many of the astrophysical science goals in the years to come. To this extent, four tunerless balanced waveguide receivers have been designed to cover the entire 180 – 720 GHz frequency range. The theory of operation and physical layout are discussed in Secs. 8.2 & 8.3. In principle 12 GHz of IF bandwidth is possible, however due to hardware constraints only 4 GHz will initially be utilized. The receiver optics are set up for dual frequency (2 color) observations in the 230/460 GHz and 345/660 GHz atmospheric frequency bands. Not only does this scheme provide a new mode of observation for the CSO, by utilizing the lower frequency channel it also facilitates pointing of the telescope in mediocre weather.

In addition to the new balanced receivers, we have also designed a specialized 2-channel, quasi-optically LO balanced continuous comparison (correlation) receiver.

*Parts of this Chapter were published as a contribution in the *Proceedings SPIE*, 21-25 Jun., Glasgow, Scotland, United Kingdom, (2004), J. W. Kooi, A. Kovács, B. Bumble, G. Chattopadhyay, M. L. Edgar, S. Kaye, R. LeDuc, J. Zmuidzinas, and T. G. Phillips, with the 2SB section submitted for publication to the *IEEE Trans. Microwave Theory and Techniques* in August (2008), F. P. Mena, J. W. Kooi, A. M. Baryshev, C. F. J. Lodewijk, R. Hesper, G. Gerlofsma, T. M. Klapwijk, and W. Wild.

It is to operate in the 280 – 420 GHz atmospheric window, and has as science goal the study and redshift determination of molecular CO and ionized carbon (C^+) in distant galaxies. As a backend correlator, we anticipate the use of WASP [3, 4], a 16 MHz/channel analog spectrometer from the University of Maryland, although an AOS [5] or FFTS [6] is also possible. The balanced- and specialized correlation receivers have much of their hardware in common.

The third and last Section of this Chapter covers the theory, design, implementation, and measurement results of a 600 – 720 GHz sideband separation receiver. This mixer development is funded by the instrumentation program of NOVA [7], the Dutch research school for astronomy, and is the first 2SB receiver to operate at such a high frequency.

Sideband separating receivers (2SB) have the advantage of separate signal and image sidebands at the mixer IF port. In practice the sideband ratio of submillimeter receivers rarely exceeds 13 dB; 10 dB being the ALMA specification [8]. There are a variety of reasons for this. Sec. 8.5 addresses these in some detail. What is important to the current discussion is that a limited sideband ratio ($\leq$ 20 dB) is rarely adequate for single dish observations. This is unlike interferometers (ALMA [9], CARMA [10], IRAM [11], SMA [12]...), where signals in the upper and lower sideband can be reconstructed from the spatial phase information contained in the observation. Significant to ground based telescopes, both single dish and interferometer, is a reduction in atmospheric noise when the undesired sideband is properly terminated. The disadvantages of 2SB mixers over balanced receivers are the higher LO power requirement, no immunity to amplitude noise in the local oscillator, and increased complexity.

Someday even more advanced structures such as "balanced sideband separation–" or "dual-polarization balanced sideband separation" mixers may be realized in the submillimeter and terahertz regime, however the complexity of such mixers with today's technology (2008) is prohibitive. For such mixers to be successful a more integrated approach then taken in this thesis will be needed. For extended line sources, a good alternative to the use of sideband separating–, or balanced sideband separating mixers, is the multi-pixel double sideband focal plane array of Chap. 9. Even though for ground based instruments the per pixel sensitivity is less than the more complex (balanced) sideband separating receiver, the large number of pixels provides the speed necessary to map extended astronomical sources. And as an added benefit, arrays receivers provide a means of correcting for correlated sky noise.

8.2 Balanced mixer theory

In this Section we review the balanced mixer theory, and how this results in a reduction in sensitivity to local oscillator amplitude noise. In principle, a single balanced mixer can be formed by connecting two reverse biased mixers to a 180° or 90° input hybrid, as shown in the top and bottom panels of Fig. 8.1.
Quantitatively, we can use an exponential to describe the non-linearity of a diode mixer [13]. It should be noted that SIS tunnel diodes have very sharp I/V curves when compared to Schottky diodes, and can by their quantum mechanical nature exhibit unity or even positive gain (Sec. 4.1). However, in principle this ought not

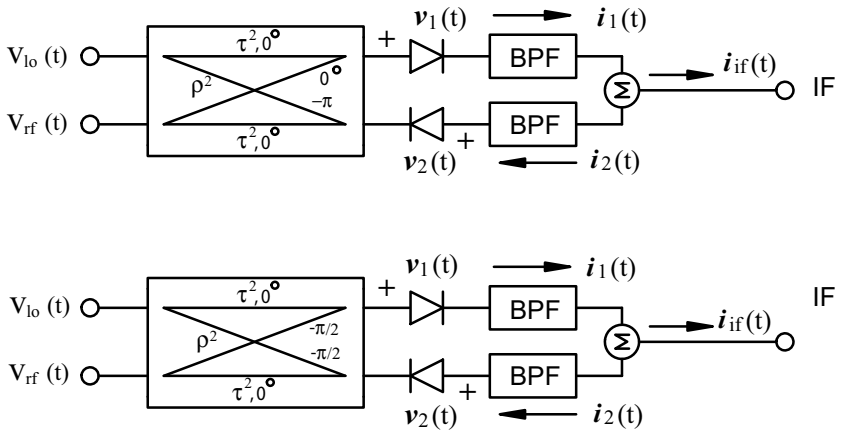

Figure 8.1: LO and RF currents in a single (2-diode) balanced mixer. In practice, the summing node in the IF can be implemented with a Wilkinson [14] in-phase power combiner or 180° IF hybrid. In our design, all IF circuitry is planar and has been designed using Ansoft's 3D electromagnetic simulator (HFSS). In the case of the CSO mixers, the band pass filter (BPF) is 3 – 9 GHz. *Top*) 180° RF input hybrid. *Bottom*) 90° RF input hybrid.

to make a difference in the fundamental performance of the balanced mixer under discussion. Using a polynomial series to represent the exponential current i_1 through diode 1 we find

$$i_1(t) = a_0 + a_1 v_1(t) + \frac{a_2 v_1(t)^2}{2!} + \frac{a_3 v_1(t)^3}{3!} \cdots = \sum_{n=0}^{\infty} \frac{a_n v_1(t)^n}{n!}. \tag{8.1}$$

Because the voltage across diode 2 is reversed from diode 1, e.g. $v_2(t) = -v_1(t)$, we obtain

$$i_2(t) = b_0 - b_1 v_2(t) + \frac{b_2 v_2(t)^2}{2!} - \frac{b_3 v_2(t)^3}{3!} \cdots = \sum_{n=0}^{\infty} (-1)^n \frac{b_n v_2(t)^n}{n!}. \tag{8.2}$$

Here the terms a_n and b_n represent the mixer conversion gain (magnitude, not power). From Eqs. 8.1 & 8.2 we observe that the term n=0 yields the dc component, n=1 the fundamentals, n=2 the second order difference and product terms, and n=3 the harmonic and intermodulation products. Due to the device capacitance in submillimeter or terahertz mixers, the intermodulation product may be ignored. It is nevertheless interesting to consider the effect from a theoretical point of view. It should also be noted from (8.1) and (8.2) that the product terms decrease by $n!$. Thus we will not consider the fourth order term. In our calculations the phase and differential gain in the upper and lower sidebands are assumed equal, and are represented by the general term ω_{rf}.

8.2.1 The 180° balanced mixer

In the case of a 180° input hybrid we find

$$v_1(t) = \left[\rho V_{rf} \cdot e^{i\omega_{rf}t} + \tau V_{lo} \cdot e^{im\omega_{lo}t}\right], \qquad \rightarrow \rightarrow \tag{8.3}$$

where V_{rf} and V_{lo} are the magnitudes of the RF and LO input signal, and m the LO harmonics $1, 2, 3....$ In the equations, zero phase is indicated by a right arrow. The voltage across diode 2 is seen as

$$v_2(t) = \left[\tau V_{rf} \cdot e^{i\omega_{rf}t} - \rho V_{lo} \cdot e^{im\omega_{lo}t}\right]. \qquad \rightarrow \leftarrow \tag{8.4}$$

Defining the power transmission and coupling terms of a hybrid coupler as ρ^2 and τ^2, then for an ideal hybrid τ^2, $\rho^2 = 1/2$ and $\tau^2 + \rho^2 = 1$ so that energy is conserved. In the case of a non-ideal hybrid (Secs. 8.2.2 & 8.2.4) we define the power imbalance as $G_h = (\rho/\tau)^2$.

At the summing node (ignoring device capacitance and IF bandpass filter) the IF current is

$$i_{if}(t) = i_1(t) - i_2(t). \tag{8.5}$$

Assuming an ideal hybrid (G_h=1), and substituting Eq. 8.3 into 8.1 and Eq. 8.4 into 8.2, while solving for i_{if}(t) under the assumption that the mixer gain terms $a_n \equiv b_n$, we find for a perfectly balanced mixer, with an 180° input hybrid that,

$$i_{if}(t) = \begin{cases} a_1 V_{rf} \cdot e^{i\omega_{rf}t} + \\ \frac{a_2}{2!}[V_{rf} V_{lo} \cdot e^{i\omega_{rf}t} \cdot e^{im\omega_{lo}t}] + \\ \frac{a_3}{4 \cdot 3!}[V_{rf}^3 \cdot e^{i3\omega_{rf}t} + 3V_{rf}V_{lo}^2 \cdot e^{i(\omega_{rf}+2m\omega_{lo})t}]. \end{cases} \tag{8.6}$$

The first term is the RF signal, which is deeply embedded in noise for radio-astronomy receivers. The second (product) term yields the sum and difference frequencies of the RF and LO signal, e.g. the IF. The third term is found to yield the RF third harmonic and intermodulation component ($2m\nu_{lo} \pm \nu_{rf}$, $m = 1, 2, 3, ...$). Note that the intermodulation component is not entirely eliminated in the case of a single balanced mixer. Of course for submillimeter or terahertz mixers all but the difference product terms are negligible due to inherent device capacitance.

8.2.2 Amplitude noise immunity of a 180° balanced mixer

Consider an amplitude modulated noise signal superimposed on the LO signal such that

$$V'_{lo}(t) = (V_{lo} + V_n(t)) \cdot e^{i(\omega_{lo})t} \ , \quad V_n(t) \ll V_{lo} \ . \tag{8.7}$$

In this case at the output of an ideal 180° hybrid ($\rho, \tau = 1/\sqrt{2}$) we obtain the following voltages,

$$v_1(t) = \frac{1}{\sqrt{2}}\left[V_{rf} \cdot e^{i\omega_{rf}t} + (V_{lo} + V_n(t)) \cdot e^{i\omega_{lo}t}\right], \qquad \rightarrow \rightarrow \tag{8.8}$$

and

$$v_2(t) = \frac{1}{\sqrt{2}}\left[V_{rf} \cdot e^{i\omega_{rf}t} - (V_{lo} + V_n(t)) \cdot e^{i\omega_{lo}t}\right], \qquad \rightarrow \leftarrow \tag{8.9}$$

Substituting $v_1(t)$ and $v_2(t)$ in Eqs. 8.1 & 8.2, and solving for $i_{if}(t)$ (Eq. 8.5) with ideal mixer gain terms $a_n \equiv b_n$, we again find the IF current

$$i_{if}(t) = \begin{cases} a_1 V_{rf} \cdot e^{i\omega_{rf}t} + \\ \frac{a_2}{2!}\left[(V_{rf}V_{lo} + V_{rf}V_n(t)) \cdot e^{i\omega_{rf}t} \cdot e^{i\omega_{lo}t}\right] \\ \frac{a_3}{4\cdot 3!}\left[V_{rf}^3 \cdot e^{i3\omega_{rf}t} + 3\big(V_{rf}V_{lo}^2 + 2V_{rf}V_{lo}V_n(t) + V_{rf}V_n^2(t)\big) \cdot e^{i(\omega_{rf}+2\omega_{lo})t}\right] . \end{cases} \tag{8.10}$$

The first term of Eq. 8.10 has no $V_{lo}(t)$ component. The third term includes the intermodulation product $V_{rf}V_{lo}^2$ which is ~ 0 in the submillimeter. In the second product term $V_{rf}V_{lo} \gg V_{rf}V_n(t)$, and

$$\frac{a_2}{2!}V_{rf}V_n(t)\cos(|(\omega_{lo} - \omega_{rf})t|) \sim 0 . \tag{8.11}$$

We see that amplitude noise in the local oscillator has minimal effect on the IF output. Of course, a perfect balanced mixer does not exist, especially in the submillimeter or terahertz regime. Hence it is constructive to analyze the response for a "non-ideal" case.

Consider a balanced mixer with unequal gain and phase response. In general, gain imbalance at the IF summing node results from imbalance in the hybrid ($\sqrt{G_h}$) and imbalance in the conversion gain (a_2, b_2) between the two mixer elements (for example non-identical I/V curves). The phase error in each leg of the RF hybrid may be taken into account by φ_1 and φ_2. In this way the hybrid phase error $\Delta\varphi = \varphi_2$-$\varphi_2$. It is easily seen (see for instance Fig. 8.6b) that the mounting accuracy of the individual mixer chips is liable to introduce a larger phase error than the RF or IF hybrid. Given an unbalanced RF hybrid we find,

$$v_1(t) = \rho V_{rf} \cdot e^{i\omega_{rf}t} + \tau(V_{lo} + V_n(t)) \cdot e^{i(\omega_{lo}t - \varphi_1)}, \qquad \rightarrow \rightarrow \tag{8.12}$$

and

$$v_2(t) = \rho V_{rf} \cdot e^{i\omega_{rf}t} - \tau(V_{lo} + V_n(t)) \cdot e^{i(\omega_{lo}t - \varphi_2)}, \qquad \rightarrow \rightarrow \tag{8.13}$$

Calculating the product term for $i_{if}(t) = i_1(t) - i_2(t)$ while normalizing to b_2 with $V_n(t) \ll V_{lo}$ gives

$$i_{if}(t) = \frac{a_2}{b_2}\sqrt{G_h}\cos(\Delta\varphi) \cdot V_{lo}V_{rf}\cos(|(\omega_{lo} - \omega_{rf})t|). \tag{8.14}$$

$\Delta\varphi$ may now be generalized to include the device and wirebond contact phase errors. Let G_m be the mixer gain imbalance $(a_2/b_2)^2$, the noise rejection of a balanced mixer can then be defined as

$$NR = 20 \cdot log\Big[1 - \sqrt{G_m G_h}\cos(\Delta\varphi)\Big]. \tag{8.15}$$

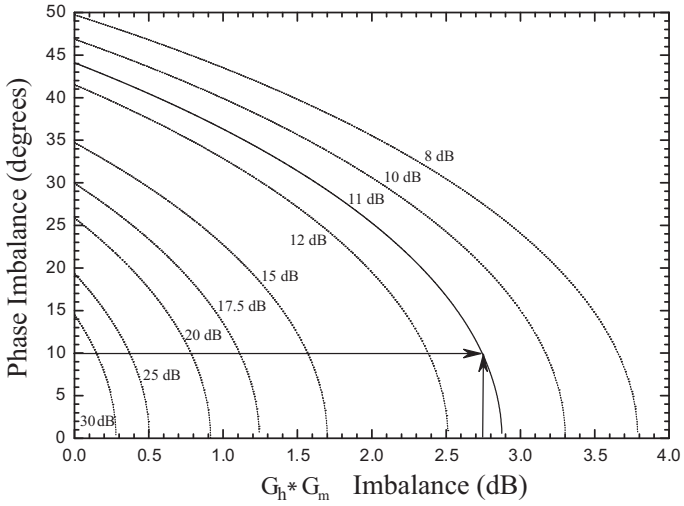

Figure 8.2: Amplitude rejection of the single balanced-input mixer. Imbalance in the IF backend (Sec. 8.3.2) is not included in this plot. This may however be included as part of G_m in Eq. 8.25. Given a RF hybrid imbalance of 1.25 dB, mixer gain imbalance of 1.5 dB and a differential phase error of 10°, we expect a 11 dB reduction amplitude noise from the LO port. These values are representative of what can be expected in a realized mixer (Sec. 8.3).

If, for example, in a realistic scenario, the imbalance in the 180° hybrid is 1.25 dB ($\sqrt{G_h}$=0.866), the mixer conversion gain imbalance 1.5 dB ($\sqrt{G_m}$=0.841), and the overall phase error at the summing node 10 degrees, then the amplitude noise rejection of the single balanced mixer will be $\approx$ 11 dB (Fig. 8.2).

8.2.3 The 90° balanced mixer

Balanced mixers based on 180° input hybrid circuitry have certain advantages over quadrature-hybrid (90°) balanced mixers. The most important characteristics are better LO-RF isolation and improved harmonic intermodulation product suppression. In the case of a 90° hybrid the RF/LO port isolation may be seen to depend critically on the mixer input reflection coefficient. For SIS mixers this is usually rather poor, typically $\leq$ -8 dB (Sec. 7.2.2). Unfortunately, 180° hybrids are large (Rat-race baluns or waveguide magic Tee's) and difficult to fabricate at frequencies above a few hundred GHz. The analysis presented here evaluates the quadrature 2-diode single balanced mixer. Following a similar treatment to that of the 180° input hybrid, we define the RF and LO voltages at the input of the quadrature-hybrid as (Fig. 8.1).

$$V_{lo}(t) = V_{lo} \cdot e^{i(m\omega_{lo}t - \pi/2)}, \tag{8.16}$$

and

$$V_{rf}(t) = V_{rf} \cdot e^{i\omega_{rf}t}. \tag{8.17}$$

For mathematical simplicity, we use an arbitrary LO phase of $-\pi/2$. Voltages at the output of an ideal quadrature hybrid with $\rho, \tau = 1/\sqrt{2}$ are thus found as

$$v_1(t) = \frac{1}{\sqrt{2}}\left[V_{lo} \cdot e^{i(m\omega_{lo}t - \pi/2)} + V_{rf} \cdot e^{i(\omega_{rf}t - \pi/2)}\right], \qquad \downarrow\downarrow \tag{8.18}$$

and

$$v_2(t) = \frac{1}{\sqrt{2}}\left[V_{lo} \cdot e^{i(m\omega_{lo}t - \pi)} + V_{rf} \cdot e^{i\omega_{rf}t}\right]. \qquad \leftarrow\rightarrow \tag{8.19}$$

where m represents the LO harmonics $1, 2, 3....$ Note that in $v_1(t)$ the LO and RF voltages are in phase, whereas in $v_2(t)$ the LO and RF voltages are 180° out of phase, as would be expected. Substituting Eqs. 8.18 & 8.19 into Eqs. 8.1 & 8.2, and summing the IF currents, as in Eq. 8.5, yields

$$i_{if}(t) = \begin{cases} \frac{a_1}{\sqrt{2}}\left[V_{rf} \cdot e^{i(\omega_{rf}t - \pi/4)} - V_{lo} \cdot e^{i(m\omega_{lo}t + \pi/4)}\right] + \\ \frac{a_2}{2!}\left[V_{lo}V_{rf} \cdot e^{im\omega_{lo}t} \cdot e^{i\omega_{rf}t}\right] + \\ \frac{a_3}{\sqrt{2}e^{i\pi/4}8\cdot 3!}\left[V_{rf}^3 e^{i3\omega_{rf}t} + 3V_{lo}^2 V_{rf} e^{i(2m\omega_{lo}+\omega_{rf})t} - 3iV_{lo}V_{rf}^2 e^{i(2\omega_{rf}+m\omega_{lo})t} - \right. \\ \left. iV_{lo}^3 e^{i3\omega_{lo}t}\right]. \end{cases} \tag{8.20}$$

As before, the fundamental, harmonic, and intermodulation products are severely attenuated by the inherent device capacitance of the submillimeter or terahertz mixing element. It is, however, constructive to observe the difference between the 180° and 90° hybrid balanced mixers. In general, the 180° balanced mixer has superior fundamental and intermodulation product suppression capabilities, which explains the popularity of the 180° hybrid at microwave frequencies. However at frequencies $\gg$ 100 GHz this advantage is greatly reduced. For this reason, submillimeter or terahertz mixers may be configured with quadrature hybrids, rather than the larger and more complex 180° hybrids. Of special interest is the second order term in Eq. 8.20. By taking the real part with $m = 1$, it follows that the IF current simplifies to

$$i_{if}(t) = \frac{a_2}{2!}V_{lo}V_{rf}\cos(|(\omega_{lo} - \omega_{rf})t|). \tag{8.21}$$

a_2 represents the system gain assuming that the hybrid and mixers are perfectly balanced. This is the same result as obtained in the case for the 180° balanced mixer (Eq. 8.6)!

8.2.4 Amplitude noise immunity of a 90° balanced mixer

Again, consider an amplitude modulated (noise) signal (Eq. 8.7) incident on the LO port of an ideal 90° hybrid. The output of the hybrid with $\rho, \tau = 1/\sqrt{2}$ yields

$$v_1(t) = \frac{1}{\sqrt{2}}\left[V_{rf} \cdot e^{i(\omega_{rf}t - \pi/2)} + (V_{lo} + V_n(t)) \cdot e^{i(\omega_{lo}t - \pi/2)}\right], \qquad \downarrow\downarrow \tag{8.22}$$

and

$$v_2(t) = \frac{1}{\sqrt{2}}\left[V_{rf} \cdot e^{i\omega_{rf}t} + (V_{lo} + V_n(t)) \cdot e^{i(\omega_{lo}t - \pi)}\right], \qquad \leftarrow\leftarrow \tag{8.23}$$

Substituting $v_1(t)$ and $v_2(t)$ into Eqs. 8.1 & 8.2, and solving for i_{if}(t) with $a_n \equiv b_n$, we find

$$i_{if}(t) = \begin{cases} \frac{a_1}{\sqrt{2}}\left[V_{rf} \cdot e^{i(\omega_{rf}t - \pi/4)} - (V_{lo} + V_n(t)) \cdot e^{i(\omega_{lo}t + \pi/4)}\right] + \\ \frac{a_2}{2!}\left[(V_{rf}V_{lo} + V_{rf}V_n(t)) \cdot e^{i\omega_{rf}t} \cdot e^{i\omega_{lo}t}\right] + \\ \frac{a_3 e^{-i\pi/4}}{\sqrt{2}} 8{\cdot}3!\left[V_{rf}^3 e^{i3\omega_{rf}t} + 3(V_{lo} + V_n(t))^2 V_{rf} e^{i(2\omega_{lo} + \omega_{rf})t} - \right. \\ \left. 3i(V_{lo} + V_n(t))V_{rf}^2 e^{i(2\omega_{rf} + \omega_{lo})t} - i(V_{lo} + V_n(t))^3 e^{i3\omega_{lo}t}\right] . \end{cases} \tag{8.24}$$

Unlike the 180° balanced mixer, the noise in the fundamental and third (odd) order term remains! Fortunately, at submillimeter frequencies these terms vanish due to the inherent device capacitance of the mixer and IF band pass filter (Fig. 8.1).

As with the 180° balanced mixer, an ideal 90° balanced mixer does not exist, especially in the submillimeter or terahertz regime. Hence, it is constructive to analyze the response for a non-perfect scenario. Following a similar analysis as for the 180° balanced mixer, we write $v_1(t)$ and $v_2(t)$ to include unequal hybrid gain ($\sqrt{G_h}$), mixer conversion gain (a_2/b_2), and phase imbalance $\Delta\varphi$. After the band pass filter (BPF) and summing node we again find the reduction in amplitude noise at the IF as,

$$NR = 20 \cdot log\left[1 - \sqrt{G_h G_m}\cos(\Delta\varphi)\right]. \tag{8.25}$$

The balanced mixer noise reduction as a function of gain and phase imbalance is graphically presented in Fig. 8.2.

8.3 Realization of 90° balanced-input receivers

The balanced receivers proposed for the CSO are implemented in (tunerless) full height waveguide [15] to minimize RF loss and fabrication difficulties. As shown graphically in Fig 8.3, four frequency bands are used to cover the entire 180 – 720 GHz atmospheric window. The balanced mixers will reside in two cryostats, one of which will house the 180 – 280 GHz and 380 – 520 GHz balanced mixers, the other the 280 – 420 GHz and 580 – 720 GHz balanced mixers [16].

To supply the needed LO pump power, planar multiplier sources [17] are mounted inside the cryostat and connected to the 15 K stage. This has the advantage of a ≈ 50 % increase in available LO power over multipliers that operate at room temperature. It also reduces complexity in the optics, improves reliability of the multipliers, and reduces thermal noise. We calculate [18] that each SIS junction requires roughly $\frac{1}{2}$ μW of pump power (α=$eV_{lo}/h\nu \approx 0.7$ on average). Because two SIS junctions are used in a single balanced mixer configuration, we require ~ 1 μW of LO pump power at the mixer LO input port. In reality the LO power requirement is slightly higher due to Ohmic loss in the waveguide (Sec. 5.1). Since the cooled multipliers are able to produce ample LO power over the described frequency bands, it is necessary to add attenuation in the LO-mixer path. In practice, this can be accomplished

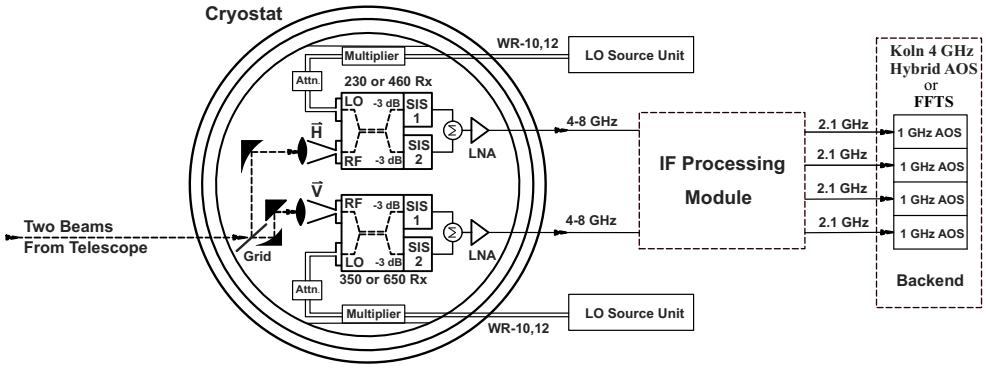

Cryostat 1: 180-280 GHz, 380-520 GHz
Cryostat 2: 280-420 GHz, 580-720 GHz

Figure 8.3: Block diagram of the CSO facility instrumentation upgrade to balanced receivers. Only one of the two cryostats is shown. The LO source signal (63 – 105 GHz) enters the cryostat via an Au plated stainless steel waveguide. The tunerless multipliers [17] are mounted on the 15 K stage of a hybrid cryostat. This has the advantage of simplifying LO injection, and increasing the overall reliability. The LO signals enter the balanced mixers via a cold fixed tuned attenuator. This is necessary to reduce LO power at the mixer to ~ 1 μW. It also minimizes standing waves between the mixer and multiplier and thermal noise from the LO. Each cryostat receives two (orthogonally polarized) beams from the sky, which are routed via a cold wire-grid to the appropriate mixer (Fig. 8.4). This technique facilitates dual frequency (2 color) observations, which improves observing efficiency and assists pointing of the high frequency receivers in mediocre weather.

with a directional coupler or fixed tuned (preset) attenuator. A preset attenuator has the advantage of being simple, relatively inexpensive, and if necessary manually adjustable at room temperature. The effect of employing a cooled attenuator is similar to the use of a beamsplitter with quasi-optical LO injection (Fig 8.16); it reduces the multiplier-mixer cavity standing wave, and lowers the injected thermal noise from the local oscillator. Additional reduction in LO amplitude and spurious noise is provided by the "noise canceling properties" of the balanced mixer as observed from Eq. 8.25. Assuming a (calculated) amplitude noise rejection of 11 dB (Sec. 8.2.2) we estimate that a phase locked Gunn oscillator/multiplier LO source has an amplitude noise contribution of a mere 0.1 K. The use of a synthesized source is likely to increase this by a few Kelvin (or less), still a very small fraction of the overall receiver noise budget. In Fig. 8.4 we show a rendering of the 230 GHz and 460 GHz balanced mixer, LO hardware, and optical components on the 4 K work surface.

8.3.1 Improved quadrature-hybrid waveguide coupler

As was seen, the balanced (and correlation, Sec. 8.4) receiver requires either a 180° or 90° phase shift between the two mixer ports. Due to ease of fabrication, we use a 90° branch line waveguide coupler. The design is a modification from the narrower bandwidth split block version, developed for the Atacama Large Millimeter Array (ALMA) [9] by Claude and Cunningham *et al.* [19]. Design and optimization of the wideband quadrature-hybrid coupler were done in HFSS [20]. From 280 – 420 GHz,

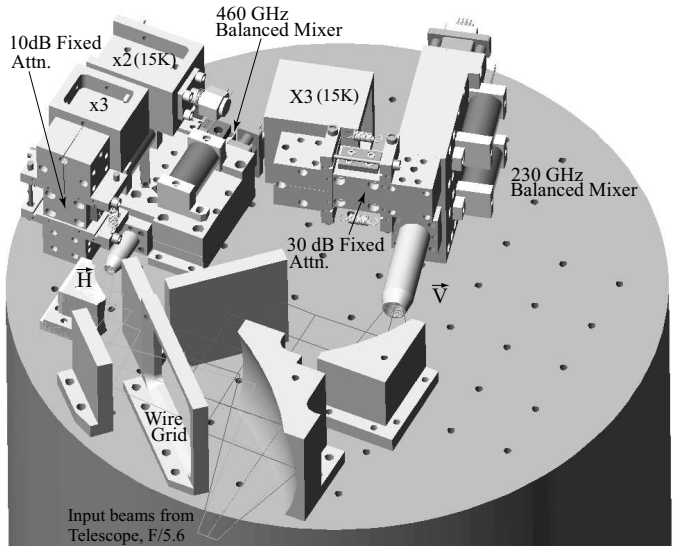

Figure 8.4: Rendering of the 230/460 GHz precision-cryogenics [21] hybrid cryostat with 230 GHz and 460 GHz balanced mixer blocks, multiplier hardware and associated optics. All hardware is manufactured, and currently awaits final assembly and testing. The first balanced receiver cryostat is expected to be installed at the observatory [2] in late 2009.

the coupled power imbalance is 0 ± 0.75 dB, while the predicted phase imbalance is less than $90 \pm 2°$. Design parameters are compiled in Table 8.1, and the predicted performance is shown in Fig. 8.6.

In order to achieve the required bandwidth, phase, and coupling, it was necessary to maximize the number of branches (n). Analyzing the computer simulation results we realized that

$$n * S = \frac{\lambda_g}{2} \quad \& \quad W = \frac{\lambda_o}{4} \ , \tag{8.26}$$

where n denotes the number of coupling sections.

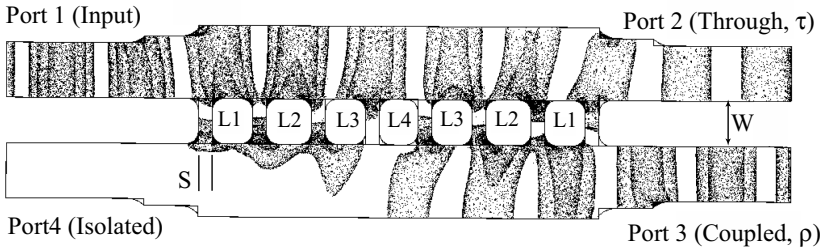

Figure 8.5: Electric field distribution in the quadrature waveguide coupler. The phase difference between port 2 and 3 is $90 \pm 1.5°$. S sets the coupling, and W the center frequency.

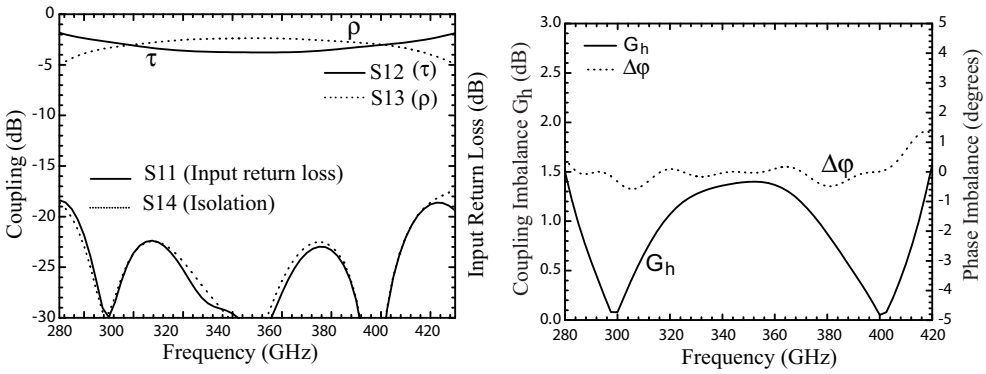

Figure 8.6: *Left*) Predicted coupling performance of the 90° hybrid. τ and ρ are defined as in Eq. 8.3. *Right*) Phase and power imbalance of the quadrature-hybrid coupler, $20{\cdot}\log(\rho/\tau)$.

In order to achieve a practical mechanical design we decided, after consultation with Custom Microwave Inc. [22], to fix the width of the branch (air) lines to ≈ 74 μm. This then determined the number of coupler branches for each frequency band. To maximize S, the width of the waveguide (b-dimension) inside the coupler has been increased by a 32.5 %. Increasing the waveguide width beyond this excites the TE_{01} mode, thereby degrading the high frequency performance of the coupler. The separation of the two waveguides is $\lambda_o/4$, as measured at the center of the band.

Table 8.1: Hybrid coupler parameters used in Fig. 8.6. S denotes the branch line width, L the length between the branch lines, and W the separation between the two waveguides.

a-dim (μm)	b-dim (μm)	S (μm)	L1 (μm)	L2 (μm)	L3 (μm)	L4 (μm)	W (μm)
680	270	74	205	231	205	190	203

8.3.2 Integrated IF and Wilkinson in-phase power combiner

In a mixer configuration, the active device is terminated into a desired IF load impedance (Sec. 4.1.10), the bias lines EMI filtered and injected via a bias Tee, and the IF output dc-isolated such as shown in Fig. 8.7.

Electrical isolation of the IF output is usually accomplished with a small series capacitor, by means of either a soldered contact or with wire bonds. Unfortunately, the series resonance of physical capacitors are, by design, often located near the upper edge of the IF band. Moreover, since the dc-blocking capacitor passes the mixer IF output, failure results in a complete loss of signal. Indeed, component failure can occur in many ways. This is most likely due to stress from repeated thermal cycling.

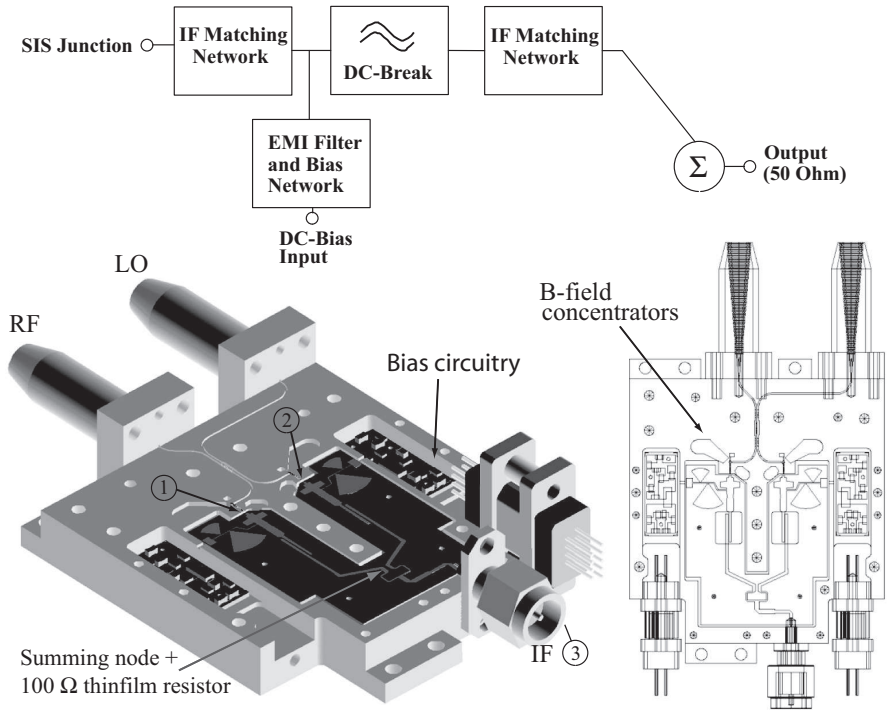

Figure 8.7: Balanced mixer block layout. The IF board is entirely planar by design, and combines the IF match, dc-break, bias Tee, EMI filter, and Wilkinson power combiner. The E-field component of the incoming signal is horizontally polarized along the waveguide split. Josephson noise suppression in the SIS tunnel junctions is accomplished by independently (not shown) adjusted magnetic fields.

As an alternative approach, we investigate the use of parallel coupled suspended microstrip lines as a compact bandpass filter [23, 24, 25], Fig. 8.8. For this filter to work, the ground plane directly underneath the filter has been removed, and the IF board positioned on top of a machined cutout (resonant cavity). There are several discontinuities in this structure. When combined, they form the bandpass filter poles. The advantages are, simplicity of design (only one lithography step), accurate

Table 8.2: Coupling parameters of the dc-break shown in Fig. 8.8. H_{sub} denotes the substrate height, W the width of the coupled lines, L their length, S the spacing, H_{cav} the cavity depth, H_{air} the air height above the substrate, L_c the cavity length, and W_c the cavity width. The center frequency is 6 GHz.

Substrate	ε_r	H_{sub} (μm)	W (μm)	L (mm)	S (μm)	H_{cav} (μm)	H_{air} (mm)	W_c x L_c (mm)
Alumina	9.90	635	480	5.72	120	585	2.5	5.08 x 6.1

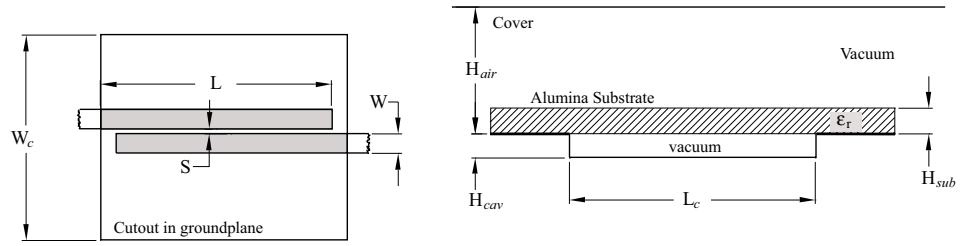

Figure 8.8: Schematic layout of the parallel coupled suspended microstrip lines The design parameters are compiled in Table 8.2 with actual implementation depicted in Fig. 8.7.

knowledge of the phase, and improved reliability. The disadvantage is its size, $\lambda_g/4$ ($\sim$ 6 mm at 6 GHz), and octave bandwidth.

Details of the blocking filter are summarized in Table 8.2. The spacing S, and cavity depth HC set the coupling. The tolerance values should be held to $\pm$ 5 %. In the balanced mixer design the SIS junctions are biased, thanks to symmetry in the I/V curves, in opposite polarity (Fig. 8.1). This has the advantage that the IF currents may be summed in phase, which is readily achieved with an in phase Wilkinson power combiner [14]. The design presented in Fig. 8.7 is entirely planar, the only component being a 100 Ohm thin-film balancing resistor. This is a 1 % laser trimmed NiCr resistor, fabricated directly onto the alumina IF circuit board [26]. In

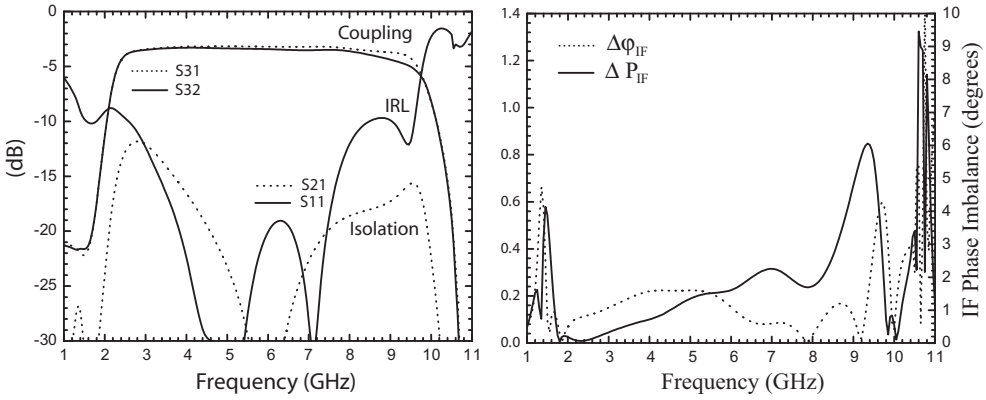

Figure 8.9: *Left*) Coupled power from the IF board (SIS) input ports 1 & 2, Fig. 8.7, to the IF output port (3). By design, terminating port 3 into 50 Ω provides a 20 Ω impedance at ports 1 & 2. The impedance at these ports is on purpose kept low (20 Ω) to minimize noise saturation in the SIS tunnel junctions. The termination impedance presented to the actual SIS junctions is 14 Ω or $\sim$ 2.7 R_n (Fig. 4.8, Sec. 7.2.2). The available IF bandwidth is 3 – 9 GHz, well in excess of the planned 4 – 8 GHz intermediate frequency. The calculated isolation between the two junction ports is $\sim$ 20 dB. It should be noted that the isolation is quite critically dependent on the quality of the 100 Ω balancing (thin film) resistor in the Wilkinson bridge. *Right*) Simulated IF power and phase imbalance. ΔP_{IF}, $\Delta\varphi_{IF}$ are $\leq$ 0.4 dB and 1.5° respective.

the design, we have made extensive use of HFSS [20], a 3-D electromagnetic field circuit simulator. The most important performance curves are depicted in Fig. 8.9.

8.3.3 SIS Junctions with integrated IF matching

As outlined in Sec. 7.2.2, the use of high current density junctions increases the instantaneous RF bandwidth of the mixer, and minimizes the effect of absorption loss in the normal and superconducting films of the front-end matching network (Chap. 5).

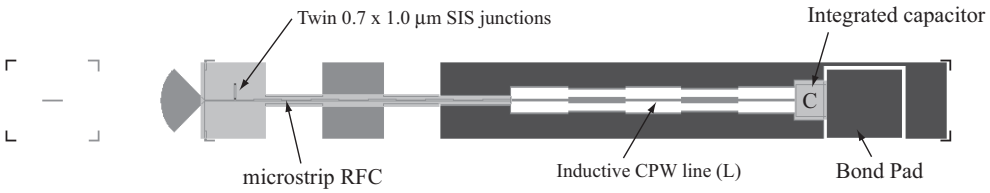

Figure 8.10: 350 GHz junction layout. The radial probe waveguide antenna is visible on the left side. The IF is taken out via a microstrip RF choke (on 300 nm SiO, ε_r=5.6) which connects to a high impedance CPW transmission line (inductive) and shunt capacitor. This LC mechanism provides a π tuning network with the combined capacitance of the probe, twin junction RF tuning structure, and microstrip RF choke. The IF passband of mixers under discussion has been optimized to cover 1 – 13 GHz (Fig. 8.11d).

Circuit designs of high current density niobium SIS junctions (4 bands) were submitted to JPL in spring 2003 for fabrication. Since that time the devices has been fabricated, lapped and diced [27]. The new SIS tunnel junctions all share the same 50 μm thick quartz wafer. The junction design employs twin SIS junctions with AlN barriers and a R_nA product of 7.6 $\Omega \cdot \mu m^2$ (J_c=25 kA/cm^2 current density). Supermix [18], a flexible software library for high-frequency superconducting circuit simulation has been used exclusively in the design process. The predicted balanced mixer results are derived from harmonic balanced superconducting SIS mixer simulations in combination with extensive 2.5D (Sonnet [28]) and 3D em-field (HFSS [20]) analysis of the RF and IF mixer circuitry. This may well be the first time that a superconducting mixer of this complexity has been simulated in its entirety. Both RF and IF matching is realized on chip, yielding a theoretically flat IF response to 13 GHz. All designs have been optimized for maximal conversion gain and minimal noise temperatures across the respective bands (Fig. 8.12). For a more details description of the RF and IF design, please refer to Secs. 7.2.2 & 7.3.3.

8.3.4 Predicted performance

In Fig. 8.11a we show the calculated performance [29] of three typical LO unpumped I/V curves from AlN-barrier wafer B030926 [30]. The junction characteristics are reasonably well matched, with slight variations in the definition of the energy gap and device area, effecting the mixer gain performance (Fig. 8.11b, c). The gap voltage though being a bit reduced does not appear to significantly impact the mixer noise performance of the 600 – 720 GHz receiver. In Fig. 8.11b we show the estimated

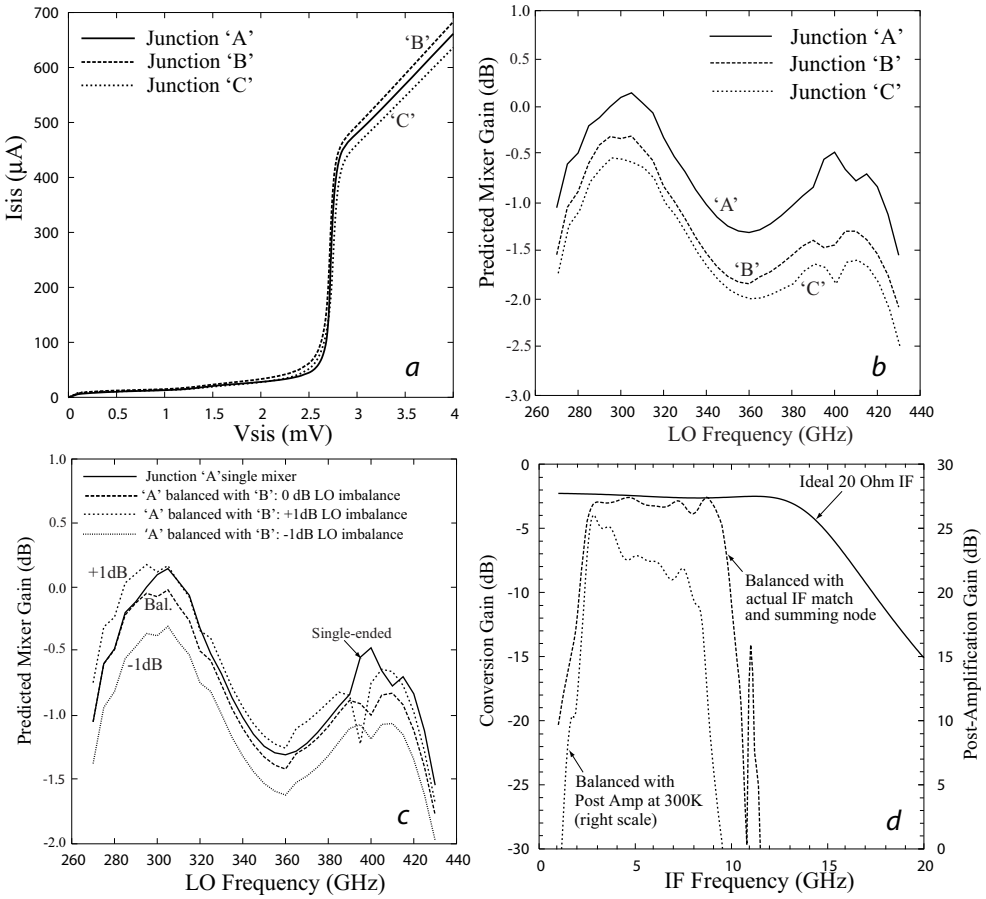

Figure 8.11: *a*) Three typical unpumped I/V curves from batch B030926. *b*) calculated mixer gain for the three devices under identical LO pump level. The effect for the change in I/V curve is approximately 1 dB. *c*) Effect of unbalancing the LO by ± 1 dB on the mixer gain (minimal). *d*) IF coupling and the effect of adding post amplification.

conversion gain with the mixer tuned for optimal noise performance. As expected, junction 'A' with the sharpest gap provides the best conversion gain, and hence the lowest noise temperature. Note that the mixer conversion gain variation among the three junctions is reasonably small (less than 1 dB). Fig. 8.11c shows the predicted mixer gain for a balanced configuration. Since a physically realizable balanced set-up involves the use of two non-identical mixers, the questions arises how much degradation of the mixer gain performance may be expected vs. a single mixer. For reference, the conversion gain of a single mixer is plotted for junction 'A'. We compare this result with the conversion gain of balanced mixer that uses both junctions 'A' and 'B'. A further limitation of the balanced design is that the LO power as a function of frequency is not equally split between the two junctions. This arrangement for a typical ± 1 dB LO pumping imbalance is also shown in Fig. 8.11c.

From this analysis we may conclude that gain imbalance due to 1) device characteristics, and 2) LO power imbalance is not expected to significantly affect the overall balanced mixer performance (Fig. 8.12). This is important since it means that the individual SIS junctions may be biased at the same, but opposite polarity, voltage setting.

Finally, in Fig. 8.11d we shown the expected IF coupling efficiency at a LO frequency of 350 GHz. It is apparent that the SIS junctions produce, in theory, a flat gain from 0 – 13 GHz. This assumes an ideal 20 Ohm termination. In case of the CSO balanced mixers, the specified mixer IF passband is 4 – 8 GHz. The actual receiver IF bandwidth is limited to 3.5 – 8.25 GHz by the cooled isolator [31] and low noise (T_n=2 K) Chalmers University amplifier [32]. When we include the cryostat cable loss and external room temperature IF amplification [33], we see that the bandwidth reduces to 3.5 – 8 GHz with an expected gain slope of approximately -6 dB. This is in good agreement with actual IF measurements on the technology development receiver (Sec. 7.3.3).

In Fig. 8.12, we show the (calculated) balanced receiver and mixer noise temperature from 180 – 720 GHz in 4 waveguide bands. To obtain a realistic estimate for the balanced receiver noise, we used the measured optics losses of the existing CSO

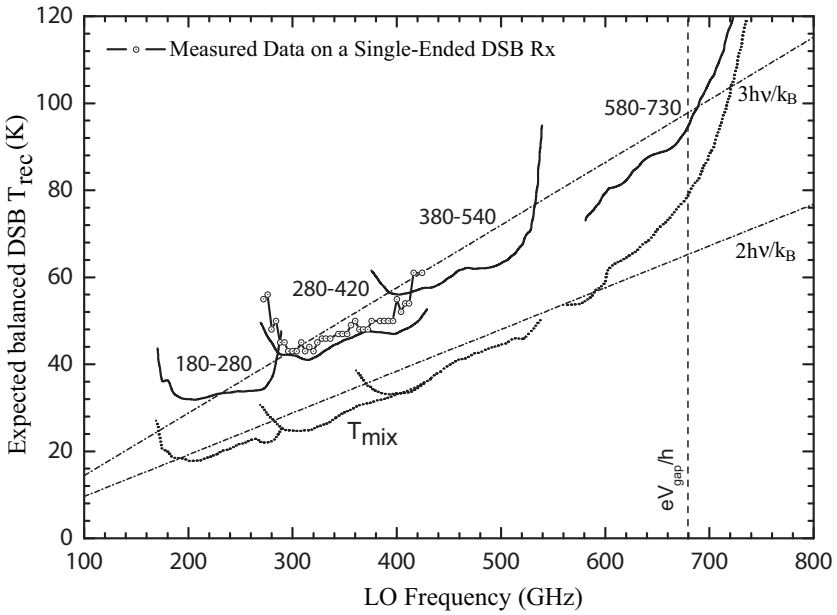

Figure 8.12: Estimated double sideband receiver noise temperatures for the balanced mixers constructed of junctions 'A' and 'B' (see I/V and gain characteristics in Fig. 8.11). The noise estimate was calculated by Supermix [18], and includes the 90° input hybrid, IF-match and summing node, LNA and isolator, and a realistic optics model. The LO noise contribution is negligible due to the noise rejection properties of the balanced mixers (calculated to be ≈ 11 dB), and the fact that the LO is injected via a cooled attenuator. The mixer noise follows the $2h\nu/k_B$ line. This may be used to estimate receiver temperatures for different IF and optics configurations (Eq. 7.6).

receivers minus LO thermal noise. Superimposed in the plot are the measured results of Chap. 7.

To understand how, for a given amount of precipitable water vapor, the balanced receiver noise temperatures of Fig. 8.12 refer to the top of the atmosphere, we follow the procedure outlined in Sec. 8.5.9. The 50 % precipitable water percentile for Mauna Kea is 2 mm, whereas the 25 percentile is 1 mm, and the 75 percentile is 3 mm [34]. The balanced receiver noise temperature in the simulation follows three times the quantum noise limit ($3\ h\nu/k_B$). We find from Fig. 8.13 that for observations above 370 GHz less than 1 mm of precipitable water vapor is permitted between the telescope and space ($\tau_{225\ GHz} \leq 0.064$). This occurs on average $\sim$ 25 % of the time on Mauna Kea.

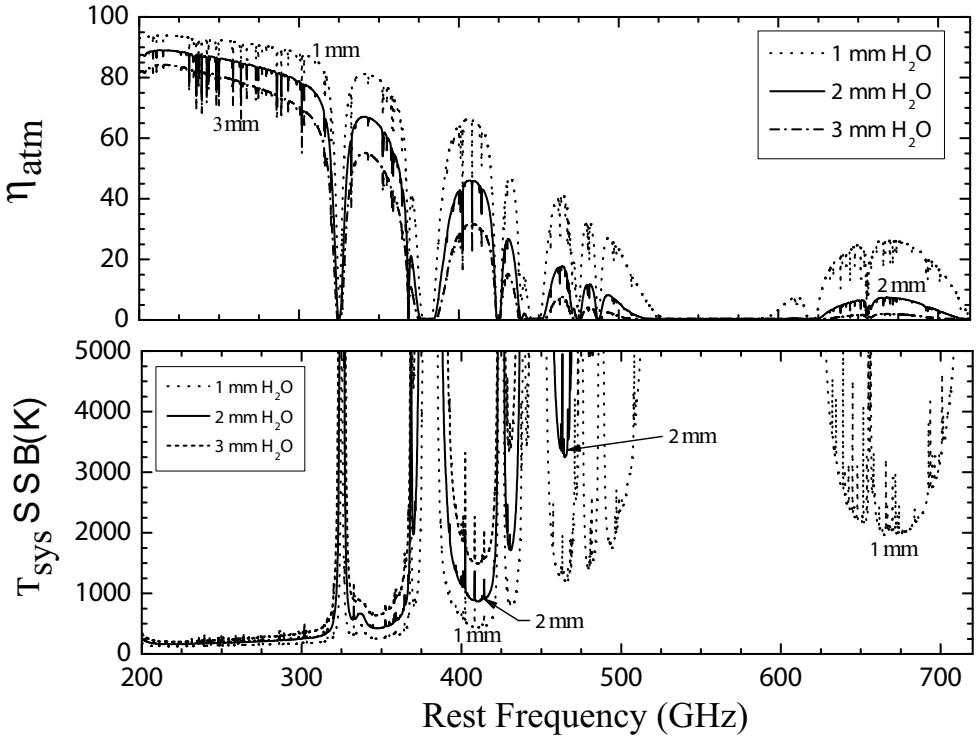

Figure 8.13: *Top*) Atmospheric transmission on Mauna Kea, HI, for 1, 2, and 3 mm precipitable water vapor (pwv). The medium precipitable water vapor for Mauna Kea is $\sim$ 2 mm (S. Radford [34]) which translates into an optical depth (τ) of 0.1 at 225 GHz. The atmospheric transmission is based on a model by J. Pardo *et al.* [35]. Calculations are for 1.1 airmass (65° elevation). *Bottom*) Estimated SSB system temperature as a function of frequency and precipitable water vapor. 1 mm pwv corresponds to a 25 percentile on Mauna Kea.

8.4 The correlation receiver

8.4.1 Introduction

For many distant galaxy projects, an improvement in sensitivity of a factor of 4-6 is needed. For single dish observations this can only be obtained by use of a more sophisticated design. Improving sensitivity is best achieved by constructing a 2-detector receiver with one beam continuously on-source, and one beam continuously off-source. In this manner the two detectors operate in what is known as a correlation or continuous comparison mode (Predmore *et al.* 1985 [36]).

The 280 – 420 GHz continuous comparison (correlation) receiver presented here has two beams on the sky; a signal and reference beam. The signal and reference beams are coupled to two tunerless SIS mixers using only cooled reflecting optics, and a RF quadrature hybrid coupler (Sec. 8.3.1). The IF outputs are after amplification correlated against each other, canceling common mode signals in both channels. This includes gain fluctuations from turbulent atmospheric cells directly above the telescope. In principle, this technique results in flat baselines with white noise that integrates down indefinitely without platforming or baseline distortion. An instrument like this is therefore especially well suited for high redshift extragalactic molecular line identification, and spectroscopy of distant point sources. For the backend correlator, we anticipate the use of WASP [3, 4], a 16 MHz/channel analog spectrometer from the University of Maryland, though an AOS [5] as square law detector may also be used. The balanced mixers described in Sec. 8.2 and the specialized correlation receiver have much of their hardware in common. A block diagram of this design is shown in Fig. 8.14.

8.4.2 Theory

Referring to Fig. 8.14, we start our analysis by considering the two inputs to the continuous comparison, or correlation receiver. Here $V_{in}(t)$ represents the signal from an astronomical source. For terrestrial observations this includes noise and gain fluctuations from the atmosphere. The second input to the comparison, or correlation receiver, is a reference signal $V_{ref}(t)$. This input may be derived from a variable internal cold load (CBB) with a temperature (flux) similar to that of the input signal. While such a scheme may be adequate for space based observations, for ground observations it suffers from excluding the atmosphere from the reference beam. For terrestrial observations it is therefore more appropriate to propagate the reference beam through the telescope and onto the sky, at a small angular offset from the signal beam. For the CSO [1, 2], the field-of-view (FOV) of the telescope is ~ 5 arc-minutes in the Cassegrain focus position. Given physical constraints inside the cryostat (Fig. 8.16) and a plate scale of ($4.6''$/mm) the designed signal-reference beam separation on the sky is $2.15'$. The disadvantage of this approach is that for extended sources, such as molecular clouds, the reference beam will not be entirely off the source.

The correlation mixer signal input beam, $v_1(t)$, thus includes the observed signal $V_s(t)$, some fraction of the cosmic background radiation depending on how much of

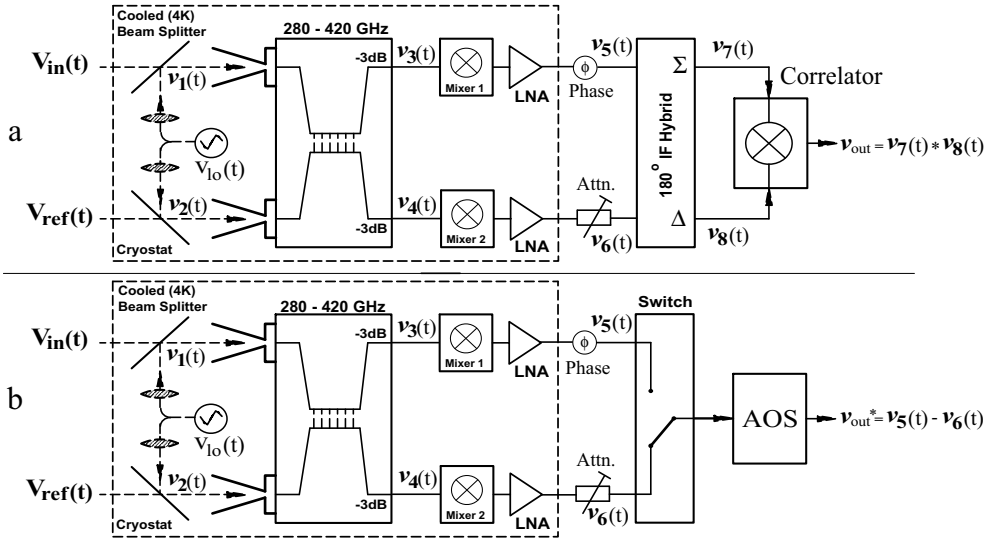

Figure 8.14: Block diagram of a continuous comparison (correlation) receiver. The instrument may be implemented with either a correlator (*a*) or acousto-optical backend spectrometer *b*). Both backend configurations are addressed in Sec. 8.4.2.

the beam is filled by the source, the LO signal $\mathrm{V}_{lo}(\mathrm{t})$, and noise from the atmosphere $\mathrm{V}_{n1}(\mathrm{t})$ of which some fraction is correlated with the reference beam, $\mathrm{V}_c(\mathrm{t})$. The reference input beam, $v_2(t)$, being trained off the source, includes 2.7 K of cosmic background radiation, uncorrelated atmospheric noise $\mathrm{V}_{n2}(\mathrm{t})$, the LO signal $\mathrm{V}_{lo}(\mathrm{t})$, and correlated noise with the signal beam $\mathrm{V}_c(\mathrm{t})$. In the analysis we include the contribution of the cosmic background radiation in $\mathrm{V}_{n1}(\mathrm{t})$ & $\mathrm{V}_{n2}(\mathrm{t})$. Note that in our design (Fig. 8.14) the local oscillator signal is injected quasi-optically in phase. This can also be seen in Fig. 8.16 where we show a rendering of the correlation receiver inside the cryostat. Injecting the LO in-phase has the advantage that common-mode amplitude noise is present in both signal and reference beam, and may thus be included in $\mathrm{V}_c(\mathrm{t})$. Also included in $\mathrm{V}_c(\mathrm{t})$ are correlated gain fluctuations from the atmosphere directly above the telescope, and possible instabilities from the LO standing wave in the telescope. Thus we find that

$$V_{in}(t) = V_s \cdot e^{i\omega_s t} + V_{n1} \cdot e^{i\omega_{n1} t} + V_c \cdot e^{i\omega_c t} \tag{8.27}$$

and

$$V_{ref}(t) = V_{n2} \cdot e^{i\omega_{n2} t} + V_c \cdot e^{i\omega_c t} \ , \tag{8.28}$$

with

$$v_1(t) = V_{in}(t) + \frac{1}{2}V_{lo} \cdot e^{i\omega_{lo}t} \tag{8.29}$$

and

$$v_2(t) = V_{ref}(t) + \frac{1}{2}V_{lo} \cdot e^{i\omega_{lo}t} \ . \tag{8.30}$$

The signal and atmospheric phase is arbitrary and has been set to 0° for convenience. In general the signal is deeply embedded in the combined noise from the atmosphere and mixer. Again referring to Fig. 8.14, we find the voltages after passing the 90° RF hybrid coupler,

$$v_3(t) = \begin{cases} \sqrt{\tau^2+\rho^2}\left[\frac{V_{lo}}{2} \cdot e^{i(\omega_{lo}t-\theta)} + V_c \cdot e^{i(\omega_c t-\theta)}\right] + \\ \tau(V_{n1} \cdot e^{i\omega_{n1}t} + V_s \cdot e^{i\omega_s t}) + i\rho V_{n2} \cdot e^{i\omega_{n2}t} \end{cases} \tag{8.31}$$

and

$$v_4(t) = \begin{cases} \sqrt{\tau^2+\rho^2}\left[\frac{V_{lo}}{2} \cdot e^{i(\omega_{lo}t-\theta)} + V_c \cdot e^{i(\omega_c t-\theta)}\right] + \\ \tau V_{n2} \cdot e^{i\omega_{n2}t} + i\rho(V_{n1} \cdot e^{i\omega_{n1}t} + V_s \cdot e^{i\omega_s t}) \ . \end{cases} \tag{8.32}$$

For a lossless hybrid, $\tau^2 + \rho^2$=1, and $\theta = tan^{-1}(\rho/\tau) \sim 45°$. In general ρ and τ are frequency dependent (Fig. 8.6) and an imbalance results in a phase shift of the local oscillator signal at the mixer input, and down converted IF output. Following a similar treatment to that of the 180° balanced mixer with mixer conversion gain imbalance $G_m = (a_2/b_2)^2$, we obtain the down-converted IF voltages $v_5(t)$ and $v_6(t)$,

$$v_5(t) = a_2 G_{if1}\left[i\tau\sqrt{G_h+1}V_c + \left[\tau(V_{n1}+V_s) + i\rho V_{n2}\right] \cdot e^{-i\theta}\right] \cdot e^{i(\omega_{if}t-\varphi_1-\phi)} \tag{8.33}$$

and

$$v_6(t) = b_2 G_{if2}\left[i\tau\sqrt{G_h+1}V_c + \left[\tau V_{n2} + i\rho(V_{n1}+V_s)\right] \cdot e^{-i\theta}\right] \cdot e^{i(\omega_{if}t-\varphi_2)} \ . \tag{8.34}$$

G_h is defined in Sec. 8.2.1 as the RF hybrid imbalance, $(\rho/\tau)^2$. The difference in IF amplifier gain (G_{if1}/G_{if2}) and IF phase (ϕ) may be removed via external calibration, as shown in Fig. 8.14. The phase difference $\Delta\varphi = \varphi_1$-$\varphi_2$ is attributed to the (frequency dependent) phase error in the 90° RF hybrid (Fig. 8.6).

8.4.2.1 Correlator back-end processor

A digital or analog correlator multiplies two instantaneous IF voltage signals with varying delay. This provides the auto-correlation function in the time domain and, after taking a fast Fourier transform (FFT), a spectrum in the frequency domain. Before doing this multiplication, IF output signals $v_5(t)$ and $v_6(t)$ are routed via a commercial 180° hybrid [37]. This is required to cancel correlated signals from the RF input (V_c). The output voltages of an ideal 180° hybrid are $v_7(t)$=$\frac{1}{2}$[$v_5(t)+v_6(t)$], and $v_8(t)$=$\frac{1}{2}$[$v_5(t) - v_6(t)$]. After normalization to G_h and G_m we obtain,

$$v_7(t) = \begin{cases} \frac{1}{2}\Big[\sqrt{G_m}\big(i\sqrt{G_h+1}V_c + V_{n1} + V_s + i\sqrt{G_h}V_{n2}\big)\cdot e^{i(\omega_{if}t-\theta-\varphi_1)} + \\ \big(i\sqrt{G_h+1}V_c + V_{n2} + i\sqrt{G_h}(V_{n1}+V_s)\big)\cdot e^{i(\omega_{if}t-\theta-\varphi_2)}\Big] \end{cases} \tag{8.35}$$

and

$$v_8(t) = \begin{cases} \frac{1}{2}\Big[\sqrt{G_m}\big(i\sqrt{G_h+1}V_c + V_{n1} + V_s + i\sqrt{G_h}V_{n2}\big)\cdot e^{i(\omega_{if}t-\theta-\varphi_1)} - \\ \big(i\sqrt{G_h+1}V_c + V_{n2} + i\sqrt{G_h}(V_{n1}+V_s)\big)\cdot e^{i(\omega_{if}t-\theta-\varphi_2)}\Big] \end{cases} \tag{8.36}$$

Multiplying Eqs. 8.35 & 8.36 provides $v_{out}(t)$. There are many factors in this product, most of which $\rightarrow 0$ due to multiplication with uncorrelated noise voltages V_{n1} and V_{n2}. The relevant terms are

$$v_{out}(t) \propto \frac{1}{2}\Big[(G_h+G_m)V_s^2 + (1-G_hG_m)V_c^2\Big]\cdot e^{i(\omega_{if}t-2\theta-\Delta\varphi)}\ . \tag{8.37}$$

For an ideal RF input hybrid with $\theta = tan^{-1}(\sqrt{G_h}) = 45°$, $\Delta\varphi$=0 (no IF phase imbalance), and a perfect balance between the two mixers (G_m=1), we find that $v_{out}(t) \propto V_s^2$ with all correlated input signals canceled. Thus the correlation receiver operates, in principle, at 100 % efficiency. The correlation rejection ratio may now be found as

$$CR = 20\cdot log\Big[\frac{1-\sqrt{G_hG_m}cos(\theta-45°)cos(\Delta\varphi)}{\sqrt{G_h+G_m}}\Big]\ . \tag{8.38}$$

Interestingly, this result is very similar to Eq. 8.15. Possible IF phase imbalance (ϕ) may again be included in $\Delta\varphi$.

To estimate the actual performance of the 280-420 GHz correlation receiver under construction, we once again assume a RF input-hybrid imbalance of $\sim$ 1.25 dB (Fig. 8.6), a mixer conversion gain imbalance of 1.5 dB and a cumulative phase mismatch of 10 degrees. All other imbalances are assumed calibrated out. For this scenario the correlation rejection ratio equals -13.3 dB with 85.4 % of V_s coupled to the IF, e.g.

$$\eta_c = \sqrt{\frac{(G_h+G_m)}{2}}\ . \tag{8.39}$$

η_c is the correlation efficiency, set by the imbalance of the input hybrid and mixer gain. Under ideal conditions $\eta_c \rightarrow 1$. In the above discussion, the effect of the 180° hybrid has been ignored (ideal). Taking into account a commercial 180° IF hybrid with $G'_h = \pm$ 0.3 dB and $\Delta\theta' = 8°$, we find that the correlation receiver rejection ratio reduces to -11.9 dB.

From this discussion it is clear that proper gain and phase calibration of the correlation receiver IF chain is very important. This may be accomplished by injecting an external (coherent) reference signal in the signal and reference beams of the correlation receiver. Another option is to modulate the local oscillator with a 6 GHz tone. The LO sidebands created in this way are likely somewhat unbalanced however, adding an calibration uncertainty.

8.4.2.2 AOS back-end processor

Aside from using a digital or analog correlator as the IF output processor, it is also possible to use an acousto-optical spectrometer (AOS). This configuration is shown in Fig. 8.14b. The analysis is somewhat simpler in that no 180° hybrid is required. In our application the AOS is used as a square law detector. In this case the output voltage is obtained by taking the difference $v_5^2 - v_6^2$ in software. Each phase is read separately by the backend spectrometer. The duty cycle of the acquisition/subtraction maybe as high as 10 Hz, well below the expected Allan variance stability time of the instrument (Chap. 7, Appendix A). We find that

$$v_5^2(t) - v_6^2(t) \propto \left[(G_h + G_m)V_s^2 + (1 - G_h G_m)V_c^2\right] \cdot e^{i(\omega_{if} t - 2\theta - \Delta\varphi)} \ . \qquad (8.40)$$

This is identical to Eq. 8.37. For an ideal RF input hybrid and a perfect balance between the two mixers, we find that $v_5^2(t) = v_6^2(t) \ \propto \ 2V_s^2$. This makes sense since V_s is measured in both phases. Thus the correlation receiver operates, in principle, with 100 % efficiency when connected to an AOS backend, with the added advantage that no 180° IF hybrid is required. The correlation rejection efficiency and astronomical signal throughput are described by Eqs. 8.38 & 8.39.

8.4.3 Observational analysis

It is expected that the rejection of gain variation, plus the extra signal from continuous comparison provides an improvement in integration time efficiency of approximately 4.4 over the existing waveguide tuned 280 – 420 GHz receiver. The 280 – 420 GHz band was chosen not only because of the astronomical opportunities, but also because waveguide techniques work well here, atmospheric and optical loss is relatively low, the (CSO) telescope main beam efficiency high (74 %), and beam dilution for point sources (CSO has a 20″ diffraction limited beam at 345 GHz) acceptable. Thus the 280 – 420 GHz atmospheric windows are judged most promising to provide search opportunities for red-shifted CII lines (z = 3.7 – 5.8). It should be noted that yet more sensitivity, with a single dish system, may be obtained for point source detection, by (in addition to the above) also separating the sidebands (Sec. 8.5). To achieve this, 4 mixers and either 2 or 4 wideband backends, depending on the technique used, are required. Even further sensitivity improvement may be obtained by utilizing both polarization. Given the cost and complexity it was deemed most appropriate to construct the described 2 pixel balanced correlation receiver first.

The expected improvement in sensitivity from using a correlation receiver comes from not having to chop on & off source, e.g. a factor 2 in time plus the chopping efficiency (η_c) in Eq. 3.1.

To obtain an estimate of the expected rms noise level in one night of integration, let us assume reasonable weather with an optical depth (τ_{atm}) of 0.15 at 345 GHz, airmass of 1.1, 74 % measured main beam efficiency of the telescope (η_{mb}), a DSB (balanced) receiver noise temperature of 50 K, and a 100 MHz of spectral resolution channel bandwidth. And unlike the existing single-ended receivers (see also Chap. 3), which suffer from plateauing effects in the mK range due to systematics and drift

noise [38], let us assume that the correlation receiver under development behaves ideal with (white) IF output noise that integrates down radiometrically (Eq. 3.1).

Referred to the top of the atmosphere, $T_{sys}(SSB)$ for a single pixel can then be estimated from,

$$T_{sys}^{SSB} = 2 * \frac{[T_{rec}^{DSB} + T_{atm}(1 - \eta_s e^{-A \cdot \tau_{atm}})]}{\eta_s e^{-A \cdot \tau_{atm}}} \ , \tag{8.41}$$

with η_s the spillover efficiency (0.95). In Eq. 8.41, A is the airmass as measured from zenith. $\theta = cos(1/A)^{-1} = 25°$. And because

$$T_{sky} \approx 0.95 * T_{amb}, \tag{8.42}$$

with $T_{amb} \sim 270$ K on Mauna Kea, HI, we find from the radiometer equation [39] a 1σ rms antenna noise temperature of ≈ 120 μK in 8 hours of integration time:

$$T_A^* = \frac{\sqrt{2} T_{sys}^{SSB}}{\sqrt{(\eta_c \Delta\nu T_{int})}} \ \ (K). \tag{8.43}$$

This is approximately a factor of 25 over what is commonly achievable in a single night with a standard single pixel DSB receiver at the CSO [2].

8.4.4 Physical implementation

The correlation mixer hardware is shown in Fig. 8.15. Signal and reference beams are coupled via two identical corrugated feedhorns [22] with a 1.322 mm waist (f/D=2.4 at 345 GHz). The location of the phase center is 1.67 mm behind the feedhorns aperture. Internal, the signals are routed via a 90° hybrid to two SIS junctions (Sec. 8.3.3). As with the balanced receivers, the IF matching network and integrated bias Tee is designed to cover 3 – 9 GHz. The design is entirely planar which minimizes phase errors and facilitates assembly/reliability. This type of IF network was developed in 2004 for HIFI mixer bands 3 & 4 [24] and successfully adapted for the "technology

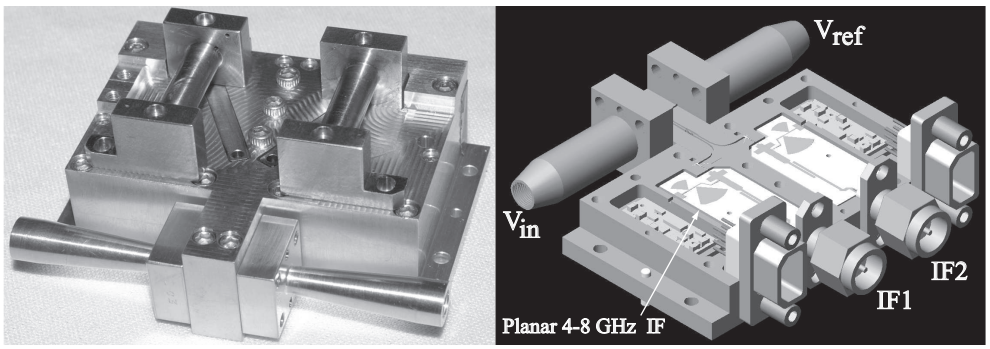

Figure 8.15: The correlation mixer. The physical mixer block [22] is shown in the left panel with a rendered view to the right. Josephson noise in the SIS tunnel junctions may be individually suppressed via two electro-magnets mounted on top of the mixer block.

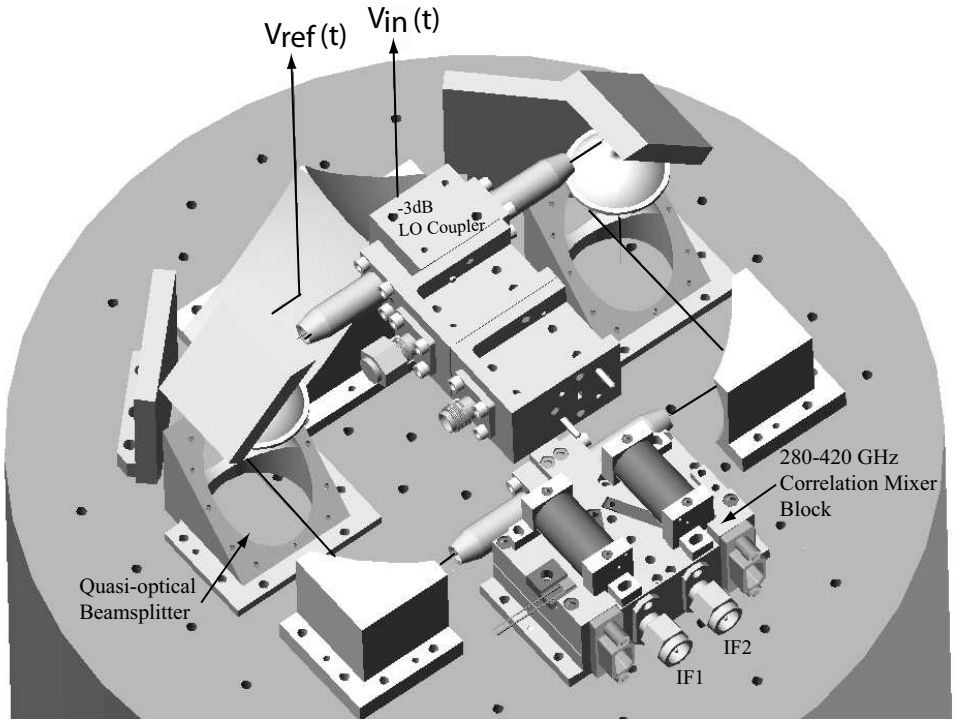

Figure 8.16: Rendered view of the balanced correlation receiver. The LO is injected in phase as depicted schematically in Fig. 8.14. This scheme offers a high degree of LO amplitude noise cancellation (Eq. 8.38). The two beams are physically separated by 28 mm which, given the CSO Cassegrain plate scale of 4.6″/mm, provides a 2.15′ offset on the sky. This is well within the 3.5′ FOV of the telescope.

development" receiver (Trex) presented in Chap. 7. It should be noted that in principle the AlN SIS devices presented in Sec. 8.3.3 support an IF frequency to 13 GHz. However due to IF amplifier and backend processing constraints it was decided to implement the first generation correlation receiver with a 4 – 8 GHz IF passband. Fig. 8.16 shows the physical layout of the correlation receiver. All components including the mirrors have been manufactured and as of the fall of 2008 are awaiting assembly and integration as part of the telescope facility heterodyne receiver instrumentation upgrade.

8.5 The sideband separating receiver

8.5.1 Introduction

An improvement over double-sideband (DSB) heterodyne detection is made when the signal and image sidebands are made available separately at the IF output. This is accomplished with a sideband separation mixer, which allows simultaneous detection

of both the upper and lower sidebands. If, as is often the case, the astronomical line of interest is located in one of the sidebands, the image sideband may then be terminated on a cold load, providing enhanced noise reduction over more conventional DSB receiving techniques. Despite these advantages the sideband separating mixer has until very recent [40, 41, 42, 43, 44] not been implemented in the submillimeter, where the required waveguide dimensions were prohibitively small. This has certainly been the case for the $600 - 720$ GHz atmospheric window (band 9 ALMA). The current state-of-the-art micro-milling technology has changed all this, and has permitted a waveguide design of a sideband separating heterodyne mixer at these high frequencies.

The 2SB mixer presented here provides a significant improvement over the more traditional double-sideband configuration (Chap. 3), albeit with increased complexity. The entire design is based on an analytical model [45], and verified by HFSS [20]. This allows the mixer performance to be studied under varying input parameters, such as SIS junction RF impedance, machining tolerance, LO termination reflection, and IF hybrid imbalance.

8.5.2 Sideband separating mixer layout

From a variety of possible sideband separating schemes, we have selected the configuration shown in Fig. 8.17. The core of the suggested mixer consists of a quadrature input hybrid, two -9 dB LO diplexers, three termination loads, and two superconductor-insulator-superconductor (SIS) junctions. We have opted for waveguide technology in the construction of the RF components. The RF modeling process is described in more detail in Sec. 8.5.5. To maximize the width of the branch lines, we have in the design of the quadrature hybrid increased the waveguide b-dimension by 32.5 % (Sec. 8.3.1). This is the maximum possible before the TE_{01} mode gets excited at the high end of the frequency band. The waveguide termination consists of a cavity at

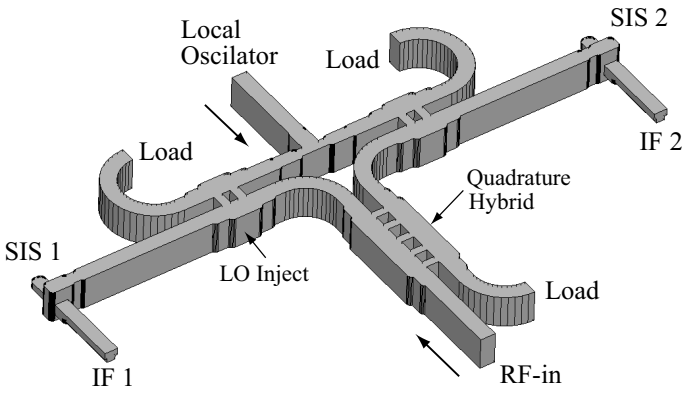

Figure 8.17: Core of the proposed implementation. The input is coupled via a quadrature hybrid with zero and ninety degree phase delay to a pair of SIS mixers. LO coupling to each SIS junction is -12 dB with the remainder terminated. The waveguide dimensions for the structure are 145×310 μm.

the end of the waveguide that is partially filled with commercially available carbon loaded epoxy MF112 [46, 47, 48].

8.5.3 Theory

The operation of a sideband separating mixer is most easily understood by looking at the phase relationship between the upper sideband (USB) and lower sideband (LSB). Referring to Fig. 8.18, we have at the output of the quadrature mixer,

$$v_1(t) = V_{rf}\left[\tau_{rf} \cdot e^{i(\omega_{rf}t-\theta_1)} + \tau'_{rf} \cdot e^{-i(\omega_{rf}t-\theta_1)}\right] \cdot V_{lo}e^{i\omega_{lo}t} \ , \qquad \rightarrow \rightarrow \tag{8.44}$$

and

$$v_2(t) = V_{rf}\left[\rho_{rf} \cdot e^{i(\omega_{rf}t-\pi/2)} + \rho'_{rf} \cdot e^{-i(\omega_{rf}t-\pi/2)}\right] \cdot V_{lo}e^{i\omega_{lo}t} \ . \qquad \downarrow \downarrow \tag{8.45}$$

The unprimed quantities are from the USB and the primed quantities from the LSB. θ_1 represents the phase error in the RF quadrature hybrid (Fig. 8.6) which in most cases constitutes $\leq 2^\circ$. Note that the local oscillator signal is injected in phase. After down-conversion to the IF, and passing through a bandpass filter we obtain,

$$v_3(t) = a_2 V_{if}\left[\tau_{rf}e^{i(\omega_{if}t-\theta_1-\phi)} + \tau'_{rf}e^{-i(\omega_{if}t-\theta_1-\phi)}\right], \qquad \rightarrow \rightarrow \tag{8.46}$$

and

$$v_4(t) = b_2 V_{if}\left[\rho_{rf}e^{i(\omega_{if}t-\pi/2)} + \rho'_{rf}e^{-i(\omega_{if}t-\pi/2)}\right]. \qquad \downarrow \downarrow \tag{8.47}$$

Here a_2 and b_2 represent the mixer gain, as in Eqs. 8.1 & 8.2 and ϕ the phase error introduced by chip misalignment in the waveguide. Propagating v_3 through the IF hybrid with 0° phase delay gives v_3", while propagation of v_4 with 90° phase delay gives v_4". Note that the phase of negative frequencies is shifted 180° with respect to the phase of positive frequencies. θ_2 is the phase error in the IF. In this case we find

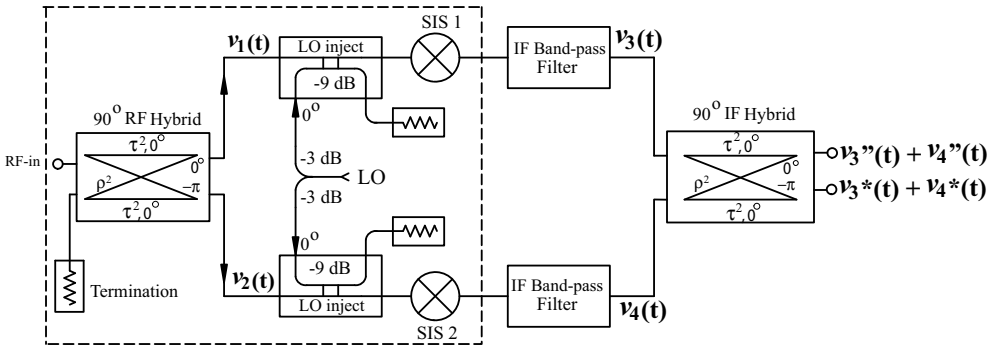

Figure 8.18: Diagram of the 2SB mixer. The IF hybrid is external to the mixer block as indicated by the dashed outline.

$$v_3"(t) = a_2 V_{if}\left[\tau_{rf}\tau_{if}e^{i(\omega_{if}t-\theta_1-\phi-\theta_2)} + \tau'_{rf}\tau'_{if}e^{-i(\omega_{if}t+\theta_1+\phi+\theta_2)}\right], \qquad \rightarrow \rightarrow \quad (8.48)$$

and

$$v_4"(t) = b_2 V_{if}\left[\rho_{rf}\rho if e^{i(\omega_{if}t-\pi)} + \rho'_{rf}\rho'_{if}e^{-i\omega_{if}t}\right]. \qquad \leftarrow \rightarrow \quad (8.49)$$

For an ideal mixer with $a_2 = b_2$, $\rho = \tau = \sqrt{2}$, and zero phase error we find after summing v_3" and v_4" that the upper sideband cancels, leaving only the lower sideband,

$$v_{LSB}(t) = a_2 V_{if} \cdot e^{-i\omega_{if}t} \ . \quad (8.50)$$

Likewise, propagating v_3 through the IF hybrid with a 90° phase delay gives v_3^*, while propagation of v_4 with 0° phase delay provides v_4^*,

$$v_3^*(t) = a_2\left[\tau_{rf}\rho_{if}e^{i(\omega_{if}t-\pi/2-\theta_1-\phi-\theta_2)} + \tau'_{rf}\rho'_{if}e^{-i(\omega_{if}t+\pi/2+\theta_1+\phi+\theta_2)}\right]. \qquad \downarrow \uparrow \quad (8.51)$$

and

$$v_4^*(t) = b_2\left[\rho_{rf}\tau_{if}e^{i(\omega_{if}t-\pi/2)} + \rho'_{rf}\tau'_{if}e^{-i(\omega_{if}t-\pi/2)}\right]. \qquad \downarrow \downarrow \quad (8.52)$$

In this case summing v_3^* and v_4^* (ideal mixer) cancels the lower sideband, leaving only the upper sideband

$$v_{USB}(t) = -ia_2 V_{if} \cdot e^{i\omega_{if}t} \ . \quad (8.53)$$

Thus we see that by introducing a 90° phase delay at the RF input and IF output, the upper and lower sidebands may be separated. It should be noted that sideband separation may also be achieved with a 0° or 180° phase shift in the RF, and with a 90° additional phase shift from the LO and IF. This again constitutes the required 180° phase shift needed to achieve successful separation of the sidebands [13, 44].

When we assume that the RF input hybrid and IF output hybrid have identical response functions (similar physics), then we find the ratio of upper to lower sideband,

$$\frac{|USB|}{|LSB|} = \frac{a_2\tau\rho + b_2\rho\tau}{a_2\tau^2 + b_2\rho^2} \quad (8.54)$$

which $\rightarrow 1$ for an ideal single sideband mixer.

A figure of merit of a 2SB mixer is the leakage of signal from one sideband to another under non-ideal conditions. Defining the mixer gain imbalance $G_m = (a_2/b_2)^2$, the quadrature hybrid imbalance $G_h = (\rho/\tau)^2$, and the total phase error $\Delta\varphi = (\theta_1 + \phi + \theta_2)$, then the signal to image sideband ratio becomes,

$$RR = -10 * log\Big(\frac{1 - 2\sqrt{G}cos(\Delta\varphi) + G)}{1 + 2\sqrt{G}cos(\Delta\varphi) + G}\Big) \ . \quad (8.55)$$

Where $G = [G_m \cdot G_h(rf) \cdot G_h(if)]$ equals the single sideband differential mixer gain. In Fig. 8.19 we depict RR as a function of amplitude and phase imbalance. The described G_m, G_h, and $\Delta\varphi$ are used in the computer simulations of Sec. 8.5.5.

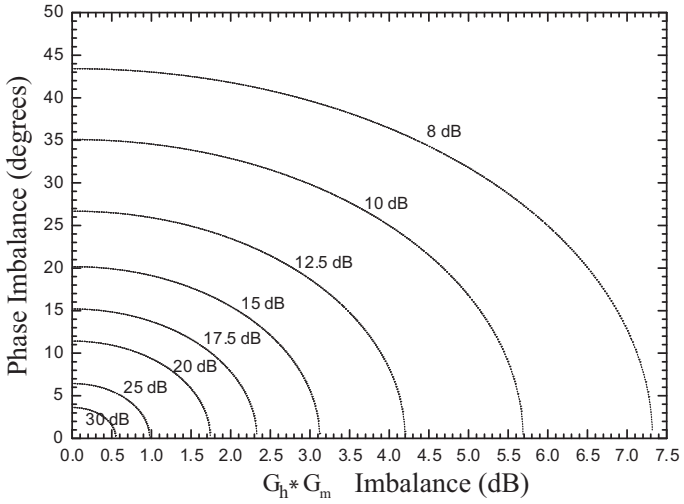

Figure 8.19: Sideband separation rejection of a sideband separating mixer as a function of amplitude and phase imbalance.

8.5.4 SIS junction and waveguide transition simulations.

To couple the TE_{10} waveguide mode to the thin-film microstrip that feeds the SIS junctions we use a full-height "across-the waveguide" radial probe [49, 50, 51]. This kind of probe has an inductive, quarter-wavelength, meandering transmission line that crossed the waveguide (Fig. 8.20a). It has the advantage of simplifying the way the IF signal is extracted. Care must however be taken not to excite higher order modes that result in high-Q resonances in the probe's passband. To further optimize the performance of the probe we have, similar to Sec. 7.2.1, added a capacitive tuning step 0.08 guide wavelength (λ_g) in front of the radial probe. From 580 – 740 GHz the probe impedance locus is $50 + i20\ \Omega$ as shown in Fig. 8.20b.

Based on successful experience with the DSB ALMA band 9 mixer development [52], a single $Nb/AlO_x/Nb$ SIS junction with integrated RF matching network [53] was employed. Although high current density junctions with AlN barriers have intrinsic higher RF bandwidth (Sec. 7.2.2), we have selected the former as, for the moment, the fabrication process is more reliable. The preference of single junctions, over the twin junction design in Chap. 7, is two-fold. It facilitates higher uniformity, important to the balance in the sideband separation mixer, and secondly it permits easier suppression of the Josephson currents through the tunnel barrier. The device characteristics of the junction and RF matching network are provided in Table 8.3 and Table 8.4. Further insight in the behavior of the mixer can be gained by taking the SIS junction RF admittance, obtained from a fit to the LO pumped I/V curve [54], into account in the computer simulations. With this information, and considering the superconducting RF tuning structure shunted by the 80 fF geometric junction capacitance, we are able to de-embed the RF junction impedance to the radial probe waveguide transition reference plane. As evidenced from Fig. 8.20b,

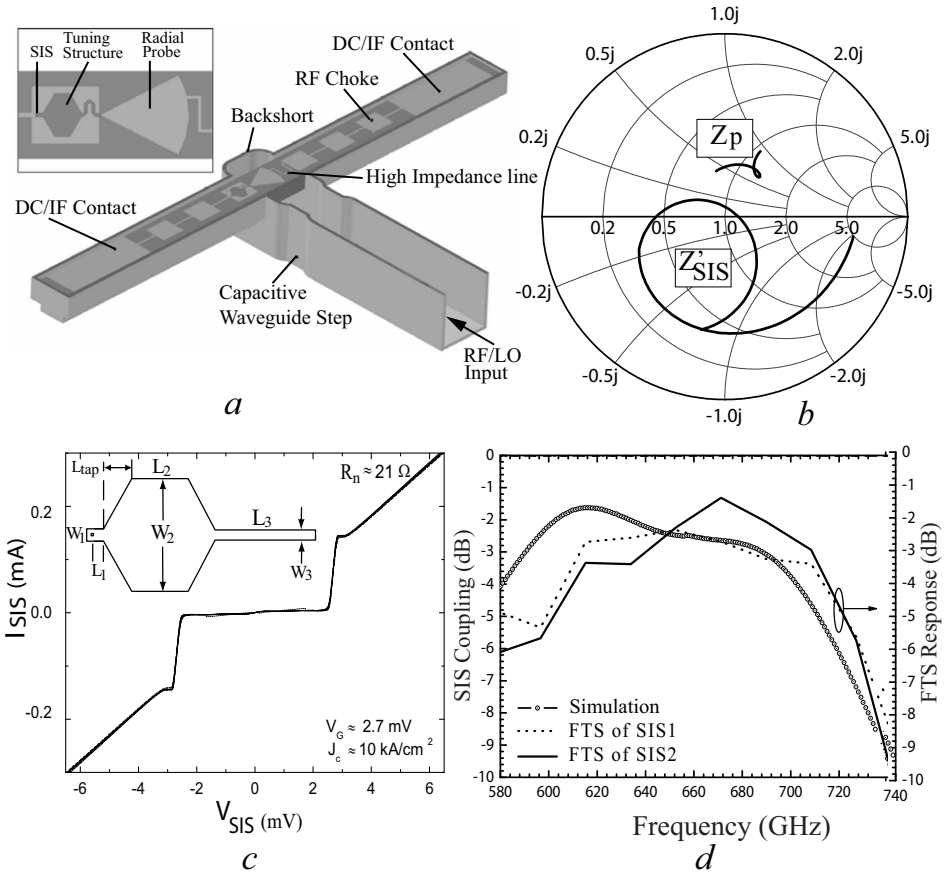

Figure 8.20: *a*) Device mounted in the IF channel. *b*) Radial probe and SIS junction input impedance for a LO pump level of $\alpha \equiv eV_{LO}/\hbar\omega = 0.7$. *c*) Eight measured IV curves (no LO applied). *d*) Coupling efficiency from the waveguide to the SIS junction with the mixer block as build. Superimposed are direct detection FTS measurements of the both junctions (arbitrary units).

there is a (slight) coupling mismatch between the de-embedded junction impedance (Z'_{sis}) and radial probe transition (Z_p). For optimal coupling $Z'^{*}_{sis} = Z_p$, which given a locus of $35 + i17\Omega$, provides a coupling efficiency of ~ 63 % (-2 dB) over the 600-720 GHz ALMA band 9 frequency band. Please note that the AlO_x barrier SIS design is based on a 40 Ohm waveguide transition impedance locus. The RF coupling loss due to the difference between the "theoretical" vs. "actual" probe impedance is ≈ 0.75 dB. The incurred RF mismatch, Ohmic loss in the waveguide (Sec. 8.5.5), and IF loss (Sec. 8.5.6) form a plausible explanation for the somewhat higher than expected SSB receiver noise temperature (Fig. 8.24).

The SIS junctions were fabricated on 50 μm thick quartz. The simulations in the next Section include the "across the waveguide" radial probe transition, the superconducting thin-film RF matching network, and RF admittance of the LO pumped

Table 8.3: SIS junction parameters as used in the 2SB measurements [53].

R_nA ($\Omega \cdot \mu m^2$)	Area (μm^2)	C_s (fF/μm^2)	ε_r	σ_{Nb} (S/m)	t_{gnd} (nm)	t_{top} (nm)	t_{SiO2} (nm)
25.0	1.0	80.0	3.8	$1 \cdot 10^7$	200	500	250

Table 8.4: SIS RF matching network (Fig. 8.20a). Values obtained from D. Ludkov *et al.*, TU Delft [55]. All dimensions in microns.

W_1	W_2	W_3	L_1	L_2	L_3	L_{tap}
5.5	50.0	4.5	5.0	41.5	44.0	12.45

SIS junction (α=0.6, V_{sis} = 2.1 mV) [54].

8.5.5 2SB computer simulations results

The layout presented in Fig. 8.17 has been modeled in a linear circuit simulator [45] with custom code written to accurately model the hybrid structures (verified by HFSS finite element simulations). This technique has the advantage that non-ideal termination impedances and waveguide dimensions maybe examined in real time. In an ideal situation, the SIS junctions are well matched to the probe impedance,

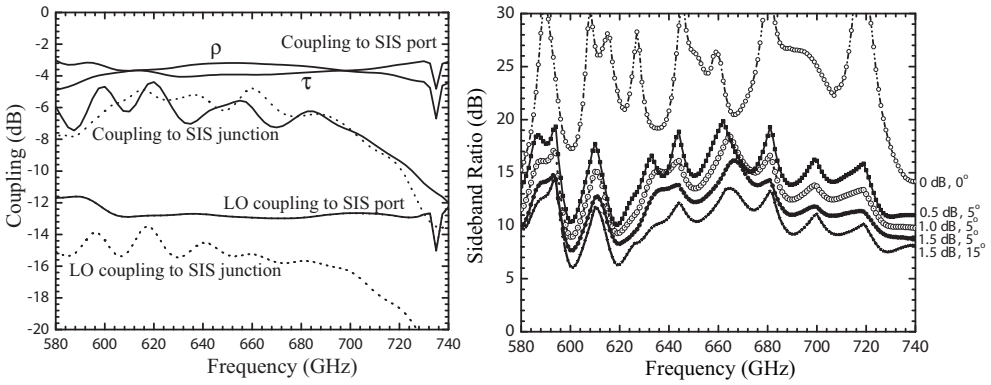

Figure 8.21: *Left*) Signal and LO coupling to the SIS port (radial probe transition) and to the SIS junction. The coupling includes the RF mismatch to the junction (RF impedance). *Right*) Sideband rejection ratio as a function of the IF quadrature hybrid power and phase imbalance. This plot shows the importance of having a well balanced IF hybrid. In the above calculations, the input return loss of the waveguide termination is assumed > -25 dB, and the mixer gain imbalance 0.25 dB (G_m), with a 5° phase error (θ_2) due to device misalignment in the waveguide.

the waveguide terminations ideal, and the IF hybrid 100 % balanced. This maybe regarded as an "upper" performance limit. By design 12 % (-9 dB) of the LO signal is coupled into the signal path, and it follows from reciprocity that 88 % of the LO signal is terminated. A loss of 88 % of available LO power was deemed acceptable. In general, a complex waveguide structure such as shown in Fig. 8.17 has noticeable Ohmic loss, estimated $\sim$ 0.9 dB from the surface impedance of gold at room temperature and roughness in the guide (Sec. 5.1). At liquid helium temperatures (4.2 K), thanks to an increase in electrical conductivity (RRR is assumed 10), the loss in the waveguide reduces to $\sim$ 0.37 dB. Because this loss is present in both arms it has no effect on the sideband rejection ratio, however it does degrade the overall mixer gain and receiver noise temperature.

In Fig. 8.21 we show the calculated coupling from the signal and LO port to the SIS port and SIS junction. The balance in LO power coupling is critically dependent on the homogeneity of the LO termination impedances. This effects the mixer LO pump level and resultant mixer gain. Thus a load termination with minimal reflection (return loss) and a high degree of reproducibility is very important [48].

8.5.6 Integrated planar IF

To facilitate reliability and modeling, we have opted for a planar IF filtering and matching design (inset Fig. 8.22). This design is compact and highly repeatable with regards to phase and amplitude. In this way it helps to minimize the differential phase error at the mixer IF output. The circuit itself contains the IF match, dc-break, bias

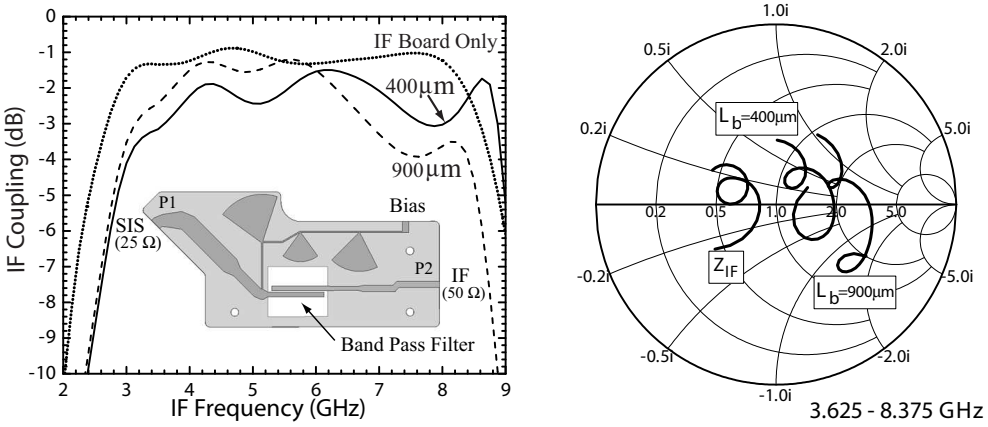

Figure 8.22: *Left*) Calculated transmission for only the IF circuit board, and for the combined SIS (Z_{00} = 200 Ω)–wirebond–IF circuit board. The connection to the SIS junction is done through a 0.9 mm and 0.4 mm length bond wire. *Right*) Complex IF impedance at the SIS port input port (P1) of the IF circuit board, and at the SIS junction. The parasitic capacitance of the junction (80 fF) and RF matching network (239 fF) have been included in the calculation. The wirebond (L) and combined parasitic capacitance (C) act as an impedance transformer, and reduce the available IF bandwidth. For a 0.9 mm wirebond length the highest IF frequency is $\sim$ 7 GHz, whereas for a 0.4 mm wirebond length this limit is pushed to $\sim$ 8.75 GHz. The Smith chart is normalized to 50 Ω.

Tee, and EMI filter. The design is similar to that presented in Sec. 8.3.2 and Chap. 7. At the heart of the structure is a pair of parallel coupled suspended transmission lines [23], which form a 3 – 9 GHz band pass filter. The entire (planar) structure has been designed in microwave office [45] and HFSS [20].

In the design of the IF matching network we have taken into account the combined parasitic RF-matching network and geometric capacitance of the junction, calculated to be 307 fF, the RF choke, and the wire bond inductance that connects the SIS chip to the IF board.

8.5.7 Physical implementation

The original circuit board design is based on a 0.3-0.4 mm IF wirebond length and $R_n = 10\ \Omega$ AlN-barrier SIS junction. However due to junction availability and construction issues, 21 Ω AlO_x-barrier SIS junctions with ~ 0.9 mm wirebond contact length were employed. Unfortunately, the higher than expected wirebond inductance "resonates" with the RF choke, thin-film RF matching network and parasitic junction capacitance as shown in the right panel of Fig. 8.22. Having understood the problem, we have made modifications to the Radiometer Physics [56] manufactured 2SB mixer block. Preliminary measurements with high current density AlN-barrier SIS junctions and a 0.4 mm IF contact confirm a flat IF passband response. The mixer IF output impedance (Z_{00}) is approximately 200 Ω and is derived from the slope of LO pumped junction below the energy gap (Sec. 4.1.7.2) [54]. This is somewhat larger than what may be expected with high J_c AlN junctions. For the IF board substrate

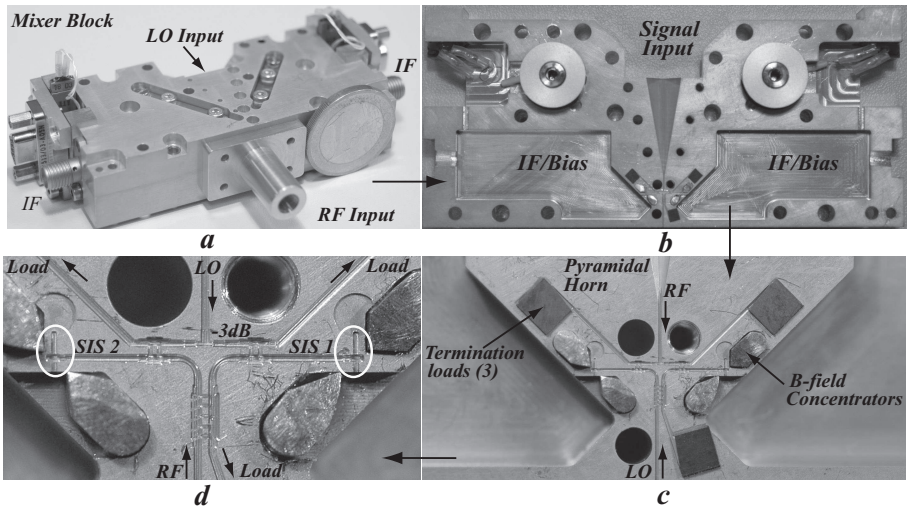

Figure 8.23: *a*) Composite view of the mixer block. *b*) Upper half of the mixer block. *c*) Close up view of the magnetic field poles, and termination loads. *d*) Zoomed in view of the waveguide structure and IF channel that houses the SIS junctions.

material we have opted for Alumina (ε_r=9.9) with a height of 635 μm. The 1 dB loss in coupling is the result of loss in the Alumina substrate (loss tangent = 0.002). At cryogenic temperatures the substrate loss is expected to reduce to $\sim$ 0.3 dB. The variation in the IF impedance at the junction's IF output port (right panel Fig. 8.22) and ripple in the transmission (dBS21) is due to a mismatch between the junction (no integrated IF matching), wirebond, and the 25 Ohm IF board input impedance. This mismatch can to some extent be alleviated with a more integrated "on-chip" IF design approach [49], Sec. 7.2.2.

To facilitate ease of construction, the 2SB mixer has been constructed in a split-block format (Fig. 8.23). Conventional machining was used for the large features, whereas micro-machining was employed for the smaller RF features [56]. Both parts of the block were made of copper which was then gold plated with a thickness of $\sim$ 2 μm. The fabricated unit is rather compact (8 cm x 2 cm x 3 cm). It contains all the RF components, the IF filter board, the dc-bias circuit, and the magnetic probes needed to suppress the Josephson currents in the SIS junctions. A close inspection of the fabricated block showed that all the waveguides and cavities are approximately 5 μm wider than designed. The reasons appear to be in the etching of the copper block during the gold plating process. However, the erosion is rather uniform throughout the mixer block. We have repeated the simulation process with the measured dimensions and find that the design is robust as long as symmetry of the RF components is maintained.

8.5.8 Measurement results

The direct detection response of both SIS junctions has been measured on a Fourier transform spectrometer (FTS). The results are in good agreement with the calculated response shown in Fig. 8.20d. The noise temperatures were measured using the conventional Y-factor method. As in Chap. 7, the input loads are obtained in accordance with the Callen & Welton formulism [57]. To measure the sideband ratio we used a modified setup similar to that described in [58].

The receiver noise temperature and sideband ratio (RR) for both output ports were determined at several LO pumping frequencies and recorded as a function of IF frequency. The results are summarized in Fig. 8.24. Both quantities are close to the ALMA specifications, as indicated by the horizontal dashed lines. For the receiver noise temperature 80 % of the band should not exceed 335 K while across the designated frequency bands all noise temperatures should be $<$ 500 K [8]. The image rejection ratio in all instances should be $\leq$ 10 dB. Although the noise temperature complies with the ALMA specifications, the IF noise temperature increases above $\sim$ 7 GHz. This is understood to be the result of a mismatch between the actual SIS junction and IF matching network, and has recently been resolved (Sec. 8.5.7). Unlike the junction designs in Chap. 7 and Sec. 8.3.3, no on chip IF matching network has yet been integrated with the Delft SIS junctions employed in the current measurements.

The obtained image rejection is in close agreement with the modeled prediction in Fig. 8.21. From our simulations we deduce that the IF hybrid has on average an imbalance of 1 dB with a 5° phase error. Indeed, these values are very close to

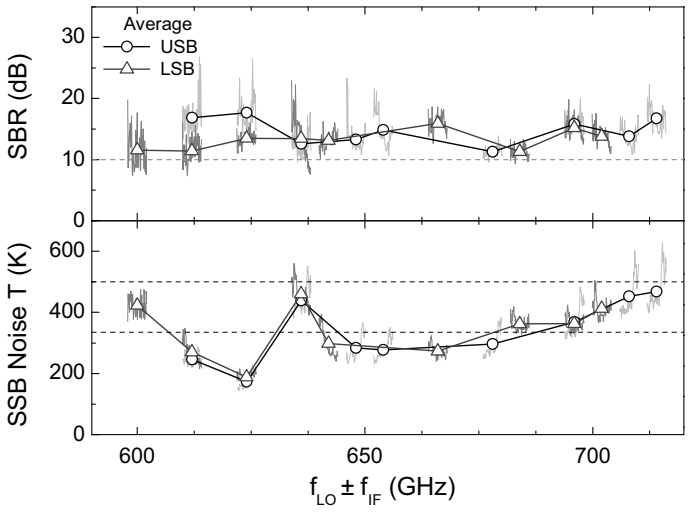

Figure 8.24: Noise temperatures and sideband rejection ratio as function of RF signal. The noise temperatures have been corrected for the finite rejection ratio. Horizontal dashed lines correspond to the ALMA specifications, see text for details.

experimental values obtained at 77 K [59]. The hybrid in question is a commercial unit that has been optimized for operation at ambient temperature. It is reasonable to assume therefore that with a custom quadrature hybrid, optimized to operate at 4 K, that an improvement of 0.5 dB in power imbalance and 2-3 % in phase is possible. In this case the sideband rejection ratio is expected to improve by $\sim 4-5$ dB (Fig. 8.21b). Alternatively, a significant improvement in the sideband ratio is obtained if the 90 degree IF hybrid is omitted altogether. This may be accomplished in the future with the use of high-speed digitizing electronics and specialized DSP software. Finally, in Table 8.5 we show a breakdown of the measured receiver noise temperature at 648 GHz. Here T_{opt} is the estimated equivalent front end optics noise temperature and T_{IF} the IF noise temperature. This includes the cooled IF hybrid and 4 – 8 GHz isolator [31]. G_{mix} is the single sideband mixer conversion gain and G_{opt} the front-end optics loss.

In future designs it is not unrealistic to expect an improvement in the mixer conversion gain of up to ~ 1.5 dB with a more optimized (AlN-barrier) SIS junction RF coupling design, better matched IF load termination, and on chip integrated IF matching network. In this scenario we estimate an improvement of ~ 34 K in the measured SSB noise temperature of Fig. 8.24. Ohmic loss in the waveguide structure, estimated $\sim 0.75-1.5$ dB from our measurements, and loss in the IF matching network/output-Hybrid will remain. Only improved micromaching or electroplating techniques are liable to reduce the front end loss. Loss simulations [20] with perfect waveguide walls and a RRR=10 ratio of the room temperature conductivity of Au upon cooling to LHe temperatures, indicate a minimum front end loss of 0.37 dB.

Table 8.5: Measured and calculated receiver parameters at $f_{LO} = 648$ GHz

Parameter	USB	LSB
T_{rec}^{SSB} (K)	290	262
T_{opt} (K)	9	9
T_{IF} (K) †	8.2	8.2
T_{mix}^{SSB} (K)	190	157
G_{mix}^{DSB} (dB) ‡	-9	-9
G_{opt} (dB)	-0.25	-0.25
$T_{mix}^{SSB}/(G_{opt})$ (K)	201	166
$T_{IF}/(G_{opt}G_{mix}^{SSB})$(K)	80	67
Measured α_{SIS1}	0.55	0.60
Measured α_{SIS2}	0.56	0.62

† Corrected for IF reflection.
‡ Including Ohmic loss in RF and IF.

8.5.9 Atmospheric noise and the effect on 2SB and DSB receivers

In this Section we look into the system noise temperature, referred to the top of the atmosphere, of a 2SB and DSB receiver as a function of atmospheric opacity, and compare the results. Technically speaking this is important if we want to understand the improvement of a 2SB receiver over a DSB receiver with equivalent SIS technology [52] during actual observation conditions. It is also scientifically important to anticipate the system performance as a function of frequency and precipitable water vapor, as this determines the required integration time and achievable rms noise level (Eq. 8.43). In the example presented here we use Chanjnantor, a high elevation plateau in the northern Chilean Andes. It is also the selected site of the Atacama Large Millimeter Array (ALMA) [9].

In our analysis we follow Jewell and Lamb ([60, 61]), but modify the equations to include noise in the upper and lower sideband separately. This is essential as the sidebands are 12 GHz apart. The result presented here is identical to that reported in Eq. 7.10. A model of the atmosphere is provided by J. Pardo *et al.* [35]. For a SSB receiver with the signal in the upper sideband (USB) we can write the system temperature as

$$T_{sys,SSB}^{SSB,usb}(\nu) = \frac{\left[T_{rec}^{SSB}(\nu) + T_{ant}^{usb}(\nu) + RR \cdot T_{ant}^{lsb}(\nu)\right]}{\eta_s \cdot e^{-A\tau^{usb}(\nu)}} \ , \tag{8.56}$$

where RR is the sideband response (≤ 0.1 for ALMA). T_{ant} is the antenna brightness temperature in the appropriate sideband, and η_s the antenna spillover efficiency. In the above equation, T_{rec}^{SSB} is the single sideband receiver noise temperature. In case

of an ideal SSB receiver RR=0.

The antenna brightness temperature may be obtained from

$$T_{ant}(\nu) = \eta_s T_{sky}\left[1 - e^{A\tau(\nu)}\right] + (1-\eta_s)T_s + \eta_s T_{bg} e^{-A\tau(\nu)} \ . \tag{8.57}$$

T_{sky} and T_s are the sky and antenna spillover temperatures, approximately 95 % of the ambient temperature. T_{bg} is the cosmic background temperature (2.725 K).

For a true DSB receiver RR=1, and Eq. 8.56 with the signal in the upper sideband may be rewritten as

$$T^{DSB,usb}_{sys,SSB}(\nu) = \frac{\left[2T^{DSB}_{rec}(\nu) + T^{usb}_{ant}(\nu) + T^{lsb}_{ant}(\nu)\right]}{\eta_s \cdot e^{-A\tau^{usb}(\nu)}} \ . \tag{8.58}$$

In Fig. 8.25 we show the results of our atmospheric simulations. The mean precipitable water vapor on Chanjnantor is 1 mm, which corresponds to a $\tau_{225\ GHz}$=0.05. For the 600-720 GHz receiver, observations are likely planned only in excellent weather conditions with stable atmospheric phase. This is the case for 0.5 mm precipitable water, which occurs approximately 25 % of the time.

For this condition the atmospheric brightness temperature drops to just below 150 K. This is demonstrated in panel *b*. In panel *c* we plot the SSB system noise temperature of the discussed single sideband mixer, and the ALMA baselined DSB mixer [52]. For the SSB mixer, we use the measured 235 K mean noise temperature with RR = -10 dB, and for the ALMA band 9 DSB mixer we use a measured (mean) receiver noise temperature of 140 K. Under the described conditions $T^{SSB}_{sys,SSB}$= 990 K and the $T^{DSB}_{sys,SSB}$=1180 K. Finally in panel *d* we calculate the $T^{DSB}_{sys,SSB}/T^{SSB}_{sys,SSB}$ ratio. With increasing water vapor the sky brightness temperature increases, and the maximum obtainable improvement by using a SSB receiver is $\sim$ 1.3. This is however during bad weather (2 mm pwv) when observations will not be carried out. The reason that the improvement of using a SSB receiver is not more, has to do with the receiver noise temperature. Simply put, the more sensitive the receiver the more background limited the instrument will be [60, 61]. Under good weather conditions the improvement of using a SSB over DSB receiver is somewhat less than 1.3 (zero in space), on average $\sim$ 16 %. This still equates to a 35 % time saving when compared to a true double sideband receiver. This is significant, and provides for example 10 extra ALMA antenna's (at "no" cost)! It should also be pointed out that, discounting phase scintillations, the 2SB receiver allows for observations in marginal weather conditions, thus extending the fraction of time observations can be made in the important 600 – 720 GHz atmospheric window.

From these results it is clear however that single pixel 2SB receivers are not necessarily the end-all. For mapping of large molecular clouds as well as airborne, high altitude balloon and space observations, receivers such as the balanced, correlation, or DSB multi-pixel arrays of Chap. 9 are likely preferred. This is certainly the situation for terahertz HEB receivers where, due to the mixer gain instability, sensitivity to local oscillator amplitude noise, LO standing waves, and non-uniformity in the devices single sideband operation will be difficult to achieve. In fact, the optimal receiver configuration for HEB mixers is probably the balanced type [64].

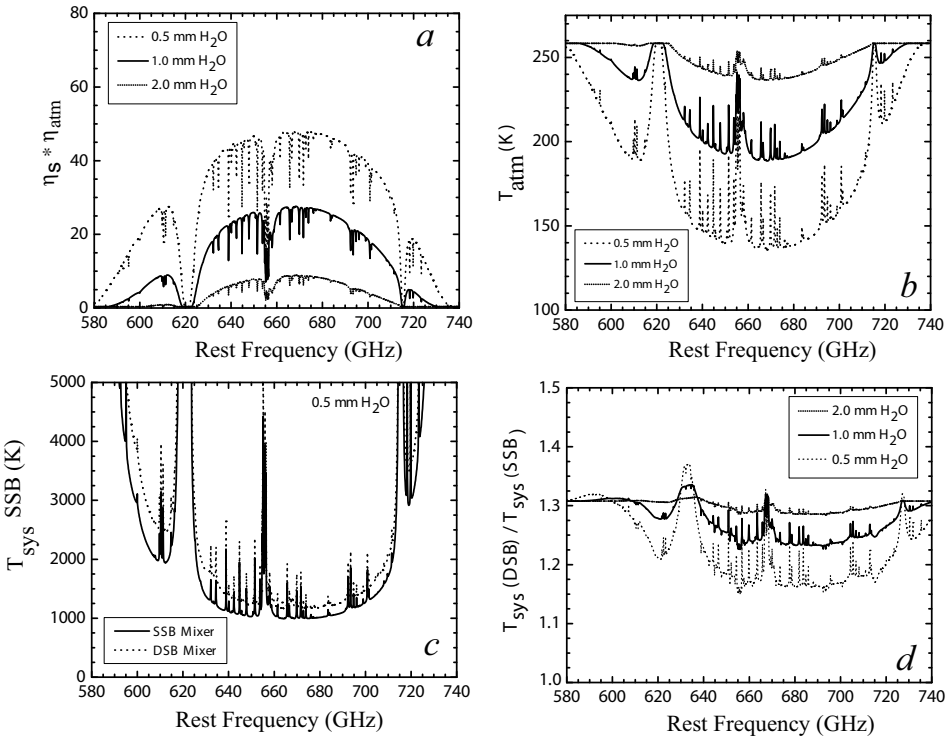

Figure 8.25: Results of ALMA band 9 calculations at Chanjnantor, a 5000 m elevation plateau in the northern Chilean Andes. *a*) Atmospheric transmission convolved with a 90 % telescope spillover efficiency for three amounts of precipitable water. For Chanjnantor the medium precipitable water vapor is 1 mm over the period 1995-2006 (S. Radford [34]) The atmospheric transmission is based on a model by J. Pardo [35]. The calculations are for 1.1 airmass. *b*) Antenna brightness temperature on the sky, as a function of precipitable water vapor. *c*) Estimated SSB system temperature for 0.5 mm precipitable water. Statistically this occurs 25 percent of the time. In the calculations the single sideband rejection ratio is assumed -10 dB (ALMA spec). For reference we also plot the SSB system noise temperature of the baselined ALMA band 9 DSB receiver (text). *d*) Improvement that may be gained in the SSB system noise temperature with the use of a SSB-, rather than a DSB receiver.

8.6 Summary

In this Chapter we have taken a detailed look into the characteristics, design, and principles of operation of a singly balanced receiver, the correlation or continuous comparison receiver, and the sideband separating (2SB) receiver. The principle limitation of these advanced heterodyne receivers lies in the implementation, complexity, and tolerance control of the very small waveguide dimensions, and the continued advancement of high current density AlN-barrier SIS junctions with integrated "on-chip" IF matching circuitry. The latter facilitates the increased instantaneous RF and IF bandwidth demanded by the scientific community. At the present time, conventional micro-milling technology allows mixer block construction up to $\sim$ 700 GHz,

albeit at a significant expense. In recent years micromachining using photolithography combined with (Cu) electroplating has undergone significant technological advancement [62]. This promising technique may in the not too distant future facilitate complex waveguide structures to be electroformed for use at terahertz frequencies.

Despite these significant advances, the fundamental construction of the mixer blocks remains a challenge. Further improvement may therefore be obtained with a more integrated design approach, such as has been taken by the integrated receiver [63], scheduled for atmospheric observations from the "Terahertz LImb Sounder" (TELIS) high altitude balloon experiment, and/or the silicon-on-insulator (SOI) development of Chap. 9.

Bibliography

[1] T. G. Phillips, "The Caltech Submillimeter Observatory", *IEEE MTT-S Int.*, pp. 1849-1852, Jun., (2007).

[2] [Online]. Available: http://www.submm.caltech.edu/cso/

[3] A. I. Harris and J. Zmuidzinas, "A Wideband Lag Correlator for Heterodyne Spectroscopy of Broad Astronomical and Atmospheric Spectral Lines", *Rev. Sci. Instrumentation*, Vol 72, No. 2, pp. 1531-1538, (2001).

[4] A. I. Harris, *Proc. of SPIE, Millimeter and Submillimeter Detectors*, Kona, HI. (2002).

[5] J. Horn, O. Siebertz, F. Schmilling, C. Kunz, R. Schieder, and G. Winnewisser, "A 4 x 1 GHz Array Acousto-Optical Spectrometer", *Experimental Astronomy*, Vol. 9, Issue 1, pp. 17-38, Jan., (1999).

[6] B. Klein, S. D. Philipp, I. Krmer, C. Kasemann, R. Gsten and K. M. Menten, "The APEX digital Fast Fourier Transform Spectrometer", *A&A*, pp 454, L29-L32, (2006).

[7] The Netherlands Research School for Astronomy [Online]. Available: http://www.strw.leidenuniv.nl/nova/

[8] [Online]. Available: http://www.alma.nrao.edu

[9] [Online]. Available: http://www.alma.info/

[10] [Online]. Available: http://www.mmarray.org/

[11] [Online]. Available: http://iram.fr/

[12] [Online]. Available: http://sma-www.harvard.edu/

[13] S. A. Maas, *Microwave Mixers*, 2^{nd} Edition.

[14] E. J. Wilkinson, "An N-way Hybrid Power Divider", *IRE, Microwave Theory and Techniques*, Vol MTT-13, pp. 116-118, Jan. (1960).

[15] J. W. Kooi, G. Chattopadhyay, S. Withington, F. Rice, J. Zmuidzinas, C. K. Walker, and G. Yassin, "A Full-Height Waveguide to Thin-Film Microstrip Transition with Exceptional RF Bandwidth and Coupling Efficiency" *Int J. IR and MM Waves*, Vol. 24, No. 3, Sept, (2003).

[16] J. W. Kooi, A. Kovács, B. Bumble, G. Chattopadhyay, M. L. Edgar, S. Kaye, R. LeDuc, J. Zmuidzinas, and T. G. Phillips, "Heterodyne Instrumentation Upgrade at the Caltech Submillimeter Observatory II," *Proc. SPIE*, 21-25 Jun., Glasgow, Scotland, United Kingdom, (2004).

[17] Virginia Diodes Inc., 321 West Main Street, Charlottesville, Va 22903, USA.

[18] J. Ward, F. Rice and J. Zmuidzinas, "Supermix: a flexible software library for high-frequency circuit simulation, including SIS mixers and superconducting components", *10th Int. Symp. on Space Terahertz Tech.*, University of Virginia, Charlottesville, VA, Mar. (1999).

[19] S. M. X Claude and C. T. Cunningham, "Design of a Sideband-Separating Balanced SIS Mixer Based on Waveguide Hybrids," *ALMA* Memo 316, Sep., (2000).

[20] Ansoft Corporation, Four Station Square, Suite 200, Pittsburgh, PA 15219-1119, USA.

[21] [Online]. Available: http://www.precisioncryo.com/

[22] Custom Microwave Incorporated, Custom Microwave, Inc., 940 Boston Avenue Longmont, CO 80501, USA.

[23] W. Menzel, L. Zhu, K. Wu, and F. Bögelsack "On the design of novel compact broadband planar filters," *IEEE Trans. Microwave Theory Tech.*, Vol. 51, no. 2, pp. 364-370, Feb. (2003).

[24] G. de Lange, SRON, NL, Private Communication.

[25] H. Golstein, SRON, NL, Private Communication.

[26] American Technical Ceramics, One Norden Lane, Huntington Station, NY 11746, USA.

[27] R. Kehl Engineering, 384 Umbarger Rd., Units B & C, San Jose, Ca 95111.

[28] Sonnet, Sonnet Software, Liverpool, NY, 2005.
[Online]. Available: http://www.sonnetusa.com/

[29] Supermix simulations were accomplished by A. Kovács, with supervision and input from the author.

[30] B. Bumble, Jet Propulsion Laboratory (JPL), Ca., Private Communication.

[31] Pamtech, 4053 Calle Tesoro, Camarillo, Ca 93012, USA.

[32] N. Wadefalk, A. Mellberg, I. Angelov, M. Barsky, S. Bui, E. Choumas, R. Grundbacher, E. Kollberg, R. Lai, N. Rorsman, P. Starski, J. Stenarson, D. Streit, and H. Zirath, "Cryogenic, Wide-band, Ultra-low-noise IF Amplifiers operating at Ultra-Low dc-Power," *IEEE Trans. Microwave Theory and Techniques*, Vol. 51, No. 6, pp. 1705-1711, Jun., (2003).

[33] [Online]. Available: http://www.cttinc.com/

[34] S. Radford. Private communication.

[35] J. R. Pardo, J. Cernicharo, and E. Serabyn, "Atmospheric Transmission at Microwaves (ATM): An Improved Model for mm/submm applications", *IEEE Trans. on Antennas and Propagation*, Vol. 49, no. 12, pp. 1683-1694, Dec., (2001).

[36] C. R. Predmore, N. R. Erickson, G. R. Huguenin, and P. Goldsmith, "A Continuous Comparison Radiometer at 97 GHz", *IEEE, Microwave Theory and Techniques*, Vol MTT-33, No. 1, pp. 44-51 , Jan., (1985).

[37] [Online]. Available: http://www.krytar.com/

[38] J. W. Kooi, G. Chattopadhyay, M. Thielman, T. G. Phillips, and R. Schieder, "Noise Stability of SIS Receivers," *Int J. IR and MM Waves*, Vol. 21, No. 5, May, (2000).

[39] J. D. Kraus, "Radio Astronomy", *2nd Edition*, pp. 7-8

[40] A. R. Kerr, S, -K. Pan, E. F. Lauria, A. W. Lichtenberger, J. Zhang, M. W. Pospieszalski, N. Horner, G. A. Ediss, J. E. Effland, R. L. Groves, "The ALMA Band 6 (211-275 GHz) Sideband-Separating SIS mixer-Preamplifier", *Proc. 15th Int. Symposium on Space Terahertz Technology, Northampton*, MA, 27-29 April (2004).

[41] S. M. X. Claude, "Sideband-Separating SIS Mixer for ALMA band 7, 275-370 GHz," *Proc. 14th Int. Symposium on Space Terahertz Technology*, Tuscon, Az, 22-24 April (2003).

[42] D. Maier, S. Devoluy, M. Schicke, and K. F. Schuster, "230 GHz SSB SIS Mixer for Band 3 of the new Generation Receivers for the Plateau de Bure Interferometer", *Proc. 16th Int. Symposium on Space Terahertz Technology*, Chalmers, Göteborg, Sweden, May, (2005), S03-02.

[43] F. P. Mena, J. W. Kooi, A. M. Baryshev, D. F. J. Lodewijk, R. Hesper, and W. Wild, Construction of a Sideband Separating Heterodyne Mixer for Band 9 of ALMA *Proc. 17th Int. Symposium on Space Terahertz Technology*, California Institute of Technology, Pasadena, Ca., Mar., (2007), to be published.

[44] V. Vassilev, V. Belitsky, C. Risacher, I. Lapkin, A. Pavolotsky, and E. Sundin, "Design and Characterization of a Sideband Separating SIS Mixer for 85-115 GHz", in *Proc. of SPIE*, Vol. 5498, Ground-based Telescopes, edited by J. Zmuidzinas, W. S. Holland, and S. Withington, (SPIE, Glasgow, UK, 23-25 June, 2004).

[45] Microwave Office, Applied Wave Research Inc. El Segundo, CA 90245, USA.

[46] G. A. Ediss, A. R. Kerr, H. Moseley, and K. P. Stewart, "FTS Measurements of Eccosorb MF112 at Room Temperature and 5 K from 300 GHz to 2.4 THz", *ALMA* Memo 273, 2 Sep., (1999). [Online]. Available: http://www.alma.nrao.edu/memos/

[47] http://www.eccosorb.com/

[48] F. P. Mena and A. Baryshev, "Design and Simulation of a Waveguide Load for ALMA-band 9", *ALMA* Memo 513, 5 Jan., (2005). [Online]. Available: http://www.alma.nrao.edu/memos/

[49] J. W. Kooi, A. Kovács, M. C. Sumner, G. Chattopadhyay, R. Ceria, D. Miller, B. Bumble, R. LeDuc, J. A. Stern, and T. G. Phillips, "A 275-425 GHz Tunerless Waveguide Receiver Based on AlN SIS Technology", *IEEE Trans. Microwave Theory and Techniques*, Vol. 55, No. 10, pp. 2086-2096, Oct. (2007).

[50] C. Risacher, V. Vassilev, A. Pavolotsky, and V. Belitsky, "Waveguide-to-Microstrip Transition with Integrated Bias-T", *IEEE Microwave and Wireless Components Letters*, Vol. 13, No. 7, pp. 262 - 264, Jul., (2003).

[51] C. Risacher, V. Belitsky, V. Vassilev, I. Lapkin, and A. Pavolotsky, "A 275-370 GHz SIS Receiver with Novel Probe Structure", *Int. Journal Infrared and Millimeter Waves*, Vol. 26, No. 6, pp. 867 - 880, May, (2005).

[52] A. M. Baryshev, R. Hesper, F. P. Mena, B. D. Jackson, J. Adema, H. Schaeffer, J. Barkhof, W. Wild, M. Candotti, C. Lodewijk, D. Loudkov, T. Zijlstra, O. Noroozian, and T. M. Klapwijk, "Design and development of a 600-720 GHz receiver for ALMA Band 9", *Proc. 17th Int. Symposium on Space Terahertz Technology*, (2006), P1-17.

[53] C. F. J. Lodewijk, M. Kroug, and T. M. Klapwijk, "Improved design for low noise Nb SIS devices for band 9 of ALMA (600-720 GHz)", *Proc. 16th Int. Symposium on Space Terahertz Technology*, Chalmers, Göteborg, Sweden, May, (2005), S03-05.

[54] J. R. Tucker and M. J. Feldman, "Quantum Detection at Millimeter Wavelengths", *Rev. Mod. Phys.*, Vol. 57, pp. 1055-1113, Oct. (1985).

[55] D. Ludkov, Kavli Institute of NanoScience, Delft University of Technology, Lorentzweg 1, 2628 CJ Delft, The Netherlands, private communication.

[56] Radiometer Physics GmbH., [Online]. Available: http://www.radiometer-physics.de

[57] H. B. Callen and T. A. Welton, "Irreversibility and generalized Noise," *Phys. Rev.*, Vol. 83, no. 1, pp. 34-40, Jul., (1951).

[58] A. R. Kerr, S. -K Pan, and J. E. Effland, ALMA Memo 357 (2001) [Online]. Available: http://www.alma.nrao.edu/memos/

[59] S. Mahieu, Institute de Radio-Astronomie Millimétrique, France, Priv. comm,. Jan. (2006).

[60] P. R. Jewell and J. G. Mangum, "System Temperatures, Single Versus Double Sideband Operation, and Optimum Receiver Performance", *ALMA* Memo 170, Apr, (1997).

[61] J. W. Lamb, "SSB vs. DSB for Submillimeter Receivers", *ALMA* Memo 301, Apr., (2000).

[62] A. Pavolotsky, D. Meledin, C. Risacher, M. Pantaleev, and V. Belitsky, "Micromachining Approach In Fabricating of THz Waveguide Components", *EMN04*, 20-21 Oct., Paris, France, (2004).

[63] V. P. Koshelets, A. B. Ermakov, L. V. Filippenko, A. V. Khudchenko, O. S. Kiselev, A. S. Sobolev, M. Yu. Torgashin, P. A. Yagoubov, R. W. M. Hoogeveen, and W. Wild, "Superconducting Integrated Submillimeter Receiver for TELIS", *IEEE Trans. Appl. Superconductivity*, Vol. 17, No. 2, pp. 336-342, Feb., (2007).

[64] D. Meledin, A. Pavolotsky, V. Desmaris, I. Lapkin, C. Risacher, V. Perez, D. Henke, O. Nystrom, E. Sundin, D. Dochev, M. Pantaleev, M. Fredrixon, M. Strandberg, B. Voronov, G. Goltsman, and V. Belitsky, "A 1.3 THz Balanced Waveguide HEB Mixer for the APEX Telescope," accepted for publication in *IEEE Microwave Theory and Technique*, (2008).

Chapter 9

Towards integrated array receivers*

9.1 Introduction

Essentially all HEB receivers operating above 800 GHz are implemented with quasi-optical (twin-slot, log-periodic, dipole) antenna structures. This despite the fact that waveguide technology offers the prospect of higher throughput, better telescope coupling efficiency, and large format imaging arrays with well aligned beams on the sky. There are several reasons for the popularity of open structure mixers in the terahertz regime.

Mechanically machined waveguide mixer blocks are expensive, especially for the small structures needed at terahertz frequencies. Then there is the issue of waveguide loss (Sec. 5.1), available RF bandwidth, how to handle the tiny quartz substrate that supports the active device, and reliability of the assembly process. Fortunately, most of these obstacles can be overcome by employing silicon-on-insulator (SOI) substrates, as outlined in this Chapter. It shall be seen that the presented work is applicable to both single element and multi-element array receivers.

We begin the discussion with a SIS mixer on a 1 μm silicon-nitride (Si_3N_4) mem-

*The material described in this Chapter has been published in the following papers: J. W. Kooi, J. Pety, B. Bumble, C. K. Walker, H. G. LeDuc P. L. Schaffer, and T. G. Phillips, *IEEE Trans. Microwave Theory and Techniques*, Vol. 46, No. 2, pp. 151-161, Feb., (1998).
J. W. Kooi, C. Dröuet d'Aubigny, R. B. Bass, C. Walker, A. W. Lichtenberger, *Applied Superconductivity Conference Jacksonville*, FL, Oct., (2004).
R. B. Bass, A. W. Lichtenberger, R. Weikle, J. W. Kooi, C. K. Walker, S.-K. Pan, *Proc. sixth European Conference on Applied Superconductivity*, Sorento, Italy, Sep. 14, (2003).
C. Groppi, C. Walker, C. Kulesa, P. Puetz, D. Golish, P. Gensheimer, A. Hedden, S. Bussmann, S. Weinreb, T. Kuiper, J. Kooi, G. Jones, J. Bardin, H. Mani, A. Lichtenberger, and G. Narayanan, *astro-ph/0606061v1*, (2006).
C. Groppi, C. Walker, C. Dröuet d'Aubigny, C. Kulesa, A. Hedden, D. Prober, I. Siddiqi, J. Kooi, A. Lichtenberger, and G. Chin, *Proc. SPIE, Astronomical Telescopes and Instrumentation*, v. 4855, (2002).

brane, operational in the 800 – 920 GHz frequency range. This technology, though feasible for SIS mixers, limits the IF gain bandwidth of HEB mixers. The reason is that surface properties of the Si_3N_4 membrane at the NbN HEB interface adversely effects the phonon escape time. It is very likely that the thermal conductivity of the silicon-nitride membrane and/or acoustic mismatch plays an important role in this process. Experiments show that the situation is mostly corrected [1, 2] by adding a MgO buffer layer between the HEB and Si_3N_4 membrane (Details in Chap. 6). To circumvent this problem we explore the use of ultra-thin "silicon-on-insulator" (SOI) substrates with integrated gold beamleads. Not only do ultra-thin silicon substrates open up the terahertz regime to multi-pixel HEB waveguide mixer arrays, it also facilitates large scale SIS focal plane arrays at submillimeter wavelength.

In this Chapter we trace the evolution from single SIS junctions on silicon-nitride membrane, to ultra-thin silicon substrate HEB mixers, to finally the design, implementation, and measurement of a 64 pixel SOI based (scalable to terahertz frequencies) 345 GHz SIS focal plane array receiver.

9.2 SIS mixer fabrication on 1 μm thick Si_3N_4 membranes

Traditional waveguide junctions are constructed on quartz supporting substrates. To avoid RF leakage, via surface modes in the substrate, the cutoff frequency of these modes needs to be well above the operation frequency of the mixer. For frequencies above 800 GHz the required thickness of the quartz ($\leq$ 35 μm), and the dimensions of the substrate channel that hold the junction ($\leq$ 80 μm) become unmanageable in size with the traditional approach. To avoid this problem we have explored the idea of fabricating a SIS junction on a silicon-nitride (Si_3N_4) membrane. The membrane is mounted on a smooth pedestal, or base, that is centered on a full height rectangular waveguide. This is shown graphically in Fig. 9.1. In this case the optically polished flat copper pedestal serves as a ground plane for the RF choke supported microstrip

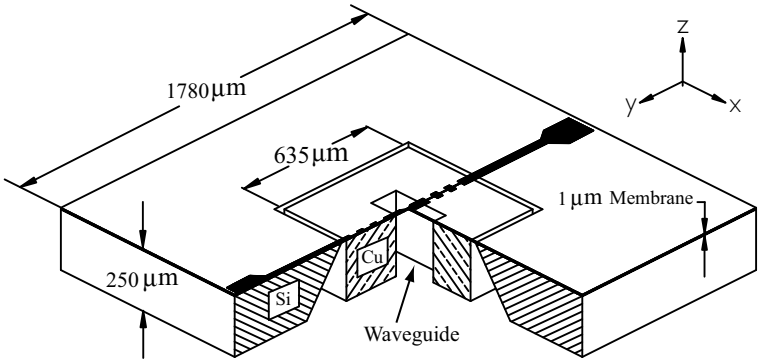

Figure 9.1: Rendering of the 1μm Si_3N_4 membrane, RF choke, and silicon support structure that houses the SIS tunnel junction and RF matching network.

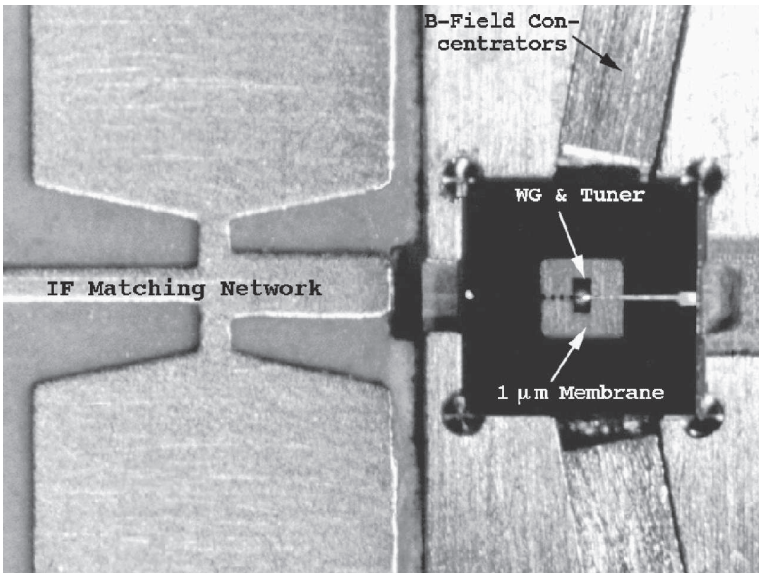

Figure 9.2: View of the silicon-nitride membrane situated in the mixer block. The membrane extends 50 μm over the pedestal to house the RF choke. Looking through the membrane one sees the waveguide (250 x 125 μm) and outline of the circular tuner low impedance section (100 μm dia, about twice the size of a human hair.) The IF frequency is 1 – 2 GHz.

mode. When properly in contact with the pedestal, the RF choke on top of the membrane provides a short circuit at the waveguide wall. The mixer block is based on a design by Ellison *et al.* [3]. The membrane itself is supported by a silicon frame etched along the 111 crystal plane. An improved version of this design incorporates a suspended RF stripline, which provides up to 12 μm dimensional freedom in the Z-direction.

The silicon frame is glued into a "moat" by means of a 50 % solution of nail polish (polyester resin) in butylacetate (solvent). Securing devices this way has the advantage that they are easily removed with acetone, yet cycle securely to liquid helium (LHe) temperatures. As far as we can tell, I/V characteristics of both LHe dipped junctions and those cooled in a vacuum cryostat are identical. This is a good indication that the thermal conductivity of the silicon-nitride membrane is high enough to prevent heating of the SIS junction. Fig. 9.2 shows the membrane supported SIS junction on its pedestal. Looking through the membrane (ε_r=7) we see the circular backshort.

9.2.1 Device fabrication

Devices are fabricated on (100) oriented silicon wafers which are 254 μm thick, 51 mm in diameter, and polished on both sides. The Si_3N_4 is grown under conditions for reduced stress by low pressure chemical vapor deposition (LPCVD) to a thickness of 1 μm. Fabrication of the $Nb/AlO_x/Nb$ tunnel junction is accomplished by a standard

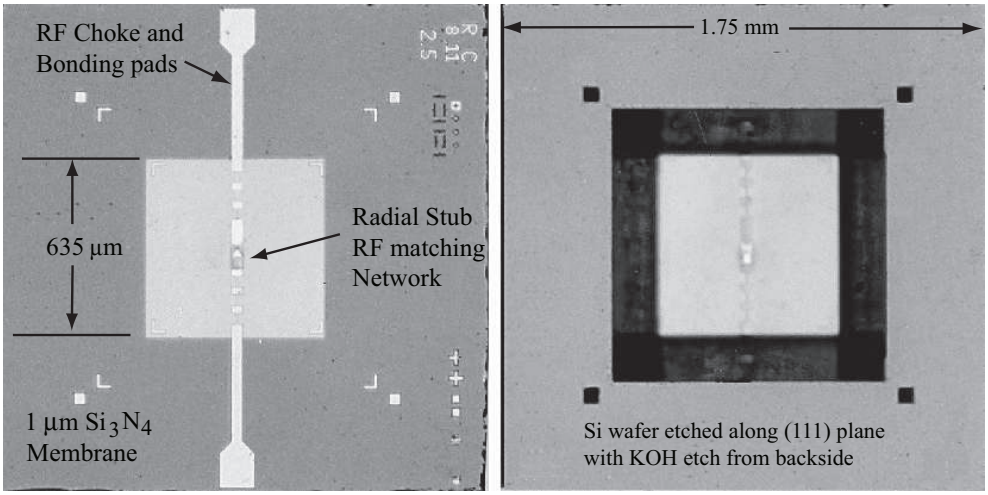

Figure 9.3: Top and bottom view of the (100) oriented silicon and 1 μm Si_3N_4 membrane.

trilayer deposition technique [4, 5].

Exposed silicon areas on the back side are then anisotropically etched in a bath of 30 % KOH solution at 70 °C (Fig. 9.3). Etching stops after about eight hours when only the front side membrane and the sides with (111) silicon planes are left exposed. The devices on the front are protected from the KOH solution by an "O"-ring enclosure. A layer of wax on the device side also helps localize wafer damage if one of the Si_3N_4 windows happens to break during KOH etching. After the etching is complete individual 1.78 mm $\times$ 1.78 mm chips are diced from the wafer using a diamond saw.

Device yield with this process is typically lower than similar devices made on either silicon or quartz substrates. We have not determined exactly how to increase yield, however many devices with current densities of about 12 kA/cm^2 and sub-gap to normal state resistance ratios of greater than 10 have been fabricated on multiple wafer runs.

9.2.2 Measured performance

In Fig. 9.4 we show the measured performance of the 1 μm thick silicon-nitride SIS mixer. Using the "shot noise" method described in Sec. 7.3.2 [6, 7] we calculate an overall mixer conversion gain of -12.6 dB, DSB mixer noise temperature of 248 K, and IF noise temperature (referred to the output of the mixer) of 6.2 K. These results are in good agreement with computer simulations where we are able to separate the total front-end loss (8.3 dB) from the actual mixer down-conversion loss (4 dB) [8]. From FTS measurements the estimated optics loss is $\sim$ 1.1 dB, and RF mismatch $\sim$ 0.42 dB. This leaves a niobium film absorption loss of approximately 6.8 dB (79 %), due to antenna, choke and RF matching network (Fig. 9.3). The calculated absorption loss is about one and a half times the loss expected from the Mattis-Bardeen theory

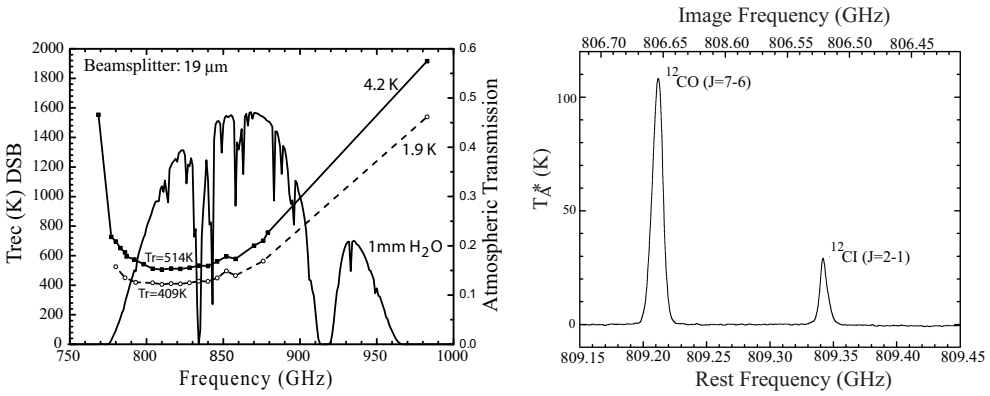

Figure 9.4: *Left*) Frequency response of the 850 GHz Si_3N_4 based waveguide receiver. The receiver employs a radial-stub RF matching network (Fig. 5.4) and two mechanical circular tuners. When installed at the Caltech Submillimeter Observatory(CSO) the receiver noise temperature decreased by 8 % across the band (475 K @ 809 GHz). This is attributed to the lower LHe bath temperature (3.55 K) at the 4200 meter altitude site. *Right*) A spectrum of the Orion Bar in $^{12}CO_{J=7\rightarrow6}$ and $CI_{2\rightarrow1}$, taken at the Caltech Submillimeter Observatory.

(65.4 %) [9].

When the mixer was cooled from 4.2 K to 1.9 K the receiver noise temperature dropped by $\sim$ 20 % to 409 K DSB. Interpretation of the measurements indicates that the mixer gain improved by approximately 12 % to -3.5 dB, which is similar to what has been observed below the gap [10]. We attribute this effect to the sharpening of the I/V curve. Due to the slightly higher energy gap ($\approx$ 2.9 mV), an additional 12 % improvement in the front-end transmission is obtained from the reduction in niobium film absorption loss.

9.3 HEB mixers on ultra-thin silicon substrates

9.3.1 Introduction

The attractive material properties of quartz include a low loss tangent (tanδ=0.0002) and low dielectric constant (ε_r=3.8). Quartz is also compatible with a variety of micro-fabrication processes and can be processed in wafer form. However, as the frequency increases circuit elements and waveguide dimensions necessarily become smaller. In practice it is found that, due to handling and mechanical strength, the practical thickness of quartz is limited to $\sim$ 35 μm. This thickness dictates a usable upper frequency of approximately 800 GHz (waveguide fill factor and substrate modes), though with special care and expertise this limit may be pushed to $\sim$ 1 THz [11]. For these reasons, quartz is an highly impractical material with which to work in the terahertz regime.

Recent research in the field has been aimed at finding better materials to advance the terahertz field, and in particular spectroscopic array receivers. Materials such as silicon-nitride (previous Section) have shown promise due to high mechanical strength,

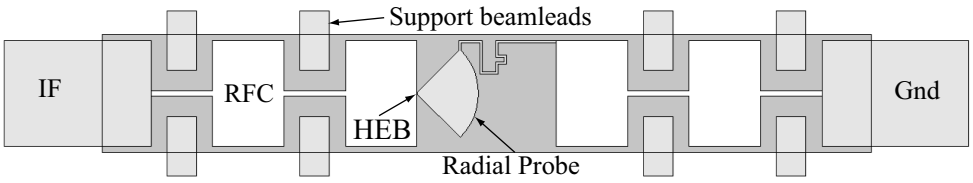

Figure 9.5: An "across-the-waveguide" 3 micron thick SOI substrate with integrated beamleads. The HEB is located at the throat of the radial probe waveguide transition.

even at a thickness of only 1 μm, and low dielectric constant (ε_r=7). However since the IF response time of HEB mixers is coupled to the electron-phonon interaction time (Chap. 6), the relatively low thermal conductivity of silicon-nitride in comparison to silicon excludes this material for use with phonon cooled HEB mixers if IF bandwidth is to be maximized [1, 2, 12].

Another issue to take into consideration with the choice of substrate material and geometry is that most HEB devices produced to date have not proven particularly uniform across an entire wafer. Thus basing a focal plane array design on the uniformity of single wafer is risky. A better approach is to have many densely packed HEB mixer chips which (after processing) can be dc pre-selected, and/or independently mounted/removed. The added advantage of such a design is that the chips can then also be used in any type of mixer configuration, e.g. array, balanced or sideband separating.

Yet another substrate consideration is the fact that to date published results of HEB terahertz mixers are essentially all quasi-optical, silicon based, single pixel, and with designs that are not necessarily scalable to the kind of imaging arrays we are proposing to build. Moreover, the extremely large instantaneous signal bandwidth of HEB mixers coupled to very broad bandwidth quasi-optical techniques leads to a non-negligible direct (continuum) detection current as discussed in Sec. 4.3.2 [13]. Using a band-limited waveguide approach will reduce the direct detection effect.

An important added advantage of the waveguide approach with focal plane arrays is that mechanical feedhorns produce well-defined on axis Gaussian beam patterns. The latter is very important and especially so in array applications. With focal plane arrays, HEB mixers, and scalability in mind, we have focused our research on ultra thin "silicon-on-insulator" (SOI) substrates.

Silicon has excellent mechanical properties when it is very thin (on the order of a few microns). The deleterious effects of the high dielectric constant and loss tangent are also significantly diminished if the substrate thickness is reduced. In addition, the superconducting detectors we involve ourselves with require cryogenic cooling. At a few Kelvin, the carriers in silicon freeze out and the material becomes a near perfect insulator. With these properties in mind, and the fact that HEB fabrication is highly compatible with silicon as a base substrate (Sec. 9.3.3), it becomes self-evident that ultra-thin silicon is potentially a good replacement for quartz substrates in the terahertz regime. It is worth noting that the SOI approach is equally well applicable to SIS arrays for frequencies below a terahertz (Sec. 9.4).

We have applied the ultra-thin SOI mixer technology to a single element HEB

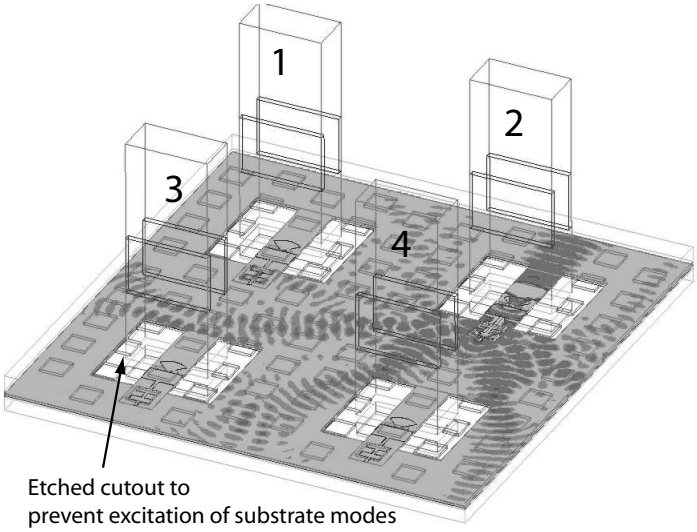

Figure 9.6: Example of a small 2 x 2 array. In the substrate, with pixel #2 excited, crosstalk is $\sim$ -40 dB. In this scenario the array is monolithic with a silicon micro-machined backshort cavity (not shown).

mixer at 1.6 THz, and SuperCam; an integrated SIS array receiver in the frequency range 300 – 400 GHz [14]. Future work is likely to include scaling SuperCam to the important 600 – 720 GHz atmospheric window and to design small spectroscopic imaging arrays centered at the 1.4 THz molecular N^+, and 1.9 THz atomic C^+ lines. To accommodate designs up to several terahertz we have baselined 3 μm silicon substrates [15], with integrated beamleads for the ground and IF/dc-bias connections.

Collaborations with the research group at the University of Virginia (UVa), have allowed development of the new ultra-thin mixer chip technology. Results were first published in the proceedings of the EUCAS 2003 conference [16], and have since been further developed and improved. The use of integrated micron thick gold beamleads simplifies the electrical connection and placement of the chip. This is an important aspect of the SOI process, which is a promising new technology that enables the complex mixer design from Chap. 8, and the array receivers discussed in this Chapter, to be realized and extended to the terahertz frequency regime.

9.3.2 Silicon-On-Insulator (SOI) morphology

Until quite recently it has been difficult to take advantage of silicon for the described terahertz applications as it could not be manufactured or processed at the required micron thickness necessary. In addition, it is also necessary that the silicon is single crystal material such that grain stresses are not introduced. These difficulties are overcome by a relatively recent technology development called “silicon-on-insulator”

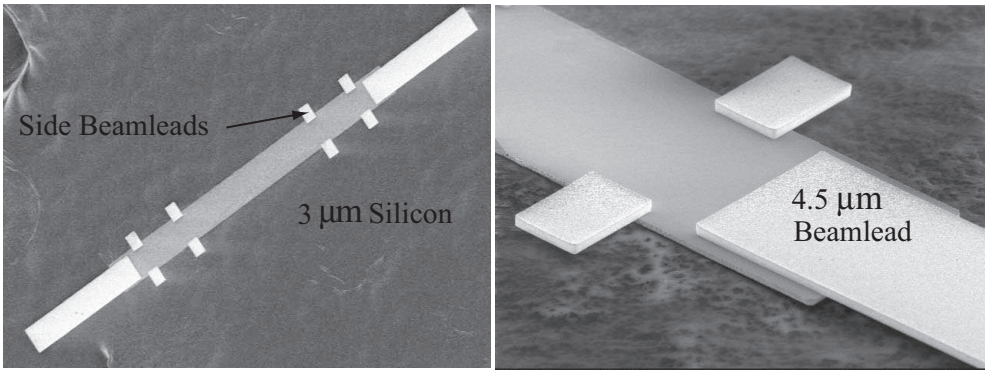

Figure 9.7: *Left*) Top-down SEM image of an ultra-thin silicon chip with gold beamleads. The dimensions of the silicon chip are 800 μm by 76 μm. *Right*) A close up SEM image of the top side of an ultra-thin silicon chip with 4.5 μm gold beamleads. Processing/picture by R. B. Bass. [16]

(SOI). Physically, a SOI wafer is the combination of a standard thickness silicon "handle" wafer, a SiO_2 insulator layer above it, and an ultra-thin silicon "device" layer fused to the oxide. The thick silicon handle gives the wafer mechanical strength for most of the device processing, while the thin device layer serves as the eventual final substrate layer. The SiO_2, or buried oxide, provides a barrier between the two silicon layers and can also be used as an etch stop. Historically SOI wafers were originally invented for the semiconductor industry to solve the problem of leakage current and parasitic capacitance between MOSFETs.

The SOI process is not only a convenient solution to the problem of making ultra-thin mixers, it also offers some significant micro-fabrication advantages in comparison to quartz mixer processes. For one, almost any mixer chip shape can be realized because the chip outline is defined by lithography and RIE etching. This is opposed to quartz, where the chip geometry is limited to a rectangular shape by the (diamond saw) dicing that is required to define and separate individual chips. Secondly, ultra-thin silicon chips with small lateral dimensions (on the order of a few tens to few hundred microns) are actually ideal from a mechanical perspective. The chips are flexible rather than brittle and can be subject to much physical handling and deformation without destruction. Another advantage of eliminating dicing processes is that beamleads can now be easily integrated into the device structure with front side processing. Beamleads are essentially gold tabs that extend from the edges of the chip and provide a means for making electrical, thermal, and mechanical connections to other chips or circuit fixtures. In effect, the chip can be suspended in the waveguide block with no need for special support structures. A possible observed disadvantage of the Au beamleads is that the mixer chip, once mounted in the waveguide, cannot be removed without significant damage (destruction) to the described beamleads.

9.3.3 SOI Processing

Conventional approaches to fabricating thin silicon chips involve chemically etching the silicon at a known etch rate to the desired thickness. However, limits imposed by variations in etch conditions limit this approach to only tens of microns. Etch rates may be slowed near the stop-point by heavily doping the silicon with boron, but this approach too is not capable of achieving thickness tolerances of less than several microns due to the spread in the doping profile. Our approach begins by fabricating the superconducting circuit and beamleads atop the device layer of a "silicon-on-insulator" (SOI) substrate. We use SOI wafers with a nominal device layer thickness of 3 μm [15] and a tolerance of less than 0.5 μm. The chip is then mounted, device side down, on top of a quartz carrier wafer. A combination of mechanical lapping and chemical etching is used to remove the handle silicon from the buried oxide layer. The oxide layer is patterned using backside photolithographic alignment through the quartz chip. The patterned oxide serves as an etch mask for a chemical or reactive ion etching of the exposed device silicon. The silicon device is etched through to the quartz carrier and gold beamleads, thereby defining the individual chips. It is our observation that the 3 μm ultra-thin chips suffer less dielectric loss and are actually much more robust than quartz chips which are easily a factor ten thicker. For a more detailed process description, we refer to Bass *et al.* [17].

9.3.4 "Symmetric" SOI-based waveguide transition

The combination of HEB mixers with silicon micro-machining techniques promises to open up the terahertz regime to large format spectroscopic imaging arrays. The potential for such systems are many, examples are atmospheric research, astrophysics, and security systems. In our designs we have made extensive use of 3D electromagnetic simulations [18] to help define the fabrication and tolerance specifications of the above mentioned ultra-thin beamlead chip technology. At the terahertz frequencies we concern ourselves with the tolerance to device misalignment, which becomes increasingly more unforgiving, needs to be addressed.

Critical to our design concept, we utilize beamleads on the SOI chip to set the vertical alignment (Z-dimension). From our computer simulations we find the tolerance in the substrate height location to be much greater that the manufacturer specified substrate variation of 0.5 μm. Sideways alignment of the beamlead chip is determined by the mechanical accuracy of the IF channel width. For conventional machining techniques the achievable tolerance is typically $\pm$ 2.5 μm, which limits the upper frequency to about 2 THz. If improved tolerance is desired or machining cost prohibitive, lithographic electroplating such as is being explored at Chalmers University [19], or traditional silicon micro-machining [20] may be more appropriate. In our design small side beamleads support the chip at either side of the waveguide, while the ground and IF beamleads make electrical contact with the block and IF circuit board. The chip itself can either be secured with Crystal bond [21] or an epoxy such as EPO-TEK H20E [22]. Once secured the IF and ground beamleads may then be tag bonded to the (gold plated) mixer block and IF circuit board. Due to the thinness and softness of the gold beamleads it is possible, if so desired, to compress the

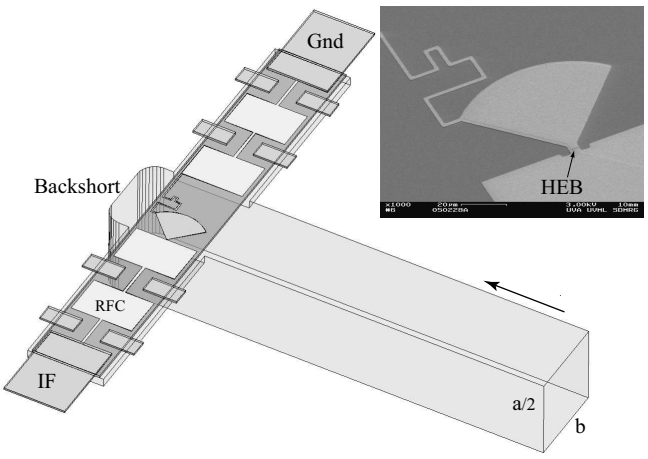

Figure 9.8: Cross-sectional view of a single pixel E-plane splitblock HEB waveguide mixer. Operating frequency is 700 – 1100 GHz. The substrate and waveguide dimensions are given in Table 9.1. Unlike an H-plane splitblock, there are no currents in the plane of the splitblock. This has the advantage that in the event of imperfect contact no RF loss is introduced.

beamleads when the top and bottom mixer block are joined. The deformation of the beamleads has negligible effect on the waveguide geometry. It should be noted that the University of Virginia developed SOI/beamlead technology is not limited to high frequency mixers alone, but can also be adapted to a large variety of waveguide based microwave circuits, such as multipliers, couplers, or even direct detection cameras. In Fig. 9.9 we show the calculated 700 – 1100 GHz "across-the-waveguide" response overlaid with the mean atmospheric transmission at Chajnantor, Chile. The achievable instantaneous bandwidth of the SOI/HEB mixer combination is 44 %, equivalent to two terrestrial atmospheric windows.
Under the assumption that mapping is the primary science goal, the loss in sensi-

Table 9.1: Symmetric waveguide design parameters of Fig. 9.8.

Element	Dimension (μm)
Waveguide dimension	240×120
SOI substrate	$3 \times 100 \times 660$
Air height below substrate	12.5
Air height above substrate	25
Backshort radius	25
Distance backshort-substrate	46
Radius radial probe	53
RF choke (high impedance)	53×4
RF choke (low impedance)	90×61

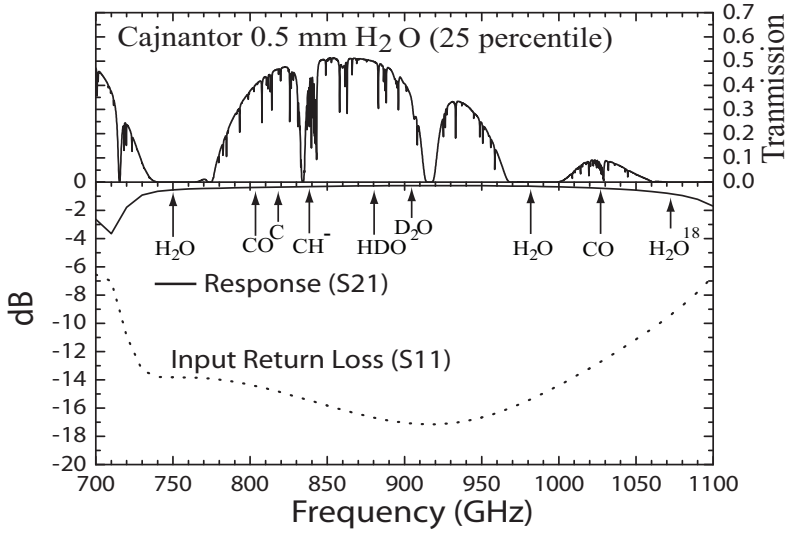

Figure 9.9: Frequency performance of the SOI symmetric radial probe transition of Fig. 9.8. Overlaid is the zenith atmospheric transmission at Chajnantor, Chile, for a 0.5 mm column of precipitable water vapor (pwv). The elevation is 4.8 km, and the barometric pressure 560 mbar [23].

tivity when array receivers are implemented with HEB mixers, as compared to more sensitive SIS junctions, may be overcome with a > 4 pixel array.

It should be noted that HEB spectroscopic imaging arrays do not require a magnetic field to suppress Josephson oscillations. This is an important advantage of HEB mixer based array receivers.

9.3.5 "Asymmetric" SOI-based waveguide transition

Greater signal bandwidth can be achieved by implementing an asymmetric SOI waveguide transition that does not go across the waveguide. This is similar to the broad bandwidth tunerless design in Chap. 7. Here we have implemented the design by means of silicon micromachining technology with the probe in the plane of the E-field. The details of the design are shown in Fig. 9.10 with the dimensions listed in Table 9.2. The SOI substrate is suspended by the IF, ground, and support beamleads. This has the advantage of fixing the height (Z) dimension. In the silicon base, the substrate channel and backshort are etched using reactive-ion etching (RIE) with lithographic precision. Because the shape of the SOI substrate at the extremities is somewhat arbitrary we have chosen to increase the width to 200 μm for ease of handling. The width (w) of the substrate itself is determined by the lowest order cutoff mode

$$w = \frac{c}{2 f_{max} K_{eff}} \quad . \tag{9.1}$$

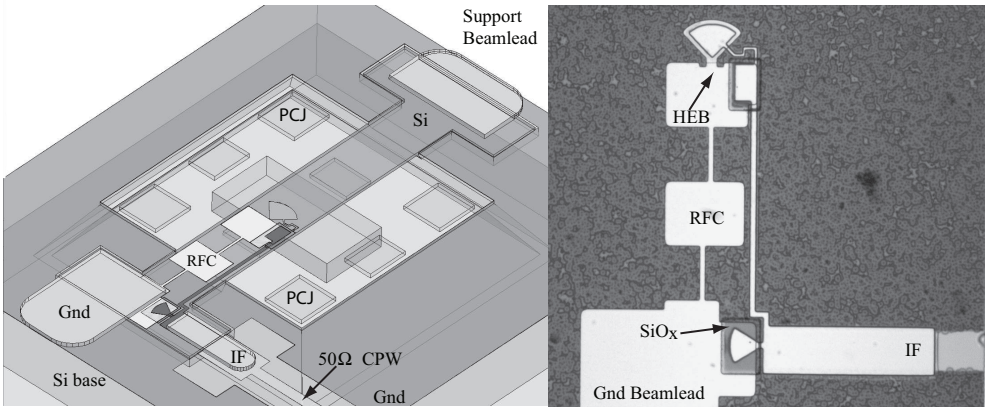

Figure 9.10: *Left*) Design of a silicon micro-machined single pixel HEB mixer. See text for details. The mixer is designed to operate from 1.3-2.2 THz. *Right*) Physical implementation at UVa (B. Bass *et al.* In this photograph the silicon handle has not yet been removed. Probe radius is 23 μm.

$K_{eff} = 1.6$ for 3 μm thick suspended silicon, as derived from HFSS [18]. Etched along the 111 crystal plane are 2 μm high, KOH etched, photonic crystal junctions (PCJ). These form quarter-wave RF chokes [24] and minimize electric field leakage from the backshort-horn cavity vacuum space (15 μm). The IF signal is taken off the silicon substrate by means of a 50 Ω coplanar wave (CPW) transmission line. Fig. 9.11 shows the simulated coupling, not accounting for possible direct detection. The RF bandwidth is 1300 – 2200 GHz, or 53 % !

Table 9.2: Asymmetric waveguide design parameters of Fig. 9.10.

Element	Dimension (μm)
waveguide dimension	132×66
SOI substrate	$3 \times 55 \times 320$
Air height below substrate	6
Air height above substrate	6
Backshort radius	—
Distance backshort-substrate	27
Radius radial probe	23
RF choke (high impedance)	29×2
RF choke (low impedance)	43×33
PCJ size	$42 \times 42 \times 4$

When we compare this to the atmospheric transmission of the stratosphere (Sofia, $\sim$ 13 km), with a mean precipitable H_2O of 7 μm, we see that in principle this single SOI based mixer design covers all important HIFI terahertz frequency lines. When implemented it is advisable to add an optical band limiting [25, 26] metal mesh filter

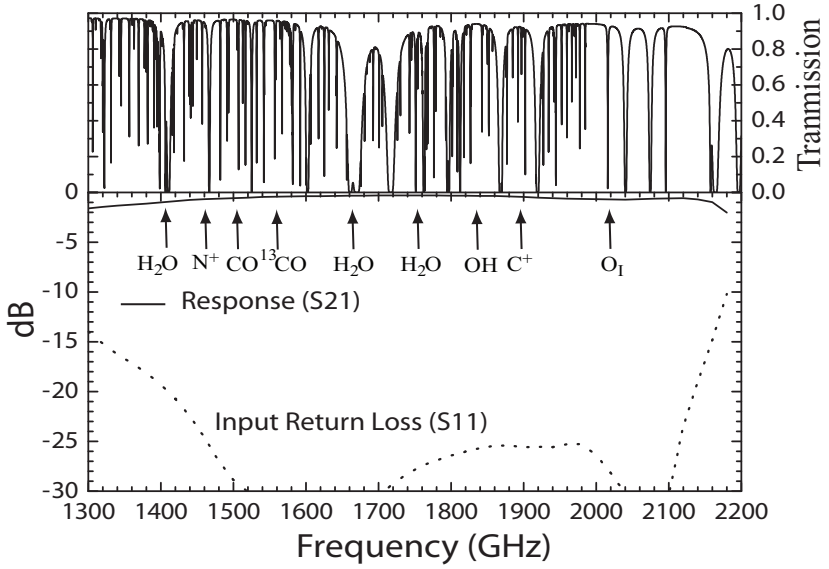

Figure 9.11: Calculated coupling efficiency and input return loss for the asymmetric silicon micromachined mixer in Fig. 9.10. Overlaid is the zenith atmospheric transparency at airborne altitude (SOFIA). Elevation is 13 km, the mean precipitable column of H_2O 7 μm, barometric pressure 163 mbar, average temperature -56.3 °C, and relative humidity 5.6 % [23].

to reduce direct detection in the HEB mixer (Sec. 4.3.2).

9.4 Large format arrays based on SOI technology

In this Section we discuss SuperCam [27], a 64 pixel, super-heterodyne camera designed for operation in the astrophysical important 870 μm atmospheric window at the 10-meter Heinrich Hertz Telescope (HHT) [28]. While the possibility of such heterodyne arrays has been discussed for more than two decades (Gillespie & Phillips 1979 [29]), only recently have advances in mixer technology, device fabrication, micromachining, and digital signal processing made this concept a reality. Astronomical interest in array receivers stems from the fact that instead of mapping an extended source, such as a molecular cloud, by slowly rastering a single pixel over the object by means of repeated motions of the telescope, a multi-pixel array receiver has a much larger field of view (FOV) and can map a source with significantly greater efficiency. When one considers the telescope overhead time, with the repeated pointings required to accommodate a single pixel instrument, array receivers become particularly attractive. An additional factor to take into consideration with observations of extended (line) emissions from the ground in the submillimeter or terahertz frequency regime, is the variability of sky opacity. Multi-pixel array receivers take full advantage of good weather conditions when they present themselves, and will therefore map larger

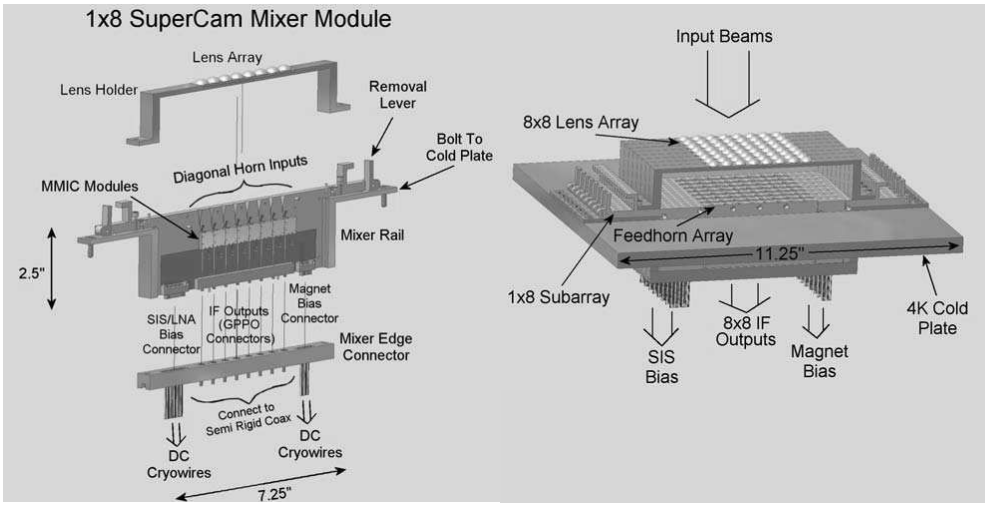

Figure 9.12: *left*) Assembly diagram of a single 1x8 mixer module. *Right*) Assembly diagram of the complete 8x8 array. Courtesy D. Golish, UAz.

regions of the sky under more or less identical conditions, thus allowing for better internal consistency. Under poor weather conditions, correlated sky noise across the array may be subtracted. This provides enhanced baseline quality, much like the correlation receiver discussed in Chap. 8.

The 64 pixel SuperCam array presented in this Chapter will be used to address fundamental questions about the physics and chemistry of molecular clouds in the Galaxy and their relation to star and planet formation. The advent of a spectroscopic imaging array provides an order of magnitude increase in mapping speed over what is now available, and is expected to revolutionize how observational astronomy is performed in this important wavelength regime. Array receivers may therefore change submillimeter (and terahertz) astronomy, similar to the way bolometric submillimeter cameras such as Sharc, Scuba, and Bolocam [30, 31, 32] have led to an explosion of new results.

Unlike the situation with bolometric detectors, heterodyne receiver systems are coherent, retaining information about both the amplitude and phase at the mixer IF output (Sec. 2.3). It should be noted that spectroscopy can in principle be performed in this same wavelength regime by the combination of incoherent detectors with frequency dispersive quasi-optical devices such as gratings and Fabry-Perot interferometers. However, as we have seen in Sec. 2.3.2, the limited resolving power limits the observable velocity resolution.

The array technology presented here is by design directly scalable to terahertz frequencies. Aside from astrophysics, it also has immediate application in remote sensing of the Earth and its atmosphere. In the following Sections, we focus on the design of a SOI substrate waveguide-to-thinfilm microstrip transition, the design of the SIS junction RF matching network, and integrated MMIC IF low noise amplifier. However, before we get to these subjects we first discuss the camera construction and

lessons learned from past efforts.

9.4.1 Camera layout

SuperCam is constructed by stacking eight, 1 x 8 rows of fixed tuned, SIS mixers. For reference, the assembly of a sub-array is shown in Fig. 9.13. The IF output of each mixer is connected to a low-noise "microwave monolithic integrated circuit" (MMIC) amplifier that has been integrated into the mixer block in close proximity to the SIS junction. The intended instantaneous IF bandwidth of each pixel is 2 GHz, centered at an IF frequency of 5 GHz. However due to the wideband performance of

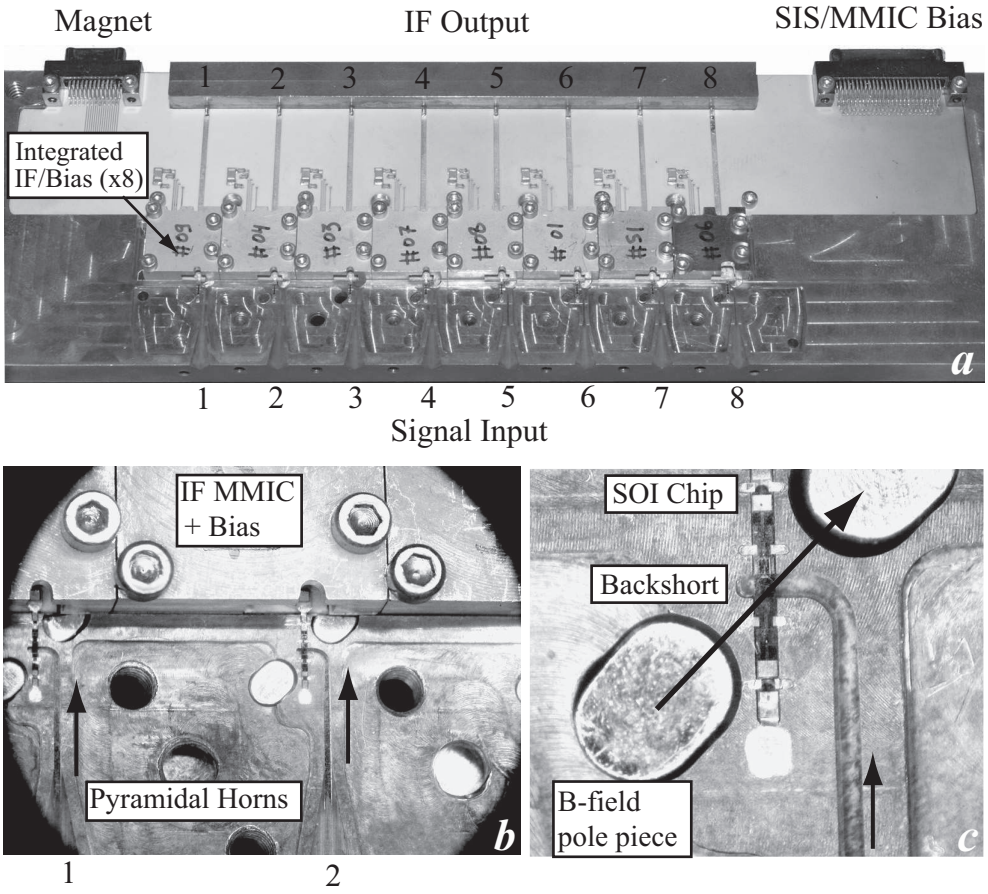

Figure 9.13: Detailed view of a 1 x 8 sub-array. LO and RF signals enter the front of the mixer block via eight pyramidal horns. Eight superconducting magnets are integrated at the backside of the block (not visible). These allow the magnetic field for each junction to be set individually. The IF output, after $\sim$ 35 dB "on board" amplification, are taken out toward the rear of the sub-array. At this same interface plane SIS mixer, MMIC, and magnet bias signals enter the IF circuit board. For further details please see text.

the integrated IF MMIC (Sec. 9.4.6) we are able to achieve $\sim$ 6 GHz instantaneous IF bandwidth. For the backend spectrometer we utilize sixteen 1 GHz wide A/D converters feeding real time FFT digital signal processors [33]. Each mixer has its own electro-magnet to suppress unwanted Josephson noise.

In addition, each pixel in the array has the SIS junction and MMIC amplifier bias individually optimized under computer control. The required local oscillator power is provided by a X-band synthesized frequency multiplier whose output is divided between the pixels via a matrix of waveguide power dividers. From the very onset, an important science driver in the array concept has been scalability to higher frequencies. To conserve helium, the mixer array is cooled to 4 K by a closed-cycle refrigeration system.

Unlike all other millimeter/submillimeter arrays composed of individual mixers and discrete components, the SuperCam array has a high degree of integration. Efficient packaging is essential to the successful implementation of the array. Each of the 1 x 8 mixer sub-arrays is constructed from tellurium copper using a splitblock technique. A low loss, dielectric lens couples energy from the telescope into a diagonal feedhorn. This type of horn offers excellent Gaussian beam coupling at the expense of significant cross-polarization. Since SuperCam is a single polarization design with no polarization selective optics, the cross-polarization introduced by the horns will not impact the instrument performance.

Fig. 9.13 shows a detailed view of the 1 x 8 sub-array. The RF and local oscillator signals enter the sub-array via eight pyramidal horns. Using fundamental TE_{10} mode waveguide the signals are coupled to the SIS junction via a, by now familiar, broadband "across-the-waveguide" radial probe waveguide to thin-film microstrip transition (Secs. 9.3.4 & 9.4.3). The substrate that supports the SIS junction and RF matching network is 3 μm SOI (Sec. 9.3.2). As shown in Fig. 9.13c the magnetic field, needed to suppress Josephson oscillations, is applied at 45 degrees. To prevent IF feedback oscillations from the eight broadband and high gain MMIC amplifiers, each module is covered by a precision machined housing. This housing also covers the SIS and MMIC bias circuitry. Even so, cavity modes are easily excited, and to minimize coupling across the MMIC a high dielectric constant IF board is recommended. The IF signals are extracted toward the rear of the block via eight 50 Ω microstrip transmission lines. Magnet and SIS/MMIC bias signals enter the Rogers TMM4 IF board via a set of Omnetics connectors.

Light from the telescope enters the cryostat through a 127 mm diameter anti-reflection (AR) coated, crystalline quartz vacuum window and passes through an IR blocking filter on the 40 K radiation shield before illuminating the 4 K mixer array. SuperCam uses a Sumitomo SRDK-415E-A71A cryocooler. The cooler has 1.5 W of thermal load capacity at 4.2 K and 45 W at 40 K with orientation-independent operation. The operating temperature of the cryocooler is stabilized by the addition of a helium gas pot on the second stage. For further information on the cryogenics we refer to Groppi *et al.* [14].

9.4.2 LO power distribution

With an array receiver, LO power must be efficiently distributed among all pixels. Depending on the mechanical and optical constraints of the array, local oscillator distribution can be achieved by either quasi-optical or waveguide injection. With the quasi-optical approach, dielectric beam splitters or holographic phase gratings are used to divide the LO energy between array pixels [34]. The multiple LO beams can then be combined with the sky beams before entering the array mixers using a traditional (Mylar) beam splitter, Martin-Puplett interferometer, or Fabry-Perot interferometer [35]. The quasi-optical approach works well for modest sized arrays. However, for the large format being presented here, the size of the required quasi-optical power splitter and diplexer become prohibitive. Therefore we have implemented a hybrid waveguide/quasi-optical LO power injection scheme. The LO power [25] at the output of the array is coupled to an eight-way waveguide power divider with a splitblock machinable waveguide twist. Each of the power divider outputs provides the drive power for a 1 x 8 sub-array via an identical 8 way corporate divider with diagonal waveguide feedhorn outputs. Accounting for conduction and surface roughness losses, we expect this 64-way network to add an additional 2 dB of LO power loss compared to a lossless divider. The described mixer blocks and LO distribution system are fabricated at the University of Arizona (UAz) with a Kern MMP micro-mill [36].

9.4.3 3 μm thick silicon splitblock waveguide transition

Similar to the HEB SOI design of Sec. 9.3, we extend the use of 3 μm thick silicon substrate to SuperCam. The choice of 3 μm SOI facilitates scalability, and eases modal excitation when going "across-the-waveguide" (Fig. 9.15). The addition of support beamleads has no effect on the RF performance as long as the cavity that houses the beamleads is evanescent.

The beamlead cavity may be extended to facilitate the use of Crystal bond wax [21]. In our design side beamleads are crucial in setting the substrate height with respect to the center of the waveguide, and for securing the chip. The width of the support beamlead cavity is 120 μm. This provides 10 μm space on either side of the support beamlead, which in principle can be reduced. Alignment tolerance issues are addressed in Sec. 9.4.5.

To mount the ultra-thin silicon chip in the mixer block the following general procedure is followed (P. Puetz and H. Mani [37]). The mixer block is first cleaned with isopropyl alcohol (IPA) in an ultrasonic bath. Following cleaning, some Crystal bond wax [21] is put in the side beamlead pockets, making sure that the pockets are not overfilled. The selected SOI device may be picked up using, for example, a fine natural haired paint brush and positioned carefully on top of the mixer block in correct orientation, and as close as possible to the final position. The mixer block should already have alcohol applied to junction area. Care must be taken to pick up the junction so that it is right side up, and the IF side of the junction is in the correct orientation. Beam leads may be aligned, and alcohol added with for instance a paintbrush. Finally, the mixer block is heated until the Crystal bond wax melts. Once the chip is secure in place, the IF beam lead is "Tack bonded" with a flat bonding

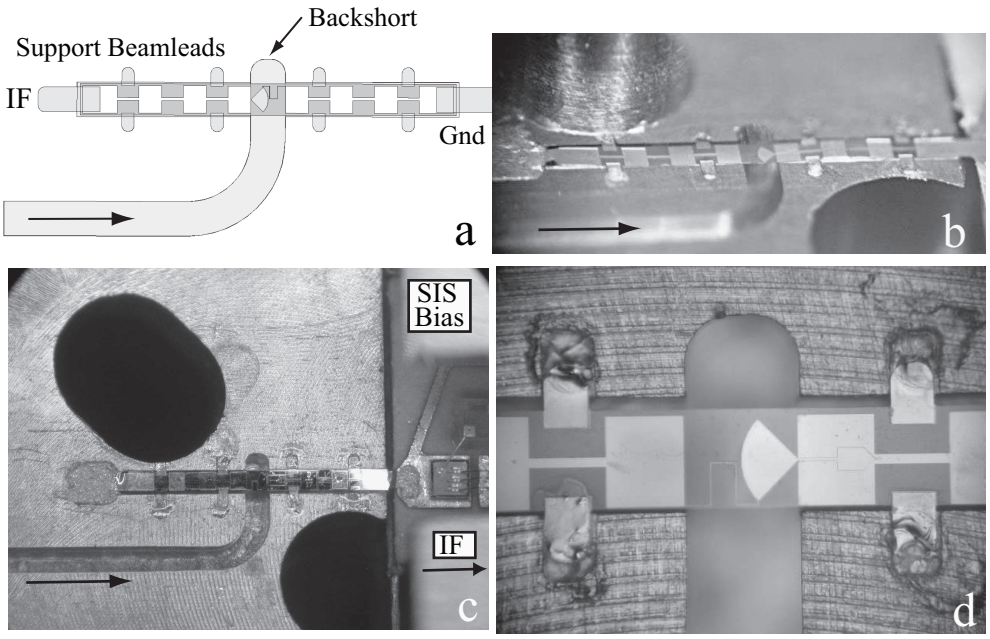

Figure 9.14: Composite view of the SuperCam waveguide-to-mictrostrip transition. The side beamleads are important in determining the Z-dimension. See text for further details.

tool. If needed, conductive H20E silver epoxy [22] may be used to reinforce the IF and contact GND beam leads mechanically. In this case the epoxy should be cured at a low temperature (95°) for 2 hours.

In Fig. 9.14a we show a rendition of the SOI chip with integrated beamleads. HFSS [18] has been used exclusively in the design of the "across-the-waveguide" transition.

Table 9.3: Geometric parameters of the SuperCam waveguide-to-SIS transition in Fig. 9.14.

Element	Dimension (μm)
Waveguide dimension	600×280
SOI substrate	$3 \times 254 \times 3048$
Air height below substrate	65
Air height above substrate	35
Backshort radius	115
Distance backshort-substrate	200
Radius radial probe	140
RF choke (high impedance)	175×24
RF choke (low impedance)	186×220

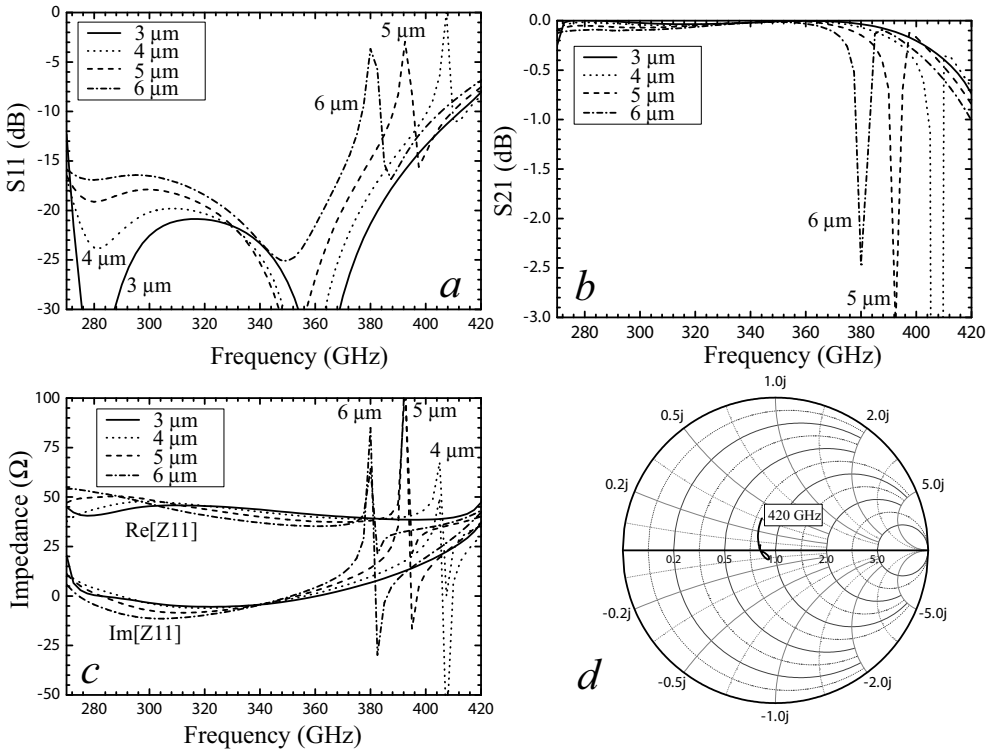

Figure 9.15: Coupling performance of the SOI "across-the-waveguide" microstrip transition. *a*) Input return loss. For a discussion on the excited substrate resonance see text. *b*) Coupling efficiency. *c*) Real and imaginary probe impedance. *d*) Probe impedance in the complex plane (Smith chart).

The backshort radius is 115 μm and is located 200 μm in front of the chip. Additional parameter details are provided in Table 9.3. In Fig. 9.14b we show a photograph taken at an oblique angle (courtesy P. Puetz). The side, ground, and IF beamleads are clearly visible. The width of the IF channel is such that it provides 12.5 μm space on either side of the silicon chip. The IF beamlead serves to extract the IF signal and inject the SIS bias. Just visible in Fig. 9.14c is the dc blocking capacitor. Errors due to chip misalignment, such as are evident in Fig. 9.14d, are at this wavelength small when compared to the tolerance in SIS junction and RF matching network parameter variation (Sec. 9.4.4).

The performance of the waveguide transition is shown in Fig. 9.15. When going across the waveguide, to facilitate the SIS dc-bias return, high Q resonant mode(s) are easily excited in the operational TE_{10} mode waveguide band. This may be understood from Withington and Yassin's assessment [38], in that by going across the waveguide the probe's input impedance is influenced by the parallel sum of one more non-propagating modal impedances. This is especially noticeable with the very broad bandwidth performance of the asymmetric radial probe (Chap. 7, Sec. 9.3.5). In case of the 3 μm thick silicon substrate, the modal resonance may be pushed to $\sim$ 440 GHz

(1.76 f_c) with an empirical design [18] of the inductive meandering transmission line that extends across the waveguide. When the silicon substrate thickness is increased, all other parameters being the same, the discussed resonance shifts down in frequency. For narrower band applications this design constraint eases considerably. Fortunately the tolerance of available SOI thickness is 0.5 μm, well within the required limit.

From the computer simulations, we see for 3 μm SOI excellent performance in the frequency range 270 – 420 GHz ($\sim$ 37 % instantaneous bandwidth). It should be noted that the SIS bias return may be accomplished via the integrated side beamleads. Taking a "conservative" approach we have not attempted this with the SuperCam chip design. However, this technique has been indirectly demonstrated with the single pixel AlN-barrier design of Chap. 7. Future designs may well follow the "asymmetric approach" with bias return via the side beamleads. It being natural to the SOI approach with integrated beamleads technology, while avoiding the fort mentioned modal excitation problems.

9.4.4 SIS junction design and predicted performance

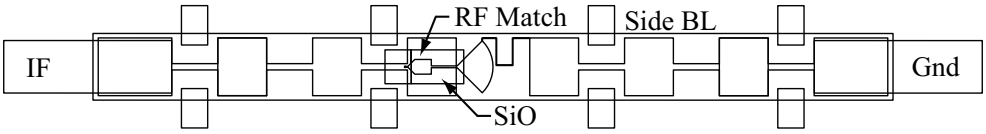

Figure 9.16: SOI junction layout with IF, ground, and 8 side beamleads (top/bottom). The side beamleads provide structural support and set the substrate height in the waveguide. The IF/ground beamleads are "tagged" down with a wirebond probe tip. All beamleads are 4.5 μm thick. Junction Fab: A. W. Lichtenberger *et al.*, UVa.

The SIS junction design for SuperCam is based on AlO_x-barrier technology. The reasons for this choice are several. AlO_x as a SIS barrier is a mature technology, which goes along well with the "conservative" approach. In addition SuperCam being primarily a mapping instrument of $^{12}CO_{J=3\rightarrow2}$ (345 GHz) and $^{13}CO_{J=3\rightarrow2}$ (330 GHz) does not require the very large RF bandwidth offered by high-current density AlN-barrier technology, as outlined in Chap. 7. A final consideration is the use of optical vs. e-beam lithography. Low-current density AlO_x-barriers have a R_nA product that allows the junction area to be defined optically for a 20 Ω normal state resistance. This is important as the junction connects directly to the integrated (50 Ω) MMIC

Table 9.4: SuperCam nominal SIS junction parameters.

R_nA ($\Omega\mu m^2$)	Area (μm^2)	J_c (kA/cm^2)	C_s ($fF/\mu m^2$)	ε_r	t_{gnd} (nm)	t_{top} (nm)	$t1_{SiO}$ (nm)	$t2_{SiO}$ (nm)
23.0	1.13	8.2	82.0	4.3	175	450	225	225

Table 9.5: SuperCam SIS RF matching network parameters. All dimensions in microns.

W_1	W_2	W_3	L_1	L_2	L_3	L_{tap}
2.0	56.0	7.0	9.5	63.0	98.5	27.0

amplifier (Sec. 9.4.6). With a proper IF matching network design the integrated MMIC terminates the SIS junction IF port into $\sim 2.5 \cdot R_n$. As was seen in Sec. 4.1.10, this termination impedance provides broad IF bandwidth with an acceptable mixer conversion loss [39].

Our design thus calls for a (single) SIS junction with 20 Ω normal state resistance. The use of a single junction is important when yield, and the ability to suppress the Josephson noise (Sec. 4.1.2) are taken into consideration. Given the parameters of Table 9.4 and a 1.13 μm^2 nominal junction area, the parasitic device capacitance shunting R_n is $\sim$ 92 fF.

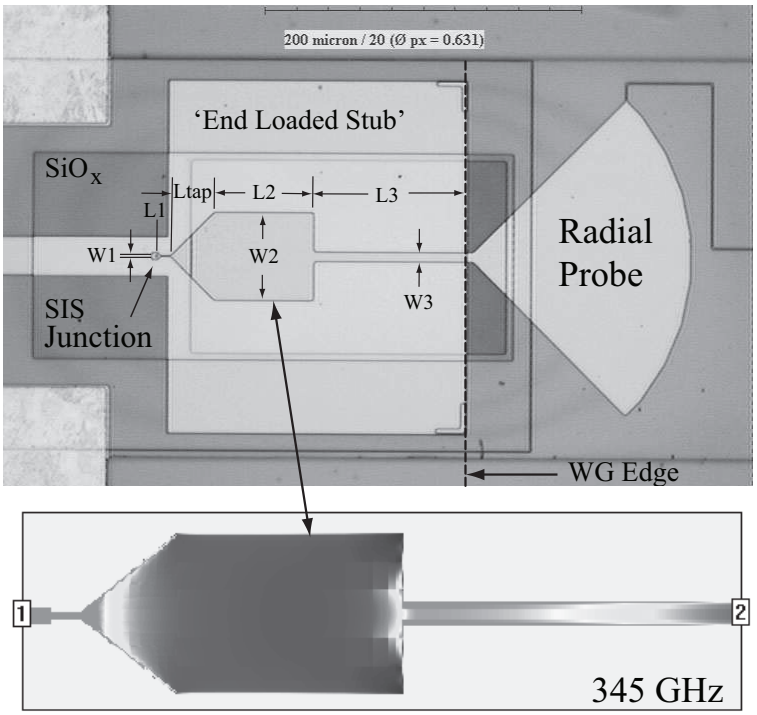

Figure 9.17: *Top*) 1000× photograph of the radial probe transition and junction area. The meandering transmission line across the waveguide is 2 μm by design. However due to undercutting the actual width is $\sim$ 1 μm. The same is true for $W1$. *Bottom*) Current distribution in the "end-loaded" stub RF matching network at 345 GHz based on Sonnet [40].

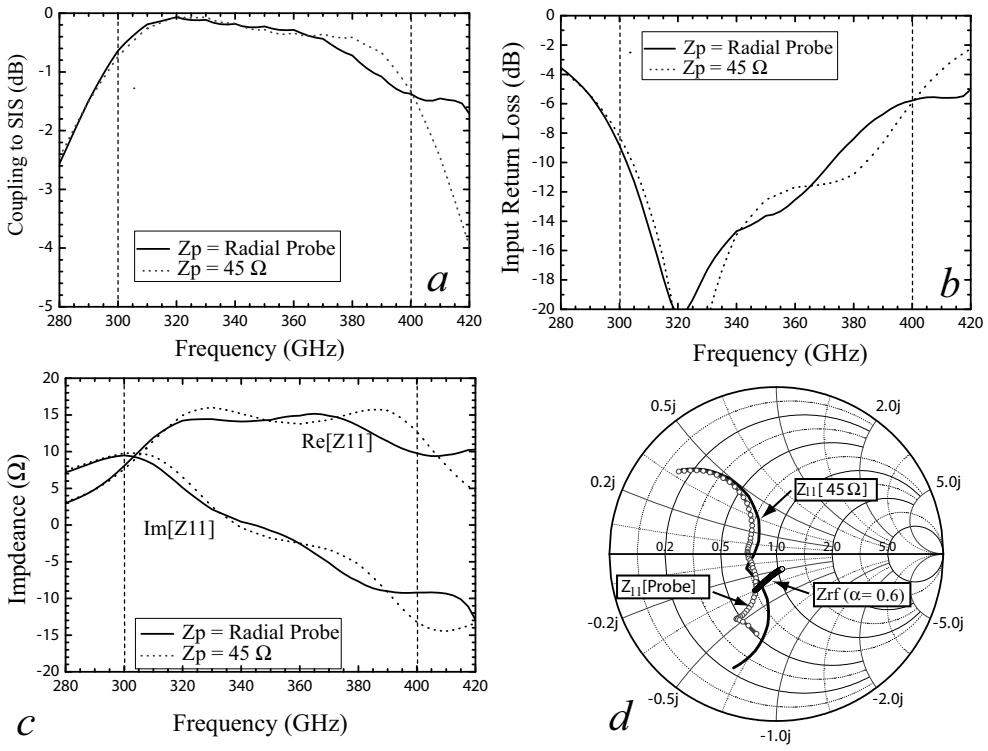

Figure 9.18: *a*) RF coupling efficiency between the waveguide and SIS junction. The dotted line is the response for a 45 Ω "ideal" antenna impedance. *b*) Input return loss at the SIS port. *c*) Real and imaginary impedance presented to the SIS junction. *d*) The same, but in the complex plane normalized to R_n (20 Ω).

To match this parallel R_nC combination to the radial probe antenna impedance we employ an "end-loaded" stub, similar to the one described in Sec. 4.1.8. In the design of the RF matching network we have used Pcircuit, a superconducting linear circuit simulator, originally written by Zmuidzinas and Bin *et al.*, in combination with Sonnet [40, 41]. The top panel of Fig. 9.17 shows the final product, with the current density distribution at 345 GHz shown in the bottom panel. The low impedance Section of the "end-loaded" stub is tapered to minimized stray capacitance of the transition.

The actual dimensions of the RF matching network are shown in Table 9.5. To calculate the coupling efficiency between the waveguide and LO pumped SIS junction (α=0.6) we combine the S-parameters of HFSS (radial-probe transition), with Sonnet (2D niobium film RF matching network), and the from the Tucker theory obtained SIS junction RF impedance.

The broadband performance shown in Fig. 9.18 is in large part due to the very wide bandwidth radial probe waveguide transition, which in the frequency range of interest presents a more or less constant 45 Ω impedance. The ωRC product of the

junction limits the overall bandwidth. Traditional waveguide to thinfilm microstrip transitions provide a smaller RF bandwidth [42]- [44] than the radial probe transition, and the coupling to the junction becomes a convolution of the waveguide transition with the ωRC product of the junction. In Fig. 9.18 the dashed lines indicate the design goal; 300 – 400 GHz.

9.4.5 Tolerance to misalignment and fabrication

In Fig. 9.19 we show the effect of a $\pm$ 10 μm sideways chip misalignment in the waveguide. The SuperCam design specification is 300 – 400 GHz, and even with the substrate 10 μm out of the waveguide do we find this goal easily met. The reason for the minor effect has to do with the small fractional change in probe radius, as measured from the waveguide wall, and the effect it has on the real impedance of the radial probe transition [45]. A much more significant effect is experienced by a change in the critically tuned parallel R_n, C_j combination. This is evident in the right panel of Fig. 9.19 where, keeping the R_nA product constant, we vary the SIS junction area. Changing this parameter effects both R_n and C_j and thus the overall response function.

Parametric junction variations also indicate that the SiO_x thickness ought to be kept to within $\pm$ 15 %. A variation in the R_nA product (J_c, Eq. 4.10) results primarily in a small coupling loss. Here too a variation of $\pm$ 15 % is acceptable. In the R_nA variation calculations (not shown) the junction capacitance is assumed 82 fF/μm^2. The most efficient method therefore to compensate for possible device process variations is to vary the junction area. An area variation of $\pm$ 17 % corresponds to a diameter variation of 1.1 - 1.3 μm. It may be assumed that the R_nA product across the 2 inch diameter SOI wafer is relatively constant. In the SuperCam design, we have opted for 25 % of the wafer with a (circular) junction diameter of 1.1 μm, 50 % with 1.2 μm, and 25 % with 1.3 μm, as depicted in the right panel of Fig. 9.19.

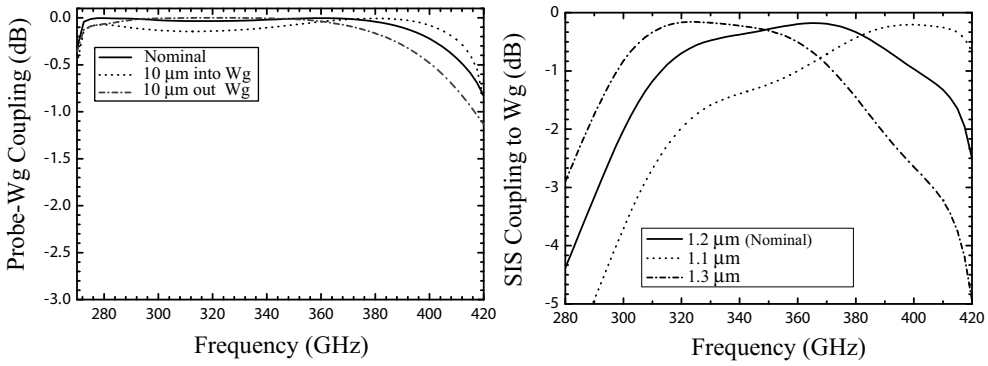

Figure 9.19: *Left*) Effect of a $\pm$ 10 μm lateral chip misalignment in the waveguide. The radial probe frequency is centered on 345 GHz. *Right*) SIS junction coupling efficiency as a function of device area (junction diameter) variation. The R_nA product is held constant at 23 $\Omega - \mu$m^2.

9.4.6 Integrated IF

During the past 4 years wideband, very low noise, cryogenic monolithic microwave integrated circuit (MMIC) amplifiers have been developed by Sander Weinreb's group at Caltech, with foundry fabrication at TRW (now Northrop Grumman Space Systems, NGST) and HRL. The MMIC's use indium phosphide, 0.1 micron gate length, high electron-mobility transistors (HEMT's). These devices match the requirements of densely packed focal plane arrays in terms of size, dc power dissipation, yield, and bandwidth.

The IF output of the SIS junction is bonded directly to the input matching network of a low-noise, InP MMIC amplifier module, located in the mixer sub-array (Fig. 9.13). SuperCam's IF center frequency is 5 GHz which is the standard IF frequency at the HHT. It also lies conveniently within the operating range of the existing generation of IF amplifier modules. The chip is mounted in an 11 mm $\times$ 11 mm amplifier module that contains integrated bias tees for the SIS junction and the WBA-13 MMIC amplifier chip. The module achieves a noise temperature of $\sim$ 5 K and consumes 8 mW of power at 4 K. An amplifier module has been integrated into a single pixel SIS mixer block and verified to operate as expected. Allan variance times and mixer noise temperatures are unchanged within the measurement errors compared to a similar mixer used with an external commercial LNA and cryogenic isolator.

The computer simulation of Fig. 9.21 are referenced to the SIS junction. We plot the IF response for three LO pumped differential sub-gap mixer impedances, ranging from 3.3 R_n to 10 R_n (67-200 Ohm). Actual measurement by Puetz *et al.* gave optimal receiver sensitivity with a sub-gap slope of 3.3 R_n (Fig. 9.24). The MMIC unit has $\sim$ 35 dB of available gain in the 4 – 9 GHz passband. This is more than adequate and ensures that the noise contribution from room temperature post amplification is negligible ($\leq$ 0.5 K, Eq. 2.27).

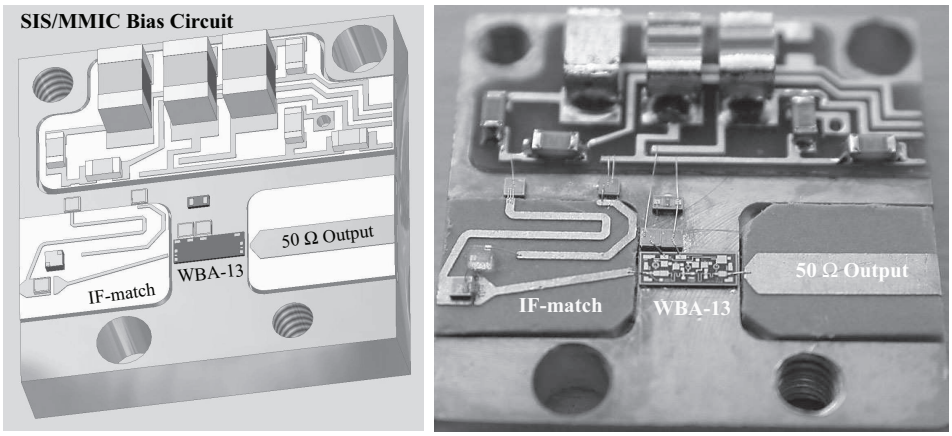

Figure 9.20: *Left*) Model of the integrated MMIC and IF input/output matching network. Rendition courtesy N. Wadefalk. *Right*) Physical implementation. The dielectric constant of the IF board should be kept as high as possible to maximize MMIC input to output port isolation.

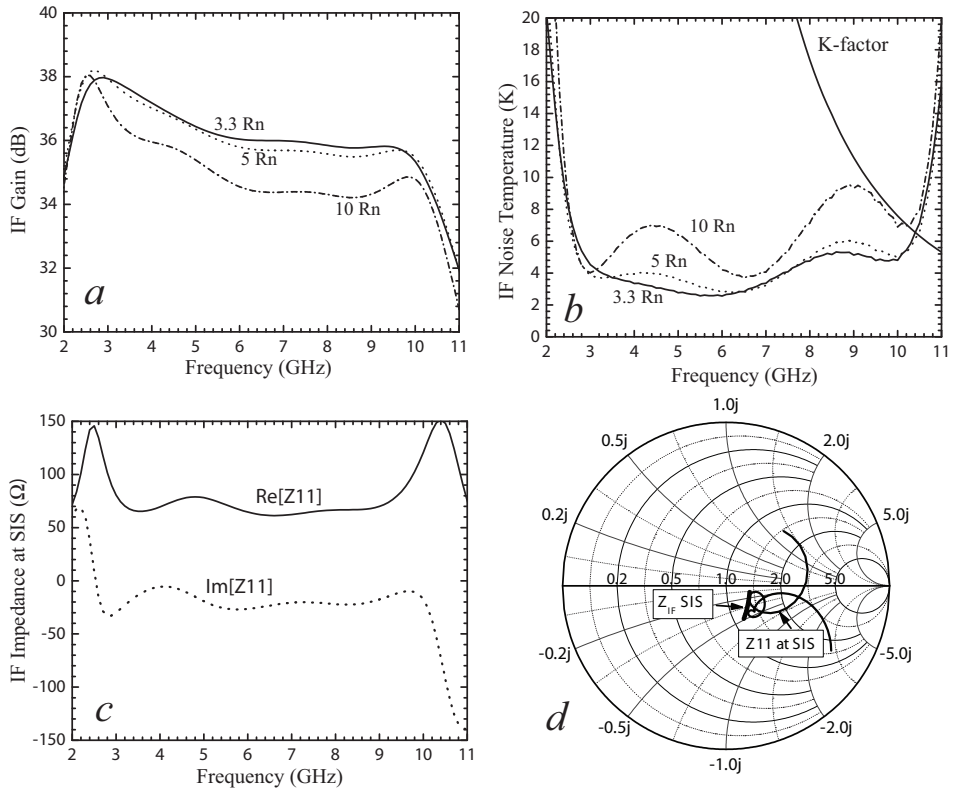

Figure 9.21: *Top*) Gain and noise temperature of the WBA-13 MMIC when connected to a SuperCam SIS junction for three LO pumped (sub-gap) differential source impedances. In all cases the parasitic junction capacitance shunts the source impedance. The K-factor indicates that the MMIC module is unconditionally stable. This does not include electromagnetic feedback. *c*) IF load impedance presented to the SIS junction. *d*) Complex plane. The IF load impedance presented at the junction, overlaid with the SIS junction intrinsic IF output impedance (3.3 R_n) shunted by the 92 fF parasitic Al_2O_3 barrier capacitance. See also Sec. 4.1.10.

As may be seen from Fig. 9.21b the IF noise temperature is quite insensitive to the SIS IF impedance (sub-gap slope) for values < 5 R_n. This is by design, e.g. R_n was chosen based on these results (Sec. 9.4.4). The amplifier is stable (K-factor) for all frequencies where the MMIC has gain. It should however be noted that with $\sim$ 35 dB of gain, feedback from the output to input is likely. A careful design of the IF amplifier housing/cover is therefore called for. In panel 9.21c we show the IF impedance presented at the junction. In the frequency range of interest this is approximately 70-i20 Ω. The IF design (N. Wadefalk & J. Kooi) has been optimized for minimum, and flat, noise performance. The presented performance includes the RF choke, thin-film RF matching network capacitance ($\sim$ 257 fF), and beamlead contact (Fig. 9.14c). The use of a beamlead contact, rather than the traditional (inductive) wirebond, is of considerable benefit for frequencies > 6 GHz. This is an additional advantage of the integrated SOI beamlead approach. Finally, in panel

9.21d we depict the IF impedance presented to the junction in the complex plane. The 3.3 R_n source impedance, shunted with the junction parasitic capacitance (92 fF) is also indicated (Z_{IF} SIS).

9.4.7 Fourier transform spectrometer (FTS) measurements

A SIS junction can be used as a direct detector. Combined with a Michelson interferometer (FTS) [46] and Fourier transform of the obtained interference spectrum, the RF frequency response of the junction can be obtained. It has in practice been found that the direct detection response of a SIS mixer is an accurate tracer of the conversion gain and instantaneous RF bandwidth. This can be understood in that the passband response of a SIS mixer is determined by the RF matching network and parasitic junction capacitance. The local oscillator power ($\alpha = 0$) has little effect on this and the optical coupling efficiency to the junction. Secondly, the IF frequency in case of a heterodyne response is a small fraction of the LO frequency, which itself lies within the designated RF passband.

The responsivity of a SIS direct detector can be derived from the LO pumped dc I/V curve [47]

$$I_{dc}(V_o, V_{LO}) = \sum_{n=-\infty}^{\infty} J_n^2(\alpha) I_{dc}\left(V_o + n\hbar\omega/e\right) \ , \tag{9.2}$$

where α presents the photon energy normalized LO pump level

$$\alpha = eV_{LO}/\hbar\omega \ . \tag{9.3}$$

For a direct detector the incoming radiation is very small ($\alpha \sim 0$) and only single photon processes are important. From [48] we obtain the increase in direct current as

$$\Delta I_{dc} = \frac{1}{4V_\omega^2} \frac{I_{dc}(V_o + \hbar\omega/e) - 2I_{dc}(V_o) + I_{dc}(V_o - \hbar\omega/e)}{(\hbar\omega/e)^2} \ . \tag{9.4}$$

Following Tucker and Feldman, the actual dissipative RF current in the SIS junction, in the limit of a small ac voltage, is found to reduce to

$$I_\omega = V_\omega \frac{I_{dc}(V_o + \hbar\omega/e) - I_{dc}(V_o - \hbar\omega/e)}{2(\hbar\omega/e)} \ . \tag{9.5}$$

Since the RF power absorbed in the junction (P_{RF}) is equal to $V_\omega I_\omega/2$, and the responsivity of a direct detector defined as the change in direct detection current in response to a change in the (ac) input signal power level, we find that

$$R = \frac{\Delta I_{dc}}{P_{RF}} = \frac{e}{\hbar\omega} \frac{I_{dc}(V_o + \hbar\omega/e) - 2I_{dc}(V_o) + I_{dc}(V_o - \hbar\omega/e)}{I_{dc}(V_o + \hbar\omega/e) - I_{dc}(V_o - \hbar\omega/e)} \ . \tag{9.6}$$

It is interesting to observe that the responsivity of an ideal tunnel junction (Eq. 9.6) reduces to $e/\hbar\omega$ for $V_{gap} - V_o < \hbar\omega/e > V_{gap} + V_o$. In all cases V_o represents the dc bias voltage and V_{gap} the superconducting energy gap voltage ($\sim$ 2.8 mV for niobium).

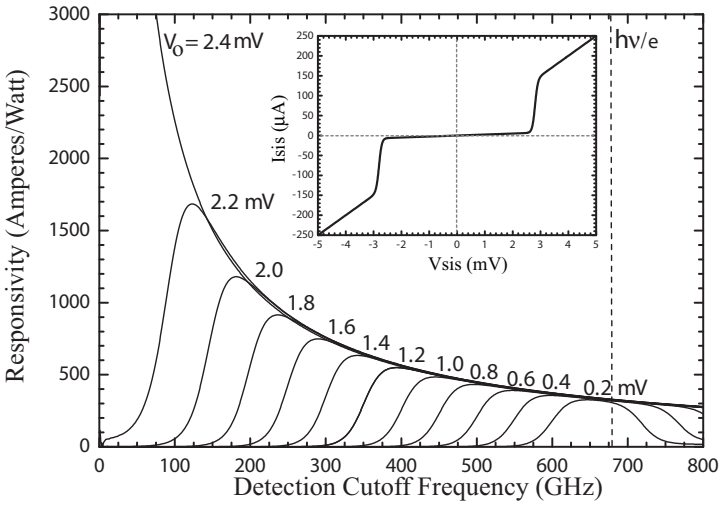

Figure 9.22: Direct detection responsivity of a SIS junction as a function of dc bias (V_o) and frequency. In all cases R_n=20 Ω, the energy gap 2.8 mV, the gap smearing ±50 μV, and the $R_{sub-gap}/R_n$ ratio (junction quality) 15. The responsivity of the SuperCam device is $\sim$ 0.6 μA per nW change in RF input power ($k_B T \Delta\nu$ in the Rayleigh-Jeans limit). To cover the low frequency end of the band, the required dc-bias voltage is $\geq$ 1.7 mV. Biasing at a voltage close to the gap also increased the detector responsivity to incoming photons.

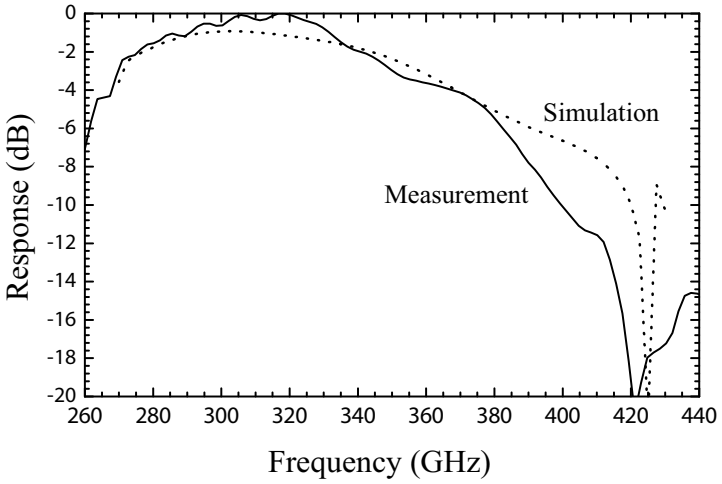

Figure 9.23: Measured and modeled direct detection response of device D17-0 from wafer T3-217. The suck-out at 420 GHz is due to modal excitation from the inductive meandering line across the waveguide (Fig. 9.15). From our computer simulation we understand the premature roll-off to be due to undercutting of the niobium (top layer) transmission lines. The pyramidal feedhorn response is not included in the simulation and may explain the response above 380 GHz.

In Fig. 9.22 we plot the responsivity for a range of bias voltages. Photons with energies less than $V_{gap} - V_o$ do not provide sufficient energy to allow electrons to tunnel through the barrier, as evidenced from the cutoff frequencies. The measured and simulated direct detection response of the SuperCam junction shown in Fig. 9.17 is plotted in in Fig. 9.23. The actual device was of wafer T3-217 (A. W. Lichtenberger *et al.*, UVa). Due to undercutting on the wafer the "end-loaded" RF matching network was tuned low in frequency (increased inductance of $L1$, Fig. 9.17). The mixer block used for the measurement uses an integrated pyramidal feedhorn.

9.4.8 Heterodyne results

The heterodyne response for a single pixel with integrated IF is shown in the left panel of Fig. 9.24. This data was taken by Patrick Puetz *et al.* in the spring of 2007, and represents "first light" for a SuperCam pixel. For consistency the response of a SIS device from wafer T3-217 is plotted. From the experimental measurement, we derive a LO pumped sub-gap differential impedance of 66.7 Ω or 3.3 R_n. This is very close to the optimal design value in Sec. 9.4.6. In the right panel of Fig. 9.24 we show the modeled and measured heterodyne performance for several devices vs. the ideal response. Clearly the response is very sensitive to SIS fabrication tolerances.

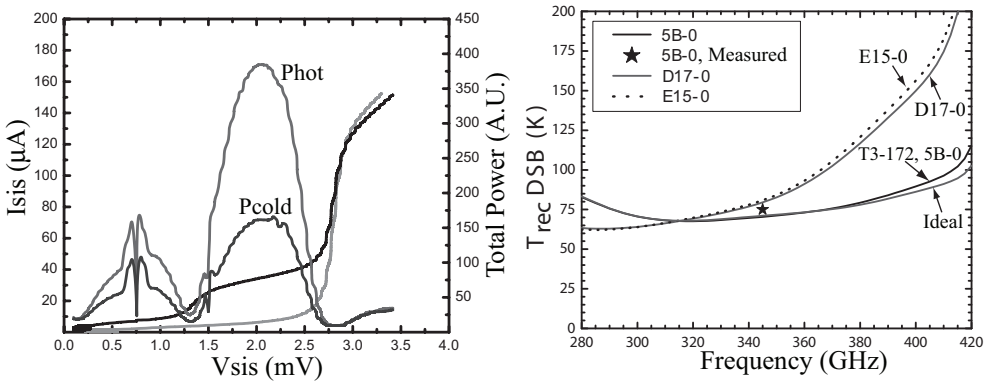

Figure 9.24: *Left*) Measured heterodyne response of wafer T3-172. The receiver noise temperature at 345 GHz ($^{12}CO_{J=3\rightarrow2}$) was 75 K. The magnetic field was tuned to the second Josephson minima which occurred at a B-field current of 31 mA. Data courtesy Patric Puetz. *Right*) Measured heterodyne response vs. the model for a variety of devices from the wafer T3-217.

9.5 Summary

In this Chapter we have taken a closer look into the development of heterodyne imaging arrays. We have traced the development of silicon-nitride membranes to ultra thin silicon-on-insulator (SOI) as a potential candidate for large format, scalable, SIS and HEB substrate material. The use of SOI material is highly competitive with existing (industrial) fabrication processes, offers for phonon-cooled HEB mixers a

compatible substrate, and has the additional advantage in the way gold beamlead may be integrated. Not only does this technology open the door to multi-pixel focal plane arrays, it also facilitates the more complex receiver designs of Chap. 8. Finally, because the individual chips are etched, rather than diced, the shape is arbitrary. This is especially advantageous in the terahertz regime since "handles" or "frames" can be integrated as part of the design. The use of SOI thus facilitates modularity and ease of assembly. These features not only benefit far-infrared astronomy, but are also likely to impact such fields as medical instrumentation, atmospheric research, and surveillance.

Bibliography

[1] P. P. Munoz, S. Bedorf, M. Brandt, T. Tils, N. Honingh, and K. Jacobs, "THz Waveguide Mixers with NbTiN HEBs on Silicon Nitride Membranes", *IEEE Microwave and Wireless Components Letters*, Vol. 16, Issue 11, pp. 606 - 608, Nov. (2006).

[2] S. Cherednichenko, V. Drakinskiy, J. Baubert, J. M. Krieg, B. Voronov, G. Gol'tsman, and V. Desmaris, "Gain bandwidth of NBN hot-electron bolometer terahertz mixers on 1.5 μm Si_3N_4/SiO_2 membranes", *J. Appl. Phys*, Vol. 101, issue 12, 124508, (2007).

[3] B. N. Ellison and R. E. Miller, "A Low Noise 230 GHz SIS Receiver," *Int. J. IR and MM Waves*, Vol. 8, 609-625, (1987).

[4] M. Gurivch, M. A. Washington, and H. A. Huggins, "High quality refractory Josephson tunnel Junction utilizing thin aluminum layers", *Appl. Phys. Lett.*, Vol. 42, 472-474, (1983).

[5] H. G. LeDuc, B. Bumble, S. R. Cypher and J. A. Stern, *Second International Symposium on Space Terahertz Technology*, Pasadena, CA, Feb. 26-28 (1991).

[6] S. Rudner, M. J. Feldman, E. Kollberg, and T. Claeson, "Superconducting-Insulator-Superconducting Mixing with Arrays at Millimeter-Wave Frequencies", *J. Applied Physics*, Vol. 52, pp. 6366-ff, (1981).

[7] D. P. Woody, R. E. Miller, and M. J. Wengler, "85-115 GHz Receivers for Radio Astronomy", *IEEE Trans. Microwave Theory Tech.*, Vol. 33, pp. 90-95, Feb., (1985).

[8] J. W. Kooi, J. Pety, B. Bumble, C. K. Walker, H. G. LeDuc P. L. Schaffer, and T. G. Phillips, "A 850 GHz Waveguide Receiver Employing a Niobium SIS Junction Fabricated on a 1μm Si_3N_4 Membrane", *IEEE Trans. Microwave Theory and Techniques*, Vol. 46, No. 2, pp. 151-161, Feb., (1998).

[9] D.C. Mattis and J. Bardeen, "Theory of the anomalous skin effect in normal and superconducting metals," *Phys. Rev.*, Vol. 111, pp. 412-417, (1958).

[10] J. W. Kooi, C. K. Walker, H. G. LeDuc, T. R. Hunter, D. J. Benford, and T. G. Phillips, "A Low Noise 665 GHz SIS Quasi-Particle Waveguide Receiver," *Int. J. IR and MM Waves*, Vol. 15, No. 3, 477-492, (1994).

[11] B. D. Jackson, G. de Lange, T. Zijlstra, M. Kroug, J. W. Kooi, J. A. Stern, and T. M. Klapwijk, "Low-Noise 0.8-0.96 and 0.96-1.12 THz Superconductor-Insulator-Superconductor Mixers for the Herschel Space Observatory", *IEEE Trans. Microwave Theory and Techniques*, Vol. 54, No. 2, pp. 547-558, Feb., (2006).

[12] J. W. Kooi, C. K. Walker, and J. Hesler, "A Broad Bandwidth Suspended Membrane Waveguide to Thinfilm Microstrip Transition", *9^{th} Int. Conference on Terahertz Electronics*, 15th - 16th Oct., (2001).

[13] J. J. A. Baselmans, A. Baryshev, S. F. Reker, M. Hajenius, J. R. Gao, T. M. Klapwijk, Yu. Vachtomin, S. Maslennikov, S. Antipov, B. Voronov, and G. Gol'tsman, *Appl. Phys. Lett.*, Vol. 86, 163503, (2005).

[14] C. Groppi, C. Walker, C. Kulesa, P. Puetz, D. Golish, P. Gensheimer, A. Hedden, S. Bussmann, S. Weinreb, T. Kuiper, J. Kooi, G. Jones, J. Bardin, H. Mani, A. Lichtenberger, and G. Narayanan, "SuperCam, a 64-pixel heterodyne imaging array for the 870 micron atmospheric window", *astro-ph*/0606061v1, (2006)

[15] Virginia Semiconductor Inc. [Online]. Available: http://www.virginiasemi.com/

[16] R. B. Bass, A. W. Lichtenberger, R. Weikle, J. W. Kooi, C. K. Walker, and S.-K. Pan, "Ultra-Thin SOI beamlead Chips for Superconducting Terahertz Circuits", *Proc. 6^{th} European Conference on Applied Superconductivity*, Sorento, Italy, Sep. 14, (2003).

[17] R. B. Bass, J. C. Schultz, A. W. Lichtenberger, R. M. Weikle, S.-K. Pan, E. Bryerton, C. K. Walker, and J. W. Kooi, "Ultra-Thin Silicon Chips for Submillimeter-Wave Applications", *15^{th} Int. Symp. on Space Terahertz Technology*, Apr. 27-29, pp. 392-399, MA, (2004).

[18] HFSS, Ansoft Corporation, Pittsburgh, PA, (2005).

[19] A. Pavolotsky, D. Meledin, C. Risacher, M. Pantaleev, and V. Belitsky, "Micromachining Approach In Fabricating of THz Waveguide Components", *EMN04*, 20-21 Oct., Paris, France, (2004).

[20] Walker, Drouet D'Aubigny, Groppi, Papapolymerou, Chin, and Lichtenberger, "A New Laser Micromachining System for the Fabrication of THz Waveguide and Quasi-Optical Components" *11^{th} Int. Symp. on Space THz Tech.*, Ann Arbor, MI, May (2000).

[21] [Online]. Available: http://www.crystalbond.com/

[22] EPO-TEK H20E conductive epoxy.
[Online]. Available: http://www.epotek.com/

[23] J. R. Pardo, J. Cernicharo, and E. Serabyn, "Atmospheric Transmission at Microwaves (ATM): An Improved Model for mm/submm applications", *IEEE Trans. on Antennas and Propagation*, Vol. 49, no. 12, pp. 1683-1694, Dec., (2001).

[24] J. Hesler, "A photonic crystal joint (PCJ) for Metal Waveguides" *IEEE, MTT-S, Microwave Symp. Digest*, Vol. 2, pp 783-786, (2001).

[25] Virginia Diodes Inc., 321 West Main Street, Charlottesville, VA 22903, USA.

[26] [Online]. Available: http://www.terahertz.co.uk/

[27] SORAL, [Online]. Available: http://soral.as.arizona.edu/

[28] HHT, [Online]. Available:
http://www.mpifr-bonn.mpg.de/div/hhertz/smt-mpifr.html/

[29] A. R. Gillespie and T. G. Phillips, "Array Detectors for Millimetre Line Astronomy", *A & A*, Vol. 73, 14. (1979).

[30] [Online]. Available: http://www.submm.caltech.edu/%7ecdd/sharcii.html/

[31] [Online]. Available: http://www.roe.ac.uk/ukatc/projects/scubatwo/

[32] [Online]. Available: http://www.cso.caltech.edu/bolocam/

[33] Omnisys Instruments AB, Gruvg. 8 , SE-421 30 Västra Frölunda, Sweden newblock[Online]. Available: http://www.omnisys.se/

[34] U.U. Graf and S. Heyminck, "Fourier gratings as submillimeter beam splitters", *IEEE Trans. on Antennas and Propagation*, Vol. 49, Issue 4, pp. 542 - 546, Apr. (2001).

[35] P. F. Goldsmith, *QuasiOptical Systems*, Piscataway, NJ: IEEE Press, (1998).

[36] Kern, Micro- und Feinwerktechnik,
[online]. Available: http://www.kern-microtechnic.com/

[37] Private Communication.

[38] S. Withington and G. Yassin, "Analytical Expression for the Input Impedance of a Microstrip Probe in Waveguide," *Int. J. IR and MM Waves*, Vol. 17, pp. 1685-1705, Nov., (1996).

[39] J. W. Kooi, F. Rice, G. Chattopadhyay, S. Sundarum, S. Weinreb and T. G Phillips, "Regarding the IF Output Conductance of SIS Tunnel Junctions and the Integration with Cryogenic InP MMIC Amplifiers", *Proc. 10^{th} Int. Symp. Space Terahertz Technology*, University of Virginia, Va, Mar., (1999).

[40] SONNET, Sonnet Software, Liverpool, NY, (2005).

[41] A. R. Kerr, "Surface Impedance of Superconductors and Normal Conductors in EM simulators", NRAO, Charlottesville, VA [Online]. Available: http://www.alma.nrao.edu/memos/html-memos/alma381/memo245.pdf

[42] C-Y. E. Tong, R. Blundell, and S. Paine, "Design and Characterization of a 250-350-GHz Fixed-Tuned Superconductor-Insulator-Superconductor Receiver", *IEEE Microwave Theory and Techniques*, Vol. MTT-44, pp. 1548-1556, Sep., (1996).

[43] Y. Delorme, M. Salez, B. Lecomte, I. Péron, F. Dauplay, A. Féret, J. Spatazza, J. -M. Krieg, and K. F. Schuster, "Space-Qualified SIS Mixers for Herschel Space Observatory's HIFI Band 1 Instrument", *Proc. 16th Int. Symposium on Space Terahertz Technology*, Chalmers, Göteborg, Sweden, May, (2005), S08-05.

[44] B. D. Jackson, G. de Lange, T. Zijlstra, M. Kroug, J. W. Kooi, J. A. Stern, and T. M. Klapwijk, "Low-Noise 0.8-0.96- and 0.96-1.12 THz Superconductor-Insulator-Superconductor Mixers for the Herschel Space Observatory", *IEEE Microwave Theory and Techniques*, Vol. MTT-54, No. 2, pp. 547- 558, Feb., (2006).

[45] J. W. Kooi, G. Chattopadhyay, S. Withington, F. Rice, J. Zmuidzinas, C. K. Walker, and G. Yassin, "A Full-Height Waveguide to Thin-Film Microstrip Transition with Exceptional RF Bandwidth and Coupling Efficiency", *Int J. IR and MM Waves*, Vol. 24, No. 3, pp. 261 - 284, Sept., (2003).

[46] P. F. Goldsmith, *QuasiOptical Systems*, Piscataway, NJ: IEEE Press, pp. 256-258, (1998). Chap. 9.4, Inteferometers, pp 256-258.

[47] J. R. Tucker, "Quantum limited detection in tunnel junctions mixers", *IEEE J. Quantum Phys.*, Vol. 15, no 11, pp. 1234-1258, (1979).

[48] J. R. Tucker and M. J. Feldman, "Quantum Detection at Millimeter Wavelengths", *Rev. Mod. Phys.*, Vol. 57, pp. 1055-1113, Oct., (1985).

Chapter 10

Stability of heterodyne receivers at terahertz frequencies*

Abstract - In this Chapter we discuss the stability of terahertz receivers based on small volume NbN phonon cooled hot electron bolometers (HEB). The stability of these receivers can be broken down in two parts: The intrinsic stability of the HEB mixer, and the stability of the local oscillator (LO) signal injection scheme. Measurements show that the HEB mixer stability is limited by gain fluctuations with a $1/f$ spectral power distribution. In a 60 MHz noise bandwidth this results in an Allan variance stability time of $\sim$ 0.3 s. Measurement of the spectroscopic Allan variance between two intermediate frequency (IF) channels results in a much longer Allan variance stability time, i.e. 3 s between a 2.5 GHz and a 4.7 GHz channel, and even longer for more closely spaced channels. This implies that the HEB mixer $1/f$ noise is strongly correlated across the IF band, and that the correlation gets stronger the closer the IF channels are spaced. In the second part of the paper we discuss atmospheric and mechanical system stability requirements on the LO – mixer cavity path length. We calculate the mixer output noise fluctuations as a result of small perturbations of the LO – mixer standing wave, and find very stringent mechanical and atmospheric tolerance requirements for receivers operating at terahertz frequencies.

*This Chapter is published as J. W. Kooi, J. J. A. Baselmans, A. Baryshev, R. Schieder, M. Hajenius, J. R. Gao, T. M. Klapwijk, B. Voronov, and G. Gol'tsman, in the *Journal of Applied Physics*, Vol. 100, 064904, Sep. (2006).

10.1 Introduction

NbN phonon cooled hot electron bolometer (HEB) mixers are currently the most sensitive heterodyne detectors at frequencies above 1.2 THz [1, 2]. The present day state-of-the-art mixers combine good sensitivity (8–15 times the quantum limit) with an intermediate (IF) noise bandwidth of 4 – 6 GHz [3, 4, 5, 6] up to RF frequencies of at least 5 THz. As a consequence, HEB mixers are increasingly baselined as terahertz heterodyne receivers on astronomical platforms, such as the European space agency's far-infrared space observatory (Herschel), the NASA/DLR stratospheric observatory for Infrared astronomy (SOFIA), and the Atacama pathfinder experiment (APEX) [7, 8, 9]. For this reason it is very important to have a good understanding of the time stability of (HEB mixer based) heterodyne terahertz receivers, as this determines the optimal observation strategy.

When an astronomical source is observed long integrations are generally called for since the signals are deeply embedded in the noise. To extract the weak signals, synchronous detection or Dicke switching [10] (signal – reference) is typically employed to circumvent instabilities in the receiving system. For extended sources this maybe accomplished by slewing the entire telescope back and forth, whereas in the case of point sources within the field of view of the telescope, nutating the secondary (or tertiary) mirror is often employed. A practical lower limit for slewing the telescope is generally 15–20 s, while chopping the secondary mirror can perhaps be as fast as 0.2 s (4 Hz). If the noise in the receiver system is completely uncorrelated (white), the subtraction rate (modulation frequency) has no effect on the signal to noise ratio. This can be deduced from the well known radiometer equation [10] which states that white noise integrates down with the square root of the integration time

$$\sigma = \frac{\langle s(t) \rangle}{\sqrt{\Delta\nu \cdot T_{int}}} \; . \tag{10.1}$$

Here $s(t)$ presents the instantaneous output voltage of a spectrometer channel or continuum detector, σ the standard deviation (rms voltage) of the signal, $\Delta\nu$ the effective noise fluctuation bandwidth, and T_{int} the integration time of the measurement. For a general treatment we will use T instead of T_{int} from now on.

In practice the power spectrum of low frequency gain fluctuations and drift noise can be characterized by $S(f) \propto 1/f^{\alpha}$ with $1 \leq \alpha < 3$. Typically $1/f$ (flicker) noise with $\alpha = 1$ originates from electronic devices, though the influence of atmospheric fluctuations in a receiver is often seen to have similar characteristics. Drift noise can be characterized by $2 \leq \alpha < 3$, where chaotic processes lead to power laws somewhere in between. White noise, generally of radiometric origin, is described by $\alpha = 0$. A measurement of the Allan variance, defined as $\sigma_A^2 = \frac{1}{2} \cdot \sigma_D^2$, is proposed as a powerful tool to discriminate between the various noise terms in the receiver [11, 12]. Here σ_D^2 is the variance of the difference of two contiguous measurements of integration time T. It can be shown [11] that for a noise power spectrum $S(f) \propto 1/f^{\alpha}$, that the Allan variance is proportional to $T^{\alpha-1}$. For a noise spectrum that contains respectively drift noise, $1/f$ noise, and white noise, the general shape of the Allan variance as a function of integration time is

$$\sigma_A^2(T) = aT^\beta + b + c/T \ , \quad \beta = \alpha - 1 \ , \tag{10.2}$$

where $1 < \beta < 2$. In practice the last term in the above equation dominates for short integration times and the Allan variance decreases as T^{-1}, as expected for white noise ($\alpha = 0$). For longer integration times, the drift will dominate as shown by the term aT^β. In this case, the variance starts to increase with a slope β, which is experimentally found to be between 1 and 2. On certain occasions, such as with the HEB mixers under discussion, it is observed that the variance plateaus. This is denoted by the constant b, and is representative of $1/f$ gain fluctuation (flicker) noise with $\alpha = 1$. Plotting the normalized $\sigma_A^2(t)$ on a log-log plot demonstrates the usefulness of this approach in analyzing the receiver noise statistics. The minimum in the plot, the crossover from white noise to $1/f$ or drift noise, is known as the Allan stability time or Allan minimum time (T_A). Note that T_A is a function of the noise fluctuation bandwidth $\Delta\nu$ according to

$$T_A'/T_A = (\Delta\nu/\Delta\nu')^{\frac{1}{\beta+1}} \ . \tag{10.3}$$

Hence the Allan time shifts to higher integration times for smaller bandwidths. For the sake of optimum integration efficiency, one is advised to keep the integration time below that of the receiving system. In actual synchronous detection measurements n samples of difference data (signal – reference) are taken, each with a period T. These differences are then averaged so that the total observed time equals $n \cdot (2T)$. If the period T is not well below the Allan stability time of the system, then apart from loss in integration efficiency, there will be a problem with baseline subtraction. In the averaged output spectrum this will manifest itself as a baseline ripple which limits how well the noise integrates down with time. Hence it is of great importance to know the system Allan time and to adjust the measurement strategy accordingly.

In this paper we discuss the stability from two different perspectives. In the first part we consider the fundamental stability of the HEB mixers themselves. We discuss a set of dedicated measurements of the Allan variance on small volume phonon cooled HEB mixers. We start with a measurement of the total power (continuum) Allan variance at 673 GHz. At this frequency there are few uncertainties in the experimental system. Afterwards we measure the total power and the spectroscopic Allan variance at 1.462 THz with an identical HEB mixer at its optimal operating point. In the second part of the paper we discuss the stability of the receiver setup as a whole. We give a theoretical analysis of the mechanical and atmospheric stability issues required to build successful receivers at THz frequencies. Due to the much shorter wavelengths, as well as the increasing air loss when compared to for example the 650 GHz atmospheric window, the constraints on mechanical design are much more stringent than at submillimeter frequencies. A set of measurements on HEB based receivers between 673 GHz and 2.814 THz with various LO injection schemes is used to give a solid experimental validation of the theoretical analysis.

10.2 Stability of small volume HEB mixers

10.2.1 Experimental setup

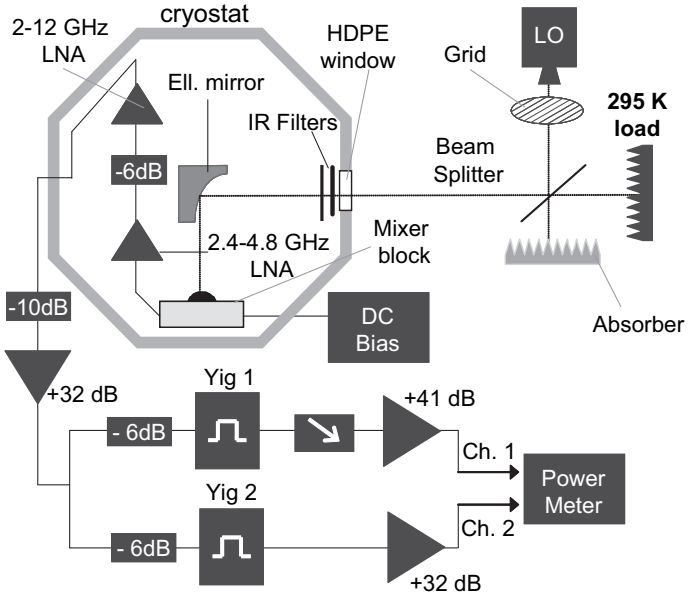

Figure 10.1: Schematic picture of the experimental setup.

We describe here in detail the experimental setup used to measure the spectroscopic Allan variance. The device under consideration is a small volume NbN phonon cooled HEB, with a NbN film thickness of about 5 nm, a length of 0.2 μm, and a width of 1.5 μm. The device has a critical current $Ic = 51$ μA at 4.2 K, and a normal state resistance of 175 Ω at 11 K. The contact pads between the NbN bridge and the antenna are made by cleaning the NbN layer *in-situ* prior to the deposition of 10 nm NbTiN and 40 nm of Au. For details regarding the fabrication we refer to Refs. [3] and [13]. To couple the RF radiation to the HEB, we use a twin slot antenna [14] designed to give an optimum response at 1.6 THz. In the experiment a quasi- optical coupling scheme is used in which the HEB mixer chip is glued to the center of an elliptical silicon lens. A schematic picture of the setup is shown in Fig. 10.1.

The lens is placed in a mixer block with internal bias-T, and thermally anchored to the 4.2 K plate of an Infrared Laboratories liquid helium cryostat. We use one layer Zitex G104 at 77 K, two layers at 4.2 K as infrared filter, and a 0.9 mm high density polyethylene (HDPE) sheet as vacuum window. A parabolic mirror converts the fast beam from the silicon lens into a f/D = 23.7 collimated beam with a 3 mm waist located at the cryostat window. The local oscillator consists of a JPL 1.45 – 1.55 THz multiplier chain, SN 2 [15], with its input signal provided by a commercial Rhode and Schwarz synthesizer. The chain operates at 1.462 THz where it has a peak output power of 11 μW. A wire grid sets the LO signal attenuation to obtain

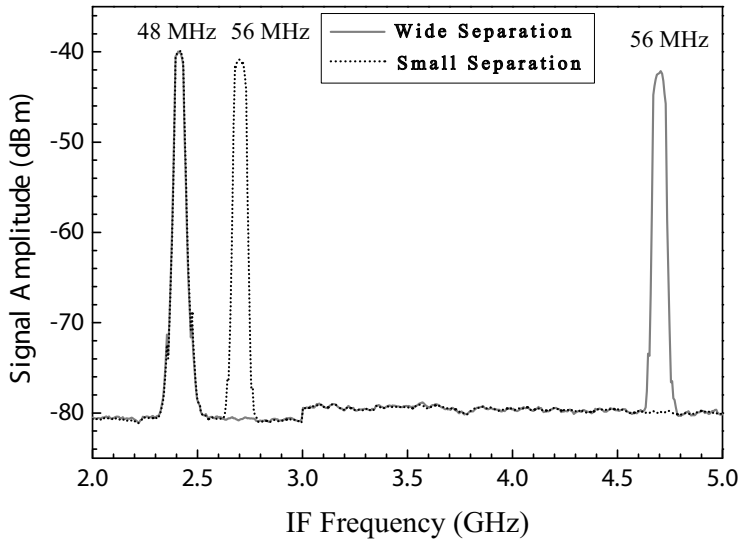

Figure 10.2: IF power spectrum of the combination of Channels 1 and 2, as shown in Fig. 10.1. Two measurements are combined in this plot, corresponding to two frequency settings of the YIG filter. In the text the HEB noise properties of closely spaced channels (2.4/2.7 GHz) and widely spaced channels (2.4/4.7 GHz) are studied.

the desired pumping level for the mixer. The IF output of the mixer unit connects via a 10 cm semi-rigid Al coax cable to the input of a InP based low noise amplifier (LNA), SRON/Kuo-Liang SN 2, with 2.4 – 4.8 GHz bandwidth, 25–26 dB of gain, and a noise temperature of 5 K. Because of its low gain this amplifier is connected to a second cryogenic amplifier, a Sandy Weinreb 2 – 14 GHz SN 20B InP microwave monolithic integrated circuit(MMIC) with 35–36 dB gain and 5 K noise. In between the two amplifiers is a 6 dB attenuator to prevent standing waves. The signal is further amplified at room temperature and split using a 3 dB power splitter. After the splitter we use in each channel a room temperature GaAs amplifier with a tunable attenuator in one of the channels. A dual frequency power head is then used to measure the power output as a function of time $P(t')$ for two IF channels simultaneously at a rate of 40 times per second. This has been done for IF frequencies very close to each other at the low end of the IF band (2.4 GHz and 2.7 GHz), and for two frequencies near the IF band edges (2.4 GHz and 4.7 GHz). The attenuator equalizes the power in both channels. This is important, since the power meter is a wideband detector with the result that the ratio of in band signal power to the total power, as seen by the detector, will change the effective measurement bandwidth, and hence the measured Allan variance.

In Fig. 10.2 we give the channel spectral response for both frequency settings. The two channel IF system enables us to do a measurement of the Allan variance in two single IF bins simultaneously. It also enables us to perform a measurement of the spectroscopic (differencing) Allan variance, which is the Allan variance of the difference of two IF channels set to different frequencies [16]. This is the Allan variance

of the quantity $s(t')$ given by

$$s(t') = \frac{1}{\sqrt{2}}\left[\left(\frac{x_i(t')}{\langle x\rangle} - \frac{y_i(t')}{\langle y\rangle}\right)+1\right]\cdot\frac{\langle x\rangle + \langle y\rangle}{2} \tag{10.4}$$

with $x(t')$ and $y(t')$ the original measurements of the powers in each IF channel as a function of time t'. The spectroscopic Allan variance gives the relative stability between channels in an IF band, whereas the total power Allan variance provides the absolute stability per channel bin. Hence it is the spectroscopic Allan variance that is relevant for spectral line measurements. For continuum observations it is the single channel or total power Allan variance that is relevant, with the added difficulty that for continuum observations larger bandwidths are typically used, resulting in a decrease in stability (Eq. 10.3).

10.2.2 Continuum stability

In the first experiment we measure the bias dependent stability of a small volume HEB mixer, identical to the one described in Sec. 10.2.1, at a LO frequency of 673 GHz.

We use a similar, but somewhat simpler experimental setup as described in Sec. 10.2.1. A single channel IF system is used, consisting of a mixer block with an external bias-T, a 1 – 2 GHz Berkshire GaAs LNA with a 4 K noise temperature, 40 dB gain, followed by a room temperature amplifier (the same as the last amplifier in channel 1 as discussed in Sec. 10.2.1 and shown in Fig. 10.1). The IF power is filtered in a 80 MHz bandwidth around 1.45 GHz, and detected with a single channel Agilent power meter at 200 readings per second. The 80 MHz noise bandwidth enables us to omit the additional amplifier after the filter. As LO source we use a phase locked Gunn

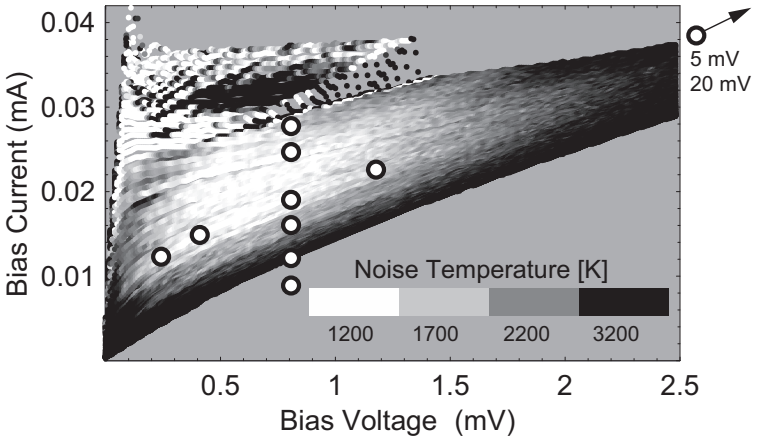

Figure 10.3: Noise temperature obtained for all bias points at 673 GHz. We obtain $T_{N,DSB}$=1100 K, only slightly inferior to the value of $T_{N,DSB}$ = 900 K obtained at the antenna center frequency of 1.6 THz. The dots indicate the bias points where the Allan variance has been obtained. The lowest point represents a completely flat pumped IV curve, where the mixer has no heterodyne response.

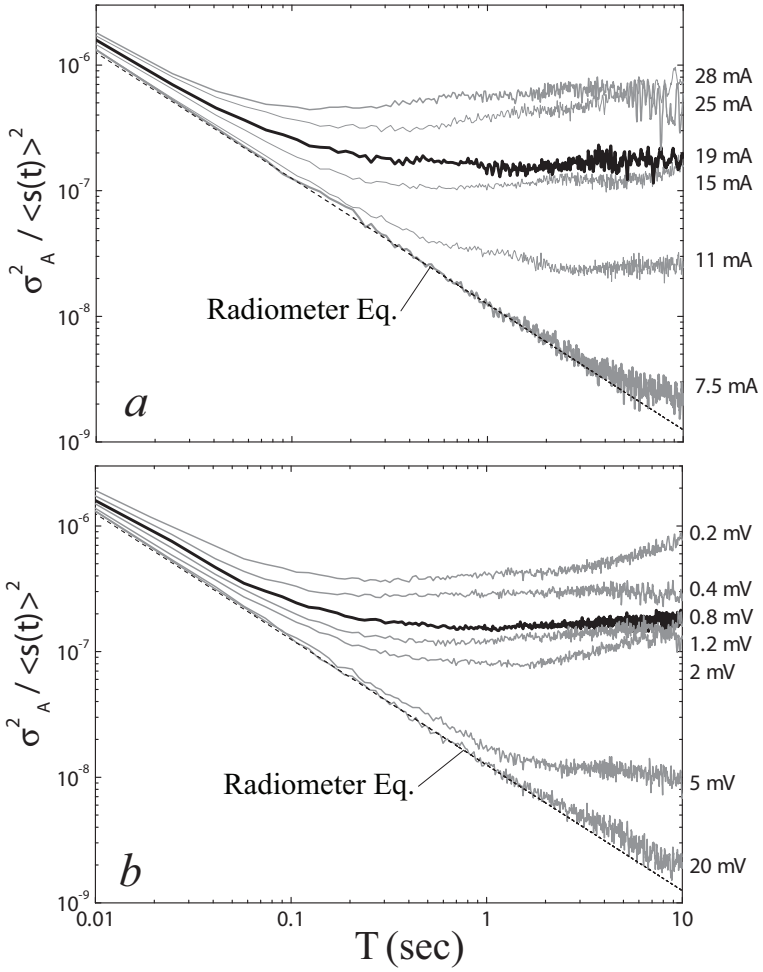

Figure 10.4: (a) Normalized total power Allan variance at optimal bias voltage (0.8 mV) for different levels of LO power as indicated by the resulting mixer bias current. (b) Normalized Allan variance as a function of DC bias voltage at optimal LO power. All bias points are shown as dots in Fig. 10.3, LO frequency is 673 GHz and $\Delta\nu \sim 80$ MHz.

oscillator followed by a multiplier chain with a signal output frequency of 673 GHz. The measurements were performed at night in a closed room and we have taken at least 10 minutes of data for every measurement. All the data have been used to calculate the Allan variance. The 673 GHz measured receiver noise temperature (Fig. 10.3, $T_{N,DSB}$) is 1100 K, only slightly inferior to the 900 K DSB value at the antenna peak frequency of 1.6 THz.

Also indicated in Fig. 10.3 are all the bias points where we have measured the Allan variance. Results of the measurements are shown in Fig. 10.4, where panel **a**

gives the dependence on LO pump level (i.e. bias current) at the optimal bias voltage, and panel **b** the bias voltage dependence at the optimal LO pump level. Note that the thick line represents, in both plots, the total power Allan time at the optimal operating point. Here T_A is 0.3 s in the 80 MHz noise spectral bandwidth of the setup. A deviation from the radiometer equation by a factor 2 is already present at ≈ 0.08 s. The plateau in the Allan variance plot indicates that the stability of the NbN HEB mixer suffers from substantial fluctuations in gain, with a $1/f$ power dependence. This is much unlike, for example, SIS mixers where the output noise is primarily dominated by white (-1 slope) and drift noise (positive slope) [12]. We also observe that T_A increases slowly with increasing DC bias voltage and with increasing LO power (decreasing bias current). However, a noticeable increase in stability is achieved only at bias points (V > 2 mV or $I \sim 11\mu$A) where the receiver sensitivity is already strongly reduced (see Fig. 10.4). Moreover, we can use the lowest curves in both panels of Fig. 10.4 to estimate the stability of the experimental setup. The lowest line in Fig. 10.4**a** is obtained at such a high LO power that the mixer is driven completely normal, i.e. no heterodyne response is observed. The same is true for the line in Fig. 10.4**b**, which is obtained at a high DC bias of 20 mV. In both cases the HEB mixer conversion gain approaches zero, and the HEB behaves as a resistor with a white noise spectrum. As such we would expect a -1 slope in the Allan variance plot. The deviation above ≈ 7 s is due to instabilities in the setup. Being so far away it does not affect the HEB mixer stability measurements we concern ourselves with in this paper. From these results we must conclude that significant gain fluctuations, with a $1/f$ like spectral distribution, limit total power integration times of a small area NbN HEB mixer to about 0.1 s in a 80 MHz noise bandwidth, or ≈ 10 ms in a 1 GHz continuum channel. The single channel Allan variance in a typical 1.5 MHz noise spectral bandwidth of an acousto-optical spectrometer [11] is approximately 0.8 s. HEB mixer stability is therefore far inferior to the stability of superconductor-insulator-superconductor (SIS) mixers at the same LO frequency [12]. This has been verified by measuring the stability of a 675 GHz waveguide coupled SIS receiver in the same room using a similar coupling scheme and the same LO source.

10.2.3 Spectroscopic stability

In the next experiment we measure the spectroscopic Allan variance, using the exact setup as described in Sec. 10.2.1. The HEB mixer used is a different mixer from the one used in the previous experiment, however it is from the same batch and has an identical normal state resistance, critical current and sensitivity. The 1.462 THz measurements have again been performed in one single evening – night, and in a closed room to minimize disturbances. For every measurement we have taken 48 minutes of data, and we have used the entire data set to calculate the Allan variance. To verify the stability of our setup, and in particular the electrical stability of the amplifiers, YIG filters, and the HEB dc bias power supply, we have biased the HEB mixer to 20 mV. The resultant spectroscopic and single channel calibrations are shown by the gray lines in Fig. 10.5. We observe that the spectroscopic line begins to deviate at ≈ 7 s (~ 50 MHz bandwidth) from the radiometer equation (Eq. 10.1), whereas the single channel calibration starts to deviate at about 1 second. This is indicative that some

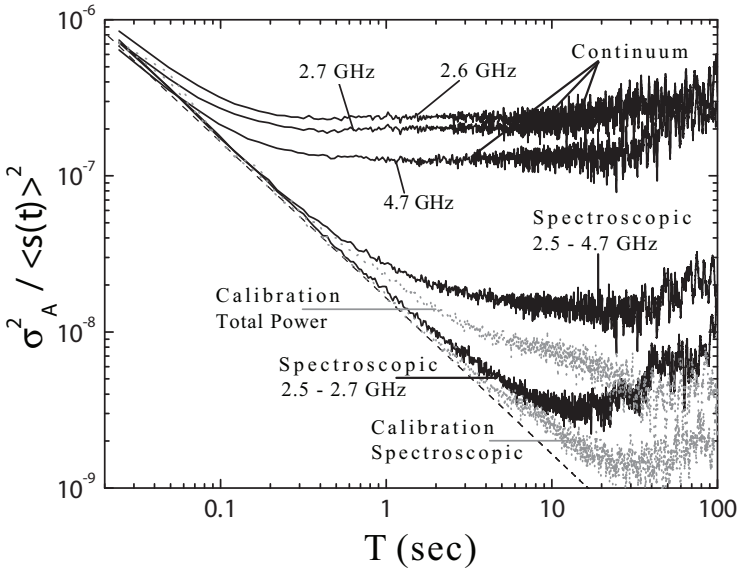

Figure 10.5: Normalized spectroscopic and total power Allan variance at 1.462 THz for a small volume twin-slot HEB mixer. $\Delta\nu \sim 60$ MHz, refer to Figs. 10.1 & 10.2 for details.

of the drift components in the setup are correlated within the IF band, and that the stability of the setup is therefore slightly worse than in the single channel experiment. This may be related to the fact that the cryogenic amplifiers used in this experiment are InP based. InP devices are known to have more gain fluctuations than their GaAs counterparts. In both situations however, the stability of the setup is much greater than that of the HEB mixer. Allan variance analysis of the 1.462 THz single channel data shows, once again, that the output noise of a hot electron bolometer suffers from substantial $1/f$ gain fluctuations (0 slope in the Allan variance diagram). The Allan minimum time of 0.4 s is virtually identical to that obtained at optimum bias at 673 GHz (same twin slot device), with a slightly larger filter bandwidth (Fig. 10.4).

The improvement in Allan time by spectroscopic differencing two (or more) channels, as shown in Fig. 10.5 is seen to be significant; a factor of 10 or better. The spectroscopic Allan variance between 2.4 GHz and 2.7 GHz channels yield an Allan time of 12–13 s. For the 2.4 GHz an 4.7 GHz channels we obtain an Allan time of 2–3 s, however the deviation from the radiometer equation now occurs at 0.8 s, as opposed to 6 s for the closely spaced channels. In addition, the instability in the widely spaced channels is governed by $1/f$ noise, whereas for the closely spaced channels drift noise is limiting the Allan time. Hence the calculation for the effective integration time in a 1.5 MHz spectral noise bandwidth is a little less straightforward than in the single channel case. Using a $1/f$ spectrum for the widely spaced channels we obtain, in a 1.5 MHz noise bandwidth, a useful integration time of ~ 80 s.

For the 2.4 GHz and 2.7 GHz bins we obtain ~ 75 s, assuming drift noise with $\beta = 1$. Spectroscopic measurements are thus seen to eliminate virtually all $1/f$ mixer

noise. Note that the differencing result between 2.4 GHz and 4.7 GHz presents roughly the largest practical bandwidth of an HEB mixer, as the device noise bandwidth is limited to about 4 – 5 GHz [3, 4, 5]. The physical reason for the gain instability is likely related to random processes in the distributed hot spot mixing region of the bridge, and it is therefore not unreasonable to expect the HEB output noise to be highly correlated. Closely spaced IF channels exhibit a higher degree of correlated noise than the channels that are spaced further apart. The explanation for this phenomena is that the HEB gain bandwidth causes the mixer output noise, dominated by thermal fluctuation noise, to roll off at frequencies above 2 – 3 GHz. As a result the HEB output noise at low IF frequencies is dominated by thermal fluctuation noise, whereas, at higher IF frequencies the relative Johnson noise contribution increases. For this reason the spectroscopic subtraction is less perfect between IF channels with a large frequency difference. It is also important to note is that the traditional way of doing total power Y-factor measurements may not be appropriate for HEB mixers, unless detection methods at time scales less than the single channel Allan time ($<$ 0.3 s) are employed.

We conclude that the observed $1/f$ gain fluctuations are not only a fundamental property of NbN phonon cooled HEB mixers, but that they are also highly correlated across the IF band. Spectroscopic measurements are therefore very efficient in removing most of the hot electron bolometer output instability, which explains why successful heterodyne spectroscopy observations are possible [17, 18]. Continuum observations, such as for example sky dips or absolute temperature calibration, will on the other hand be challenging. It is not inconceivable that device geometry, film properties, and/or magnetic field have an effect on the HEB gain fluctuation noise. As such, small differences in the Allan minimum time may be expected between the different mixer groups. Note that the reported measurements here are in good agreement with other reported stability measurements on similar devices, taking into account variations in (noise) bandwidth [19].

10.3 Atmospheric and mechanical receiver stability

In the previous Section we have focused on the fundamental stability limit of small area HEB based receivers. Up to $\sim$ 1.46 THz we have seen that the stability of the system is limited by that of the mixer. However, with the development of HEB mixers to frequencies of 5 THz [8, 4] and above, the demands of atmospheric and mechanical stability on the receiving system increases.

In most submillimeter and terahertz receivers the required local oscillator power is coupled to the mixer via optical means, regardless of mixer type. Local oscillator injection is performed most easily via a thin beam splitter, which acts as a directional coupler or diplexer, though it is also possible to use a dual-beam interferometer such as a Fabry-Perot or Martin-Puplett interferometer [20]. Inevitably, due to the finite return loss of the mixer and local oscillator, a standing wave is setup in the LO – mixer cavity. As the LO – mixer cavity path length changes, be it due to air or mechanical fluctuations, the standing wave in the LO – mixer cavity changes am-

Table 10.1: Atmospheric parameters. Air opacity, path length variation ΔL, and air path attenuation for a 1 meter column of air. P_{atm}=990 mBar, T=20.15 °C, and relative humidity 55 %.

Frequency (THz)	0.673	1.462	1.630	2.814
Opacity, τ (np)	0.01857	0.1238	0.6265	1.0727
ΔL (μm)	62.002	66.202	138.76	140.17
Attenuation (dB)	0.081	0.538	2.72	4.658

plitude. Amplitude modulation of the local oscillator signal results in short and long term gain instability ($1/f$ noise and drift) at the output of the mixer. Measurements at submillimeter wavelength, with a 10 % reflective beam splitter, typically show a LO – mixer standing wave amplitude of 4 % – 5 %. In the terahertz regime, due to shorter wavelength, it is this standing wave that will easily dominate the receiver stability budget. In the next few Sections we provide a theoretical analysis of this important effect, and compare it to experimental data at 0.673, 1.462, 1.630, and 2.814 THz.

10.3.1 LO path length loss

The (LO) electric field propagating in the z direction can be described as

$$E_{lo} = E_{lo}(0) \cdot e^{-\gamma z} \cdot e^{i\omega t} \ , \tag{10.5}$$

with the time averaged power density as

$$P_{lo} = P_{lo}(0) \cdot e^{-\tau z} \ . \tag{10.6}$$

γ is known as the complex propagation constant, τ the opacity/meter, and $P_{lo}(0)$ the peak LO power at $z = 0$ meters. The air opacity and the change in optical path length ΔL, defined as the path length increase due to water vapor in a 1 meter column of air, have been modeled by Juan Pardo [21] [22] and provided in Table 10.1. Uncertainty in the atmospheric opacity is estimated to be no more than 5 %. The conditions used are as follows: Atmospheric pressure 990 mBar, temperature 20.15 °C, and relative humidity 55 %. Note that in the case of turbulent air, it is not the absolute path length we concern ourselves with, but the deviation in path length due to changes in the refractive index of air.

10.3.2 Standing waves in the LO – mixer path

Following Schieder [23] and Goldsmith [20], we define the incident LO power on the mixer, P_{lo}, as

$$P_{lo} = P_{lo}(0) \cdot |r_{bs}|^2 \cdot A_i(\nu_{lo}) \ . \tag{10.7}$$

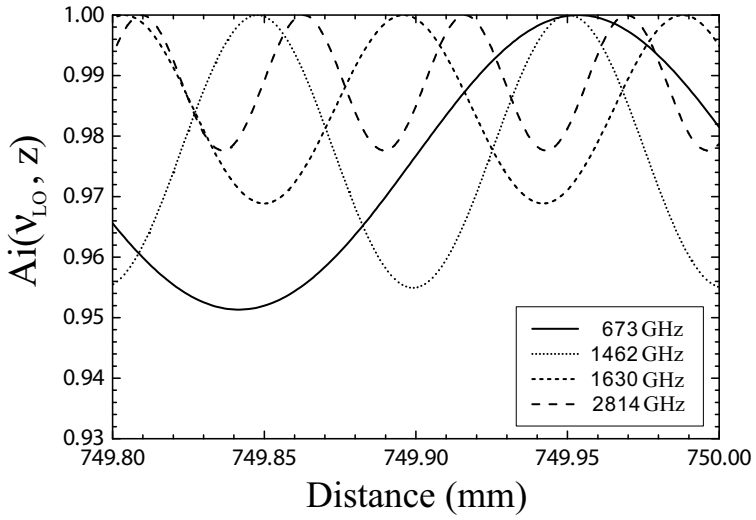

Figure 10.6: Standing wave for a cavity path length of $z = 0.75$ meter. Note the effect of atmospheric loss (damping) on the standing wave amplitude at the shorter wavelength. Shown here are the last 200 μm. In the example $|r_m|^2$ was taken to be -10 dB, $|r_{lo}|^2$ = -8 dB, and $|r_{bs}|^2$ = -10 dB. Without atmospheric loss (space, or a high dry mountain site), the peak-to-peak standing wave amplitude in the example would be 4.934 %.

$|r_{bs}|^2$ is the beam splitter or diplexer power reflection coefficient, $P_{lo}(0)$ the LO power at the LO source output, and $A_i(\nu_{lo})$ the Airy function that describes the fractional transmitted power as a function of the LO – mixer distance z.

$$A_i(\nu_{lo}) = \frac{1}{1 + F sin^2(\frac{\delta}{2})} \ , \quad \delta = \frac{4\pi n z}{\lambda} \ , \tag{10.8}$$

where n is the refractive index of air, given by $n = (1 + \Delta L/z)$ and F the finesse of the LO – mixer cavity

$$F = \frac{4|r|^2}{(1 - |r|^2)^2} \ . \tag{10.9}$$

Here $|r|^2$ represents internal reflections in the LO – mixer cavity. Rewriting Eq. 10.9 to include loss, we substitute $|r|^2 \rightarrow |r|^2 e^{-\tau z}$ so that

$$F = \frac{4|r|^2 e^{-\tau z}}{(1 - |r|^2 e^{-\tau z})^2} \ . \tag{10.10}$$

Now substituting Eq. 10.10 into Eq. 10.8, and expressing the Airy function in terms of the propagation constant β gives

$$A_i(\nu_{lo}) = \frac{\left(1 - |r|^2 e^{-\tau z}\right)^2}{\left(1 - |r|^2 e^{-\tau z}\right)^2 + 4|r|^2 e^{-\tau z} sin^2(\beta n z)}, \tag{10.11}$$

where $|r|^2$ can be expresses in terms of the mixer reflection coefficient $|r_m|^2$, the LO source reflection coefficient $|r_{lo}|^2$, and the beam splitter or diplexer reflection coefficient $|r_{bs}|^2$ according to

$$|r|^2 = |r_{bs}|^2 \sqrt{|r_m^2 \cdot r_{lo}^2|} \ . \tag{10.12}$$

Looking at Eq. 10.11, we see that the Airy function has a ripple period of $\beta nz = \pi$. This describes the standing wave pattern between the LO port and the mixer input via the beam splitter. In the next Sections we examine the importance of tuning to the peak of the LO – mixer cavity standing wave ($\beta nz = 0,\ \pi,\ 2\pi, \cdots$), rather than on a steep slope ($\beta nz = \pi/4,\ 3\pi/4, \cdots$).

Consider, as an example, a typical mixer with an input reflection coefficient of -10 dB ($|r_m|^2$=0.10), a LO source reflection coefficient of -8 dB ($|r_{lo}|^2$=0.16), and a 10 % (-10 dB) beam splitter to inject the local oscillator signal. In Fig. 10.6 we plot the Airy function (Eq. 10.11) for the last 200 μm of a $z = 0.75$ meter LO – mixer cavity path length.

If there were no atmospheric loss (space or vacuum cryostat), the peak-to-peak amplitude variation for the given parameters would be 4.934 %. In actuality, for a 0.75 meter path length, the standing wave amplitude has attenuated to $\approx$ 4.8 % for a 673 GHz local oscillator signal, 3.1 % for the 1.630 THz CH_2F_2 FIR laser line, and 2.2 % for the quantum cascade laser (QCL) line at 2.814 GHz [24] (close to the 2.774 THz water line). Interestingly, a 5 % standing wave value agrees well with measurements at 230 GHz, 352 GHz, 690 GHz, and 807 GHz obtained at the Caltech Submillimeter Observatory (CSO). A nice confirmation that the assumed mixer, LO source, and beam splitter reflections are reasonable. From Eq. 10.11 it is clear that as $r_{bs} \rightarrow 0$ that the LO – mixer standing wave amplitude also vanishes to zero. It is advantages therefore to use a LO diplexing scheme with a small coupling coefficient. Of course at terahertz frequencies, except for when an FIR laser is employed, this may not be practical due to the limited available LO power.

10.3.3 Estimate of allowed LO power fluctuations

To estimate the level of local oscillator fluctuations that may be tolerated without degrading the receiver stability below that of the mixer stability, one has to consider the sensitivity of the mixer IF output power with respect to the input LO power (dP_{if}/dP_{lo}). Assuming that the mixer acts as a standard square law detector, the IF output will be proportional to changes in the input signal. For this reason, tiny LO fluctuations (amplitude noise) at the mixer input show up as instability at the mixer IF output. Since atmospheric and mechanical vibrations typically have a $1/f$ spectral distribution, care should be taken to keep these fluctuations on timescales longer than the intrinsic stability time of the (HEB) mixer. From the total power stability measurements (see Fig. 10.4, 10.5) and using Eq. 10.1 with $T = T_A$, we find that local oscillator changes at the mixer ($\sigma/\langle s(t)\rangle$) in excess of 0.025 % result in output fluctuations larger than the (small volume) HEB mixer $1/f$ noise. In this case the local oscillator signal fluctuations begin to dominate the HEB mixer total power stability budget.

10.3.4 Sensitivity to atmospheric turbulence

To estimate the level of local oscillator fluctuations in the presence of turbulent air, we calculate the change in LO power (Eq. 10.11) against the percentage change in optical path length ΔL. If the air were to be absolutely stable, or humidity very low as would be the case on a high mountain, we would expect $dP_{lo} \rightarrow$ zero. Note that the loss term in Eq. 10.11 has a damping effect on the LO standing wave amplitude. For instance, if a mixer is to be operated close to a water line, fluctuations in the refractive index of air will be significant and modulate the standing wave amplitude. This is however somewhat mitigated by the increased absorption in air (Fig. 10.6). The increase in sensitivity to air turbulence with frequency is therefore not only a function of wavelength, but also of atmospheric opacity.

In Fig. 10.7 we plot the result of this calculation for four frequencies, evaluated for a LO – mixer path length of $z = 0.75$ meter, and a 10 % reflecting beam splitter. When the LO – mixer standing wave is tuned to a peak ($\beta nz = 0,\ \pi,\ 2\pi, \cdots$), the effect of air turbulence on the local oscillator signal at the mixer is smallest. In this situation, assuming a maximum LO signal fluctuation of 0.025 % (Sec. 10.3.3), the allowed atmospheric path length change due to air turbulence at 1.462 THz is $\pm$ 4.8 %. At the 1.630 THz CH_2F_2 FIR laser line this is $\pm$ 2.4 %, and at the 2.814 THz quantum cascade laser line [24] it has become a mere $\pm$ 1.3 %. At 650 GHz the atmosphere has essentially NO influence on the local oscillator signal, as is observed in practice. Reducing the path length and/or atmospheric humidity (high mountain)

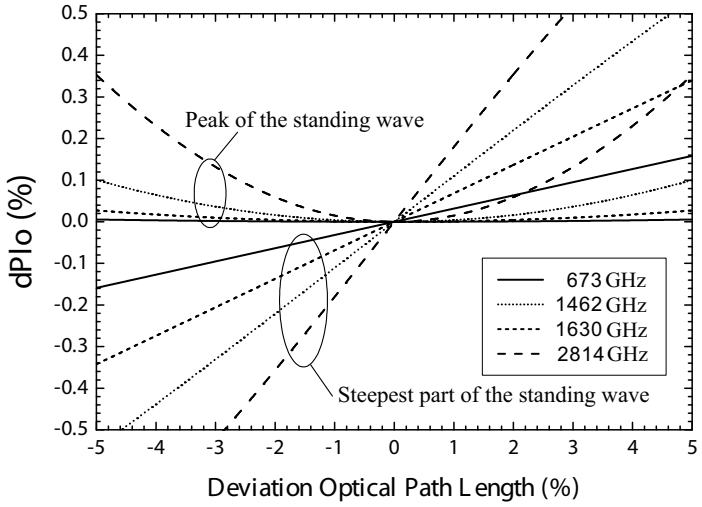

Figure 10.7: Change in LO power as a function of a change in optical path length for a $z = 0.75$ meter cavity. $|r_m|^2$ is -10 dB, $|r_{lo}|^2$ -8 dB, and $|r_{bs}|^2$ -10 dB. Shown is a situation where the cavity length is tuned to the peak of the LO – mixer standing wave ($\beta nz = 0,\ \pi,\ 2\pi, \cdots$), and where dP_{lo}/dz has a maximum. For a 0.025 % change in LO power (Sec. 10.3.3), the maximum allowed change in optical path length is just a few percent. The situation degrades by approximately a factor of three in the case of a dual beam interferometer style LO diplexing scheme.

will considerably improve the situation. However, when a dual beam interferometer type of LO injection scheme is employed [20], the allowed optical path length change decreases by approximately a factor of 3. This assumes a 1 dB loss in the optics setup.

If we tune the local oscillator frequency to the most sensitive part of the standing wave ($\beta nz = \pi/4,\ 3\pi/4, \cdots$), we see a large increase in LO power fluctuation for a given change in optical path length. It is absolutely critical therefore, as far as terahertz receiver stability is concerned, that the LO – mixer cavity is tuned to a peak of the LO power standing wave. In practice this may be done by adjusting the LO frequency or by a small positional move of the cryostat along the axis of propagation.

10.3.5 Sensitivity to mechanical fluctuations

As an example of the effect of mechanical path length fluctuations, consider the same mixer with an input reflection coefficient of -10 dB, LO source reflection coefficient of -8 dB, and a 10 % reflecting beam splitter to inject the LO signal. Evaluating Eq. 10.11 for small perturbations in z, we obtain an estimate for the allowed mechanical path length change of the LO – mixer cavity.

Given again a 0.025 % local oscillator signal stability (Sec. 10.3.3), the mechanical stability of the instrument at 1.462 THz needs to be better than $\pm$ 2.4μm, $\pm$ 2.6 μm at 1.630 THz, and a mere $\pm$ 1.8 μm at 2.814 THz. As seen in the previous Section, if a dual beam interferometer style diplexer is employed the sensitivity to mechanical change increases approximately threefold. In this case mechanical stability on the

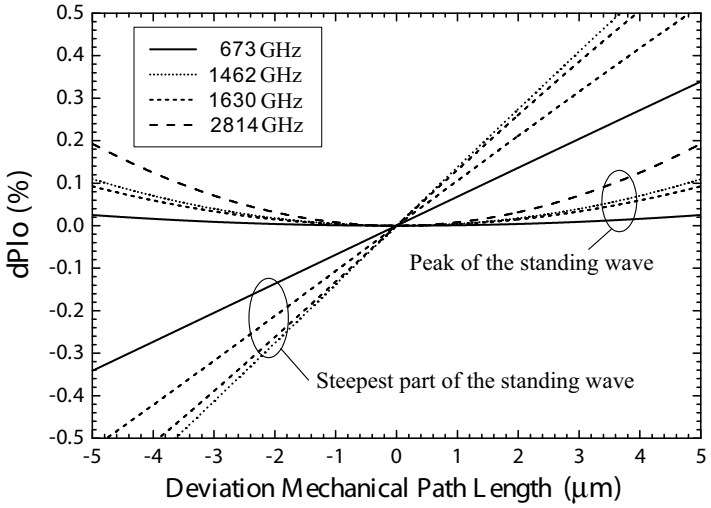

Figure 10.8: Change in LO power as a function of a change in mechanical path length for a $z = 0.75$ meter cavity. $|r_m|^2$ equals -10 dB, $|r_{lo}|^2$ -8 dB, and $|r_{bs}|^2$ -10 dB. Data is given when the cavity length is tuned to a peak of the standing wave, and on the steepest slope where $\beta nz = \pi/2,\ 3\pi/2, \cdots$. When dP_{lo}/dz has a maximum the mechanical stability requirements become considerably more stringent.

order of 0.75 μm (or less) is called for. This specification places stringent thermal requirements on the hardware. For example: Given a thermal expansion of aluminum at room temperature of $2.25 \cdot 10^{-5}\ K^{-1}$, a 75 cm LO – mixer cavity path length, and a total integration/calibration period of 20 minutes, then the maximum allowed temperature drift will be $\sim$ 132 mK/hour. At a physical temperature of 100 K the situation improves by approximately a factor of 2, due to a decrease in the thermal expansion of Aluminum. These numbers suggest that in the terahertz regime LO injection is best accomplished in a temperature controlled environment, or at cryogenic temperatures where thermal fluctuations are minimized. Furthermore, the analysis suggests that if the LO – mixer cavity length is fixed (LO source and receiver cannot be moved), that observations be done at discrete frequencies such that βnz is a multiple of π radians. This is the free spectral range, which for $z = 75$ centimeters equals 200 MHz.

10.4 Experimental validation

To experimentally study the effect of the atmosphere and mechanics at higher frequencies, we have repeated the stability measurement using a quantum cascade laser (QCL) as the local oscillator source [24]. As mixer a spiral antenna coupled, large

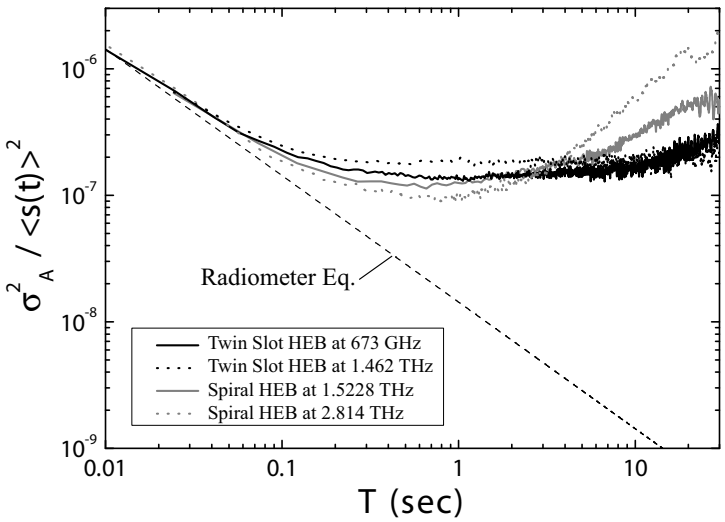

Figure 10.9: Normalized total power Allan variance stability measurements for variety of local oscillator sources, devices and LO frequencies. In all cases the HEB output noise exhibits an Allan minimum time of 0.2 – 0.3 s. For the 1.4624 THz and 673 GHz data the HEB output noise at the longer integration times is entirely dominated by gain fluctuation noise with a $1/f$ spectral distribution. At 1.5228 THz and 2.814 THz atmospheric and mechanical drift becomes progressively worse. Note that at 1.5228 THz the LO signal was injected directly, whereas in all other experiments a very thin beam splitter was employed ($|r_{bs}|$= -12 dB at 2.814 THz, and -15 dB for all other frequencies).

volume (0.4 x 4 μm) hot electron bolometer was used. We show, in Fig. 10.9 the measured Allan variance at 2.814 THz, using the QCL as LO source [24] with a 6 μm Mylar beam splitter. The measured Allan variance at 1.5228 THz was obtained with a solid state LO source similar to the one used in the experiments described in Sec. 10.2. The LO is coupled directly to the mixer in this case.

Superimposed on the plots are also the results from Fig. 10.4. Note that the Allan variance time is roughly identical for all datasets, being governed by intrinsic HEB $1/f$ gain fluctuation noise. However, at 2.8 THz we see the combined effect of atmospheric and mechanical drift. The same is true, to a lesser extent, for the 1.5228 THz data. The clear presence of drift in the 1.5228 THz data contrasts the absence of drift at 1.4624 THz, despite the fact that atmospheric properties and mechanical tolerances are very similar for both frequencies. The explanation for this is that in the 1.462 THz measurement a 3.5 μm beam splitter had been used, whereas in the 1.5228 THz experiment the local oscillator signal was coupled directly to the mixer. The much stronger drift component at 1.5228 THz is consistent with the developed theory, and provides an indication of what may happen if a room temperature dual beam interferometer style diplexer is used to inject the local oscillator signal. Because the HEB output noise is so dominated by internal $1/f$ gain fluctuations, the discussed atmospheric and mechanical stability issues in the case of HEB mixers is somewhat muted below 2 THz, unlike for example would be the case with SIS or Schottky based receivers.

10.5 Conclusion

We have studied the stability of HEB heterodyne receivers from two perspectives. First we have measured the stability of an HEB mixer in a laboratory setup at 0.673, 1.462, 1.630, and 2.814 THz. We find that phonon cooled NbN HEBs have significant short term gain fluctuation noise, and that up to at least 2.8 THz $1/f$ noise dominates the mixer stability budget. This instability limits the useful integration time to about 0.3 s in a 80 MHz total power noise fluctuation bandwidth. The physical origin of the gain fluctuation noise is unclear, however it is conjectured that it may be related to thermal or quantum processes in the hot-spot region of the mixer. It is therefore advisable to establish sensitivity of terahertz HEB mixers via synchronous or spectroscopic means, keeping integration times below the intrinsic Allan variance stability time of the mixer (Sec. 2.3.5).

The level of improvement that may be gained from using the spectroscopic measurement (statistically differencing two or more uncorrelated IF channels) depends on how correlated the noise is across the HEB IF band. Depending on the IF bandwidth under consideration, we have observed a factor of 10 – 15 improvement in stability with a small area 0.15 x 1.0 μm phonon cooled HEB. This is significant, as it demonstrates for the first time that the $1/f$ output noise of the HEB mixer is highly correlated, and why therefore hot electron bolometers may still be used as effective heterodyne mixing elements (for more details, we refer to Sec. A.5). It should be noted that if science goals call for the hot electron bolometer mixer to be used in continuum observations, that spectroscopic stability measurements are not a good guide

for performance. Whichever stability method is relevant (continuum or spectroscopic) will thus depend on the science objectives of the instrument.

Finally, we have studied the effect of atmosphere, mechanics, and temperature on the stability on terahertz mixers from the point of view of the LO – mixer cavity standing wave. It is found that operating terahertz receivers at the peak of the LO – mixer standing wave is important. Due to the very stringent thermal requirements, a dual beam interferometer style LO injection scheme such as a Fabry-Perot or Martin-Puplett interferometer is found best employed cold, i.e. at cryogenic temperatures.

It should be noted that one possible means of mitigating amplitude instability from the LO signal path is by employing the balanced style receiver configuration as briefly discussed in Sec. 2.3.5, and technically laid out in Sec. 8.2. For terahertz HEB receiver systems this appears a very promising technological advancement [25].

There are of course other mechanisms that cause a mixer to behave unstable or erratic [11, 12]. Fortunately, spectroscopic measurement greatly reduce many of these problems as fluctuations are often highly correlated (Sec. A.4). However, if the spectroscopic Allan stability time of the instrument is less then 20 s, the typical position switching time of a telescope, observations of extended astronomical sources may become problematic.

Aside from adequate spectroscopic stability time, there is also the issue of absolute intensity calibration. For this, the differential stability of the atmosphere and that of the instrument itself has to preferably exceed a few minutes if observation efficiency is not to be impacted (see also Sec. 2.3.6).

Bibliography

[1] E. M. Gershenzon, G. N. Goltsman, I. G. Gogidze, A. I. Eliantev, B. S. Karasik and A. D. Semenov, Millimeter and submillimeter range mixer based on electronic heating of superconducting films in the resistive state, *Sov. Phys. Supercondcutivity*, Vol. 3, 1582 (1990).

[2] D. E. Prober, *Superconducting terahertz mixer using a transition-edge microbolometer*, *Appl. Phys. Lett.*, Vol. 62, 2119 (1993).

[3] J. J. A. Baselmans, J. M. Hajenius, J. R. Gao, T. M. Klapwijk, P. A. J. de Korte, B. Voronov, and G. Gol'tsman, Doubling of sensitivity and bandwidth in phonon cooled hot electron bolometer mixers, *Appl. Phys. Lett*, Vol. 84, 1958 (2004).

[4] A. D. Semenov, H.-W. Hübers, J. Schubert, G. N. Gol′tsman, A. I. Elantiev, B. M. Voronov, and E. M. Gershenzon, Design and Performance of the lattice-cooled hot-electron terahertz mixer, *J. Appl. Phys*, Vol. 88, 6758 (2000).

[5] S. Cherednichenko, P. Khosropanah, E. Kollberg, M. Kroug, H. Merkel, Terahertz superconducting hot-electron bolometer mixers, *Physica C*, Vol.407, 372-376 (2002).

[6] P. Yagoubov, M. Kroug, H. Merkel, E. Kollberg, G. Gol'tsman, S.Svechnikov and E. Gershenzon, Noise temperature and local oscillator power requirement of NbN phonon cooled hot electron bolometric mixers at terahertz frequencies, *Appl. Phys. Lett.*, Vol. 73, 2814 (1998).

[7] Herschel; http://sci.esa.int/

[8] Sofia; http://www.sofia.usra.edu/

[9] Apex; http://www.apex-telescope.org/

[10] J. D. Kraus, Radio Astronomy, (McGraw-Hill, New York, 1966), Chaps. 3 & 7.

[11] R. Schieder and C. Kramer, Optimization of Heterodyne Observations using Allan variance Measurements, *Astron. Astrophys*, Vol. 373, 746-756 (2001).

[12] J. W. Kooi, G. Chattopadhyay, M. Thielman, T. G. Phillips, and R. Schieder, Noise Stability of SIS receivers, *Int J. IR and MM Waves*, Vol. 21 (5), (2000).

[13] M. Hajenius, J. J. A. Baselmans, J. R. Gao, T. M. Klapwijk, P. A. J. de Korte, B. Voronov and G. Goltsman, Low noise NbN superconducting hot electron bolometer mixers at 1.9 and 2.4 THz, *Supercond. Sci. Technol*, Vol. 17, S224-S228 (2004).

[14] W. F. M., Ganzevles, L. R. Swart, J. R. Gao, P. A. J. de Korte, and T. M. Klapwijk, Direct response of twin-slot antenna-coupled hot-electron bolometer mixers designed for 2.5 THz radiation detection, *Appl. Phys. Lett.*, Vol. 76, 3304 (2000).

[15] G. Chattopadhyay, E. Schlecht, J. Ward, J. Gill, H. Javadi, F. Maiwald, and I. Mehdi, An All Solid-State Broadband Frequency Multiplier Chain at 1500 GHz, *IEEE Transactions on Microwave Theory and Techniques*, Vol. 52, 5, 1538 (2004).

[16] V. Tolls, R. Schieder, and G. Winnewisser, The Cologne Acousto-Optical Spectrometers, *Experimental Astronomy*, Vol. 1, 101 (1989).

[17] J. Kawamura, T. R. Hunter, C. E. Tong, R. Blundell, D. C. Papa, F. Patt, W. Peters, T. Wilson, C. Henkel, G. Goltsman, and E. Gershenzon, Ground-based CO spectroscopy toward Orion, *Astron. Astrophys*, Vol. 394, pp271-274 (2002).

[18] M. C. Wiedner, G. Wieching, F. Bielau, K. Rettenbacher, N. H. Volgenau, M. Emprechtinger, U. U. Graf, C. E. Honingh, K. Jacobs, K. M. Menten, L. Lyman, R. Güsten, S. Philipp, D. Rabanus, J. Stutyki, and F. Wyrowski, First observations with CONDOR, a 1.5 THz heterodyne receiver *Astron. Astrophys*, Vol. 454, L33-L39 (2006).

[19] T. Berg, S. Cherednichenko, V. Drakinskiy, H. Merkel, E. Kollberg, and J. W. Kooi, Stability measurements of NbN HEB receiver at THz frequencies, *Proc. 15^{th} Int. Symp. on Space THz*, Tech., Northampton, Ma (USA) (2004).

[20] P. F. Goldsmith, *Quasioptical Systems (IEEE)*, New York, (1998), Chap. 9.

[21] J. R. Pardo, E. Serabyn, M. C. Wiedner, and J. Cernicharo, Measured telluric continuum-like opacity beyond 1 THz, *J. Quant. Spec. and Radiat. Transfer*, Vol. 96/3-4, 537-545 (2005).

[22] J. R. Pardo, J. Cernicharo, and E. Serabyn, Atmospheric Transmission at Microwaves (ATM): An Improved Model for mm/submm applications, *IEEE Trans. on Antennas and Propagation*, Vol. 49 (12), 1683-1694 (2001).

[23] R. Schieder, (private communication).

[24] J. R. Gao, J. N. Hovenier, Z. Q. Yang, J. J. A. Baselmans, A. Baryshev, M. Hajenius, T. M. Klapwijk, A. J. L. Adam, and T. O. Klaassen, B. S. Williams, S. Kumar, Q. Hu, and J. L. Reno, Terahertz heterodyne receiver based on a quantum cascade laser and a superconducting bolometer, *Appl. Phys. Lett*, Vol. 86, 244104 (2005).

[25] D. Meledin, A. Pavolotsky, V. Desmaris, I. Lapkin, C. Risacher, V. Perez, D. Henke, O. Nystrom, E. Sundin, D. Dochev, M. Pantaleev, M. Fredrixon, M. Strandberg, B. Voronov, G. Goltsman, and V. Belitsky, "A 1.3 THz Balanced Waveguide HEB Mixer for the APEX Telescope," accepted for publication in *IEEE Microwave Theory and Technique*, (2008).

Appendix A

The Allan variance method*

A.1 Introduction

There is a strong interest in the submillimeter astronomy community to increase the IF bandwidth of SIS receivers in order to better facilitate broad spectral linewidth and continuum observations of extragalactic sources. However, with an increase in IF bandwidth there is a decrease in the mixer total power stability. This in turn effects the integration efficiency and the quality of the measurement. In order to better understand the noise mechanisms responsible for reducing the receiver stability, we employ a technique first described by D.W. Allan and later elaborated upon by Schieder *et. al.*

Radio astronomy receivers in general look at very weak signals deeply embedded in noise. To extract the weak signals, synchronous detection ("signal on" - "signal off") is typically employed. This is done by either slewing the entire telescope back and forth so as to get the beam on/off the source, or by nutating the secondary mirror (subreflector) of the telescope at a relatively fast rate. The problem in both these cases is the dead time between observations, i.e., chopping efficiency (η_c). A practical lower limit for slewing the whole telescope is typically 15 s, while chopping the secondary mirror can perhaps be as fast as 0.2 s (5 Hz). Frequency switching is possible and can be accomplished at a much higher rate. It suffers however from modulation of the LO-mixer standing wave (Chap. 10) [1], local oscillator power stability, and for terrestrial observations changes in the atmospheric transmission. For the high resolution Heterodyne Instrument (HIFI) on ESA's Herschel satellite [2, 3] frequency switching is baselined as one of the observation modes.

If the noise in the receiver system is completely uncorrelated (white), it turns out that the rate of chopping (modulation frequency) has no effect on the final signal to noise ratio. This can be deduced from the well known radiometer equation (A.1) which

*The material described in this Appendix has been published in the following paper: J. W. Kooi, G. Chattopadhyay, M. Thielman, T. G. Phillips, and R. Schieder, in *Int. J. IR and MM Waves*, Vol. 21 (5) (2000).

states that uncorrelated noise with a Gaussian like spectral distribution integrates down with the square root of integration time

$$\sigma = \frac{\langle x(t) \rangle}{\sqrt{(\Delta\nu * T)}} \ . \tag{A.1}$$

Here σ is the standard deviation (rms voltage) of the signal, $\langle x(t) \rangle$ the signal mean, $\Delta\nu$ the effective fluctuation bandwidth, and T is the total integration time of the data set.

In practice however, the noise in radiometers, and in particular SIS and HEB mixers, appears to be a combination of low frequency drift (correlated noise), $1/f$ electronic noise and white (uncorrelated) noise. Hence, there is an optimum integration time, known as the Allan stability time (T_A), after which observing efficiency is lost. In actual synchronous detection measurements n samples of difference data ("signal on" - "signal off") are taken, each with a period T. These differences are then averaged so that the total observed time equals $n * (2T)$. If the period T is larger than the Allan stability time (T_A) of the system, then apart from loss in integration efficiency, there will be a problem with proper baseline subtraction. This manifests itself in baseline ripples at the output of the spectrometer which limits how well the noise integrates down with time (Sec. 2.3.5).

A.2 Theoretical considerations

To optimize observation efficiency, it is important to find the best secondary mirror (subreflector) chopping rate. This requires a knowledge of the nature of the receiver noise fluctuations. In practice, we employ a method developed by Allan [4], Barnes [5], and further elaborated on by Schieder *et al.* [6, 7].

Following Schieder's analysis of synchronous detection, two sets of contiguous data samples are taking, each with the same integration time (T). The first measurement is the "on-source" signal $s(t)$, and the second measurement the "off-source" reference $r(t)$. In the analysis, it is assumed that there is no dead time between the data samples. If we define the first measurement as the integrated signal $s(t)$ over a period T

$$s(T) = \int_0^T s(t)\ dt \ , \tag{A.2}$$

and the second measurement as:

$$r(T) = \int_T^{2T} r(t)\ dt \ , \tag{A.3}$$

than difference of the two measurements is

$$d(T) = s(T) - r(T) \ . \tag{A.4}$$

If μ is defined as the mean of $d(T)$, and σ^2 the variance of $d(T)$ then

$$\sigma^2(T) = \langle (d(T) - \mu)^2 \rangle = \langle d(T)^2 \rangle - \langle d(T) \rangle^2 \ . \tag{A.5}$$

Here $\langle d(T)^2 \rangle$ is the mean (expectation value) of the difference squared and $\langle d(T) \rangle^2$ the squared mean of the difference. From [4] we find the Allan variance defined as

$$\sigma_A^2(T) = \sigma^2(T)/2 \ , \tag{A.6}$$

so that

$$\sigma_A^2(T) = \frac{1}{2} \langle (d(T) - \langle d(T) \rangle)^2 \rangle \ . \tag{A.7}$$

Because we look in astronomy at signals deeply embedded in the noise and are only interested in how the noise integrates down with time, we can make the simplification that there is essentially no signal present in $s(t)$. This means that the average of $d(T) = \langle d(T) \rangle = 0$, and we have under this condition the special situation that

$$\sigma_A^2(T) = \frac{1}{2} \langle d(T)^2 \rangle \ . \tag{A.8}$$

Since in practice the data is only available in discreet form, we can use the more general expression of Eq. A.7 for a spectrometer channel k with fluctuation bandwidth $\Delta\nu$ as

$$\sigma_{A,k}^2(T) = \frac{1}{2(N-1)} \sum_{n=1}^{N} (d_k(n) - \langle d_k \rangle)^2 \ , \quad \langle d_k \rangle = \frac{1}{N} \sum_{n=1}^{N} d_k(n) \ . \tag{A.9}$$

N equals the number of discrete time samples taken. Thus for a spectrometer with K channels, the average Allan variance spectrum (Fig. A.1b) can then be obtained by summing the variance of each individual channel, e.g.

$$\sigma_A^2(T) = \frac{1}{K} \sum_{k=1}^{K} \sigma_{A,k}^2(T) \tag{A.10}$$

Other weightings are possible, for this we refer to Ossenkopf *et al.* [8].

The mathematical treatment of Eq. A.6 can be found in [5] for different types of noise spectra. If the noise spectral density is represented by a power law, then

$$S(f) = f^{-\alpha}, \quad \alpha = [1, 3] \tag{A.11}$$

and one finds that

$$\sigma_A^2(T) \ \propto \ T^{\,\alpha-1} \ . \tag{A.12}$$

$\alpha = 0$ stands for the white (uncorrelated) noise part of the spectrum, e.g.

$$\sigma_A^2(T) = \frac{\langle s(t) \rangle^2}{2\Delta\nu T} \ , \tag{A.13}$$

$\alpha = 1$ for $1/f$ noise, and $\alpha \geq 2$ for correlated low frequency (drift) noise. Using a simple power law to characterize low frequency drift noise might not be correct however. A more accurate representation would be to describe the noise by a correlation function

$$g(\tau) = \langle r(t) * r(t+\tau) \rangle \ . \tag{A.14}$$

The Allan variance can then be expressed as:

$$\sigma_A^2(T) = \frac{1}{T^2} \int_{-T}^{T} (T - |\tau|)(g(\tau) - g(T+\tau)) \ d\tau \ . \tag{A.15}$$

Because we are interested only in integration times less than the correlated (drift) noise time scale, the correlation function can be expanded in a power series with only a few terms:

$$g(\tau) = g(0) - a\tau^{\beta} \ \pm \ \ldots , \qquad \beta = 1, 2, ... \tag{A.16}$$

From equation (A.15) we obtain

$$\sigma_A^2(T) \ \propto \ T^{\beta} \ . \tag{A.17}$$

Combining equation (A.12) and equation (A.17) we find that for a noise spectrum that contains drift, white noise, and $1/f$ noise that the Allan variance takes the form

$$\sigma_A^2(T) = aT^{\beta} + \frac{b}{T} + c \ , \tag{A.18}$$

where a, b, and c are appropriate constants and $\beta = \alpha - 1$. For short integration times, the variance decreases as $\frac{1}{T}$, as expected from the radiometer equation (A.1). For longer integration times, the drift will dominate as shown by the term aT^{β}. In that case, the variance starts to increase with a slope β which is experimentally found to be between 1 and 2. For SIS and HEB mixers it is frequently observed that the variance plateaus after some time T. This is attributed to the constant c and is representative of flicker or $1/f$ noise in the device under test.

Plotting $\sigma_A^2(T)$ on a log-log plot demonstrates the usefulness of this approach in analyzing the radiometer noise statistics (Fig. A.1b). As a reference it is meaningful to superimpose radiometric noise with a T^{-1} slope. The latter represents the uncorrelated (white) noise part of the spectrum. The minima in the plot gives the Allan time (T_A), the crossover from white noise to $1/f$ or drift noise. Often however, there is no clear minima, and a factor $\sqrt{2}$ deviation from the rms radiometric noise is then a useful definition of the Allan time. For the sake of optimum integration efficiency, one is advised to keep the integration time well below the system Allan time (Sec. 2.3.5).

Finally, it is often of interest to estimate what happens to the Allan stability time if spectrometer channels are binned to reduce the rms noise in an observed spectrum, or if the IF bandwidth of the radiometer is increased. Solving equation (A.18) for T as a function of receiver binned IF bandwidth $\Delta\nu'$ we get

$$T'_A/T_A = (\Delta\nu/\Delta\nu')^{\frac{1}{\beta+1}} \ . \tag{A.19}$$

β the slope of the drift noise as discussed above. When the uncorrelated (white) noise component of the mixer spectral output power is reduced (by for example binning of spectrometer channels), the intersect between radiometric (A.1) and drift noise (A.17) occurs at an earlier time. Where exactly the two curves intersect depends on the statistical nature of the long term drift.

A.3 Total Power Allan variance

As an example we show in Fig. A.1 the time series and total power Allan variance (also known as the continuum Allan variance) of HIFI HEB mixer band 6a (H-polarization) as measured during the instrument level test phase (ILT) in May 2007. As we shall see, this plot contains a wealth of information. The IF output frequency of the HEB mixer is 2.4 – 4.8 GHz [9], which after being up-converted, and then back down-converted to match the 4 – 8 GHz wideband acousto-optical spectrometer (WBS) [10] input, translates to AOS subband1 (4.8 – 3.8 GHz), subband2 (3.8 – 2.8 GHz), and subband3 (2.8 – 2.4 GHz). "Full" corresponds to the total 2.4 GHz available HEB IF bandwidth. The left panel of Fig. A.1 depicts the averaged normalized time series of the full, and the three individual spectrometer subbands. It should be noted that the HEB mixer is most sensitive in the 2.4 – 3.4 GHz IF frequency range (Chap. 6) [9], and as a results it may be expected that WBS subband 3 is the most unstable. This is indeed the case as is evident from the top curve in Fig. A.1b. The offsets between the three spectrometer subband Allan times are due to excess noise in each of the IF subchannels. Averaged over the entire IF bandwidth, the calculated fluctuation

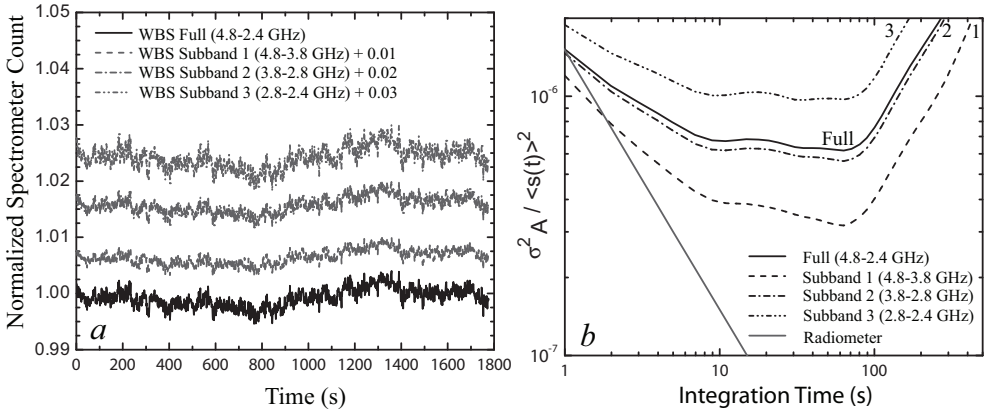

Figure A.1: *Left*) Time series for HIFI B6a HEB mixer, H-polarization, LO frequency = 1447 GHz. Curves have been offset for clarity. The statistical details of the noise are brought out by the Allan variance plot on the right. *Right*) The derived continuum, or total power Allan variance. The "full" (2.4 GHz) spectrometer response deviates a factor 2 from the radiometric noise at 3 s. This may be considered the effective total power "Allan variance minimum time" (T_A). See text for details.

noise bandwidth ($\Delta\nu$) is 1.3 MHz. This is somewhat less than the spectrometer [10] intrinsic noise bandwidth of 2.3 MHz, indicative of some excess (non-radiometric) noise.

Again referring to Fig. A.1b, we see that the noise integrates down with a slope slightly less than $(\Delta\nu T)^{-1}$ between 1 s and 7 s. Judging from the -1 radiometer slope, we have a factor 2 loss in integration efficiency at ~ 3 s. This may be considered the effective "Allan minimum time". The reason that there is not a clear minimum in the Allan variance plot is that HEB mixers exhibit significant $1/f$ fluctuation noise (zero slope), in this case between ~ 10 s – 90 s. Above approximately 90 s, drift noise begins to dominate. In this particular example the drift slope $\beta = +1.2$. For a further discussion on this subject we refer to Chap. 10.

A.4 Spectroscopic Allan variance

The spectroscopic Allan variance measures deviations from the continuum level fluctuations [8]. As such it corresponds to the subtraction of the spectrometer mean continuum level, known as the zeroth order baseline correction, as proposed by Schieder, Ossenkopf, and Siebertz [7, 8, 11]. This is allowed since most heterodyne observations are intended for line observations, rather than continuum or flux calibration. For continuum observations incoherent detectors are better suited (Chap. 2). The spectroscopic normalization for two channels is given by Eq. 10.4. For K spectrometer channels the signal in each channel ($d_k(n)$) at time n may be normalized by subtraction of the instrument zero level in the particular channel (z_k), and then by dividing the difference by the temporal average of each channel

$$s'_k(n) = \frac{d_k(n) - z_k}{\big\langle d_k(n) - z_k \big\rangle_n} \ , \quad z_k = \frac{1}{N}\sum_{n=1}^{N} d_k(n) \ . \tag{A.20}$$

To now obtain the difference for the spectroscopic Allan variance computation, we substract the normalized mean summed over all spectrometer channels of interest, e.g.

$$s_k(n) = s'_k(n) - \big\langle s'_k(n) \big\rangle_k \ . \tag{A.21}$$

$s_k(n)$ may then be substituted for $d_k(n)$ in Eq. A.9 to obtain the spectroscopic Allan variance for each channel.

In Fig. A.2a we show the spectroscopic Allan variance. In this case a zeroth order correlated noise baseline is subtracted. We see a substantial improvement in the statistical variance of the spectra. The noise now integrates down radiometrically, for about 50 s in case of the subbands, and 15 s for the full spectrometer band (4.8 – 3.8 GHz). The $1/f$ gain fluctuation noise that dominates the continuum Allan variance of Fig. A.1b has been nearly completely removed! Taking the ratio of the spectroscopic to the total power Allan variance (Fig. A.2b), we find that statistically the largest improvement (factor 10+) is gained by spectrometer subband 3 at integration times > 10 s. This is good news as most galactic (narrow line) observations will be planned in this subband, being the most sensitive region of the HEB IF passband [9].

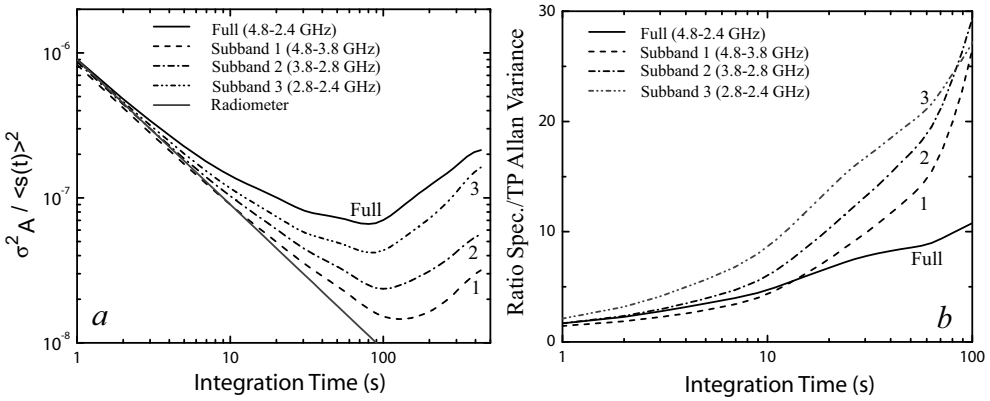

Figure A.2: *Left*) Spectroscopic Allan variance for the B6a HEB mixer subbands and full spectrometer band (2.4 GHz). The Allan times, defined as a factor of two deviation from the radiometric noise (white) are: T_A(full)=14.9 s, T_A(subband1)=111 s, T_A(subband2)=50.5 s, and T_A(subband3)=30.7 s. The noise fluctuation bandwidth is 2.3 MHz. *Right*) Ratio of the spectroscopic to the total power (Fig A.1b) Allan variance. Not surprising, the greatest improvement is obtained at long integration times. Spectrometer subband 3 offers the greatest improvement, as it constitutes only 400 MHz of bandwidth and is the most unstable (highest sensitivity) to start out with. H-polarization for the mixer band, LO frequency = 1447 GHz

For spectral line broadened extragalactic observations the full spectrometer will need to be used in which case a factor six improvement over the continuum stability is obtained.

It should be noted that the HIFI B6a results presented here serve as an example of system stability. Actual HEB mixer stability (Chap. 10) [1] may be better in a more optimized environment such as space, or possibly worse in a poorly designed ground based application. The balanced approach of Chap. 8, by virtue of reduced sensitivity to local oscillator amplitude noise, is expected to improve the HEB mixer system stability.

A.5 Improvement of spectroscopic over total power Allan variance

To further compare the improvement in spectroscopic Allan variance over continuum Allan variance, we compare in Fig. A.3 the ratios of HIFI SIS band 2 (736 GHz) and HEB mixer band 6 (1652 GHz). For the HEB mixer, subband 1 has the lowest sensitivity (4.4 – 4.8 GHz), and also shows the least improvement. The loss in sensitivity of an HEB mixer is caused by the roll of in mixer gain, as described in Sec. 6.5, overlaid by the frequency response of the diplexer used to inject the LO signal. For the band 2 SIS mixer the sensitivity is uniform across all spectrometer subbands. In this case a beam splitter is used to inject the LO signal. Why the spectroscopic-over continuum Allan variance ratio is not more uniform is not entirely clear, except to note that the 7 – 8 GHz IF channel (subband 4) has always the worst stability

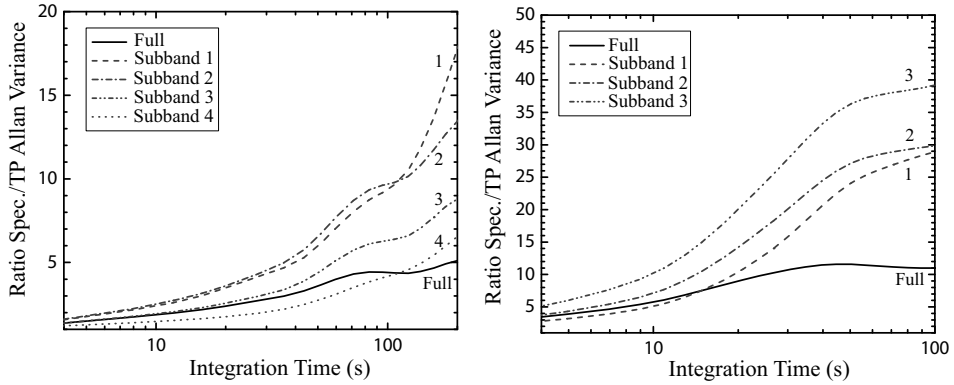

Figure A.3: *Left*) Improvement ratio of the spectroscopic Allan variance for HIFI SIS mixer band 2b. LO frequency is 736 GHz. *Right*) Improvement ratio of the spectroscopic Allan variance for HIFI HEB mixer band 6b. LO frequency is 1652 GHz. Note that the plots have different scales. The behavior of the individual subbands is noticeably different. The removal of a zeroth order baseline has significantly more effect on a per subband bases for an HEB mixer than SIS mixer. This indicates that the source of HEB instability (see also Chap. 10) is highly correlated in an HEB mixer. The most likely culprits are: LO instability and optical standing waves. SIS mixer band 2 is a beamsplitter band, and HEB mixer band 6 uses a diplexer to inject the LO signal. Due to the finite diplexer passband and roll of in mixer gain, HEB subband 1 has considerably lower sensitivity than subband 3. For both mixer bands, we have plotted the vertically polarized IF output channel.

performance. It is likely that we see an additive effect of the many subcomponents in the IF- and backend system. In general it appears therefore that the noise of a SIS mixer is less correlated in the higher end of the IF band.

Significantly, a greater amount of spectroscopic- over continuum Allan variance improvement is obtained in the HEB mixer band than the SIS mixer band. There are several explanations for this. First, as we have seen in Sec. 4.3, the HEB is a power sensor. This is opposed to a SIS junction that is sensitive to quasi-particle tunneling through a thin barrier (Sec. 4.1). Second, HEB mixers operate in the terahertz frequency regime. As such they are more sensitive to optical standing waves than SIS mixers, which primarily operate below 1 THz. This is the subject of Sec. 10.3.2. And finally, the LO sources that pump the mixers are more complex at higher operating frequencies (HEB mixers), and thus more susceptible to amplitude noise which increases approximately as $20log_{10}(N^2)$ [12]. N is the local oscillator multiplication factor. Hence the argument that a balanced HEB mixer configuration is liable to have improved system stability performance.

Bibliography

[1] J. W. Kooi, J. J. A. Baselmans, A. Baryshev, R. Schieder, M. Hajenius, J. R. Gao, T. M. Klapwijk, B. Voronov, and G. Gol'tsman, "Stability of Heterodyne Terahertz Receivers", *Journal of Applied Physics*, Vol. 100, 064904, Sep. (2006).

[2] Th. de Graauw, N. Whyborn, E. Caux, T. G. Phillips, J. Stutzki, X. Tielens, R. Güsten, F. P. Helmich,
W. Luinge, J. Pearson, P. Roelfsema, R. Schieder, K. Wildeman, and K. Wavelbakker, "The Herschel-Heterodyne Instrument for the Far-Infrared (HIFI)", [Online]. Available: herschel.esac.esa.int/Publ/2006/SPIE2006_HIFI_paper.pdf

[3] [Online]. Available: Herschel; http://sci.esa.int/

[4] D. W. Allan, "Statistics of Atomic Frequency Standards", *Proc. IEEE*, Vol. 54, No. 2, pp 221-230, (1969).

[5] A.B Barnes, "Characterization of frequency stability", *IEEE Trans. Instrument Measurements*, Vol. IM-20, no. 2, pp. 105-120, (1971).

[6] R. Schieder, "Characterization and Measurement of System Stability", *SPIE*, Vol 598, Instrumentation for Submillimeter Spectroscopy (1985).

[7] R. Schieder and C. Kramer, "Optimization of Heterodyne Observations using Allan variance Measurements", *Astron. Astrophys.*, Vol. 373, 746-756 (2001).

[8] V. Ossenkopf, "The stability of spectroscopic instruments: A unified Allan variance computation scheme", *A & A*, Vol. 479, 915-926 (2008).

[9] A. Cherednichenko, V. Drakinskiy, T. berg, P. Khosropanah, and E. Kollberg, "Hot-electron bolometer terahertz mixers for the Herschel Space Observatory", *Rev. Sci. Instrum.*, Vol. 79, 034501, (2008).

[10] R.Schieder, O. Siebertz, F. Schloeder, C. Gal, J. Stutzki, P. Hartogh, and V. Natale, "Wide-Band Spectrometer for HIFI-FIRST", *Proc. of "UV, Optical, and IR Space Telescopes and Instruments"*, J. B. Breckinridge, P. Jakobsen Eds., SPIE 4013, 313-324, Jul., (2000).

[11] O. Siebertz, "Akusto-optisches Spektrometer mit variabler Auflsung", PhD thesis, University Cologne, (1998).

[12] N. Erickson, "AM Noise in Drives for Frequency Multiplied Local Oscillators", *Proc. 15th Int. Symp. on Space Terahertz technology*, Northampton, MA, (2004), pp. 135-142.

Appendix B

Transmission properties of Zitex*

B.1 Introduction

Advances in submillimeter SIS receivers necessitate the use of very-low-loss components in order to achieve theoretical performance. Often these optical elements are cooled to 4 K, where their properties are less well measured. The advanced SIS receivers of Chaps. 7–9 achieve noise temperatures as low as 3–5 times the quantum noise limit ($h\nu/k_B$), of which up to 30 % may stem from optical loss. Modern bolometric instruments have comparable optical efficiencies. Clearly, choosing materials with optimum dielectric constants, low absorption loss and optimal cryogenic performance is very important.

To reduce the loading on cold optical elements operating in the far-infrared, room temperature infrared radiation must be blocked efficiently while allowing the desired wavelengths to pass unattenuated [1, 2]. Quartz is a low-loss material when a suitable antireflection coating like Teflon is applied, but this is difficult and restricts the wavelengths over which it can be used as a highly transmissive element [3]. Teflon itself is a good IR block, but transmits power in the 5–10 μm range and longward of 50 μm, limiting its usefulness. Several more absorbing materials, such as Fluorogold and Fluorosint, have been used for low frequency applications, but their slow spectral cut-off characteristics are not ideal for receivers operating above $\sim$ 400 GHz [3, 4].

With this in mind we have measured (Table B.1) the power absorption coefficient, refractive index, and thermal conductivity of Zitex at 290 K, 77 K, and 4 K in the 1 to 1000 μm spectral range. This was accomplished with the use of three Fourier Transform Spectrometers (FTS) [5]. Zitex [6] is a sintered Teflon material with voids of 1–60 μm and a filling factor of 50 %. Several different varieties are available, divided

*A subsection of the material described in this Appendix has been published in the following paper: D. J. benford, M. C. Gaidis, and J. W. Kooi, *Proc. 10^{th} Int. Symp. Space Terahertz Technology*, (1999), pp. 402 ff.

Table B.1: Zitex samples measured.

Grade	Pore Size (μm)	Thickness (mm)	Filling Factor†	NIR data	FIR data	Submm data
G104	5–6	0.10	0.45	√		
G106	4–5	0.16	0.50	√		
G108	3–4	0.20	0.55	√	√	
G110	1–2	0.25	0.60	√	√	
G115	1–2	0.41	0.60	√		
G125	∼3	3.53	∼0.5	√		√
A155	2–5	0.27	0.40	√		

† Relative density of Teflon.

into two categories by manufacturing process. Zitex A is designed to reproduce filter paper. It has many narrow linear paths through it and is a rough but soft sheet. It is available in 11 grades with effective pore sizes ranging from 3 μm to 45 μm and in thicknesses from 0.13 mm (0.005") to 0.64 mm (0.025"). Zitex G is made of sintered Teflon spheres of small sizes, resulting in a denser, smoother material. Available in 5 grades, the pore sizes range from 1.5 μm to 5.5 μm and is available in standard thicknesses of 0.10 mm (0.004") to 0.38 mm (0.015"), although larger thicknesses are available.

Zitex is similar in geometry to glass bead filters, in which dielectric spheres are embedded in a suspending material with a different index of refraction. A single sphere of radius a in a material of index n will scatter strongly for wavelengths $\lambda \lesssim \pi a(n-1)$ [7]. Thus, for Teflon ($n = 1.44$ [8]), a sphere of radius 10 μm produces a shadow for wavelengths shortward of 15 μm. At short wavelengths a perfectly randomly scattering screen will redistribute the optical power in an incident beam equally in all directions, resulting in a large loss for well-collimated beams.

Zitex is an effective IR block, with thin (200μm) sheets transmitting less than 1 % in the 1–50 μm range while absorbing $\lesssim$ 10 % at wavelengths longer than 200 μm. Some variation in the cutoff wavelength is seen, tending to be a shorter wavelength cutoff for a smaller pore size. In addition, the thermal conductivity of Zitex at cryogenic temperatures has been measured, and is found roughly one-half that of bulk Teflon.

B.2 Zitex G104, G106, G108, G110, G115, & A155

The samples of G104 and G106 were measured in the near- to mid-infrared to derive a transmission and an effective absorption coefficient, as shown in Fig. B.1. The absorption coefficient α for a sheet of thickness d is calculated from the transmission t_{rf} as $-\ln(t_{rf})/d$. Since some wavelength-dependent fraction of the loss $(1 - t_{rf})$ is

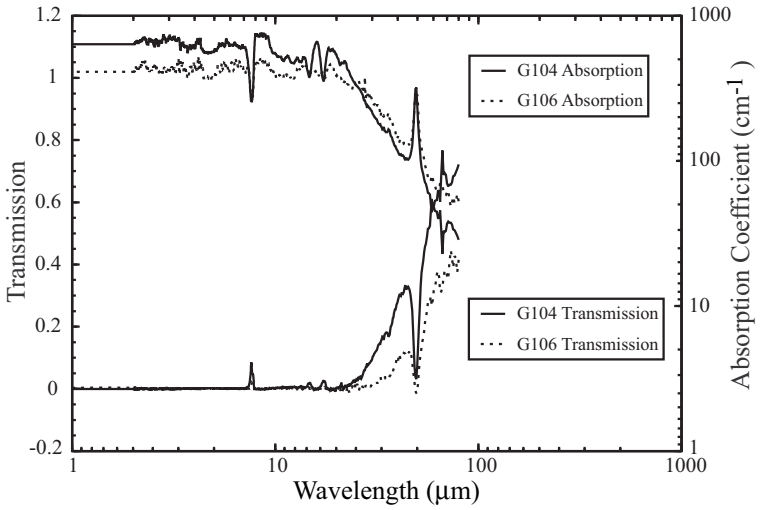

Figure B.1: Transmission and effective absorption coefficient in nepers per cm of single sheets of Zitex G104 and G106 (pore sizes 5–6 μm and 4–5 μm, respectively).

from scattering and some from absorption, the absorption coefficient cannot be used to estimate the transmission of arbitrary thicknesses. It does, however, provide a useful means of comparison with other, more purely absorptive, materials.

Combining sets of data in the near- through far-infrared for samples of G108 and G110 allows to build a more complete picture of the turn-on profile of Zitex near 100 μm, as shown in Fig. B.2.

B.3 Multiple Layers

A LHe-cooled receiver is likely to have several layers of infrared-blocking filtration in the optical path. As a result, it is natural in the case of a scattering material like Zitex to question its efficiency in a multilayer application. Layering single-, double-, and triple sheets of Zitex in close proximity (limited only by the natural wavy contours of the thin sheets) shows that scattering is the dominant loss mechanism and that multiple sheets are not substantially more effective than single sheets [5].

Using Zitex A155 sheets spaced by roughly 7 mm, we find the transmission shown in Fig. B.3. At mid-infrared wavelengths, the Zitex still appears to be dominated by scattering since the effective absorption coefficient of two layers is less than that for of one layer. However, at far-infrared wavelengths, the transmission appears to be increasingly determined by absorption alone, presumably in the bulk of the Teflon; the absorption is similar to that of Birch [9].

B.4 Temperature Variation

For many materials (e.g., quartz), the absorption of mid-infrared radiation is known to vary as the temperature changes [10]. To determine if there was any effect of the

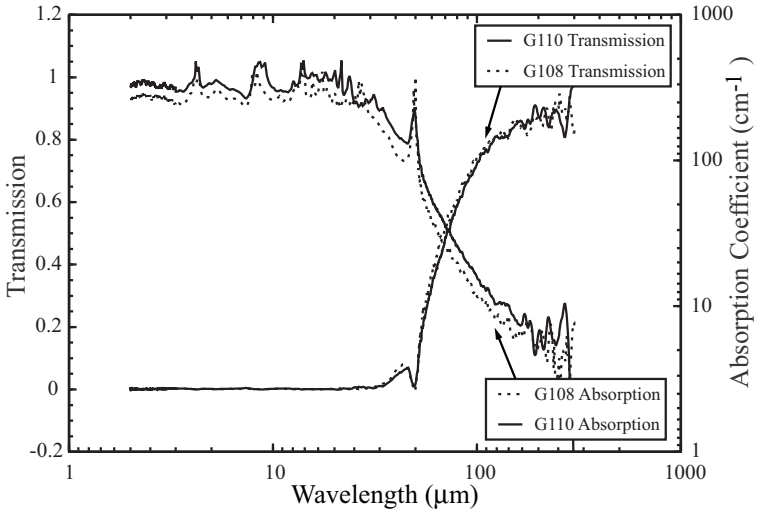

Figure B.2: Transmission and effective absorption coefficient in nepers per cm of single sheets of Zitex G108 and G110 (pore sizes 3–4 μm and 1–2 μm, respectively) using near-, mid-, and far-infrared data.

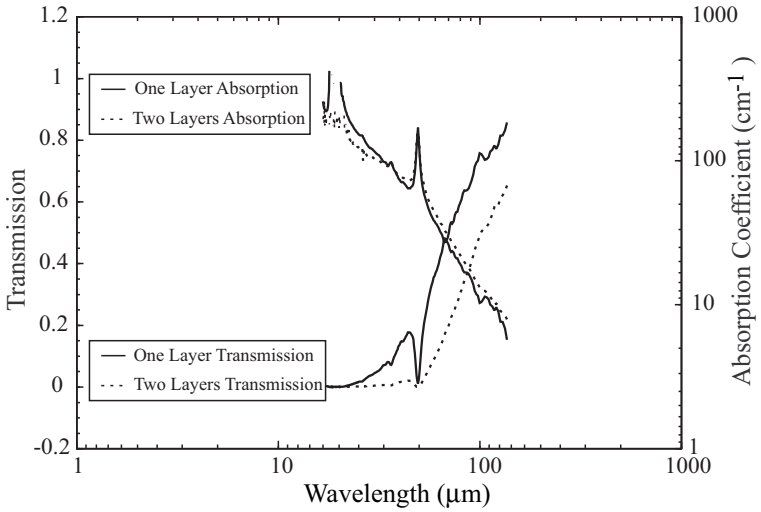

Figure B.3: Transmission of single and double layers of Zitex in an $f/4$ beam with ~ 7 mm spacing. At mid-IR wavelengths, the Zitex acts as two scattering surfaces; at far-IR wavelengths, like an absorber. Adding 7 mm of space between the layers extends the turn-on to longer wavelength.

temperature on the transmission of Zitex, we measured the transmission of samples of G110 at 300 K and 77 K in the far-infrared near the turn-on region. No significant variation in the transmission was seen upon cooling which is to be expected for dielectric scattering.

B.5 Refractive Index

Measuring the refractive index of a material of low dielectric constant is difficult near 1 THz for a nondispersive FTS. Only the thick sample of G125 could be measured, via a determination of the fringe spacing in the 3.5 mm thick slab. The fringe spacing, averaged between 13 and 45 cm^{-1} (200 – 800 μm or 400 – 1350 GHz), was 1.18 cm^{-1}. This provides a refractive index for Zitex of $n = 1.20 \pm 0.07$ at a temperature of 2 K. This can be compared to Teflon, which has $n = 1.44$ [8]; with a filling factor of ~ 50 %, the expected refractive index is $n = 1.22$, exactly as measured.

B.6 Thermal Conductivity

The thermal conductance of a thick slab of Zitex was measured in the direction along the sheet using an apparatus developed for the purpose of measuring lateral thermal conductance in sheets [11]. At cryogenic temperatures ($T \leq 150$ K), the conductivity of Zitex is found well fit by $K(T) = 0.01\,T^{0.58}$ $\mathrm{W\,K^{-1}m^{-1}}$. This value is half the bulk conductivity of Teflon [12], indicating that the porous nature of Zitex does not substantially affect its thermal conductance beyond the geometric reduction.

However, since Zitex sheets tend to be thin ($\sim$ 0.3 mm), even the small power incident on Zitex when used as a near-infrared blocking filter will raise its temperature by a significant fraction. This suggests the use of two layers for good blocking, whereas one Teflon layer might have been sufficient to handle the optical loading. Since the loss in Zitex at long wavelengths is so low however, the two layer solution is likely to be more efficient than the use of solid Teflon.

Bibliography

[1] J. W. Kooi, M. Chan, B. Bumble, H. G. Leduc, P.L. Schaffer, and T. G. Phillips, "230 and 492 GHz Low-Noise SIS Waveguide Receivers employing tuned Nb/AlO_x/Nb tunnel junctions", *Int. J. IR and MM Waves*, Vol. 16, No. 12, pp. 2049-2068, Dec. (1995).

[2] T. R. Hunter, D. J. Benford, and E. Serabyn, "Optical Design of the Submillimeter High Angular Resolution Camera (SHARC)", *PASP*, Vol. 108, p. 1042 (1996).

[3] D. J. Benford, J. W. Kooi, and E. Serabyn, "Spectroscopic Measurements of Optical Components Around 1 Terahertz", *Proc. 9^{th} Int. Symp. on Space Terahertz Technology*, p. 405 (1998).

[4] J. W. Lamb, "Miscellaneous Data on Materials for Millimetre and Submillimetre Optics"," *Int. J. IR MM Waves*, Vol. 17, no. 12, pp. 1997–2034 (1996).

[5] D. J. benford, M. C. Gaidis, and J. W. Kooi, "Transmission Properties of ZITEX in IR-Submm", *Proc. 10^{th} Int. Symp. Space Terahertz Technology*, (1999), pp. 402ff.

[6] Norton Performance Plastics, Wayne, New Jersey. (201) 696-4700.

[7] S. Sato, S. Hayakawa, T., Matsumoto, H. Matsuo, H. Murakami, K. Sakai, A. E. Lange and P. L. Richards, "Submillimeter wave low pass filters made of glass beads", *Applied Optics*, Vol. 28, no. 20, p. 4478 (1989).

[8] J. Kawamura, S. Paine, and D. C. Papa, "Spectroscopic Measurements of Optical elements for Submillimeter Receivers", *Proc. 7^{th} Int. Symp. on Space Terahertz Technology*, pp. 349 (1996).

[9] J. R. Birch, "The Far-Infrared Optical Constants of Polypropylene, PTFE, and Polystrene", *Infrared Phys.*, Vol. 6, no. 1, pp. 33–38 (1992).

[10] F. Bréhat and B. Wyncke, "Measurements of the Optical Constants of Crystal Quartz at 10K and 300K in the Far Infrared Spectral Range: 10-600 cm^{-1}"," *Int. J. IR MM Waves*, Vol. 18, no. 9, pp. 1663–1679 (1997).

[11] D. J. Benford, T. J. Powers, and S. H. Moseley, "Thermal Conductivity of Kapton Tape", *Cryogenics*, Vol. 39, no. 1, pp. 93–95 (1999).

[12] G. E. Childs, L. J. Ericks, and R. L. Powell, "Thermal Conductivity of Solids at Room Temperature and Below", *NIST-NBS Monograph* #131, (1973).

Appendix C

AR coated HDPE windows*

C.1 Introduction

Pressure windows, infrared blocking filters, and lenses are by definition made of dielectric materials with refractive indexes > 1 (vacuum). Aside from absorption loss (Sec. 4.2.2), dielectric materials used in the above described manner also suffer from reflection loss at the interface to free space. Before addressing this issue, it is instructive to look at a dielectric slab from an optical engineering perspective. As was seen in Sec. 10.3.2, the fractional transmitted power in a cavity (voltage standing wave inside the dielectric slab) can be described by an Airy function

$$A_i(\nu) = \frac{1}{1 + F sin^2(\frac{\delta}{2})} \ , \quad \delta = \frac{4\pi n d}{\lambda_0} \ . \tag{C.1}$$

n is the refractive index of the material, d the thickness of the dielectric slab, λ_0 the free space wavelength, and F the finesse

$$F = \frac{4|r|^2}{(1 - |r|^2)^2} \ . \tag{C.2}$$

For normal incidence, r the magnitude of the reflection is polarization independent and may be obtained from

$$\mid r_\perp \mid = \frac{n-1}{n+1}, \quad n = \sqrt{\varepsilon_r} \ . \tag{C.3}$$

The Airy function has a maximum value (no internal reflection) for $\delta = 0,\ 2\pi,\ 4\pi, \cdots$, and a minimum for $\delta = \pi,\ 3\pi, \cdots$.

Traditionally z-cut quartz is used for vacuum windows, and infrared-blocking filters, because of its high transparency in the submillimeter, relatively low dielectric

*A subsection of the material described in this Appendix has been published in the following paper: D. J. Benford, J. W. Kooi, and E. Serabyn, *Proc. 9^{th} Int. Symp. on Space Terahertz Technology*, p. 405 (1998).

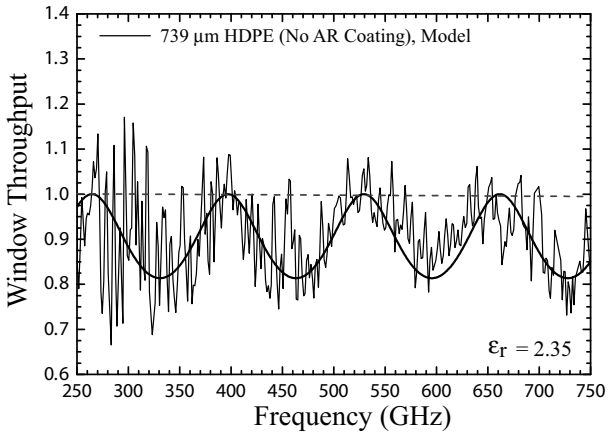

Figure C.1: Measured and modeled transmission of a 739 μm thick high-density polyethylene (HDPE) pressure window. From a fit against the model we obtain a dielectric constant $\varepsilon_r = 2.35$. The increase in noise below 350 GHz is due to the decrease in the FTS bolometer responsivity.

constant (ε_r=3.8), and opaqueness to helium and other gasses. However, the refractive index is high enough to cause substantial reflections loss. As an example, we find for quartz a maximum constructive interference amplitude (1-Ai_{quartz}) of 0.3403. This corresponds to a 34 % voltage reflection loss, which in power corresponds to a worst case scenario loss of 11.56 %. Of course this is only at one frequency, with the mean reflected power obtained from $r_\perp^2 \sim 10$ %.

To minimize reflection loss, antireflection coating of the dielectric slab's surface is frequently utilized. In the case of quartz, only Teflon has the ideal dielectric constant and required low loss tangent for appropriate antireflection material. Unfortunately, adhesion of Teflon to quartz is very difficult and therefore costly. This is especially so in the submillimeter where a quarter-wave antireflection coating requires substantial thickness. Other materials such as silicon ($\varepsilon_r = 11.8$) with as antireflection coating Parylene-c [1] have been investigated. However the dielectric constant of Parylene-c ($\varepsilon_r = 2.62$) and material absorption loss are not ideal, vacuum deposition is specialized, and signal bandwidth due to the high dielectric constant of silicon (Eq. C.1) limited. For this reason antireflection coated silicon windows/infrared blocks have seen limited application in the submillimeter frequency regime.

An interesting alternative to quartz is high-density polyethylene (HDPE). This material is used by many research groups to make lenses, infrared-blocking filters, and vacuum pressure windows. HDPE has good transmission well into the far infrared, good to excellent blockage of helium and other atmospheric gasses, and a low dielectric loss tangent (Eq. 4.84). To obtain the dielectric constant of HDPE we measured the transmission of a 739 μm thick slab on a Fourier transform Spectrometer (FTS). The result is shown in Fig. C.1.

Fitting our model to the measurement we derive a dielectric constant (ε_r) of 2.35. Given the thickness of the sample, we calculate (Eq. C.1) a signal (amplitude) transmission of 0.8415. This is in good agreement with the measurement.

C.2 Antireflection coating

Antireflection (AR) coating of the surface is generally best understood from an electrical circuit analysis point of view. Similar to Eq. 4.54, we can describe the input impedance of a general transmission line as

$$Z_s = Z_0 \frac{Z_l + iZ_0 tan(\beta l)}{Z_0 + iZ_l tan(\beta l)} = \frac{Z_l cos(\beta l) + iZ_0 sin(\beta l)}{Z_0 cos(\beta l) + iZ_l sin(\beta l)} \ . \tag{C.4}$$

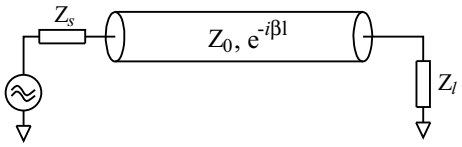

Figure C.2: General transmission line model of Eq. C.4.

β is the propagation constant $= 2\pi/\lambda$, Z_l the load impedance at the end of the transmission line (Z_{slab}), Z_s the input impedance of the transmission line which ideally equals the free space impedance $\eta_0 = 377\ \Omega$ for minimum reflection, Z_0 is the impedance of the intermediate (antireflection) dielectric layer, and βl the electrical length. For $\beta l = \pi/2$ (or multiple thereof),

$$Z_s = \frac{Z_0^2}{Z_l} \quad \rightarrow \quad \eta_0 = \frac{Z_0^2}{Z_{slab}} \ , \tag{C.5}$$

so that $Z_0 = \sqrt{\eta_0 Z_{slab}}$. The relative dielectric slab impedance normalized to the free space impedance is $Z_{slab}/\eta_0 = 1/\varepsilon_r$. And thus we see that Z_0, the antireflection layer impedance, relative to the dielectric slab equals $Z_{slab}/Z_0 = \sqrt{\varepsilon_r}$. A quarter wavelength in the AR layer material is obtained for $d_{AR} = \lambda_0/4\sqrt{n}$, $n = \sqrt{\varepsilon_r}$.

In Fig. C.3 we show a measurement and simulation of a 230 GHz Teflon AR coated quartz window (2.5 mm thick). The internal reflections (Fabry-Perot pattern) perfectly cancel at 230 GHz. At the edges of the band (180 GHz & 280 GHz), the voltage reflection loss has degraded $\sim$ 8–10 % (1 % in power).

C.3 Multi-layer antireflection coating

To model (multi-layer) antireflection coatings, it is most convenient to express the transmission line with impedance Z_0 and electrical length γl as an ABCD matrix. γ is the complex propagation constant $\alpha + i\beta$ as in Eq. 4.77. In this way any number of layers can be build up by cascading the ABCD matrixes, similar to what is shown in Fig. C.4. The ABCD matrix of a transmission line can be described as a 2-port:

$$\begin{bmatrix} A & B \\ C & D \end{bmatrix} = \begin{bmatrix} cosh(\gamma l) & Z_0 sinh(\gamma l) \\ Y_0 sinh(\gamma l) & cosh(\gamma l) \end{bmatrix} \ . \tag{C.6}$$

Cascading yields,

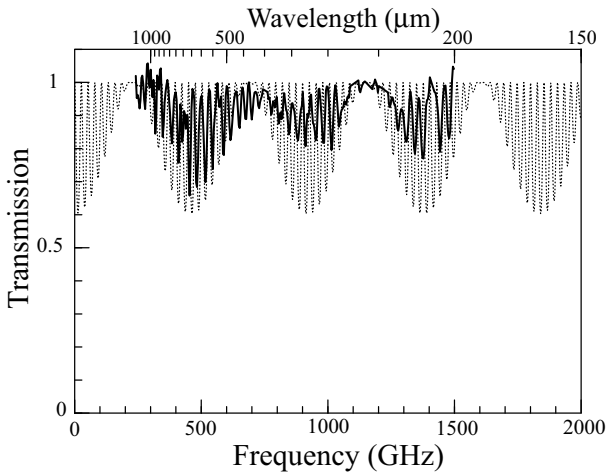

Figure C.3: Transmission of an antireflection coated quartz window designed for the 230 GHz region.

$$\begin{bmatrix} V_1 \\ I_1 \end{bmatrix} = \begin{bmatrix} A_1 & B_1 \\ C_1 & D_1 \end{bmatrix} \begin{bmatrix} A_2 & B_2 \\ C_2 & D_2 \end{bmatrix} \begin{bmatrix} A_3 & B_3 \\ C_3 & D_3 \end{bmatrix} \begin{bmatrix} V_2 \\ I_2 \end{bmatrix} . \tag{C.7}$$

Multiplying the individual matrixes yields the overall ABCD matrix. The equivalent two-port S-parameter matrix can then be calculated [2]

$$\begin{bmatrix} S11 & S12 \\ S21 & S22 \end{bmatrix} = \begin{bmatrix} \frac{A+B/Zs-CZ_s-D}{A+B/Zs+CZ_s+D} & \frac{2(AD-BC)}{A+B/Zs+CZ_s+D} \\ \frac{2}{A+B/Zs+CZ_s+D} & \frac{-A+B/Zs-CZ_s+D}{A+B/Zs+CZ_s+D} \end{bmatrix} . \tag{C.8}$$

The matrix will be reciprocal (no non-linear elements) so that $S11 = S22$ and $S12 = S21$. In this case $S11$ represents the input return loss (reflected power equals $20\log_{10}$[S11]) and S21 the forward transmission (power transmission = $20\log_{10}$[S21]).

To investigate the use of low cost infrared blocks and vacuum windows we have [3] antireflection coated HDPE with Zitex. Zitex, being 50 % porous Teflon has a melting point of $\sim$ 327 °C, significantly higher that that of HDPE (130–137 °C). Using a thin (25–50 μm) layer of low-density polyethylene (LDPE) [4] with a melting point $\sim$ 10 °C

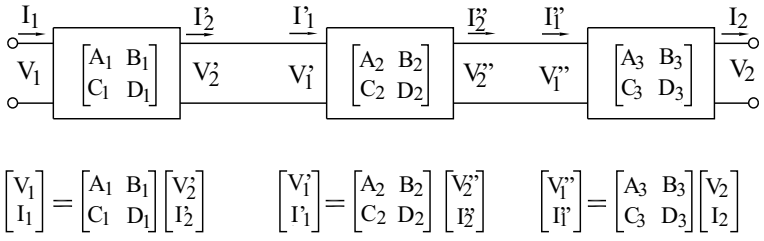

Figure C.4: Antireflection layers and dielectric slab modeled as a series of cascaded ABCD matrixes.

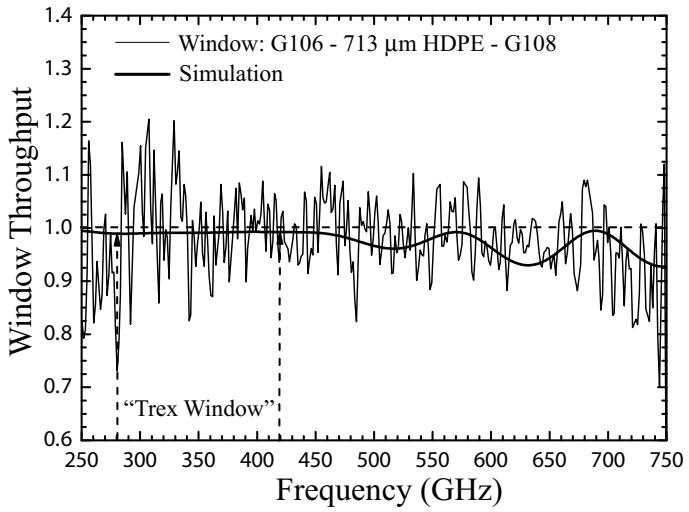

Figure C.5: Measured and modeled 713 μm HDPE window with G106 and G108 Zitex AR coating. This window is presently used on the "Technology Development Receiver" of Chap. 7. The expected reflection loss is on the order of 2 % ($\sim$ 6 K). Careful leak checks of the cryostat revealed no noticeable permeability to helium.

below that of HDPE as a glue, we have under pressure (1/4 ton) and heat (125 ° C) successfully fused a "sandwich" of Zitex-LDPE-HDPE-LDPE-Zitex.

To maximize the RF bandwidth while minimizing reflection, it was found through computer simulations [5] that the use of Zitex with different sheet thickness on either side of the HDPE window is preferred. In Fig. C.5 we show the measured and simulated response of a vacuum window made of 713 μm high-density polyethylene (HDPE), antireflection coated with a single layer (150 μm) G106 Zitex on one side, and a single layer (200 μm) G108 on the other side. The pressure window was designed to cover the 280 – 420 GHz technology receiver passband of Chap. 7. The calculated transmission is better than 98 % between 280 GHz – 420 GHz, with an input return loss $<$ -20 dB. As is evident from the FTS measurement, the method works very well with the benefit of having essentially no cost associated with it!

As a final note, ALMA [6] has developed excellent five-layer quartz vacuum windows (Zitex-HDPE-quartz-HDPE-Zitex), albeit at a significant complexity and cost. The performance of the described Zitex-LDPE-HDPE-LDPE-Zitex "sandwich" is very competitive with these excellent multi-layer windows. Because the thinnest sheet of Zitex is 100 μm (G104), the application of the Zitex-LDPE-HDPE-LDPE-Zitex technique is limited to $\sim$ 750 GHz. Above this frequency range, HDPE with antireflection grooves [7], quartz windows with suitable AR coated (Teflon), or possibly Parylene coated silicon windows will need to be utilized.

Bibliography

[1] A. J. Gatesman, J. Waldman, M. Ji, C. Musante, and S. Yagvesson, "An antireflection coating for silicon optics at terahertz frequencies", *IEEE Microwave and Wireless Components Letters*, Vol. 10, no. 7, Jul. (2000).

[2] D. M. Pozar, "*Microwave Engineering*", John Wiley & Sons, Inc., 3rd Edition, (2005).

[3] Tasos Vayonakis, private communication.

[4] Carlisle Plastics Company, Inc., 320 South Ohio Avenue, New Carlisle, OH 45344, USA.

[5] Microwave Office, Applied Wave Research Inc. El Segundo, CA 90245, USA.

[6] D. Koller, A. R. Kerr, and G. A. Ediss, "Proposed Quartz Vacuum Window Designs for ALAM bands 3 - 10", NRAO, Charlottesville, VA [Online]. Available: http://www.alma.nrao.edu/memos/html-memos/alma397/memo397.pdf

[7] P. F. Goldsmith, *Quasioptical Systems (IEEE)*, New York, (1998), Chap. 5.

Nederlandse Samenvatting

Waarnemingen in het verre infrarood

Moderne sterrenkunde begon met Galileo Galilei in 1610, toen hij de in 1608 uitgevonden "Hollandschen Kijcker" van de in Middelburg woonachtige Nederlander Hans Lipperhey nabouwde ($\sim 20\times$ vergroting), en voor het eerst waarnemingen deed van de maan, Jupiter, de sterren als ook van de Orion nevel en de Pleiaden (de zeven zusters). Zo ontdekte hij de meest prominente manen van Jupiter; IO, Europa, Ganymede, en Callisto, en publiceerde hij de resultaten van zijn onderzoek in een boekje van 60 bladzijden; de "Sidereus Nuncius" ("Boodschapper van de sterren"). Door het succes van zijn waarnemingen wordt Galileo in 1615 streng gewaarschuwd niet het model van Copernicus (planeten draaien om een centrale zon) te propageren.

Sinds die tijd is het duidelijk geworden dat planeten systemen zoals de onze hun onstaan ontleden uit de nucleaire synthese van protosterren, en dat de meeste elektromagnetische energie, of te wel fotonen, zich in het verre infrarood bevindt. Voor het laatste zijn twee redenen: Het uitdijende heelal en het feit dat het heelal globaal gesproken koud is. In alle richtingen waar we ook kijken is er een gloed van ~ 3 K boven het absolute nul punt. Dit was voor het eerst ontdekt in 1965 door Arno Penzias en Robert Wilson (Nobel prijs 1978), indertijd bij Bell Labs. Inmiddels weten we door o.a. de COBE [1] en WMAP [2] satellieten, dat de kosmische achtergrond straling een temperatuur heeft van 2.725 ± 0.002 K. De tweede reden dat het koud is in het heelal heeft te maken met de grote en vrijwel lege ruimte tussen de sterren. Dit is ook de reden dat het 's nachts donker is in plaats van licht (de Olbers Paradox). Toch bevat ons melkweg stelsel grote hoeveelheden microscopische interstellaire stof ("rook"), en moleculaire gas wolken.

Hoe nu precies de nucleaire synthese in protosterren tot stand komt in het interstellair medium (ISM) is het studie gebied van de astrofysicus en astrochemicus. Zij vinden bijvoorbeeld dat sterren en planeten systemen geboren worden in enorme grote en koude moleculaire wolken die door de zwaartekracht en schok lokaal samen worden geperst. Normaal zal druk verhoging leiden tot een temperatuur verhoging, en dus een tegen druk. Echter door fotonen (kwanta deeltjes van licht) uit te stralen in het verre infrarood, zijn de grote moleculaire wolken in staat thermische energie te verliezen, en dus een dichtheid te bereiken waar protostellaire formatie plaats kan vinden. Dit proces is alleen waarneembaar in het verre infrarood, ook wel bekend als het submillimeter gebied, met een golflengte van $0.1 - 1$ mm. Dit komt omdat in het visuele en het nabije infrarode gedeelte van het elektromagnetische spectrum

Figure S.1: Grote wolken van kosmisch "stof" en moleculair gas zijn de geboorte plaats van protosterren en zonnen systemen, in dit geval in de Arend (Eagle) nebula. Foto credit: IAC, Daniel Lopez.

microscopische stof deeltjes het licht verstooien. Door nu de atomische en moleculaire rotatie lijnen van atomen en moleculen te bestuderen, zoals bijvoorbeeld C^+, N^+, C^0, CO, H_2O, HCN, HDO ... krijgen we een idee wat er gebeurt in het interstellaire medium (ISM).

Maar er is meer. Ook sterren stelsels buiten ons melkweg stelsel hebben stof en moleculair gas waaruit de miljarden en miljarden sterren ontstaan. Dus het bestuderen van ons melkweg stelsel geeft een beeld van hoe de natuur- en scheikundige processen er ook daar aan toegaan, en mogelijk ook hoe sterren stelsels tot stand komen.

In het algemeen gesproken kan interstellaire "stof" worden waargenomen met lage spectrale resolutie cameras. Dit geeft een goed idee waar de sterren vormen, maar geeft geen informatie over de complexe chemische interacties in het ISM en de net geboren jonge sterren (YSO). Voor dit is een veel hogere spectrale resolutie nodig.

De heterodyne ontvangers omschreven in dit proefschrift maken dit soort waarnemingen mogelijk. Ze opereren op het temperatuur niveau van vloeibaar helium (4.2 K, Heike Kamerlingh Onnes, 1908), en zijn gebaseerd op het feit dat een elektron in staat is door een microscopisch dunne grenslaag te tunnelen als die een kwanta van licht met genoeg energie ontvangt (foton). De reden voor deze complexiteit is dat fotonen in het verre infrarood weinig energie hebben ($E = h\nu$). h is Planck's constante

(6.626×10^{-34} J·s) en ν de frequentie. Met de heterodyne ontvangers omschreven in dit proefschrift, kunnen we niet alleen het interstellaire medium in ons eigen melkweg stelsel, maar ook in andere sterren stelsels waarnemen. Verder is het ook mogelijk om de atmosfeer van planeten en kometen in ons eigen zonnestelsel te bestuderen. Het waarnemen van water en zuurstof kan echter alleen vanuit de ruimte plaatsvinden daar de atmosfeer van de Aarde dit belemmert (Fig. 2.8) [3, 4, 5]. Door moleculen zoals CO, CO_2 H_2O ... waar te nemen leren we een heleboel over de atmosfeer van een andere planeet, de verticale wind snelheden, en de temperatuur verdeling. Hoogst relevant zijn ook waarnemingen in onze eigen atmosfeer van Ozon (O_3), ClO, de hydroxil OH, en broeikas gassen (CO, CH_4, NO). Bijvoorbeeld, methaan (CH_4), O_2 en O_3 komen in onze atmosfeer voor omdat er biologisch leven is op Aarde.

Een andere, ook erg belangrijke factor is de H/D ratio van ons zonnesysteem. Dit is de ratio van de waterstof en deuterium. Het kan worden aangenomen dat deze ratio het zelfde is voor alle planeten en kometen in ons zonnesysteem omdat allen tegelijkertijd zijn ontstaan, zo'n 4.5 miljard jaar geleden. Door nu de isotopen ratio van HDO en $^{18}H_2O$, $^{17}H_2O$ te meten in kometen en in de atmosfeer van planeten kan de heden ten dagen H/D worden vast gesteld, hetgeen weer informatie verleent over de atmosferische evolutie. Ook voor dit soort metingen zijn hoge spectrale resolutie heterodyne ontvangers zoals omschreven in dit proefschrift nodig. En ook HIFI [6] aan boord van het ruimtelijke observatorium Herschel [7] zal binnenkort de technologie uiteengelegd in dit proefschrift gebruiken voor o.a. dit soort waarnemingen.

Uitleg van het proefschrift

Moderne astrofysica vraagt om hoge spectrale mogelijkheden, frequentie flexibiliteit, gevoeligheid, bandbreedte, stabiliteit, en gebruikers gemak. Om deze daadwerkelijk te maken onderzoekt dit proefschrift geavanceerde heterodyne technieken in het submillimeter en verre infrarood gedeelte van het elektromagnetische spectrum.

Het proefschrift begint met een introductie van het submillimeter en verre infrarood vak gebied. In hoofdstuk 2 worden de wetenschappelijke en operationele eisen uiteen gelegd zoals o.a. beschreven in de vorige sectie. Niet alleen gevoeligheid, maar ook factoren zoals frequentie resolutie, de stabiliteit van het instrument, kalibratie, en bandbreedte bepalen wat soort detector het meest geschikt is voor een gegeven wetenschappelijke onderzoek.

In hoofdstuk 3 worden verschillende ontvanger structuren uiteen gelegd. Dit is nodig om de voor en nadelen af te kunnen wegen. Hoofdstuk 4 omschrijft de theorie van SIS en HEB mengtrappen (mixers). Een nieuwe soort supergeleidende-isolator-supergeleidende (SIS) AlN grenslaag structuur wordt geïntroduceerd in het eerste gedeelte van hoofdstuk 4. In het tweede gedeelte wordt de aandacht gericht op de hete elektronen bolometer (HEB) mengtrap. We gebruiken test resultaten van het HIFI instrument [6], en bestuderen technisch problematiek zoals elektrothermische terugkoppeling en het "direct detectie" fenomeen. In hoofdstuk 5 introduceren we de eerste AlN grenslaag SIS heterodyne ontvanger. Door het succes van deze hoog frequent ontvanger is de technologie overgenomen in HIFI mengtrap banden 3 & 4.

Dan in hoofdstuk 6 richten we de aandacht op het gelimiteerde midden frequentie (MF) bereik van de HEB mengtrap. Omdat een HEB mengtrap werkt op het principe

van elektronen en fononen interactie, en bijbehorende tijd constanten, is de elektronen relaxatie tijd relatief langzaam. Dit duidt zich in een vrij kleine MF bandbreedte, die wetenschappelijke waarnemingen met een gelimiteerde snelheids resolutie te gevolgen heeft.

Hoofdstuk 7 beschrijft "Trex", een geavanceerde heterodyne ontvanger die geinstaleerd is bij het Submillimeter Observatorium van Caltech, gelegen op Mauna Kea, een vulkanische berg van 4.2 km hoogte in Hawaii. Deze ontvanger maakt gebuikt van de in hoofdstuk 4 afgeleide theorie. De ontvanger is net zoals de ontvanger in hoofdstuk 5 te gebruiken door wetenschappers over de gehele wereld.

Hoofdstuk 8 concentreert zich op de theorie, en de implementatie van drie soort ontvangers: De "gebalanceerde" of te wel balanced ontvanger, de "correlatie" ontvanger, en een ontvanger die de boven en onder zijbanden splitst (sideband separating receiver). Alle drie ontvangers zijn uniek. De laatste is ontwikkeld voor ALMA band 9 (600 – 720 GHz), en is de meest geavanceerde mixer in dit frequentie gebied tot nu toe.

Hoofdstuk 9 gaat in op de ontwikkeling van meerdere beeldpunt (multiple pixel) heterodyne ontvangers. De bijdrage aan SuperCam, een 64 beeldpunt hoge spectrale resolutie ontvanger voor het in kaart brengen van $^{12}\mathrm{CO}_{J=3\rightarrow2}$ en $^{13}\mathrm{CO}_{J=3\rightarrow2}$ (330 en 345 GHz) in ons melkweg stelsel, wordt beschreven. Tevens is er ook onderzoek naar meerdere beeldpunt ontvangers voor het verre infrarood gebied. Dit soort ontvangers is zeer aantrekkelijk, maar technisch moeilijk uitvoerbaar. Door de hoge waarnemings efficiency, bijvoorbeeld van grote objecten aan de hemel (koude wolken in het interstellair medium) zijn dit soort geavanceerde ontvangers erg belangrijk. Ook kan met deze categorie ontvangers eventuele atmosferische turbulentie verwijderd worden door correlatie tussen de verschillende beeldpunten. Dit principe wordt momenteel grootschalig toegepast op bolometric cameras, die soortgelijk staan aan CCD in het visuele en nabije infrarood.

Uiteindelijk wordt in hoofdstuk 10, de stabiliteit van de HEB mengtrappen onder de loep genomen, en factoren onderzocht die leiden tot instabiliteit. Zoals vermeld in hoofdstuk 2, stabiliteit van het instrument is erg belangrijk voor de kwaliteit, efficiency, en de kalibratie nauwkeurigheid van de waarneming.

Bibliography

[1] [Online]. Available: http://lambda.gsfc.nasa.gov/product/cobe/

[2] [Online]. Available: http://map.gsfc.nasa.gov/

[3] [Online]. Available: http://sunland.gsfc.nasa.gov/smex/swas/

[4] [Online]. Available: http://www.ssc.se/?id=7180/

[5] [Online]. Available: http://www.sci.esa.int/iso/

[6] Th. de Graauw, N. Whyborn, E. Caux, T. G. Phillips, J. Stutzki, X. Tielens, R. Güsten, F. P. Helmich, W. Luinge, J. Pearson, P. Roelfsema, R. Schieder, K. Wildeman, and K. Wavelbakker, "The Herschel-Heterodyne Instrument for the Far-Infrared (HIFI)", [Online]. Available: herschel.esac.esa.int/Publ/2006/SPIE2006_HIFI_paper.pdf

[7] [Online]. Available: http://sci.esa.int/

Acknowledgements

After many years of research, and a lot of work, this thesis is finished. Of course the story does not end here. The development of submillimeter and terahertz coherent detection technology will continue; for astronomical, Earth science, commercial, and military applications. But for now the time has come to thank the many people, colleagues, collaborators, and family members with whom I have had the pleasure to interface over the many years.

First I like to thank my promotores, Wolfgang Wild and Teun Klapwijk for their guidance and support. Wolfgang, thank you very much for the informative discussions on observation techniques, the rigorous proof reading of this thesis, and the joint proposal work on the ALMA Band 9 sideband separating mixer of Chapter 8. Teun I like to thank you for the many stimulating discussions on a wide range of physics topics, some of which have actually made it into this thesis. Thank you also for the time you have taken to proof read this thesis, and the many useful suggestions. I also like to take the opportunity to thank the reading committee members; Thijs de Graauw, Reynier Peletier, and Victor Belitsky for their part in this thesis.

Next up I like to thank Prof. Tom Phillips for providing the environment for successful research. It is certainly true that this work would not have been possible without the countless trips to the CSO (HI). I also like to acknowledge Prof. Zmuidzinas of Caltech for his physical insight and discussions on the many issues raised in this thesis.

Then I thank Prof. Chris Walker of the University of Arizona, with whom I have had many dealings during the past 18 years. Our collaboration has taken us to many places, even as remote and far away as the South Pole. The discussion of focal plane array technology in Chapter 9 would certainly not have been possible without the many fruitful late night discussions and e-mails.

I also like to acknowledge Prof. Rudolf Schieder and colleagues of the University of Köln. Your visit to Caltech in 1998 was instrumental in providing an understanding of the fundamental sources of gain instability in heterodyne receivers. This work eventually led to the stability characterization of the HIFI instrument at SRON in 2007, and the timely discovery of a number of system related stability problems. Left unattended, they would have significantly impaired the capabilities of the HIFI instrument on board the soon to be launched Herschel space observatory.

There are also the numerous persons and colleagues with whom I have had dealings with over the years. In the humble realization that I cannot possibly name everyone,

I shall make an attempt anyhow. First I like to thank my colleagues at JPL; John Pearson, Goutam Chattopadhyay, and John Ward for the productive friendship, and the many stimulating discussions we have had over the years. I also like to thank Rick LeDuc, Bruce Bumble, and Jeffrey Stern for their input in SIS junction fabrication, and the excellent devices produced over the years.

Next up I take the opportunity to thank Prof. Arthur Lichtenberger and his group at the University of Virginia for his skill and dedication in making SIS junctions on SOI substrates for the SuperCam array, and Jian–Rong Gao at the Delft University of Technology for his help and patient support in the research area of increasing the IF bandwidth of hot electron bolometer mixers.

A bit closer to home, the author thanks Chip Sumner and Dave Miller of Caltech for their tremendous help with the AlN-barrier SIS receivers of Chapters 7 and 8, and Tasos Vayonakis and Mick Edgar for general advice on a wide range of topics. And then there is the HILO based staff of the Caltech Submillimeter Observatory, Hawaii. Thanks to you all for putting up with me for so many years.

On the LNA front, I like to recognize the very valuable input from Prof. Sander Weinreb and Hamdi Mani at Caltech, and Niklas Wadefalk, Piotr Starski at the Chalmers University of Technology, Sweden. Sergey Cherednichenko and Erik Kollberg, also at Chalmers, thank you too for your help with all the HIFI HEB mixer work. Prof. Yngvesson of the University of Massachusetts thank you for all your feedback and the productive times we had at the South Pole. You see where it led.

Stafford Withington and Richard Hills at the Cavendish Laboratory, University of Cambridge, UK, thank you as well for your help with the initial development of the radial waveguide probe transition and the many instrumental discussions over the years. The same holds true for Ghassan Yassin at Oxford University, UK.

At SRON, the Netherlands, I acknowledge the generous help and electronics insight of Hans Golstein, as well as that of Ronald Hesper for the many technical discussions on material properties, the use of the FTS, and the late night "Groene Weide" dinners. And then there is Andrey Baryshev, always an interesting source of stimulating discussion and help around the lab. Thanks Andrey for all the blah! Thanks too to Jochem Baselmans, for all the excitement in the HEB lab, and help on Chapter 10 of this thesis. Good luck with your KIDs. Pourya Khosropanah thank you for many practical discussions on taming the little HEB monsters.

Thank you too Prof. Patricio Mena, now at the astronomical instrumentation group of the Universidad de Chile, for a very productive working relationship on the ALMA Band 9 sideband separating receiver. May this continue.

Then on the HIFI front, I like to acknowledge Pieter Dieleman for his support in measuring the HEB IF impedance, and his willingness to let me use the HIFI wideband spectrometer for non-HIFI purposes. Gert deLange, thank you for allowing me to play a role in mixer bands 3 and 4. Thank you too for the positive interactions over the years. As you can see, some of the discussions have been implemented in Chapters 7 & 8. Willem Jellema, thank you for all your diligent work on "fixing" the HIFI instability problems, and the many useful optical engineering discussions, some of which have made it to the CSO (cover).

On the integrated receiver front, I like to thank Prof. Valery Koshelets of the

Russian academy of Science for a very productive collaboration and friendship, and giving me an opportunity to work on some IF design issues. Thank you too to all my colleagues and friends at the Group for Advanced Receiver Development (GARD), Chalmers TU, Sweden. May we continue our fruitful collaboration it the future. And finally, I like to acknowledge Gerard Beaudin, Jean-Michel Krieg, Yan Delorme and colleagues at the Observatoire de Paris for the very fruitful collaboration on HIFI mixer band 1, and the many productive visits and interaction over the years. It has been great!

Lastly, I like to thank my late father Else Kooi, my mother Cornelia Kooi-Liefting, my two brothers Gerard and Frank Kooi, and my sister Marion Kooi, along with their spouses. And last but not least, the time has come to thank my more immediate family – my wife Helen, and my two sons David and Andreas Kooi. Thank you for your love and understanding and helping me make this thesis a reality.

Jacob W. Kooi

Refereed publications

1. "A 275-425 GHz Tunerless Waveguide Receiver Based on AlN SIS Technology", J. W. Kooi, A. Kovács, M. C. Sumner, G. Chattopadhyay, R. Ceria, D. Miller, B. Bumble, R. LeDuc, J. A. Stern, and T. G. Phillips, *IEEE Trans. Microwave Theory and Techniques*, Vol. 55, No. 10, pp. 2086-2096, Oct. (2007).
2. "A 275-425 GHz Tunerless Waveguide Receiver Based on AlN SIS Technology", J. W. Kooi, A. Kovács, M. C. Sumner, G. Chattopadhyay, R. Ceria, D. Miller, B. Bumble, R. LeDuc, J. A. Stern, and T. G. Phillips, *IEEE Trans. Microwave Theory and Techniques*, Vol. 55, No. 10, pp. 2086-2096, Oct. (2007).
3. "IF Impedance and Mixer Gain of NbN Hot-Electron Bolometers", J. W. Kooi, J. J. A. Baselmans, J. R. Gao, T. M. Klapwijk, M. Hajenius, P. Dieleman, A. Baryshev, and G. de Lange, *Journal of Applied Physics*, Vol. 101, 044511, Feb. (2007).
4. "Full characterization and analysis of a terahertz heterodyne receiver based on a NbN hot electron bolometer", M. Hajenius, J. J. A. Baselmans, A. Baryshev, J. R. Gao, T. M. Klapwijk, J. W. Kooi, W. Jellema, and Z. Q. Yang, *Journal of Applied Physics*, Vol. 100, 074507, Oct. (2006).
5. "Stability of Heterodyne Terahertz Receivers", J. W. Kooi, J. J. A. Baselmans, A. Baryshev, R. Schieder, M. Hajenius, J. R. Gao, T. M. Klapwijk, B. Voronov, and G. Gol'tsman, *Journal of Applied Physics*, Vol. 100, 064904, Sep. (2006).
6. "Low-Noise 0.8-0.96 and 0.96-1.12 THz Superconductor-Insulator-Superconductor Mixers for the Herschel Space Observatory", B. D. Jackson, G. de Lange, T. Zijlstra, M. Kroug, J. W. Kooi, J. A. Stern, and T. M. Klapwijk, *IEEE Trans. Microwave Theory and Techniques*, Vol. 54, No. 2, pp. 547-558, Feb., (2006).
7. "NbN Hot Electron Bolometer Mixers: Sensitivity, LO Power, Direct Detection and Stability", J. J. A. Baselmans, M. Hajenius, J. R. Gao, A. Baryshev, J. W. Kooi, T. M. Klapwijk, B. Voronov, P. de Korte, and G. Gol'tsman, *IEEE Tran. Applied Supercon.*, Vol. 15, No. 2, pp. 484-489, Jun., (2005).
8. "A Full-Height Waveguide to Thin-Film Microstrip Transition with Exceptional RF Bandwidth and Coupling Efficiency", J. W. Kooi, G. Chattopadhyay, S. Withington, F. Rice, J. Zmuidzinas, C. K. Walker, and G. Yassin *Int. J. IR and MM Waves*, Vol. 24, No. 3, Sept, (2003).
9. "Deuterium Enhancement in Water toward Orion IRc2 Deduced from HDO Lines above 800 GHz", J. R. Pardo, J. Cernicharo, F. Herpin, J. Kawamura, J. W. Kooi, and T. G. Phillips, *Astrophysical Journal*, 562:799-803, Dec., (2001).
10. "The Antarctic Submillimeter Telescope and Remote Observatory (AST/RO)", Stark, A. A., Bally, J., Balm, S. P., Bania, T. M., Bolatto, A. D., Chamberlin, R. A.,

Engargiola, G., Huang, M., Ingalls, J. G., Jacobs, K., Jackson, J. M., Kooi, J. W., Lane, A. P., Lo, K.-Y., Marks, R. D., Martin, C. L., Mumma, D., Ojha, R., Staguhn, J., Stutzki, J., Walker, C. K., Wilson, R. W., Wright, G. A., Zhang, X., Zimmermann, P., and Zimmermann, *Publications of the Astronomical Society of the Pacific*, 113, pp. 567-585, (2001).

11. "A Low Noise NbTiN-based 850 GHz SIS Receiver for the Caltech Submillimeter Observatory", J. W. Kooi, J. Kawamura, J. Chen, G. Chattopadhyay, J. R. Pardo, J. Zmuidzinas, T. G. Phillips, B. Bumble, J. Stern, and H. G. LeDuc, *Int. J. IR and MM Waves*, Vol. 21, No. 9, Sep., (2000).
12. "Noise Stability of SIS Receivers", J. W. Kooi, G. Chattopadhyay, M. Thielman, T. G. Phillips, and R. Schieder, *Int. J. IR and MM Waves*, Vol. 21, No. 5, May, (2000).
13. "Low-noise Submillimeter-wave NbTiN Superconducting Tunnel Junction Mixers", J. Kawamura, J. Chen, D. Miller, J. W. Kooi, J. Zmuidzinas, B. Bumble, H. G. LeDuc, J. A. and Stern, *Applied Physics Letters*, Vol. 75, 4013-4015, (1999).
14. "Low Loss NbTiN Films for THz SIS Mixer Tuning Circuits", J. W. Kooi, J. A. Stern, G. Chattopadhyay, H. G. LeDuc, B. Bumble, and J. Zuidzinas, *Int. J. IR and MM Waves*, Vol. 19, No. 3, Mar., (1998).
15. "A 850 GHz Waveguide Receiver Employing a Niobium SIS Junction Fabricated on a 1μm Si_3N_4 Membrane", J. W. Kooi, J. Pety, B. Bumble, C. K. Walker, H. G. LeDuc P. L. Schaffer, and T. G. Phillips, *IEEE Trans. Microwave Theory and Techniques*, Vol. 46, No. 2, pp. 151-161, Feb., (1998).
16. "Detection of the $^3P_2$ - $^3P_1$ Submillimeter Transition of 13CI in the Interstellar Medium: Implication for Chemical Fractionation", J. Keene, P. Schilke, J. W. Kooi, D. C. Lis, D. M. Mehringer, and T. G. Phillips. *Astrophysics, astro-ph*/9712071, 4 Dec., (1997).
17. "The Development of an 850 GHz Waveguide Receiver using Tuned SIS Junctions on 1μm Si_3N_4 Membranes", J. W. Kooi, M. S. Chan, M. Bin, B. Bumble, H. G. Leduc, C. K. Walker, and T. G. Phillips, *Int. J. IR and MM Waves*, Vol. 16, No.2, pp. 349-362, Feb., (1995).
18. "230 and 492 GHz Low-Noise SIS Waveguide Receivers Employing Tuned Nb/AlO_x/Nb Tunnel Junctions", J. W. Kooi, M. Chan, B. Bumble, H. G. Leduc, P. L. Schaffer, and T. G. Phillips, *Int. J. IR and MM Waves*, Vol. 16, No. 12, pp. 2049-2068, Dec., (1995).
19. "A Low Noise 665 GHz SIS Quasi-Particle Waveguide Receiver", J. W. Kooi, C. K. Walker, H. G. LeDuc, T. R. Hunter, D. J. Benford, and T. G. Phillips, *Int. J. IR and MM Waves*, Vol. 15, No. 3, 477-492, (1994).
20. "A Low Noise 345 GHz Waveguide Receiver Employing a tuned 0.50 μm^2 Nb/AlO_x/Nb Tunnel Junction", J. W. Kooi , M. Chan, B. Bumble, and T. G. Phillips, *Int. J. IR and MM Waves*, Vol. 15, No. 5, May, (1994).
21. "A Low-noise 500 GHz SIS Waveguide Receiver", C. K. Walker, J. W. Kooi, M. Chan, H. G. Leduc, P. L. Schaffer, J. E. Carlstrom, and T. G. Phillips, *Int. J. IR and MM Waves*, Vol. 13, pp. 785-798, Jun., (1992).
22. "A Low Noise 230 GHz Heterodyne Receiver Employing a 0.25 μm^2 Nb/AlO_x/Nb Tunnel Junction", J. W. Kooi, M. Chan, T. G. Phillips, B. Bumble, and H. G. Leduc, *IEEE Trans. Microwaves Theory and Techniques*, Vol. 40, No. 5, pp. 812-815, May, (1992).

Conference papers

1. "HIFI Stability as Measured During ILT Phase", J. W. Kooi, V. Ossenkopf, M. Olberg, R. Shipman, R, and D. Teyssier, *19th Int. Symp. Space Terahertz Technology*, Apr. 28-30, Groningen, NL, (2008).
2. "Ultra-Thin Silicon Chips for Submillimeter-Wave Applications", R.B. Bass, J. C. Schultz, A. W. Lichtenberger, R. M. Weikle, S.-K. Pan, E. Bryerton, C. K. Walker, J. W. Kooi, *15th International Symposium on Space Terahertz Technology*, Apr. 27-29, pp. 392-399, MA, (2004).
3. "Fabrication and Characterization of Niobium Diffusion-Cooled Hot-Electron Bolometers on Silicon Nitride Membranes", A. M. Datesman, J. C. Schultz, A. W. Lichtenberger, D. Golish, C. K. Walker, and J. W. Kooi, *Applied Superconductivity Conference Jacksonville*, FL, Oct., (2004).
4. "Heterodyne Instrumentation Upgrade at the Caltech Submillimeter Observatory II", J. W. Kooi, A. Kovacs, B. Bumble, G. Chattopadhyay, M. L. Edgar, S. Kaye, R. LeDuc, J. Zmuidzinas, and T. G. Phillips *Proc. SPIE*, 21-25 Jun., Glasgow, Scotland, United Kingdom, (2004).
5. "Stability of HEB receivers at THz frequencies", T. Berg, S. Cherednichenko, V. Drakinskiy, P. Khosropanah, H. Merkel, E. Kollberg, and J. W. Kooi, *Proc. SPIE*, 21-25 Jun., Glasgow, Scotland, United Kingdom, (2004).
6. "Regarding Atmospheric and Mechanical Stability Requirements of (LO-Pumped) Mixers", J. W. Kooi, R. Schieder, J. Baselmans, M. Hajenius, A. Baryshev, R. Hesper, *15th Int. Symp. Space Terahertz Technology*, Apr. 27-29, MA, (2004).
7. "Ultra-Thin SOI Beam Lead Chips for Superconducting Terahertz Circuits", R. B. Bass, A. W. Lichtenberger, R. Weikle, J. W. Kooi, C. K. Walker, S.-K. Pan, *Proc. 6th European Conference on Applied Superconductivity*, Sorento, Italy, Sep. 14, (2003).
8. "Broad Bandwidth Suspended Membrane Waveguide Transition for use in Silicon Micromachined Mixer blocks at THz Frequencies", J. W. Kooi, C. Dröuet d'Aubigny, R. B. Bass, C. Walker, A. W. Lichtenberger, *Proc. 14th Int. Symp. Space Terahertz Technology*, (2003), pp. 127.
9. "Heterodyne Array Development at the University of Arizona", C. Groppi, C. Walker, C. Kulesa, G. Narayanan, K. Jacobs, U. Graf, R. Schieder, and J. W. Kooi, *Proc. 14th Int. Symp. Space Terahertz Technology*, (2003), pp. 189-203.
10. "Beam Lead Fabrication Using Vacuum Planarization", R. B. Bass, J. C. Schultz, A. W. Lichtenberger, C. Walker, and J. W. Kooi, *Proc. 14th Int. Symp. Space THz Technology*, Tucson, AZ, Apr., (2003).

11. "Integrated Heterodyne Array Receivers for Submillimeter Astronomy", Walker, C. K., Groppi, C., Dröuet d'Aubigny, C., Kulesa, C., Hedden, A., Prober, D., Siddiqi, I., Kooi, J. W. , Chen, G., and Lichtenberger, A. W. *Proc. SPIE, Astronomical Telescopes and Instrumentation*, v. 4855, (2002).
12. "Heterodyne Instrumentation Upgrade at the Caltech Submmillimeter Observatory", J. W. Kooi, A. Kovac, S. Kaye, J. Dama, J. Zmuidzinas, and T.G. Phillips *Proc. SPIE*, Kona, Hawaii, Aug., (2002).
13. "Terahertz Initiatives at the Antarctic Submillimeter Telescope and Remote Observatory (AST/RO)", Stark, A. A., Lane, A. P., Martin, C. L., Chamberlin, R. A., Kooi, J. W., and Walker, C. K. *Proc. 13th Int. Symp. Space THz Technology*, Cambridge, MA, 26-28 Mar. (2002), pp. 133-142.
14. "A Broad Bandwidth Suspended Membrane Waveguide to Thinfilm Microstrip Transition", J. W. Kooi, C. K. Walker, and J. Hesler *Proc. 19th Int. Conference on Terahertz Electronics*, Oct., (2001).
15. "PoleSTAR: An 810 GHz Array Receiver for AST/RO", C. K. Walker, C. Groppi, D. Golish, C. Kulesa, A. Hungerford, C. Drouet d'Aubigny, K. Jacobs, U. Graf, C. Martin, and J. W. Kooi, *Proc. 12th Int. Symp. Space THz Technology*, San Diego, CA, (2001), pp. 540-552.
16. "Regarding the IF Output Conductance of SIS Tunnel Junctions and the Integration with Cryogenic InP MMIC Amplifiers", J. W. Kooi, F. Rice, G. Chattopadhyay, S. Sundarum, S. Weinreb and T. G Phillips, *Proc. 10th Int. Symp. Space Terahertz Technology*, University of Virginia, Va, Mar., (1999).
17. "Transmission Properties of ZITEX in IR-Submm", D. J. benford, M. C. Gaidis, J. W. Kooi, *Proc. 10th Int. Symp. Space Terahertz Technology*, (1999), pp. 402ff.
18. "Fabrication and DC-Characterization of NbTiN Based SIS Mixers for use between 600 and 1200 GHz", J. A. Stern, B. Bumble, H. G. Leduc, J. W. Kooi, and J. Zmuidzinas, *Proc. 14th Int. Symp. Space Terahertz Technology*, (1999), pp 305-313.
19. "Heterodyne Instrumentation at the CSO", J. W. Kooi, P. L. Schaffer, B. Bumble, R. LeDuc, and T. G. Phillips *Proc. SPIE*, Kona, Hawaii, Mar., (1998).
20. "Development of SIS mixers for 1 THz", J. Zmuidzinas, J. W. Kooi, J. Kawamura, G. Chattopadhyay, B. Bumble, H. G. LeDuc, and J. A. Stern, *Proc. SPIE*, Vol. 3357, pp. 53-61, (1998).
21. "Spectroscopic Measurements of Optical Components around 1 THz", D. J. benford, J. W. Kooi, and E. Serabyn, *Proc. 9th Int. Symp. Space Terahertz Technology*, Pasadena, California, Mar., (1998).
22. "Fabrication and DC-Characterization of NbTiN Based SIS Mixers for the Use between 600 and 1200 GHz". J. A. Stern, B. Bumble, H. G. LeDuc, J. W. Kooi, J. Zmuidzinas, *Proc. 9th Int. Symp. Space Terahertz Technology*, Pasadena, California, Mar., (1998).
23. "Fabrication and DC-Characterization of NbTiN Based SIS Mixers for Use between 600 and 1200 GHz", J. A. Stern, B. Bumble, H. G. Leduc, J. W. Kooi, and J. Zmuidzinas, *Proc. 10th Int. Symp. Space Terahertz Technology*, (1999), pp. 305-313.
24. "A 665 GHz Waveguide Receiver Using a Tuned 0.5 μm^2 Nb/AlO$_x$/Nb Tunnel Junction", J. W. Kooi, M. S. Chan, H. G. Leduc, and T. G. Phillips, *Proc. 7th Int. Symp. Space Terahertz Technology*, Charlottesville, Va, Mar., (1996).